

**FLUIDS ENGINEERING DIVISION**

Editor  
**J. KATZ (2005)**

Assistant to the Editor  
**L. MURPHY (2005)**

Associate Editors  
**M. J. ANDREWS (2006)**  
**S. BALACHANDAR (2005)**  
**A. BESHOK (2008)**  
**K. S. BREUER (2006)**  
**G. L. CHAHINE (2006)**  
**S. GOGINENI (2006)**  
**A. GOTTO (2007)**  
**F. F. GRINSTEIN (2006)**  
**T. J. HEINDEL (2007)**  
**H. JOHARI (2006)**  
**J. LEE (2006)**  
**Y. T. LEE (2007)**  
**J. A. LIBURDY (2007)**  
**P. LIGRANI (2008)**  
**T. J. O'HERN (2008)**  
**H. PIOMELLI (2007)**  
**S. ROY (2007)**  
**D. SIGINER (2005)**  
**K. D. SQUIRES (2005)**  
**Y. TSUJIMOTO (2006)**  
**S. P. VANKA (2007)**

**PUBLICATIONS DIRECTORATE**  
Chair, **A. G. ERDMAN**

**OFFICERS OF THE ASME**  
President, **H. ARMEN**  
Executive Director, **V. R. CARTER**  
Treasurer, **T. D. PESTORIUS**

**PUBLISHING STAFF**  
Managing Director, Engineering  
**T. G. LOUGHLIN**  
Director, Technical Publishing  
**P. DI VIETRO**  
Production Coordinator  
**A. HEWITT**  
Production Assistant  
**M. ANDINO**

**THE 2004 FREEMAN SCHOLAR LECTURE**

- 189 **Sniffers: Fluid-Dynamic Sampling for Olfactory Trace Detection in Nature and Homeland Security**  
Gary S. Settles

**TECHNICAL PAPERS**

- 219 **Experimental Investigation of the Turbulent Boundary Layer of Surfaces Coated With Marine Antifouling**  
M. Candries and M. Atlas
- 233 **Modeling of Wall Pressure Fluctuations Based on Time Mean Flow Field**  
Yu-Tai Lee, William K. Blake, and Theodore M. Farabee
- 241 **Vortex-Induced Vibration Characteristics of an Elastic Square Cylinder on Fixed Supports**  
Z. J. Wang and Y. Zhou
- 250 **Effects of Wall Roughness on Particle Velocities in a Turbulent Channel Flow**  
Michael Benson, Tomohiko Tanaka, and John K. Eaton
- 257 **Wind-Driven Rivulet Breakoff and Droplet Flows in Microgravity and Terrestrial-Gravity Conditions**  
G. McAlister, R. Ettema, and J. S. Marshall
- 267 **Numerical Study of Cavitation in Cryogenic Fluids**  
Ashvin Hosangadi and Vineet Ahuja
- 282 **Cavitation Properties of Oils Under Dynamic Stressing by Tension**  
P. R. Williams and R. L. Williams
- 290 **Computational Analysis of Pressure and Wake Characteristics of an Aerofoil in Ground Effect**  
Stephen Mahon and Xin Zhang
- 299 **Experimental and Numerical Investigation of the Flow Field in the Tip Region of an Axial Ventilation Fan**  
Xiaocheng Zhu, Wanlai Lin, and Zhaohui Du
- 308 **Periodic Velocity Measurements in a Wide and Large Radius Ratio Automotive Torque Converter at the Pump/Turbine Interface**  
S. O. Kraus, R. Flack, A. Habsieger, G. T. Gillies, and K. Dullenkopf
- 317 **Slip Factor for Centrifugal Impellers Under Single and Two-Phase Flow Conditions**  
José A. Caridad and Frank Kenyery
- 322 **Experimental Analysis on Tip Leakage and Wake Flow in an Axial Flow Fan According to Flow Rates**  
C.-M. Jang, D. Sato, and T. Fukano
- 330 **Hydrodynamic Design of Rotodynamic Pump Impeller for Multiphase Pumping by Combined Approach of Inverse Design and CFD Analysis**  
Shuliang Cao, Guoyi Peng, and Zhiyi Yu
- 339 **Improvements in Fixed-Valve Micropump Performance Through Shape Optimization of Valves**  
Adrian R. Gamboa, Christopher J. Morris, and Fred K. Forster
- 347 **Numerical Simulation and Experimental Measurement of Pressure Pulses Produced by a Pulp Screen Foil Rotor**  
Mei Feng, Jaime Gonzalez, James A. Olson, Carl Ollivier-Gooch, and Robert W. Gooding

(Contents continued on inside back cover)

This journal is printed on acid-free paper, which exceeds the ANSI Z39.48-1992 specification for permanence of paper and library materials. ©™  
♻️ 85% recycled content, including 10% post-consumer fibers.

Transactions of the ASME, Journal of Fluids Engineering (ISSN 0098-2202) is published bimonthly (Jan., Mar., May, July, Sept., Nov.) by The American Society of Mechanical Engineers, Three Park Avenue, New York, NY 10016. Periodicals postage paid at New York, NY and additional mailing offices.

POSTMASTER: Send address changes to Transactions of the ASME, Journal of Fluids Engineering, c/o THE AMERICAN SOCIETY OF MECHANICAL ENGINEERS, 22 Law Drive, Box 2300, Fairfield, NJ 07007-2300.

CHANGES OF ADDRESS must be received at Society headquarters seven weeks before they are to be effective. Please send old label and new address.

STATEMENT from By-Laws. The Society shall not be responsible for statements or opinions advanced in papers or printed in its publications (B7.1, Par. 3).

COPYRIGHT © 2005 by the American Society of Mechanical Engineers. Authorization to photocopy material for internal or personal use under those circumstances not falling within the fair use provisions of the Copyright Act, contact the Copyright Clearance Center (CCC), 222 Rosewood Drive, Danvers, MA 01923, tel: 978-750-8400, www.copyright.com. Request for special permission or bulk copying should be addressed to Reprints/Permission Department, Canadian Goods & Services Tax Registration #126148048.

- 358 Vortex Breakdown in a Differentially Rotating Cylindrical Container  
Teruaki Koide and Hide S. Koyama
- 367 A New Class of Synthetic Jet Actuators—Part I: Design, Fabrication and Bench Top Characterization  
J. L. Gilarranz, L. W. Traub, and O. K. Rediniotis
- 377 A New Class of Synthetic Jet Actuators—Part II: Application to Flow Separation Control  
J. L. Gilarranz, L. W. Traub, and O. K. Rediniotis
- 388 Development of an Experimental Correlation for a Pressure Loss at a Side Orifice  
Ho-Yun Nam, Jong-Man Kim, Kyung-Won Seo, and Seok-Ki Choi

## TECHNICAL BRIEFS

- 393 New Mixing-Length Approach for the Mean Velocity Profile of Turbulent Boundary Layers  
M. H. Buschmann and M. Gad-el-Hak
- 397 Effect of Initial Temperature Profile on Recovery Factor Computations  
B. W. van Oudheusden
- 400 Measurements in the Transition Region of a Turbine Blade Profile Under Compressible Conditions  
E. J. Walsh and M. R. D. Davies

## ERRATUM

- 404 Erratum: "A Simplified Model for Determining Interfacial Position in Convergent Microchannel Flows" [Journal of Fluids Engineering, 2004, 126(5), pp. 758–767]  
T. R. Harris, D. L. Hitt, and N. Macken

The ASME Journal of Fluids Engineering is abstracted and indexed in the following:

*Applied Science & Technology Index, Chemical Abstracts, Chemical Engineering and Biotechnology Abstracts (Electronic equivalent of Process and Chemical Engineering), Civil Engineering Abstracts, Computer & Information Systems Abstracts, Corrosion Abstracts, Current Contents, Ei EncompassLit, Electronics & Communications Abstracts, Engineered Materials Abstracts, Engineering Index, Environmental Engineering Abstracts, Environmental Science and Pollution Management, Excerpta Medica, Fluidex, Index to Scientific Reviews, INSPEC, International Building Services Abstracts, Mechanical & Transportation Engineering Abstracts, Mechanical Engineering Abstracts, METADEX (The electronic equivalent of Metals Abstracts and Alloys Index), Petroleum Abstracts, Process and Chemical Engineering, Referativnyi Zhurnal, Science Citation Index, SciSearch (The electronic equivalent of Science Citation Index), Shock and Vibration Digest, Solid State and Superconductivity Abstracts, Theoretical Chemical Engineering*

# Sniffers: Fluid-Dynamic Sampling for Olfactory Trace Detection in Nature and Homeland Security—The 2004 Freeman Scholar Lecture

**Gary S. Settles**

e-mail: gss2@psu.edu  
Department of Mechanical and Nuclear  
Engineering, Penn State University,  
University Park, PA 16802

*Vertebrates aim their noses at regions of interest and sniff in order to acquire olfactory trace signals that carry information on food, reproduction, kinship, danger, etc. Invertebrates likewise position antennae in the surrounding fluid to acquire such signals. Some of the fluid dynamics of these natural sensing processes has been examined piecemeal, but the overall topic of sniffing is not well investigated or understood. It is, however, important for several human purposes, especially sampling schemes for sensors to detect chemical and biological traces in the environment. After establishing some background, a general appraisal is given of nature's accomplishments in the fluid dynamics of sniffing. Opportunities are found for innovation through biomimicry. Since few artificial ("electronic") noses can currently sniff in the natural sense, ways are considered to help them sniff effectively. Security issues such as explosive trace detection, landmine detection, chemical and biological sniffing, and people sampling are examined. Other sniffing applications including medical diagnosis and leak detection are also considered. Several research opportunities are identified in order to advance this topic of biofluid dynamics. Though written from a fluid dynamics perspective, this review is intended for a broad audience. [DOI: 10.1115/1.1891146]*

## 1 Introduction

Sniffing for chemical traces is as old as nature itself. It dominates the lives of most animal species, relegating touch, hearing, and sometimes even vision to lower status. Animals depend on olfaction for food, reproduction, kin recognition, and danger alert [1]. The first three of these require little sniffing in humans, but recognizing danger is still very important to us in the 21st century.

The study of olfaction is a well-established scientific discipline, but hardly a stagnant one. Zwaardemaker's book on vertebrate olfaction [2] already listed over 200 references in 1895, but at this writing, researchers R. Axel and L. B. Buck have just been awarded the Nobel Prize in Medicine for their research on odorant receptor genetics. Some of the many recent surveys of the field are given in Refs. 1 and 3–6. These authors discuss olfaction from the perspectives of neuroscience, psychology, zoology, chemistry, anatomy, and communication. Few, however, have included the perspective of fluid dynamics.

But fluid dynamics is central to olfaction, and it is therefore surprising that sniffing flows have not attracted much attention to date. Biofluid dynamics has been mainly concerned with the larger themes of blood flow, respiration, and external locomotion flows [7,8], and has left the fluid dynamics of sniffing mostly unexplored.

Hence the time is right to investigate this topic, especially in that—until recently—no technology could begin to emulate the animal nose. Now, however, we have artificial or "electronic" noses [9,10] with substantial and growing capabilities. They need samplers—*sniffers*—of comparable aptitude.

The closely related issue of chemical trace sampling has likewise received little attention. S. F. Hallowell, head of the U.S.

Department of Homeland Security's Transportation Security Lab, said "Chemists have been so fixed on detector development [that] that's exactly what we got: very well-developed detectors that have no front ends. We're going to have to reach out to other disciplines to develop novel sampling systems" [11]. Fluid dynamics is the principal discipline that must fulfill this need.

**1.1 Scope.** This is an unusual Freeman Lecture: Rather than a detailed review of a current fluids topic, it attempts to bring together several diverse fields—some outside the traditional fluids realm—in order to introduce a novel biofluid dynamics topic. Rather than the culmination of a career, it is an attempt to strike out in a new direction.

Of course, not all chemical sensing methods require fluid-dynamic sniffing *per se*. An early distinction is made here between trace and bulk detection, for example. The latter involves non-olfactory methods to sense significant quantities of a target material such as a concealed explosive or other contraband. Also, direct-contact methods like swabbing can acquire trace samples without an overt fluid-dynamic step.

A similar distinction is made between standoff and point detection [12]. Standoff detection requires physical separation between the sensor and the site of interest. In this paper, except for air-scenting and chemical plume tracing, sniffers are considered to be point-detection devices.

The well-developed fields—some broader than others—that bear on the present topic include:

1. Biofluid dynamics [7,8].
2. Animal olfaction, neurophysiology, and evolution.
3. Artificial olfaction, often called the "electronic nose."
4. Airborne particle sampling of the sort used to determine air quality [13]. (In [14] more than 1000 such instruments manufactured by 240 companies were identified.)
5. Inhalation toxicology, where laboratory animals are used to

Contributed by the Fluids Engineering Division for publication in the JOURNAL OF FLUIDS ENGINEERING. Manuscript received by the Fluids Engineering Division, February 10, 2005. Review conducted by J. Katz.

- assess human responses to inhaled pollutants [15,16].
6. Ventilation, especially inlets and hoods for industrial capture and local exhaust of fumes [17–20].
  7. Electronics cooling, where high convective heat transfer occurs in confined spaces [21,22].
  8. Aerobiology [23–25], “the science of the aerial transport of microorganisms...together with their transfer to the air, their deposition, and the ensuing consequences...” C. S. Cox [23].
  9. Analytical chemistry, the science of identifying and quantifying compounds using laboratory instruments, e.g., [26].

**1.2 Goals.** Lighthill, in the introduction to his *Mathematical Biofluidynamics* [7], wrote “The value of seeing any biofluiddynamic problem...against the background of a systematic comparative survey of the biological function in question in many different groups of animals, can hardly be overestimated.” Such a survey of sniffers is the principal aim of this paper. It is intended for a broad audience, including zoologists, biologists, environmentalists, anatomists, and physiologists as well as the fluids community. It also aims to encourage the fluids community to consider olfaction and the olfaction community to include fluid dynamics. The role of sniffers is examined in nature, instruments, and applications, the state-of-the-art is summarized, and future developments are projected. It is, in other words, a fluids engineer’s view of olfaction.

## 2 Fluid Dynamics of Sniffing and Sampling

A brief overview of some pertinent fluid dynamics is given here as a resource for nonfluids-oriented readers. This is no substitute for a basic fluid mechanics course, but it does include some history and a collection of pertinent—if little-known—fluids issues. The breadth of the topic and that of the anticipated audience precludes mathematical rigor in favor of an approach based on physical reasoning, phenomenology, similarity, and scaling.

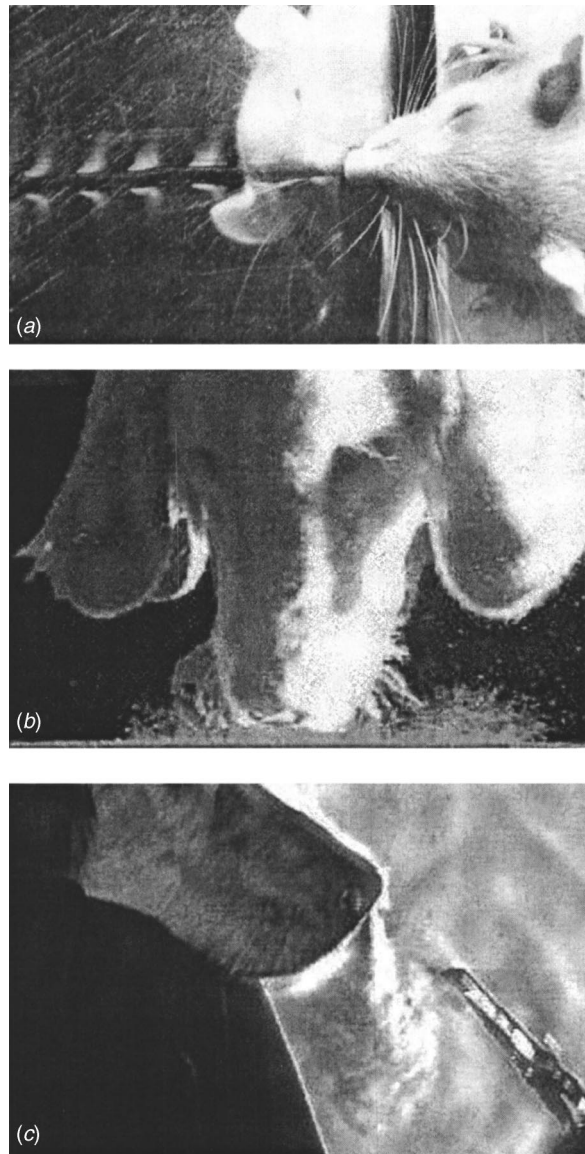
**2.1 Flow Visualization.** As elegantly stated by Kline [27] and Roshko [28], solutions of the equations of fluid motion have limited value without some accompanying phenomenological insight, usually gained from flow visualization [29]. This marriage of fluids, optics, and artistry serves research for purposes of discovery, exploration, illustration, qualitative insight, and nowadays quantitative measurement. Modern flow visualization includes a computational element and benefits from both computer and laser technology.

The visualization of olfactory flows apparently began with Paulsen [30], who placed litmus paper inside the nasal cavity of a human cadaver head and caused the head to “inhale” ammonia. This early surface-flow visualization method revealed elements of the internal airflow pattern. In the same era, Zwaardemaker [2] observed the flow of breath from the human nostril by way of moisture condensation on a cold mirror. This method is still useful in modern times, [31] and Fig. 1(a).

More modern attempts to visualize the airflow in the human nasal cavity used transparent plastic models ranging in scale from 1:1 [32] to 20:1 [33]. Computational fluid dynamics (CFD) simulations, e.g., [16,34], agreed with experiment in that only a fraction of the inspired airflow reaches the olfactory region.

Brueggemann and Jeckstadt also reached that conclusion in 1938 [35] following chemical tracer and dust deposition studies in the nasal cavity of a dog. Dawes [36] used cigarette smoke to visualize the airflow through a thin slice of a dog’s nose between clear plastic plates. Such particle visualization is also important in external airflow studies of chemical plume tracing [37,38] and ventilation exhaust effectiveness [39].

Underwater, Teichmann used dye to study the water flow through the olfactory lamellae of an eel [40]. Similar visualizations of both the antennule flows of crustaceans and the chemical



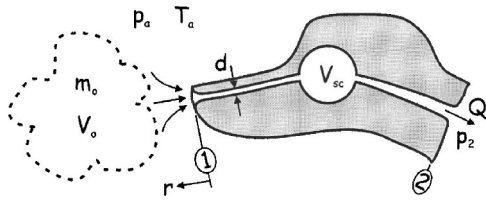
**Fig. 1** Examples of olfactory flow visualization in nature. (a) condensed moisture traces of a rat sniffing on a Zwaardemaker mirror, a form of surface flow visualization, courtesy F. Bojsen-Møller, and (b) tracer particles disturbed by a dog sniffing a horizontal surface, and (c) schlieren image of the exhalation from a dog’s nose [47]

plumes they detect are shown in [41–43]. Invoking fluid-dynamic similarity, human [44,45] and lab-rat nasal flow patterns were examined in water models with dye injection.

In contrast, the optical flow visualization methods (schlieren, shadowgraph, and interferometry [29,46]) were used only once for olfactory research, [47] and Fig. 1(c). This requires special optics but has the advantage of imaging air currents without tracer particles. A National Research Council study recommends Schlieren imaging for the detection of explosive vapor plumes [48].

In summary, there is a wealth of resources on flow visualization [29] that can be used in future olfactory research. Visualization should always be done first; it defines the flow phenomena and sets the stage for more quantitative and detailed measurements. It teaches you the physics of the flow.

**2.2 Definitions and Assumptions.** Sniffing is sampling the surrounding fluid by olfaction, and a sniffer is the apparatus—whether natural or artificial—that sniffs. A sniffer has an external



**Fig. 2 Diagram of a basic sniffing process (the actual interior of a dog's nose is much more complicated than this)**

*nares*, or nostril, and a nasal cavity containing olfactory sensors in vertebrates and in artificial noses (though the latter do not also breathe.) Invertebrates have their olfactory sensors outside their bodies, but we consider them to be sniffers as well. Sometimes the sensor is stationary with respect to a moving fluid, other times the sniffer transports fluid through a stationary sensor apparatus. Either way, mass transfer by fluid flow is required for olfaction.

Olfaction is the sensory detection of an odor or scent, some chemical signal in the environment. The sources of such chemicals need not be present for olfaction to occur. Moreover, only *trace* amounts, not bulk amounts, are required. A trace is a very small chemical signal—sometimes only a few molecules. W. J. McGann has defined trace detection as “the process of sample collection, detection, and identification of targeted substances not measurable by any other means.” For present purposes we draw no distinction between trace detection thus defined and olfaction.

Incompressible single-phase fluid flow is assumed throughout this paper. Solid particles, when present, represent a negligible mass fraction. Weak odorant concentrations are passive scalars that do not change the gas properties. Reactions between sensors and odorants do not alter the energy level of the flow. Three-dimensional (3D) unsteady flow occurs in the most general sense, although lower dimensionality and quasisteady flow are assumed in many practical examples. The flow may be laminar, transitional, or turbulent, depending upon a Reynolds number that ranges broadly over the phenomena of interest. Viscosity is ignored in external flows away from surfaces. For internal flows a lumped friction loss is assumed for simplicity. All body forces are neglected. Readers unfamiliar with these assumptions should consult a basic fluid mechanics text, e.g., [49,50].

The equations to be solved, then, are the Navier-Stokes equations of continuum fluid motion, generally by numerical computation and experimental analog. Often, though, the external flows of sniffers lend themselves to simpler solutions like potential-flow approximations, where fluid rotation is neglected. Software is available to do these simple solutions, e.g., [51], and some examples are shown later. The underlying theory is covered in fluids texts and does not bear repeating here. However, potential-flow theory is inadequate for the flow inside an animal's nose or an artificial nose, where friction is important. Several complete Navier-Stokes solutions of such nasal flows in rats, monkeys, and people were done by Subramaniam et al. [16], Kimbell et al. [52,53], Kepler et al. [54], and Kimbell and Subramaniam [55].

**2.3 Modeling and Scaling.** A simple modeling exercise can help to introduce the key parameters of sniffing. Consider the rudimentary sniffer sampling the atmosphere in Fig. 2. (Much of this paper concerns ingenious ways of sample acquisition by sniffing, the simplest of which is shown in this figure.) A certain mass  $m_o$  of odorant is dispersed in the air within an odor cloud of volume  $V_o$ , yielding an average odorant mass concentration  $C_o = m_o/V_o$ . A sampler, or nose, approaches the vapor cloud closely enough that much of the cloud lies within the “reach” of the nose, i.e., the maximum distance over which it can induce a significant airflow. By inhaling a volume  $V_i$  through the nostril at ① over time interval  $\Delta t$ —“sniffing”—the nose transfers odorant from  $V_o$  to its internal sensor chamber, which has a volume  $V_{sc}$ , at a flow

rate  $Q = V_i/\Delta t$ .

The sniff is caused by a reduction in pressure  $p_2$  compared to ambient pressure  $p_1 = p_a$ . The pressure differential  $\Delta p = p_1 - p_2$  induces the desired airflow. Conservation of mass between stations ① and ② requires that  $U_1/U_2 = A_1/A_2$ , where  $U$  is the airspeed and  $A$  is the duct cross-sectional area. The steady-flow energy equation between stations ① and ②, ignoring any heat transfer, is

$$\frac{p_1}{\rho} + \frac{U_1^2}{2} = \frac{p_2}{\rho} + \frac{U_2^2}{2} + g(h_f + \sum h_m) \quad (1)$$

where  $g$  is gravitational acceleration and  $\rho$  is the gas density. This familiar relation reveals that wall-friction losses  $gh_f$  and “minor” losses  $g\sum h_m$  occur at the expense of the fluid kinetic energy inside the nose, and are balanced by the pressure differential according to

$$\Delta p = p_1 - p_2 = \frac{\rho K(U_2^2 - U_1^2)}{2} \quad (2)$$

where  $K$  is a lumped nondimensional loss coefficient expressing the sum of wall friction plus any duct losses caused by sudden expansions, contractions, bends, etc.  $K$  is not known *a priori* for a complicated nasal passage, but it can be evaluated from Eq. (2) using basic pressure and velocity data from experiments or computations.

This textbook material stresses to artificial nose designers the importance of minimizing the minor losses. Each of these wastes a portion of the velocity head  $1/2\rho U^2$ , and such flow energy loss must be made up by the lung or blower or pump that drives the sniffing process (see Sec. 5.3.2). Narrow flow constrictions are also lossy [45]. Inside an animal, too many minor losses overload the lungs and impede olfaction, if not respiration itself [56]. In an artificial nose, after the airstream has been sampled and interrogated, a *diffuser* is needed to recapture the potential energy of the flow before it is discharged to the atmosphere.

Returning to Fig. 2, if no extraneous unscented air is inhaled and  $V_{sc} \ll V_o$ , then the odorant concentration in the sensor chamber is simply  $C_{sc} = C_o$ . Of course this is unlikely, for in reality the nose also inhales some extraneous ambient air  $V_a$ , thus reducing the concentration of odorant in the sensor chamber by a sampling efficiency factor  $\eta_s \sim V_a/V_i$ . The sensed odorant concentration, then, is  $C_{sc} = \eta_s C_o$ . Other inefficiencies can occur, such as signal loss to the walls of the nasal passages. When particles are present in the odorant cloud, they may also be lost during sniffing by settling or impaction [57]. Realistically, then, the odorant concentration  $C_{sc}$  in the sensor chamber is often much less than  $C_o$ , which itself is usually tenuous in the environment. In other words there is an “impedance mismatch” due to poor sampling efficiency, by analogy with the transfer of electrical energy.

Large impedance mismatches in sniffers are often dealt with by *preconcentration*, in which a fraction  $m_s$  of the odorant mass  $m_o$  is sampled, usually by being adsorbed or impacted upon a surface during the sniff, and the large original volume of air  $V_i$  is discarded. (The additional apparatus and ductwork required to do this are not shown in Fig. 2.) After the capture, artificial noses use a much smaller volume of carrier gas  $V_p$  to collect the odorant mass, which is thermally desorbed from the surface, and convey it to the sensor chamber. This process takes time, but yields a preconcentration factor  $\eta_p = V_i/V_p$  as large as 1000 or more, greatly ameliorating the impedance mismatch. Natural noses have evolved the ability to sense trace odorants directly via the sensory tissue upon which they collect: a much-faster and more elegant approach.

Having arrived at an odorant concentration  $C_{sc}$  in the sensor chamber by sniffing, noses sense the odorant by way of a chemical reaction. In nature, odorant molecules interact directly with receptor cells mediated by a mucous layer, for example. True artificial noses mimic this, while other man-made detector types usually interrogate the captured odorant by spectroscopy. The

natural response to odorant concentration is the psychophysical power law (Stevens' law)  $R \sim C_{sc}^n$ , where  $n$  is less than 1 and is dependent upon the particular odorant species [58,59].

Now from a different viewpoint, the total odorant mass  $m_s$  sampled during the sniff is given by

$$m_s = \eta_s \cdot Q \cdot C_o \cdot \Delta t \quad (3)$$

This shows that higher sniffing flow rates and longer sniffs increase  $m_s$ . But does that mean greater olfactory sensitivity? Stuiver [44] reasoned that a higher flow rate reduces odorant dwell time upon the receptors and thus elicits less olfactory response. Mozell et al. and Hahn, Scherer, and Mozell [58,60] further noted that increasing  $Q$  by raising  $\Delta p$  with fixed  $\Delta t$  in olfaction studies also increases  $V_i$  and changes several variables at once, causing confusion. The design of the sensor chamber also bears upon this question (discussed in Sec. 5.3).

A longer sniff at the same flow rate, however, clearly does expose the receptors to more odorant mass according to this simple quasisteady-state model (which neglects *adaptation*, the loss of sensor response with time). Dogs can do this in case of weak or inaccessible scents by taking 1/2 Hz "long sniffs" in place of their normal  $\sim 5$  Hz sniff rate [47,61–63].

Finally, the Reynolds number  $Re_d = Ud/\nu$  governs the nature of this flow, where  $d$  is the nasal passage diameter and  $\nu$  is the kinematic viscosity of the air. Below  $Re_d \sim 2000$ – $3000$ , laminar flow is expected in simple ducts, though not necessarily in the complicated nasal passages of *macrosmatic* animals—those with keen olfactory powers. Since  $\nu$  is roughly constant at about  $1.5 \times 10^{-5} \text{ m}^2/\text{s}$  for air in the near-ambient temperature range, the Reynolds number varies mainly with airflow rate  $Q$  and physical scale  $d$ . The anterior nasal passages of terrestrial vertebrates range from about 1 mm diameter in the rat [64] to a centimeter or more in the largest animals. Given rat respiratory flow rates in the 100 ml/min–900 ml/min range, a typical  $Re_d$  is about 350 and laminar nasal flow is assumed [53], at least initially. In humans, however, the issue is controversial [45].

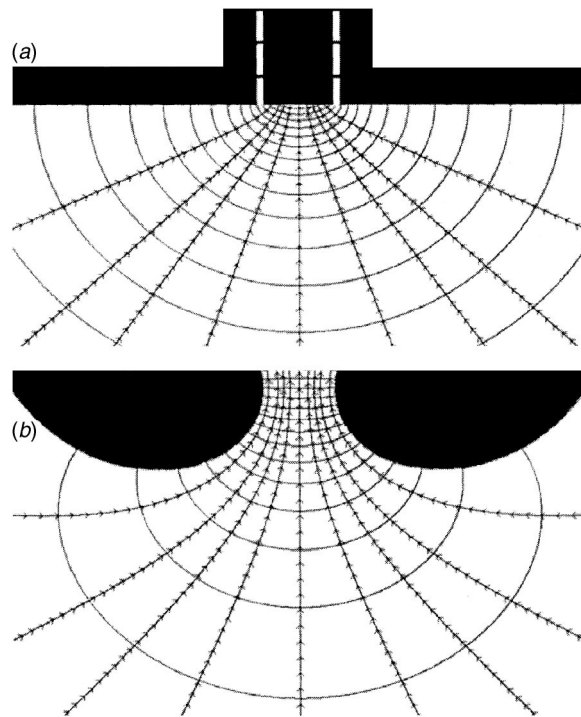
Underwater,  $\nu$  is an order of magnitude smaller than in air but the pertinent length scale is also often much reduced. The chemosensory hairs (*aesthetascs*) of crustaceans, for example, operate with  $Re_d \sim 1$ , where the interplay of fluid viscosity and inertia is delicately balanced, [65] and Chap. 15 of [66].

**2.4 Potential-Flow Inlets.** The potential flow approximation, mentioned earlier, naturally describes the flow of ideal fluids into suction orifices like the nostrils of present concern. We can examine external sniffing airflows by simple means, so long as  $Re$  is large and both wall friction and flow separation are either avoided or ignored. Ventilation engineering takes major advantage of this as is detailed in several references [17–19,67,68].

In brief summary, potential flow theory reveals that a simple inlet is not directional. Wile E. Coyote's ACME vacuum cleaner may suck in all sorts of objects from a distance, but that only works in the cartoon world. In reality an inlet draws fluid equally from all available directions, so its influence drops rapidly with distance. Consequently, except for the case of airborne scent plumes, sniffing is not a stand-off activity and proximity is essential for a nose to acquire a localized scent.

Potential flow also explains the inefficiency of a simple free-standing pipe as an air inlet: Even when aimed at something, it draws air equally from behind as well as from in front. It further has a high loss coefficient, 0.93, meaning that it wastes 93% of the velocity head  $1/2\rho U^2$ . A flanged inlet, Fig. 3(a) is an improvement: The forward reach is extended by excluding any suction from the rear hemisphere. Still, the sharp-edged inlet orifice has a loss coefficient of 0.49. Whether a nose is powered by lungs or batteries, such an unnecessary pressure loss is a burden.

Nature abhors sharp edges in favor of smooth, bulbous, aerodynamic nostril inlets like the one shown in Fig. 3(b). Also called a *bellmouth*, this inlet has a very small loss coefficient. Here is an



**Fig. 3 Streamlines (arrowed) and equipotential lines (solid) for (a) a flanged, sharp-edged inlet and (b) a bulbous "natural" bellmouth inlet. (These planar 2D potential flow solutions are shown only for illustration purposes)**

important design principle for artificial noses: avoid the sharp edge and the step change in area. It is the natural thing to do.

A definition of the "reach" of an inlet is the size of the region upwind of the inlet from which all of the fluid is ultimately captured [19]. In Fig. 2, in order for the sampling efficiency  $\eta_s$  to approach unity, the reach of the sniffer shown must at least encompass the entire odorant cloud. Industrial local-exhaust ventilation has the same problem: The exhaust hood must reach out to collect fumes from welding, for example, and not let any escape. Given the limited reach of a potential-flow inlet, this is quite a challenge. For the case of Fig. 2, approximated as a simple sink flow, the induced airspeed  $u = Q/\pi r^2$  drops linearly with distance  $r$  forward of the nostril inlet.

Potential-flow inlets scale up or down geometrically without regard for nondimensional numbers like  $Re$ , so the reach of an inlet also grows linearly with its diameter  $d$  because  $Q = \pi d^2 U_1/4$ . This works against the small-diameter tubing used in wand-type leak samplers, e.g., [69]. They have little reach even at the extreme  $U_1$  corresponding to choked flow, and must be physically inserted into an odorant cloud to sample it.

**2.5 Turbulent Jets.** There is a key distinction between the behavior of potential-flow inlets just described and fluid jets: while inlets are omnidirectional, jets can be vectored. Aim an air jet in a certain direction and it maintains that direction in still air. The "reach" of a jet, then, is many times longer than the reach of an inlet having the same flow rate  $Q$ . Jets thus project fluid momentum at a distance.

The turbulent jet literature is vast. Useful surveys of it for present purposes are found in Chap. 4 of [17] and in [70–72]. The recent discovery of synthetic jets is also pertinent [73].

A jet entrains fluid from all directions perpendicular to its axis, which causes it to grow linearly in diameter with increasing distance downstream. The volumetric entrainment rate of turbulent jets is approximately  $0.25x/A^{1/2}$ , where  $x$  is the distance from the nozzle and  $A$  is the nozzle cross-sectional area [70].

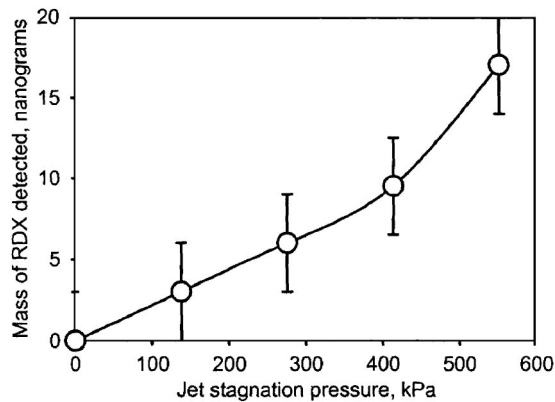


Fig. 4 Portal results of liberated RDX particle mass as a function of impinging-jet stagnation pressure [83]

When a jet impinges upon a solid surface it tends to attach and to exhibit starting impinging jet behavior [74]. Free jets impinge upon surfaces to become wall jets [75].

Even though jets seem at first antithetical to the present goal of sniffing, they can be useful on at least two counts. First there is jet-assisted olfaction, where jets help to focus the suction of a sniffer in the forward direction to improve its reach, Secs. 4.3.1 and 5.2.4. Second is the use of jet momentum to stir up the environment, resuspending settled particles and making them available for olfaction as shown in Fig. 1(b).

Phares, Smedley, and Flagan at Caltech have studied the second topic at length [76]. They explored the effects of  $Re_d$ , nozzle height, and jet velocity profile on particle removal using both normal [77] and oblique [78] jets, and found that surface particles respond to the shear stress imposed upon them by jet impact [79]. Particle removal depends on particle size and jet duration as well [80]. With these results in hand, they examined previous resuspension theories and proposed a new model. Other recent investigators [81] also studied this topic, and one [82] suggested an analogy with heat transfer enhancement by pulsed jets.

In applied experiments in the Penn State Gas Dynamics Laboratory [83], short-duration air jets from round nozzles impinged upon human subjects whose clothing was contaminated by 10-micron-range trace particles of the explosive cyclotrimethylene-trinitramine (RDX). Dislodged particles were collected (Sec. 6.3.2) and quantified with results shown in Fig. 4. In addition to the shear-stress mechanism described above, inertial detachment of particles also occurs due to jet impact ruffling of the clothing. No matter what the mechanism, though, jet impingement has become the principal means of liberating trace particles from people for analysis and detection in a reasonably nonintrusive manner.

The quasilinear response shown in Fig. 4 is understandable in that the nozzle-to-person distance was fixed in the experiments and the nozzle exit was sonic. Since jet momentum is conserved, an increase in stagnation pressure thus produces a proportional increase in jet momentum, which is thought to be responsible for inertial particle removal from clothing.

**2.6 Particles and Stokes Number.** Can particles in a flow follow streamlines, as molecules do by definition? This question is answered by considering the nondimensional Stokes number, the ratio of the aerodynamic response time of a particle to the characteristic flow time,

$$Stk = \frac{\rho_p \cdot d_p^2 \cdot U}{18 \cdot \mu_f \cdot L_c} \quad (4)$$

where  $\rho_p$  is particle density,  $d_p$  is diameter,  $\mu_f$  is fluid viscosity, and  $L_c$  is a characteristic length, such as the size of a flow obstruction. As  $Stk$  approaches 0, particles have no significant inertia

and they faithfully follow streamlines, but for  $Stk$  greater than about 1, impaction of particles upon obstructions is likely. This is the basis of devices called *impactors* that collect particles from flowing fluids.

Consider airborne particles of unit specific gravity and 10  $\mu\text{m}$  diameter, having masses of about a nanogram each. If  $U = 30$  m/s and  $L_c = 1$  m, roughly the speed of a car and the size of its windshield, then  $Stk = 0.009$  and the subject particles will be likely to flow around the windshield without striking it. But if  $L_c = 5$  mm, the diameter of the radio antenna, then  $Stk = 1.8$  and impaction is much more likely. Calculations like this are useful in the design of particle collectors, the loss of particles during transport in tubes, particle settling time, terminal speed, and the deposition of inhaled particles in the nose and lungs [57,84–86].

**2.7 Advection Versus Diffusion.** Advection is bulk fluid motion whereas diffusion is the molecular spreading of one fluid into another without bulk motion. These distinct phenomena are often confused in the olfaction literature. In Feynman's [87] classic classroom example gone wrong, diffusion is taught by opening a bottle of ammonia and waiting for the student in the back of the room to say "I smell it." But if diffusion is the only transport mechanism, he will not smell it by the end of the class, or even the end of the semester. In reality, the ammonia molecules are quickly transported by the advection of air currents around the room and by thermal convection currents generated by the people in the room.

This point is often made but the confusion persists, even though it may be just an imprecise choice of terms. Airborne odor transport in the nasal cavities of vertebrates has been attributed to diffusion [3,88,89], but that too is unlikely.

Vogel draws an elegant comparison between diffusion and advection for a popular audience ([90], p. 182). Diffusion only works over short distances and thus depends on the size of the flow in question, "But even in air, diffusion remains glacially slow for what we regard as ordinary distances."

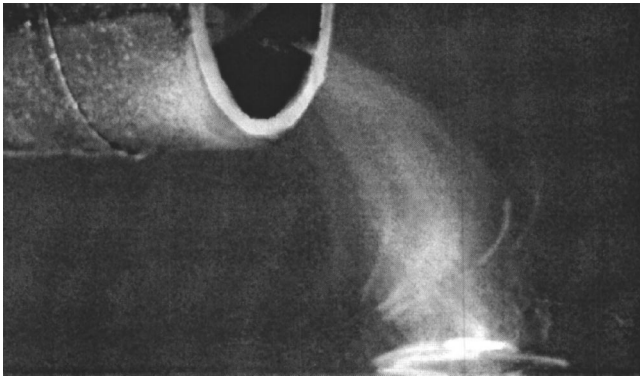
The relative rates of advective versus diffusional transport in fluids are described by the nondimensional Péclet number,  $Pé = L_c U / D$ , where  $D$  is the diffusion coefficient of an odorant molecule in the fluid of interest. When  $Pé = 1$ , the rates are equal. Returning to the rat's-nose example of Sec. 2.3, let  $L_c = 1$  mm and  $U \sim 5$  m/s [53]. Diffusion coefficients of typical odorant molecules in air are broadly in the range of 0.1–0.3  $\text{cm}^2/\text{s}$  [91], yielding a rat's-nose Péclet number of several hundred. Only at much-lower airspeeds and length scales can diffusion matter in this sniffing example. But there are certainly cases where diffusion matters in olfactory sensing, such as lobster "sniffing" [92,93].

Griffy [94] calculated the time required for a trinitro-toluene (TNT) bomb to produce a saturated TNT vapor level in a room by pure diffusion: hundreds of days. He concluded that airborne explosive vapor detectors are unlikely to succeed unless they are orders of magnitude more sensitive than needed to detect equilibrium vapor levels. But let us not abandon vapor detection altogether, so long as there are air currents to convey the signal and sniffers poking their noses into nooks and crannies (see also Sec. 5.2.2).

**2.8 Vortex Flow.** The potential-flow vortex is a rotating flow with a strength determined by its core singularity. It has no radial velocity, circular streamlines, and a circumferential velocity field that dies off as the inverse of radius from the core. Vortex flows are covered in elementary fluids textbooks, but see also Lugt's scholarly book [95] that appeals to a broad audience.

What relevance do vortices have to sniffing? At least one man-made sniffer uses an apparent vortex as its operating principle [96]. The puffs on either side of the dog's nose in Fig. 1(b) are the starting vortices of impinging nostril jets. The bellmouth nostril flowfield of Fig. 3(b) is produced by twin counter-rotating vortices (hidden inside the nostrils), and so on. Vortices are everywhere.

One vortex of special interest is the *intake* or *inlet* vortex. There



**Fig. 5 Inlet vortex into a vacuum cleaner hose with a cross breeze, visualized by coating the ground plane with talcum powder**

are photos of vortex cores extending from the idling jet engines of parked aircraft, touching the ground like mini tornadoes and sucking up debris. It is a common fallacy that the jet engine creates its own inlet vortex [97], but researchers in E. M. Greitzer's lab at Massachusetts Institute of Technology have demonstrated that a cross breeze is also required [98] in all cases except those of inlets with swirl vanes [99]. The cross breeze sheds a line vortex from the engine inlet lip that turns downward and attaches to the ground.

The inlet vortex can be duplicated on a tabletop using a vacuum cleaner and fan according to Stong [100]. This instructive demonstration is not difficult (Fig. 5), but its stability is greatly improved if one places a screen or flow straightener after the fan producing the cross breeze.

**2.9 Frequency of Animal Sniffing.** Although dependable fluid-dynamic data on olfaction are rare, enough exist to estimate the nondimensional sniffing frequency of at least a few animals. This is the Strouhal number,  $Str = fd/U$ . For the rat, dog, and human, respectively, the available data are approximately as follows: dimensional sniffing frequency  $f = 10, 5,$  and  $2$  Hz, characteristic nostril dimensions  $d = 1, 7,$  and  $13$  mm, and characteristic airspeed  $U = 8, 5,$  and  $3$  m/s [33,47,53,89]. These values yield Strouhal numbers of about 0.008 for the dog and human and 0.0014 for the rat. Thus sniffing is a slow process compared to the flapping of animal appendages for propulsion, where Strouhal numbers are up to two orders of magnitude larger. A quasisteady-flow approximation is justified in the analysis of sniffing airflows [33] at this low frequency. It may be that animal sniffing rates are based, at least in part, on the need to provide sharp gradients of odorant rather than a constant odorant level to the olfactory sensors. Adaptation works against high sensitivity in the limit as the sniffing rates approaches zero.

### 3 Traditional Sampling Issues and Methods

Sampling the environment is important to society. So much has been written on this topic, including several thorough reviews, that it serves the present purpose only to give a brief overview with some key references, noting the issues relevant to sniffing.

**3.1 Airborne Particle Sampling.** The U.S. Clean Air Act controls particles in the atmosphere in order to protect public health and prevent environmental damage. Airborne particulates in the  $<10 \mu\text{m}$  ( $PM_{10}$ ) and  $<2.5 \mu\text{m}$  ( $PM_{2.5}$ ) aerodynamic diameter range are regulated by law according to National Ambient Air Quality Standards. Compliance is monitored by samplers that draw in ambient air and collect the airborne particles by any of several means, including impactors, cyclones, filters, and electrostatic precipitators [13,25,101,102].

The aspiration efficiency of these sampling inlets is one con-

cern, since they must sample a representative population of airborne particles. Isokinetic sampling helps to accomplish this. Outdoor samplers also require inlets that are insensitive to the wind direction. Rooftop inlets are often symmetric about a vertical axis for this reason, while thin-walled sharp-edged inlet tubes can be shrouded to make them less sensitive to variable wind direction. There are many commercial samplers available, from the liters/min range up to about a 19 liters/s flow rate for large rooftop models [84].

Aside from filtration [101], impaction (Sec. 2.5) is the most common means of separating the particles from the airstream in these samplers [13,84,102]. Multistage impactors further classify particles into several size ranges. This matters in air pollution measurement but is not an issue in olfaction; a single-stage impactor can sample all the particles above a minimum diameter together if purely for chemical detection.

A dog's nose collects particles by impaction in the nasal vestibule region, where the respiratory mucosa are moist and sticky [103]. Preventing impacted particles from bouncing or blowing off is likewise an issue in man-made impactors, where a wide variety of sticky coatings is used [13,84,102,104].

Another approach is the virtual impactor, which preconcentrates particles in the sampled airstream by a factor of 6:1, 20:1 [84] or even 25:1 [105]. The particles remain airborne, which helps transport them to an analyzing instrument. Design rules for virtual impactors are given in [84].

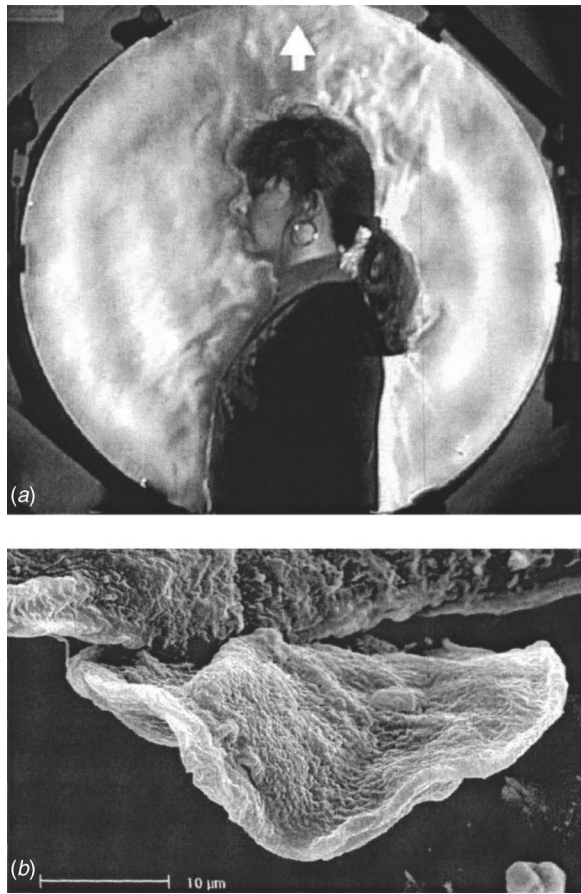
Other than inert particles, there are also bioaerosols to be sampled [12,25,106–108]. With such a bewildering array of species already present in the air, detecting a biological warfare attack is a problem [109]. The sampling step must not harm these live airborne particles, since a culture is often required to identify them [110]. The analysis step may also require a liquid sample like that provided by impingers and some cyclone samplers, purification may be needed, and a high sample concentration is called for [12].

**3.2 Indoor Sampling.** Indoor air quality considers the adverse health effects of smoking, sick building syndrome, insufficient ventilation, etc. [111–113]. Airborne sampling indoors began with the realization that the dangerous pollution sources are under our noses, including chlorinated water, dry-cleaned clothes, mothballs, air fresheners, cooking, paint strippers, solvents, radon gas, and especially tobacco smoke [112]. Large government-sponsored studies like Particle Total Exposure Assessment Methodology (PTEAM) [114–116] in the United States and others abroad showed that personal  $PM_{10}$  exposure levels measured by lapel samplers are significantly higher than either outdoor or indoor levels measured by fixed samplers.

**3.2.1 Personal activity cloud or human boundary layer?** Without questioning the results or significance of PTEAM, here is an alternative fluid-dynamic interpretation. A "personal activity cloud" was proposed by PTEAM investigators as the source of the measured discrepancy in exposure levels [116,117]. Wallace [118] explains: "It is almost as if the participants were walking about in their own personal cloud of particles, a sort of Pigen effect, after the character in the (Charles Schulz) *Peanuts* comic strip."

The cloud analogy and the comic-strip reference are sadly misleading, though, for what actually happens is not a cloud at all but rather a rising thermal boundary layer that separates to form the *human thermal plume* (Fig. 6(a) [46]). It was first shown by Clark and Cox [24], Lewis et al. [119], and Clark and Edholm [120] that the temperature difference between people and ambient air drives a natural-convection boundary layer beginning at the feet and separating from the head and shoulders. Thus the "cloud" analogy overlooks the strong vertical transport ( $U \sim 0.25$  m/s,  $Q$  up to 50 liters/s [121]) in the airflow about a person. This transport not only presents floor-level contaminants to one's breathing zone, but also entrains the surrounding air and its particle burden at all other levels below the breathing zone. Quoting [122], "The natural con-





**Fig. 6 (a) Schlieren image of the rising boundary layer and thermal plume from a human being (L. J. Dodson) [46] and (b) scanning electron microscopy image of a desquamated human skin flake, H. A. Gowadia [123,124]. According to Syrotuck [125], “They are cornflake in shape which gives them an aerodynamic characteristic.”**

vection boundary layer around the human body is capable of transporting particles such as dust, skin scales, pollens, and spores and provides a link in the chain of airborne infection.”

A second problem with the PTEAM interpretation is its disregard for the role of human skin flakes: “body cloud emissions are...not considered here as a component of the personal activity cloud effect” [117]. In fact, human skin is easily the most prevalent particulate in the human thermal boundary layer and plume. A complete layer of human skin is desquamated every 1–2 days [24], releasing a million skin scales/min with a  $14\ \mu\text{m}$  average diameter and a size range of  $5\text{--}50\ \mu\text{m}$  (see Fig. 6(b) [123,124]). Most inhaled air comes from the human boundary layer that contains these particles, from which 6000 to 50,000  $5\text{--}50\ \mu\text{m}$  particles/liter of air enter the human nose. Most clothing is permeable to this particle stream. Ordinary house dust is found under microscopic examination to consist of 70%–90% human skin flakes covered with microorganisms. According to Syrotuck [125], if you walk at  $1\ 1/3\ \text{m/s}$  (3 mph) you leave behind 500 skin flakes/m. The weight of this evidence on the significance of skin flakes in the human microenvironment ought to be hard to ignore (see also [125–128]).

Moreover, human skin flakes contain mitochondrial DNA, even though they have no cell nuclei and thus no nuclear DNA [129]. We thus continuously shed gross samples of our mitochondrial DNA into the surrounding air. Anthropologists sequencing tiny remnants of ancient mitochondrial DNA must be scrupulous to avoid contamination from their own airborne skin. We cannot sup-

press this shedding of our DNA, and collecting it for analysis is certainly possible according to principles to be described later (Sec 6.3). Ethical questions about this possibility remain to be resolved, however.

Meanwhile note that a thorough study of the airflow in the human breathing zone, including flow visualization, quantitative measurements, and CFD [130] has apparently not been done, so there is much still to learn about the reach of inhalation, the penetration of exhaled nostril jets, particle intake, and the proper location of personal samplers. Where to locate a personal sampler on a breathing person, considering the nose inlet flow and upward boundary layer motion, still remains an open question. In seeming proof that nothing is sacred, even intranasal samplers are used to sample incoming particles inside human nostrils, thus avoiding this pitfall [131].

**3.2.2 Personal samplers.** References [14,15] describe the state-of-the-art of small battery-powered personal samplers to be worn by human subjects for particle exposure monitoring in studies like those just described and in industrial hygiene assessments. Typically a battery-powered diaphragm pump draws in the sampled air at a few liters/min through a sorbent tube, filter, impactor, or cyclone. The inlet is usually connected by tubing to the pump, and is attached to a subject’s collar or lapel to sample breathing-zone air. A miniaturized five-stage personal cascade impactor is available [132] to classify particle sizes. The SKC Corporation’s Button Sampler is a collar-clip filter sampler with a porous curved-surface inlet having low wind sensitivity [133].

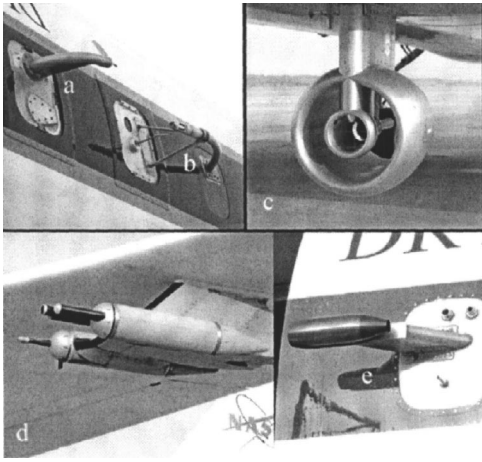
Mannequins are used to test personal samplers [134,135], but they do not always properly simulate people. A department-store mannequin is the worst case, for it has neither body heat nor skin flakes and it cannot breathe [136]. Human subjects are thus preferable to mannequins here and in any experiments involving the human thermal boundary layer and plume.

**3.2.3 Hand vacuums.** Hand vacuums are simple, versatile, filter-type “dustbuster” sniffers. They see regular use in sampling the clothing and luggage of aircraft passengers. The filters are made of cellulose fibers, glass or quartz fibers, membranes, polycarbonate pore material, or plastic foam. In security screening the filter is removed and heated in a desorber, driving off collected traces to be detected, usually, by an ion mobility spectrometer [137].

**3.2.4 Wand-type sniffer probes.** Wand-type sniffer probes were singled out in Sec. 2.4 for their short reach. Nevertheless a simple probe or wand at the end of a hose is a popular way to poke around and sniff for something. Leak detectors often use wands for gas collection and they are considered prior art in several inventions, e.g., [138]. A search of the technical and patent literature for the term “sniffers” mostly yields such leak-detection equipment with long hoses and hand-held, pointed wands intended to pinpoint leaks [69,139]. In one case a filter at the end of a long hand-held hose samples particles in clean room environments [140], while in another a heated probe tube feeds a portable gas sampling system [141]. A person probing with a sniffer wand is like an elephant exploring with its trunk: Both animals are too bulky to get into tight places without the aid of an olfactory extension tube.

**3.3 Outdoor Sampling.** Sniffing outdoors raises further complicating issues having to do with flight, the weather, and chemical plumes.

**3.3.1 Sampling by flight vehicles.** Sampling by flight vehicles involves a mobile sniffer moving rapidly through a relatively immobile atmosphere. Man-made flight platforms for air sampling range from miniature unmanned aerial vehicles (UAVs) [142–145] to full-sized aircraft [146–148]. Beginning in the 1970s, NASA’s 5.5 m-wingspan Mini-Sniffers [149] pioneered UAV sampling of the atmosphere at high altitudes. Since then the potential of UAVs



**Fig. 7 Sampling inlet probes on the NASA-Dryden DC-8, (a) heated, Teflon-lined PANAK probe, (b) U. Hawaii shrouded probe [147], (c) nacelle-mounted ATHOS probe [146], (d) wing-tip mounted aerosol scattering spectrometer probes, and (e) shrouded POPS probe (NASA photos)**

for biological agent detection has been explored [144,145], and a recent Defense Advanced Research Projects Administration (DARPA) program spawned microair vehicles that could be similarly employed for sniffing [142,150].

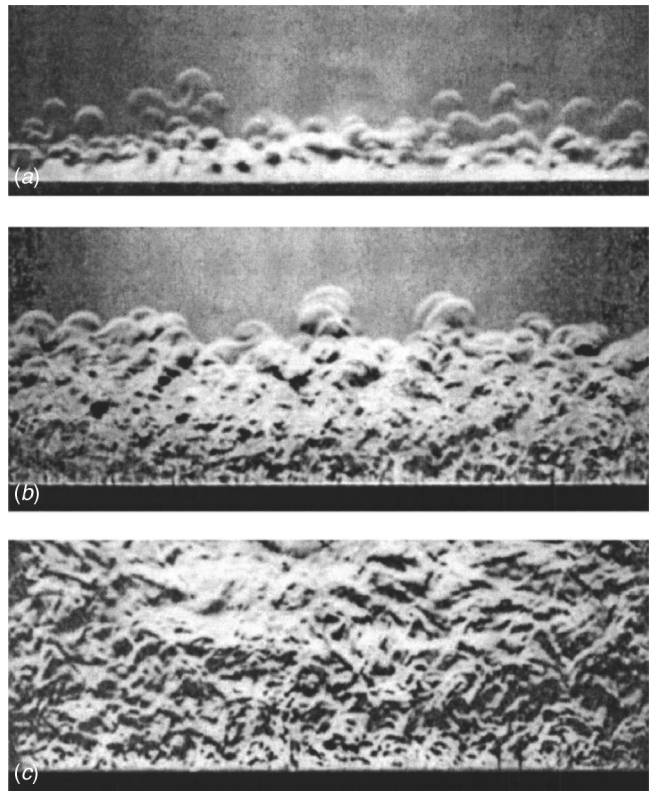
In contrast, take the current Intercontinental Chemical Transport Experiment-North America as an example of sampling from full-scale aircraft [151]. Its principal flight vehicle, the NASA-Dryden DC-8, with sampling probes of all sorts. Five are shown in Fig. 7 [146,147]. Most of these feature shrouded inlets to minimize flow angularity effects, after Kiel's original shrouded Pitot probe from the early days of aeronautics [152].

In principle, it appears easy enough to extend a tube through an airplane window and sample the air. Some further design refinements are obvious, like mounting the probe on a strut to get it outside the airplane's boundary layer. For chemical species in the upper atmosphere, though, there is the concern that they will react with the walls of the tube. Particle sampling is an even greater concern: Recalling the Stokes number from Sec. 2.5, when  $U$  is hundreds of m/s it becomes hard to prevent particles from impacting inside the probe rather than being conveyed to the instruments inside the aircraft. Likewise the airflow angle with respect to the probe axis is not well known. These issues combine to make airborne sampling probe design challenging.

Wind-tunnel tests [153] are often used to verify that new probe types can achieve isokinetic sampling and deliver a true particle sample. A good reference summarizing inlet probe design for aircraft samplers is [154]. The topic is revisited in Sec. 4.3.13, where we will see how birds solve this problem.

**3.3.2 Micrometeorology.** In nature, sniffing must take place outdoors under all manner of weather conditions. Sun or clouds; calm, steady, or gusty winds; moisture levels; the temperatures of the air and terrain, all play a role. The broad field of micrometeorology [155,156] is not reviewed here, rather just a few issues pertinent to sniffing.

First, consider the wind [157]. The lowest atmospheric level is a turbulent planetary boundary layer (PBL) that we perceive as wind. Meteorological calm, 2.2 m/s or 5 mph, is still a significant breeze for bioaerosols [107], insects, and even people, whose thermal plumes become wakes at a much-lower airspeed (Sec. 6.3). Sniffers operate in the smallest local regime of micrometeorology, the bottom 2 m or so of the PBL's roughness layer [156]. Even so, ill winds readily disrupt sniffing by dispersing chemical traces [158]. Moths, for example, cannot track pheromone plumes when



**Fig. 8 Schlieren images of high-Rayleigh-number thermal convection from a suddenly heated horizontal surface, simulating the earth at sunup on a windless day, courtesy J. C. Molendord [167]. (a) Early thermals, (b) a forest of starting thermal plumes develops, with both their crowns and stalks visible, and (c) fully developed thermal convection field. These pictures compliment those in the literature using tracer-particle visualization. Here an integrated view is shown, though one can imagine the depth effect**

the breeze is too stiff [159]. On the other hand wind interactions with obstacles offer opportunities for olfaction, such as sniffing the recirculating flow downstream of a building [160].

Moisture levels are still another matter. Although the effect of temperature and humidity on human olfaction is controversial [59], various investigators [161,162] show that an increased soil moisture level generally aids olfactory trace detection by animals, whether of buried food or land mines. Extreme aridity, on the other hand, may so dry the mucous membranes of a dog's nose as to inhibit olfaction.

Also there is the issue of the buoyant odor-bearing thermal plume [70,155,163–165]. As an example, consider the following landmine detection scenario [125,166]: The surface temperature of the soil varies some 30°C daily, depending on local conditions. This desorbs some trace explosives—where present—from the soil surface over a buried landmine, creating an airborne vapor signal. What becomes of this signal, however, depends on micrometeorology. On sunny days a strong temperature gradient develops above the soil, which can be 40°C hotter than desert air. This produces unstable thermal convection, transporting any desorbed explosive vapor upward and away. Measurements show that typical thermals arise from surface areas of 1 or more m<sup>2</sup>, rise at speeds of about 1/4 m/s, and occur at frequencies in the range of 4/min [155]. Visualized thermals (Fig. 8 [167]) show typical mushroom-shaped convection cells. Under such adverse micrometeorological conditions no stable layer of trace explosive can be expected above a buried landmine.

The situation improves, though, from sunset until morning. A stable boundary layer often forms above cool soil in the summer.

Through the night, explosive vapor from buried landmines can accumulate in this layer. Thus mines are most detectable during the evening, night, and early morning in calm weather when the ground is moist.

Given a prevailing wind, however, the situation is dramatically complicated by mixed free and forced convection, both unstationary and fully turbulent. In sunny weather, thermals are sheared horizontally and mixed out by turbulence. A light horizontal breeze, less than 1 m/s, is enough to tilt the thermals over significantly. For higher wind speeds, forced convection dominates and any explosive vapor from a minefield is quickly diluted and transported away in the PBL. Not even trained dogs can locate landmines under such adverse weather conditions.

**3.3.3 Chemical plume tracing.** This naturally leads to a recent “hot” research topic, chemical plume tracing. The ability to follow tenuous outdoor plumes in nature rewards many animals with food or sex. The fluid dynamics of plumes and how to follow them is thus a part of sniffing as we define it here. It was also the subject of a recent DARPA/Office of Naval Research (ONR) program that funded multidisciplinary studies to understand chemical plumes in nature and to develop artificial plume tracing systems. More details are available in [41,92,168,169].

Briefly, much of the research to date concerned insects in the atmosphere and crustaceans in the ocean. The small-scale plumes these creatures track are nonetheless large enough that the Reynolds number dictates fully turbulent flow. They are highly intermittent, having large scales comparable to the plume width and a cascade of finer-scale eddies [41,170]. They spread downstream and contain streamwise and cross-stream chemical gradients in their mean structure [43,171–174].

An animal’s response to this intermittent stimulus is complicated. Insects and crustaceans have sensory appendages that provide them with plume information [42,175,176]. Lobsters, for example, flick their antennules to sample the environment [92,93,177]. Both chemical orientation (chemotaxis) and flow orientation (anemotaxis) are invoked [175,178,179]. Generally upwind progress toward the plume source is modulated by turns and sometimes by “casting” [168,180]. Weissburg takes an overall view of the fluid dynamics underlying this animal behavior [170].

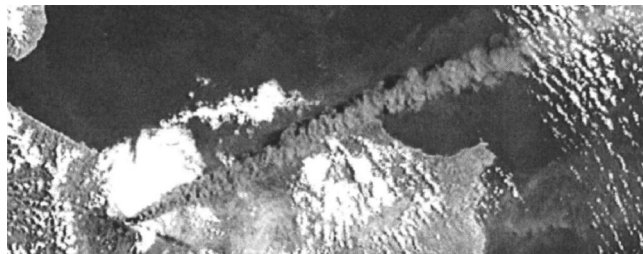
Robots employ such natural plume-tracing principles with varying degrees of success. Man-made chemosensors are currently inferior to natural ones in terms of speed [169], but nevertheless several robotic plume tracers have been developed and tested [41,181–185], including the “Robolobster” [186].

Standoff detection of small localized chemical plumes is a current security concern [48]. Understanding explosive vapor plume dynamics, for example, is helpful in the development of spectroscopic standoff detectors. Such plumes may have very low concentrations of chemical vapor (see Sec. 2.6), but they can be sought and interrogated based on their buoyancy or momentum, which drives the trace chemical transport.

These small-scale plumes are in stark contrast to the huge natural and man-made plumes that have grave environmental and security implications [187]. They are sometimes visibly tagged with particles, as in Fig. 9, but also sometimes quite invisible. Several horrific plume accidents now serve as case studies, including Bhopal and Chernobyl [188–190]. Large-scale computational plume modeling, e.g., [191], is driven by the knowledge that plume-generating weapons of mass destruction are within the grasp of terrorists. Plume dispersion in cities, driven by convoluted local meteorology due to buildings, is especially challenging [192,193].

## 4 Nature’s Sniffers and Biomimicry

**4.1 Narial Morphology and Evolution.** Almost no one except Negus [194] and Bang [195] has shown enough interest in the external animal nares—the nostrils—to do a morphological study. It cannot be done justice here for several reasons, but at least one can take a peripheral look and open a prospectus for



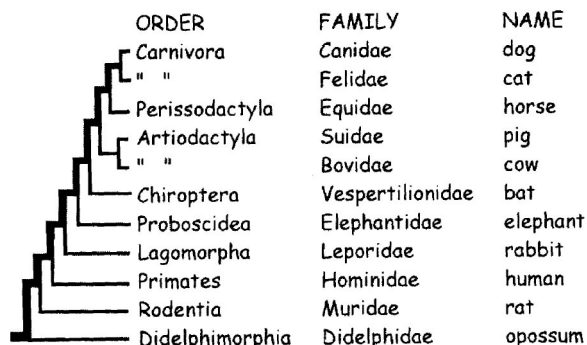
**Fig. 9** Satellite photo of the ash plume from the eruption of Mount Etna on October 29, 2002. The plume direction is SSE over eastern Sicily, the city of Siracusa, and the Mediterranean Sea. The lateral scale is roughly 200 km, and the scale of the largest visible eddy (i.e., the plume width) is perhaps 10 km. Photo PIA03733 by the NASA GSFC/LaRC/JPL MISR Team

further study. In that the few fluid-dynamic studies of sniffers conducted to date have yielded interesting results, e.g., [16,32–34,47,65,92,93,176,196], there is clearly more to learn from nature’s broad range of sniffing systems. What man-made sniffers have to offer thus far is paltry in comparison.

Here we will examine an abridged but representative phylogenetic cross section of the animal kingdom, with at least one example from each vertebrate class (mammals, birds, reptiles, amphibians, and fish), but only examples from the arthropod phylum of invertebrates. Special emphasis is given to the morphology of mammalian sniffers (Fig. 10). Taxonomic and phylogenetic information is obtained from [197–200], and anatomical terminology [201] is adopted except for a few common-usage lapses.

Nature, over some 300 million years, has explored animal sniffing systems quite thoroughly. Fossil animal DNA was recently recovered and studied up to about 100,000 years ago; enough to address some far-reaching evolutionary questions and shake up the old phylogeny in places [202]. For example, from fossil mitochondrial DNA and other evidence, the *Canidae* appear to have arisen as a distinct family of carnivores some 50 million years ago [199,200]. Within this family the wolf, dog, fox, raccoon, bear, weasel, and jackal have nearly identical nostrils. The *Hyaenidae* appeared separately about the same time, and are more closely related to the *Viverridae* and *Felidae* than to dogs according to the DNA record [200]. Hyenas nonetheless sport very dog-like muzzles and nares.

Despite all her diversity, though, nature never developed one of our most clever man-made devices: the turbomachine. Bellows action remains the natural way to pump fluids [203]. On this account a small, low-power pump or fan gives artificial olfaction a



**Fig. 10** An abridged phylogeny of mammals for the study of external nares evolution. For brevity the common name is given in place of the scientific species name. Time progresses nonlinearly from left to right for compactness, and branches indicate evolutionary divergences of a group (the lower arm) from the general mammalian stock

certain advantage over nature's devices: It can inhale air continuously and efficiently, and exhale it somewhere else. Even so, when it comes to mimicking nature's olfactory sensors, their fluid-dynamic sophistication and their direct connection to the brain, we are still far behind.

**4.2 Biomimicry.** T. H. Huxley said "Sit down before fact as a little child, be prepared to give up every conceived notion, follow humbly wherever and whatever abysses nature leads, or you will learn nothing." Biomimicry is innovation inspired by observing nature, learning her lessons and deliberately copying them in man-made devices [204]. Here, for example, the study of narial morphology may lead to better sniffers for the new generation of artificial noses now becoming available. This dual need for fundamental studies of mammalian olfactory systems has been recognized by funding agencies including the U.S. National Science Foundation [205].

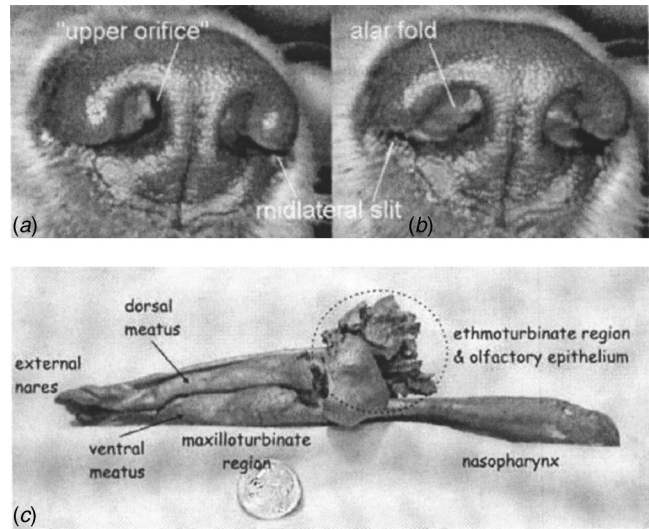
**4.3 Internal-Flow Noses of the Vertebrates.** In mammals and many other vertebrate species, nasal passages lead from the external naris through a maxillo-turbinate region, past the olfactory mucosa—nature's sensor chamber—to the nasopharynx and thence to the lungs [3,206]. Olfaction is further aided in some species by a dedicated olfactomotor system [63] that drives nostril motion during sniffing by way of elaborate musculature.

Every species shown in Fig. 10 is macroscopic except humans. In two cases, mammals of the same order are compared in order to emphasize diverse narial evolution in closely related species. All species shown are also of the infraclass *Eutheria* (placental mammals) except the opossum, a marsupial, who belongs to the infra-class *Metatheria*.

One must beware here, given nature's penchant for multiple functionality, not to confuse other roles with olfaction. Respiration is intimately connected with olfaction in all of the considered species. Nasal turbinates, for example, are not "turbulators" (mixing devices), but rather air-conditioning devices for heat and moisture exchange [36,206–209]. They provide additional olfactory surface area and generate vorticity even so. Further concern arises in using the fossil record to trace olfactory evolution, since fossils do not preserve the soft nasal tissues.

**4.3.1 Dog.** The dog's nose is recognized as the gold standard of olfactory acuity. There are many good sniffers shown in Fig. 10, but dogs are easiest to train for olfactory detection. Our closest animal companions, they are the cheerful butt of endless sniffing humor because we cannot appreciate the rich olfactory environment as they can. They are the ultimate mobile, instinctive, intelligent sniffing platforms.

A brief history of canine olfaction research begins in 1938, when it was shown experimentally that the majority of inspired air bypasses the olfactory epithelium, which is offset from the main airway of the nasal cavity [35]. Dawes' experiments [36] then revealed that currents from the main airstream pass freely into the olfactory region during expiration as well. Becker and King [210] likewise found different pathways for inspired and expired air. Neuhaus [211–213], however, was the first to carry out extensive research on canine olfactory acuity in the 1950s. He found that a dog can detect 1 mg of butyric acid dispersed throughout  $10^8$  m<sup>3</sup> of air, i.e., the volume of an entire town. Negus [194,206] made a broad comparison of olfaction among many species with the dog as chief sniffer. Syrotuck [125] examined canine scenting and tracking in terms of physical and chemical phenomena. He estimated that the detectable "ground scent" left by a human might last 8–16 h. Zuschneid [61] discovered the long canine sniffs. Neuhaus [89] further examined the anatomy of the nasal passages and the role of sniffing in olfaction. Schreider and Raabe [64] showed 29 transverse sections through a beagle's nose, revealing the elaborate scrollwork of the turbinates. Recently Johnston et al. [214,215] and Williams et al. [216,217] developed laboratory olfactometry for dogs and measured the dog's response to trace



**Fig. 11 External nares of a Golden Retriever (a) during inhale and (b) during exhale portions of sniffing cycle [47], and (c) solid cast of the nasal cavity of a dog reconstructed from CAT scans [62] (cast provided courtesy T. S. Denny Jr., Auburn University)**

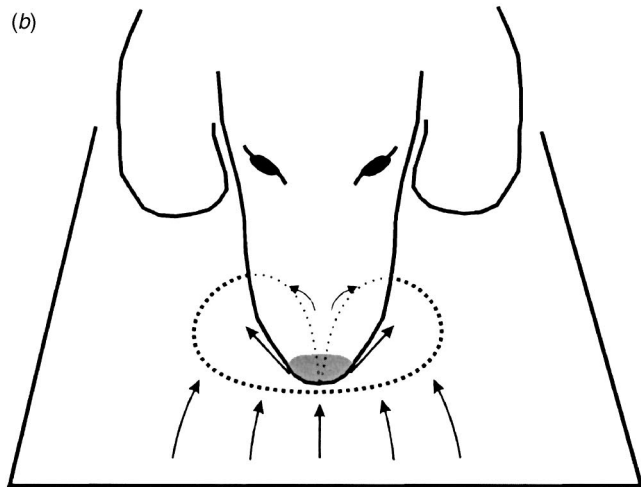
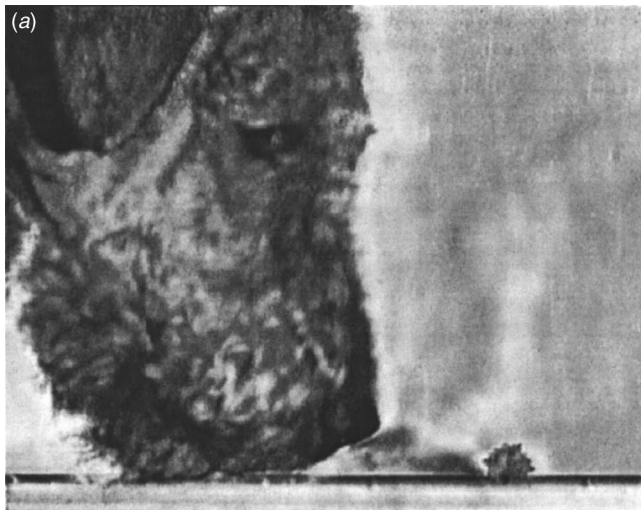
chemicals (see also Sec. 6.1). Thesen et al. [218] and Steen et al. [219] studied canine olfaction in outdoor tracking experiments. Morrison [62] and Johnston et al. [103] reported basic experiments on the canine olfactory system, including tomography of the nasal cavity and a particle deposition study. Most recently, Settles et al. [47] visualized the airflows associated with the canine external nares during sniffing. Based on this historical record, modern anatomical references now reveal the detailed internal structure of the dog's nose [220,221].

The canine external nares are shown in Figs. 11(a) and 11(b). Negus [194] first noted that mammalian nostrils give direction to the inspired air, then Stoddart [3] found that the nasal swell body (*alar fold*) just inside the nostril controls the direction of the air-flow into the nose. The high-speed video observations underlying Figs. 11(a) reveal the opening of an "upper orifice" above the alar fold during the inspiration phase of sniffing. Upon expiration, however, this pathway closes, the nostril flares [Fig. 11(b)], and air is ejected ventrally and laterally through the midlateral slits (*nasal sulcae*) [47].

Figure 11(c) [62] shows the upper and lower airway (*dorsal* and *ventral meatus*) leading from the external naris into the maxilloturbinate region of the canine nasal cavity. The external naris motion just described, driven by several olfactomotor muscles [220], causes the dorsal meatus to receive inspired air and the ventral meatus to deliver the spent air for expiration. The dorsal and caudal direction of the inspired air channels it directly toward the olfactory region of the dog's nose.

The expired air jets, on the other hand, are vectored by the shape of the "nozzle" formed by the alar fold and the flared nostril wings (*nasal ala*), Fig. 11(b). Thus the external naris acts as a variable-geometry flow diverter [47]. This has three advantages: (1) it avoids distributing the scent source by expiring back toward it; (2) it stirs up particles [Fig. 1(b)] that may be subsequently inspired and sensed as part of the olfactory process; and (3) it entrains the surrounding air into the vectored expired jets [Figs. 1(b), 1(c), and 12], thus creating an air current toward the naris from points rostral to it. This "ejector effect," shown in Fig. 12, is an aid to olfaction: "jet-assisted olfaction," in other words.

We also observed that the "reach" of the canine nares during sniffing is up to about 10 cm, though the dog always narrows this distance essentially to zero if allowed. Since the nostril inflow is omnidirectional (Sec. 2.4), the detailed spatial distribution of a

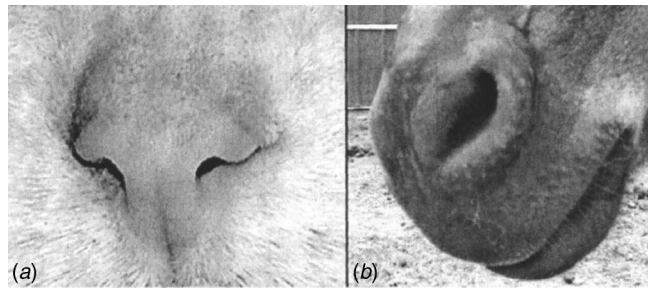


**Fig. 12** (a) Schlieren image revealing the “ejector effect” of expired air jets during canine sniffing that draws in air from a warm forward scent source and (b) diagram illustrating the region of expired jet impact upon a ground plane (dotted line) and the induced airflow caused by jet entrainment [47]. See also Fig. 1(b)

scent source is only discernable when the nose is brought into very close proximity with it [47]. Canines [218,222] and other macrosmatic animals [223,224] need to “read” detailed olfactory “messages” such as scent overmarks left by other animals. Their ability to do this requires *proximity sniffing*, and is analogous to our visual reading of text. So, in order to properly interrogate chemical traces it really is necessary for a dog to poke its nose into everyone’s business.

Proximity, however, is not required in air scenting of chemical traces borne by plumes, another canine specialty [125]. Steen et al. [219] discovered that an air-scenting bird dog can maintain continuous nasal inspiration for up to 40 s. They propose that open-mouth respiration produces a low nasopharyngeal pressure to induce this continuous olfactory airflow.

Negus [194] suggested that macrosmatic mammals sight down their long snouts to focus upon food they are about to seize. We observed, however, that a dog approaching a scent source on the ground first scanned its vicinity [47]. Instead of aiming directly at the source, the nose was instead lowered to close nostril proximity with the ground before reaching the source [Fig. 12(a)]. Then the dog advanced toward the scent source, pausing when the nostrils were directly overhead, sniffing all the while. Often the dog



**Fig. 13** External nares of (a) a domestic shorthaired cat and (b) a burro, *Equus asinus*, photo by L. J. Dodson

scanned past the scent source, allowing the expired air jets to impinge directly upon it. Finally the nose returned to a position directly above the source for a few more sniff cycles. This behavior promotes visual as well as olfactory inspection and provides a local survey of the spatial scent distribution. It also disturbs particles in the vicinity of a scent source by the impingement of the expired air jets.

Syrotuck sees this environmental disturbance during sniffing as an aid to olfaction [125]. Morrison examined the uptake of fine ( $0.5\ \mu\text{m}$ – $5\ \mu\text{m}$ ) charcoal powder inside the dog’s nasal cavity following sniffing [62]. Particles were found predominantly in the anterior nasal cavity ventral to the maxilloturbinates. However, upon vigorous sniffing, particles reached as far into the nasal cavity as the olfactory ethmoturbinates. Moist mucosa are important here, since moisture is the solvent that carries both vapor and particle-borne chemical traces to the olfactory receptors [125]. When the dog’s nose is wet and cold, it can act as both a particle and a vapor trap.

Finally, the warmth of the expired canine air jets may act to volatilize latent chemical traces on surfaces. Many biological odors vaporize at or near body temperature, and the vapor pressure of TNT, for example, increases by a factor of 4 between 20 and 30°C [225].

**4.3.2 Cat.** The cat’s nose, Fig. 13(a), is in stark contrast with that of its canine relatives. Though macrosmatic, the entire *Felidae* family (ocelot, domestic cat, panther, puma, lynx, Asian leopard cat, caracal, and bay cat [226]) appears to lack the variable geometry and multifunctionality of the canine external nares. While a proper aerodynamic study has not been done, almost no nostril motion is observed when the domestic cat sniffs. Clearly a sophisticated canine-type nostril is not a prerequisite for olfactory ability, even among carnivores.

**4.3.3 Horse.** The horse *Equus caballus* and its relatives are odd-toed ungulates and prey animals. They have wide oval nostrils and long straight nasal passages allowing a high respiratory airflow rate while running, when dilator muscles cause the nostrils to flare. The nostrils contract upon expiration to produce prominent ventrally-expired jets that are visible due to moisture condensation in winter. Horses sniff to identify food, kin, and sexual status, and to acquire olfactory warnings of the predators that they suspect are lurking behind every bush. Unlike dogs, horses and their relatives have dry rhinaria.

**4.3.4 Pig.** The swine nose is spade shaped and has several uses. Moulton [207] considers it to be a “chemotactile” organ. Like elephants, pigs use their snouts for tasks that their feet cannot accomplish. The pig nostril inlet orifice, Fig. 14(a), is well rounded according to the discussion of Sec. 2.4. In fact, it is a simple flanged bellmouth inlet with a hint of an inverted-comma shape.

**4.3.5 Cow.** Like pigs, cows are members of the great ungulate prey order *Artiodactyla*, which also includes the antelope, deer,

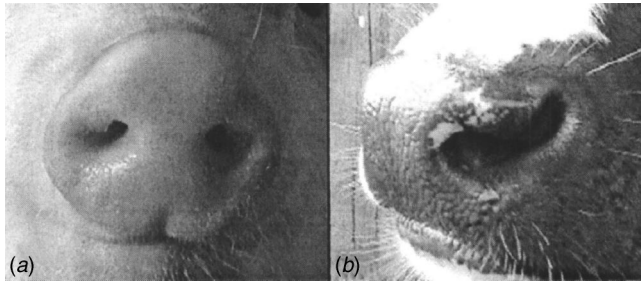


Fig. 14 External nares of (a) a piglet and (b) a calf, photos by L. J. Dodson

goat, sheep, camel, caribou, moose, giraffe, and hippopotamus. Many of these animals have opposed, laterally oriented, inverted-comma-shaped nostrils as seen distinctly in the cow, Fig. 14(b). The inverted-comma nostril shape, upon constriction, narrows the air passage to a crescent [194]. This suggests some distant connection with the canine midlateral nostril slit, but in fact none of the prey animals has a nostril of sufficient mobility to modulate the airflow in a canine fashion. At least two ungulates, though, have variable-geometry nostrils for other purposes: The camel's nostrils close to keep out the sand, while the moose's nostrils close underwater [227].

**4.3.6 Bat.** The bat's naris is some two orders of magnitude smaller than that of the *Bovidae* just discussed. The insectivorous Little Brown Bat, *Myotis lucifugus*, common in North America, has broad nostrils with an inverted-comma shape. The elaborate nose "leaves" of some bat species are for ultrasonics, though, not olfaction. The bat's forwardly oriented nostrils aid olfaction in flight by ram-air sampling. Some bats can discern the edibility of insects they pursue by using "wake olfaction" [3].

**4.3.7 Elephant.** The elephant's trunk is a unique and celebrated multipurpose chemotactile organ. Elephants are quite macrosmatic even though their external nares and olfactory mucosa are separated by a considerable length of trunk. The trunk not only explores proximity scents but also acts as a periscope for directional air scenting [228]. Other trunk functions include grasping food, drinking, spraying water, respiration, greeting, hand-like tactile operations, trumpeting, and fighting [228]. Its cross section shows two oblong central nasal tubes formed of connective tissue and lined with mucosa. These open into the elephant's nasoturbinate at their posterior extremity [229]. As noted earlier, the elephant is a natural prototype for hand-held wand-type sniffer probes.

**4.3.8 Rabbit.** Glebovskii and Marevskaya [230] found that rabbit nostril motion, driven by the narial muscles, is directly connected with high olfactory brain activity. Inspiration is accompanied by nostril dilation, reducing airway resistance. "The tip and *alae nasi* move upward while the floor of the nostril sinks." A sharp rise in airway resistance then signals the onset of expiration. Glebovskii and Marevskaya further describe the rabbit narial muscles as "the propiomotor apparatus of the olfactory analyzer." Zwaardemaker mirror tests by Bojsen-Møller and Fahrenkrug [31] showed that expired air is directed ventrally and laterally in the rat and rabbit, as in the dog. The rabbit's nose, Fig. 15(a), resembles a cap over a vectored duct. Little else is known about the mobile nostril function of this macrosmatic mammal. A rabbit nostril aerodynamics study along the lines of [47] is certainly called for.

**4.3.9 Human.** Our nose is retrograde and macrosmatic, but heavily investigated. Sources on human nasal airflow include both popular [231] and scholarly [232] accounts, historically significant works [2,233], and recent review articles [5,234–236]. The decline of the primate olfactory genes leading up to humankind is

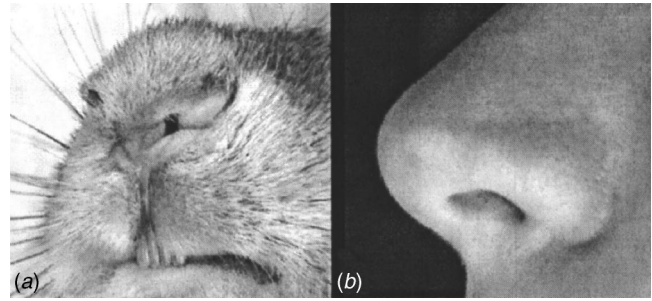


Fig. 15 External nares of (a) cottontail rabbit, *Sylvilagus obscurus* and (b) human, *Homo sapiens*

also well documented [237,238]. Though less elaborate than the other animal noses, our nose [Fig. 15(b)] is still sensitive, interesting, and comparatively well studied.

Section 3.2.1 described the rising human boundary layer and its particles. We stand erect and our nostrils are directed downward so they inevitably sample this boundary layer, unlike the case of a four-legged animal with a long snout. Expired air jets are directed ventra-rostrally and are usually fast and turbulent, allowing almost no rebreathing of the exhaled air [239].

Keyhani et al. carried out a steady laminar Navier-Stokes solution of airflow into the human nasal cavity with  $Re=610$  based on the external-naris hydraulic diameter [240]. Results show that the internal path taken by inspired air depends upon its entry point at the nostril, with only the anterior tip of the orifice supplying the air that eventually reaches the olfactory epithelium. Because of this, 90% of the inspired air is not sampled for olfactory content, as already known from work cited earlier. The flowfield computed by Keyhani et al. was then used to derive an olfaction model [240] that yields the odorant mass flux sensed by the nose and addresses some of the questions raised in Sec. 2.3.

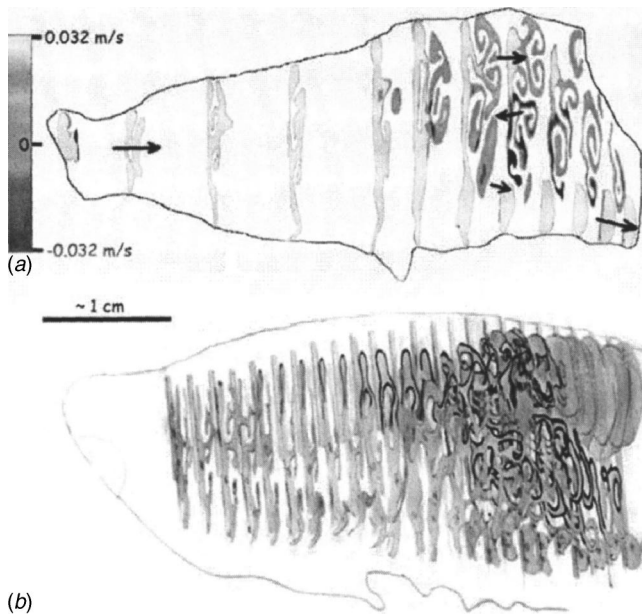
Subramaniam et al. [16] did a similar CFD solution at  $Re=1360$  for an inhalation toxicology study. Here, recirculating flow in the nasal vestibule and nasopharynx produced a more-intricate overall flow pattern with even less airflow to the olfactory region.

*In vitro* flow visualization experiments on human nasal aerodynamics were described in Sec. 2.1. The appearance of turbulence in some of the results [241], however, raises questions about the laminar-flow CFD simulations just described. A low nostril inlet  $Re$  does not guarantee laminar flow throughout, especially in such contorted passages, but no turbulent or unsteady CFD results are currently available.

Finally, Sobel et al. [242] study the neurophysiology of human olfaction *in vivo*, finding that it is not the movement of nose muscles that primes the human brain for olfaction, but rather the rush of air up the nose. Differences in the airflow rate between nostrils cause each nostril to be sensitized to different odorants, so each nostril conveys slightly different olfactory information to the brain [242]. Further, sniffing for a scent and actually smelling it activate different brain regions [243], and sniffs are modulated in response to odor content, higher odorant concentrations inducing lower-volume sniffs [63].

**4.3.10 Rat.** The laboratory rat holds a unique position in science. For reasons similar to those given for humans, we know a lot about rats although, unlike humans, rats are macrosmatic. Lab rats have perhaps 1500 olfactory genes of which only some 20% are "junk" DNA [237].

Human carcinogen response is assessed by two-year, 1/2 million-dollars-each rat studies carried out by the U.S. National Toxicology Program [112]. Extrapolation of the results from lab rats to humans to assess human health risks is problematic, though, given large interspecies differences in nasal respiratory physiology and airway anatomy [16]. Inhalation toxicology nevertheless uses live rats or their nasal molds to measure the depo-



**Fig. 16** (a) CFD solution of airspeed in the F344 rat's nasal cavity [53,247], courtesy J. S. Kimbell and (b) sectional anatomy of an albino rat's nasal cavity with darkened olfactory epithelium [248], courtesy J. S. Kauer

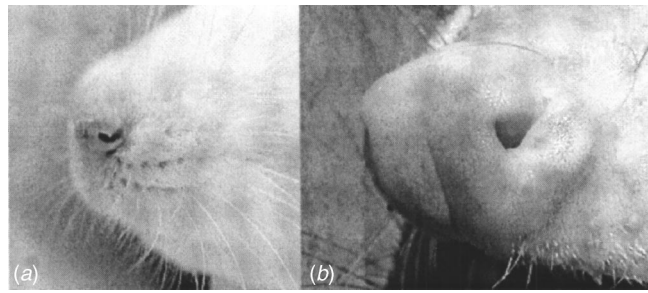
sition of respirable particulates [244–246]. The albino lab rat is thus the key to determining safe levels of human exposure to toxic inhalants.

A CFD solution of the Navier-Stokes equations for the airflow in the passages of a lab rat's nose yields some insight into this process, Fig. 16(a) and [53,247]. As in dogs and humans, most of the inspired air bypasses the rat's olfactory zone and exits via the nasopharynx. However, the airstream that actually reaches the sensory ethmoturbinates enters dorsally, reverses direction medially, and finally exits ventrally through the nasopharynx as indicated by arrows in Fig. 16(a). Of course CFD only approximates the convoluted geometry of an actual rat's nose, Fig. 16(b) [248].

Like the rabbit and dog, the rat has active, variable-geometry external nares. In both ground and air scenting the nose pitches and the nostril twitches [249]. In some rats the external nares flare and the nose hairs (*vibrissae*) move rhythmically, projecting during inspiration and retracting during expiration [3]. The inverse-comma-shaped narial orifice directs expired airflow ventrally and laterally, causing relatively little anterior air exchange [250] and forming two fan-shaped areas of condensation on the Zwaardemaker mirror, Fig. 1(a) [31]. A bout of sniffing grows to yield a maximum airflow rate at its conclusion. Youngentob et al. suggest a “sniffing index” describing many characteristics of the rat's sniffing strategy [251]. During a discrimination task, rats suddenly switch from a low (2–5 Hz) sniffing rate to a high rate of 8 Hz–10 Hz for unknown reasons [252]. Here, too, a proper aerodynamic study of external nostril airflows is needed.

**4.3.11 Opossum.** While dogs and cats diverged from a common ancestor some 50 million years ago, the opossum has not changed significantly in 90 million years. He is both ancient and modern, since he continues to compete effectively with placentals today. His chief current challenge is to stay out of the road.

The opossum has the long, well-equipped snout and multiple turbinates of a macrosmatic animal [194]. The external naris aperture, Fig. 17(b), is laterally oriented and not obviously variable in geometry, although there are no known studies of it. Moulton [207] notes that olfactory structures are most prominent among older animals like the opossum, not in the higher primates and



**Fig. 17** (a) External nares of a Sprague-Dawley lab rat provided by M. J. Kennett, Penn State University and (b) external nares of the opossum *Didelphis virginiana*

aquatic mammals.

**4.3.12 Fish.** Here we leave the mammalia to consider other vertebrates, many of whom have simple immobile external nares compared to those of the dog, rabbit, and rat. Like mammals, fish need their sense of smell for habitat and kin recognition, food, reproduction, and predation avoidance. Detailed accounts of fish olfaction are given by Negus [194], Kleerekoper [253], and Stoddart [3].

The key issue in fish olfaction for present purposes is its separation from the respiratory gill flowfield. Anterior and posterior naris holes or slits supply through flow to a chamber filled with *lamellae* that provide a large sensory surface area (see also Sec. 5.3.1). To overcome the internal olfactory pressure drop, fish use either passive or active water circulation. The former requires relative motion between fish and water, where sometimes a ridge or scoop just aft of the anterior naris assists olfaction by recovering dynamic pressure there while the flow vents to local static pressure downstream. Active olfactory water circulation may be driven by cilia or may occur as an accessory to respiratory jaw motion.

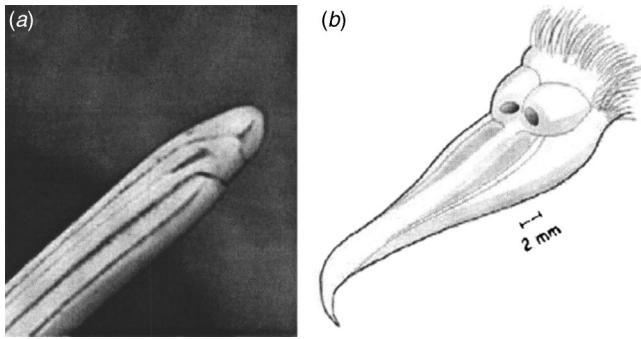
Some fish feature highly specialized naris adaptations. *Polypterus bichir*, for example, has a fluted Pitot-tube-like anterior naris extension [3], while in moray eels both anterior and posterior nares may be extended. Some *Tetraodon* species have their entire olfactory apparatus out on a stalk [253].

Shark olfaction is almost as adept as their ability to generate interest and fear in people. The Great White and many other shark species have flush anterior nares located on the underside of the snout, feeding water to an olfactory chamber of spectacular sensitivity. Sharks track prey wakes [254] by the chemical plume tracing methods described in Sec. 3.3.3. Here is yet another opportunity to study, for the first time, the fluid dynamics of shark olfaction.

**4.3.13 Birds.** Birds sometimes have only rudimentary sniffing apparatus [3], but in other species olfaction is key to their feeding and nesting behavior, and even to navigation. Airborne sniffing, for example, allows scavengers like the turkey vulture to locate their malodorous meals. Atmospheric trace gases also provide olfactory navigational cues to some birds [255], the young learning prevalent trace gradient patterns at home [256] and then using this knowledge to navigate by olfactory detection of natural airborne volatiles [257].

Many birds have simple round or oval nostril holes in the posterior region of the beak. They also have turbinates [209] that function much like those of mammals. Sometimes the naris is covered by skin or feathers, and often the anterior turbinate protrudes into the orifice [195]. Such obstructions suggest that these species are not keen sniffers.

Only one bird, the highly specialized kiwi, has its nostril orifice at the tip of a long beak like a wand-type sniffer. It probes the soil for worms, so a posterior naris location would be worthless. The beak tip, Fig. 18(a), consists of an anterior probe, a longitudinal



**Fig. 18** (a) Close-up image of the Great Spotted Kiwi's beak tip, copyright Chris Smuts-Kennedy, reproduced by permission. (b) The upper beak of the tube-nosed Dove Prion, *Pachypytia desolata*, redrawn from [258]

slit nostril, and a lower mandible. One wonders if naris plugging by soil and olfactory signal deposition in the long nostril tubes are worrisome to the macrosomatic kiwi.

The *Procellariiformes* [195,258] are seabirds that include petrel and albatross species, all with highly developed olfactory systems and distinct tubular nostrils. They can follow the trace odor of a food source for many km over the ocean. Following the discussion of airborne sampling in Sec. 3.3.1, it is hard for a fluid dynamicist to see such nostrils, Fig. 18(b), without thinking "Pitot tubes." These nostril protrusions recover the impact pressure or velocity head  $1/2\rho U^2$  during flight, automatically providing a pressure boost to overcome losses in the olfactory system, and doing so without additional effort from the bird. Pennycuik also suggests a related Pitot-tube function—that of an airspeed indicator—allowing the bird to sense and take advantage of gust energy in the separated flows downstream of oceanic wave crests [259]. *Procellariiformes* tap this unlimited energy source in order to soar almost effortlessly over long distances.

**4.3.14 Reptiles and amphibians.** Reptiles and amphibians generally have rudimentary olfactory apparatus. Most have only a simple pair of external naris holes flush with the front or top of the head [3]. Olfactory power varies among species, though, and some lizards, snakes and crocodilia are macrosomatic. Waterproof naris closure and "snorkel" nostrils adorn the newt, crocodile, salamander, and frog [3,260]. Frogs even have flap-separated anterior and posterior olfactory regions suited for sniffing in water or air, respectively [237].

Not much is known about dinosaur olfaction, but Witmer [261] places the *T. rex* external naris well forward of its usually-depicted location in order to provide room for a more significant internal olfactory apparatus. Also *Rhomaleosaurus* is believed to have had National Advisory Committee for Aeronautics (NACA)-scoop-type naris inlets inside its mouth, venting externally [262].

**4.4 External-Flow Noses of the Invertebrates.** Here the sensor chamber of the vertebrates is turned inside out: no chamber at all, just sensor-bearing antenna stalks extending into the surrounding fluid. Treelike sensor structures have evolved in both air and water to present a large surface area for olfaction. The fluid dynamics of these *aesthetascs* has received a lot of recent attention [93,170,176,196,263].

For brevity we consider here the morphology of only a few invertebrate sniffers from the phylum *Arthropoda*.

**4.4.1 Crustaceans.** Lobster "sniffing" was introduced in Sec. 2.7 in terms of diffusion and in Sec. 3.3.3 in terms of chemical plume tracing. Lobsters have twin antennae with lateral flagella bearing fine sensory aesthetascs, Fig. 19. There are differences in species [41], but in general the antennae are flicked in order to sample the environment [92,93]. This sniffing behavior is gov-



**Fig. 19** Lateral flagellum of one antennule of the clawed lobster *Homarus americanus*. Proximal diameter shown is 1.4 mm. Hairlike projections are aesthetascs and guard hairs (out of water and in disarray). See [92] for electron microscopy images

erned by the aesthetasc Reynolds number  $Re$  which determines "leakiness," i.e., how much water passes between them. This  $Re$  tends to be near unity, so the lobster can sample with a fast downstroke and hold the signal with a slower upstroke [176,264]. Péclet numbers are large for these motions, but diffusion acts when the antennae are still.

Similar principles apply to other crustaceans, including the crayfish, crab, and Mantis shrimp [41,65,177,196]. These sought-after species take advantage of zones of high mean flow speed, which increases turbulence and degrades a predator's ability to track a chemical plume. Thus fast flows provide a hydrodynamic refuge from olfactory-mediated predation [179].

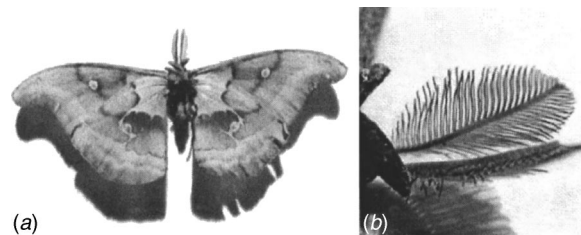
**4.4.2 Insects.** Chemical plumes are as important to insects in the air as to crustaceans underwater [168,265,266]. Moths tracing a pheromone plume are the classic example. The same Reynolds number effect on the apparent porosity of branched antennae [90,267,268] arises, though the comblike moth antennae do not flick and are spectacularly different in appearance than those of the lobster (Fig. 20). Some moths respond to pheromone signals by flapping their wings to induce airflow through their antennae without flying [268], an aspect of insect behavior that has already attracted biomimicry [182].

Here briefly consider mankind's worst enemy, that supreme terrorist and chief vector of biological warfare, the mosquito (Fig. 21). With a human death toll of over one million/year, mosquitoes as killers easily outrank all the worst human tyrants combined [269].

Mosquito host location is known to be an insect-sniffing and chemical-plume-tracing issue [168,270,271]. Humans give off a variety of *kairomones*, chemical signals ( $CO_2$ , lactic acid, etc.) that attract mosquitoes [272]. The thermal convection currents produced by vertebrates carry these trace chemicals [270,273], and mosquitoes fly upwind to locate their sources [180]. *Anopheles gambiae*, for example, flew an upstream zigzag path in a wind tunnel odor plume [272]. In another study, smelly human feet were a noteworthy mosquito attractant [274].

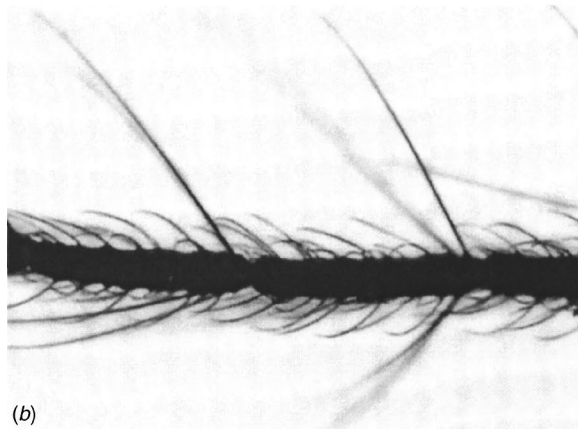
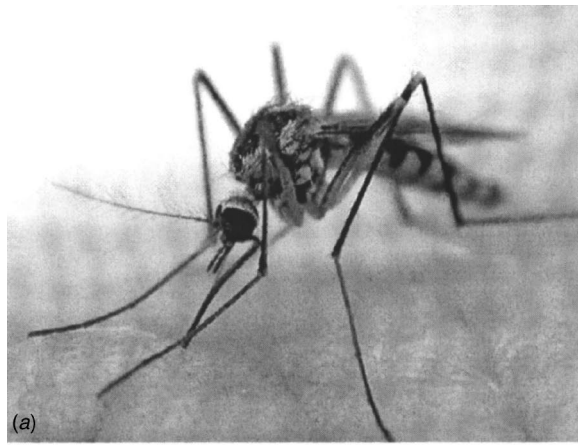
An important human goal is to interrupt mosquito-host interactions, thus inhibiting the spread of disease [275]. The host-location sensilla are on the mosquito antennae, Fig. 21, and palps [272,276,277]. At normal flight speed a 1- $\mu m$ -diameter mosquito sensillum hair has a Reynolds number of about 0.06.

An outsider needs extra caution around this intricate topic. There are many mosquito species with different behaviors, for example [272]. Nonetheless some fluid dynamics seems to be missing here, namely: (1) a proper understanding of the human



**Fig. 20** (a) Giant silkmoth moth, *Antheraea polyphemus*, wingspan 8 cm and (b) closeup of feathery antennae





**Fig. 21 (a) Mosquito feeding on a human hand. Courtesy Philip Myers, <http://animaldiversity.ummz.umich.edu>. One antennal flagellum is visible. (b) Microgram of a mosquito antennal flagellum, about 20  $\mu\text{m}$  in diameter, showing two complete segments, the long *sensilla chaetica*, and the numerous shorter *sensilla trichodea*, photo by J. M. Listak**

thermal plume and wake behavior (Secs. 3.2.1 and 6.3.3) and (2) a knowledge of the mosquito's flight envelope and limitations. For example, in one popular book on mosquitoes the human scent plume is said to be heavier than the surrounding air [269]. Normal flight speed is quoted at 1 m/s and maximum speed at 1 1/3 m/s [269,278], yet there is little information on the inhibition of mosquito bites as a function wind speed or host motion. Finally, although our knowledge of insect aerodynamics has benefited greatly from studies of the innocuous dragonfly, where are the parallel studies of mosquito aerodynamics? The mosquito appears to be a fragile insect, all rickety and strung out like a Wright Flyer. If we knew more about her aerodynamics, it might suggest ways to push her beyond her flight envelope.

**4.5 Directional Olfaction.** Von Békésy claimed directional odor perception if as little as a 10% concentration difference was presented to the left and right human nostrils [279]. Later research questioned this [280], but there is still considerable evidence that at least some animals practice and depend upon "stereolfaction" [3,242,281]. In addition to *chemotaxis* and *anemotaxis*, described earlier, the terms *klinotaxis*, swinging the head from side to side, and *tropotaxis*, stereolfaction via widely-separated naris inlets, are used.

Stoddart [3] suggests that nostril adaptation goes with neck stiffness, and that stiff-necked fish need tropotaxis more than supple-necked land species. Tube-nosed bats appear to use tropotactic olfaction in flight, where turning the head would produce unwanted aerodynamic forces. Dogs practice klinotaxis, moving

their heads while tracking or scenting, and probably also anemotaxis based on the differential wind cooling of their wet noses [125,218]. Moulton [207], on the other hand, notes that the close narial spacing of many mammals does not apparently provide a sufficient lateral signal difference to discern an odor gradient by tropotaxis. The myth of tropotaxis due to the widely spaced nares of hammerhead sharks was debunked by Kajiura et al. [282], who found that an anterior groove on the shark's cephalofoil integrates the olfactory input, thus providing no more tropotactic separation than that of any other shark species.

Finally, Atema [42] demonstrated that the lateral separation of lobster antennae is sufficient for "eddy chemotaxis" in turbulent odor plumes. He also found that the sharpness of odor peaks in passing eddies can provide "odor landscape" information about the lobster's location relative to the plume's source.

## 5 Artificial Olfaction

**5.1 Artificial (Electronic) Noses.** Artificial noses are devices featuring several nonspecific odorant sensors interrogated by a pattern-recognition system in order to identify a broad range of odorants [9]. This definition excludes specific sensors like gas leak detectors and mass spectrometers, but these will also be considered later. Still very much a work-in-progress since they were introduced a few decades ago, artificial noses already augment limited human olfactory skills by being less subjective, and they may even supplant the trained canine sniffer someday by having similar sensitivity but being willing to work longer hours.

**5.1.1 Overview of current artificial noses.** Gardner and Bartlett [9] give a brief history of electronic noses and a discussion of current commercial devices. Similar overviews are found in [283,284], while Yinon [285] summarizes "e-noses" for explosive detection. Artificial noses currently have nonspecific sensors based on a variety of principles including quartz microbalances, surface acoustic wave (SAW) technology, capacitance, metal oxide semiconductors, calorimetric or amperometric sensors, and photopolymers.

Most of the present commercial devices are ponderous benchtop analytical instruments that do not sniff and are not considered further here. A few portable or handheld noses deserve further attention, but most of them also lack any real ability to sniff. Only the Smiths Detection Cyranose [286] has both an internal sampling pump and a wand-type inlet with a flared end that can be considered a sniffer. The Applied Sensor VOCcheck and Microsensor Systems Vaporlab handheld e-noses have pumps but no sniffers (apparently only fittings are provided for direct connection to an odor source).

The Nomadics "FIDO" artificial nose can be either handheld or wand-mounted (for landmine detection) [287]. Ambient air is drawn through the sensor, after which there is a clean-air purge. A similar prototype device employs a small vacuum tank to sniff air at ground level [288]. The Z-nose [289] uses SAW and gas-chromatograph technology in a hand-held sensor with a 10 s sampling time. Gelperin's e-nose [290,291] inhales the air surrounding an object through a perforated platform located over a sensor array.

The Tufts Medical School/CogniScent Inc. Scentinel [6,292,293] is not yet a commercial device, but is nonetheless notable for the biological inspiration behind its sensors and its pattern matching [294]. Moreover it is a true sniffer with a snout, a flanged inlet and a through-flow sensor chamber. It can even inhale and exhale like an animal.

**5.1.2 Related nonartificial-nose handheld detectors.** A popular and useful nonartificial-nose detector for explosives, drugs, and chemical agents is the ion mobility spectrometer or IMS [295,296]. At least two commercial handheld devices are available, the GE Security VaporTracer, Fig. 22, and the Smiths Detection Sabre 2000. Both have internal pumps to acquire air samples,



**Fig. 22 The GE Infrastructure Security VaporTracer sniffing a briefcase**

but the volume of air that an IMS can directly accept is only some ml/min. A third IMS device, the Implant Sciences Quantum Sniffer, takes a different approach discussed in Sec. 5.2.4.

The Sandia Microhound [297] uses a micro-IMS and a SAW sensor, and inhales air through a flanged inlet. The Mesosystems Biocapture [298] impacts and liquefies samples for analysis, but details of its sniffer are not available. Finally, two Thermedics Inc. patents [299,300] describe handheld shrouded sampling guns that apply heat and air-jet puffers to surfaces, then inhale air across a preconcentrator. These devices are without any known commercialization.

*5.1.3 Desired characteristics of sniffers for artificial noses.* Ideally an optimum sniffer ought to:

1. Have sufficient “reach” to acquire the desired explosive trace signal without physical contact,
2. Localize the scent source (except for those special sniffer types designed to sample broad areas like the sides of vehicles),
3. Display immunity to ambient conditions, especially the breeze,
4. Have simplicity, mobility, light weight, small size, and reasonable power requirements, and
5. Have the ability to disturb surface environments enough to dislodge and collect particles as well as vapor traces.

## 5.2 Airborne Trace Sampling for Artificial Olfaction.

*5.2.1 Headspace sampling versus sniffing.* In most benchtop instruments of analytical chemistry, including the majority of commercial e-noses, the saturated vapor above a sample in a container is drawn by carrier gas through tubing into the input of the instrument. This is headspace sampling [301], and while it is essential in laboratory practice, it is distinct from aerodynamic sampling—sniffing—as defined here. Few animals have the luxury to squat on a lab bench, have odor samples delivered to them, and suck the samples through a straw.

*5.2.2 Particles versus vapor.* There is a controversy in explosive detection circles over whether one actually detects particles or vapor traces or both. A key paper on this topic is Davidson and Stott [302], who draw a distinction between volatile explosives (vapor pressure higher than nitroglycerin) and nonvolatiles: vapor detection of nonvolatiles usually depends upon solvents, impurities, or breakdown products, whereas the vapor of volatile explosives like tri-acetone-tri-peroxide (TATP) is directly detectable. Such volatile vapors are readily adsorbed, however, by such things as the packing materials found inside cargo containers.

In general we should be ready to sniff and detect both particles and vapors, since they provide complimentary information about the odorant source. Particle sampling is the more difficult of the two, but it has the advantages of larger signal levels and of indicating the actual chemical species, not just its vapor byproducts.

Approaches to resuspend particles from surfaces include mechanical agitation and vacuuming, swabbing, vibration, thermal

desorption, shock waves, pulse-pressurization, and jet puffers (Sec. 2.5). Wrapping and handling an improvised explosive device, for example, is likely to generate a particle field that may be detectable even if the vapor of the explosive is not [303,304].

Griffy’s calculation [94] was mentioned in Sec. 2.7 with a caution about giving up on vapor detection. Vapor diffusion is a slow process, but some sniffers can get in such close proximity to an odorant source that they can get a good sniff even so. Further, vapors are readily transported in thermal plumes [48].

On the other hand, given the extremely low vapor pressure of explosives like pentaerythritol-tetranitrate (PETN) and RDX, it is certain that particles, however small, play a role in the detection of these substances by sniffing. Nonvolatile explosives strongly adsorb to solids [305], including the ever-present airborne particles in the human thermal plume (Sec. 3.2.1).

*5.2.3 Preconcentration.* Preconcentration and the “impedance mismatch” were introduced in Sec. 2.3, while impactors were described in Sec. 3.1. How it is done in practice, though, deserves a little further elaboration.

Traditional preconcentration methods of analytical chemistry involve passing an air sample through a permeation tube filled with a sorbent material, such as activated charcoal, silica gel or Tenax™. That material is subsequently thermally desorbed to release trapped chemical traces [306–309]. Personal samplers, Sec. 3.2.2, often work this way. But given the small size and high pressure drop of a typical sorbent tube, this approach is slow and ineffective for high-flow-rate sniffing.

Membrane filters can serve the same purpose as permeation tubes and can be desorbed in a similar fashion [13,101,310], but are likewise not suited for high flow rates.

A third approach, more adaptable to rapid sniffing of larger air volumes, is to collect the trace odorant on a metal surface in a flow-through preconcentrator [310–313]. Depending upon the odorant, various treatments can be applied to the metal to enhance molecular or particle deposition. The metal can then be heated electrically to quickly desorb captured traces. A secondary carrier gas flow is needed during desorption, when the main airstream either stops or is shunted away. Cold metal surfaces especially attract trace chemicals like explosives, but moisture condensation is an associated problem [314].

When the desired airborne trace material is in particulate form, impactors or cyclones (Sec. 3.1) make suitable preconcentrators. For example, biological pathogens like spores and bacteria are usually impactable, as are explosives or chemical agents attached to human skin flakes or textile fibers. Virtual impactors preconcentrate such particle-laden airstreams by discarding most of the airflow while keeping the particles.

*5.2.4 Jet-assisted olfaction.* One of nature’s lessons (Sec. 4.3.1 and Figs. 1 and 12) is to put exhaled air jets to work assisting the sniffing process. Thus the dog and probably the rat and rabbit can disturb surface particles, inhale them, and desorb odorants from them in the nasal mucosa—a natural preconcentration system.

How can we use this knowledge in a man-made sniffer? Since respiration is unnecessary, auxiliary air jets adjacent to the sniffer inlet are required to disturb surface particles, as first suggested by McGown, Bromberg, and Noble [299]. Beyond that, though, it was also shown in Sec. 4.3.1 that the dog’s exhaled jets produce an ejector effect that can improve the reach of the sniffer. Extended reach is just as important for man-made sniffers, since proximity sniffing is not always possible and is occasionally even dangerous.

At least two schemes are available to extend the reach of a sniffer, the first borrowed from the field of ventilation. C. P. N. Aaberg [315] invented an elegant inlet reach extender using auxiliary jets, Fig. 23. The central inlet, facing downward in the figure, takes in flow rate  $Q_c$  while an additional airflow  $2Q_j$  at above-ambient pressure discharges laterally forming turbulent jets. The

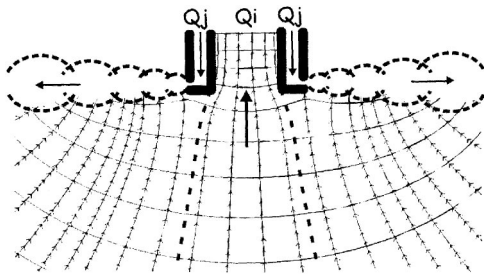


Fig. 23 2D potential-flow simulation of an Aaberg inlet

jet entrainment makes this device appear to be a much larger inlet with an extended reach, but only the central streamtube between the vertical dashed lines is actually taken into the inlet. Thus the otherwise-omnidirectional potential-flow inlet is effectively focused toward the forward direction by jet assistance.

The ventilation community has embraced this concept for local fume exhaust (usually axisymmetric rather than planar as in Fig. 23), and several studies are reported [316–319]. The ratio of the jet to inlet momentum flux is found to control the reach, which can be several times that without jets [320]. This jet assist is not free, but is well worth it in the exhaust of welding fumes, where the extended reach avoids having the inlet in the welder's face.

The Aaberg principle has never been applied to chemical trace sniffing and is suggested here for the first time. It has the advantage that the large volume of air that must be moved in order to achieve a long reach is not all inhaled, thereby reducing the pre-concentration chore.

The second jet-assisted sniffer scheme is that of Motchkine, Krasnobaev, and Bunker [96]. Here the auxiliary jet flow is passed through tangential nozzles or vanes to produce swirl between the inlet (right) and the surface being sampled (left) in Fig. 24. On the centerline of this "cyclone" a sampling orifice withdraws a flow rate  $Q_s$ . According to [96] "The cyclonic motion...creates a tube consisting of a wall of moving gas that behaves like an extension of the tube that formed the external sampling orifice." No mention is made of a vortex core, but data are shown indicating a favorable pressure gradient along the centerline from the sampled surface to the sampling orifice over separation distances up to 15 cm. This jet-assisted inlet is used in the Implant Sciences Quantum Sniffer, a commercial IMS detector that was developed under U.S. Navy funding.

**5.2.5 Isolation from ambient wind.** All of the sniffing inlets discussed thus far, whether jet assisted or not, are subject to disruption by a lateral breeze. The effect is shown qualitatively in Fig. 25, where a mild breeze interrupts the sampling of a boundary layer by a simple flanged inlet [47].

In the animal world, the only remedy for this is proximity: If your nostrils are touching the sampled surface, then the wind is

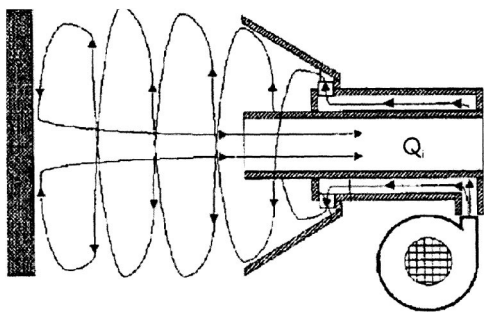


Fig. 24 Diagram of a cyclone sampling nozzle for an ion mobility spectrometer, from [96]

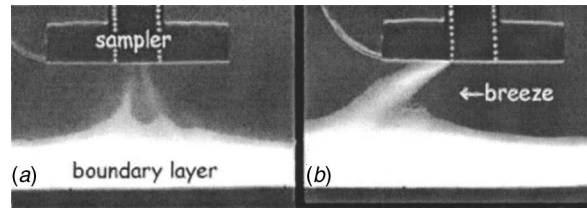


Fig. 25 Schlieren photos of a flanged inlet sampling a thermal boundary layer (a) in still air and (b) with a light lateral breeze from the right [47]

not an issue. However, practical considerations require man-made sniffers to have a finite standoff distance and no hard contact (especially in landmine detection).

No real solutions to this problem are available, just a few ideas. Baturin, [17] Chap. 6, for example, describes a method to estimate inlet streamlines in a crossflow. No remedy is given other than increasing the inlet suction. Likewise shrouded probes are effective against cross flows in flight and wind tunnels, Sec. 3.3.1, but are not a cure for the present difficulty.

One approach that might work is a "soft" shroud made of rubber, brush fibers, screen, or porous filter material. To succeed, the lateral pressure drop across it must balance the dynamic pressure of the crossflow. Experiments by Cant, Castro, and Walklate [321] reveal that high-porosity screens have little effect, whereas low-porosity screens act like solid surfaces to the crossflow. Near 50% porosity, interesting things happen.

An air curtain [322] has also been suggested for this purpose. It might succeed if its entrainment can be made to serve the purpose of jet-enhanced olfaction described above; otherwise it is likely to exacerbate the problem.

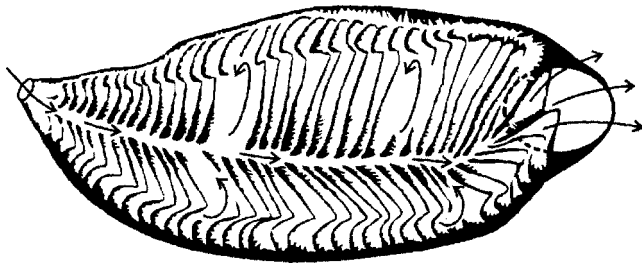
In any case, aerodynamic sniffer isolation from the effects of an ambient breeze is an important topic for further research.

**5.2.6 Signal loss in sampling tubes.** Signal loss in sampling tubes is an analytical chemistry concern that carries over to the present topic. Most animals have short sampling tubes, the elephant and kiwi excepted. Man-made tubes cannot be inert to all trace chemicals, and explosive molecules, for example, adhere to Teflon, glass, Pyrex, quartz, nickel, stainless steel, gold, platinum, copper, fused silica, aluminum, and plastic [307,310]. Heated transfer lines are used to avoid such deposition except when particles are being transferred [302]. In that case there is also the concern that particles will impact and stick to tubing walls downstream of bends, etc. [13,57,323].

**5.3 Sensor Chamber Fluid Dynamics for Artificial Olfaction.** Sensor chamber fluid dynamics is virgin territory: only one previous investigation is known [324]. Insofar as all present artificial noses carry their olfactory sensors internally like vertebrates, we consider only that case here. Further, we avoid the confusing multifunctionality of the mammalian nasal cavity (olfaction+respiration+air-conditioning) by examining the separate olfactory chambers of fish. Reynolds number scaling allows us to move freely between air and water in this regard.

**5.3.1 The eel as a role model.** Specifically, consider the common freshwater eel, *Anguilla anguilla*, as a role model for sensor chamber fluid dynamics [3,40,253,325]. As shown in Fig. 26, a simple anterior naris on the left leads directly onto the medial passage of a chamber packed full of olfactory lamellae. Acting as flow turning vanes as well as sensor surfaces, the lamellae direct the water laterally and ventrally (into the page). Cilia induce rotation between the lamellae as shown, bringing the flow up along the sides of the chamber to its roof, where it is collected and discharged out the posterior naris.

This highly three-dimensional flow encounters a large sensory surface, ensures that the entire flow is thoroughly sampled, and



**Fig. 26** The path of water through the olfaction chamber of an eel, top view, redrawn from illustrations in [40,253,325]

does it all in a compact volume. (The scale shown is at most a few centimeters, but could be an order of magnitude larger in air at the same  $Re$ .) This compactness is an asset to the animal and it provides a quick olfactory response time. Artificial nose designers can scarcely find a better natural example than this.

Though air-breathing vertebrates favor turbinate over lamellae, this sort of olfactory sensor chamber is nonetheless broadly characteristic of all vertebrates. According to Stoddart [3], “There is an inlet to, and an outlet from, a chamber in which is held a thin sensory membrane of sometimes immense area.”

**5.3.2 Pressure losses, fans, and pumps.** In Sec. 2.3 the flow losses in a sensor chamber and the energy required to overcome them were introduced. These pressure losses need to be frictional, as required by the analogy described below, not due to flow separation. Separation losses do not arise from effective olfaction, just bad design. Principles of good design can be found, for example, in [326,327].

In artificial olfactory systems a pump or fan supplies the motive power to overcome losses and induce a flow through a sensor chamber [14]. Such a device produces its maximum overall pressure differential (head) when there is no flow, thus no loss through the sensors. As the flow rate (capacity)  $Q$  through the sensors rises, the pump or fan’s ability to sustain a given pressure differential drops. Where the two curves meet is the operating point of the olfactory system. Every undergraduate fluids engineering student learns to draw such head/capacity curves for pumping systems. Designers of artificial noses should learn to draw them too (see, e.g., [49]).

**5.3.3 Expansion of a sensor chamber from a small inlet.** What limits how fast the eel’s olfaction chamber in Fig. 26 expands in area downstream of the tiny anterior naris? Lighthill [7] first considered this issue in terms of the branching of the arteries and bronchial tubes. Briefly, the area increase slows the flow and raises the static pressure, so except at low Reynolds numbers there is a danger of flow separation. Lighthill’s rule-of-thumb to avoid this allows no more than a 20% increase in flow cross-sectional area per channel bifurcation. At least in the arteries, nature seems to obey this rule. Cross-sectional area data are not available for the eel’s olfactory chamber, but are available for the comparable case of a beagle’s nose [64]. These data show that the maxilloturbinate region expands about linearly in cross section to seven times its initial area over a downstream distance of only 35 mm. According to Lighthill’s rule, a bifurcation should occur initially every mm or so to prevent separation. This is hard to check with the available data, but it is clear that the maxilloturbinate burgeson with branching complexity in this region. Thus separation prevention goes hand-in-hand with the need for large heat-exchanger surface area in the beagle’s maxilloturbinate.

**5.3.4 Heat and mass transfer analogy.** Osborne Reynolds (1842–1912) recognized that mass, heat, and momentum are transferred by similar physical mechanisms (molecular motion in laminar flow, eddy motion in turbulent flow). The analogy between these fluxes—Reynolds analogy—is useful in sensor cham-

ber design, where a high mass transfer rate of odorant molecules to olfactory surfaces is desired. Concomitant momentum transfer by friction is required by the analogy, and heat transfer may also occur. Thus odorant mass transfer is related to the fluid power required to overcome sensor-chamber friction losses. The empirical relations describing Reynolds analogy are well-known and readily available, e.g., [91,327,328], and do not bear repeating here.

The utility of Reynolds analogy in sniffing for chemical traces was first recognized by Fraim et al. [311], who designed an explosives preconcentrator based on heat exchanger technology. In modern microelectronics, strong thermal generation occurs in a small confined space and must be removed by a fluid flow. The analogy with an olfactory sensor chamber is obvious from the above, so we can learn design principles from the volumes that have been written on electronics cooling, e.g., [21,22,327,329].

Finned heat exchangers expose large surface areas to the flow for efficient heat transfer, a principle already in use in nature in the nasal turbinates, as well as in the air-conditioning industry [91]. One must make sure the flow is along the fin channels and not across them, or the process becomes stalled. For flow in odd-shaped ducts the Reynolds number is based on the hydraulic diameter  $D_h = 4A/P$ , where  $A$  is the cross-sectional area and  $P$  is the duct perimeter. Loss coefficients are known for many situations, e.g., discharging the flow abruptly from a small tube into a large chamber (which dissipates one velocity head, Sec. 2.3). Loss formulas are likewise known for screens, grids, protuberances, and rough channel walls.

In particular, the stacked eel lamellae of Fig. 26 are strikingly similar to the finned heat sinks used to cool electronics [21]. Heat-sink design principles encourage low flow speeds to minimize the pressure loss for a given performance level. Straight fins are shown to outperform other fin shapes (e.g., cylinders) [327]. Fins and lamellae should also be aerodynamic, with rounded leading edges and tapered trailing edges.

## 6 Homeland Security Applications

Down through the ages, civilization only flourished in enclaves sufficiently well-defended to prevent the ravages of barbarians. The terms “homeland security” and “terrorism” were not popular then, but the results of a security failure were nonetheless devastating. Fluid mechanics has been important in homeland security all along, providing standoff barriers against invasion, weapons technologies, mobility, etc. [330].

Many believe that the modern solution to the asymmetry of the terrorist threat lies in technology. Here we discuss a piece of that technology that concerns gaining information by detecting chemical traces in the air or water. Like the prey animals discussed earlier, we need constant environmental awareness but, unlike them, we cannot sleep standing up.

Homeland security thus requires continuous environmental monitoring. The unusual, however minor, can be a crucial warning of an impending attack. For example Carranza et al. [331], while monitoring the atmosphere for heavy metal traces, noticed a magnesium spike on the July 4th holiday—not terrorism that time, but it could have been.

**6.1 Canine Detection.** So much has been written about training dogs for chemical trace detection that it serves present purposes merely to cite some key references and give a brief commentary.

Much of the scientific basis of canine detection was learned recently at the Auburn University College of Veterinary Medicine, Auburn, Alabama [66,332,214–217]. There, operant conditioning experiments yielded sensitivity curves like those of Fig. 27, that quantify the threshold levels of specific trace chemicals that dogs can detect. These data also set the sensitivity standard for artificial noses, a standard that has already been exceeded in at least one case [292].

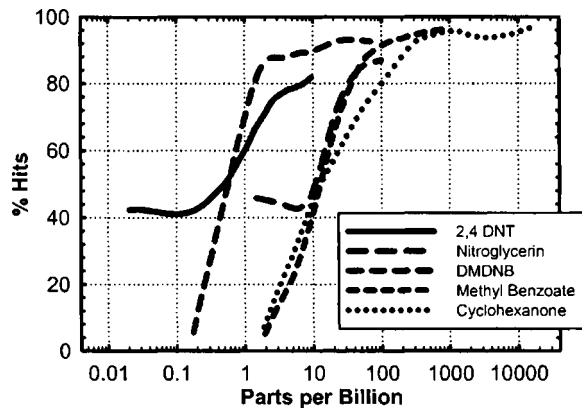


Fig. 27 Canine olfaction sensitivity curves measured at Auburn University, redrawn from <http://www.vetmed.auburn.edu/ibds/>. Except for methyl benzoate, a cocaine derivative, all trace chemicals shown are explosive-related

Extraneous odors present while sniffing can interfere with a dog's ability to detect a scent and can therefore raise the thresholds shown in Fig. 27, but to do so requires a comparatively enormous extraneous odorant level [217].

Dogs respond to the most-volatile compounds present in an explosive, not necessarily to the explosive species itself. For example in detecting C-4 plastic explosive, the dog is not likely to respond directly to the explosive component RDX, which has a very low vapor pressure, but rather to compounds like cyclohexanone, a solvent used in RDX production [215,216,333].

Gazit and Terkel report [334] that heavy exercise interferes with a dog's olfactory ability, since the dog cannot sniff while panting. They also use a microphone to pick up the sound of sniffing, which provides useful feedback to the dog handler [335].

While handlers have commented on the most desirable traits of their dogs [336], the desirable traits of handlers appear to need more work [332,337]. Being the brains of the team, the dog handler has a responsibility to be aware of the issues discussed here, such as human skin flakes, chemical plumes, micrometeorology, and the aerodynamics of air and ground sniffing. Syrotuck [125] should be required reading. Thermal plumes can also sometimes be visible to the unaided eye of the handler [46,48,338]. These fluid-dynamic issues might well be illustrated in a training video for dog handlers.

Despite the issues of expense and limited duty cycle, canine trace detection is a trusted mainstay of homeland security that will not soon be replaced by artificial nose technology. Furton and Myers [333] found that detector dogs still represent the best explosive detection means available, since artificial sniffers suffer from poor sampling systems, interference from masking odorants, and limited mobility.

**6.2 Cargo Screening.** Cargo screening has become politicized because of the high cargo volume crossing national borders and the extreme measures that are needed to screen a significant fraction of it for explosive, chemical, or biological weapons. Air, sea, rail, and truck cargo are all at risk. Methods that rely upon radiation to probe cargo containers are cumbersome and expensive, detection dogs do not have access to cargo interiors, and manual unloading for inspection requires far too much time and labor to be practical.

Still, sniffing the air inside cargo containers—without opening them—for trace contraband is an approach that can be both effective and affordable, and there is a precedent for it. Fine et al. [339], for example, patented a method to do this by injecting compressed air into a cargo container, applying suction, collecting the sampled air in a hood, and interrogating its contents for trace chemicals.

Another example is the MDS Sciex CONDOR system, which searched cargo containers for explosive traces using a suction probe fitted with a brush that fed an adsorption cartridge with an airflow flow rate of 25 liters/s [340]. The interior of containers or the exterior of cargo pallets was sampled by contact with the brush for about 30 s, whereupon the cartridge was removed and desorbed into a mass spectrometer. Cargo containers were also sampled through their ventilator ports or through a 10 cm array of drilled holes that ended up not being acceptable to the cargo industry [302]. This substantial system employed a 9 m heated sampling line and applied mechanical agitation even to full-sized sea containers. Inside the container they found a gradient of particle dispersion leading up to the source [302]. Trace contamination was even detected in some containers not holding any bulk explosives: Once upon a time Kilroy had been there.

Still another approach to cargo sampling is the British Remote Air Sampling for Canine Olfaction (RASCO) system [341,342]. A probe inserted into a cargo container pumps out a volume of air through a polymer mesh sample canister that is later presented to a detection dog for analysis. Sixty liters/min are drawn through the canister for 2 min. Success appears to depend upon a significant explosive vapor headspace inside the container. A related general discussion of collecting and transporting chemical traces in evacuated flasks, canisters, sampling bags, and sorbent canisters is given in [306]. If you cannot get the proboscis to the signal, take the signal to the proboscis.

Jenkins [343] patented a method to interrogate baggage by placing it in a compartment provided with vacuum and vibration. Airborne chemical traces thus liberated are drawn into a detector. A recent adaptation of this approach to cargo trace detection is the Ray Detection Discovery CERT system [344], which uses heat, pressurization, vibration, and gas jets to dislodge explosive traces from palletized air cargo in an airtight enclosure.

Finally, research on cargo trace detection is currently under way at Penn State, University Park, PA [345], funded by the U.S. Transportation Security Administration. The goal is to understand the internal airflows of cargo containers and to sample these flows for trace detection without opening the containers.

**6.3 People Sampling.** People sampling is a unique topic in all of chemical trace detection. Aircraft passengers are aware of the danger of terrorism, but are also very sensitive to the invasion of their personal space. A NRC study of passenger screening found that there is a strong relationship between public acceptance and the perception of risk [346]. It nonetheless irks passengers to wait in long lines, parcel out their belongings, and take off their shoes. Being sniffed by a dog is particularly offensive. People-sniffer developers need to be aware of these issues, just as terrorists are surely aware of them. But despite all this, the total U.S. annual people-screening outlay is expected to grow from \$590 million in 2001 to \$9.9 billion in 2010 [347].

Hallowell [348] reviewed the available technology for people screening in 2001. Since then several approaches have seen further development. One study recommended that research into the "vapor space" surrounding a suicide bomber might lead to improved means of detection [48]. Misconceptions about that space and its true nature—the human thermal plume—were described in Sec. 3.2.1. Here we discuss recent people-sampling developments in light of what is now known about the aerodynamics and heat transfer around people.

**6.3.1 Human olfactory signature.** The human olfactory signature was pioneered as a topic of study by Dravnieks [314,349]. Human scent arises from bioeffluents and from bacteria acting upon the skin and its secretions [125]. People also carry with them an olfactory image of their recent environment [222,314]. Any successful scheme to detect trace chemicals on people must take account of this olfactory signature and its conveyance by the human thermal plume and wake.

Dravnieks developed a "body tube" sampler to acquire chemi-

cal trace signals from people [349]. Bethune et al. [350] and May and Pomeroy [126] used similar “dispersal chambers” for bacteriological studies of human subjects. Such enclosures are only practical for people-sampling in the lab, but they have been instrumental in contamination studies [351,352] and in aviation security research leading up to the present portal technology [123,124,353,354].

There is anecdotal evidence that artificial noses were deployed to detect troops in the Vietnam jungle, and more recently in the caves of Afghanistan. Building upon genetic research with mice, the current DARPA Unique Signatures program seeks an exploitable chemosignal corresponding to an individual’s genetically determined odor type. If found, it will be used to develop a detector for the presence of “high-level-of-interest individuals within groups of enemy combatants.”

**6.3.2 Portals for screening people.** Portals for screening people have generated many patents, e.g., [355–358], but only a few practical devices. Some of the approaches that failed include “wind-tunnel” portals that moved massive amounts of air, “saloon-door” portals that required physical contact with subjects, and “telephone-booth” portals that were too confining or too slow. During the development of these devices a goal of 6 s/person sampling time was set by the U.S. Federal Aviation Administration (FAA), but was difficult to achieve.

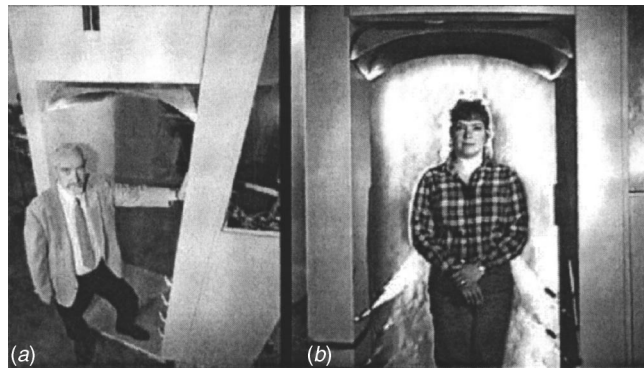
General reviews of people-screening portals are given in [348,310]. The role of air jets was described earlier in Sec. 2.5, and related material on explosive trace standards and computations of the human thermal plume is found in [130,359–363].

The first published investigation of portal aerodynamics is probably Schellenbaum [364], who examined various airflow directions in tube-type and booth-type portals. He used a department-store mannequin (see Sec. 3.2.2), so his results take no account of the human thermal plume. He recommended a downward airflow over the subject with collection at foot level.

Hobbes and Conde [365] studied the aerodynamics of an “open-clamshell”-type portal by CFD simulation. This portal drew a large flux of air—350 liters/s for 10 s—horizontally across the human subject and into inlets for subsequent interrogation. The induced airspeed was up to 2.4 m/s, more than ten times the commonly accepted maximum for comfortable room ventilation [366]. Vortical recirculation was generated on the lee side of the subject. Air-jet puffer effects and the release of explosive vapor as a passive contaminant were also simulated. Although this portal design lacked sophistication, it was the first study to apply the tools of fluid dynamics to people sampling.

Sandia National Laboratories developed a vertical-downflow portal in the 1990s [356,368,367,358], a version of which is now commercialized as the Smiths Detection Sentinel II. A human subject enters the portal and turns 90 deg, whereupon an array of air-jet puffers and two ceiling slot-jets sweep the body for chemical traces. The cross-sectional area of the open portal is reduced near the floor, where a portion of the induced downflow is collected for analysis by an IMS detector. This is purely jet-assisted sniffing, since thermal convection from the human subject cannot play a significant role. It bears a similarity to air-shower or air-douche devices used for particle removal from clothing in clean room practice ([17] Chap. 14, and [369]).

Quite a different approach is taken in the GE Security EntryScan<sup>3</sup>, Fig. 28, which uses the natural upward motion of the human thermal plume to collect and preconcentrate the plume overhead for IMS interrogation [357]. This is convection-assisted sniffing, but air-jet puffers also play a role in both ruffling the subject’s clothing to release particles and in encouraging the upward airflow. An aerodynamic contraction (see, e.g., [370]) is used overhead to capture the human thermal plume at a flow rate up to 50 liters/s and pass it through a 10×10 cm metal-mesh preconcentrator.



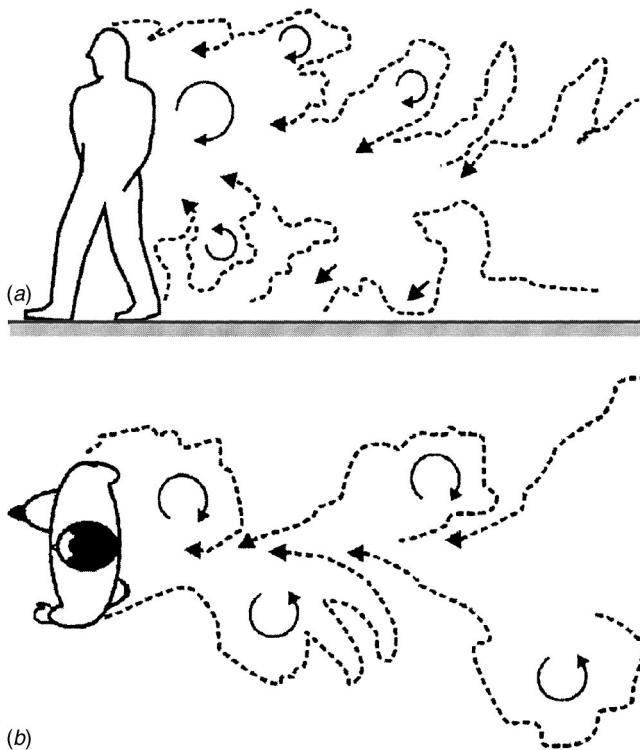
**Fig. 28 (a) The author standing in a prototype version of the GE Infrastructure EntryScan<sup>3</sup> explosive detection portal (Penn State photo by Greg Grieco) and (b) schlieren image of portal with subject (L.J. Dodson) and with air-jet puffers firing**

Several years of research on this portal at Penn State [83,124,353,354,371] have yielded the following results, summarized briefly:

1. The human thermal plume is a natural whole-body sampling system, from the toes to the top of the head.
2. As shown in Fig. 4, *brief* puffer-jet impingement (e.g., 50 ms) is the principal means of liberating trace particles for detection.
3. Most of the readily-available signal from a human subject can be had in a few seconds of overhead sampling time.
4. The detectability of 10  $\mu\text{m}$ -range explosive particulate traces originating beneath the clothing is affected by clothing porosity only when the porosity is less than about 4%.
5. Layered clothing reduces the chemical trace signal level, but the signal remains measurable.
6. Trace explosive sources beneath the clothing transfer to both the clothing and the skin, but remain highest in the vicinity of the source.
7. Human skin flakes do not figure prominently in the transport of dry crystalline explosive traces in the human thermal plume.
8. Lateral air currents in the range of normally acceptable ventilation drafts do not substantially affect the performance of an open portal such as the one tested here.
9. When pure explosive vapor was released inside the portal, up to 25% of it was captured and detected by the present metal-mesh pre-concentrator.

**6.3.3 Human aerodynamic wake.** For a lateral airspeed  $U$  (or walking speed in still air) of more than about 0.2 m/s the human thermal plume ceases to exist. Instead, the thermal boundary layer of a person is swept downstream to form a wake. This can be seen by comparing the Reynolds number  $Re$  and the Grashof number  $Gr = g\beta\Delta TL^3/\nu^2$ , where  $\beta$  is the volumetric thermal expansion coefficient,  $\Delta T$  is the temperature difference, and  $L$  is the characteristic width of the human body [372]. Without lateral airspeed  $U$ ,  $Re \rightarrow 0$  and  $Gr/Re^2 \gg 1$ , meaning that the flow is dominated by free convection. On the other hand, for ordinary walking speeds in the  $U = 1$  m/s range,  $Gr/Re^2 \ll 1$  and the flow is dominated by forced rather than free convection. Since  $\Delta T$  no longer matters in the latter flow regime, we use the expression “human aerodynamic wake.”

Several investigators have studied lateral airflow effects on the flow about stationary humans, mostly motivated by air pollution control and the reduction of worker exposure [135,373–377]. In a different reference frame, however, a person walking with speed  $U$  in still air produces an aerodynamic wake in which the wake



**Fig. 29** Diagrams of motion in the human aerodynamic wake from smoke flow visualization experiments [372,378], (a) median plane and (b) dorsal plane

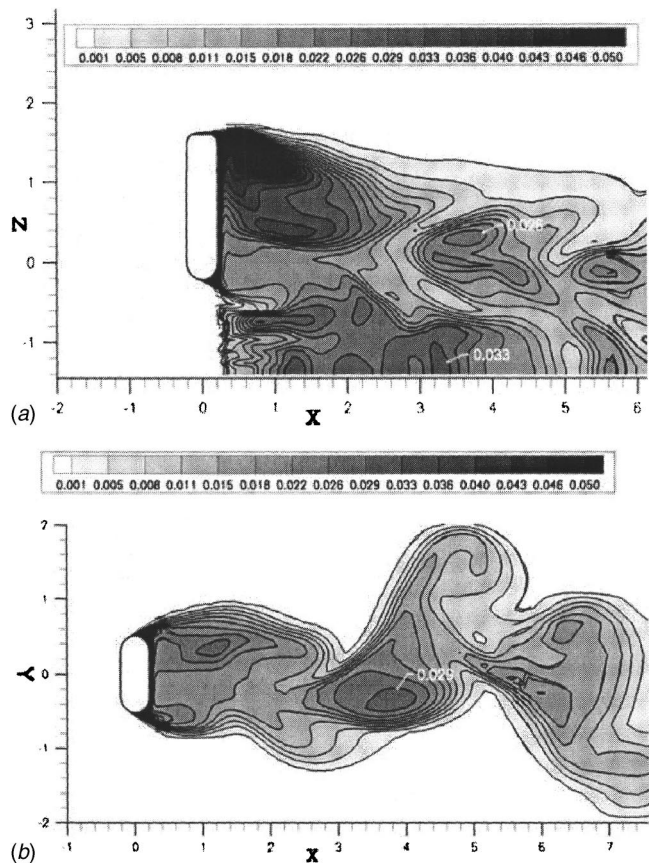
flow follows the person. The human chemical trace signature, formerly in the human boundary layer, becomes distributed in this wake. It is common experience that a walking person's scent in still air is noticeable to a fixed observer only after that person walks by.

This has been exploited as a means of "sniffing" human chemical traces by sampling the wakes of walking people [372,378,379]. The advantage over the portal technology described above is that people are already walking in security scenarios such as airports and, by not making them stop and stand, the sampling time can be reduced substantially. For example, experiments [378] have shown that the wakes of two walking people, one following the other, are aerodynamically independent for separation times greater than about 2 s.

The Penn State work [372,378,379], still in progress, has characterized the human aerodynamic wake as the unsteady vortex shedding from an irregular 3D cylindrical body (Fig. 29). The irregularity mostly concerns the legs, which act as individual shedding cylinders with through-flow between them. This causes the wake to dissipate more rapidly downstream of the legs than downstream of the torso, where a large recirculation zone occurs. There is also a downwash component that causes the lower wake to interact with the ground and to spread laterally. Despite these several complicating aspects, the human wake nevertheless shows unmistakable Kármán vortex shedding in the dorsal plane shown in Figs. 29(b) and 30(b).

A CFD solution of the Reynolds-averaged Navier-Stokes equations [372], despite a simplified representation of the human body, is able to portray all the significant aspects of the human wake flow that are seen in the experiments. For example, a scalar contaminant representing a chemical trace from the human body decays exponentially with distance downstream as the wake mixes out with the surrounding air. Thus one should sample the early wake just downstream of a walking person in order to acquire the maximum trace signal strength.

The design of a portal to sample the human aerodynamic wake



**Fig. 30** Corresponding to Fig. 29, computed instantaneous motion of a scalar contaminant in the aerodynamic wake of a simulated human [372], (a) median plane and (b) dorsal plane

was first suggested in [357]. It appears possible to take advantage of the wake's momentum in this regard [378,379]. However, compared to the case of the human thermal plume, sampling a much larger volume of air over a shorter time interval will be a severe test of pre-concentrator technology.

**6.4 Landmine Detection.** Landmine detection is another severe test for sniffers, as described in Sec. 3.3.2, because of weak trace signals outdoors in the weather and terrain. At the same time the global landmine crisis [380–383] extracts a shocking human and economic price and demands solutions.

Dogs are the principal detectors of buried landmines, even though it puts them and their handlers at risk. The DARPA Dog's Nose program in the late 1990s sought to produce artificial noses of similar sensitivity, and several of such were actually developed [287,288,292,384], though none has supplanted the dog so far. Yinon [310] and Pamula [384] have both surveyed this topic in more detail than present space allows.

Briefly, as part of the mentioned DARPA program an Explosives Fate and Transport Team characterized the trace signal level that one can expect to find above a buried landmine [162,385–387]. Trace explosives and related mine compounds enter the surrounding soil, collect below the mine, and percolate to the surface in a "halo" pattern about the mine location. Moisture and daily variations in soil temperature aid this process. For the ubiquitous 2,4,6-TNT mine, the prevalent trace signal is from 2,4-DNT, which is more volatile than TNT and is present in the military-grade explosive as a contaminant. It is this "odor signature" that a dog actually detects, rather than the bulk explosive [215].

The mass of explosive-related compounds in contaminated soil above a buried mine was found to be on the order of tens of

micrograms/kilogram of soil. 2,4-DNT vapor is also present in the boundary layer directly above a typical anti-personnel mine, but only at a concentration of perhaps 100 picograms/liter at equilibrium under ideal atmospheric conditions, and such conditions are not usual [387].

Overall, then, the chances are bleak of sniffing explosive-related vapor in the air above a buried mine. Anecdotal evidence from dog handlers that their dogs air-scented landmines at 5 m must describe extraordinary rather than usual circumstances.

Soil particles, though, are another matter, since they carry a thousand-fold higher concentration of explosive-related signal. A dog's ability to stir up, inspire, and probably desorb trace chemicals from such particles was discussed in Sec. 4.3.1 and in [103,166]. Some developers of landmine sniffers also attempt to take advantage of soil particles by thermally desorbing traces from the soil using laser radiation before sniffing [388], by disturbing loose particles using air jets [310,384] or ultrasonics [389], or by collecting particles electrostatically [390].

Finally, Mineseeker.com [391] floats a mini blimp over a minefield and uses radar to locate landmines. One could lower an elephantlike sampling trunk with assisting air jets almost to ground level and sniff for them as well.

**6.5 Biohazard Detection.** The topic of sniffing for bioaerosols was introduced in Sec. 3.1, including some unique sampling and detection problems and the issue of distinguishing biowar agents from the natural airborne background. Chemical plumes—one way of dispersing biowar agents—were likewise covered in Sec. 3.3.3 and aerobiology was introduced in Sec. 1.1. Further references are also available on sampling biological aerosols [106,108], biosensors [392], and chemical and biological terrorism [12].

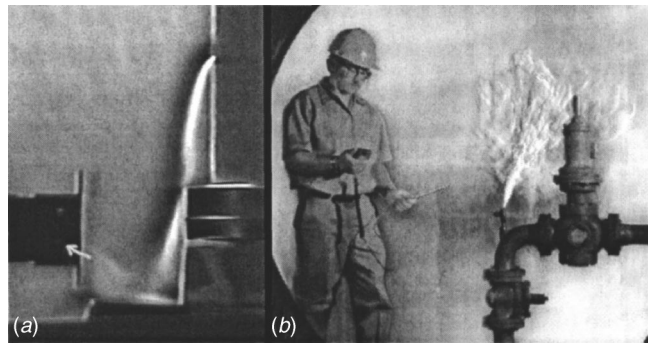
Consider the anthrax letters that were mailed in the United States in late 2001. Finely powdered anthrax spores in ordinary paper envelopes became airborne due to handling, costing several lives and contaminating two large mail-handling facilities [393]. Postal delivery-bar-code sorters squeezed the air and spores out of the envelopes by belts and rollers.  $1\ \mu\text{m}$ – $3\ \mu\text{m}$  anthrax spores can pass easily through the  $20\ \mu\text{m}$  pores of a typical paper envelope even if it remains unopened. Tearing open an anthrax-filled envelope was found to cause massive airborne contamination.

The Northrop-Grumman Corporation, Baltimore, MD, subsequently developed a biohazard detection system (BDS) for the U.S. Postal Service to detect any such future attacks upon the postal system. BDS compresses mail to force the air out of envelopes and captures it in a sampling hood positioned over the first pinch point in the mail processing operation. From the sampled airflow a Spincon high-volume liquid-based cyclone collector acquires biological particles and uses the polymerase chain reaction and DNA matching to detect the trace presence of such species as *Bacillus anthracis* in the mail. BDS is a fully automated system that sounds an alert when a biohazard is detected.

## 7 Other Applications

**7.1 Medical Diagnosis.** Since the beginning of medicine, human body and breath odors have been used to diagnose disease [394,395]. Dozens of diseases are known by their characteristic odors, such as acetone breath from diabetes [396], the putrid odor of scurvy, and the sour odor that precedes mononucleosis [397]. Also included are characteristic odors due to chemical poisoning and substance abuse, and even schizophrenia [398]. The popular press has made much of pet dogs purportedly sniffing out cancer in their owners. However, lacking quantification and in the face of modern laboratory analysis, olfaction in medical diagnosis has languished.

One reason for this is that most methods of artificial olfaction for medical diagnosis are intrusive and slow. Dravnieks et al. [314,349] and Distelheim and Dravnieks [399] used a "body tube" sampler (Sec. 6.3.1) and gas chromatograph (GC)-mass-



**Fig. 31 (a) Schlieren image of an acetone vapor leak cascading downward and being inhaled (arrow) by the snout of the Cogniscent artificial nose (b) a hand-held, wand-type sniffer probe is used to search for a natural gas leak, visualized by large-field schlieren optics [46,408,411]**

spectrometric analysis. Cotton swabs, breath bags [400,401], and skin headspace collectors [402,403] all work without the need for actual sniffing.

Gardner and Bartlett [9] speculated that "Perhaps in the future the electronic nose will be able to sniff the human body directly..." That future has already arrived in the form of portals that sample the human thermal plume, Sec. 6.3 and [83,120,124,357,371]. However, modern nonintrusive portal technology has yet to be applied outside the realm of explosive trace detection for security screening.

Nonetheless there is considerable recent activity in artificial olfaction for medical diagnosis, mostly using only intrusive sampling methods. Applications include staph, strep, and e-coli infections, breath signals for uremia and liver cirrhosis, urinary tract infections, tuberculosis, and airway inflammation [9,404,405]. Continuous e-nose monitoring of disease stages and global disease surveillance have been suggested [406] but not yet realized.

Clearly, modern sniffing for medical diagnosis still has many hurdles to overcome, as described by Persaud, Pisanelli, and Evans [407]. Despite its enormous potential, this application is presently more driven by sensor research and development [392] than by sampling issues, and there is not yet a commercial realization even of a breath analyzer. The medical arena is a difficult one; human variations can produce different odors from the same disease, misdiagnoses are bad news, and chemical interference is common. Also the funding tends to favor therapeutic rather than diagnostic instrument development. Finally, even though current lab analyses of blood samples and cultures take days, any replacement technology must at least achieve the accuracy of the current methods.

**7.2 Leak Detection.** Wand-type leak-detector sniffer probes, Fig. 31 [408], were discussed in Sec. 3.2.4 and elsewhere. They have very broad industrial applications in leak-testing turbines, condensers, heat exchangers, tanks, refrigerant systems, and pipelines. Explosive rocket propellant leaks must be found, as must leaking solvents or fuels that pose fire, explosion, or environmental hazards. Natural gas leaks are expensive as well as dangerous.

Usually a hand-held sniffer probe acquires a sample by suction and conveys it to a sensor such as a helium or flame-ionization detector. The sampling time rises rapidly with the hose length, and for long hoses of typical 1-cm-or-less diameter it becomes prohibitive. Example calculations for sensitivity, standoff distance, linear speed of probe motion, response time, and calibration are given in [139].

Some other sniffer types are not hand held, but rather vehicle mounted. In one case, Boreal Laser's aircraft-mounted GasFinderAB system is flown over natural gas pipelines, sampling and analyzing the air for leaks. Dogs are also trained to sniff for gas



leaks.

Hand-held sniffer probes are accurate and sensitive, but searching is slow and coverage of large areas is labor intensive. Broad-field standoff optical methods can supplement probe detection by covering large areas quickly at reduced sensitivity levels. At least three such approaches have been suggested: (1) IR thermography [409], which depends upon a thermal difference between leaking gas and the ambient air and usually only examines ground signatures; (2) Schlieren imaging [46,410,411], which requires a small refractive-index difference but images the air itself rather than the ground; and (3) laser absorption [412], which can detect isothermal airborne leak plumes but requires expensive and cumbersome equipment.

## 8 Summary and Future Directions

**8.1 Summary.** For convenience, the high points of this tour of the world of sniffers are repeated in list form:

1. Little previous effort has been spent on the biofluid dynamics of sniffing or on the design of sniffers for artificial olfaction.
2. Nature favors energy-efficient faired bellmouth-type inlets rather than sharp-edged holes.
3. Brief air-jet impingement is the principal means of liberating trace particles from surfaces for detection by sniffing.
4. The proper model for airflow about the human body in still air is the human thermal boundary layer and plume, not the "personal activity cloud."
5. Plumes bearing chemical traces can be classified and understood based on their buoyancy and momentum.
6. Nature teaches proximity sniffing, but the most advanced natural nostrils, such as the variable-geometry dog's nose, also use exhaled air jets to enhance the reach and particle uptake of the process.
7. A vertebrate does not require variable-geometry external nares in order to be macrosmatic, but several of those examined here do have them. We know something of their function in dogs, but almost nothing in the case of other animals.
8. The natural narial sampling orifice of terrestrial vertebrates is typically either round, inverse-comma shaped, or slit shaped.
9. A proboscis, nostril, and mobile platform are required for vertebrate sniffing, but proboscis length is only weakly constrained by nature, as demonstrated by the elephant and kiwi.
10. Small turbomachines can move fluids for olfaction more effectively than nature's usual bellows action.
11. Macrosmatic terrestrial vertebrates usually have large nostrils for high airflow rates and long straight snouts to provide enough space for both the olfactory and the air-conditioning apparatus.
12. None of the animals can afford the time to collect and later desorb odorants. They acquire the odorant by sensor cells generating neuronal signals that are sent directly to the brain in real time.
13. The peak mammalian sniff rate of a few hertz ignores higher-frequency information, such as some of that contained in chemical plumes. This suggests that a man-made continuously-inhaling sniffer could gain an advantage in frequency response by not having to accommodate respiration.
14. For olfactory sensor chamber design the best model is the fish: simple, elegant, and not complicated by dual use. Mounting the sensor chamber off to the side, as in the dog's nose, appears just to be nature's way of accommodating olfaction with respiration.
15. Reynolds analogy plays an important role in olfactory sensor chamber design.

16. Mankind's worst enemy, the mosquito, has received little attention from fluid dynamicists.
17. Invertebrates who track chemical plumes use the Reynolds number to control the effective porosity of their antennae sensor hairs during sniffing.
18. We can understand a lot about natural sniffers but not all, because biomimicry is a sort of reverse engineering: The final product is available, but no logical path is revealed to get there.
19. Compared to nature, the sniffers now used in man-made detectors and artificial noses are almost devoid of sophistication. Several possibilities are suggested for their improvement.
20. Vapor and particle sampling are both important in nature as well as in artificial olfaction.
21. In people sniffing, the human thermal plume is a natural whole-body sampler, from the toes to the top of the head.
22. The human aerodynamic wake has been characterized, at least initially, by both experiments and computations.
23. Modern nonintrusive portal technology for sniffing people has yet to be applied to medical diagnosis or anything else outside the realm of explosive trace detection for security screening.
24. This paper has collected scattered information and has associated diverse fields in the hope of establishing a "new" topic in biofluid dynamics.

**8.2 Future Directions.** Future directions for the further understanding and development of sniffers are summarized in the following list:

1. Study the nostril aerodynamics of the rabbit, rat, and opossum in order to broaden the present knowledge of natural sniffing systems.
2. Carry out an experimental and computational fluid-dynamic study of an eel's or shark's olfactory capsule as a primary example for sensor chamber design in artificial olfaction.
3. Study the internal aerodynamics of the dog's nose by particle image velocimetry (PIV) measurements and CFD simulation as another important example for artificial olfaction sensor chamber design.
4. Carry out flow visualization, PIV velocity measurements, and a CFD simulation of the airflow around the upper human body, breathing zone, exhaled jets, cough, and sneeze.
5. Perform turbulent and unsteady-flow CFD simulations of the flow inside the human and dog's nose.
6. Gain a better understanding of mosquito aerodynamics, the effects of ambient wind, mosquito plume tracing, and potential aerodynamic strategies to defeat mosquito host location.
7. Beginning at the fundamental level, examine current and prospective new artificial sniffer types in terms of practicality, efficiency, proper use of fluid-dynamic principles, and the performance criteria stated in Sec. 5.1.3.
8. Conduct research to better understand jet-assisted olfaction.
9. Study more effective means of aerodynamic sniffer isolation from the effects of an ambient breeze.
10. Develop ways to replace the present adsorb-desorb-analyze-detect cycle with more direct olfactory sensing, as in nature.
11. Develop flexible, controllable "elephant trunk" snouts for land-based robot sniffers in order to improve their olfactory mobility and performance by aiming their trunks at local regions of interest.
12. Apply modern nonintrusive portal sampling technology to human medical diagnosis.
13. Produce an educational film on the fluid mechanics of scent plumes, skin flakes, and the aerodynamics of scenting for the dog handler and the artificial nose user.

Finally, various studies and working groups have made similar suggestions for future research, including more study of mammalian olfaction, sampling, and preconcentration [205], biomimetic sensing focused on distributed low-cost sensors [48], factories of the future filled with cheap tiny olfactory and other sensors [413], rapid wristwatch-sized biodelectors [414], low-power, distributed, unattended, miniaturized remote sensors, robotic “insects” with onboard sampling and sensors, and rat packs with global positioning system transponders trained to detect explosives in city sewers [48]. Some of this speculation is far fetched, but we can reasonably expect that sniffers will eventually no longer be *ad hoc* afterthoughts in artificial olfaction, as they are now in almost every case. Small, portable, inexpensive e-noses with integral sniffers will eventually become common useful tools, although trained canine detectors will not soon become obsolete. The genetic detectors, e.g., [237,415], will also have more to say about the origin and function of the various noses reviewed here. Meanwhile fluid dynamicists have a lot of interesting work to do on this topic.

## Acknowledgments

The author thanks the ASME Freeman Scholar Committee for providing him the opportunity to write this review. The paper benefited especially from critiques by S. Vogel, D. M. Stoddart, and L. R. Witmer. The author also thanks B. A. Craven, J. S. Kauer, A. Kepecs, M. J. Kennett, P. Mielle, E. G. Paterson, N. Sobel, and J. E. White for helpful discussions, T. S. Denny, Jr. for the dog’s nose cast, and the several gracious contributors of images who are acknowledged in the figure descriptions. The author finally thanks his laboratory staff, L. J. Dodson and J. D. Miller, and his students for their support. Some elements of the reviewed research were supported by the US Federal Aviation Administration, the Transportation Security Administration, and DARPA. Opinions expressed in this paper do not necessarily reflect the policies of these sponsoring agencies.

## References

[1] Eisenberg, J. F., and Kleiman, D. G., 1972, “Olfactory Communication in Mammals,” *Annu. Rev. Ecol. Syst.*, **3**, pp. 1–32.  
 [2] Zwaardemaker, H., 1895, *Die Physiologie des Geruchs*, W. Engelmann, Leipzig, Germany.  
 [3] Stoddart, D. M., 1980, *The Ecology of Vertebrate Olfaction*, Chapman & Hall, New York, pp. 1–33.  
 [4] Axel, R., 1995, “The Molecular Logic of Smell,” *Sci. Am.*, **273**(4), pp. 154–159.  
 [5] Doty, R. L., 2001, “Olfaction,” *Annu. Rev. Psychol.*, **52**, pp. 423–452.  
 [6] Kauer, J. S., and White, J. E., 2001, “Imaging and Coding in the Olfactory System,” *Annu. Rev. Neurosci.*, **24**, pp. 963–979.  
 [7] Lighthill, M. J., 1975, *Mathematical Biofluidynamics*, SIAM, Philadelphia.  
 [8] Weinbaum, S., 1996, “Biofluid Mechanics,” in *Research Trends in Fluid Dynamics: Report from US National Commission on Theoretical & Applied Mechanics*, J. L. Lumley, ed., Springer, New York, pp. 296–309.  
 [9] Gardner, J. W., and Bartlett, P. N., 1999, *Electronic Noses—Principles and Applications*, Oxford University Press, Oxford.  
 [10] Pearce, T. C., Schiffman, S. S., Nagle, H. T., and Gardner, J. W., eds., 2002, *Handbook of Machine Olfaction*, Wiley, New York.  
 [11] Rouhi, A. M., 1997, “Detecting Illegal Substances,” *Chem. Eng. News*, **75**(39), pp. 24–29.  
 [12] National Research Council, 1999, *Chemical and Biological Terrorism: Research and Development to Improve Civilian Medical Response*, National Academy Press, Washington, DC.  
 [13] Watson, J. G., and Chow, J. C., 2001, “Ambient Air Sampling,” in *Aerosol Measurement: Principles, Techniques, and Applications*, 2nd Ed., P. A. Baron and K. Willeke, eds., Wiley, New York, pp. 821–844.  
 [14] Monteith, L. E., and Rubow, K. L., 2001, “Air Movers and Samplers,” in *Air Sampling Instruments for Evaluation of Atmospheric Contaminants*, 9th Ed. American Conference of Governmental Industrial Hygienists, Cincinnati, OH, pp. 233–280.  
 [15] Singh, M., and Sioutas, C., 2003, “Assessment of Exposure to Airborne Particles,” in *Indoor Environment: Airborne Particles and Settled Dust*, L. Morowska and T. Salthammer, eds., Wiley, New York, pp. 374–386.  
 [16] Subramaniam, R. P., Richardson, R. B., Morgan, K. T., Kimbell, J. S., and Guilmette, R. A., 1998, “Computational Fluid Dynamics Simulations of Inspiratory Airflow in the Human Nose and Nasopharynx,” *Inhalation Toxicol.*, **10**(5), pp. 473–502.

[17] Baturin, V. V., 1972, *Fundamentals of Industrial Ventilation*, Pergamon, New York, pp. 12–24.  
 [18] Heinsohn, R. J., 1991, *Industrial Ventilation*, Wiley, New York.  
 [19] Heinsohn, R. J., and Cimbala, J. M., 2002, “Ideal Flow,” in *Indoor Air Quality Engineering*, Marcel Dekker, New York, pp. 517–580.  
 [20] Goodfellow, H. D., and Tähti, E., eds., 2001, *Industrial Ventilation Design Guidebook*, Elsevier, New York.  
 [21] Kordyban, T., 1998, *Hot Air Rises and Heat Sinks: Everything You Know About Cooling Electronics is Wrong*, ASME, New York.  
 [22] Remsburg, R., 2001, *Thermal Design of Electronic Equipment*, CRC, Boca Raton.  
 [23] Cox, C. S., 1987, *The Aerobiological Pathway of Microorganisms*, Wiley-Interscience, New York.  
 [24] Clark, R. P., and Cox, R. N., 1973, “The Generation of Aerosols from the Human Body,” in *Airborne Transmission and Airborne Infection: Concepts and Methods*, J. F. Hers and K. C. Winkler, eds., Wiley, New York, pp. 413–426.  
 [25] Burge, H. A., 1995, “Aerobiology of the Indoor Environment,” *Occup. Med.*, **10**(1), pp. 27–40.  
 [26] Higson, S. P. J., 2003, *Analytical Chemistry*, Oxford University, Oxford, UK.  
 [27] Kline, S. J., 1960, “The Importance of Flow Visualization,” *Symposium on Flow Visualization*, ASME, New York, 1, pp. 1–9.  
 [28] Roshko, A., 1995, “Flow Visualization As a Basic Research Tool,” in *Flow Visualization VII*, Crowder, J. P. ed., Begell House, New York, pp. 983–994.  
 [29] Merzkirch, W., 1987, *Flow Visualization*, Academic, New York.  
 [30] Paulsen, E., 1882, “Experimentelle Untersuchungen Über Die Strömungen Der Luft in Der Nasenhöhle,” *Sitzungsber. K. Preuss. Akad. Wiss.*, **85**, p. 348ff.  
 [31] Bojsten-Møller, F., and Fahrenkrug, J., 1971, “Nasal Swell-Bodies and Cyclic Changes in the Air Passage of the Rat and Rabbit Nose,” *J. Anat.*, **110**(1), pp. 25–37.  
 [32] Hornung, D. E., Leopold, D. A., Youngentob, S. L., Sheehe, P. R., Gagne, G. M., Thomas, F. D., and Mozell, M. M., 1987, “Airflow Patterns in a Human Nasal Model,” *Arch. Otolaryngol. Head Neck Surg.*, **113**(2), pp. 169–172.  
 [33] Hahn, I., Scherer, P. W., and Mozell, M. M., 1993, “Velocity Profiles Measured for Airflow Through a Large-Scale Model of the Human Nasal Cavity,” *J. Appl. Physiol.*, **75**(5), pp. 2273–2287.  
 [34] Keyhani, K., Scherer, P. W., and Mozell, M. M., 1997, “Numerical Simulation of Airflow in the Human Nasal Cavity,” *ASME J. Biomech. Eng.*, **117**, pp. 429–441.  
 [35] Brueggemann, J., and Jeckstadt, S., 1938, “Über Den Weg Des Luftstromes Durch Die Nase Des Hundes (On the Direction of the Airstream Through the Dog’s Nose),” *Pflügers Archiv, European Journal of Physiology*, **239**, pp. 293–303.  
 [36] Dawes, J. D. K., 1952, “The Course of the Nasal Airstreams,” *J. Laryngol. Otol.*, **66**(12), pp. 583–593.  
 [37] Ishida, H., Yamanaka, T., Kushida, N., Nakamoto, T., and Moriizumi, T., 2000, “Study of Real-Time Visualization of Gas/Odor Flow Image Using Gas Sensor Array,” *Sens. Actuators B*, **65**(1–3), pp. 14–16.  
 [38] Yamanaka, T., Ishida, H., Nakamoto, T., and Moriizumi, T., 1998, “Analysis of Gas Sensor Transient Response by Visualizing Instantaneous Gas Concentration Using Smoke,” *Sens. Actuators, A*, **69**(1), pp. 77–81.  
 [39] Saunders, C. J., and Fletcher, B., 1996, “Jet Enhanced Local Exhaust Ventilation,” *Ann. Occup. Hyg.*, **37**(1), pp. 15–24.  
 [40] Teichmann, H., 1959, “Vergleichende Untersuchungen an Der Nase Der Fische (Comparative Investigations on the Nose of the Fish),” *Z. Morphol. Oekol. Tiere*, **43**, pp. 171–212.  
 [41] Grasso, F. W., and Basil, J. A., 2002, “How Lobsters, Crayfishes, and Crabs Locate Sources of Odor: Current Perspectives and Future Directions,” *Curr. Opin. Neurobiol.*, **12**(6), pp. 721–727.  
 [42] Atema, J., 1996, “Eddy Chemotaxis and Odor Landscapes: Exploration of Nature with Animal Sensors,” *Biol. Bull.*, **191**(1), pp. 129–138.  
 [43] Webster, D. R., and Weissburg, M. J., 2001, “Chemosensory Guidance Cues in a Turbulent Chemical Odor Plume,” *Limnol. Oceanogr.*, **46**(5), pp. 1034–1047.  
 [44] Stuijver, M., 1958, “Biophysics of the Sense of Smell,” PhD thesis, University of Groningen, Germany.  
 [45] Schreck, S., Sullivan, K. J., Ho, C. M., and Chang, H. K., 1993, “Correlations Between Flow Resistance and Geometry in a Model of the Human Nose,” *J. Appl. Physiol.*, **75**(4), pp. 1767–1775.  
 [46] Settles, G. S., 2001, *Schlieren and Shadowgraph Techniques: Visualizing Phenomena in Transparent Media*, 1st Ed., Springer, New York.  
 [47] Settles, G. S., Kester, D. A., and Dodson-Dreibelbis, L. J., 2003, “The External Aerodynamics of Sniffing,” in *Sensors and Sensing in Biology and Engineering*, F. G. Barth et al., eds., Springer, New York, pp. 323–355.  
 [48] Board on Chemical Sciences and Technology, 2004, “Existing and Potential Standoff Explosives Detection Technologies,” US National Research Council Report, National Academies Press, Washington DC.  
 [49] White, F. M., 2002, *Fluid Mechanics*, McGraw-Hill, Boston.  
 [50] Batchelor, G. K., 2000, *An Introduction to Fluid Mechanics*, Cambridge University, Cambridge, UK.  
 [51] Chahine, A., Chahine, G. L., Duraiswami, R., Billard, J. Y., and Nieuwstadt, F. T. M., 1995, “Two-Dimensional Potential Flow Instruction and Analysis on Personal Computers,” *ASME J. Fluids Eng.*, **220**, pp. 89–93.  
 [52] Kimbell, J. S., Gross, E. A., Joyner, D. R., Godo, M. N., and Morgan, K. T., 1997, “Application of Computational Fluid Dynamics to Regional Dosimetry of Inhaled Chemicals in the Upper Respiratory Tract of the Rat,” *Toxicol. Appl. Pharmacol.*, **121**(2), pp. 253–263.

- [53] Kimbell, J. S., Godo, M. N., Gross, E. A., Joyner, D. R., Richardson, R. B., and Morgan, K. T., 1997, "Computer Simulation of Inspiratory Airflow in All Regions of the F344 Rat Nasal Passages," *Toxicol. Appl. Pharmacol.*, **145**(2), pp. 388–398.
- [54] Kepler, G. M., Richardson, R. B., Morgan, K. T., and Kimbell, J. S., 1998, "Computer Simulation of Inspiratory Nasal Airflow and Inhaled Gas Uptake in a Rhesus Monkey," *Toxicol. Appl. Pharmacol.*, **150**(1), pp. 1–11.
- [55] Kimbell, J. S., and Subramanian, R. P., 2001, "Use of Computational Fluid Dynamics Models for Dosimetry of Inhaled Gases in the Nasal Passages," *Inhalation Toxicol.*, **13**(5), pp. 325–334.
- [56] Koch, D. A., Arnold, S., Hubler, M., and Montavon, P. M., 2003, "Brachycephalic Syndrome in Dogs," *Compendium on Continuing Education for the Practicing Veterinarian*, **25**(1), pp. 48.
- [57] Brockmann, J. E., 2001, "Sampling and Transport of Aerosols," in *Aerosol Measurement: Principles, Techniques, and Applications*, 2nd Ed., P. A. Baron and K. Willeke, eds., Wiley, New York, pp. 143–195.
- [58] Hahn, I., Scherer, P. W., and Mozell, M. M., 1994, "A Mass-Transport Model of Olfaction," *J. Theor. Biol.*, **167**(2), pp. 115–128.
- [59] Anonymous, 2001, "Odors," in *ASHRAE Fundamentals Handbook*, American Society of Heating, Ventilation, and Air-Conditioning Engineers, Atlanta, pp. 13.1–13.8.
- [60] Mozell, M. M., Hornung, D. E., Sheehe, P. R., and Kurtz, D. B., 1986, "What Should be Controlled in Studies of Smell?," in *Clinical Measurement of Taste and Smell*, H. L. Meiselman and R. S. Rivlin, eds., MacMillan, New York, pp. 154–169.
- [61] Zuschneid, K., 1973, "The Olfactory Acuity of the Dog (Die Riechleistung Des Hundes)," PhD thesis, School of Veterinary Medicine, Free University of Berlin, Berlin, Germany.
- [62] Morrison, E. E., 2000, "Canine Detection of Illicit Drugs: Sensory Apparatus Technology," Battelle Report A185183, Columbus, OH.
- [63] Johnson, B. N., Mainland, J. D., and Sobel, N., 2003, "Rapid Olfactory Processing Implicates Subcortical Control of an Olfactory System," *J. Neurophysiol.*, **90**(2), pp. 1084–1094.
- [64] Schreider, J. P., and Raabe, O. G., 1981, "Anatomy of the Nasal-Pharyngeal Airway of Experimental Animals," *Anat. Rec.*, **200**, pp. 195–205.
- [65] Mead, K. S., Koehl, M. A. R., and O'Donnell, M. J., 1999, "Stomatopod Sniffing: The Scaling of Chemosensory Sensillae and Flicking Behavior with Body Size," *J. Exp. Mar. Biol. Ecol.*, **241**(2), pp. 235–261.
- [66] Vogel, S., 1994, *Life in Moving Fluids: The Physical Biology of Flow*, Princeton University, Princeton, NJ.
- [67] Olander, L., 2001, "Exhaust Hoods," in *Industrial Ventilation Design Guidebook*, H. D. Goodfellow, and E. Tähti, eds., Elsevier, New York, pp. 814–916.
- [68] Anonymous, 1999, "Industrial Local Exhaust Systems," in *ASHRAE Applications Handbook*, ASHRAE, Atlanta, pp. 29.1–29.21.
- [69] Jackson, C. N., Sherlock, C. N., and Moore, P. O., 1998, "Leak Testing, Part 3: Test Techniques Providing Electronic Indications of Leak Locations," in *Non-destructive Testing Handbook, Second Edition*, ASNT, Columbus, OH, 1, pp. 30–33.
- [70] List, E. J., 1982, "Mechanics of Turbulent Buoyant Jets and Plumes," in *Turbulent Buoyant Jets and Plumes*, W. Rodi, ed., Pergamon, New York, pp. 1–68.
- [71] Abramovich, G. N., and Schindler, L., 1963, *The Theory of Turbulent Jets*, MIT, Cambridge, MA.
- [72] Zhivov, A., 2001, "Air Jets," in *Industrial Ventilation Design Guidebook*, H. D. Goodfellow, and E. Tähti, eds., Elsevier, New York, pp. 446–517.
- [73] Glezer, A., and Amitay, M., 2002, "Synthetic Jets," *Annu. Rev. Fluid Mech.*, **34**, pp. 503–529.
- [74] Lai, H. Z., Naughton, J. W., and Lindberg, W. R., 2003, "An Experimental Investigation of Starting Impinging Jets," *ASME J. Fluids Eng.*, **125**(2), pp. 275–282.
- [75] Glauert, M. B., 1956, "The Wall Jet," *J. Fluid Mech.*, **1**(5), pp. 625–643.
- [76] Phares, D. J., Smedley, G. T., and Flagan, R. C., 2000, "The Inviscid Impingement of a Jet with Arbitrary Velocity Profile," *Phys. Fluids*, **12**(8), pp. 2046–2055.
- [77] Smedley, G. T., Phares, D. J., and Flagan, R. C., 1999, "Entrainment of Fine Particles From Surfaces by Gas Jets Impinging at Normal Incidence," *Exp. Fluids*, **26**(4), pp. 324–334.
- [78] Smedley, G. T., Phares, D. J., and Flagan, R. C., 2001, "Entrainment of Fine Particles From Surfaces by Gas Jets Impinging at Oblique Incidence," *Exp. Fluids*, **30**(2), pp. 135–142.
- [79] Phares, D. J., Smedley, G. T., and Flagan, R. C., 2000, "The Wall Shear Stress Produced by the Normal Impingement of a Jet on a Flat Surface," *J. Fluid Mech.*, **418**, pp. 351–375.
- [80] Phares, D. J., Smedley, G. T., and Flagan, R. C., 2000, "Effect of Particle Size and Material Properties on Aerodynamic Re-Suspension From Surfaces," *J. Aerosol Sci.*, **31**(11), pp. 1335–1353.
- [81] Ibrahim, A. H., Dunn, P. F., and Brach, R. M., 2003, "Microparticle Detachment From Surfaces Exposed to Turbulent Air Flow: Controlled Experiments and Modeling," *J. Aerosol Sci.*, **34**(6), pp. 765–782.
- [82] Ziskind, G., Yarin, L. P., Peles, S., and Gutfinger, C., 2002, "Experimental Investigation of Particle Removal From Surfaces by Pulsed Air Jets," *Aerosol Sci. Technol.*, **36**(5), pp. 652–659.
- [83] Settles, G. S., Thomas, M. A., Ferree, H. C., Jonassen, D. R., Miller, J. D., and Dodson, L. J., 2005, "The Aerodynamics of a Chemical Trace Detection Portal for Screening People," in preparation.
- [84] Marple, V. A., Olson, B. A., and Rubow, K. L., 2001, "Inertial, Gravitational, Centrifugal, and Thermal Collection Techniques," in *Aerosol Measurement: Principles, Techniques, and Applications*, 2nd Ed., P. A. Baron and K. Willeke, eds., Wiley, New York, pp. 229–260.
- [85] Baron, P. A., and Willeke, K., 2001, "Gas and Particle Motion," in *Aerosol Measurement: Principles, Techniques, and Applications*, 2nd Ed., P. A. Baron and K. Willeke, eds., Wiley, New York, pp. 61–82.
- [86] Morawska, L., and Salthammer, T., 2003, "Fundamentals of Indoor Particles and Settled Dust," in *Indoor Environment: Airborne Particles and Settled Dust*, L. Morawska and T. Salthammer, eds., Wiley, New York.
- [87] Feynman, R. P., 1999, "Diffusion," in *The Feynman Lectures on Physics, Vol. 6, Kinetics and Heat*, Audio Recording, Basic Books, New York.
- [88] Stitzel, S. E., Stein, D. R., and Walt, D. R., 2003, "Enhancing Vapor Sensor Discrimination by Mimicking a Canine Nasal Cavity Flow Environment," *J. Am. Chem. Soc.*, **125**(13), pp. 3684–3685.
- [89] Neuhaus, W., 1981, "The Importance of the Sniffing in Canine Olfaction (Die Bedeutung des Schnüffels für das Riechen des Hundes)," *Zeitschrift für Säugetierkunde*, **46**, pp. 301–310.
- [90] Vogel, S., 2003, *Comparative Biomechanics: Life's Physical World*, Princeton University, Princeton, NJ.
- [91] Anonymous, 2001, "Mass Transfer," in *ASHRAE Fundamentals Handbook*, ASHRAE, Atlanta, pp. 5.1–5.13.
- [92] Goldman, J. A., and Koehl, M. A. R., 2001, "Fluid Dynamic Design of Lobster Olfactory Organs: High Speed Kinematic Analysis of Antennule Flicking by *Panulirus Argus*," *Chem. Senses*, **26**(4), pp. 385–398.
- [93] Koehl, M. A. R., Koseff, J. R., Crimaldi, J. P., McCay, M. G., Cooper, T., Wiley, M. B., and Moore, P. A., 2001, "Lobster Sniffing: Antennule Design and Hydrodynamic Filtering of Information in an Odor Plume," *Science*, **294**(5548), pp. 1948–1951.
- [94] Griffy, T. A., 1992, "A Model of Explosive Vapor Concentration II," in *Proceedings of the Fourth International Symposium on the Analysis and Detection of Explosives*, J. Yinon, ed., Kluwer-Academic, New York, pp. 503–511.
- [95] Lugt, H. J., 1983, *Vortex Flow in Nature and Technology*, Wiley, New York.
- [96] Motchkine, V. S., Krasnobaev, L. Y., and Bunker, S. N., Aug. 21, 2003, "Cyclone Sampling Nozzle for an Ion Mobility Spectrometer," U.S. Patent App. US2003/0155506A1.
- [97] Colehour, J. L., and Farquhar, B. W., 1971, "Inlet Vortex," *J. Aircr.*, **8**(1), pp. 39–43.
- [98] De Siervi, F., Viguier, H. C., Greitzer, E. M., and Tan, C. S., 1982, "Mechanisms of Inlet Vortex Formation," *J. Fluid Mech.*, **124**, pp. 173–207.
- [99] Chen, P., Soundra-Nayagam, M., Bolton, A. N., and Simpson, H. C., 1996, "Unstable Flow in Centrifugal Fans," *ASME J. Fluids Eng.*, **118**(1), pp. 128–133.
- [100] Stong, C. L., 1971, "Experiments With Wind: A Pendulum Anemometer and Miniature Tornadoes," *Sci. Am.*, **224**(10), pp. 108–112.
- [101] Lippmann, M., 2001, "Filters and Filter Holders," in *Air Sampling Instruments for Evaluation of Atmospheric Contaminants*, 9th Ed., American Conference of Governmental Industrial Hygienists, Cincinnati, OH, pp. 281–314.
- [102] Hering, S. V., 2001, "Impactors, Cyclones, and Other Particle Collectors," in *Air Sampling Instruments for Evaluation of Atmospheric Contaminants*, 9th Ed., American Conference of Governmental Industrial Hygienists, Cincinnati, OH, pp. 315–375.
- [103] Johnston, J. M., Morrison, E. E., and Boussom, T. M., 2002, "The Role of Particles in Canine Olfactory Detection," unpublished.
- [104] Chang, M. C., Kim, S., and Sioutas, C., 1999, "Experimental Studies on Particle Impaction and Bounce: Effects of Substrate Design and Material," *Atmos. Environ.*, **33**(15), pp. 2313–2322.
- [105] Misra, C., Geller, M. D., Shah, P., Sioutas, C., and Solomon, P. A., 2001, "Development and Evaluation of a Continuous Coarse (PM10-PM2.5) Particle Monitor," *J. Air Waste Manage. Assoc.*, **51**(9), pp. 1309–1317.
- [106] Macher, J. M., and Burge, H. A., 2001, "Sampling Biological Aerosols," in *Air Sampling Instruments for Evaluation of Atmospheric Contaminants*, 9th Ed., American Conference of Governmental Industrial Hygienists, Cincinnati, OH, pp. 662–701.
- [107] Solomon, W. R., 2003, "How Ill the Wind? Issues in Aeroallergen Sampling," *J. Allergy Clin. Immunol.*, **112**(1), pp. 3–8.
- [108] Mehta, S. K., Bell-Robinson, D. M., Groves, T. O., Stetzenbach, L. D., and Pierson, D. L., 2000, "Evaluation of Portable Air Samplers for Monitoring Airborne Culturable Bacteria," *Am. Ind. Hyg. Assoc. J.*, **61**(6), pp. 850–854.
- [109] Lacey, J., 1997, "Guest Editorial: Sampling and Rapid Assay of Bioaerosols," *J. Aerosol Sci.*, **28**(3), pp. 345–348.
- [110] Griffiths, W. D., Stewart, I. W., Futter, S. J., Upton, S. L., and Mark, D., 1997, "Development of Sampling Methods for the Assessment of Indoor Bioaerosols," *J. Aerosol Sci.*, **28**(3), pp. 437–457.
- [111] Heinsohn, R. J., and Cimbala, J. M., 2002, *Indoor Air Quality Engineering*, Marcel Dekker, New York.
- [112] Wallace, L. A., 2001, "Human Exposure to Volatile Organic Pollutants: Implications for Indoor Air Studies," *Annu. Rev. Energy Environ.*, **26**, pp. 269–301.
- [113] Anonymous, 2001, "Indoor Environmental Health," in *ASHRAE Fundamentals Handbook*, ASHRAE, Atlanta, GA, pp. 9.1–9.20.
- [114] Thomas, K. W., Pellizzari, E. D., Clayton, C. A., Whitaker, D. A., Shores, R. C., Spengler, J., Ozkaynak, H., Froelich, S. E., and Wallace, L. A., 1993, "Particle Total Exposure Assessment Methodology (PTEAM) 1990 Study—Method Performance and Data Quality for Personal, Indoor, and Outdoor Monitoring," *J. Expo Anal Environ. Epidemiol.*, **3**(2), pp. 203–226.
- [115] Clayton, C. A., Perritt, R. L., Pellizzari, E. D., Thomas, K. W., Whitmore, R. W., Wallace, L. A., Ozkaynak, H., and Spengler, J. D., 1993, "Particle Total Exposure Assessment Methodology (PTEAM) Study—Distributions of Aerosol and Elemental Concentrations in Personal, Indoor, and Outdoor Air

- Samples in a Southern California Community," *J. Expo Anal Environ. Epidemiol.*, **3**(2), pp. 227–250.
- [116] Ozkaynak, H., Xue, J., Spengler, J., Wallace, L., Pellizzari, E., and Jenkins, P., 1996, "Personal Exposure to Airborne Particles and Metals: Results From the Particle Team Study in Riverside, California," *J. Expo Anal Environ. Epidemiol.*, **6**(1), pp. 57–78.
- [117] Rodes, C. E., Kamens, R. M., and Wiener, R. W., 1991, "The Significance and Characteristics of the Personal Activity Cloud on Exposure Assessment Measurements for Indoor Contaminants," *Indoor Air*, **2**, pp. 123–145.
- [118] Wallace, L. A., 1993, "The TEAM Studies," *EPA Journal*, **19**(4).
- [119] Lewis, H. E., Foster, A. R., Mullan, B. J., Cox, R. N., and Clark, R. P., 1969, "Aerodynamics of the Human Microenvironment," *Lancet*, **322**(7609), pp. 1273–1277.
- [120] Clark, R. P., and Edholm, O. G., 1985, *Man and His Thermal Environment*, E. Arnold, London.
- [121] Homma, H., and Yakiyama, M., 1991, "Examination of Free Convection Around Occupant's Body Caused by Its Metabolic Heat," *ASHRAE Trans.*, **94** Part 1(3118), pp. 104–124.
- [122] Clark, R. P., and Cox, R. N., 1974, "An Application of Aeronautical Techniques to Physiology. 2. Particle Transport within the Human Microenvironment," *Med. Biol. Eng.*, **12**(3), pp. 275–279.
- [123] Gowadia, H. A., 2000, "The Natural Sampling of Airborne Trace Signals Associated with the Human Body," PhD thesis, Pennsylvania State University, University Park, PA.
- [124] Gowadia, H. A., and Settles, G. S., 2001, "The Natural Sampling of Airborne Trace Signals From Explosives Concealed Upon the Human Body," *J. Forensic Sci.*, **46**(6), pp. 1324–1331.
- [125] Syrotuck, W. G., 1972, *Scent and the Scenting Dog*, Arner, Rome, NY.
- [126] May, K. R., and Pomeroy, N. P., 1973, "Bacterial Dispersion from the Body Surface," in *Airborne Transmission and Airborne Infection: Concepts and Methods*, J. F. Hers and K. C. Winkler, eds., Wiley, New York, pp. 426–432.
- [127] Clark, R. P., and Shirley, S. G., 1973, "Identification of Skin in Airborne Particulate Matter," *Nature (London)*, **246**(5427), pp. 39–40.
- [128] Clark, R. P., 1974, "Skin Scales Among Airborne Particles," *J. Hyg. (Lond)*, **72**(1), pp. 47–51.
- [129] Sykes, B., 2001, *The Seven Daughters of Eve*, Norton, New York.
- [130] Murakami, S., 2002, "CFD Study on the Micro-Climature Around the Human Body with Inhalation and Exhalation," in *Proceedings of ROOMVENT 2002, 8th International Conference on Air Distribution in Rooms*, Copenhagen, 8–11, Technical University of Denmark.
- [131] Renstrom, A., Karlsson, A. S., and Tovey, E., 2002, "Nasal Air Sampling used for the Assessment of Occupational Allergen Exposure and the Efficacy of Respiratory Protection," *Clin. Exp. Allergy*, **32**(12), pp. 1769–1775.
- [132] Misra, C., Singh, M., Shen, S., Sioutas, C., and Hall, P. A., 2002, "Development and Evaluation of a Personal Cascade Impactor Sampler (PCIS)," *J. Aerosol Sci.*, **33**(7), pp. 1027–1047.
- [133] Hauck, B. C., Grinshpun, S. A., Reponen, A., Reponen, T., Willeke, K., and Bornschein, R. L., 1997, "Field Testing of New Aerosol Sampling Method With a Porous Curved Surface As Inlet," *Am. Ind. Hyg. Assoc. J.*, **58**(10), pp. 713–719.
- [134] Aizenberg, V., Choe, K., Grinshpun, S. A., Willeke, K., and Baron, P. A., 2001, "Evaluation of Personal Aerosol Samples Challenged with Large Particles," *J. Aerosol Sci.*, **32**(6), pp. 779–793.
- [135] Guffey, S. E., Flanagan, M. E., and van Belle, G., 2001, "Air Sampling at the Chest and Ear As Representative of the Breathing Zone," *Am. Ind. Hyg. Assoc. J.*, **62**(4), pp. 416–427.
- [136] Fletcher, B., and Johnson, A. E., 1989, "Comparison of Personal and Area Concentration of Measurements, and the Use of a Mannequin in Sampling," *Proceedings Ventilation '88*, Vincent, J. H., ed., BOHS, London, pp. 161–167.
- [137] Fetterolf, D. D., and Clark, T. D., 1993, "Detection of Trace Explosive Evidence by Ion Mobility Spectrometry," *J. Forensic Sci.*, **38**(1), pp. 28–39.
- [138] Baret, G., and Gevaud, R., Aug. 30, 1994, "Helium Leak Detector," U.S. Patent 5,341,671.
- [139] Jackson, C. N., Sherlock, C. N., and Moore, P. O., 1998, "Leak Testing, Part 5: Sampling Detector Probe Testing of Systems Pressurized with Helium Tracer Gas," in *Nondestructive Testing Handbook*, 2nd Ed., ASNT, Columbus, OH, I, pp. 478–489.
- [140] DeSorbo, M. A., 2001, "Fingerprinting Particles 'Automatically,'" *Cleanrooms*, **15**(10), pp. 1–54.
- [141] Anonymous, 2004, "Portable Gas Sample Extraction Probe PSP4000-H/C/T," M&C Products Analysetechnik GmbH, Ratingen, Germany.
- [142] Grasmeyer, J. M., and Keennon, M. T., 2001, "Development of the Black Widow Micro Air Vehicle," AIAA Paper No. 2001-0127.
- [143] Mueller, T. J., and DeLaurier, J. D., 2003, "Aerodynamics of Small Vehicles," *Annu. Rev. Fluid Mech.*, **35**, pp. 89–111.
- [144] Anderson, G. P., King, K. D., Cuttino, D. S., Whelan, J. P., Ligler, F. S., MacKrell, J. F., Bovais, C. S., Indyke, D. K., and Foch, R. J., 1999, "Biological Agent Detection With the Use of an Airborne Biosensor," *Field Anal. Chem. Tech.*, **3**(4–5), pp. 307–314.
- [145] Ligler, F. S., Anderson, G. P., Davidson, P. T., Foch, R. J., Ives, J. T., King, K. D., Page, G., Stenger, D. A., and Whelan, J. P., 1998, "Remote Sensing Using an Airborne Biosensor," *Environ. Sci. Technol.*, **32**, pp. 2461–2466.
- [146] Brune, W. H., Faloon, I. C., Tan, D., Weinheimer, A. J., Campos, T., Ridley, B. A., Vay, S. A., Collins, J. E., Sachse, G. W., Jaegle, L., and Jacob, D. J., 1998, "Airborne in-Situ OH and HO<sub>2</sub> Observations in the Cloud-Free Troposphere and Lower Stratosphere During SUCCESS," *Geophys. Res. Lett.*, **25**(10), pp. 1701–1704.
- [147] Porter, J. N., Clarke, A. D., Ferry, G., and Pueschel, R. F., 1992, "Aircraft Studies of Size-Dependent Aerosol Sampling Through Inlets," *J. Geophys. Res.*, [Atmos.], **97**(D4), pp. 3815–3824.
- [148] Sheridan, P. J., and Norton, R. B., 1998, "Determination of the Passing Efficiency for Aerosol Chemical Species Through a Typical Aircraft-Mounted, Diffuser-Type Aerosol Inlet System," *J. Geophys. Res.*, [Atmos.], **103**(D7), pp. 8215–8225.
- [149] Reed, R. D., 1978, "High-Flying Mini-Sniffer RPV—Mars Bound," *Astronaut. Aeronaut.*, **16**(6), pp. 26–39.
- [150] Spedding, G. R., and Lissaman, P. B. S., 1998, "Technical Aspects of Microscale Flight Systems," *Journal of Avian Biology*, **29**(4), pp. 458–468.
- [151] Singh, H., Jacob, D., Pfister, L., and Crawford, J., 2002, "INTEX-NA: Intercontinental Chemical Transport Experiment—North America," National Aeronautics and Space Administration White Paper, [http://cloud1.arc.nasa.gov/intex-na/overview/white\\_paper.pdf](http://cloud1.arc.nasa.gov/intex-na/overview/white_paper.pdf).
- [152] Kiel, G., 1935, "Total-Head Meter with Small Sensitivity to Yaw," National Advisory Committee for Aeronautics, Technical Memorandum 775, <http://naca.larc.nasa.gov/reports/1935/naca-tm-775/>.
- [153] Cain, S. A., Ram, M., and Woodward, S., 1998, "Qualitative and Quantitative Wind Tunnel Measurements of the Airflow Through a Shrouded Airborne Aerosol Sampling Probe," *J. Aerosol Sci.*, **29**(9), pp. 1157–1169.
- [154] Soderman, P. T., Hazen, N. L., and Brune, W. H., 1991, "Aerodynamic Design of Gas and Aerosol Samplers for Aircraft," National Aeronautics and Space Administration Technical Memorandum 103854.
- [155] Sutton, O. G., 1953, *Micrometeorology*, McGraw-Hill, New York.
- [156] Arya, P. S., 2001, *Introduction to Micrometeorology*, Academic, New York.
- [157] DeBlieu, J., 1998, *Wind: How Air Flow Has Shaped Life, Myth, and the Land*, Houghton Mifflin, Boston, MA.
- [158] Shivik, J. A., 2002, "Odor-Adsorptive Clothing, Environmental Factors, and Search-Dog Ability," *Wildlife Soc. Bull.*, **30**(3), pp. 721–727.
- [159] Schouet, L. P., and Miller, T. A., 1994, "Automated Pheromone Traps Show Male Pink-Bollworm (Lepidoptera, Gelechiidae) Mating Response Is Dependent on Weather Conditions," *J. Econ Entomol.*, **87**(4), pp. 965–974.
- [160] Anonymous, 2001, "Airflow Around Buildings," in *ASHRAE Fundamentals Handbook*, ASHRAE, Atlanta, GA, pp. 16.1–16.12.
- [161] Vander Wall, S. B., 1998, "Foraging Success of Granivorous Rodents: Effects of Variation in Seed and Soil Water on Olfaction," *Ecology*, **79**(1), pp. 233–241.
- [162] Jenkins, T. F., Walsh, M. E., Miyares, P. H., Kopczinski, J. A., Ranney, T. A., George, V., Pennington, J. C., and Berry, T. E., 2000, "Analysis of Explosives-Related Chemical Signatures in Soil Samples Collected Near Buried Land Mines," U.S. Army Corps of Engineers Report ERDC TR-00-5, Hanover, NH.
- [163] Turner, J. S., 1973, *Buoyancy Effects in Fluids*, Cambridge University, Cambridge, UK.
- [164] List, E. J., 1982, "Turbulent Jets and Plumes," *Annu. Rev. Fluid Mech.*, **14**, pp. 189–212.
- [165] Scorer, R. S., 1958, *Natural Aerodynamics*, Pergamon, New York.
- [166] Settles, G. S., and Kester, D. A., 2001, "Aerodynamic Sampling for Landmine Trace Detection," in *Proc. SPIE—Detection and Remediation Technologies for Mines and Minelike Targets*, VI, Dubey, A. C., et al., eds., International Society for Optical Engineering, Bellingham, WA, 4394, pp. 890–898.
- [167] Mollendorf, J. C., Arif, H., and Ajmiran, E. B., 1996, "Developing Flow and Transport Above a Suddenly Heated Horizontal Surface in Water," *Int. J. Heat Mass Transfer*, **27**(2), pp. 273–289.
- [168] Carde, R. T., 1996, "Odour Plumes and Odour-Mediated Flight in Insects," in *Ciba Foundation Symposium on Olfaction in Mosquito-Host Interactions*, Associated Scientific, Amsterdam, pp. 54–70.
- [169] Ishida, H., and Morizumi, T., 2003, "Machine Olfaction for Mobile Robots," in *Handbook of Machine Olfaction*, T. C. Pearce et al., eds., Wiley, New York, pp. 399–417.
- [170] Weissburg, M. J., 2000, "The Fluid Dynamical Context of Chemosensory Behavior," *Biol. Bull.*, **198**(2), pp. 188–202.
- [171] Murlis, J., Willis, M. A., and Carde, R. T., 2000, "Spatial and Temporal Structures of Pheromone Plumes in Fields and Forests," *Phys. Entomol.*, **25**(3), pp. 211–222.
- [172] Vickers, N. J., 2000, "Mechanisms of Animal Navigation in Odor Plumes," *Biol. Bull.*, **198**(2), pp. 203–212.
- [173] Finelli, C. M., Pentcheff, N. D., Zimmer-Faust, R. K., and Wetthey, D. S., 1999, "Odor Transport in Turbulent Flows: Constraints on Animal Navigation," *Limnol. Oceanogr.*, **44**(4), pp. 1056–1071.
- [174] Moore, P. A., and Atema, J., 1991, "Spatial Information in the Three-Dimensional Fine Structure of an Aquatic Odor Plume," *Biol. Bull.*, **181**(12), pp. 408–418.
- [175] Moore, P. A., Zimmer-Faust, R. K., Bement, S. L., Weissburg, M. J., Parrish, J. M., and Gerhardt, G. A., 1992, "Measurement of Microscale Patchiness in a Turbulent Aquatic Odor Plume Using a Semiconductor-Based Microprobe," *Biol. Bull.*, **183**(8), pp. 138–142.
- [176] Koehl, M. A. R., 1996, "Small-Scale Fluid Dynamics of Olfactory Antennae," *Marine Freshwater Behav. Physiol.*, **27**(2–3), pp. 127–141.
- [177] Mead, K. S., Wiley, M. B., Koehl, M. A. R., and Koseff, J. R., 2003, "Fine-Scale Patterns of Odor Encounter by the Antennules of Mantis Shrimp Tracking Turbulent Plumes in Wave-Affected and Unidirectional Flow," *J. Exp. Biol.*, **206**(1), pp. 181–193.
- [178] Murlis, J., Elkington, J. S., and Carde, R. T., 1992, "Odor Plumes and How Insects Use Them," *Annu. Rev. Entomol.*, **37**, pp. 505–532.

- [179] Weissburg, M. J., and Zimmer-Faust, R. K., 1993, "Life and Death in Moving Fluids: Hydrodynamic Effects on Chemosensory-Mediated Predation," *Ecology*, **74**, pp. 1428–1443.
- [180] Geier, M., Bosch, O. J., and Boeckh, J., 1999, "Influence of Odour Plume Structure on Upwind Flight of Mosquitoes Towards Hosts," *J. Exp. Biol.*, **202**(12), pp. 1639–1648.
- [181] Ishida, H., Nakamoto, T., and Moriizumi, T., 1998, "Remote Sensing of Gas/Odor Source Location and Concentration Distribution Using Mobile System," *Sens. Actuators B*, **49**(1–2), pp. 52–57.
- [182] Ishida, H., Nakamoto, T., Moriizumi, T., Kikas, T., and Janata, J., 2001, "Plume-Tracking Robots: A New Application of Chemical Sensors," *Biol. Bull.*, **200**(2), pp. 222–226.
- [183] Devez, R., Thiel, D., Russell, A., and Mackay-Sim, A., 1994, "Odor Sensing for Robot Guidance," *Int. J. Robot. Res.*, **13**, pp. 232–239.
- [184] Li, W., Farrell, J. A., and Carde, R. T., 2001, "Tracking of Fluid-Advection Odor Plumes: Strategies Inspired by Insect Orientation to Pheromone," *Adaptive Behavior*, **9**(3–4), pp. 143–170.
- [185] Dusenbery, D. B., 2003, "Mechanisms for Gradient Following," in *Sensors and Sensing in Biology and Engineering*, Springer-Verlag, Vienna, Chap. 21, pp. 291–303.
- [186] Grasso, F., Consi, T., Mountain, D., and Atema, J., 1996, "Locating Odor Sources in Turbulence with a Lobster Inspired Robot," in *From Animals to Animats: Proceedings of the International Conference on Simulation Adaptive Behavior*, P. Maes et al., eds., MIT, Cambridge, MA, pp. 104–112.
- [187] Anonymous, 2003, "Following Toxic Clouds: Science and Assumptions in Plume Modeling" *Hearing Before Subcommittee on National Security, Emerging Threats & International Relations, Committee on Government Reform, U.S. House of Representatives, 108th Congress, 1st Session, Serial No. 108-91*, US GPO Report 1016-A, <http://purl.access.gpo.gov/GPO/LPS47967>
- [188] Sharan, M., and Gopalakrishnan, S. G., 1997, "Bhopal Gas Accident: a Numerical Simulation of the Gas Dispersion Event," *Environ. Model. Software*, **12**(2–3), pp. 135–141.
- [189] Gudiksen, P. H., Harvey, T. F., and Lange, R., 1989, "Chernobyl Source Term, Atmospheric Dispersion, and Dose Estimation," *Health Phys.*, **57**(5), pp. 697–706.
- [190] List, E. J., 1996, "Environmental Fluid Mechanics," *Research Trends in Fluid Dynamics: Report from US National Commission on Theoretical & Applied Mechanics*, J. L. Lumley ed., Springer, New York, pp. 148–166.
- [191] Sullivan, T. J., Ellis, J. S., Foster, C. S., Foster, K. T., Baskett, R. L., Nasstrom, J. S., and Schalk, W. W., 1993, "Atmospheric Release Advisory Capability-Real-Time Modeling of Airborne Hazardous Materials," *Bull. Am. Meteorol. Soc.*, **74**(12), pp. 2343–2361.
- [192] Cowan, I. R., Castro, I. P., and Robins, A. G., 1997, "Numerical Considerations for Simulations of Flow and Dispersion Around Buildings," *J. Wind. Eng. Ind. Aerodyn.*, **67–68**, pp. 535–545.
- [193] Boris, J., 2002, "The Threat of Chemical and Biological Terrorism: Preparing a Response," *Comput. Sci. Eng.*, **4**(2), pp. 22–32.
- [194] Negus, V. E., 1958, *The Comparative Anatomy and Physiology of the Nose and Paranasal Sinuses*, Livingstone, London.
- [195] Bang, B. G., 1971, "Functional Anatomy of the Olfactory System in 23 Orders of Birds," *Acta Anat. Suppl.* (Basel), **79**, pp. 1–76.
- [196] Stacey, M. T., Mead, K. S., and Koehl, M. A. R., 2002, "Molecule Capture by Olfactory Antennules: Mantis Shrimp," *J. Math. Biol.*, **44**(1), pp. 1–30.
- [197] U.S. Department of Agriculture, 2004, "Integrated Taxonomic Information System On-Line Database," <http://www.itis.usda.gov>.
- [198] Arnason, U., Adegoke, J. A., Bodin, K., Born, E. W., Esa, Y. B., Gullberg, A., Nilsson, M., Short, R. V., Xu, X. F., and Janke, A., 2002, "Mammalian Mitogenomic Relationships and the Root of the Eutherian Tree," *Proc. Natl. Acad. Sci. U.S.A.*, **99**(12), pp. 8151–8156.
- [199] Carroll, R. L., 1997, *Patterns and Processes of Vertebrate Evolution*, Cambridge University, Cambridge, England.
- [200] Wayne, R. K., 1993, "Molecular Evolution of the Dog Family," *Trends Genet.*, **9**(6), pp. 218–224.
- [201] International Committee on Veterinary Gross Anatomical Nomenclature, 1972, *Nomina Anatomica Veterinaria*, World Association of Veterinary Anatomists, New York.
- [202] Wayne, R. K., Leonard, J. A., and Cooper, A., 1999, "Full of Sound and Fury: The Recent History of Ancient DNA," *Annu. Rev. Ecol. Syst.*, **30**, pp. 457–477.
- [203] Vogel, S., 1994, "Nature's Pumps," *Am. Sci.*, **82**(5), pp. 464–471.
- [204] Benyus, J. M., 1997, *Biomimicry*, William Morrow & Co., New York.
- [205] Moniz, E. J., and Baldeswiler, J. D., 2003, "Approaches to Combat Terrorism (ACT): Opportunities for Basic Research," National Science Foundation, [http://www.mitre.org/public/act/10\\_22\\_final.pdf](http://www.mitre.org/public/act/10_22_final.pdf)
- [206] Negus, V. E., 1960, "Further Observations on the Air-Conditioning Mechanism of the Nose," *Ann. R. Coll. Surg. Engl.*, **27**, pp. 171–204.
- [207] Moulton, D. G., 1967, "Olfaction in Mammals," *Am. Zool.*, **7**, pp. 421–429.
- [208] Hillenius, W. J., 1992, "The Evolution of Nasal Turbinates and Mammalian Endothermy," *Paleobiology*, **18**, pp. 17–29.
- [209] Geist, H. R., 2000, "Nasal Respiratory Turbinate Function in Birds," *Physiological and Biochemical Zoology*, **73**(5), pp. 581–589.
- [210] Becker, R. F., and King, J. E., 1957, "Delineation of the Nasal Airstreams in the Living Dog," *Arch. Otolaryngol.*, **65**(5), pp. 428–436.
- [211] Neuhaus, W., 1953, "Über die Riechschärfe des Hundes für Fettsäuren," *Zeitschrift für Vergleichende Physiologie*, **35**, pp. 527–552.
- [212] Neuhaus, W., 1955, "Die Unterscheidung von Luftquantitäten bei Mensch und Hund nach Versuchen Mit Buttersäure," *Zeitschrift für Vergleichende Physiologie*, **37**, pp. 234–252.
- [213] McCartney, W., 1968, *Olfaction and Odours: An Osmophysiological Essay*, Springer-Verlag, Berlin.
- [214] Johnston, J. M., Myers, L. J., Waggoner, L. P., and Williams, M., 1994, "Determination of Canine Olfactory Thresholds using Operant Laboratory Methods," *Proceedings Substance Detection Systems*, Proc. SPIE, **2092**, pp. 238–243.
- [215] Johnston, J. M., Williams, M., Waggoner, L. P., Edge, C. C., Dugan, R. E., and Hollowell, S. F., 1998, "Canine Detection Odor Signatures for Mine-Related Explosives," in *Proceedings of SPIE, Detection Remediation Technology for Mines and Mine-like Targets III*, Proc. SPIE, **3392**, Part 1, pp. 490–501.
- [216] Williams, M., Johnston, J. M., Cicoria, M., Paletz, E., Waggoner, L. P., Edge, C. C., and Hollowell, S. F., 1998, "Canine Detection Odor Signatures for Explosives," *Proc. SPIE*, **3575**, pp. 291–301.
- [217] Williams, M., Johnston, J. M., Cicoria, M., Paletz, E., Waggoner, L. P., Edge, C. C., and Hollowell, S. F., 1998, "Effects of Extraneous Odors on Canine Detection," *Proc. SPIE*, **3575**, pp. 355–362.
- [218] Thesen, A., Steen, J. B., and Doving, K. B., 1993, "Behaviour of Dogs During Olfactory Tracking," *J. Exp. Biol.*, **180**, pp. 247–251.
- [219] Steen, J. B., Mohus, I., Kvesetberg, T., and Walloe, L., 1996, "Olfaction in Bird Dogs During Hunting," *Acta Physiol. Scand.*, **157**(1), pp. 115–119.
- [220] Evans, H. E., 1993, *Miller's Anatomy of the Dog*, Saunders, Philadelphia.
- [221] Anderson, W., Anderson, B. G., and Smith, B. J., 1994, *Atlas of Canine Anatomy*, Lea & Febiger, Philadelphia.
- [222] Thomas, E. M., 1993, *The Hidden Life of Dogs*, Houghton Mifflin, Boston, MA.
- [223] Johnston, R. E., and Bhorade, A., 1998, "Perception of Scent Over-Marks by Golden Hamsters (*Mesocricetus Auratus*): Novel Mechanisms for Determining Which Individual's Mark is on Top," *J. Comp., Psych.*, **112**(3), pp. 230–243.
- [224] Ferkin, M. H., Dunsavage, J., and Johnston, R. E., 1999, "What Kind of Information do Meadow Voles, *Microtus Pennsylvanicus*, Use to Distinguish Between the Top and Bottom Scent of an Over-Mark?," *J. Comp., Psych.*, **113**(1), pp. 43–51.
- [225] Achter, E. K., Hobbs, J. R., Fine, D. H., Dionne, B. C., and Rounbehler, D. P., 1986, "Vapor Pressure of Explosives," *J. Energ. Mater.*, **4**(1–4), pp. 447–472.
- [226] Johnson, W. E., and O'Brien, S. J., 1997, "Phylogenetic Reconstruction of the Felidae Using 16S rRNA and NADH-5 Mitochondrial Genes," *J. Mol. Evol.*, **44**(Suppl 1), pp. S98–S116.
- [227] Clifford, A. B., and Witmer, L. M., 2004, "Case Studies in Novel Narial Anatomy: 2. The Enigmatic Nose of Moose (*Artiodactyla: Cervidae: Alces Alces*)," *J. Zool.*, **262**, pp. 339–360.
- [228] Shoshani, J., 1997, "It's a Nose! It's a Hand! It's an Elephant's Trunk!," *Natural History*, **106**(10), pp. 37–43.
- [229] Mariappa, D., 1986, *Anatomy and Histology of the Indian Elephant*, Indira Publishing House, Oak Park, MI.
- [230] Glebovskii, V. D., and Marevskaya, A. P., 1968, "Participation of Muscles of the Nostrils in Olfactory Analysis and Respiration in Rabbits," *Fiziol. Zh.*, **54**(11), pp. 1278–1286.
- [231] Le Guerier, A., 1992, *Scent: The Essential and Mysterious Powers of Smell*, Turtle Bay Books/Random House, New York.
- [232] Stoddart, D. M., 1990, *The Scented Ape: The Biology and Culture of Human Odour*, Cambridge University, Cambridge, England.
- [233] Proetz, A. W., 1941, *Essays on the Applied Physiology of the Nose*, Annals Publishing Co., St. Louis, Mo.
- [234] Eccles, R., 2000, "Nasal Airflow in Health and Disease," *Acta Oto-Laryngol.*, **120**(5), pp. 580–595.
- [235] Cole, P., 2000, "Biophysics of Nasal Airflow: A Review," *Am. J. Rhinol.*, **14**(4), pp. 245–249.
- [236] Lin, S. J., and Danahey, D. G., 2002, "Nasal Aerodynamics," *eMedicine*, **3**(4).
- [237] Zimmer, C., 2002, "The Rise and Fall of the Nasal Empire," *Natural History*, **111**(5), pp. 32–35.
- [238] Shepherd, G. M., 2004, "The Human Sense of Smell: Are We Better Than We Think?," *PLoS Biology*, **2**(5), pp. 572–575.
- [239] Haselton, F. R., and Sperandio, P. G. N., 1988, "Convective Exchange Between the Nose and the Atmosphere," *J. Appl. Physiol.*, **64**(6), pp. 2575–2581.
- [240] Keyhani, K., Scherer, P. W., and Mozell, M. M., 1997, "A Numerical Model of Nasal Odorant Transport for the Analysis of Human Olfaction," *J. Theor. Biol.*, **186**(3), pp. 279–301.
- [241] Simmen, D., Scherrer, J. L., Moe, K., and Heinz, B., 1999, "A Dynamic and Direct Visualization Model for the Study of Nasal Airflow," *Arch. Otolaryngol. Head Neck Surg.*, **125**(9), pp. 1015–1021.
- [242] Sobel, N., Khan, R. M., Saltman, A., Sullivan, E. V., and Gabrieli, J. D. E., 1999, "Olfaction-The World Smells Different to Each Nostril," *Nature (London)*, **402**(6757), p. 35.
- [243] Sobel, N., Prabhakaran, V., Desmond, J. E., Glover, G. H., Goode, R. L., Sullivan, E. V., and Gabrieli, J. D. E., 1998, "Sniffing and Smelling: Separate Subsystems in the Human Olfactory Cortex," *Nature (London)*, **392**(6673), pp. 282–286.
- [244] Cheng, Y. S., Hansen, G. K., Su, Y. F., Yeh, H. C., and Morgan, K. T., 1990, "Deposition of Ultrafine Aerosols in Rat Nasal Molds," *Toxicol. Appl. Pharmacol.*, **106**, pp. 222–233.
- [245] Kelly, J. T., and Asgharian, B., 2003, "Nasal Molds as Predictors of Fine and

- Coarse Particle Deposition in Rat Nasal Airways," *Inhalation Toxicol.*, **15**(9), pp. 859–875.
- [246] Kelly, J. T., Kimbell, J. S., and Asgharian, B., 2001, "Deposition of Fine and Coarse Aerosols in a Rat Nasal Mold," *Inhalation Toxicol.*, **13**(7), pp. 577–588.
- [247] Morgan, K. T., Kimbell, J. S., Monticello, T. M., Patra, A. L., and Fleischman, A., 1991, "Studies of Inspiratory Air-Flow Patterns in the Nasal Passages of the F344 Rat and Rhesus-Monkey Using Nasal Molds-Relevance to Formaldehyde Toxicity," *Toxicol. Appl. Pharmacol.*, **110**(2), pp. 223–240.
- [248] Kauer, J. S., 1968, "A Study of the Structure and Function of the Vomeronasal (Jacobson's) Organ," MA thesis, Clark University, Worcester, MA.
- [249] Welker, W. I., 1964, "Analysis of Sniffing of the Albino Rat," *Behaviour*, **22**, pp. 223–244.
- [250] Wilson, D. A., and Sullivan, R. M., 1999, "Respiratory Airflow Pattern at the Rat's Snout and an Hypothesis Regarding its Role in Olfaction," *Physiol. Behav.*, **66**(1), pp. 41–44.
- [251] Youngtob, S. L., Mozell, M. M., Sheehe, P. R., and Hornung, D. E., 1987, "A Quantitative Analysis of Sniffing Strategies in Rats Performing Odor Detection Tasks," *Physiol. Behav.*, **41**(1), pp. 59–69.
- [252] Kepecs, A., 2004 (unpublished).
- [253] Kleerekoper, H., 1969, *Olfaction in Fishes*, Indiana University, Bloomington, IN.
- [254] Pohlmann, K., Grasso, F. W., and Breithaupt, T., 2001, "Tracking Wakes: The Nocturnal Predatory Strategy of Piscivorous Catfish," *Proc. Natl. Acad. Sci. U.S.A.*, **98**(13), pp. 7371–7374.
- [255] Wallraff, H. G., 2003, "Olfactory Navigation by Birds," *Journal für Ornithologie*, **144**(1), pp. 1–32.
- [256] Wallraff, H. G., 2000, "Simulated Navigation Based on Observed Gradients of Atmospheric Trace Gases (Models on Pigeon Homing, Part 3)," *J. Theor. Biol.*, **205**(1), pp. 133–145.
- [257] Wallraff, H. G., and Andrae, M. O., 2000, "Spatial Gradients in Ratios of Atmospheric Trace Gases: A Study Stimulated by Experiments on Bird Navigation," *Tellus, Ser. B*, **52**(4), pp. 1138–1157.
- [258] Bang, B. G., 1966, "The Olfactory Apparatus of Tubenosed Birds (*Procellariiformes*)," *Acta Anat. (Basel)*, **65**, pp. 391–415.
- [259] Pennycook, C. J., 2002, "Gust Soaring as a Basis for the Flight of Petrels and Albatrosses (*Procellariiformes*)," *Avian Science*, **2**(1), pp. 1–12.
- [260] Witmer, L. M., 2001, "A Nose for All Seasons," *Natural History*, **110**, pp. 64–71.
- [261] Witmer, L. M., 2001, "Nostril Position in Dinosaurs and Other Vertebrates and its Significance for Nasal Function," *Science*, **293**, pp. 850–853.
- [262] Cruickshank, A. R. I., Small, P., and Taylor, M., 1991, "Dorsal Nostrils and Hydrodynamically Driven Underwater Olfaction in Plesiosaurs," *Nature (London)*, **352**, pp. 62–64.
- [263] Goldman, J. A., and Patek, S. N., 2002, "Two Sniffing Strategies in Palinurid Lobsters," *J. Exp. Biol.*, **205**(24), pp. 3891–3902.
- [264] Koehl, M. A. R., 2001, "Transitions in Function at Low Reynolds Number: Hair-Bearing Animal Appendages," *Math. Methods Appl. Sci.*, **24**(17–18), pp. 1523–1532.
- [265] Hansson, B. S., 1999, *Insect Olfaction*, Springer-Verlag, Berlin.
- [266] Humphrey, J. A. C., and Haj-Hariri, H., 2002, "Detection and Real Time Processing of Odor Plume Information by Arthropods in Air and Water," *Proceedings of the AFI-2002 Mini-Symposium on Advanced Fluids Information—Fusion of EFD and CFD*, Institute of Fluid Science, Tohoku University, Tokyo, pp. 47–67.
- [267] Schneider, R. W. S., Lanzan, J., and Moore, P. A., 1998, "Boundary-Layer Effect on Chemical Signal Movement Near the Antennae of the Sphinx Moth, *Manduca sexta*: Temporal Filters for Olfaction," *J. Comp. Physiol. [A]*, **182**(3), pp. 287–298.
- [268] Loudon, C., and Koehl, M. A. R., 2001, "Sniffing by a Silkworm Moth: Wing Fanning Enhances Air Penetration Through and Pheromone Interception by Antennae," *J. Exp. Biol.*, **203**(19), pp. 2977–2990.
- [269] Spielman, A., and D'Antonio, M., 2001, *Mosquito*, Hyperion, New York.
- [270] Wright, R. H., 1975, "Why Mosquito Repellents Repel," *Sci. Am.*, **233**(7), pp. 104–111.
- [271] Fox, A. N., Pitts, R. J., Robertson, H. M., Carlson, J. R., and Zwiebel, L. J., 2001, "Candidate Odorant Receptors from the Malaria Vector Mosquito *Anopheles Gambiae* and Evidence of Down-Regulation in Response to Blood Feeding," *Proc. Natl. Acad. Sci. U.S.A.*, **98**(25), pp. 14693–14697.
- [272] Takken, W., 1991, "The Role of Olfaction in Host-Seeking of Mosquitoes: A Review," *Sci. App.* **12**(1–3), pp. 287–295.
- [273] Dekker, T., Takken, W., Knols, B. G. J., Bouman, E., van de Laak, S., de Bever, A., and Huisman, P. W. T., 1998, "Selection of Biting Sites on a Human Host by *Anopheles Gambiae*, An-Arabiensis and An-Quadriannulatus," *Entomol. Exper. App.*, **87**(3), pp. 295–300.
- [274] Knols, B. G. J., Takken, W., Cork, A., and DeJong, R., 1997, "Odour-Mediated, Host-Seeking Behavior of *Anopheles Mosquitoes*: A New Approach," *Ann. Trop. Med. Parasitol.*, **91**, pp. S117–S118.
- [275] Takken, W., 1996, "Synthesis and Future Challenges: The Response of Mosquitoes to Host Odours," *Ciba Found Symp.*, **200**, pp. 302–312.
- [276] McIver, S. B., 1982, "Sensilla of Mosquitoes (Diptera: Culicidae)," *J. Med. Ethics*, **19**, pp. 489–535.
- [277] Sutcliffe, J. F., 1994, "Sensory Bases of Attractancy: Morphology of Mosquito Olfactory Sensilla—A Review," *J. Am. Mosq. Control Assoc.*, **10**(2), Part 2, pp. 309–315.
- [278] Bidlingmayer, W. L., Day, J. F., and Evans, D. G., 1995, "Effect of Wind Velocity on Suction Trap Catches of Some Florida Mosquitoes," *J. Am. Mosq. Control Assoc.*, **11**(3), pp. 295–301.
- [279] Békésy, G. v., 1964, "Olfactory Analogue to Directional Hearing," *J. Appl. Physiol.*, **19**(3), pp. 369–373.
- [280] Kobal, G., Van Toller, S., and Hummel, T., 1989, "Is there Directional Smelling?," *Experientia*, **45**(2), pp. 130–132.
- [281] Stoddart, D. M., 1979, "External Nares and Olfactory Perception," *Experientia*, **35**, pp. 1456–1457.
- [282] Kajjura, S. M., Forni, J. B., and Summers, A. P., 2005, "Olfactory Morphology of Carcharhinid and Sphyrnid Sharks—Does the Cephalofoil Confer a Sensory Advantage?," *J. Morphol.*, in press.
- [283] Vanneste, E., and Geise, H. J., 2003, "Commercial Electronic Nose Instruments," in *Handbook of Machine Olfaction*, T. C. Pearce et al., eds., Wiley, New York, pp. 161–179.
- [284] Snopok, B. A., and Kruglenko, I. V., 2002, "Multisensor Systems for Chemical Analysis: State-of-the-Art in Electronic Nose Technology and New Trends in Machine Olfaction," *Thin Solid Films*, **418**(1), pp. 21–41.
- [285] Yinon, J., 2003, "Detection of Explosives by Electronic Noses," *Anal. Chem.*, **75**(5), pp. 99A–105A.
- [286] Li, J., 2000, "The Cyanose Chemical Vapor Analyzer," *Sensors*, **17**(8), pp. 56–60.
- [287] Cumming, C., Aker, C., Fisher, M., Fox, M., IaGrone, M., Reust, D., Rockley, M., Swager, T., Towers, E., and Williams, V., 2001, "Using Novel Fluorescent Polymers As Sensory Materials for Above-Ground Sensing of Chemical Signature Compounds Emanating From Buried Landmines," *IEEE Trans. Geosci. Remote Sens.*, **39**(6), pp. 1119–1128.
- [288] Albert, K. J., Myrick, M. L., Brown, S. B., James, D. L., Milanovich, F. P., and Walt, D. R., 2003, "Field-Deployable Sniffer for 2,4-Dinitrotoluene Detection," *Environ. Sci. Technol.*, **35**(15), pp. 3193–3200.
- [289] Staples, E. J., 2001, "The ZNose," *Sensors*, **18**(6), pp. 92–97.
- [290] Gelperin, A., and Hopfield, J. J., 2002, "Electronic and Computational Olfaction," *ACS Symposium Series*, **825**, pp. 289–317.
- [291] Gelperin, A., Oct. 7, 1997, "Olfactory Sensor Identification System and Method," U.S. Patent 5,675,070.
- [292] White, J. E., Waggoner, L. P., and Kauer, J. S., 2004, "Explosives and Landmine Detection Using an Artificial Olfactory System," *Proceedings SPIE Security Defense Conference*, Orlando, Proc. SPIE, **5415**, Paper 35, pp. 521–532.
- [293] Kauer, J. S., and White, J. E., 2003, "Representation of Odor Information in the Olfactory System: From Biology to an Artificial Nose," in *Sensors and Sensing in Biology and Engineering*, Springer-Verlag, Vienna, pp. 305–322.
- [294] White, J. E., Mall, S., and Kauer, J. S., 2002, "Using Biology to Guide Development of an Artificial Olfactory System," in *Neurotechnology for Biomimetic Robots*, J. Ayers, J. L. Davis, and A. Rudolph, eds., MIT, Cambridge, MA.
- [295] Eiceman, G. A., 2002, "Ion-Mobility Spectrometry as a Fast Monitor of Chemical Composition," *Trends Analyt. Chem.*, **21**(4), pp. 259–275.
- [296] Hill, H. H., Siems, W. F., StLouis, R. H., and McMinin, D. G., 1990, "Ion Mobility Spectrometry," *Anal. Chem.*, **62**(23), pp. A1201–A1209.
- [297] Linker, K. L., Adkins, D. R., Mowry, C. D., Trudell, D. E., Pfeifer, K. B., Sanchez, R. C., and Rohde, S. B., 2001, "Micro-Explosives Detection System  $\mu$ Hound™," in *Proceedings of the 3rd FAA International Symposium on Explosives Detection and Aviation Security Technologies*, Atlantic City, NJ, U.S. Federal Aviation Administration.
- [298] Call, P., Kenning, V., and Moler, C., 2001, "BioCapture Air Sampler," <http://www.mesosystems.com/>
- [299] McGown, J. B., Bromberg, E. A., and Noble, L. W., Mar. 20, 1990, "Vapor Sampling Probe," U.S. Patent 4,909,090.
- [300] Carroll, A. L., Miskolczy, G., Fraim, F. W., Achter, E. K., and Lieb, D. P., June 23, 1992, "Hand-Held Sample Gun for Vapor Collection," U.S. Patent 5,123,274.
- [301] Kolb, B., and Ettre, L. S., 1997, *Static Headspace-Gas Chromatography: Theory and Practice*, Wiley-VCH, New York.
- [302] Davidson, W. R., and Stott, W. R., 1994, "Synergy or Dichotomy—Vapor and Particle Sampling in the Detection of Contraband," *Proceedings SPIE Conference on Substance Detection Systems*, Innsbruck, Austria, Proc. SPIE, **2092**, pp. 108–119.
- [303] Fainberg, A., 1992, "Explosives Detection for Aviation Security," *Science*, **255**(5051), pp. 1531–1537.
- [304] Steinfeld, J. I., and Wormhoudt, J., 1998, "Explosives Detection: A Challenge for Physical Chemistry," *Annu. Rev. Phys. Chem.*, **49**, pp. 203–232.
- [305] Bender, E., Hogan, A., Leggett, D., Miskolczy, G., and Macdonald, S., 1992, "Surface Contamination by TNT," *J. Forensic Sci.*, **37**(6), pp. 1673–1678.
- [306] Brown, R. H., and Monteith, L. E., 2001, "Gas and Vapor Sample Collectors," in *Air Sampling Instruments for Evaluation of Atmospheric Contaminants*, 9th Ed., American Conference of Governmental Industrial Hygienists, Cincinnati, OH, pp. 415–455.
- [307] Anonymous, 1989, "Part I—General Techniques," in *Methods of Air Sampling and Analysis*, 3rd Ed., J. P. Lodge, ed., Lewis Publishers, New York, pp. 3–58.
- [308] Brown, H. R., and Purnell, C. J., 1979, "Collection and Analysis of Trace Organic Vapor Pollutants in Ambient Atmospheres," *J. Chromatogr.*, **178**, pp. 97–80.
- [309] Bender, F., Barie, N., Romoudis, G., Voigt, A., and Rapp, A., 2003, "Development of a Preconcentration Unit for a SAW Sensor Micro Array and Its Use for Indoor Air Quality Monitoring," *Sens. Actuators B*, **93**(1–3), pp. 135–141.

- [310] Yinon, J., 1999, *Forensic and Environmental Detection of Explosives*, Wiley, New York.
- [311] Fraim, F. W., Achter, E. K., Carroll, A. L., and Hainsworth, E., 1992, "Efficient Collection of Explosive Vapors, Particles and Aerosols," *Proceedings of the 1st International Symposium on Explosives Detection Technology*, Nov. 1991, S. M. Khan, ed., Report DOT/FAA/CT-92/11 U. S. Federal Aviation Administration, Atlantic City, NJ, pp. 559–565.
- [312] Achter, E. K., Carroll, A. L., Roundbehr, D. P., Fine, D. H., and Fraim, F. W., Mar. 3, 1992, "Vapor Collector/Desorber With Metallic Ribbon," U.S. Patent 5,092,157.
- [313] Linker, K. L., 2001, "Large-Volume Sampling and Preconcentration," in *Proceedings of the 3rd FAA International Symposium on Explosives Detection and Aviation Security Techniques*, U. S. Federal Aviation Administration, Atlantic City, NJ.
- [314] Dravnieks, A., 1966, "Odors As Signatures," *New Sci.*, **31**, pp. 622–624.
- [315] Aaberg, C. P. N., Aug. 23, 1977, "Method and Apparatus for Exhausting Air from a Limited Zone," U.S. Patent 4,043,257.
- [316] Kulmala, I., 2000, "Experimental Validation of Potential and Turbulent Flow Models for a Two-Dimensional Jet-Enhanced Exhaust Hood," *Am. Ind. Hyg. Assoc. J.*, **61**(Mar./Apr.), pp. 183–191.
- [317] Burton, D. J., 2000, "Practical Applications of an Aaberg Hood," *Occup. Health Saf.*, **69**(11), pp. 37–39.
- [318] Heinsohn, R. J., and Cimbala, J. M., 2002, "Present Local Ventilation Practice," in *Indoor Air Quality Engineering*, Marcel Dekker, New York, pp. 437–515.
- [319] Rueeg, T., Gubler, D., Sprecher, P., Moser, A., and Weber, R., 2004, "Local Capture of Contaminants," *ASHRAE J.*, **46**(1), pp. 26–29.
- [320] Hunt, G. R., and Ingham, D. B., 1996, "Long Range Exhaustion—A Mathematical Model for the Axisymmetric Airflow of a Local Exhaust Ventilation Hood Assisted by a Turbulent Radial Jet," *Ann. Occup. Hyg.*, **40**(2), pp. 171–196.
- [321] Cant, R., Castro, I., and Walklate, P., 2002, "Plane Jets Impinging on Porous Walls," *Exp. Fluids*, **32**(1), pp. 16–26.
- [322] Anonymous, 2001, "Air curtains," in *Industrial Ventilation Design Guidebook*, Academic, San Diego, pp. 553–571.
- [323] Stenger, J. B., and Bajura, R. A., 1984, "Deposition in Sampling Tubes," in *Aerosols: Science, Technology and Industrial Applications of Airborne Particles*, *Proceedings of the First International Aerosol Conference*, Elsevier, New York, pp. 175–178.
- [324] Falcitelli, M., Benassi, A., Di Francesco, F., Domenici, C., Marano, L., and Pioggia, G., 2002, "Fluid Dynamic Simulation of a Measurement Chamber for Electronic Noses," *Sens. Actuators B*, **85**(1–2), pp. 166–174.
- [325] Laibach, E., 1937, "Das Geruchsorgan des Aals (*Anguilla Vulgaris*) in Seinen Verschiedenen Entwicklungsstadien," *Zoologische Jahrbucher, Abterlung fur Anatomie und Ontogenie der Tiere*, **63**, pp. 37–72.
- [326] Rae, W. H., and Pope, A. Y., 1984, *Low-Speed Wind Tunnel Testing*, Wiley, New York.
- [327] Mälhammar, A., 2004, "A Method for Comparing Heat Sinks Based on Reynolds Analogy," *Proceedings of the 10th International Workshop on Thermal Investigation of ICs and Systems*, Sophia Antipolis, France, pp. 229–234.
- [328] Eckert, E. R. G., and Drake, R. M., 1959, *Heat and Mass Transfer*, McGraw-Hill, NY.
- [329] Garimella, S. V., 1996, "Enhanced Air Cooling of Electronic equipment," in *Air Cooling Technology for Electronic Equipment*, S. J. Kim and S. W. Lee, eds., CRC, Boca Raton, FL, pp. 173–202.
- [330] Settles, G. S., 2006, "Fluid Mechanics and Homeland Security," submitted to *Annu. Rev. Fluid Mech.*, **38**.
- [331] Carranza, J. E., Fisher, B. T., Yoder, G. D., and Hahn, D. W., 2001, "On-Line Analysis of Ambient Air Aerosols Using Laser-Induced Breakdown Spectroscopy," *Spectrochim. Acta, Part B*, **56**(6), pp. 851–864.
- [332] Myers, L. J., 1992, "The Dog-Handler Team as a Detection System for Explosives: A Tail to be Told," *Proceedings of the Conference on the Aviation Security Problem and Related Technologies*, W. H. Makky, ed., SPIE CR42, San Diego, pp. 93–103.
- [333] Furton, K. G., and Myers, L. J., 2001, "The Scientific Foundation and Efficacy of the Use of Canines As Chemical Detectors for Explosives," *Talanta*, **54**(3), pp. 487–500.
- [334] Gazit, I., and Terkel, J., 2003, "Explosives Detection by Sniffer Dogs Following Strenuous Physical Activity," *App. Animal Behav. Sci.*, **81**(2), pp. 149–161.
- [335] Gazit, I., Lavner, Y., Bloch, G., Azulai, O., Goldblatt, A., and Terkel, J., 2003, "A Simple System for the Remote Detection and Analysis of Sniffing in Explosives Detection Dogs," *Behav. Res. Methods Instrum. Comput.*, **35**(1), pp. 82–89.
- [336] Rooney, N. J., Bradshaw, J. W. S., and Almey, H. E., 2004, "Attributes of Specialist Search Dogs—A Questionnaire Survey of UK Dog Handlers and Trainers," *J. Forensic Sci.*, **49**(2), pp. 300–306.
- [337] Ternes, J. W., and Prestrude, A. M., 1992, "Integration of the Human, Canine, Machine Interface for Explosives Detection," *Proceedings of the 1st International Symposium on Explosives Detection Technology*, S. M. Khan, ed., Report DOT/FAA/CT-92/11 U. S. Federal Aviation Administration, Atlantic City, NJ, pp. 891–902.
- [338] Settles, G. S., 1999, "Schlieren and Shadowgraph Imaging in the Great Outdoors," *Proceedings of the 2nd Pacific Symposium on Flow Visualization and Image Processing*, S. Mochizuki, ed., Honolulu, Pacific Center of Thermal-Fluids Engineering, Tokyo.
- [339] Fine, D. H., Fraim, F. W., MacDonald, S. J., and Thrash, K. M., Dec. 27, 1994, "Method and System for Sampling and Determining the Presence of Compounds in Containers," U.S. Patent 5,376,550.
- [340] Davidson, W. R., Stott, W. R., Akery, A. K., and Sleeman, R., 1992, "The Role of Mass Spectrometry in the Detection of Explosives," *Proceedings of the 1st International Symposium on Explosive Detection Technology*, S. M. Khan, ed., Report DOT/FAA/CT-92/11, U. S. Federal Aviation Administration, Atlantic City, NJ, pp. 663–667.
- [341] Cartwright, P. A., Alcock, N. J., Groves, D. M., Almey, H. E., and Brookes, M. D., 2001, "Development of Performance Evaluation Tubes for Remote Air Sampling for Canine Olfaction (RASCO)," in *Proceedings of the 3rd FAA International Symposium on Explosives Detection and Aviation Security Technologies*, U. S. Federal Aviation Administration, Atlantic City, NJ.
- [342] Lord, D., 2004, "RASCO: A New Cargo Screening Methodology Comes of Age," *Aviation Security International*, **9**(4), p. 34.
- [343] Jenkins, A., Mar. 9, 1976, "Inspection Apparatus," U.S. Patent 3,942,357.
- [344] Ornath, F., and Beuchler, S. S., Aug. 24, 1999, "Method and Apparatus for Sampling Contaminants," U.S. Patent 5,942,699.
- [345] Smith, D. J., 2005, "The Internal Airflow in Cargo Containers and Methods to Sample it for Chemical Trace Detection," M.S. Thesis, Pennsylvania State University, State College PA.
- [346] Anonymous, 1996, "Airline Passenger Security Screening—New Technologies and Implementation Issues," US National Research Council Report NMAB-482-1, U. S. National Academy of Science, Washington, DC.
- [347] Anonymous, 2002, "People Screening Weapon & Explosives Detection," Market Report 2003–2010, Homeland Security Research Corp., San Jose, CA.
- [348] Hallowell, S. F., 2001, "Screening People for Illicit Substances: a Survey of Current Portal Technology," *Talanta*, **54**(3), pp. 447–458.
- [349] Dravnieks, A., 1975, "Evaluation of Human Body Odor: Methods and Interpretations," *J. Soc. Cosmet. Chem.*, **26**(11), pp. 551–571.
- [350] Bethune, D. W., Blowers, R., Parker, M., and Pask, E. A., 1965, "Dispersal of *Staphylococcus Aureus* by Patients and Surgical Staff," *Lancet*, **318**, pp. 480–483.
- [351] Whyte, W., Vesley, D., and Hodgson, R., 1976, "Particle Dispersion in Relation to Operating Room Clothing," *J. Hyg. (Lond)*, **76**, pp. 367–378.
- [352] Whyte, W., 2001, *Cleanroom Technology: Fundamentals of Design, Testing, and Operation*, Wiley, New York.
- [353] Settles, G. S., Gowadia, H. A., Strine, S. B., and Johnson, T. E., 1996, "The Natural Aerodynamic Sampling of Trace Explosives From the Human Body," *Proceedings of the 2nd FAA Conference on the Aviation Security Problem and Related Technologies*, W. H. Makky, ed., SPIE CR42, Atlantic City, NJ, pp. 65–70.
- [354] Settles, G. S., Ferree, H. C., Tronosky, M. D., Moyer, Z. M., and McGann, W. J., 2001, "Natural Aerodynamic Portal Sampling of Trace Explosives From the Human Body," in *Proceedings 3rd FAA International Symposium on Explosive Detection and Aviation Security*, U. S. Federal Aviation Administration, Atlantic City, NJ.
- [355] Achter, E. K., Burke, E. J., Miskolczy, G., and Sonin, A. A., Mar. 20, 1990, "Walk-in Inspection Apparatus for Producing Air Samples," U.S. Patent 4,909,089.
- [356] Linker, K. L., Hannum, D. W., and Conrad, F. J., June 22, 1999, "Vertical Flow Chemical Detection Portal," U.S. Patent 5,915,268.
- [357] Settles, G. S., June 13, 2000, "Chemical Trace Detection Portal Based on the Natural Airflow and Heat Transfer of the Human Body," U.S. Patent 6,073,499.
- [358] Davies, J. H., Apr. 23, 2002, "Apparatus and Method for Screening People and Articles to Detect and/or to Decontaminate with Respect to Certain Substances," U.S. Patent 6,375,697.
- [359] Phares, D. J., Holt, J. K., Smedley, G. T., and Flagan, R. C., 2000, "Method for Characterization of Adhesion Properties of Trace Explosives in Fingerprints and Fingerprint Simulations," *J. Forensic Sci.*, **45**(4), pp. 774–784.
- [360] Neudorff, P., McCooye, M. A., and Elias, L., 1993, "Testing Protocol for Surface-Sampling Detectors," *Proceedings of the 4th International Symposium on the Analysis and Detection of Explosives*, J. Yinon, ed., Kluwer Academic, New York, pp. 373–384.
- [361] Sorensen, D. N., and Voight, L. K., 2003, "Modelling Flow and Heat Transfer Around a Seated Human Body by Computational Fluid Dynamics," *Build. Environ.*, **38**(6), pp. 753–762.
- [362] Murakami, S., Kato, S., and Zeng, J., 2000, "Combined Simulation of Airflow, Radiation and Moisture Transport for Heat Release From a Human Body," *Build. Environ.*, **35**(6), pp. 489–500.
- [363] Craven, B. A., and Settles, G. S., 2005, "A Computational and Experimental Investigation of the Human Thermal Plume," submitted to *J. Biomech. Eng. Schellenbaum, R. L.*, 1987, "Air Flow Studies for Personnel Explosives Screening Portals," *Proceedings of the 1987 Carnahan Conference on Security Technology: Electronic Crime Countermeasures*, Lexington, KY, IEEE, New York, pp. 101–105.
- [365] Hobbs, J. R., and Conde, E. P., 1993, "Analysis of Airflows in Personnel Screening Booths," *Proceedings of the Fourth International Symposium on the Analysis and Detection of Explosives*, J. Yinon, ed., Kluwer Academic, New York, pp. 437–453.
- [366] Daws, L. F., 1970, "Movement of Airstreams Indoors," *J. Inst. Heat. Vent. Eng.*, **37**(2), pp. 241–253.
- [367] Parmeter, J. E., Linker, K. L., Rhykerd, C. L., Hannum, D. W., and Bouchier, F. A., 1998, "Explosives Detection Portal for High-Volume Personnel Screening," in *Enforcement and Security Technologies*, Proc. SPIE, **3575**, pp. 384–391.

- [368] Linker, K. L., and Brusseau, C. A., Jan. 1, 2002, "Target Detection Portal," U.S. Patent 6,334,365.
- [369] Whyte, W., and McGeorge, D., 1994, "Evaluating the Effects of a Cleanroom Air Shower on Particle Dispersion," *Microcontamination*, **12**(9), pp. 39–41, 69.
- [370] Batill, S. M., and Hoffman, J. J., 1986, "Aerodynamic Design of Three-Dimensional Subsonic Wind Tunnel Inlets," *AIAA J.*, **24**(2), pp. 268–269.
- [371] Settles, G. S., and McGann, W. J., 2001, "Potential for Portal Detection of Human Chemical and Biological Contamination," in *Aerosense 2001: Sensor Technology and Application*, SPIE-International Society for Optical Engineering **4378**, Paper 01.
- [372] Edge, B. A., Paterson, E. G., and Settles, G. S., 2005, "Computational Study of the Wake and Contaminant Transport of a Walking Human," submitted to *ASME J. Fluids Eng.*
- [373] Rodes, C. E., Kamens, R. M., and Wiener, R. W., 1995, "Experimental Considerations for the Study of Contaminant Dispersion Near the Body," *Am. Ind. Hyg. Assoc. J.*, **56**(6), pp. 535–545.
- [374] Kim, T., and Flynn, M. R., 1991, "Airflow Pattern Around a Worker in a Uniform Freestream," *Am. Ind. Hyg. Assoc. J.*, **52**(7), pp. 287–296.
- [375] Flynn, M. R., and Miller, C. T., 1991, "Discrete Vortex Methods for the Simulation of Boundary-Layer Separation Effects on Worker Exposure," *Ann. Occup. Hyg.*, **35**(1), pp. 35–50.
- [376] Flynn, M. R., and Ljungqvist, B., 1995, "A Review of Wake Effects on Worker Exposure," *Ann. Occup. Hyg.*, **39**(2), pp. 211–221.
- [377] Murakami, S., Zeng, J., and Hayashi, T., 1999, "CFD Analysis of Wind Environment Around a Human Body," *J. Wind. Eng. Ind. Aerodyn.*, **83**, pp. 393–408.
- [378] Moyer, Z. M., 2003, "The Human Aerodynamic Wake and the Design of a Portal to Sample It," M.S. thesis, Pennsylvania State University, University Park, PA.
- [379] Craven, B. A., and Settles, G. S., 2005, "The Design of a Chemical Trace Detection Portal That Samples the Aerodynamic Wake of a Walking Person," in preparation.
- [380] Anonymous, 1998, *Hidden Killers: The Global Landmine Crisis*, U.S. Dept. of State Publication 10575.
- [381] Andersson, N., Dasousa, C. P., and Paredes, S., 1995, "Social Cost of Land Mines in 4 Countries—Afghanistan, Bosnia, Cambodia, and Mozambique," *Br. Med. J.*, **311**(7007), pp. 718–721.
- [382] Ashley, S., 1996, "Searching for Land Mines," *Mech. Eng. (Am. Soc. Mech. Eng.)*, **118**(4), pp. 62–67.
- [383] Strada, G., 1996, "The Horror of Land Mines," *Sci. Am.*, **278**(5), pp. 40–45.
- [384] Pamula, V. K., 2003, "Detection of Explosives," in *Handbook of Machine Olfaction*, T. C. Pearce et al., eds., Wiley, New York, pp. 547–580.
- [385] Phelan, J., and Webb, S. W., 1998, "Simulation of the Environmental Fate and Transport of Chemical Signatures From Buried Landmines," *Proceedings of the 1999 Detection and Remediation Technologies for Mines and Minelike Targets III*, Proc. SPIE, **3392**(1), pp. 509–520.
- [386] George, V., Jenkins, T. F., Leggett, D. C., Cragin, J. H., Phelan, J., Oxley, J., and Pennington, J., 1999, "Progress on Determining the Vapor Signature of a Buried Land Mine," *Proceedings of the SPIE Aerosense Conference*, Orlando, FL, Proc. SPIE, **3710**, pp. 258–269.
- [387] Jenkins, T. F., Leggett, D. C., Miyares, P. H., Walsh, M. E., Ranney, T. A., Cragin, J. H., and George, V., 2001, "Chemical Signatures of TNT-Filled Land Mines," *Talanta*, **54**(3), pp. 501–513.
- [388] Morgan, J. S., Bryden, W. A., Miragliotta, J. A., and Aamodt, L. C., 1999, "Improved Detection of Explosive Residues by Laser Thermal Desorption," *Johns Hopkins APL Tech. Dig.*, **20**(3), pp. 389–395.
- [389] Fair, R. B., Pollack, M., and Pamula, V. K., 1998, "MEMS Devices for Detecting the Presence of Explosive Material Residues in Mine Fields," in *Proceedings of the 1999 Detection and Remediation Technologies for Mines and Minelike Targets III*, Proc. SPIE, **3392**(1), pp. 409–417.
- [390] Fisher, M., Cumming, C., IaGrone, M., and Taylor, R., 1998, "An Electrostatic Particle Sampler and Chemical Sensor System for Landmine Detection by Chemical Signature," *Proceedings of the 1998 Detection and Remediation Technologies for Mines and Minelike Targets III*, Proc. SPIE, **3392**(1), pp. 565–574.
- [391] Morrocco, J. D., 2000, "Field Trials in Kosovo Test Mine Detection," *Aviat. Week Space Technol.*, **156**, p. 38.
- [392] Turner, A. P. F., 2000, "Biosensors—Sense and Sensitivity," *Science*, **290**(5495), pp. 1315–1317.
- [393] Cole, L. A., 2003, *The Anthrax Letters: A Medical Detective Story*, Joseph Henry Press, Washington DC.
- [394] Pope, C., 1928, "The Diagnostic Art of Smelling," *Am. J. Med.*, **34**, pp. 651–653.
- [395] Hayden, G. F., 1980, "Olfactory Diagnosis in Medicine," *Postgrad Med. J.*, **67**(4), pp. 110–118.
- [396] Tassopoulos, C. N., Barnett, D., and Fraser, T. R., 1969, "Breath-Acetone and Blood-Sugar Measurements in Diabetes," *Lancet*, **1**(1282), pp. 1286.
- [397] McSherry, J., 1986, "Sniffing Out the Diagnosis," *Can. Med. Assoc. J.*, **135**(10), pp. 1070.
- [398] Smith, K., Thompson, G. F., and Koster, H. D., 1969, "Sweat in Schizophrenic Patients: Identification of the Odorous Substance," *Science*, **166**, pp. 398–399.
- [399] Distelheim, I. H., and Dravnieks, A., 1973, "A Method for Separating Characteristics of Odors in Detection of Disease Processes 1," *Int. J. Dermatol.*, **12**(4), pp. 241–244.
- [400] Di Natale, C., and D'Amico, A., 2001, "The Electronic Nose Analysis of Breath As Potential Diagnostic Tool: the Case of Lung Cancer," *Proceedings of the Eighth International Symposium on Olfaction and the Electronic Nose*, J. R. Stetter and W. R. Penrose, eds., The Electrochemical Society, Washington DC, pp. 48–53.
- [401] Krüger, U., Körber, R., Ziegler, K.-H., Koroncz, I., Nachnani, S., and Goschnick, J., 2001, "Electronic Noses Towards Practical Application in Medical Diagnostics," *Proceedings of the Eighth International Symposium on Olfaction and the Electronic Nose*, J. R. Stetter and W. R. Penrose, eds., The Electrochemical Society, Washington DC, pp. 62–64.
- [402] Lawrence, A. H., Nanji, A. A., and Taverner, J., 1988, "Skin-Sniffing Ion Mobility Spectrometric Analysis—A Potential Screening Method in Clinical Toxicology," *J. Clin. Lab Anal.*, **2**(2), pp. 101–107.
- [403] Batterman, S. A., Franzblau, A., and Zhou, N.-Z., 1996, "Airborne Emissions at Skin Surfaces: a Potential Biological Exposure Index," *Int. Arch. Occup. Environ. Health*, **68**, pp. 268–274.
- [404] Stetter, J. R., Penrose, W. R., Kubba, S., Kocka, F., McEntegart, C. M., Roberts, R. R., and Iademarco, M. F., 2001, "Enhancement of the Sensitivity of the Electronic Nose for Bacterial Applications," *Proceedings of the Eighth International Symposium on Olfaction and the Electronic Nose*, J. R. Stetter and W. R. Penrose, eds., The Electrochemical Society, Washington DC, pp. 54–61.
- [405] Roller, C., Namjou, K., Jeffers, J. D., Camp, M., Mock, M., McCann, P. J., and Grego, J., 2002, "Nitric Oxide Breath Testing by Tunable-Diode Laser Absorption Spectroscopy: Application in Monitoring Respiratory Inflammation," *Appl. Opt.*, **41**(28), pp. 6018–6029.
- [406] Pavlou, A. K., and Turner, A. P. F., 2000, "Sniffing Out the Truth: Clinical Diagnosis Using the Electronic Nose," *Clin. Chem. Lab. Med.*, **38**(2), pp. 99–112.
- [407] Persaud, K. C., Pisanelli, A. M., and Evans, P., 2003, "Medical Diagnostics and Health Monitoring," in *Handbook of Machine Olfaction*, T. C. Pearce et al., eds., Wiley, New York, pp. 445–460.
- [408] Settles, G. S., 2004, "The Penn State Full-Scale Schlieren System," *Proceedings of the 11th International Symposium on Flow Visualization*, T. J. Mueller and I. Grant, eds., Notre Dame University, IN.
- [409] Kaminski, R. K., 1980, "Leak Detection: A Route to Conservation and Safety," *Proc. Am. Pet. Inst., Sect. 3*, **59**, pp. 37–41.
- [410] Peale, R. E., and Summers, P. L., 1996, "Zebra Schlieren Optics for Leak Detection," *Appl. Opt.*, **35**(22), pp. 4518–4521.
- [411] Settles, G. S., 1999, "Imaging Gas Leaks by Using Schlieren Optics," *Pipeline and Gas Journal*, **226**(9), pp. 28–30.
- [412] Mcrae, T. G., and Kulp, T. J., 1993, "Backscatter Absorption Gas Imaging—A New Technique for Gas Visualization," *Appl. Opt.*, **32**(21), pp. 4037–4050.
- [413] Kher, U., 2000, "Electronic Noses Sniff Out a Market or Two," *Time*, **155**(11), pp. 64–65.
- [414] Aston, C., 2001, "Biological Warfare Canaries," *IEEE Spectrum*, **38**(10), pp. 35ff.
- [415] Olender, T., Fuchs, T., Linhart, C., Shamir, R., Adams, M., Kalush, F., Khen, M., and Lancet, D., 2004, "The Canine Olfactory Subgenome," *Genomics*, **83**(3), pp. 361–372.



# Experimental Investigation of the Turbulent Boundary Layer of Surfaces Coated With Marine Antifoulings

M. Candries

e-mail: Maxim\_Candries@yahoo.com

M. Atlar

e-mail: Mehmet.Atlar@ncl.ac.uk

School of Marine Science and Technology,  
University of Newcastle-upon-Tyne,  
Newcastle-upon-Tyne, NE1 7RU,  
United Kingdom Tel: + 44 191 222 89 77  
Fax: + 44 191 222 54 91

*Turbulent boundary-layer measurements have been carried out on flat surfaces coated with two different new generation marine antifoulings. The coatings were applied on 1-m-long test sections that were fitted in a 2.1-m-long flat plate setup. The measurements were carried out in two different recirculating water tunnels by means of two-component laser Doppler velocimetry and were compared with measurements of a smooth steel reference surface and a surface covered with sand grit. Both coatings exhibited an increase in frictional resistance compared to the reference surface, but the increase was significantly smaller for the Foul(ing) Release coatings than for the Tin-free SPC coating. The coatings did not significantly affect the boundary-layer thickness. When expressed in inner variables, the coatings did not have an effect on the turbulence intensity profiles, but when expressed in outer variables, the coatings affected the near-wall turbulence intensities. [DOI: 10.1115/1.1891148]*

## 1 Introduction

At present, the most widely applied marine antifoulings are Tributyl-Tin Self-Polishing Co-Polymers (TBT-SPC), which can keep a ship free of fouling for 5 years by means of a steady release of the TBT toxin. Due to environmental side-effects related with TBT, the International Maritime Organisation (IMO) decided in October 2001 to phase out the use of TBT-SPCs by 2008. There are currently two alternatives on the market that can also offer 5 years of satisfactory antifouling performance. The first alternative, Tin-free SPC, uses the same chemical principle but, instead of TBT, gradually leaches copper-based toxins which are complemented by so-called "booster biocides." The second type, Foul(ing) Release coatings, work by an entirely different principle. Instead of killing marine organisms that have attached to the hull, they try to prevent the attachment of the organisms altogether. This is possible by their specific material characteristics. The Foul Release coatings described in this paper are silicone elastomers based on polydimethylsiloxane (PDMS). Experimental studies on the attachment of fouling organisms to different types of materials have shown that silicones are least prone to foul [1,2]. Eventually, all surfaces will foul, but experiments have also shown that the strength of attachment of the organisms to silicones is an order of magnitude lower than to other materials. Kovach and Swain [3] towed a plate, which was coated with a Foul Release system and covered by fouling, at different speeds and showed that the organisms started to release at speeds above 12 knots. These antifoulings are therefore particularly suited for ships which spend a short time in port and travel at sufficiently high speeds.

When Foul Release coatings were commercially introduced in the 1990s on a high-speed catamaran ferry, lower fuel consumption was recorded at the same service speed, implying lower drag characteristics [4]. A Ph.D. research project was therefore set up with the objective of collecting data on the drag and boundary-layer characteristics of both Foul Release and Tin-free SPC coatings, and to compare them systematically. Within this framework,

drag measurements were obtained from towing tank tests with two friction planes of different lengths [5,6]. The experiments demonstrated that the Foul Release coating exhibited between 2 and 20% less frictional resistance than the Tin-free SPC coating, depending on the quality of application. The difference in resistance has been related by Candries [6] to the respective differences in roughness, sample measurements of which are shown in Figs. 1 and 2. The difference in texture particularly may have an effect on the boundary-layer characteristics.

An experimental investigation was therefore carried out to study the structure of turbulent boundary layers that develop over surfaces coated with this new generation of marine antifoulings. To accomplish this, boundary-layer measurements were made on a replaceable flat test section coated with Tin-free SPC and Foul Release systems. The experiments were conducted in two different water tunnels using four-beam two-component Laser Doppler Velocimetry (LDV). The mean velocity profiles and flow parameters as well as the turbulent normal and shear stresses are compared with flows over smooth and sand-grit rough walls. This paper reports the details and main findings of this experimental investigation.

## 2 Experimental Facilities

The first part of the experimental work was carried out in the Emerson Cavitation Tunnel (UK), and the second part was carried out in the CEHIPAR Cavitation Tunnel (Spain).

The Emerson Cavitation Tunnel (ECT) at the University of Newcastle-upon-Tyne is 7.69 m high and 10.79 m long. The rectangular measuring test section is 1.22 m wide by 0.81 m high and 3.10 m long. Flow management devices include turning vanes placed in the tunnel corners and a honeycomb flow straightener in the entrance to the contraction section [7]. The free-stream velocities in the test section can be adjusted from 1 to 8 m/s, although the maximum velocity was restricted to 6 m/s for the present setup. The mean velocity can be maintained constant at between +1.5% and -2.5% throughout the range and the resulting free-stream turbulence intensity in the test section is ~2% [8].

The Cavitation Tunnel at the Canal de Experiencias Hidrodinámicas de El Pardo (CEHIPAR) has a parallel test section

Contributed by the Fluids Engineering Division for publication in the JOURNAL OF FLUIDS ENGINEERING. Manuscript received by the Fluids Engineering Division May 29, 2002. Revised manuscript received December 22, 2004. Review conducted by M. Plesniak.

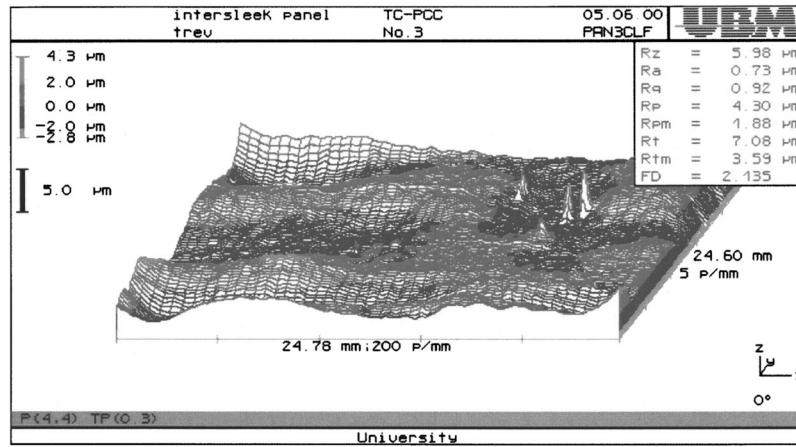


Fig. 1 Roughness measurements taken on a Foul Release coated surface

which is 0.9 m in width and height and 4.7 m long. The maximum free-stream velocity in the test section is 11 m/s but was restricted to 8 m/s for the present setup.

Five different test specimens were tested in the Emerson Cavitation Tunnel: a smooth unpainted reference surface (designated as STEEL), a surface coated with a Tin-free SPC (SPC), a surface coated with a Foul Release system applied by spraying (FR), and a surface coated with a Foul Release system applied by rollering (ROLL). The different application methods of the Foul Release system were compared because towing tank experiments had indicated that this may influence the drag characteristics [6]. A surface partially covered with sand grit (SAND) was also tested to examine the fully rough flow regime. In the CEHIPAR Cavitation Tunnel, where experimental time was restricted, only two surfaces were tested, a Tin-free SPC and a Foul Release surface, both applied by spraying (designated as CSPC and CFR, respectively). The thickness of each of the coating schemes was 350 μm.

The average roughness of each of the test specimens was measured with a BMT Hull Roughness Analyser, which is described by, e.g., Thomas [9]. This stylus instrument, widely used to measure the roughness of marine surfaces, measures the highest peak and the lowest valley perpendicular to the mean line of a 50-mm-long roughness profile at a sampling interval of 1.25 mm. An average of 270 readings was measured for each surface. In order to take the effect of surface texture into account, additional roughness parameters were measured with a UBM optical measurement system that uses the focus detection principle of a 3 mW semiconductor laser (cf. [6,9]) on 200 mm by 250 mm sample plates

that were painted alongside and were representative of the coated test specimens. A description of the test specimens, along with their reference names and some roughness parameters, is given in Table 1.

The test specimens were bolted to a flat plate mounted vertically in the Emerson Cavitation Tunnel and horizontally in the CEHIPAR Cavitation Tunnel (due to reasons of accessibility). The plate, made of mild steel, was 0.80 m wide (0.895 m for the experiments in the CEHIPAR Cavitation Tunnel), 2 m in length as two 1-m-long sections attached together, and 12 mm thick. The 15-mm-thick leading and trailing edges of the plate were tapered and the forwardmost 300 mm of the plate was covered with #40 sand grit to hasten the development of a turbulent boundary layer. The use of a strip of roughness to artificially thicken the boundary layer was proposed by Klebanoff and Diehl [10]. The forward edge of the test specimen was located 1050 mm from the leading edge of the plate. In the Emerson Cavitation Tunnel, the plate was mounted 700 mm from the front side of the water tunnel and was held in place with 6 corner brackets which supported the plate in pairs (top and bottom) at the front middle and end. The brackets have a certain degree of freedom until the bolts are fixed firmly, which allows adjustments to the free-stream pressure gradient. Six thin plates, 1 m long and 0.8 m wide, were fabricated from 3-mm-thick mild steel. One thin plate was used to cover the front section of the 12-mm-thick plate and the other five thin plates were used as the test specimens. The thin plates were held on the 12-mm-thick plate by five magnets. At the edges 18 countersunk screws were employed to fix the thin plates. Ten extra countersunk screws

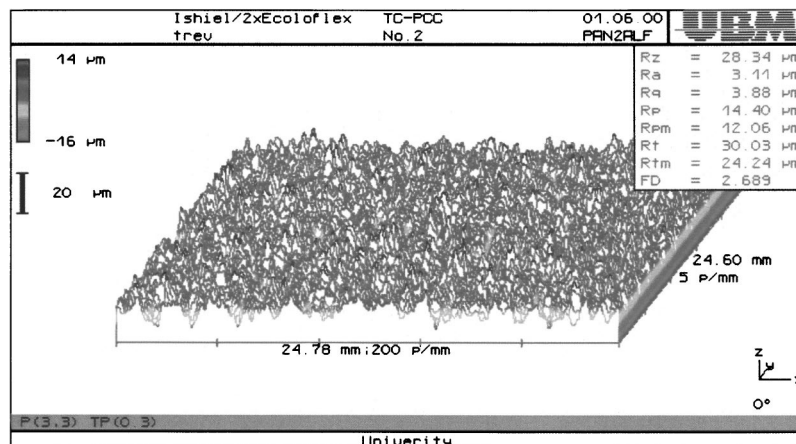


Fig. 2 Roughness measurements taken on a Tin-free SPC coated surface

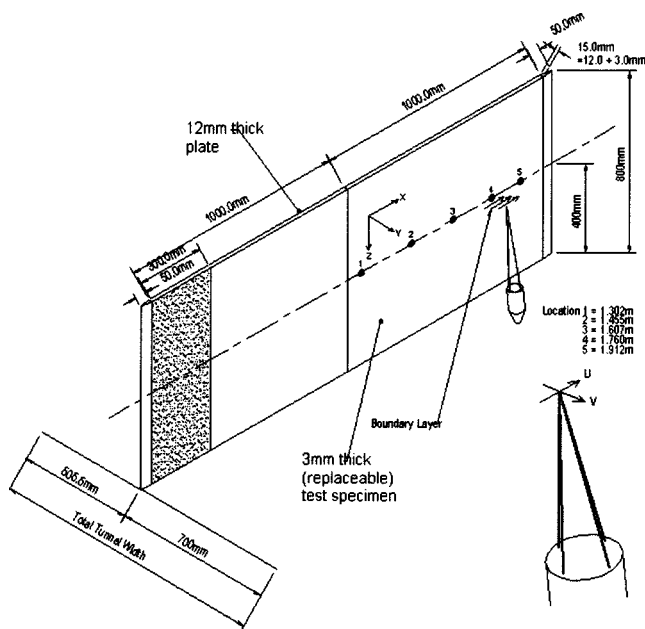
**Table 1** Description and roughness characteristics of the test specimens. AHR ( $\mu\text{m}$ ) is the average Hull roughness measured with the BMT stylus instrument; Ra ( $\mu\text{m}$ ) is the center-line average roughness height and Sa ( $^\circ$ ) is the mean absolute slope angle both over a cut-off length of 2.5 mm and a sampling interval of 50  $\mu\text{m}$ ; FD is the fractal dimension. The latter three parameters were measured with a UBM Optical Measurement System, except for the SAND surface, which fell outside the measurement range of the instrument.

Specimen	Facility	Name	AHR	Ra	Sa	FD
Steel surface	ECT	STEEL	22.9	1.21	1.44	1.68
Foul Release applied by spraying	ECT	FR	51.3	0.51	0.36	1.31
Foul Release applied by spraying	CEHIPAR	CFR	49.4	1.26	0.39	1.13
Foul Release applied by rolling	ECT	ROLL	59.7	1.11	0.43	1.21
Tin-free SPC applied by spraying	ECT	SPC	68.6	3.41	2.82	1.60
Tin-free SPC applied by spraying	CEHIPAR	CSPC	34.3	2.33	2.44	1.66
Surface covered with sand grit #40	ECT	SAND	727.3	*	*	*

were drilled 250 mm below and above the centerline. A schematic sketch of the experimental setup is shown in Fig. 3.

For the experiments in the CEHIPAR Cavitation Tunnel, the plate was mounted horizontally at 0.45 m from the bottom of the water tunnel and was held in place with 6 supports 0.21 m in length, which supported the plate in pairs at the front, middle, and end. Three thin plates were fabricated from 3-mm-thick mild steel and were held on the 12-mm-thick plate similar to the setup shown in Fig. 3. One thin plate was used to cover the front section of the 12-mm-thick plate and was partially covered with grit as mentioned. The other 2 thin plates were used as test specimens.

The velocity measurements were made with a four-beam two-component fiber-optic DANTEC laser Doppler velocimetry (LDV) system. The LDV system consists of a laser light source, a beam separator, fiber-optic couplers, a multi-color receiver, a signal processor, a personal computer, a fiber-optic probe, and a



**Fig. 3** Schematic sketch of the flat plate test fixture and experimental setup in the Emerson Cavitation Tunnel. For the experiments in the CEHIPAR Cavitation Tunnel, the plate was mounted horizontally.

three-axis computer-driven traverse. The laser beam is separated into green ( $\lambda=514.5$  nm) and blue ( $\lambda=488$  nm) light. The optical elements include a 40 MHz Bragg cell to remove directional ambiguity and a 600 mm focal length lens. The measurement process, data acquisition, and data processing are controlled by a software package called “PDA Flow and Particle Software” developed by DANTEC. The traverse allowed the position of the probe to be maintained to  $\pm 12.5$   $\mu\text{m}$  in all directions in the Emerson Cavitation Tunnel, and  $\pm 50$   $\mu\text{m}$  in the CEHIPAR Cavitation Tunnel. In order to obtain more accurate near-wall data, the probe, capturing from the bottom window of the Emerson Cavitation Tunnel and from the side window of the CEHIPAR Cavitation Tunnel, was tilted toward the plate by  $5^\circ$  and  $2.9^\circ$ , respectively. Corrections of the measurements for these tilt angles were made in the signal processor software. Silver coated (soda lime borosilicate) glass spheres with a mean particle size of 16.3  $\mu\text{m}$  (ranging from 8.4 to 24.8  $\mu\text{m}$ ) were used for seeding the flow. About 2 g of seeding was put in per week. More seeding was initially required in the CEHIPAR Cavitation Tunnel. The system was set up with a 600 mm focal length lens and a signal to noise ratio for the collected data of 1 dB in the Emerson Cavitation Tunnel and  $-3$  dB in the CEHIPAR Cavitation Tunnel.

The velocity measurements were conducted in backscatter mode over 20 s or until 4096 validated samples (whichever came first) were collected per location. The measurements were transit time averaged. The probe volume diameter was 276  $\mu\text{m}$  for the (blue) wall-normal channel and 291  $\mu\text{m}$  for the (green) streamwise channel, while the probe volume length was 8.725 and 9.199 mm, respectively. The probe volume contained 35 fringes spaced 7.709 and 8.128  $\mu\text{m}$ , respectively. The frequency bandwidth for the streamwise channel was set at 1.2 MHz for the first part and 4 MHz for the second part of the experiments, whereas for the wall-normal channel it was set at 0.12 MHz for speeds of 2 and 3 m/s and at 0.4 MHz for the higher speeds.

The validation and validated data rate measured in the Emerson Cavitation Tunnel increased from very low values near the wall to higher values in the range of 65–98% and 180–300 Hz, respectively, further away from the wall. In the CEHIPAR Cavitation Tunnel, the values away from the wall did not exceed 65–80% and 35 Hz, respectively, most likely due to poor coincidence of both channels and non-optimal alignment of the optics. The viscous length  $\nu/U_\tau$  varied from a minimum of 2.3  $\mu\text{m}$  for the SAND surface to a maximum of 17.1  $\mu\text{m}$  for the STEEL surface.

The diameter of the probe volume therefore ranged from 127 viscous lengths for the SAND surface to 17 viscous lengths for the STEEL surface.

### 3 Methods Used to Determine the Friction Velocity

A critical part of the investigation is the determination of the friction velocity  $U_\tau$ . The use of direct force measurements using a floating element gauge was considered but not applied because it would be difficult to avoid edge effects and let the gauge mimic the surrounding surface [11]. Three alternative methods were therefore applied to determine the friction velocity: two wall similarity methods, whereby the measured velocity profile is fitted to a standard profile, and the Reynolds stress method.

The first method, which is an inner-layer wall similarity method, assumes that the velocity profile follows a logarithmic form, i.e.,

$$U^+ = \kappa^{-1} \ln y^+ + C \quad (1)$$

whereby  $\kappa$  and  $C$  were taken according to the Stanford conventions as 0.41 and 5.0. This method was introduced by Clauser [12] and is better known as the "Clauser chart method." Perry and Joubert [13] later modified the method for rough surfaces by the introduction of the error-in-origin  $\epsilon$ . This method requires the determination of four parameters,  $U_\tau$ ,  $\Delta U^+$ ,  $\Pi$ , and  $\epsilon$  by iteration, and has been used for surfaces that display a fairly high roughness function, e.g., [14,15], but in this investigation the modified method did not work well for the coated surfaces. At this point, it may perhaps be added that two other methods did not work well for the coated surfaces: the momentum method (which proved to be inaccurate) and the sublayer slope method (due to lack of sufficient data points measured in the viscous sublayer).

The second method used in this study is an outer-layer similarity method, which was applied to all surfaces. This method has the advantage that the number of parameters to be determined can be reduced by one since the velocity defect law, as initially formulated by Hama [16], is valid for both rough and smooth surfaces and does not contain the roughness function  $\Delta U^+$ . Following the arguments of Bandyopadhyay [17], Perry et al. [18], Krogstad et al. [19], and Tachie et al. [20], a formulation of the velocity defect law was used which allows the optimization of the wake strength parameter  $\Pi$ :

$$w((y + \epsilon)/\delta) = 1/2\Pi[(1 + 6\Pi) - (1 + 4\Pi)((y + \epsilon)/\delta)]((y + \epsilon)/\delta)^2, \quad (2)$$

which is substituted in the velocity defect law,

$$U_e^+ - U^+ = 2\Pi/\kappa[w(1) - w((y + \epsilon)/\delta)] - 1/\kappa \ln((y + \epsilon)/\delta) \quad (3)$$

and fitted to the measured data. In the present investigation, the procedure involved optimizing  $U_\tau$  and  $\Pi$  first with  $\epsilon=0$ , and when the near-wall data showed a premature departure from the fit in the log-law region, a virtual origin was introduced to straighten the data. This had a limited effect on the values of  $U_\tau$  and  $\Pi$  and one extra iteration loop generally sufficed. One advantage of this method over the Clauser chart method is that the profile matching covers virtually the entire boundary layer as opposed to matching the profile in the logarithmic region, which is thin and for which there is only a restricted amount of data points to work with [17].

The third method used in this investigation and which was applied to all surfaces is known as the "Reynolds (or total) stress method" and is founded on the observation that at sufficiently high Reynolds numbers, the total shear stress is entirely made up of the Reynolds stress near the wall (i.e., in the constant stress region), so that a plot of  $-u'v'/U_\tau^2$  versus  $(y + \epsilon)/\delta$  should approach a maximum that is equal to unity [14,15,19,21].

The three methods have been abbreviated to the Clauser method (C), the Hama method (H), and the Reynolds Stress method (RS), respectively.

### 4 Uncertainty Estimates

Since it was anticipated that the differences between the coated surfaces would be relatively small, extra care was taken to keep the experimental uncertainties as low as possible. This involved trying several experimental configurations and the measurement of a large number of data points for each velocity profile to calculate the friction velocity accurately.

Uncertainty estimates of the measurements were made using repeatability tests. Ten replicate profiles were taken on both a smooth and a rough plate (i.e., on the STEEL and SPC specimen, respectively). The standard error for each of the measurement quantities was then calculated for both samples. In order to estimate the 95% confidence limits, the standard error on each measured quantity was multiplied by the two-tailed  $t$  value ( $t = 2.262$ ) for 9 degrees of freedom, as given by Coleman and Steele [22]. In the Emerson Cavitation Tunnel, the resulting uncertainties over a region  $50 < y^+ < 0.8\delta^+$  in the quantities  $U$ ,  $V$ ,  $u'_{rms}$ ,  $v'_{rms}$ , and  $-u'v'$  were  $\pm 1.4\%$ ,  $\pm 12.1\%$ ,  $\pm 4.5\%$ ,  $\pm 3.8\%$ , and  $\pm 11.2\%$ , respectively. The higher uncertainties on  $V$  are due to the fact that automatic recalibration of the measurement software during data acquisition had larger repercussions on the streamwise than on the wall-normal channel and occasionally caused relatively large adjustments to the mean wall-normal velocity. Due to time constraints, the uncertainty analysis in the CEHIPAR Cavitation Tunnel was limited to profiles consisting of half the number of data points collected for the measurements. The resulting uncertainty values were  $\pm 4.7\%$ ,  $\pm 26.6\%$ ,  $\pm 29.4\%$ ,  $\pm 29.9\%$ , and  $\pm 144.2\%$ , respectively.

In the Emerson Cavitation Tunnel, the uncertainty in  $c_f$  for the smooth walls was  $\pm 1.4\%$  for the Clauser method,  $\pm 4.5\%$  for the Reynolds stress method, and  $\pm 2.4\%$  for the Hama method. The uncertainty in  $c_f$  for the rough walls was  $\pm 2.5\%$  for the Reynolds stress method and  $\pm 3.1\%$  for the Hama method. The uncertainty in  $\delta$  was  $\pm 5.7\%$ . In the CEHIPAR Cavitation Tunnel, the uncertainty in  $c_f$  for the rough walls was  $\pm 4.8\%$  for the Reynolds stress method and  $\pm 6.7\%$  for the Hama method. The uncertainty in  $\delta$  was  $\pm 17.7\%$ .

### 5 Results And Discussion of the Experiments

In order to study the boundary-layer development and the effect of Reynolds number on the flow, velocity profiles were taken at different locations and for different free-stream velocities. The profile locations in the Emerson Cavitation Tunnel were at 1.302, 1.4545, 1.607, 1.7595, and 1.912 m from the leading edge ( $x/L = 0.620, 0.693, 0.765, 0.838, \text{ and } 0.910$ , respectively) and the five free-stream velocities were 2, 3, 4, 5, and 6 m/s. These locations have been numbered sequentially and each boundary-layer profile is identified by a code where the letters designate the test specimen while the following two numbers designate the free-stream velocity and the location number, respectively. For example, FR4.3 corresponds to the boundary-layer measurements taken on the sprayed Foul Release surface at 4 m/s and at the third downstream location. In order to repeat the measurements with the plate in a horizontal position and to make measurements at higher free-stream velocities, a surface sprayed with Foul Release (CFR) and Tin-free SPC (CSPC) were also tested in the CEHIPAR Cavitation Tunnel. The profile locations were at 1.4545, 1.607, and 1.7595 m from the leading edge (referred to as numbers 2, 3, and 4) and the three free-stream velocities were 3.2, 5.3, and 7.5 m/s (referred to as 3, 5, and 7 in Tables 2 and 3).

The boundary-layer parameters for the test specimens are given in Tables 2 and 3. The coatings did not have a significant effect on these flow parameters. The shape factor  $H$ , however, was significantly larger for the SAND surface, as shown in Fig. 4. Figure 4 also shows the equation for  $H$  derived by Hama [16] and Hinze [23] based on the velocity defect law and experimental data. Fig-

Table 2 Boundary-layer parameters measured in the Emerson Cavitation Tunnel at location 3 ( $\delta$ ,  $\delta_1$  and  $\theta$  in mm)

Profile	$U_e$	$Re_\theta$	$\delta$	$\delta_1$	$\theta$	H	Tu
STEEL2.3	1.94	7.99E+03	36.00	4.73	3.63	1.30	0.0211
STEEL3.3	3.05	1.23E+04	34.65	4.41	3.44	1.28	0.0186
STEEL4.3	3.98	1.59E+04	32.80	4.46	3.40	1.31	0.0264
STEEL5.3	5.27	2.04E+04	36.65	4.61	3.46	1.33	0.0231
STEEL6.3	6.06	2.39E+04	34.40	4.50	3.39	1.33	0.0262
SPC2.3	1.93	7.63E+03	34.35	4.49	3.55	1.26	0.0184
SPC3.3	3.00	1.25E+04	34.35	4.30	3.37	1.28	0.0207
SPC4.3	3.96	1.52E+04	35.25	4.22	3.34	1.26	0.0258
SPC5.3	4.99	2.11E+04	36.10	4.32	3.46	1.25	0.0214
SPC6.3	6.11	2.71E+04	40.10	4.75	3.77	1.26	0.0196
FR2.3	1.95	7.88E+03	34.90	4.91	3.69	1.33	0.0210
FR3.3	3.04	1.16E+04	34.75	4.52	3.50	1.29	0.0203
FR4.3	3.97	1.43E+04	31.75	4.23	3.29	1.29	0.0239
FR5.3	5.00	1.94E+04	36.75	4.81	3.55	1.36	0.0222
FR6.3	6.14	2.57E+04	37.45	4.79	3.69	1.30	0.0221
ROLL2.3	1.99	7.33E+03	29.50	4.40	3.31	1.33	0.0278
ROLL3.3	3.09	1.21E+04	34.30	4.62	3.52	1.31	0.0202
ROLL4.3	3.99	1.43E+04	31.30	4.39	3.24	1.36	0.0235
ROLL5.3	5.13	1.97E+04	34.30	4.71	3.42	1.38	0.0251
ROLL6.3	6.16	2.33E+04	35.30	4.34	3.37	1.29	0.0245
SAND2.3	1.99	9.66E+03	34.00	6.24	4.33	1.44	0.0234
SAND3.3	3.07	1.46E+04	33.20	6.24	4.25	1.47	0.0216
SAND4.3	3.99	1.92E+04	35.20	6.33	4.24	1.49	0.0206
SAND5.3	5.18	2.53E+04	37.20	6.34	4.30	1.48	0.0252
SAND6.3	6.19	3.10E+04	35.90	6.54	4.41	1.48	0.0236

ure 5 shows the velocity profiles at 5 m/s and 1.607 m from the leading edge for the surfaces tested in the Emerson Cavitation Tunnel. The STEEL profile follows the smooth wall log-law well in the overlap region. The other surfaces also display a linear log region that is shifted by  $\Delta U^+$  below the smooth profile.

The friction velocities  $U_\tau$ , wake strength parameters  $\Pi$ , frictional resistance coefficients  $c_f$ , and roughness functions  $\Delta U^+$  are

shown in Table 4 (only for location 3) and in Table 5. Compared to smooth walls, the wake strength parameter generally increases for rough walls [19,20,24], but Tables 4 and 5 show that  $\Pi$  decreased slightly for the coated surfaces. Significantly lower wake strength values were recorded for the measurements at 7.5 m/s. This can be attributed to slight bending of the plate due to a Venturi effect which occurred at this velocity. The wall-normal

Table 3 Boundary-layer parameters measured in the CEHIPAR Cavitation Tunnel ( $\delta$ ,  $\delta_1$ , and  $\theta$  in mm)

Profile	$U_e$	$Re_\theta$	$\delta$	$\delta_1$	$\theta$	H	Tu
CSPC3.2	3.20	1.27E+04	33.00	4.27	3.37	1.27	0.0523
CSPC3.3	3.21	1.27E+04	33.00	4.45	3.37	1.32	0.0550
CSPC3.4	3.20	1.30E+04	33.50	4.48	3.46	1.29	0.0583
CSPC5.2	5.19	2.14E+04	37.50	4.66	3.43	1.36	0.0393
CSPC5.3	5.31	2.29E+04	40.00	5.10	3.75	1.36	0.0361
CSPC5.4	5.35	2.48E+04	49.00	5.30	3.99	1.33	0.0313
CSPC7.2	7.54	3.02E+04	37.00	4.20	3.04	1.38	0.0373
CSPC7.3	7.50	2.57E+04	39.50	3.81	2.85	1.34	0.0408
CSPC7.4	7.53	3.00E+04	44.00	4.30	3.14	1.37	0.0419
CFR3.2	3.25	1.61E+04	40.70	5.10	3.80	1.34	0.0602
CFR3.3	3.34	1.51E+04	39.80	4.71	3.80	1.24	0.0778
CFR3.4	3.38	1.66E+04	44.00	4.86	3.88	1.25	0.0761
CFR5.2	5.35	2.16E+04	36.00	4.20	3.19	1.32	0.0431
CFR5.3	5.28	2.40E+04	43.50	4.56	3.86	1.18	0.0371
CFR5.4	5.34	2.56E+04	46.50	5.27	4.07	1.30	0.0335
CFR7.2	7.59	2.99E+04	39.10	3.87	3.11	1.24	0.0353
CFR7.3	7.55	2.73E+04	39.10	3.70	3.00	1.23	0.0281
CFR7.4	7.62	3.61E+04	46.00	5.13	4.03	1.27	0.0315

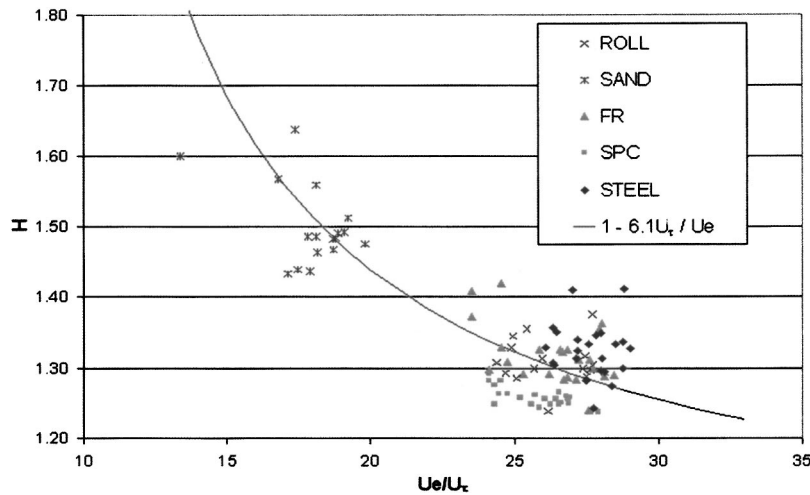


Fig. 4 von Karman shape factor  $H$  plotted against  $U_e/U_\tau$  (uncertainty in  $H$ :  $\pm 3.17\%$  for STEEL,  $\pm 0.58\%$  for SPC; uncertainty in  $U_e/U_\tau$ :  $\pm 1.07\%$  and  $\pm 1.56\%$ , respectively)

hydrodynamic force, associated with the Venturi effect caused by the accelerated flow between the plate and the tunnel wall, was strong enough to bend the thin test-plates which affected the determination of the error in origin  $\epsilon$ .

The friction velocities were calculated by three different methods for the STEEL plate: the Clauser method ( $C$ ), the Reynolds-stress method ( $RS$ ), and the Hama method ( $H$ ) for which good agreement was found. Only the latter two methods were retained on the coated surfaces and good agreement was found there as well.

The frictional resistance coefficients of the STEEL surface calculated with the Reynolds stress method were on average 2% higher than when calculated with the Clauser method, and 1.6% higher than when calculated with the Hama method. The frictional resistance profile matched well with the equation given in Monin and Yaglom [25]:

$$\frac{1}{\sqrt{c_f}} = \frac{1}{\kappa\sqrt{2}} \ln(\text{Re}_{\delta_1}) + B_4. \quad (4)$$

The empirical constant  $B_4$  was determined by least-squares regression analysis and was found to be 2.67 for the Hama method, 2.51

for the Reynolds Stress method, and 2.71 for the Clauser method (with respective correlation values of  $R^2=0.918$ ,  $0.908$ , and  $0.905$ ). It is of note that these regression lines average 4–5% higher than the original line proposed by Monin and Yaglom [25] (i.e., with  $\kappa=0.40$  and  $B_4=2.60$ ), but 10–11% lower than the line recently proposed by Tachie et al. [26] for open channel flows.

Figure 6 presents the skin friction coefficients of the STEEL surface and the three coated surfaces tested in the Emerson Cavitation Tunnel, plotted against  $\text{Re}_{\delta_1}$  for the values obtained with the Hama and Reynolds stress methods. Regression lines of the form of Eq. (4) have been included to indicate the average increase in  $c_f$ . The values for  $B_4$  and  $R^2$  for the coated surfaces are listed in Table 6. Figure 6 shows that the three coated surfaces all exhibited significantly higher  $c_f$  values compared to the smooth STEEL surface. Figure 6(a) shows that in comparison with the STEEL surface, the  $c_f$  values obtained by the Hama method increase on average by 14.7% for the SPC surface, by 10.1% for the FR surface, and by 12.4% for the ROLL surface. Figure 6(b) shows that with the Reynolds stress method the increase is 13.4%, 10.0%, and 12.8%, respectively. In comparison with the  $c_f$  values measured in the Emerson Cavitation Tunnel for the STEEL sur-

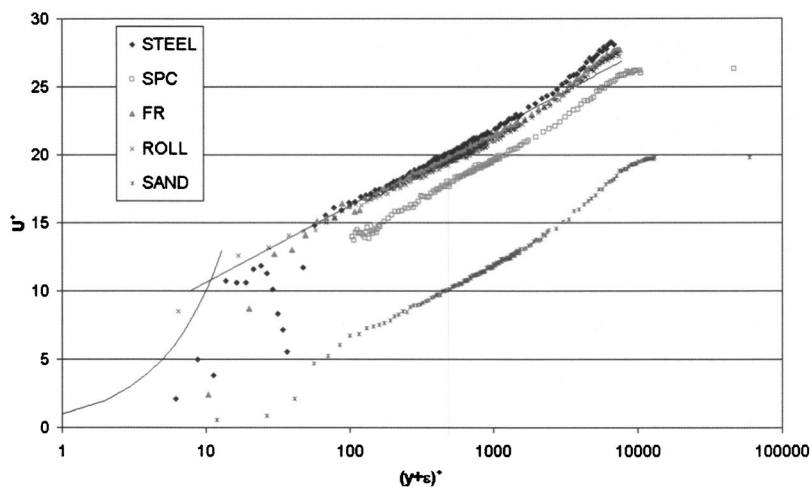


Fig. 5 Comparative velocity profiles at 5 m/s and 1.607 m from the leading edge [uncertainty in  $U^*$  for  $50 < (y+\epsilon)^+ < 0.8\delta^+$ :  $\pm 1.72\%$  for the STEEL surface,  $\pm 1.94\%$  for the rough surfaces)

**Table 4 Friction velocities and related parameters for the Emerson Cavitation Tunnel measurements at location 3**

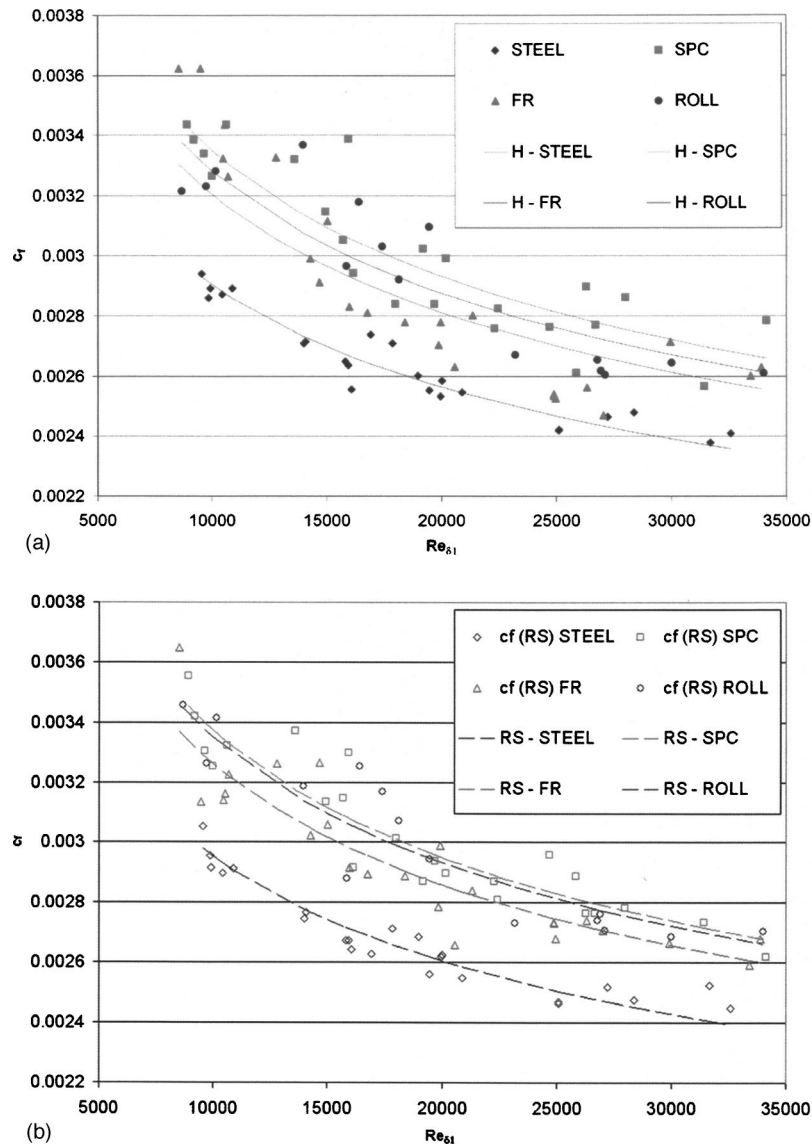
Smooth	Re <sub>s1</sub>	U <sub>t</sub> (H)	Π	δ <sup>+</sup>	c <sub>f</sub> (C)	c <sub>f</sub> (H)	c <sub>f</sub> (RS)	
STEEL2.3	10430	0.0735	0.44	3007	0.002815	0.002871	0.002899	
STEEL3.3	15806	0.111	0.42	4525	0.002633	0.002649	0.002673	
STEEL4.3	20885	0.142	0.43	5480	0.002545	0.002546	0.00255	
STEEL5.3	27233	0.185	0.40	7593	0.002429	0.002465	0.002519	
STEEL6.3	31691	0.209	0.45	8360	0.002429	0.002379	0.002526	
Rough	Re <sub>s1</sub>	U <sub>t</sub> (H)	Π	δ <sup>+</sup>	c <sub>f</sub> (H)	c <sub>f</sub> (RS)	ΔU <sup>+</sup> (H)	ΔU <sup>+</sup> (RS)
SPC2.3	9642	0.079	0.31	3015	0.003341	0.003304	1.63	1.27
SPC3.3	15939	0.124	0.32	5237	0.003389	0.003299	3.07	2.51
SPC4.3	19188	0.154	0.34	6240	0.003025	0.00287	2.11	1.20
SPC5.3	26296	0.190	0.35	8365	0.0029	0.002766	2.35	1.49
SPC6.3	34132	0.228	0.34	10756	0.002785	0.002618	2.47	1.40
FR2.3	10478	0.080	0.30	3038	0.003324	0.00314	1.78	0.85
FR3.3	15029	0.120	0.32	4565	0.003116	0.00306	1.88	1.42
FR4.3	18390	0.148	0.33	5145	0.00278	0.00289	0.89	1.18
FR5.3	26328	0.179	0.34	7202	0.002563	0.002739	0.68	1.37
FR6.3	33419	0.222	0.35	9426	0.002603	0.00259	1.49	1.20
ROLL2.3	9734	0.080	0.34	2622	0.003232	0.003262	1.25	1.14
ROLL3.3	15852	0.119	0.32	4535	0.002966	0.002881	1.38	0.77
ROLL4.3	19457	0.157	0.28	5460	0.003097	0.002945	2.44	1.57
ROLL5.3	27094	0.185	0.32	7130	0.002606	0.002707	0.98	1.28
ROLL6.3	30005	0.224	0.32	8884	0.002645	0.002687	1.44	1.43
SAND2.3	13904	0.114	0.40	4341	0.006563	0.005838	9.56	8.28
SAND3.3	21439	0.164	0.42	6098	0.005707	0.005762	9.38	9.24
SAND4.3	28691	0.209	0.52	8360	0.005488	0.00556	9.74	9.64
SAND5.3	37303	0.262	0.45	11054	0.005097	0.005415	9.68	10.04
SAND6.3	46020	0.330	0.44	13442	0.005667	0.005239	11.22	10.25

face, the  $c_f$  values calculated with the Hama and the Reynolds stress method increased on average by 12.8% and 14.0%, respectively, for the CFR surface and by 22.2% and 23.5%, respectively, for the CSPC surface, which is a significant difference within the experimental uncertainty. There is also significant difference between ROLL and SPC when calculated with the Hama method but not when calculated with the Reynolds stress method. These findings are in agreement with the findings from towing tank and rotor experiments [6] and indicate that rolling instead of spraying may jeopardize the drag benefits that newly applied Foul Release systems may offer over Tin-free SPC [6]. If these increases in

frictional resistance are compared with the roughness measurements of the coatings given in Table 1, it is clear that there is no correlation if only the parameter AHR is taken into account to characterize the roughness, as is the usual practice in naval architecture. The authors found that a correlation between roughness and drag is found if, in addition to a height parameter, a texture parameter is taken into account to characterize the roughness. The best correlation was found with a characteristic roughness measure that is the product of height parameter Ra and texture parameter Sa [27]. The values for the average increase of the roughness function for the coated surfaces, which are listed in Table 6, can

**Table 5 Friction velocity and related parameters for the CEHIPAR Cavitation Tunnel measurements**

CSPC	Re <sub>s1</sub>	U <sub>t</sub> (H)	Π	c <sub>f</sub> (H)	c <sub>f</sub> (RS)	ΔU <sup>+</sup> (H)	ΔU <sup>+</sup> (RS)
CSPC3.2	16079	0.135	0.26	0.00356	0.003773	3.68	4.13
CSPC3.3	16788	0.131	0.26	0.003331	0.003351	2.99	2.83
CSPC3.4	16877	0.131	0.21	0.003352	0.003353	3.08	2.85
CSPC5.2	29149	0.2	0.26	0.00297	0.003037	2.92	2.98
CSPC5.3	31128	0.2	0.28	0.002837	0.002848	2.48	2.31
CSPC5.4	32957	0.198	0.28	0.002739	0.002753	2.16	2.00
CSPC7.2	41666	0.278	0.11	0.002719	0.002955	2.64	3.52
CSPC7.3	34413	0.278	0.06	0.002748	0.002836	2.31	2.50
CSPC7.4	41006	0.273	0.01	0.002629	0.002697	2.14	2.27
CFR3.2	21526	0.125	0.26	0.002959	0.00324	2.11	3.04
CFR3.3	18746	0.13	0.26	0.00303	0.002975	2.07	1.61
CFR3.4	20793	0.124	0.26	0.002692	0.002713	0.77	0.65
CFR5.2	28419	0.2	0.26	0.002795	0.002879	2.06	2.22
CFR5.3	28325	0.198	0.28	0.002813	0.002838	2.13	2.02
CFR5.4	33129	0.2	0.26	0.002805	0.002946	2.49	2.91
CFR7.2	37171	0.268	0.06	0.002494	0.002606	1.16	1.55
CFR7.3	33618	0.263	0.06	0.002427	0.002461	0.52	0.49
CFR7.4	45946	0.27	0.14	0.002511	0.002531	1.78	1.67



**Fig. 6** The frictional resistance coefficients of the STEEL and coated surfaces as obtained with (a) the Hama and (b) the Reynolds stress methods (uncertainties in  $c_f$ :  $\pm 3.1\%$  for the Hama method;  $\pm 2.4\%$  for the Reynolds stress method). Least-squares regression lines of the form of Eq. (4) are included.

be derived from the regression lines of  $c_f$  shown in Fig. 6. Equation (4) was used to calculate  $c_{f,STEEL}$  and hence the roughness function for the different surfaces evaluated at the same  $Re_{\delta 1}$  values [28]:

$$\Delta U^+ = \left( \sqrt{2/c_{f,STEEL}} \right) - \left( \sqrt{2/c_f} \right). \quad (5)$$

The obtained values are listed in Tables 4 and 5. Figures 7(a)–7(c) show  $\Delta U^+$  against  $Re_{\delta 1}$  for each of the three coated surfaces tested in the Emerson Cavitation Tunnel respectively. A rise of  $\Delta U^+$  with increasing Reynolds number is expected and forms the basis for formulas which interpolate between the hydraulically smooth and fully rough flow regime like the well-known Colebrook–White law for “engineering roughness” [29,30]. Whether or not coated surfaces obey the Colebrook–White law has been a topic of discussion in the past but it is not suggested by the present data [6].

When the flow regime is fully rough, the frictional resistance becomes invariant with Reynolds number. While the coated surfaces have been measured in the transitional flow regime, the SAND surface was largely measured in the fully rough flow regime which is generally regarded to set in from equivalent sand

roughness values  $h_s^+ > 70$  to 90. The equivalent sand roughness was calculated from the average Hull roughness value with the approximation given by Canham [31] as  $h_s = 465 \mu\text{m}$ . This value is comparable to the average sand grain size of sand grit #40 (i.e., 40 holes in a standard sized screen) of  $425 \mu\text{m}$  as given by the Federation of European Producers of Abrasives. Thus,  $h_s^+$  is approximately 60 at 2 m/s and larger than 85 for all the other SAND measurements. Nikuradse’s form of the roughness function  $\chi$  is constant in the fully rough flow regime and written as [32]:

$$\chi = C + \frac{1}{\kappa} \ln h_s^+ - \Delta U^+ \quad (6)$$

It was found that  $\chi$  is indeed fairly constant for the SAND surface over the tested Reynolds number range and approximately equal to 7.08.

The turbulence intensities  $\sqrt{u'^2}/U_\tau$  and  $\sqrt{v'^2}/U_\tau$  are shown in Figs. 8 and 9 in inner and outer variables, respectively, for all the surfaces at 5 m/s and 1.607 m from the leading edge. Figure 8(a) indicates that over the region  $220 < (y + \epsilon)^+ < 1110$ , which is



**Table 6 Average roughness functions for the different surfaces and parameters of the regression lines**

	Hama method			Reynolds Stress method		
	$\Delta U^+$ (average)	$B_4$	$R^2$	$\Delta U^+$ (average)	$B_4$	$R^2$
SPC	1.80 ( $\pm 0.53$ )	1.39	0.796	1.65 ( $\pm 0.38$ )	1.33	0.873
FR	1.25 ( $\pm 0.71$ )	1.78	0.782	1.25 ( $\pm 0.44$ )	1.62	0.841
ROLL	1.54 ( $\pm 0.56$ )	1.57	0.799	1.58 ( $\pm 0.44$ )	1.39	0.859
SAND	10.39 ( $\pm 1.04$ )	-	-	9.96 ( $\pm 1.13$ )	-	-
CFR	1.68 ( $\pm 0.69$ )	1.50	0.574	1.80 ( $\pm 0.88$ )	1.25	0.439
CSPC	2.71 ( $\pm 0.51$ )	0.77	0.863	2.82 ( $\pm 0.67$ )	0.53	0.765

equivalent to  $0.02 < (y + \epsilon) / \delta < 0.11$ , the SAND surface displays a small flat “hump” in the streamwise turbulence intensity. According to Ligrani and Moffat [21], such humps are characteristic for fully rough surfaces and they are regions where the production of longitudinal turbulence energy is important. This is in accordance with the observations made with regards to the roughness function of the SAND surface. Figure 8 also indicates that at the equivalent values of  $(y + \epsilon) / \delta = 0.1$ , i.e.,  $(y + \epsilon)^+ = 762, 846, 726, 713, 1111, 945, \text{ and } 1040$  for STEEL, SPC, FR, ROLL, SAND, CSPC, and CFR, respectively, the values for  $\sqrt{u'^2} / U_\tau$  and  $\sqrt{v'^2} / U_\tau$  are  $2.1 \pm 0.2$  and  $1.1 \pm 0.1$ , respectively. This is in agreement with the values reported by Raupach et al. [33]. The near-wall region ( $y^+ < 30$ ) and in particular the peak values, which are higher than reported elsewhere, e.g., [33], have to be considered with great precaution in view of the large experimental uncertainties for  $y^+ < 50$ . When expressed in inner variables, all data collapse within the experimental uncertainty, in agreement with, for example, the channel flow experiments of Grass [34]. Kutlar and Lewkowicz [35] observed an increase in the wall-normal and spanwise (but not in the streamwise) turbulence intensities for a coarse surface when compared against a coated surface with lower roughness function. Similarly, Krogstad et al. [19] observed a significant increase in the wall-normal intensities for mesh roughness and concluded that the major effect of this type of roughness was to tilt the large-scale flow structures toward the wall-normal direction, leading to a higher degree of isotropy. Musker [36] observed increases both in the streamwise and in the wall-normal intensities over coated surfaces when compared against a smooth surface. Schultz and Swain [14] and Gangadharan et al. [37] also measured increases in both components over fouled surfaces, although there was a large degree of variability in these results due to the nature of the biofilm. In a comparison of two different types of roughness (streamwise rods and a mesh screen) for which the roughness function  $\Delta U^+$  was the same, Antonia and Krogstad [38] measured significant differences between the wall-normal intensities, and a smaller difference in the streamwise intensities. The differences in the wall-normal intensities persisted throughout the boundary layer in contradiction to the wall similarity hypothesis, which states that turbulent motions are independent from the wall roughness outside the roughness sublayer (which is of the order of a few roughness heights away from the wall) [33]. This apparent invalidity of the wall similarity hypothesis was also noted by Tachie et al. [20] in channel flow experiments with three different types of roughness (perforated plate, sand grain, and wire mesh). Recent wind tunnel experiments over grooved surfaces by Keir-

bulck et al. [23] indicated that both  $\sqrt{u'^2} / U_\tau$  and  $\sqrt{v'^2} / U_\tau$  profiles are increased compared to smooth-wall data, but that the effect is confined to the near-wall region, in support of the wall similarity hypothesis.

When expressed in outer variables, which is the scaling derived by George and Castillo [39], Fig. 9 shows that all data collapse from  $(y + \epsilon) > 0.7\delta$  within the experimental uncertainty. Figure 9(a) shows that for the SAND surface the roughness effect clearly shows up for  $(y + \epsilon) < 0.7\delta$ . Despite the relatively large uncertainties for the CEHIPAR measurements, the higher drag increases observed on CFR and CSPC seem to confirm the observations made regarding the effect of increasing roughness on the near-wall turbulence intensities, as seen in Fig. 9(c). Because of the higher free-stream turbulence levels at CEHIPAR (3.7% as opposed to  $\sim 2.3\%$  in the Emerson Cavitation Tunnel), Fig. 9(c) also shows that the turbulence intensities over the CFR and CSPC surface decay more slowly and remain higher in the outer layer.

Figure 10 compares the turbulent shear stresses of the different surfaces at  $x = 1.607$  m and  $U_e = 3$  m/s. The near-wall measurements are a direct indication of the agreement between the Hama method and the Reynolds stress method. It was found that the Reynolds shear stresses (non-dimensionalized by  $U_\tau^2$ ) seem to collapse for all the surfaces, except for SAND at location 1, where the shear stresses decay more rapidly in the outer layer. This may be the influence of the change from smooth to rough, which according to Antonia and Luxton [40] may extend over a length  $\sim 10\delta$ . At streamwise positions further away from the leading edge, all profiles collapse within the experimental uncertainty. This is in agreement with Ligrani and Moffat [21], who did not notice an influence of roughness on the Reynolds shear stresses in a zero-pressure gradient boundary layer over a flat plate. Similarly, Grass [34] observed no differences in open channel flow experiments. Krogstad et al. [19] and Tachie [41] found a moderate increase in the Reynolds shear stresses over mesh roughness, which was further evidence that the wall similarity hypothesis did not hold for that type of surface. The fact that the wall similarity hypothesis is supported by the present data justifies the use of an outer-layer wall similarity technique to determine the friction velocity.

## 6 Conclusions

The present study extends the available database of rough-wall turbulent boundary layers toward irregularly rough surfaces and, to the authors' knowledge, this is the first time LDV measure-

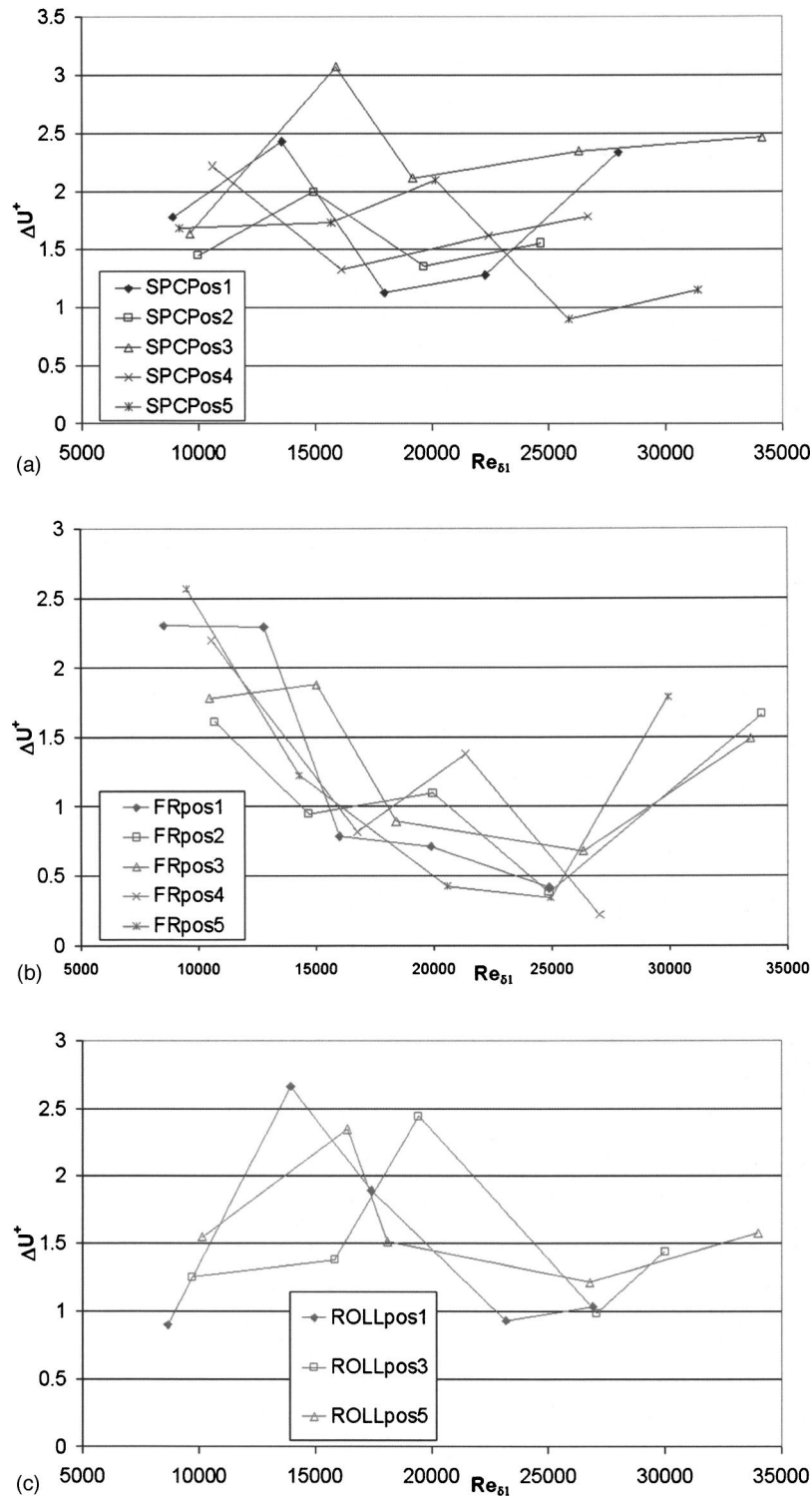


Fig. 7 Roughness function  $\Delta U^*$  versus  $Re_{\delta 1}$  at each location for (a) the surface SPC, (b) FR, and (c) ROLL (uncertainty in  $\Delta U^*$ :  $\pm 14.74\%$ ,  $Re_{\delta 1}$ :  $\pm 9.86\%$ )

ments for marine coatings have been published in the open literature. The velocity measurements indicated that the coatings generally did not have a significant effect on the boundary-layer parameters such as the boundary-layer thickness and shape factor. The friction velocity, on the other hand, was significantly increased by the coatings. Depending on the type and quality of application, the average increase was between 10% and 14% for the Foul release system, and between 13.4% and 23.5% for the

Tin-free SPC. Overall the increase in frictional resistance was less for the Foul Release coating applied by spraying than for the Foul Release coating applied by rolling. These findings are in agreement with findings from towing tank and rotor experiments.

No significant differences were found between the surfaces for the turbulence intensities and Reynolds shear stress when normalized by the friction velocity. However, when normalized by the free-stream velocity, increasing roughness had an effect for the

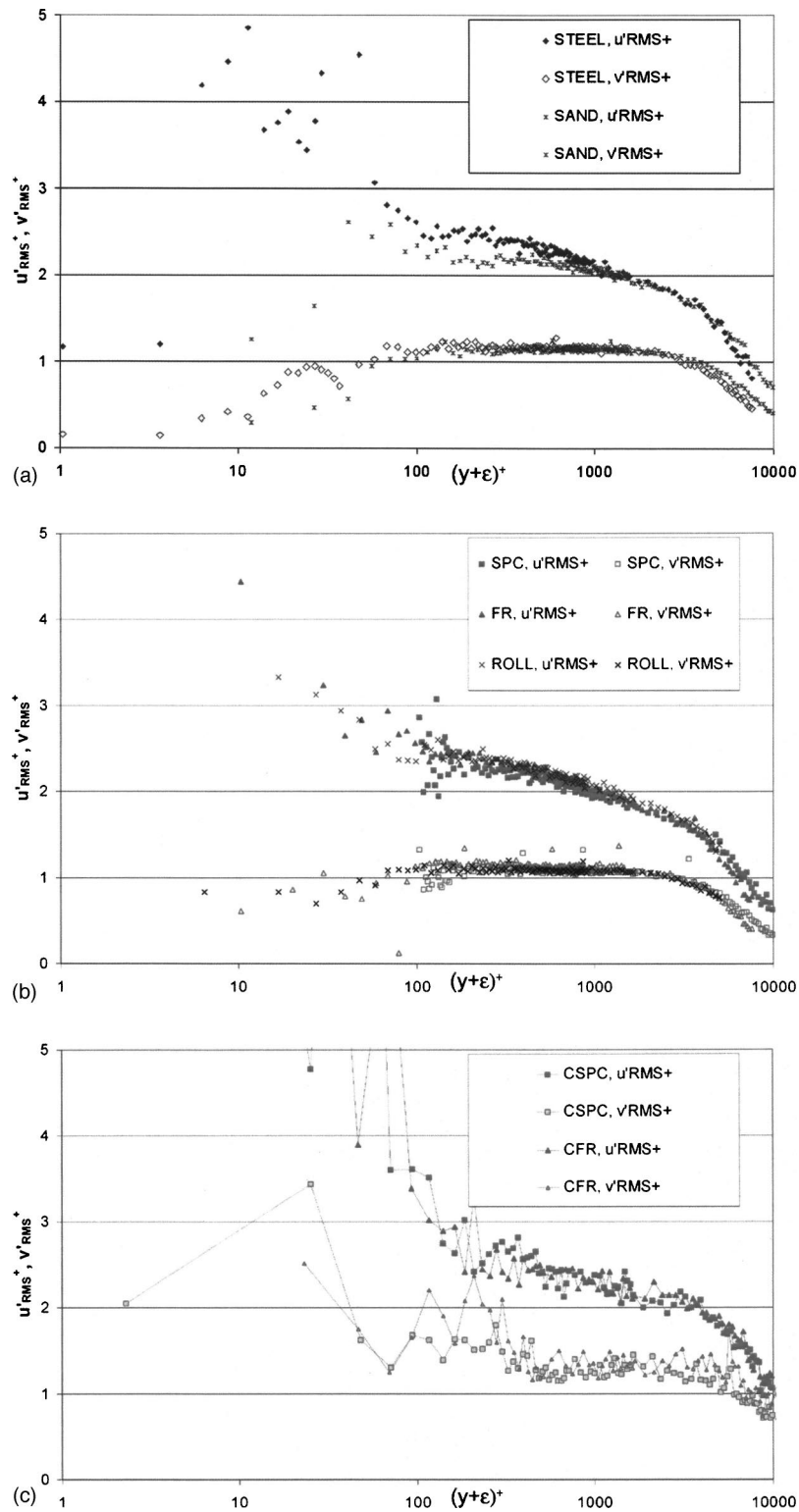


Fig. 8 Turbulence intensity profiles at  $U_e=5$  m/s and 1.607 m from the leading edge expressed in inner variables for (a) STEEL and SAND, (b) SPC, ROLL, and FR, (c) CSPC and CFR [uncertainties for the rough surfaces and for  $(y+\epsilon)^+ > 30$ :  $u'_{rms}$ :  $\pm 4.66\%$ ,  $v'_{rms}$ :  $\pm 4.00\%$  in the Emerson Cavitation Tunnel,  $\pm 29.4\%$  and  $\pm 29.9\%$ , respectively, in CEHIPAR]

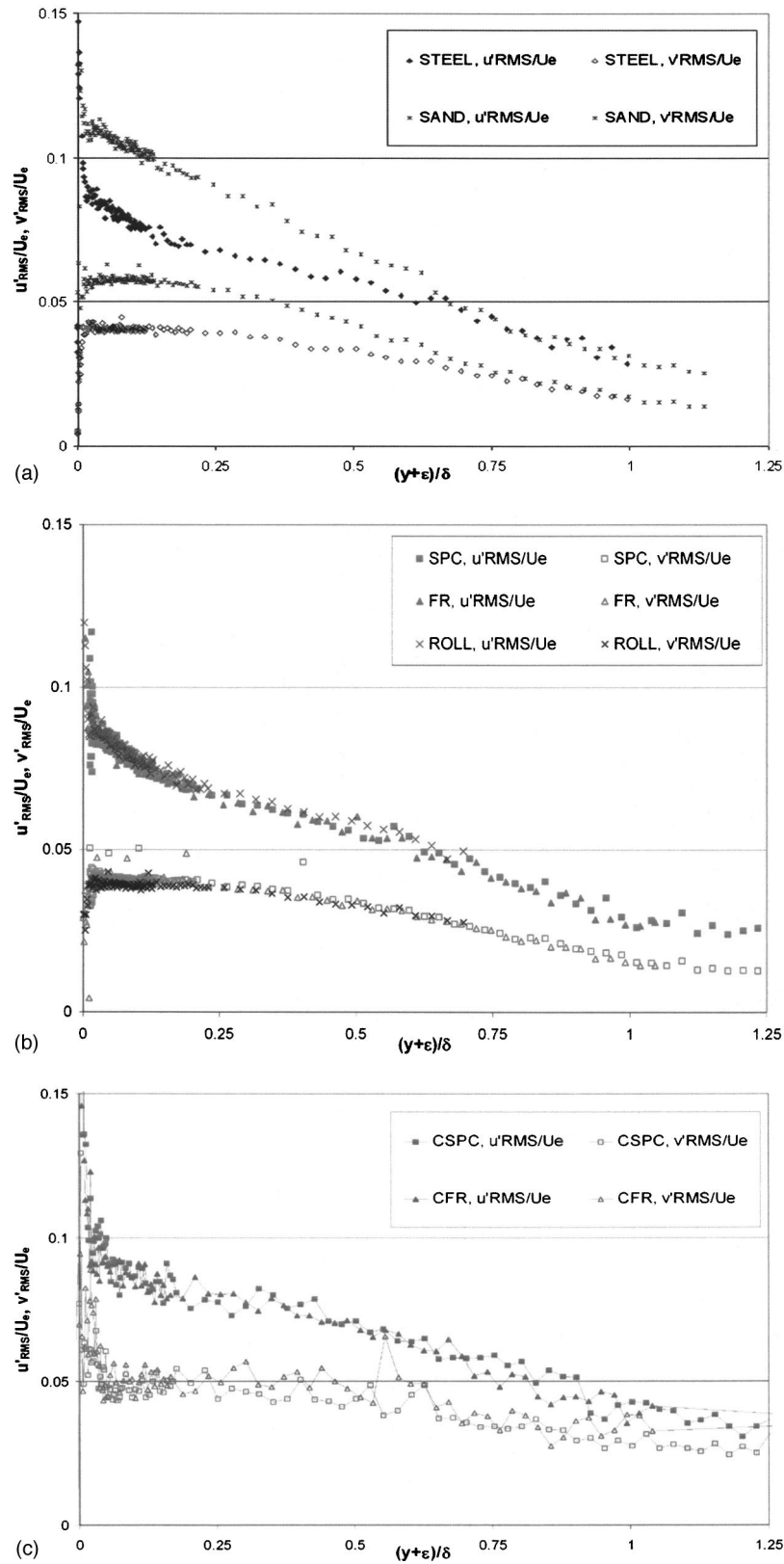


Fig. 9 Turbulence intensity profiles at  $U_e=5$  m/s and 1.607 m from the leading edge expressed in outer variables for (a) STEEL and SAND, (b) SPC, ROLL, and FR, (c) CSPC and CFR [uncertainties for the rough surfaces and for  $(y+\epsilon)/\delta > 0.02$ :  $u'_{rms}/U_e: \pm 4.54\%$ ,  $v'_{rms}/U_e: \pm 3.85\%$  in the Emerson Cavitation Tunnel,  $\pm 29.5\%$  and  $\pm 30.0\%$ , respectively, in CEHIPAR]

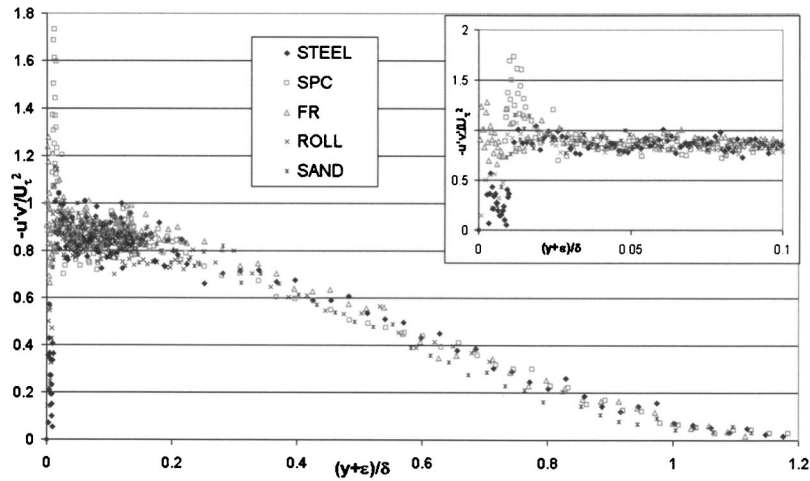


Fig. 10 Reynolds stress profiles at  $U_0=3$  m/s and  $x=1.607$  m [uncertainties for  $(y+\epsilon)/\delta > 0.02: \pm 12.14\%$ ]

near-wall turbulence intensities. In addition, it was found that the free-stream turbulence affected the rate of decay in the outer layer.

## 7 JFE Data Bank Contribution

Due to space restrictions, Tables 2 and 3 only list the measurements at location 3, but the other locations are available in the Data Bank.

## Acknowledgments

This research project was funded by EPSRC Research Grant No. 98316366, by International Coatings Ltd., and by the Engineering Design Centre at the University of Newcastle-upon-Tyne. The experiments at CEHIPAR were made possible by the European Community programme CEHMAR, which promotes the mobility and opportunities of researchers. The roughness measurements were made with the Hull Roughness Analyser of International Coatings Ltd. and with the optical measurement system at the Akzo Nobel Technology Centre. International Coatings Ltd. is thanked for the application of the paint systems and the staff at CEHIPAR are thanked for their assistance. The authors also would like to thank the various correspondents who have commented on the experiments.

## Nomenclature

AHR	= average Hull roughness
$C(=5.0)$	= smooth-wall log law constant
$c_f$	$= 2\tau_w/(\rho U_0^2)$ = local frictional resistance coefficient
FD	= fractal dimension
$h$	= a characteristic measure of roughness
$H = \delta_1/\theta$	= shape factor
$h_s$	= sand grain size
$n_{\text{mean}}$	= mean data-rate
$Re_x = U_0 x/\nu$	= Reynolds number
$Re_{\delta_1}$	$= U_0 \delta_1/\nu$ = displacement thickness Reynolds number
$Re_{\theta} = U_0 \theta/\nu$	= momentum thickness Reynolds number
Ra	= center-line average roughness height
rms	= root mean square
Sa	= mean absolute slope angle
Tu	$= \frac{\sqrt{(u'^2 + v'^2)}/2}{U_0}$ = free-stream turbulence
$U_0$	= free-stream velocity
$U_\tau$	= shear velocity

$U, V$  = average velocity components (streamwise and wall-normal)

$\dot{u}, \dot{v}$  = instantaneous velocity components

$-u'v'$  = Reynolds stress (divided by  $\rho$ )

$w$  = wake function

$x$  = streamwise distance from the leading edge of the plate

$y$  = normal distance from the wall

$Z_i$  =  $i$ th height reading of a surface profile

$\alpha$  = statistical significance level

$\delta = \delta_{0.99}$  = boundary-layer thickness

$\Delta$  = Clauser's boundary-layer thickness parameter

$\delta_1$  = displacement thickness

$\Delta U^+$  = Hama's form of the roughness function

$\epsilon$  = distance from virtual to actual origin at the wall (error in origin)

$\kappa(=0.41)$  = von Karman constant

$\nu$  = kinematic viscosity

$\theta$  = momentum thickness

$\Pi$  = wake strength parameter

$\rho$  = density

$\rho(\tau)$  = autocorrelation function

$\tau_w$  = wall shear stress

$+$  = non-dimensionalized in wall units: multiplied by  $U_\tau/\nu$  for length parameters and by  $1/U_\tau$  for velocities

$\chi$  = Nikuradse's form of roughness function

## References

- [1] Baier, R. E., 1970, "Surface Properties Influencing Biological Adhesion," in *Adhesion in Biological Systems*, R. S. Manly, ed., Academic, New York, pp. 15–48.
- [2] Meyer, A. E., Baier, R. E., and King, R. W., 1988, "Initial Fouling of Nontoxic Coatings in Fresh, Brackish and Sea Water," *Can. J. Chem. Eng.*, **66**, pp. 55–62.
- [3] Kovach, B. S., and Swain, G. W., 1998, "A Boat Mounted Foil to Measure the Drag Properties of Antifouling Coatings Applied to Static Immersion Panels," *Proc. Int. Symp. Seawater Drag Reduction*, Newport, Rhode Island, pp. 169–173.
- [4] Millett, J., and Anderson, C. D., 1997, "Fighting Fast Ferry Fouling," *Fast '97, Conference Papers*, 1, pp. 493–495.
- [5] Candries, M., Atlar, M., and Anderson, C. D., 2000, "Considering the Use of Alternative Antifouling: The Advantages of Foul Release Systems," *Conference Proceedings ENSUS 2000*, University of Newcastle-upon-Tyne, pp. 88–95.
- [6] Candries, M., 2001, "Drag, Boundary-Layer and Roughness Characteristics of Marine Surfaces Coated with Antifouling," Ph.D. thesis, Department of Marine Technology, University of Newcastle-upon-Tyne, UK, [http://www.geocities.com/maxim\\_candries/](http://www.geocities.com/maxim_candries/)

- [7] Atlar, M., 2000, "A History of the Emerson Cavitation Tunnel and its Role in Propeller Cavitation Research," *NCT '50 International Conference on Propeller Cavitation*, University of Newcastle-upon-Tyne, pp. 3–34.
- [8] Atlar, M., and Korkut, E., 1997, "Emerson Cavitation Tunnel Inflow Characteristics Based on 2-D Laser Doppler Anemometry Analysis," Report No. MT-1997-001, University of Newcastle-upon-Tyne, Newcastle-upon-Tyne.
- [9] Thomas, T. R., 1999, *Rough Surfaces*, 2nd ed., Imperial College Press, London.
- [10] Klebanoff, P. S., and Diehl, Z. W., 1952, "Some Features of Artificially Thickened Fully Developed Turbulent Boundary Layers with Zero Pressure Gradient," NACA Report No. 1110, <http://naca.larc.nasa.gov/reports/1952/naca-report-1110/>.
- [11] Hanratty, T. J., and Campbell, J. A., 1996, "Measurement of Wall Shear Stress," in *Fluid Mechanics Measurements*, 2nd ed., R. J. Goldstein (Ed.), Taylor & Francis, Philadelphia, 575–648.
- [12] Clauser, F. H., 1954, "Turbulent Boundary Layer in Adverse Pressure Gradients," *J. Aeronaut. Sci.*, **21**, pp. 91–108.
- [13] Perry, A. E., and Joubert, P. N., 1963, "Rough Wall Boundary Layers in Adverse Pressure Gradients," *J. Fluid Mech.*, **17**, pp. 193–211.
- [14] Schultz, M. P., and Swain, G. W., 1999, "The Effect of Biofilms on Turbulent Boundary Layers," *ASME J. Fluids Eng.*, **121**, pp. 44–51.
- [15] Schultz, M. P., 2000, "Turbulent Boundary Layers on Surfaces Covered with Filamentous Algae," *ASME J. Fluids Eng.*, **122**, pp. 357–362.
- [16] Hama, F. R., 1954, "Boundary Layer Characteristics for Smooth and Rough Surfaces," *Soc. Nav. Archit. Mar. Eng., Trans.*, **62**, pp. 333–358.
- [17] Bandyopadhyay, P. R., 1987, "Rough-Wall Turbulent Boundary Layers in the Transition Regime," *J. Fluid Mech.*, **180**, pp. 231–266.
- [18] Perry, A. E., Lim, K. L., and Henbest, S. M., 1987, "An Experimental Study of the Turbulence Structure in Smooth- and Rough-Wall Boundary Layers," *J. Fluid Mech.*, **177**, pp. 437–466.
- [19] Krogstad, P.-A., Antonia, R. A., and Browne, L. W. B., 1992, "Comparison between Rough- and Smooth-Wall Turbulent Boundary Layers," *J. Fluid Mech.*, **245**, pp. 599–617.
- [20] Tachie, M. F., Bergstrom, D. J., and Balachandar, R., 2000, "Rough Wall Turbulent Boundary Layers in Shallow Open Channel Flow," *ASME J. Fluids Eng.*, **122**, pp. 533–541.
- [21] Ligrani, P. M., and Moffat, R. J., 1986, "Structure of Transitionally Rough and Fully Rough Turbulent Boundary Layers," *J. Fluid Mech.*, **162**, pp. 69–98.
- [22] Coleman, H. W., and Steele, W. G., 1999, *Experimentation and Uncertainty Analysis for Engineers*, Wiley, New York.
- [23] Hinze, J. O., 1975, *Turbulence*, McGraw-Hill, New York, p. 633.
- [24] Keirsbulck, L., Labraga L., Mazouz, A., and Tournier, C., 2002, "Surface Roughness Effects on Turbulent Boundary Layer Structures," *ASME J. Fluids Eng.*, **124**, pp. 127–135.
- [25] Monin, A. S., and Yaglom, A. M., 1971, *Statistical Fluid Mechanics: Mechanics of Turbulence*, MIT, Cambridge, Vol. 1.
- [26] Tachie, M. F., Bergstrom, D. J., Balachandar, R., and Ramachandran, S., 2001, "Skin Friction Correlation in Open Channel Boundary Layers," *ASME J. Fluids Eng.*, **123**, pp. 953–956.
- [27] Candries, M., and Atlar, M., 2003, "On the Drag and Roughness Characteristics of Antifoulings," *Soc. Nav. Archit. Mar. Eng., Trans.*, **145** Part A2, pp. 35–60.
- [28] Granville, P. S., 1987, "Three Indirect Methods for the Drag Characterization of Arbitrarily Rough Surfaces on Flat Plates," *J. Ship Res.*, **31**, pp. 70–77.
- [29] Colebrook, C. F., and White, C. M., 1937, "Experiments with Fluid Friction in Roughened Pipes," *Proc. R. Soc. London, Ser. A*, **161**, pp. 367–381.
- [30] Perry, A. E., Hafez, S., and Chong, M. S., 2001, "A Possible Reinterpretation of the Princeton Superpipe Data," *J. Fluid Mech.*, **439**, pp. 395–401.
- [31] Canham, H. J. S., 1975, "Resistance, Propulsion and Wake Tests with HMS Penelope," *Transactions of the Soc. Nav. Archit. Mar. Eng., Trans.*, **117**, pp. 61–94.
- [32] Yaglom, A. M., 1979, "Similarity Laws for Constant-Pressure and Pressure-Gradient Turbulent Wall Flows," *Annu. Rev. Fluid Mech.*, **11**, pp. 505–540.
- [33] Raupach, M. R., Antonia, R. A., and Rajagopalan, S., 1991, "Rough-Wall Turbulent Boundary Layers," *Appl. Mech. Rev.*, **44**, pp. 1–25.
- [34] Grass, A. J., 1971, "Structural Features of Turbulent Flow over Smooth and Rough Boundaries," *J. Fluid Mech.*, **50**, pp. 233–255.
- [35] Kutlar, A. I., and Lewkowicz, A. K., 1990, "Investigation of the Effect of a Paint Coat on the Turbulence near a Rough Flat Plate," *International Workshop on Marine Roughness and Drag*, R.I.N.A., London, Paper 6.
- [36] Musker, A. J., 1990, "Turbulence Measurements in a Shear-Layer Associated with a Ship-Hull Roughness," *International Workshop on Marine Roughness and Drag*, R.I.N.A., London, Paper 10.
- [37] Gangadharan, S. N., Schultz, M., Collino, B., Clark, A., and Wimberly, C. R., 2001, "Experimental Investigation of *Enteromorpha clathrata* Biofouling on Lifting Surfaces of Marine Vehicles," *Mar. Technol. Soc. J.*, **38**, pp. 31–50.
- [38] Antonia, R. A., and Krogstad, P.-A., 2001, "Turbulence Structure in Boundary Layers over Different Types of Surface Roughness," *Fluid Dyn. Res.*, **28**, pp. 139–157.
- [39] George, W. K., and Castillo, L., 1997, "Zero Pressure Gradient Turbulent Boundary Layer," *Appl. Mech. Rev.*, **50**, pp. 689–729.
- [40] Antonia, R. A., and Luxton, R. E., 1971, "The Response of a Turbulent Boundary Layer to a Step Change in Surface Roughness. 1. Smooth-to-Rough," *J. Fluid Mech.*, **48**, pp. 721–761.
- [41] Tachie, M. F., 2000, "Open Channel Turbulent Boundary Layers and Wall Jets on Rough Surfaces", Ph.D. thesis, Department of Mechanical Engineering, University of Saskatchewan, Saskatoon.

# Modeling of Wall Pressure Fluctuations Based on Time Mean Flow Field

Yu-Tai Lee

e-mail: LeeYT@nswccd.navy.mil

William K. Blake

Theodore M. Farabee

Naval Surface Warfare Center, Carderock  
Division, 9500 MacArthur Blvd., West Bethesda,  
MD 20817

*Time-mean flow fields and turbulent flow characteristics obtained from solving the Reynolds averaged Navier-Stokes equations with a  $k$ - $\epsilon$  turbulence model are used to predict the frequency spectrum of wall pressure fluctuations. The vertical turbulent velocity is represented by the turbulent kinetic energy contained in the local flow. An anisotropic distribution of the turbulent kinetic energy is implemented based on an equilibrium turbulent shear flow, which assumes flow with a zero streamwise pressure gradient. The spectral correlation model for predicting the wall pressure fluctuation is obtained through a Green's function formulation and modeling of the streamwise and spanwise wave number spectra. Predictions for equilibrium flow agree well with measurements and demonstrate that when outer-flow and inner-flow activity contribute significantly, an overlap region exists in which the pressure spectrum scales as the inverse of frequency. Predictions of the surface pressure spectrum for flow over a backward-facing step are used to validate the current approach for a nonequilibrium flow. [DOI: 10.1115/1.1881698]*

## Introduction

Pressure fluctuations on the wall under a turbulent boundary layer result from turbulent velocity fluctuations throughout the layer. These wall pressure fluctuations could theoretically be predicted directly by either a direct numerical simulation (DNS) or a large eddy simulation (LES). Both DNS and LES are very computationally intensive, require a large amount of computer resources, and are used generally for low-Reynolds-number canonical-type flows. For applications with complex geometries it becomes unrealistic to apply either calculation method in a time-driven design environment.

On the other hand, steady-state flow analysis by solving Reynolds averaged Navier-Stokes (RANS) equations with either an isotropic or an anisotropic turbulence model is quickly becoming a standard procedure in designing complex fluid systems. RANS simulation provides a great deal of useful information regarding the flow characteristics. In this paper, a computationally efficient wall-pressure-spectrum prediction method is introduced using time-mean flow fields predicted by RANS simulation.

Most of the literature investigating wall pressure characteristics deals with the equilibrium turbulent boundary layer, which assumes flow with a zero streamwise pressure gradient. These efforts include the work performed by Willmarth and Wooldridge [1], Corcos [2], Blake [3,4], Olivero-Bally et al. [5], and Abraham and Keith [6] and analyses by Lilley and Hodgson [7], Landahl [8], Panton and Linebarger [9], Chase [10], Blake et al. [11], and Smol'yakov [12]. Even given the difficulty and uncertainty in measuring and predicting surface pressure fluctuations for equilibrium shear layers, studies of the wall pressure fluctuations for nonequilibrium turbulent boundary layers have started to emerge in the literature. Among these efforts, Farabee and Casarella [13,14] made wall pressure measurements for flows past backward- and forward-facing steps and tried to characterize the spectral contents of the reattachment flows. Although the flows upstream of the steps are in equilibrium, the reattached flows need to travel a long distance before again reaching equilibrium. Interest in understanding unsteady surface pressure beneath nonequi-

librium turbulent flows also extends to more complex geometries. Simpson et al. [15] investigated the characteristics of wall pressure spectra under strong flow separation. Brooks and Humphreys [16] measured and analyzed wall pressure spectra over an airfoil with a finite-span flap under NASA's airframe noise program. They used the measured surface pressures to help analyze and characterize side-flap noise, which dominates the entire airframe noise. Guo et al. [17] characterized the noise from an airfoil similar to that used in [16] and also used measured surface pressure spectra as the source term in their noise-modeling efforts.

In this paper a methodology of predicting turbulent boundary layer wall pressure spectra is presented. The method uses the predicted mean flow field obtained from RANS calculations and a spectral correlation model, and integrates across the turbulent boundary layer. Validation of the present method is demonstrated for both an equilibrium flow and a nonequilibrium flow resulting from flow over a backward-facing step (BFS).

## Methodology

We deal with turbulent boundary layers at low Mach numbers over a smooth, stationary, rigid surface. A weak coupling between the mean flow field and the acoustic field is assumed to provide a means of solving the mean flow field independently from its acoustic field.

**Mean-Flow Prediction.** The mean flow field is obtained by solving the incompressible RANS equations as follows:

$$\frac{\partial U_i}{\partial x_i} = 0, \quad \rho \frac{DU_i}{Dt} = -\frac{\partial P}{\partial x_i} + \frac{\partial \tau_{ij}}{\partial x_j} \quad (1)$$

where  $U_i$  and  $P$  are mean-flow velocity and pressure fields;  $\tau_{ij} = \mu \partial U_i / \partial x_j - \rho u_i u_j$  is the effective shear stress, which includes the laminar (first term) and the turbulent (second term) shear stresses; and  $u_i$  is the fluctuating velocity. The turbulent (or Reynolds) shear stress is further formulated using a two-equation isotropic turbulence model as

$$\frac{Dk}{Dt} = \frac{\partial}{\partial x_l} \left[ \left( C_k \frac{k^2}{\epsilon} + \nu \right) \frac{\partial k}{\partial x_l} \right] - u_i u_l \frac{\partial U_i}{\partial x_l} - \epsilon$$

Contributed by the Fluids Engineering Division for publication in the JOURNAL OF FLUIDS ENGINEERING. Manuscript received by the Fluids Engineering Division May 24, 2004; revised manuscript received, September 20, 2004. Review conducted by T. Gatski.

$$\frac{D\varepsilon}{Dt} = \frac{\partial}{\partial x_i} \left[ \left( C_k \frac{k^2}{\varepsilon} + \nu \right) \frac{\partial \varepsilon}{\partial x_i} \right] - C_{\varepsilon 1} \frac{\varepsilon}{k} \frac{\partial U_i}{\partial x_i} - C_{\varepsilon 2} \frac{\varepsilon^2}{k} \quad (2)$$

where  $k = \overline{u_i u_i} / 2$ ,  $\varepsilon = \nu \overline{(\partial u_i / \partial x_i)(\partial u_i / \partial x_i)}$ , and the following constants are defined as  $C_k = 0.09$ ,  $C_{\varepsilon 1} = 1.45$ , and  $C_{\varepsilon 2} = 1.92$ . The RANS equations (1) and the turbulence equation (2) are discretized with a cell-centered finite-volume spatial approximation, which employs a second-order upwind scheme for the convection terms and a second-order central difference scheme for the diffusion term. An implicit numerical flux linearization with the Block-Jacobi Gauss-Seidel relaxation is used to solve the discretized difference equations.

The RANS equations with the  $k$ - $\varepsilon$  turbulence model are integrated [18,19] with a scalable parallel algorithm and the message passing interface (MPI) to solve the flowfield in a multiprocessor computational environment. The computational grids, generated by the commercial software *GRIDGEN*, are multiblock surface-fitted structured grids with arbitrary block connectivity.

**Prediction of Surface Pressure Spectrum.** The equation for pressure fluctuations in turbulence is derived by taking the divergence of the momentum equation, using the continuity equation to drop terms, performing a Reynolds decomposition into mean and unsteady terms, and then subtracting the time-averaged equation, to yield

$$\nabla^2 p = -2\rho \frac{\partial U_i}{\partial x_j} \frac{\partial u_j}{\partial x_i} - \frac{\partial^2}{\partial x_i \partial x_j} \rho(u_i u_j - \overline{u_i u_j}) \quad (3)$$

Equation (3) is a Poisson equation for the fluctuating pressure  $p$  in a turbulent flow. The source terms on the right-hand side of Eq. (3) represent the mean shear-turbulence (MT) interaction (first term) and the turbulence-turbulence (TT) interaction (second term). Lilley and Hodgson [7] estimated the relative importance of these interactions and concluded that the TT terms were only 4–6% of the mean-square pressure. However, Hodgson [20], Corcos [2], and Panton and Linebarger [9] indicated that the TT contribution becomes comparable to the MT contribution in the low frequency range, i.e.,  $\omega \delta^* / U_\infty \leq 0.02$  where  $\delta^*$  is the displacement thickness. The most interesting work in this regards is perhaps that of Chang [21] who conducted an intensive study of source terms by examining velocity field statistics and partial wall pressures computed from a database generated by a DNS of a fully developed channel flow. One of Chang's major findings is that the MT and TT terms are of the same order of magnitude throughout the wave number range examined and that both have the same spectral shape as the total pressure. Although Chang's calculations were for a low Reynolds number flow, it is assumed that the above finding is applicable to higher Reynolds number flows and the TT terms are not explicitly considered in the present analysis.

Equation (3) without the TT source terms can be solved in the spectral domain, i.e., in terms of the spectral variables wave number and frequency. Adopting standard boundary layer approximations and the assumption that the flow in planes parallel to the wall is homogeneous and stationary, Eq. (3) can be Fourier transformed in the two directions on these planes and over time. With these assumptions the MT source term becomes  $-2\rho(\partial U_1 / \partial y)(\partial u_2 / \partial x)$ , where  $u_2$  is the vertical fluctuating velocity. Furthermore, since the intent is to predict the frequency spectrum of wall pressure fluctuations and since these pressures are dominantly generated by convected turbulence activity, the wave number spectrum is converted to a frequency spectrum by assuming a frozen turbulence field that convects with a velocity  $U_c(k_c)$ . Following the derivations of Kraichnan [22], Panton and Linebarger [9], Blake [4], and Chase [10] and further applying a boundary condition of zero normal pressure gradient at the wall, the frequency spectral density of the fluctuating pressure can be written

$$\Phi_{pp}(\omega) = \frac{4\tau_w^2 \delta^{*2}}{u_\tau} \int_0^{\delta^*} \int_0^{\delta^*} d\left(\frac{y}{\delta^*}\right) d\left(\frac{y'}{\delta^*}\right) \frac{d\left(\frac{U_1(y)}{u_\tau}\right)}{d\left(\frac{y}{\delta^*}\right)} \frac{d\left(\frac{U_1(y')}{u_\tau}\right)}{d\left(\frac{y'}{\delta^*}\right)} \times \left( \frac{\rho(\overline{u_2^2}(y))^{1/2}(\overline{u_2^2}(y'))^{1/2}}{\tau_w} \right) \mathcal{J}(y, y', \omega \delta^* / U_c) \quad (4)$$

where, for convenience, terms within the integrals are expressed in nondimensional form. The  $\mathcal{J}(y, y', \omega \delta^* / U_c)$  term in Eq. (4) is modeled, and all the other terms are calculated from the RANS solution described in the previous section. This modeled term represents an integration in the spanwise wave number with a Green's function and a spectral correlation function  $\phi_{22}$  for the vertical fluctuation velocity between two positions  $y$  and  $y'$  of the boundary layer. It is written explicitly as

$$\mathcal{J}(y, y', \omega \delta^* / U_c) = \int_{-\infty}^{\infty} dk_3 \left( \frac{k_c^2}{k_c^2 + k_3^2} \right) e^{-\sqrt{k_c^2 + k_3^2}(y+y')} \phi_{22}(y, y', k_3, \omega / U_c) \quad (5)$$

where  $\phi_{22}$  can be further decomposed in terms of the autospectrum of  $u_2$

$$\phi_{22}(y, y', k_3, \omega / U_c) = \sqrt{\phi_1(\omega / U_c, y) \phi_1(\omega / U_c, y')} E_{22}^N(y, y', k_3, \omega / U_c) \quad (6)$$

The last term in Eq. (6) is an interplane correlation function between  $y$  and  $y'$  and modeled using Chase's formulation [10]. The wave number spectrum of  $u_2$  is approximated using Farabee's data [23] as

$$\phi_1(k_c, y) = \frac{y_{pp}}{U_c} \frac{0.18}{1 + (k_c y_{pp} / 1.7)^2}$$

with  $\frac{y_{pp}}{\delta^*} = \frac{2.5y / \delta^* (0.9 + 2.5y / \delta^*)}{1 + (2.5y / \delta^*)^2}$  (7)

where the convective wave number is  $k_c = \omega / U_c$ .

**Modification for Anisotropic Turbulent Flows.** The RANS calculations previously described use the isotropic  $k$ - $\varepsilon$  turbulence model. This model expresses the wall normal velocity as

$$\overline{u_2^2} = \frac{2k}{3} \quad \text{with } 2k = \overline{u_1^2} + \overline{u_2^2} + \overline{u_3^2} \quad (8)$$

In order to account for the anisotropy of the turbulence field, a modification of Eq. (8) is used for predicting the normal fluctuating velocity, i.e.,

$$\overline{u_2^2} = \frac{2k}{3} f_{\text{aniso}} \quad (9)$$

where  $f_{\text{aniso}}$  is an anisotropic factor, which is derived from equilibrium flow data by averaging Klebanoff's smooth data and Corrsin's fully rough data [24] as shown in Fig. 1. Since this anisotropic factor is developed based on an equilibrium flow, a generalized form for nonequilibrium flows would require additional knowledge of the subject turbulent fields. Certainly a RANS solution obtained with a solved normal Reynolds stress turbulence model would provide the required information for the present prediction.

## Results

The proposed computational scheme for predicting the spectrum of wall pressure fluctuations is applied first to an equilibrium shear layer, and the predicted results are compared to several measured data. It is then validated for a nonequilibrium flow, i.e., flow over a backward-facing step with flow recirculation and a reattachment zone. It is recognized here that application of this analy-



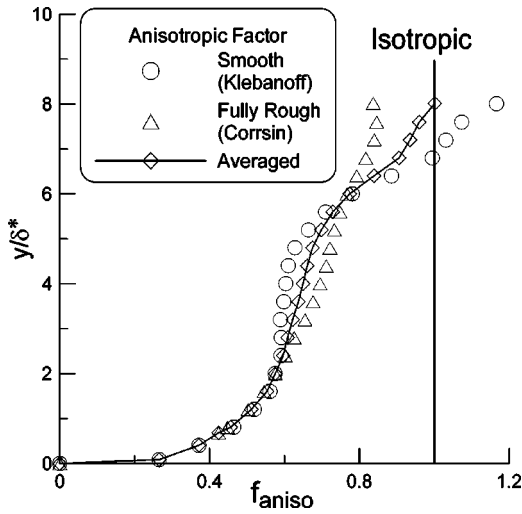


Fig. 1 The function for the anisotropic factor

sis approach to a nonequilibrium flow may be counter to the initial assumptions of in-plane homogeneity. However, it is felt that these comparisons provide a test of the robustness of the prediction approach.

**Equilibrium Flow.** The prediction model is first applied to a zero streamwise pressure gradient boundary layer flow. RANS calculations from the zero streamwise pressure gradient region of flow over an airfoil are used for this purpose. Comparisons of the wall pressure spectra predicted for both the isotropic and anisotropic cases are made in Fig. 2 to measured spectra provided by Blake [3], Farabee and Casarella [25], and Goody [26]. Figure 2(a) provides a comparison for the case in which the spectra are scaled on the length ( $\delta^*$ ), time ( $\delta^*/U_e$ ), and pressure ( $q = 1/2\rho U_e^2$ ) scales formed using outer-flow variables. Similarly, Fig. 2(b) provides a comparison using mixed (inner- and outer-) flow variables for the length  $\delta$ , time  $\delta/u_\tau$ , and pressure  $\tau_w$ . A final comparison is provided in Fig. 2(c) using the inner-flow variables based scales of  $\mu/u_\tau$ ,  $\mu/u_\tau^2$ , and  $\tau_w$  for the length, time, and pressure, respectively. It is noted that the predictions are derived from calculations at a momentum thickness Reynolds number  $Re_\theta$  of 3582, which is in the lower range of the  $Re_\theta$  for the measured data and is close to the lower  $Re_\theta$  data of Farabee and Casarella [25]. The comparisons in Fig. 2 clearly show that adopting the anisotropic correction factor  $f_{aniso}$  results in far better agreement between the predicted and measured pressure spectra. Using the isotropic  $k-\varepsilon$  turbulence model results in a pressure spectrum that overpredicts the measured spectra by 6–8 dB.

Included in Fig. 2(c) for visual reference are lines representing slopes for spectra that scale as specific powers of frequency. All three of these spectral dependencies ( $\omega^{-1}$ ,  $\omega^{-7/3}$ , and  $\omega^{-5}$ ) have been suggested to exist by various investigators ([5], for example). Detailed discussions of the scaling behavior of wall pressure spectra are provided elsewhere ([25], for example) and will not be repeated here beyond the following comments. The scaling used in Figs. 2(a) and 2(b) is based on outer-flow variables and results in excellent collapse of the measured spectra at lower frequencies. Similarly, the scaling used for Fig. 2(c) is based on inner-flow variables and results in excellent collapse of the measured spectra at high-frequencies. These observations are consistent with the argument that near-wall turbulence is the source of high-frequency wall pressures and outer-flow turbulence the source of low-frequency wall pressures. A further evaluation of the distribution of sources of wall pressure fluctuations across the boundary layer is provided next.

As Eq. (4) indicates, unsteady wall pressures come from turbu-

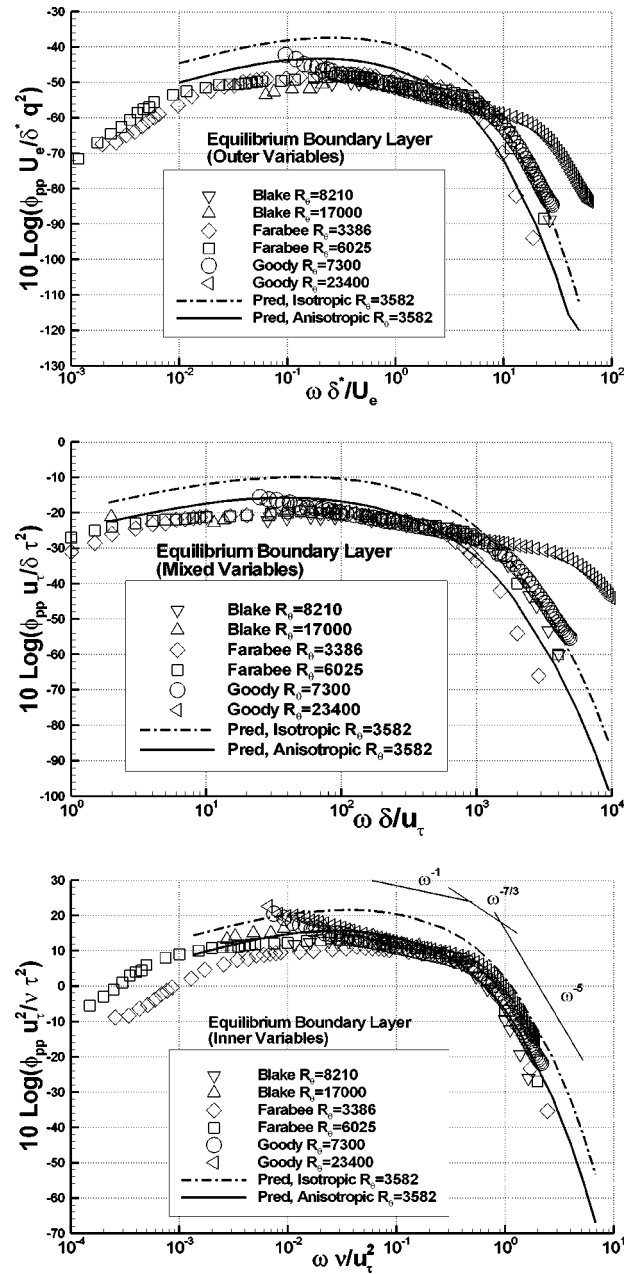


Fig. 2 Comparison of spectra for equilibrium flows using (a) outer; (b) mixed; and (c) inner variables

lence fluctuations across the entire shear layer. In order to distinguish the contributions from various parts of the shear layer, we divide the turbulent boundary layer into inner (I), middle (M), and outer (O) regions with each region defined in Eq. (10). A graphical representation of this division is shown in Fig. 3(a) and follows that used by Panton and Linebarger [9].

$$\text{Inner: } y^+ \leq 33$$

$$\text{Middle: } y^+ > 33 \text{ and } y/\delta \leq 0.2 \quad (10)$$

$$\text{Outer: } y/\delta > 0.2$$

Contributions from each region to the fluctuating wall pressure for the equilibrium layer are calculated by independently integrating the double integrals of Eq. (4) for each region and are plotted in Fig. 3(b) as functions of frequency  $\omega \delta^*/U_e$ . The regional contributions are categorized into those that originate from and affect

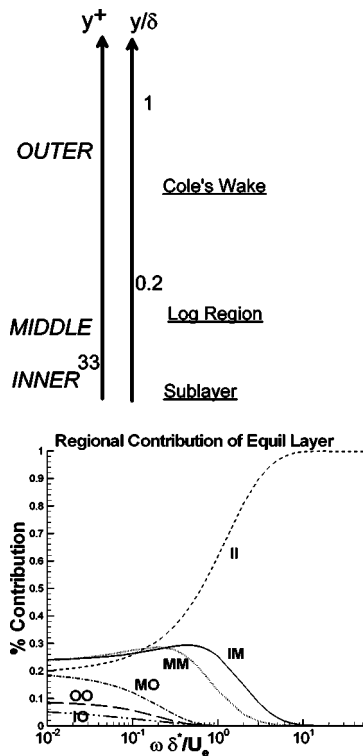


Fig. 3 Regional contributions of equilibrium flows

the same regions (II, MM, and OO), and those that originate from and affect different regions (IM, IO, and MO). For high-frequency pressure fluctuations the spectrum is dominated by the II region. This dominating feature drops quickly for  $\omega \delta^*/U_e \leq 0.5$ , where the II, IM, and MM contributions are almost equal. Note that the low-frequency contribution from MO is larger than that from IO for the entire frequency range even though regions M and O are farther away from the wall than regions I and O.

**Nonequilibrium Flows.** The present modeling scheme for predicting fluctuating wall pressure is also applied to a backward-facing step (BFS) flow. Complex flow over a BFS, as shown in Fig. 4, consists of an inflow with an equilibrium turbulent boundary layer, a recirculation region starting at the step, a free shear layer between the recirculation region and the outer flow, a reattachment region with a fluctuating reattachment point, and a redeveloped region that reconciles the reattached boundary layer back to the equilibrium layer. When the flow transitions from the recirculation region to the reattached boundary layer, highly unstable flow disturbances produce a rapid growth of vortical structures, which convect far downstream. These coherent structures domi-

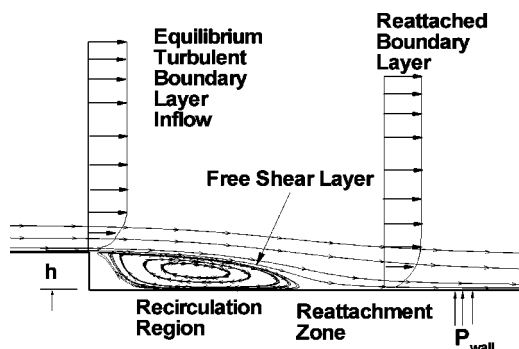


Fig. 4 Flow field over the BFS

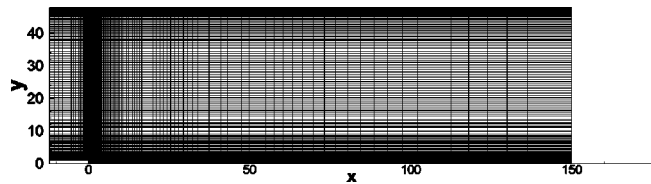


Fig. 5 Computational grid for BFS

nate the momentum transfer between flow regions and have a significant impact on the magnitude and spectral characteristics of the resulting wall pressure fluctuations. Although the flow recirculation produces all of the complex flow features for the BFS, the focus of this paper is to investigate the applicability of the current model for predicting wall pressure fluctuations from the flow in the reattached flow region.

Data from the BFS study of Farabee [23] are used for this analysis. The measurements were performed in a wind tunnel with an opening height of  $47h$ , where  $h$  is the step height of 1.27 cm. The expansion ratio at the step is 1.0213. The test wind tunnel speed is 15.36 m/s with a Reynolds number (based on  $h$ ) of 13,043. Since the data at the farthest measured station (i.e.,  $x = 72h$ ) indicate that the reattached shear layer has not completely recovered yet, the RANS computational domain (shown in Fig. 5) has a dimension of  $48h$  in height and extends from  $-12h$  to  $150h$  in the streamwise direction with the BFS located at the origin. The two-dimensional (2D) RANS calculation uses a grid of 401 nodes in the streamwise direction and 261 nodes in the transverse direction. The near wall grid has  $y^+ \cong 1$ .

The boundary condition at the wind tunnel walls is a nonslip condition. The inflow conditions at  $x/h = -12$ , shown in Fig. 6, employ the measured velocity  $U_x$  and turbulent kinetic energy  $k$  distributions with a shear layer profile thickness of  $\delta/h = 1.75$ . Since measured values of  $k$  from crosswire measurements tend to be low, single-wire data were used to estimate the total  $k$  at the inlet station. The dissipation rate is estimated based on Goldberg's formulation [27]. The outflow condition at  $x/h = 150$  is set for a zero back pressure.

The RANS prediction results with the  $k-\epsilon$  model agree well with the measured mean velocity (Fig. 7) and the turbulent kinetic energy (Fig. 8). Although the measured reattachment location fluctuates around  $x = 6h$ , the steady RANS calculation predicts the location for the reattachment point at  $x/h = 6.0$ . Since we are interested in investigating the applicability of the current methodology for reattachment flows, we will focus on the comparisons made at  $x/h = 10$ , as shown in Figs. 7 and 9. Figures 7(b) and 9(b) indicate that the RANS solution underpredicts the velocity in the logarithmic region and slightly overpredicts the turbulent kinetic energy.

Measured and calculated values of the anisotropic factor defined in Eq. (9) are plotted in Fig. 10 for various  $x/h$  locations. Calculated values for the profile used in predicting the wall pressure frequency spectra are labeled as the SM profile. Measured values were taken at four stations:  $x/h = -12, 10, 16,$  and  $54$ . It is interesting to note that the SM profile fits well with the upstream ( $x/h = -12$ ) and downstream ( $x/h = 54$ ) profiles, but underpredicts the values for the other two intermediate stations. The predicted wall pressure spectra are plotted in Figs. 11 and 12. Comparisons with the measured spectra in the reattachment region ( $x/h = 10$ ) and the re-developed region ( $x/h = 72$ ) are also shown in Fig. 11(a) and 11(b), respectively. The predicted spectrum for the downstream section agrees well with the measured spectrum. For the upstream section in the reattachment region, the calculated spectrum underpredicts the wall pressure fluctuation in the middle and high-frequency portions of the spectrum. This underprediction is associated with the combined effects of the underpredictions of the anisotropic factor, shown in Fig. 10, and the mean velocity

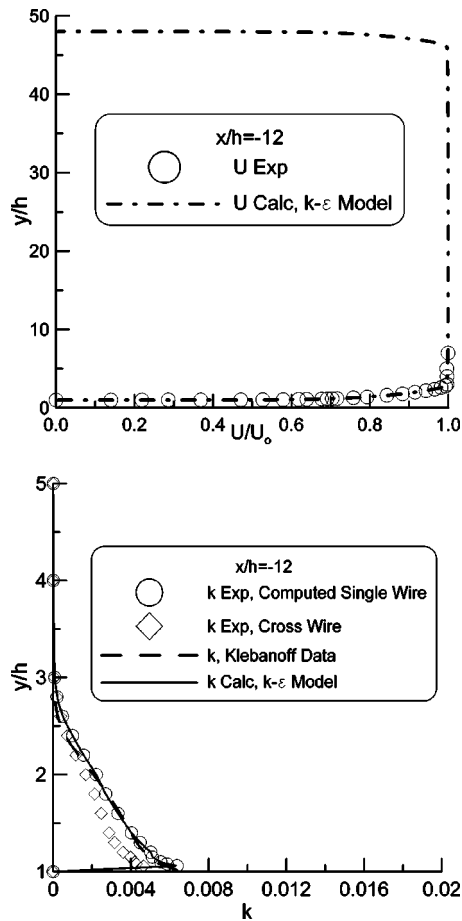


Fig. 6 Inflow conditions for the BFS calculations

shown in Fig. 7(b). Furthermore, the anisotropic factor seems to play a more important role in the prediction of the spectrum than the mean velocity. This observation is consistent with the fact that the integrand in Eq. (4) contains only the gradient of the mean velocity, which exhibits only weak variations away from the near-wall region of the boundary layer. Predicted spectra for three locations along the streamwise direction ( $x/h=10, 16,$  and  $72$ ) are shown in Fig. 12 along with a spectrum measured beneath an equilibrium boundary layer [13,14], which is provided for reference. The predicted spectra indicate that, starting from the reattachment point, the shear layer gradually recovers from the strong vortical structure. As reported by Farabee [23] even at  $x/h=72$ , the flow has not completely recovered to the equilibrium stage. It is noted that since the predictions of pressure spectra for the BFS case are made for the same flow conditions as the experimental data the set of scaling variables used to compare predicted to measured pressure spectra is immaterial. For convenience the BFS pressure spectra comparisons are made based on flow-field length, time, and pressure scales of  $\delta^*$ ,  $\delta^*/U_e$ , and  $\tau_w$ , respectively.

An examination of the regional contributions to the predicted wall pressures at  $x/h=72$  is provided in Fig. 13, which provides further evidence of the importance of turbulence activity in various regions of the boundary layer. To distinguish between the equilibrium layer and the shear layer at  $x/h=72$ , the regional contributions according to the definition in Eq. (10) are again used. The obvious difference between the two shear layers lies in the contributions from the MM, MO, and IM (particularly MM) terms, which implies interactions in the midlayer and between the midlayer and the outer and inner layers. On the other hand, the free shear layer effect between the outer layer and the recirculation region still dominates the spectrum and slows down the re-

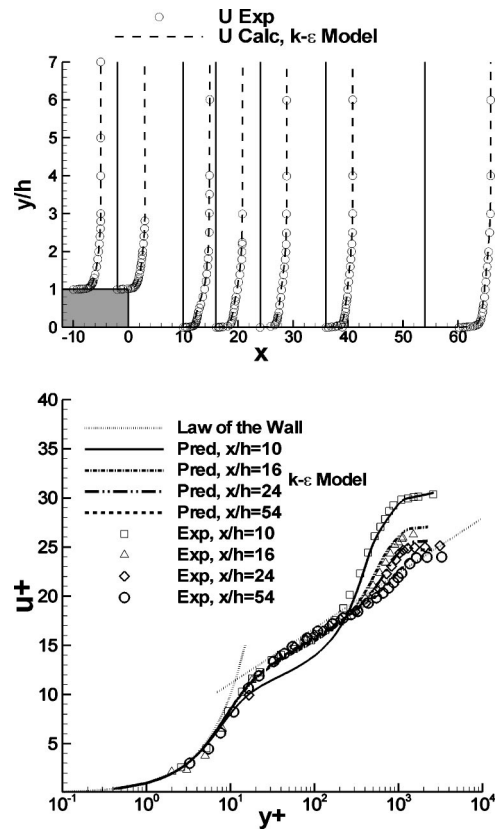


Fig. 7 Velocity comparisons for the BFS calculations

covery process for the middle- and high-frequency contents. In the comparisons of the regional contributions made between  $x/h=10$  and  $x/h=72$  (as shown in Fig. 14), the dominant contribution of MM from the free shear layer is further pronounced for the wall pressure fluctuations in the low and mid frequencies.

## Conclusions

A methodology of predicting the frequency spectrum of fluctuating wall pressure is developed based on time-mean flow characteristics of turbulent flows obtained by solving the Reynolds averaged Navier-Stokes (RANS) equations. The RANS solution is coupled with a spectral modeling scheme for predicting the fluctuating wall pressures using the vertical turbulent fluctuating velocity and gradients of the streamwise mean shear velocity. The turbulence model used in the RANS calculations is an isotropic two-equation model. The anisotropic feature of turbulence is ac-

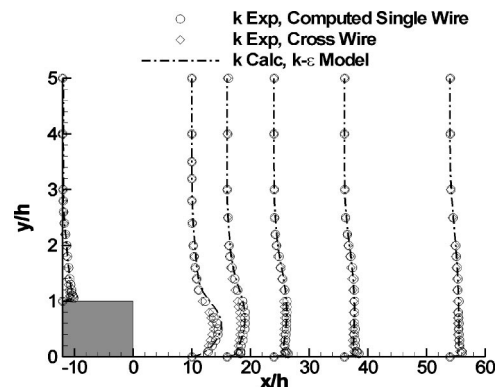


Fig. 8 Comparisons in turbulent kinetic energy for the BFS

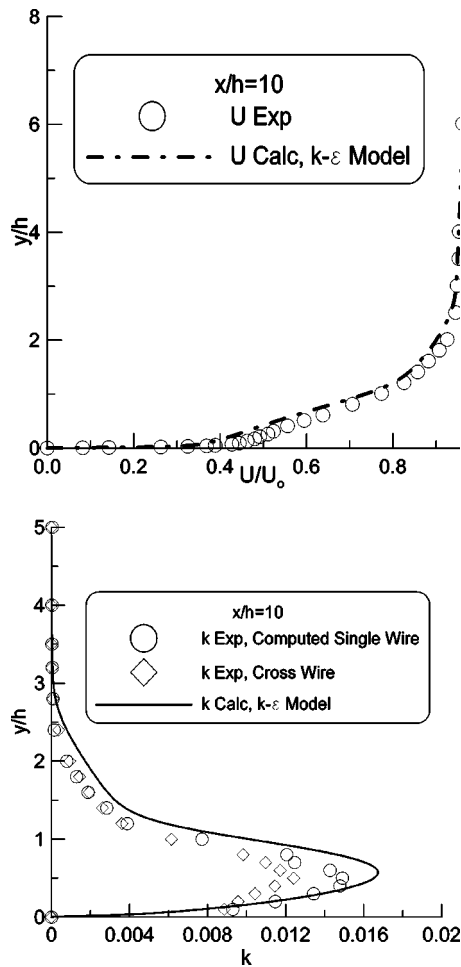


Fig. 9 Comparisons in velocity and turbulent kinetic energy for BFS at  $x/h=10$

counted for with an anisotropic factor, which is a modification to the calculated turbulent kinetic energy and is derived based on smooth and rough data of equilibrium flows. The spectral correlation model for predicting the frequency spectrum of the wall pressure fluctuation is obtained through a wave number integration of the Green's function and modeling of the streamwise and spanwise wave number spectra.

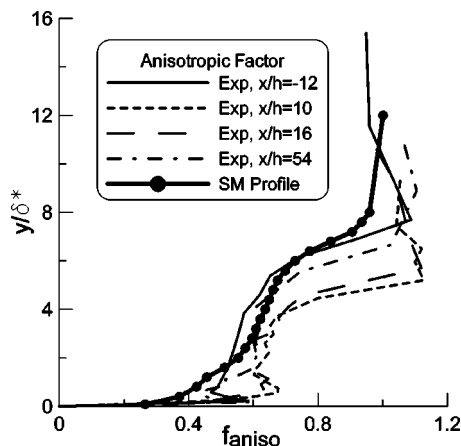


Fig. 10 Comparison in the anisotropic factor for BFS

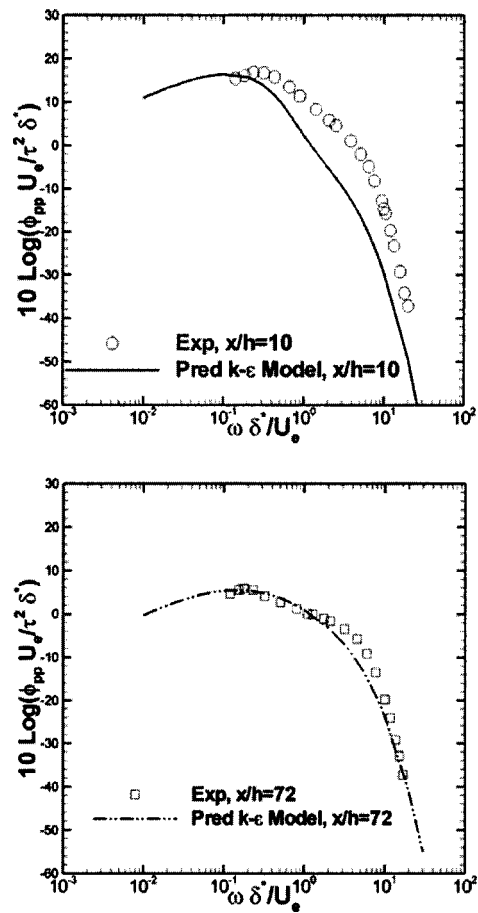


Fig. 11 Predicted and measured spectra for BFS at  $x/h=10$  and 72

Predictions for equilibrium flow agree well with measurements and reveal an overlap region that scales as an inverse of the frequency. Calculation of regional contributions of the wall pressure fluctuation indicate that the spectrum is dominated by the contribution from the near-wall region for the high-frequency spectra. The contributions are nearly evenly distributed among the parts II, IM, and MM for  $\omega \delta^+ / U_e^+ \leq 0.5$ . The contribution from MO exceeds that from IO for the entire frequency range.

Evaluation for a backward-facing step demonstrates the strength of the developed methodology in predicting the wall

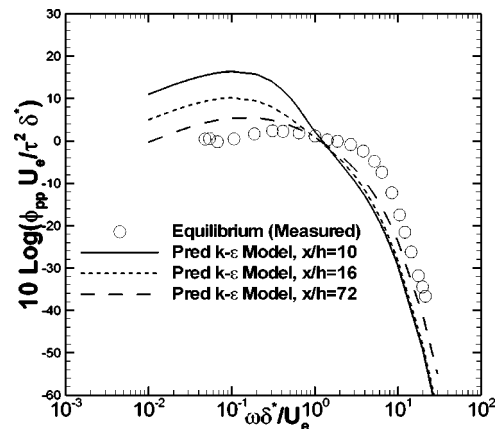


Fig. 12 Predicted spectra at three streamwise locations for BFS

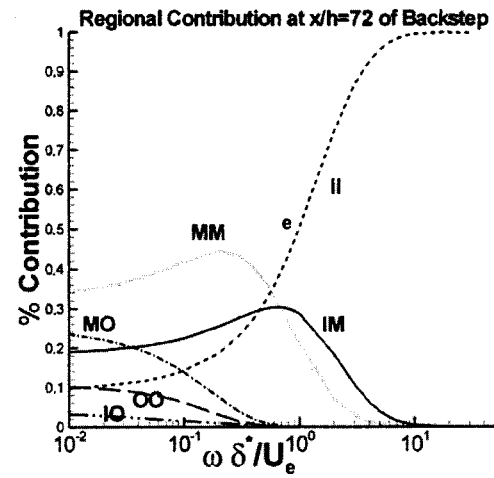
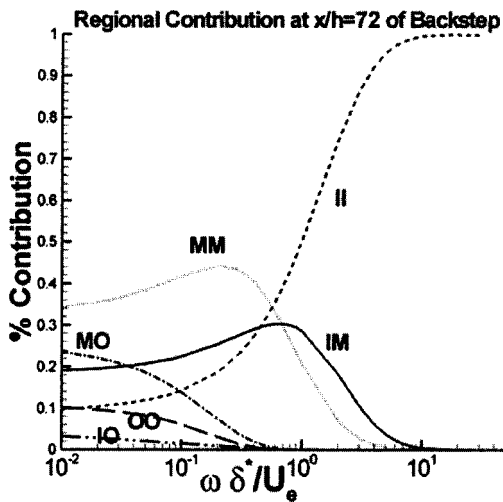
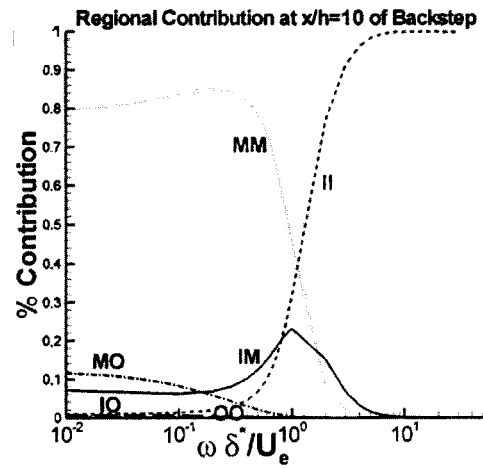
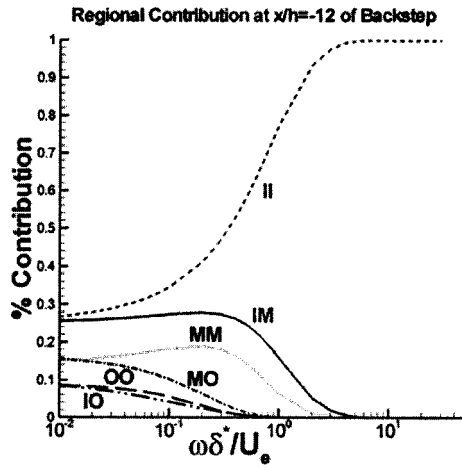


Fig. 13 Regional contributions for BFS at inlet and  $x/h=72$

Fig. 14 Regional contributions for BFS at  $x/h=10$  and  $72$

pressure spectrum for a complex flow. The flow, with recirculation and a reattachment region, generates fluctuating vortical structures in the reattachment region that convect downstream a long distance before recovering back to an equilibrium flow condition. The predicted spectrum agrees well with measurements in the redeveloped boundary layer region downstream of the reattachment region. Both the prediction and the measurement indicate that the flow at  $x/h=72$  has not yet recovered to an equilibrium flow state. In the reattachment region, however, the predicted spectrum is lower than the measured spectrum in the middle and high frequencies due to underpredictions of the vertical turbulent fluctuating velocity and the mean streamwise velocity obtained by the RANS calculations. The calculation of regional contributions reveals that the structure of the turbulence near the reattachment point, which contribute to the wall pressure fluctuations, is very different from that of the equilibrium layer.

### Acknowledgement

This work was sponsored by the Office of Naval Research under the Hydroacoustic Task (Program Element PE602121) with Dr. K. H. Kim as program monitor and very recently under the Surface Ship Flow Noise Task (Program Element PE602123) with S. C. Schreppler as program monitor. Computational resources were provided by the DoD High Performance Computing Centers.

### Nomenclature

$C_k, C_{\varepsilon 1}, C_{\varepsilon 2}$  = constants

- $E_{22}^N$  = interplane correlation function used in Eq. (6)
- $f_{\text{aniso}}$  = anisotropic factor defined in Eq. (9)
- $h$  = height of backward facing step
- $k$  = turbulent kinetic energy
- $k_c$  = convective wavenumber
- $k_i$  = wave number along  $i$ th direction
- $P, p$  = mean and fluctuating pressure
- $q = 1/2\rho U_e^2$
- $Re_\theta$  = Reynolds number based on  $\theta$
- $t$  = time
- $U_c$  = convective velocity
- $U_e$  = velocity at the edge of the boundary layer
- $U_i, u_i$  = mean and fluctuating velocity components
- $U_x$  = free-stream velocity as function of streamwise location (step flow)
- $U_\infty$  = reference velocity
- $u_\tau$  = friction velocity
- $u^+ = u/u_\tau$
- $x_i, x, y, z$  = Cartesian coordinates
- $y_{pp}$  = coordinate transformation used in Eq. (7)
- $y^+ = yu_\tau/\nu$
- $\delta$  = boundary layer thickness
- $\delta^*$  = displacement thickness
- $\varepsilon$  = turbulent dissipation rate
- $\theta$  = momentum thickness
- $\mu, \nu$  = dynamic and kinematic viscosity
- $\rho$  = density
- $\tau_{ij}$  = effective shear stress

- $\tau_w$  = wall shear stress  
 $\mathfrak{J}$  = spectral correlation function defined in Eq. (5)  
 $\Phi_{pp}(\omega)$  = frequency spectral density of the fluctuating pressure  
 $\phi_1$  = autocorrelation function for the vertical fluctuation velocity  
 $\phi_{22}$  = spectral correlation function for the vertical fluctuation velocity  
 $\omega$  = rotational frequency

## References

- [1] Willmarth, W. W., and Wooldridge, C. E., 1962, "Measurements of the Fluctuating Pressure at the Wall Beneath a Thick Turbulent Boundary Layer," *J. Fluid Mech.*, **14**, pp. 187–210.
- [2] Corcos, G. M., 1964, "The Structure of the Turbulent Pressure Field in Boundary-Layer Flows," *J. Fluid Mech.*, **18**, pp. 353–378.
- [3] Blake, W. K., 1970, "Turbulent Boundary-Layer Wall-Pressure Fluctuations on Smooth and Rough Walls," *J. Fluid Mech.*, **44**, pp. 637–660.
- [4] Blake, W. K., 1986, *Mechanics of Flow-Induced Sound and Vibration*, Academic Press, San Diego.
- [5] Olivero-Bally, P., Forestier, B., Focquenoy, E., and Olivero, P., 1993, "Wall-Pressure Fluctuations in Natural and Manipulated Turbulent Boundary Layers in Air and Water," *ASME Proc. of Flow Noise Modeling, Measurement, and Control*, ASME, New York, FED-Vol. 168, pp. 63–74.
- [6] Abraham, B. M., and Keith, W. L., 1998, "Direct Measurements of Turbulent Boundary Layer Wall Pressure Wavenumber-Frequency Spectra," *ASME J. Fluids Eng.*, **120**, pp. 29–39.
- [7] Lilley, G. M., and Hodgson, T. H., 1960, "On Surface Pressure Fluctuations in Turbulent Boundary Layers," AGARD Report No. 276.
- [8] Landahl, M. T., 1967, "A Wave-Guide Model for Turbulent Shear Flow," *J. Fluid Mech.*, **29**, pp. 441–459.
- [9] Panton, R. L., and Linebarger, J. H., 1974, "Wall Pressure Spectra Calculations for Equilibrium Boundary Layers," *J. Fluid Mech.*, **65**, pp. 261–287.
- [10] Chase, D. M., 1980, "Modeling the Wavevector-Frequency Spectrum of Turbulent Boundary Wall Pressure," *J. Sound Vib.*, **70**, Part 1, pp. 29–67.
- [11] Blake, W. K., Lee, Y. T., and Zawadzki, I., 1998, "Evolving Design Tools for Predicting Aeroacoustics of Rotating Machinery," *Proc. of FEDSM'98, 1998 ASME Fluids Engineering Division Summer Meeting*, Washington DC, ASME, New York, FEDSM98–4874.
- [12] Smol'yakov, A. V., 2001, "Noise of a Turbulent Boundary Layer Flow over Smooth and Rough Plates at Low Mach Numbers," *Acoust. Phys.*, **47**(2), pp. 218–225.
- [13] Farabee, T. M., and Casarella, M. J., 1984, "Effects of Surface Irregularity on Turbulent Boundary Layer Wall Pressure Fluctuations," *ASME J. Vib., Acoust., Stress, Reliab. Des.*, **106**, pp. 343–350.
- [14] Farabee, T. M., and Casarella, M. J., 1986, "Measurements of Fluctuating Wall Pressure for Separated/Reattached Boundary Layer Flows," *ASME J. Vib., Acoust., Stress, Reliab. Des.*, **108**, pp. 301–307.
- [15] Simpson, R. L., Chodbane, M., and McGrath, B. E., 1987, "Surface Pressure Fluctuations in a Separating Turbulent Boundary Layer," *J. Fluid Mech.*, **177**, pp. 167–186.
- [16] Brooks, T. F., and Humphreys, W. M., 2000, "Flap Edge Aeroacoustic Measurements and Predictions," AIAA Paper 2000–1975, June.
- [17] Guo, Y. P., Joshi, M. C., Bent, P. H., and Yamamoto, 2000, "Surface Pressure Fluctuations on Aircraft Flaps and Their Correlation With Far-Field Noise," *J. Fluid Mech.*, **415**, pp. 175–202.
- [18] Taylor, L. K., Arabshahi, A., and Whitfield, D. L., 1995, "Unsteady Three-Dimensional Incompressible Navier-Stokes Computations for a Prolate Spheroid Undergoing Time-Dependent Maneuvers," AIAA Paper No. 95–0313, Jan.
- [19] Chakravarthy, S., Goldberg, U. C., Peromian, O., and Sekar, B., 1997, "Some Algorithmic Issues in Viscous Flows Explored Using a Unified-Grid CFD Methodology," AIAA Paper No. 97–1944.
- [20] Hodgson, T. H., 1962, "Pressure Fluctuations in Shear Flow Turbulence," Ph.D. thesis, University of London.
- [21] Chang, P. A., 1998, "Relationships Between Wall Pressure and Velocity Field Sources," Ph.D. thesis, University of Maryland.
- [22] Kraichnan, R. H., 1956, "Pressure Fluctuations in Turbulent Flow over a Flat Plate," *J. Acoust. Soc. Am.*, **28**(3), pp. 378–390.
- [23] Farabee, T. M., 1986, "An Experimental Investigation of Wall Pressure Fluctuations beneath Non-equilibrium Turbulent Flows," Ph.D. thesis, Catholic University of America.
- [24] Hinze, J., 1975, *Turbulence*, 2nd Edition, McGraw-Hill, New York, pp. 638–656.
- [25] Farabee, T. M., and Casarella, M. J., 1991, "Spectral Features of Wall Pressure Fluctuations Beneath Turbulent Boundary Layers," *Phys. Fluids*, **3**(10), 2410–2420.
- [26] Goody, M. C., 1999, "An Experimental Investigation of Pressure Fluctuations in Three-Dimensional Turbulent Boundary Layers," Ph.D. thesis, Department of Aero. and Ocean Engineering, Virginia Tech.
- [27] Goldberg, U. C., 1991, "Derivation and Testing of a One-Equation Model Based on Two Time Scales," *AIAA J.*, **29**(8), pp. 1337–1340.

# Vortex-Induced Vibration Characteristics of an Elastic Square Cylinder on Fixed Supports

Z. J. Wang

Y. Zhou<sup>1</sup>

e-mail: mmyzhou@polyu.edu.hk

Department of Mechanical Engineering, The Hong Kong Polytechnic University, Hung Hom, Kowloon, Hong Kong

*The vortex-induced structural vibration of an elastic square cylinder, on fixed supports at both ends, in a uniform cross flow was measured using fiber-optic Bragg grating sensors. The measurements are compared to those obtained for an elastic circular cylinder of the same hydraulic diameter in an effort to understand the effect of the nature (fixed or oscillating) of the flow separation point on the vortex-induced vibration. It is found that a violent vibration occurs at the third-mode resonance when the vortex-shedding frequency coincides with the third-mode natural frequency of the fluid-structure system, irrespective of the cross-sectional geometry of the cylinder. This is in distinct contrast to previous reports of flexibly supported rigid cylinders, where the first-mode vibration dominates, thus giving little information on the vibration of other modes. The resonance behavior is neither affected by the incidence angle ( $\alpha$ ) of the free stream, nor by the nature of the flow separation point. However, the vibration amplitude of the square cylinder is about twice that of the circular cylinder even though the flexural rigidity of the former is larger. This is ascribed to a difference in the nature of the flow separation point between the two types of structures. The characteristics of the effective modal damping ratios, defined as the sum of structural and fluid damping ratios, and the system natural frequencies are also investigated. The damping ratios and the system natural frequencies vary little with the reduced velocity at  $\alpha=0$  deg, but appreciable at  $\alpha \geq 15$  deg; they further experience a sharp variation, dictated by the vortex-shedding frequency, near resonance. [DOI: 10.1115/1.1881693]*

*Keywords:* elastic cylinder, vortex-induced vibration, flow separation, damping ratio

## 1 Introduction

Flow-induced vibrations are complex and complicated, involving coupling between structural and fluid dynamics. Since the vibrations have a significant impact on the fatigue life of structures and may even have disastrous consequences, interest in documenting and predicting these vibrations is rapidly growing. Past research has largely focused on flow-induced vibrations on relatively “rigid” cylinders [1–6]. Here, a rigid cylinder is defined as one with infinite structural stiffness. Engineering structures are, strictly speaking, elastic, that is, having finite structural stiffness. There are, however, few investigations carried out on the flow-induced vibrations on elastic structures on fixed support. The dynamic characteristics of an elastic cylinder on fixed supports can be quite different from a rigid one. For example, in elastically mounted rigid cylinder cases, the first-mode vibration is predominant. Thus, it would be difficult to identify other modes. This is perhaps why the previous studies of vortex-induced vibration have mostly focused on the first-mode motion only. For an elastic cylinder fixed at both ends, the vibration modes other than the first mode are also important [7] and need to be better understood.

It is well known that, in vortex-induced vibrations, the excitation force originates from vortex shedding. Naturally, the nature (fixed or oscillating) of the flow separation point could affect the dynamics of a vibrating elastic cylinder. In the case of a circular cylinder, the separation point oscillates on the cylinder surface.

The excursion of the separation point varies from 75 to 85 deg, measured from the leading stagnation point, for Reynolds number  $Re=1.06 \times 10^5$  [8]. The separation point location and oscillation range may vary with  $Re$  [9–11] and structural vibration [12]. On the other hand, vortex shedding from a square cylinder is characterized by a fixed separation point and is dependent on  $\alpha$  [13–15]. Evidently, the separation behavior differs from that of the circular cylinder. It is of fundamental interest to see how this difference would impact on the vortex-induced vibration of an elastic cylinder on fixed supports in a cross flow.

The damping ratio models the energy dissipation of the system during vibrations and plays an important role in determining the vibration amplitude and the stability of a structure. Damping arises from the fluid surrounding the structure as well as from the structure itself. Although structural damping is related to the properties of the structure alone, fluid damping originates from viscous dissipation and fluid drag, i.e., resulting from flow separation and viscous shearing of the fluid on the surface of the structure. Evidently, fluid damping is motion dependent and not so easy to estimate. Using an autoregressive moving average (ARMA) analysis technique [16], Zhou et al. [17] estimated the fluid damping ratio based on the displacement time series obtained from a numerical simulation of a flexibly supported rigid circular cylinder in a uniform cross stream. The same technique also enabled Zhou et al. [7] to deduce the effective damping ratio, defined as the sum of structural and fluid damping ratios, from the measured strain signal of two side-by-side elastic circular cylinders in a cross flow. It would be interesting to see how the flow separation from a cylinder affects the effective damping ratio.

In a forced vibration situation, the imposed vibration may modify the vortex-shedding frequency, resulting in the lock-in

<sup>1</sup>Corresponding author.

Contributed by the Fluids Engineering Division for publication in the JOURNAL OF FLUIDS ENGINEERING. Manuscript received by the Fluids Engineering Division February 18, 2004; revised manuscript received, September 27, 2004. Review conducted by V. Otugen.

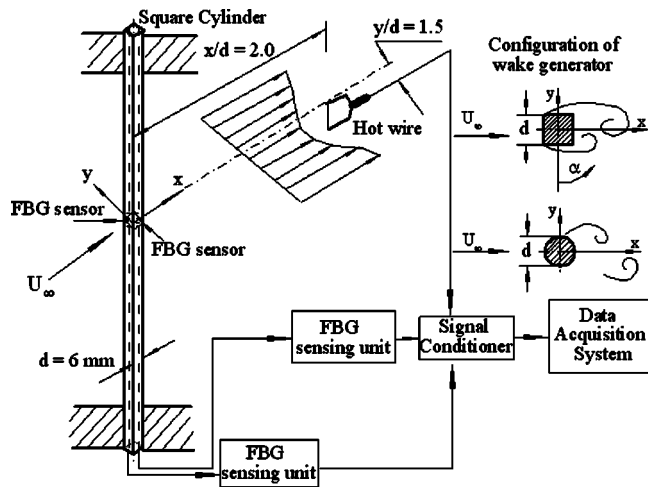


Fig. 1 Experimental arrangement

phenomenon. However, in the vortex-induced vibration case, vortex shedding is responsible for the excitation forces. Zhou et al. [7] demonstrated that the system natural frequencies of two side-by-side elastic circular cylinders on fixed support are dependent on  $U_r$  and can be modified up to 10% by vortex shedding when resonance occurs. The same can be anticipated for the system natural frequencies associated with an elastic square cylinder. In this case, one additional question is how these frequencies are dependent upon  $\alpha$ .

This work aims to study experimentally the effect of the flow separation point on the vortex-induced vibration of an elastic cylinder on fixed supports. Both circular and square cross-sectional cylinders were investigated. While a single hot wire was used to monitor the fluctuating flow velocity, two fiber-optic Bragg grating (FBG) sensors [18,19] were deployed to measure the structural responses in the longitudinal and lateral directions, respectively. Based on the measured data, the system natural frequencies and the modal damping ratios are examined in detail.

## 2 Experimental Details

**2.1 Experimental Setup.** The experiments were conducted in a suction-type wind tunnel with a square cross section (0.35 m  $\times$  0.35 m) that is 0.5 m long. In the free stream, the longitudinal turbulence intensity was 0.2%. The same tunnel was used by Zhou et al. [18], So et al. [20], and Zhou et al. [7]. Interested readers may refer to these studies for more details. An acrylic cylinder was vertically mounted in the midplane of the test section at 0.20 m downstream of the exit plane of the contraction section (Fig. 1). Both square and circular cross sections of the cylinder were investigated, which were associated with fixed and moving flow separation points, respectively. The hydraulic diameter  $d$  of both cases was 6.0 mm. The structural characteristics of the cylinders are given in Table 1. The mounting of the cylinders was designed to provide a fix-support boundary condition at both ends, implying a zero cylinder deflection at the supports. The  $Re$  investigated varied from 800 to 10,700, and the corresponding reduced velocity  $U_r$  ( $=U_\infty/f_0^{(1)}d$ , where  $f_0^{(1)}$  is the first-mode structural

natural frequency of the test cylinder) was 4–51. The blockage of the circular cylinder or the square cylinder with one of its faces normal to  $U_\infty$ , namely,  $\alpha=0$  deg, was 1.7%, but increased to a maximum of 2.4% for  $\alpha=45$  deg. The blockage effect on the mean drag was relatively small for the  $Re$  range investigated. A total of four values of  $\alpha$  were investigated for the square cylinder (i.e.,  $\alpha=0, 15, 30,$  and  $45$  deg). Great care was taken during the experiments to minimize the variation in  $f_0^{(1)}$  resulting from changing  $\alpha$ . Consequently, the  $f_0^{(1)}$  values of the square cylinder were found to be 90.2, 89.8, 89.2, and 88.7 Hz, corresponding to  $\alpha=0, 15, 30,$  and  $45$  deg, respectively.

**2.2 Dynamic Strain Measurements.** The experimental arrangement is shown schematically in Fig. 1. Two optical silicon fibers of diameter 125  $\mu$ m built with FBG sensors were used to measure simultaneously the structural responses in the longitudinal and lateral directions. The FBG sensing system was built in-house. Zhou et al. [18] and Jin et al. [19] have given a thorough discussion of the sensing principle of the FBG sensor. In the circular cylinder case, one optical silicon fiber built with the FBG sensor was buried in a groove along the trailing stagnation line of the cylinder and the other fiber along a line 90 deg from the stagnation line. The two fibers, installed flush with the cylinder surface using nail polish, measured the dynamic strain  $\epsilon_x$  due to the drag and  $\epsilon_y$  due to the lift, respectively, at the midspan of the cylinder. With a finite length of about 10 mm, the sensor grating measured the average strain over this length. In the square cylinder case with  $\alpha=0$  deg, the two optical fibers were buried in a groove along the cylinder midway on the downstream surface and on one side surface of the cylinder, respectively.

The sensors, labeled sensor 1 and sensor 2, simultaneously measured the strains  $\epsilon_1$  and  $\epsilon_2$  (or  $\epsilon_x$  and  $\epsilon_y$ ) at the midspan of the cylinder. In principle,  $\epsilon_1$  and  $\epsilon_2$  are independent of each other. Note that the optical fiber is extremely light and has a homogeneous mass distribution. Therefore, its attachment to the cylinder will not change the structural stiffness of the cylinder. Measurements of the streamwise fluctuating velocity  $u$  and cross-flow fluctuating displacement  $Y$  carried out by Zhou et al. [18] indicated a negligible effect of the attachment of the optical fiber on flow separation and  $Y$ . In the present experiment, the effect has been further minimized by burying the optical fiber in the cylinder. A major source of experimental errors comes from the non-linear relationship between the output voltage and the dynamic strain. Strictly speaking, this relation, depending on the characteristics of the selected tunable optical filter (TOF) and FBG sensors, follows a sinusoidal curve. However, given appropriate operation, the operating point occurs in the approximate linear range of the curve, thus minimizing possible errors. Based on repeated measurements, the experimental errors were determined to be  $\pm 0.15 \mu\epsilon$  for dynamic strain measurements and  $\pm 0.8 \mu$ m for dynamic displacement measurements [18]. More details about the FBG sensing principle and how to operate the system can be found in Zhou et al. [18] and Jin et al. [19]. The experimental uncertainties are summarized in Table 2.

Since the test cylinder was mounted on the working section of the tunnel, it was important to minimize tunnel vibrations, which largely originated from the fan and motor. The working section was isolated from the motor and fan through vibration absorbers. Zhou et al. [18] measured the tunnel vibrations using a Laser

Table 1 Structural characteristics of cylinders.

Cylinder	Material	$d$ (mm)	$m$ ( $\text{kg m}^{-1}$ )	$EI$ ( $\text{Nm}^2$ )	$M^*$	$f_0^{(1)}$ (Hz)			
Square	Acrylic	6.00	0.0421	0.4739	970	$\alpha=0$ deg 90.2	$\alpha=15$ deg 89.8	$\alpha=30$ deg 89.2	$\alpha=45$ deg 88.7
Circular	Acrylic	6.00	0.01926	0.224	565	94			



**Table 2** Uncertainties of the measured or calculated quantities

$Y_{rms}, X_{rms}$	$\varepsilon_{x,rms}, \varepsilon_{y,rms}$	Effective damping ratios	Natural frequencies
$\pm 7.5\%$	$\pm 8.0\%$	$\pm 12.0\%$	$\pm 0.35$ Hz

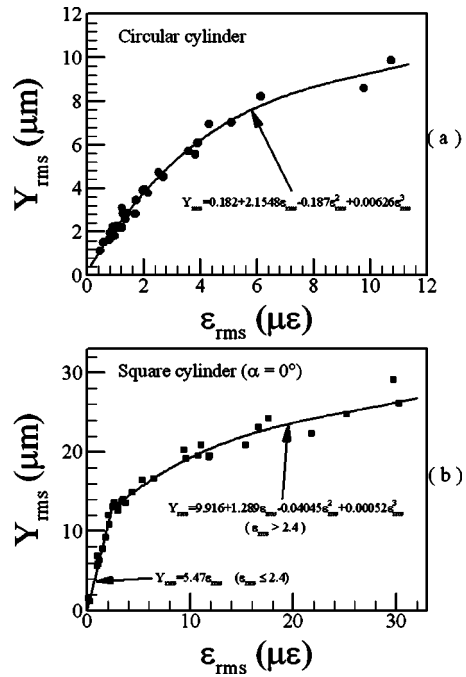
vibrometer. Their measurements indicated that the natural frequency of the working section was in the range of 20–30 Hz and the maximum vibration amplitude was only 1–2  $\mu\text{m}$ . Furthermore, the tunnel vibration caused a maximum variation of 1.1% in the spectral energy of the measured fluctuating strain around the first-mode natural frequency of the fluid-cylinder system [7], indicating a negligible tunnel vibration effect on the strain measurements.

**2.3 Fluctuating Velocity Measurements.** The streamwise fluctuating velocity  $u$  was measured using a single Tungsten wire of 5  $\mu\text{m}$  diam placed at  $x/d=2$  and  $y/d=1.5$ . The hot wire was operated at an overheat ratio of 1.8 with a constant temperature anemometer (DISA Type 55M10).

The signals  $\varepsilon_x, \varepsilon_y,$  and  $u$  or  $\varepsilon_1, \varepsilon_2,$  and  $u$  were simultaneously measured and offset, amplified and then digitized using a 12-bit A/D board and a personal computer at a sampling frequency of 6 kHz per channel. The duration of each record was 20 s, which has been verified to be sufficiently long for the rms values  $\varepsilon_{x,rms}$  of  $\varepsilon_x, \varepsilon_{y,rms}$  of  $\varepsilon_y, \varepsilon_{1,rms}$  of  $\varepsilon_1$  and  $\varepsilon_{2,rms}$  of  $\varepsilon_2$  to reach approximately their stationary state, with a variation smaller than 1%.

### 3 Bending Displacement Estimate

Zhou et al. [18] and Jin et al. [19] used the FBG sensor to measure the dynamic strain induced by the unsteady lift on a circular cylinder, which was identical to the circular cylinder presently used. The strain thus obtained was compared with  $Y$  measured using a laser vibrometer. They found that the spectra deduced from the two signals were in agreement with each other in terms of the vortex-shedding frequency and the natural frequencies of the fluid-cylinder system. Furthermore,  $Y_{rms}$  and  $\varepsilon_{y,rms}$  were linearly related for small  $\varepsilon_{y,rms}$  but nonlinearly for large  $\varepsilon_{y,rms}$ . Their data were presently fitted to a nonlinear relationship (Fig. 2(a))



**Fig. 2** Empirical correlation between  $Y_{rms}$  and  $\varepsilon_{y,rms}$ : (a) circular cylinder (data from [18]) and (b) square cylinder at  $\alpha = 0$  deg

$$Y_{rms} = F_C(\varepsilon_{rms}) = 0.182 + 2.1548\varepsilon_{rms} - 0.187\varepsilon_{rms}^2 + 0.00626\varepsilon_{rms}^3 \quad (1)$$

In order to determine the strain-displacement relationship for the square cylinder,  $Y$  at  $\alpha=0$  deg was measured, simultaneously with  $\varepsilon_y$ , using a Polytec Series 3000 dual laser beam vibrometer. One laser beam was used to measure the displacement at the mid-span of the test cylinder; the other was used to monitor the tunnel vibration at the same cross section. The differential signal from the two beams significantly reduced contamination from tunnel vibrations [20]. The measurement covers the whole  $U_r$  range presently investigated.  $Y_{rms}$  and  $\varepsilon_{rms}$  were presented in Fig. 2(b) and fitted to

$$Y_{rms} = F_s(\varepsilon_{rms}) = \begin{cases} 5.47\varepsilon_{rms} & \dots \dots \dots \varepsilon_{rms} \leq 2.4 \\ 9.916 + 1.289\varepsilon_{rms} - 0.04045\varepsilon_{rms}^2 + 0.00052\varepsilon_{rms}^3 & \dots \dots \dots \varepsilon_{rms} > 2.4 \end{cases} \quad (2)$$

The nonlinear  $Y_{rms}-\varepsilon_{rms}$  relationship for  $\varepsilon_{rms} > 2.4\mu\text{e}$  is probably due to a different mixture of vibration modes as  $U_r$  increases [18]. Theoretically, the strain-displacement relationship of a beam is independent of the cross-sectional geometry [21]. The  $\varepsilon-Y$  relationship should be essentially the same for different  $\alpha$ . Nevertheless, the axial loading may vary at different  $\alpha$ , which could indirectly affect the  $\varepsilon-Y$  relationship. This effect is by no means expected to be significant in the present investigation as indicated by the very small differentiation in the natural frequencies for different  $\alpha$  (Table 1). On the other hand, it is very difficult to measure  $Y$  if  $\alpha \neq 0$  deg. Therefore, Eq. (2) is used to estimate approximately the bending displacement based on measured dynamic strain signals for the square cylinder of  $\alpha \neq 0$  deg as well as  $\alpha=0$  deg, whereas (1) is used to calculate the bending displacement for the circular cylinder.

In the circular cylinder case, the dynamic strains  $\varepsilon_x$  and  $\varepsilon_y$  were measured using two FBG sensors (Sec. 2); the time series was given by

$$\varepsilon_x(1), \varepsilon_x(2), \dots, \varepsilon_x(i), \dots, \varepsilon_x(120,000)$$

$$\varepsilon_y(1), \varepsilon_y(2), \dots, \varepsilon_y(i), \dots, \varepsilon_y(120,000)$$

The bending displacements are approximated by

$$X(i) = F_C[\varepsilon_x(i)]$$

$$Y(i) = F_C[\varepsilon_y(i)], \quad i = 1, 2, \dots, 120,000$$

Similarly, the bending displacements  $X'(i)$  and  $Y'(i)$  for the square cylinder can be approximated by

$$X'(i) = F_S[\varepsilon_1(i)]$$

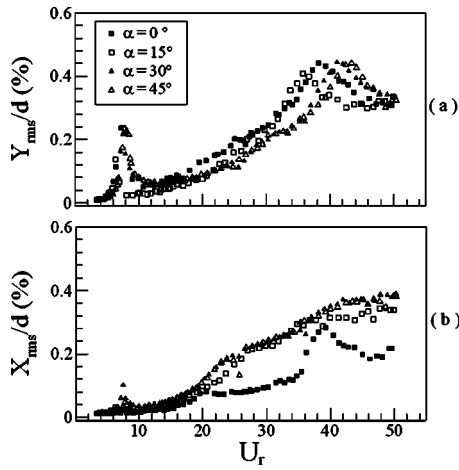


Fig. 3 Dependence on  $U_r$  of the vibration amplitude of the square cylinder: (a)  $Y_{rms}/d$  and (b)  $X_{rms}/d$

$$Y'(i) = F_S[\varepsilon_2(i)], \quad i = 1, 2, \dots, 120,000$$

When the square cylinder is placed at  $\alpha \neq 0$  deg (Fig. 1),  $X'(i)$  is not a displacement in the longitudinal direction, nor is  $Y'(i)$  in the lateral direction. Decomposing  $X'(i)$  and  $Y'(i)$ , the bending displacements in the longitudinal and lateral directions can be written as

$$X(i) = Y'(i)\cos\left(\frac{3}{2}\pi + \alpha\right) + X'(i)\cos\alpha$$

$$Y(i) = Y'(i)\sin\left(\frac{3}{2}\pi + \alpha\right) + X'(i)\sin\alpha, \quad i = 1, 2, \dots, 120,000$$

where,  $\alpha = 0, 15, 30$ , and  $45$  deg.

#### 4 Vibration Characteristics

Figure 3 presents the variation of  $X_{rms}/d$  and  $Y_{rms}/d$  with  $U_r$  for the square cylinder at various  $\alpha$  values. At  $\alpha = 0$  deg, the variation of  $Y_{rms}/d$  and  $X_{rms}/d$  shows a similar trend. Both increase for increasing  $U_r$  and their local peaks occur at the same  $U_r$ , i.e., at  $U_r \approx 7.5$  and  $38$ , respectively. It is well known that the structure of noncircular cross sections is susceptible to galloping, which is associated with a violent vibration. Parkinson and Smith [22] proposed a two-dimensional quasi-steady model of the transverse galloping of a long prism of square section in a normal steady wind. Presumably, this relationship is also valid in the present studies in view of small vibration amplitude (Fig. 3). The minimum or critical reduced velocity for galloping instability could be predicted based on this model by  $U_{r0} = U_\infty / (f_0^{(1)} d) = 8\pi M^* \zeta_s^{(1)} / A$ . Here,  $A$  is given by  $(dC_{Fy}/d\alpha)_{\alpha=0}$ , where the lateral aerodynamic force coefficient  $C_{Fy}$ , measured on a stationary cylinder, is a function of  $\alpha$ . In the present investigation,  $\zeta_s^{(1)} \approx 0.02$  and  $M^* \approx 970$ , and  $A$  is approximately given by  $3.147$  based on the data of  $C_{Fy}$  in [22].  $U_{r0}$  is then estimated to be about  $155$ , grossly greater than the present  $U_r$  range ( $< 51$ ). Therefore, the  $Y_{rms}/d$  and  $X_{rms}/d$  peaks around  $U_r \approx 7.5$  and  $38$  cannot be attributed to galloping instability.

The  $Y_{rms}/d$  peak at  $U_r \approx 7.5$  for the case  $\alpha = 0$  deg results from the resonance where the vortex shedding frequency  $f_s$  coincides with the first-mode natural frequency  $f_y^{(1)*}$  of the fluid-structure system. This is substantiated by the spectra of  $E_Y$ ,  $E_X$ , and  $E_u$  at  $U_r \approx 7.5$  (not shown), which all display a prominent peak at  $f_s^* = f_s d / U_\infty = 0.1335$ , i.e., the Strouhal number of a square cylinder [23–25]. The first-mode system natural frequency can be calculated by  $f_y^{(1)*} = f_0^{(1)} / \sqrt{1 + \pi/4M^*}$  [20]. Since the added mass is very

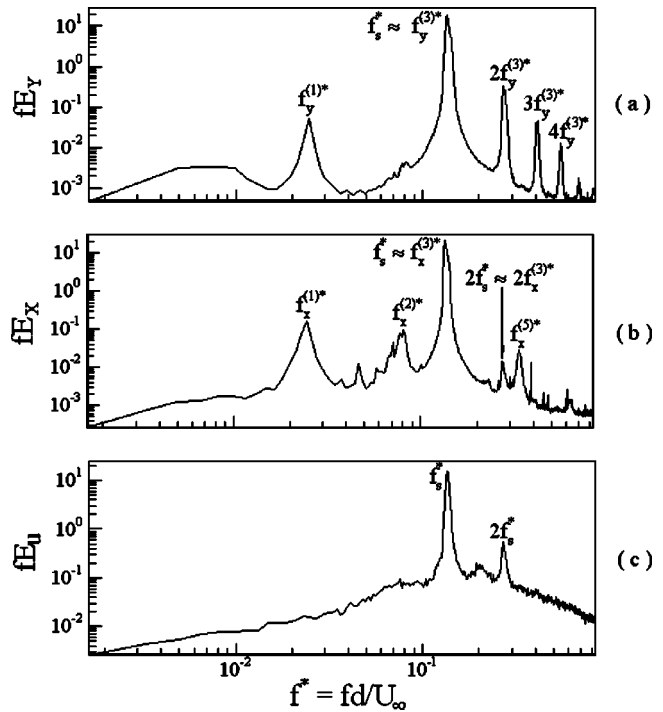


Fig. 4 (a)  $Y$  spectrum  $E_Y$ , (b)  $X$  spectrum  $E_X$ , (c)  $u$  spectrum  $E_u$  (square cylinder,  $\alpha = 0$  deg,  $U_r \approx 40$ . The hot wire was placed at  $x/d = 2$  and  $y/d = 1.5$ .)

small compared to the cylinder mass in an airflow and the mass ratio  $M^*$  is quite large ( $\approx 970$ ),  $f_y^{(1)*}$  is essentially identical to  $f_0^{(1)} = 90.2$  Hz (Table 1) or approximately equal to  $f_s$ .

In order to understand the  $Y_{rms}/d$  peak at  $U_r \approx 38$  for the  $\alpha = 0$  deg case (see Fig. 3(a)), the spectra  $E_Y$ ,  $E_X$ , and  $E_u$  at  $U_r \approx 40$  are shown in Fig. 4. The most pronounced peak in  $E_Y$  occurs at  $f_s^* \approx 0.1354$  or  $f_s = 480$  Hz, approximately equal to the third-mode natural frequency  $f_y^{(3)*}$  of the fluid-cylinder system, which can be estimated from  $f_y^{(3)*}$  using  $f_y^{(3)*} / f_y^{(1)*} = (121/22.4) = 5.402$  or  $f_y^{(3)*} = 0.1354$  [7]. Therefore, the peak at  $U_r \approx 38$  results from the third-mode resonance. The spectra at  $U_r \approx 7.5$  and  $40$  for  $\alpha = 15, 30$ , and  $45$  deg (not shown) were quite similar to those shown at  $\alpha = 0$  deg, indicating the occurrence of the first- or third-mode resonance.

The peak in  $Y_{rms}/d$  at  $U_r \approx 40$  (Fig. 3) is far more pronounced than that at  $U_r \approx 7.5$ , irrespective of the  $\alpha$  value, suggesting a more violent vibration at the third-mode resonance. A number of factors may contribute to the observation. First,  $U_r$  corresponding to the third-mode resonance is about 5.4 times that for the first-mode resonance. Flow energy associated with vortex shedding is proportional to  $U_r^2$ , implying a much higher flow excitation energy at the third-mode resonance than that at the first-mode resonance. Second, the structural damping ratio associated with the third-mode motion is less than one-fifth of that associated with the first-mode motion [7]. Since fluid damping is presently very small, the effective damping ratio corresponding to the third-mode motion is thus very small, compared with that associated with the first-mode motion. This means that the energy dissipation, when resonance occurs at  $f_s^* = f_y^{(3)*}$ , could be quite small. Finally, the fifth harmonic of  $f_y^{(1)*}$  ( $5 \times f_y^{(1)*} = 0.124$ ) is quite close to  $f_s^*$  ( $\approx 0.135$ ). This could feed additional energy to the system at resonance. The combined effect leads to a strong response in the third mode. This observation points to a significant impact that a flexural structure may have on its dynamic stability.

At  $\alpha = 15, 30$  and  $45$  deg,  $Y_{rms}/d$  displays a similar variation to

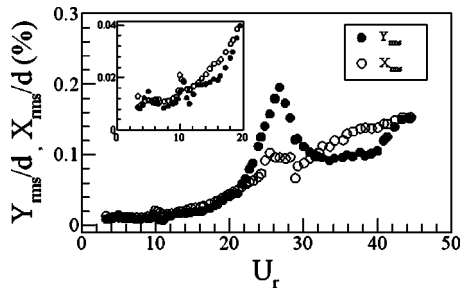


Fig. 5 Dependence on  $U_r$  of  $Y_{rms}/d$  and  $X_{rms}/d$  of the circular cylinder

that at  $\alpha=0$  deg. The peak at  $U_r \approx 38$  in  $Y_{rms}/d$  for  $\alpha=0$  deg shifts slightly to  $U_r \approx 36.2, 41.4,$  and  $42.8$  for  $\alpha=15, 30$  and  $45$  deg, respectively. The peak at  $U_r \approx 7.5$  for  $\alpha=0$  deg shifts to  $U_r \approx 6.34, 7.54,$  and  $7.94$  for  $15, 30$  and  $45$  deg, respectively. The shift is ascribed to the variation in  $f_s^*$  at different  $\alpha$  values. Chen and Liu's measurement [15] for a square cylinder showed a dependence of  $St=fd'/U_\infty$  on  $\alpha$  and  $Re$ , where  $d'$  is the cross-flow dimension of the cylinder, given by  $(\sin \alpha + \cos \alpha)d$ . For example, at  $Re=8000$ ,  $St$  is  $0.135$  for  $\alpha=0$  deg,  $0.1814$  for  $\alpha=15$  deg, but changes little with any further increase in  $\alpha$ . The fact that  $f_0^{(1)}$  varies little for different  $\alpha$  (Table 1) and is in general very close to the system natural frequency because of a small contribution from flow (Sec. 6) implies that the third-mode resonance, where  $f_s \approx f_y^{(3)}$ , will occur at  $f_0^{(3)}$  and  $U_r = U_\infty / f_0^{(1)} d = f_0^{(3)} d' / S d f_0^{(1)} d$ . Noting that  $f_0^{(3)} = 5.402 f_0^{(1)}$  [7] and  $d' = (\sin \alpha + \cos \alpha)d$ ,  $St=0.135$  for  $\alpha=0$  deg and about  $0.1814$  for  $\alpha=15, 30$  and  $45$  deg, the third-mode resonance is predicted to occur at  $U_r=40.01, 36.47, 40.68,$  and  $42.11$  for  $\alpha=0, 15, 30,$  and  $45$  deg, respectively. The shift of the peak corresponding to the first-mode resonance may be similarly explained.

$X_{rms}/d$  at  $\alpha=15, 30,$  and  $45$  deg (Fig. 3(b)) behaves rather different from that at  $\alpha=0$  deg, exhibiting only one tiny peak at  $U_r \approx 7.5$ . The small peak, as compared with  $Y_{rms}/d$ , is consistent with the observation that the fluctuating drag of a bluff body is far smaller than its fluctuating lift. For a square cylinder, the mean drag coefficient is minimum at  $\alpha \approx 13$  deg and increases for further increasing  $\alpha$  [26]. Fluctuating drag is also likely to increase [27], thus increasing  $X_{rms}/d$  for a larger  $\alpha$  (Fig. 3(b)).

For the purpose of comparison, the  $Y_{rms}/d$  and  $X_{rms}/d$  measurements of the circular cylinder were presented in Figs. 5 and 6. A detailed discussion has been given in Zhou et al. [18] about the vibration characteristics of a circular cylinder in a cross flow and need not be discussed further. The following comments will focus on the difference in the vibration behavior between the circular and square cylinders.

First, three peaks are discernible at  $U_r \approx 4.2, 10.5,$  and  $26.0$  in  $Y_{rms}/d$  of the circular cylinder, which are identified with the occurrence of the first-, second-, and third-mode resonance [18], respectively. In contrast, the square cylinder data do not show the peak corresponding to the second-mode resonance. One possible reason for this observation is that the flow separation point from a square cylinder is fixed, implying a spanwise in-phase shedding of vortex rolls, which enhances the two-dimensional nature of vortex shedding. Presumably, the vortex excitation is spanwise uniform. The second-mode vibration could then hardly be excited. In the circular cylinder case, however, the separation point oscillates over a range of  $75-85$  deg [8]. The oscillation is unlikely to be spanwise in phase, thus partially responsible for the three-dimensional nature of vortex shedding. The vortex cell has a typical spanwise extent of  $1-3d$  [11,28]. Therefore, the vortices shed from a circular cylinder is less two-dimensional than those from a square cylinder [1,25]. This will induce spanwise asymmetrical excitation force, thus exciting the second mode of vibration.

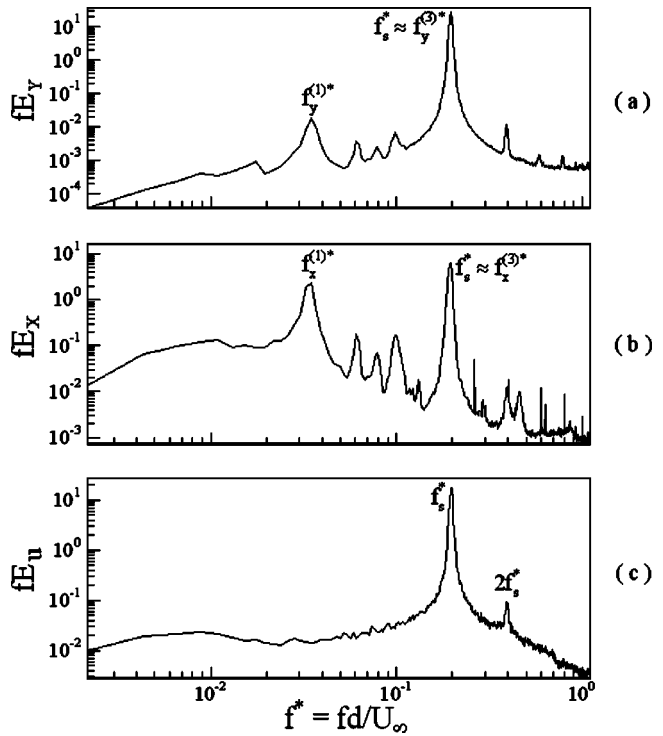


Fig. 6 (a)  $Y$  spectrum  $E_Y$ , (b)  $X$  spectrum  $E_X$ , (c)  $u$  spectrum  $E_u$  (circular cylinder,  $U_r \approx 26$ . The hot wire was placed at  $x/d=2$  and  $y/d=1.5$ .)

Second, both cylinders show the most pronounced peak in  $Y_{rms}/d$  at the third-mode resonance, but the peak at  $U_r \approx 40$  (Fig. 3) for the square cylinder is about twice that at  $U_r \approx 26$  (Fig. 5) for the circular cylinder even though the flexural rigidity of the square cylinder is larger (Table 1). As earlier discussed, this cannot be attributed to the galloping instability associated with a noncircular cross section. Rather, since vortex shedding from the square cylinder is more likely to be spanwise in-phase than that from the circular cylinder, vortices generated by the square cylinder are more coherent in the spanwise direction, thus resulting in a strong excitation force and subsequently a more violent resonance.

## 5 Effective Damping Ratios

The vortex-induced vibration of an elastic structure on fixed supports includes multiple modes. The ARMA modeling technique [16] is presently used to evaluate effective modal damping ratios based on the measured signals. Figure 7 presents the first- and third-mode effective damping ratios of the fluid-square-cylinder system along the  $y$  direction (i.e.,  $\zeta_{y,e}^{(1)}$  and  $\zeta_{y,e}^{(3)}$ , which were calculated from the  $Y$  signal. The ratios  $\zeta_{x,e}^{(1)}$  and  $\zeta_{x,e}^{(3)}$  along the  $x$  direction are given in Fig. 8. The second-mode effective damping ratios,  $\zeta_{y,e}^{(2)}$  and  $\zeta_{x,e}^{(2)}$ , exhibited relatively large scatter and therefore were not shown. A few observations can be made based on Figs. 7 and 8.

First, the effective damping ratios rise, though slowly, as  $U_r$  increases beyond 15. The structural damping ratio  $\zeta_s^{(1)}$  was estimated from plucking tests using the log-decrement method in a cross flow with a  $U_r$  range of  $0-40$  (not shown) as well as in still air. The ratio  $\zeta_s^{(1)}$  was almost constant ( $0.02$ ) except near the first-mode resonance ( $U_r \approx 5$ ), where a slight dip was observed, indicating little effect of  $U_r$  on  $\zeta_s^{(1)}$ . Apparently, the increase in the effective damping ratio is due to the rising fluid damping. It is pertinent to point out that the measured structural damping ratio is probably overestimated due to the presence of some fluid damping during measurement.

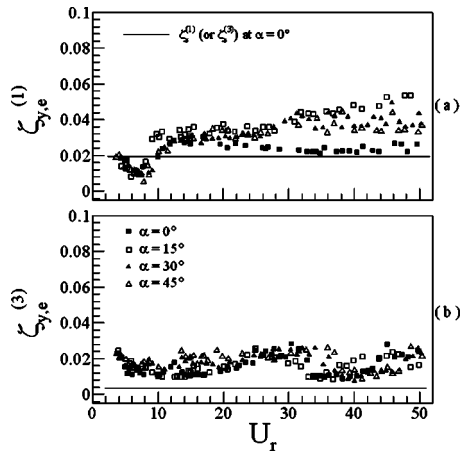


Fig. 7 Cross-flow effective damping ratios of the fluid-square-cylinder system: (a)  $\zeta_{y,e}^{(1)}$  and (b)  $\zeta_{y,e}^{(3)}$

Second, as  $U_r$  increases, the fluid damping ratios  $\zeta_{y,f}^{(1)}$  and  $\zeta_{x,f}^{(1)}$  increase little at  $\alpha=0$  deg but appreciably at  $\alpha=15, 30$ , and  $45$  deg, especially when  $U_r > 23$ , up to about 200%. The  $\alpha$  effect on  $\zeta_{y,f}^{(1)}$  and  $\zeta_{x,f}^{(1)}$  could be related to the manner the flow separates and whether reattachment occurs. At  $\alpha=0$  deg, flow separates from the upstream corners and will not reattach on the side surfaces of the cylinder [13,14], regardless of the  $U_r$  value. When the square cylinder is rotated to  $\alpha=15, 30$ , and  $45$  deg, the flow may reattach on the side surface of the cylinder, separating from one upstream corner and one trailing corner of the cylinder [15,29]. Meanwhile, the boundary layer may be accelerated, leading to a higher velocity gradient and hence a larger shear stress near the surface of the structure than that at  $\alpha=0$  deg. Since fluid damping results from viscous shearing at the structure surface and flow separation [30], the higher shear stress might give rise to higher fluid damping.

Third, the first mode effective damping ratio drops below structural damping, implying a negative fluid damping, when resonance occurs at  $U_r \approx 7.5$ , but the third-mode effective damping ratio approaches only the third-mode structural damping, instead of zero, at  $U_r \approx 40$ . The third-mode structural damping ratio in Figs. 7 and 8 is estimated by  $\zeta_s^{(3)} = \zeta_s^{(1)}(f_0^{(3)}/f_0^{(1)})$  [7]. The  $Y$  spectrum at  $U_r \approx 7.5$  (not shown) shows the presence of the first mode structural vibration only. Fluid motion acts to drive structural motion due to their synchronization, thus resulting in negative fluid

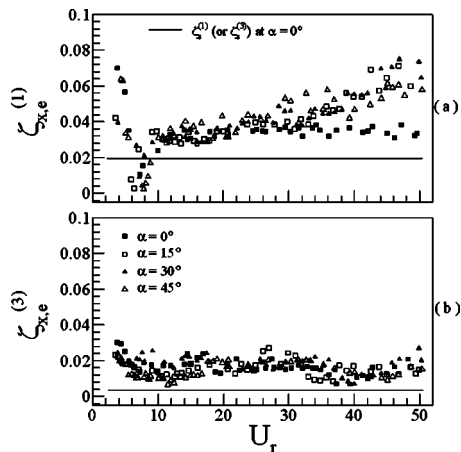


Fig. 8 Inline effective damping ratios of the fluid-square-cylinder system: (a)  $\zeta_{x,e}^{(1)}$  and (b)  $\zeta_{x,e}^{(3)}$

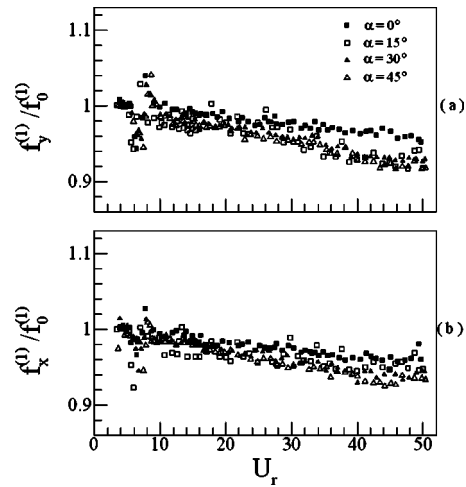


Fig. 9 Dependence on  $\alpha$  and  $U_r$  of (a)  $f_y^{(1)}$  and (b)  $f_x^{(1)}$  associated with the square cylinder

damping. On the other hand, when the third-mode resonance occurs, both the first- and the third-mode structural vibrations are present, as evident in Fig. 4(a), the former in fact being rather strong. Note that the frequency of the third-mode motion is presently about 5.4 times that of the first-mode motion; it is impossible for fluid motion to synchronize with the first- as well as the third-mode of structural motion. This could be responsible for the observation that  $\zeta_{y,e}^{(3)}$  or  $\zeta_{x,e}^{(3)}$  does not drop below  $\zeta_s^{(3)}$ .

Finally,  $\zeta_{x,e}^{(1)}$  is generally larger than  $\zeta_{y,e}^{(1)}$  for  $U_r < 12$ , implying larger inline fluid damping. This observation agrees with Granger et al.'s [31] report for a small gap flow velocity. Based on a linear assumption that the structural vibration velocity was small relatively to the free-stream velocity, Blevins' [30] analysis indicated that the inline fluid damping was twice that of the cross-flow direction for a fluid-cylinder system. The analysis is expected to be valid for small values of  $U_r$  only. When  $12 < U_r < 20$ ,  $\zeta_{y,e}^{(1)}$  and  $\zeta_{x,e}^{(1)}$  are nearly the same. For a higher  $U_r$ ,  $\zeta_{y,e}^{(1)}$  and  $\zeta_{x,e}^{(1)}$  increase. However,  $\zeta_{x,e}^{(1)}$  increases faster and becomes larger than  $\zeta_{y,e}^{(1)}$ . On the other hand,  $\zeta_{x,e}^{(3)}$  is comparable in magnitude with its counterpart in the lift direction, probably due to the relatively small contribution from the fluid damping.

The effective modal damping ratios of the circular cylinder along the  $x$  and  $y$  direction (not shown) behave quite similarly to the square cylinder at  $\alpha=0$  deg. For example,  $\zeta_{y,e}^{(1)}$  varies little with  $U_r$  and approaches zero when the first-mode resonance occurs at  $U_r \approx 4.2$ , implying a negative fluid damping. The similarity could be expected since, as resonance occurs, flow separation from the circular cylinder is likely to be more two-dimensional, thus approaching the square cylinder case.

## 6 Natural Frequencies of the Fluid-Cylinder System

The natural frequency  $f_y^{(1)}$  of the fluid-square-cylinder system is 88.7 Hz at  $\alpha=0$  deg and  $U_r \approx 7.5$ , as determined from the  $Y$  spectrum (not shown), below  $f_0^{(1)}=90.2$  Hz (Table 1). This frequency further decreases to 86.9 Hz at  $U_r \approx 40$  (Fig. 4). The spectra were deduced using a conventional fast Fourier transform (FFT) program with a frequency resolution  $\Delta f$  fixed by the sampling rate and the record length used in the FFT calculation. This  $\Delta f$  was estimated to be 0.35 Hz (Table 2). Therefore, the variation in  $f_y^{(1)}$  could not be attributed to experimental or calculation errors. It is more likely a genuine change in the system natural frequency because of different flow conditions.

It is evident in Fig. 9 that  $f_y^{(1)}/f_0^{(1)}$  or  $f_x^{(1)}/f_0^{(1)}$  exhibits a decrease with increasing  $U_r$ , which is more appreciably at  $\alpha \neq 0$  deg than at

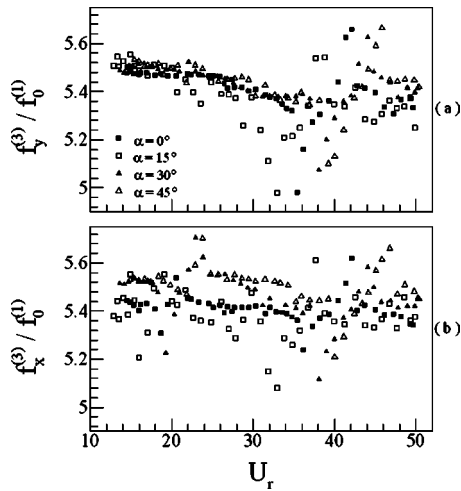


Fig. 10 Dependence on  $\alpha$  and  $U_r$  of (a)  $f_y^{(3)}/f_0^{(1)}$  and (b)  $f_x^{(3)}/f_0^{(1)}$  associated with the square cylinder

$\alpha=0$  deg. This difference becomes particularly evident when  $U_r > 20$ . A number of factors may contribute to this variation. As  $U_r$  increases, the static drag and the axial force begin to rise, thus increasing the structural rigidity [32] and the system natural frequency. This trend is opposite to experimental observation. Added mass is another factor that might change the natural frequency of the system. Sarpkaya [33] measured the added mass for a circular cylinder, which was forced to oscillate laterally in a steady current. His results indicated that the added mass might change with a variation in  $U_r$ , contributing to a variation in the system natural frequency. For the present case, the mass ratio is very large (Table 1). Therefore, a change in added mass is unlikely to be responsible for the variation in the natural frequency of the system. Finally, it has been shown in Figs. 7 and 8 that the first-mode fluid damping ratio increases appreciably, up to 200% for  $\alpha \neq 0$  deg, from  $U_r = 10$ –50. Since  $f_x^{(n)} = f_0^{(n)} \sqrt{1 - (\zeta_{x,e}^{(n)})^2}$  and  $f_y^{(n)} = f_0^{(n)} \sqrt{1 - (\zeta_{y,e}^{(n)})^2}$  [7], the increase in the damping ratio leads to a slowly decreasing natural frequency of the fluid-cylinder system. The combined effect of the three factors could be responsible for the variation in  $f_y^{(1)}/f_0^{(1)}$  or  $f_x^{(1)}/f_0^{(1)}$ . The fluid damping ratio at  $\alpha=0$  deg (Figs. 7 and 8) changes little between  $U_r=10$  and 50, in distinct contrast with those at  $\alpha=15, 30$ , and 45 deg, especially when  $U_r > 20$ . This could partially account for the observation that the variation in  $f_y^{(1)}/f_0^{(1)}$  (or  $f_x^{(1)}/f_0^{(1)}$ ) at  $\alpha=0$  deg is smaller than that at  $\alpha \neq 0$  deg.

It is interesting to note that, for all values of  $\alpha$  tested, when resonance occurs near  $U_r \approx 7.5$ ,  $f_y^{(1)}/f_0^{(1)}$  and  $f_x^{(1)}/f_0^{(1)}$  fall off sharply and then increases to a value above 1. The variation is within  $\pm 0.05 f_0^{(1)}$  in both  $x$  and  $y$  directions. A similar observation is made for the circular cylinder in the  $y$  direction (not shown). The sharp variation in  $f_y^{(3)}/f_0^{(1)}$  and  $f_x^{(3)}/f_0^{(1)}$  also occurs near the third-mode resonance. The variation is about 11% in  $f_y^{(3)}/f_0^{(1)}$  (Fig. 10(a)) and  $f_x^{(3)}/f_0^{(1)}$  (Fig. 10(b)) between  $U_r=27 \sim 48$ . The sharp variation does not occur at the same  $U_r$  for different values of  $\alpha$ , apparently linked to the occurrence of the resonance (Fig. 3(a)), as discussed in Sec. 4.

When a structure is forced to vibrate in a cross flow, the lock-in phenomenon occurs as  $f_s$  approaches the frequency of the external excitation force. For vortex-induced vibrations, however, it is vortex shedding that excites the structure. In other words, the vortex excitation force dominates. To illustrate this, the  $Y$  spectra of the square cylinder at  $\alpha=0$  deg are presented in Fig. 11 for selected  $U_r$  values. The variation of  $f_y^{(3)}/f_0^{(1)}$  is affected by  $f_s/f_0^{(1)}$  but not vice versa. This point is further highlighted in Fig. 12. At  $U_r$

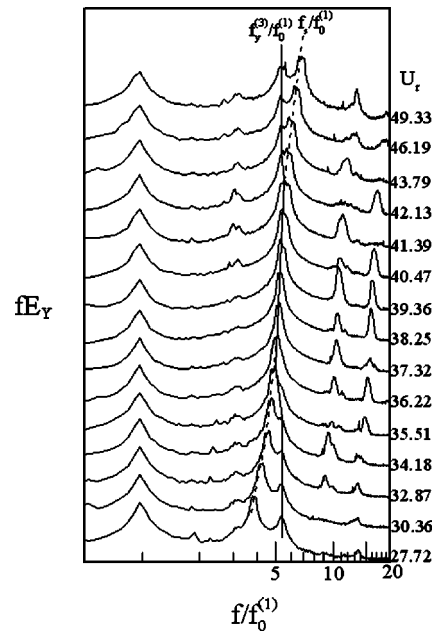


Fig. 11 Power spectra for a range of  $U_r$  (square cylinder,  $\alpha = 0$  deg). The lines are drawn to highlight the trend.

$= 35.0$ ,  $f_s/f_0^{(1)}$  and  $f_y^{(3)}/f_0^{(1)}$  are close enough to interact with each other and the resonance starts to occur. Influenced by the relatively small value of  $f_s/f_0^{(1)} = 4.7$ ,  $f_y^{(3)}/f_0^{(1)}$  drops from 5.3 to 4.96, a value approaching  $f_s/f_0^{(1)}$ . Note that  $f_s/f_0^{(1)}$  remains linear with respect to  $U_r$ , implying that  $f_y^{(3)}$  has little influence on  $f_s$ . Such interplay between  $f_s$  and  $f_y^{(3)}$  continues until they are identical or synchronize at  $U_r = 39.5$ . As  $f_s/f_0^{(1)}$  further increases with increasing  $U_r$ ,  $f_y^{(3)}/f_0^{(1)}$  follows  $f_s/f_0^{(1)}$  until eventually  $f_s/f_0^{(1)}$  and  $f_y^{(3)}/f_0^{(1)}$  are decoupled from each other at  $U_r \approx 42.0$ . The interaction between  $f_s$  and  $f_y^{(1)}$  near the first-mode resonance (not shown) is quite similar to that described above for  $f_y^{(3)}$  and  $f_s$ , except that  $f_y^{(1)}$  varies over a smaller  $U_r$  range than  $f_y^{(3)}$  apparently because the third-mode resonance, occurring at a higher  $U_r$ , is associated with greater fluid excitation energy than the first-mode resonance. Clearly, vortex shedding dominates the nonlinear interaction between the fluid excitation force and the structural vibration in the vortex-induced vibration case, thus tuning the natural frequency of the system to  $f_s$ . This observation contrasts with the lock-in phenomenon where  $f_s$  is dictated by the forced vibration frequency of the cylinder. Similar behavior also exists for the circular cylinder.

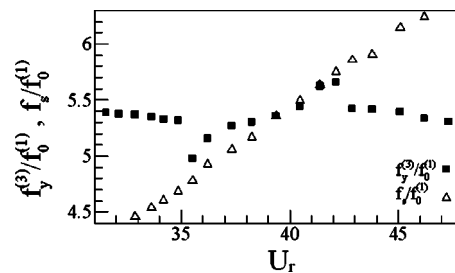


Fig. 12 Variation of  $f_y^{(3)}$  and  $f_s$  with  $U_r$  around resonance (square cylinder,  $\alpha=0$  deg)

## 7 Conclusions

The vortex-induced vibration characteristics of an elastic square cylinder, on fixed supports at both ends, in a cross flow was experimentally investigated and compared to those of a circular cylinder. The following conclusions can be drawn.

1. The vibration amplitude  $Y_{\text{rms}}/d$  at  $\alpha=0$  deg increases with  $U_r$  and displays two peaks at  $U_r \approx 7.5$  and  $U_r \approx 38$ , respectively. The peaks were the result of the excitation of the first- and third-mode resonance. When  $\alpha$  was varied, the two modes of resonance were again excited, though at slightly different  $U_r$  values because of variation in  $f_s$  at different  $\alpha$ . In contrast, two peaks in  $Y_{\text{rms}}/d$  are evident at  $U_r \approx 4.2$  and 26.0 for a circular cylinder, which are identified with the occurrence of the first- and third-mode resonance. The second-mode excitation is discernible at  $U_r \approx 10.5$  in  $Y_{\text{rms}}/d$ . The observation is linked to spanwise nonuniform vortex shedding, implying an asymmetrical excitation force along the cylinder span, which excites the second-mode vibration.
2. The peak in  $Y_{\text{rms}}/d$  due to the third-mode resonance is more pronounced than the others. This is attributed to the combined effect of the higher excitation energy, smaller effective damping ratio, and possible synchronization of vortex shedding with the higher harmonics of the first-mode vibration when the third-mode resonance occurs. The maximum vibration amplitude at the third-mode resonance for the square cylinder doubles that for the circular cylinder even though the square cylinder has a larger flexural rigidity. This is ascribed to the oscillation of the flow separation point associated with a circular cylinder, which impairs the spanwise coherence of vortex rolls and hence the excitation force acting on the structure.
3. The first-mode effective damping ratio at  $\alpha \neq 0$  deg increases appreciably faster than that at  $\alpha=0$  deg as  $U_r$  increases, especially for  $U_r > 23$ . This is likely due to the reattachment of the flow on the side walls at nonzero  $\alpha$ , which is associated with an accelerated shear layer and hence a higher velocity gradient or shear stress near the surface of the structure than that at  $\alpha=0$  deg, thus resulting in higher fluid damping. In the circular cylinder case, the first-mode effective damping ratio behaves quite similarly to that of the square cylinder at  $\alpha=0$  deg, changing little as  $U_r$  varies. The first-mode effective damping ratio approaches zero when the first-mode resonance occurs for all values of  $\alpha$  tested, implying a negative fluid damping.
4. The system natural frequencies slowly decrease as  $U_r$  increases except near resonance where a sudden variation occurs. The sudden variation is dictated by the vortex-shedding frequency and can be as large as 10% of the structural natural frequency. The Zhou et al. [7] linear analysis indicated that the  $n$ th mode natural frequency  $f_y^{(n)}$  and effective damping ratio  $\zeta_{y,e}^{(n)}$  of the fluid-structure system are related by  $f_y^{(n)} = f_0^{(n)} \sqrt{1 - (\zeta_{y,e}^{(n)})^2}$ . At resonance, the nonlinear fluid-structure interaction leads to an appreciable change in  $\zeta_{y,e}^{(n)}$ , as is evident in Figs. 7 and 8 and consequently a change in  $f_y^{(n)}$ . The slow variation is more appreciable for the square cylinder at  $\alpha \neq 0$  deg than that at  $\alpha=0$  deg or for the circular cylinder. This difference is similar to that in the fluid-damping ratio. It is suggested that the slow decrease in the system natural frequencies could be at least partially due to an increase in fluid damping. This system natural frequency behavior is observed for both cylinders, suggesting that it is independent of the nature (fixed or oscillating) of the flow separation point.

## Acknowledgments

Y. Zhou wishes to acknowledge support given to him by the Research Grants Council of the Government of the HKSAR through Grant No. POLYU5316/03E.

## Nomenclature

- $C_{Fy}$  = lateral aerodynamic force coefficient  
 $d$  = cylinder diameter or characteristics height, mm  
 $d'$  = cross-flow cylinder dimension,  $d' = (\sin \alpha + \cos \alpha)d$  for square cylinder, mm  
 $E$  = Young's modulus of elasticity of a cylinder ( $\text{N/m}^2$ )  
 $EI$  = structural stiffness ( $\text{Nm}^2$ )  
 $E_\gamma(f)$  = spectrum of fluctuation  $\gamma$ , normalized so that  $\int_0^\infty E_\gamma(f)df = 1$   
 $f$  = frequency in spectrum analysis, Hz  
 $f_s$  = vortex shedding frequency, Hz  
 $f_0^{(n)}$  =  $n$ th mode structural natural frequency, Hz,  $n=1,2,3,\dots$   
 $f_x^{(n)}, f_y^{(n)}$  =  $n$ th mode inline and cross-flow natural frequencies, respectively, of the fluid-cylinder system, Hz,  $n=1,2,3,\dots$   
 $I$  = cylinder area moment of inertia,  $\text{m}^4$   
 $m$  = cylinder mass per unit length,  $\text{kg/m}^{-1}$   
 $M^*$  = mass ratio =  $m/\rho d^2$   
 $\text{Re}$  = Reynolds number =  $U_\infty d/\nu$   
 $\text{St}$  = Strouhal number =  $f_s d/U_\infty$   
 $u$  = streamwise fluctuation velocity, m/s  
 $U_\infty$  = free-stream velocity, m/sec  
 $U_r$  = reduced velocity =  $U_\infty/f_0^{(1)}d$   
 $U_{r0}$  = critical reduced velocity for galloping instability  
 $x, y$  = coordinates in streamwise and lateral directions, respectively, measured from the center of the cylinder  
 $X, Y$  = displacements of the cylinder in the  $x$  and  $y$  directions, respectively.  $X$  and  $Y$  were derived from strain signals measured at mid-span of the cylinder using fibre-optic Bragg grating (FBG) sensors ( $\mu\text{m}$ )  
 $X', Y'$  = bending displacements of the square cylinder estimated from the strain signals  $\varepsilon_1$  and  $\varepsilon_2$ , respectively,  $\mu\text{m}$   
 $X_{\text{rms}}, Y_{\text{rms}}$  = root-mean-square values of  $X$  and  $Y$ , respectively,  $\mu\text{m}$

## Greek Symbols

- $\alpha$  = incidence angle of free stream velocity, zero when the flow is normal to one face of the square cylinder  
 $\varepsilon_1, \varepsilon_2$  = dynamic strains of the square cylinder measured by FBG sensor 1 and sensor 2, respectively,  $\mu\text{e}$   
 $\varepsilon_{1,\text{rms}}, \varepsilon_{2,\text{rms}}$  = root-mean-square values of  $\varepsilon_1$  and  $\varepsilon_2$ , respectively,  $\mu\text{e}$   
 $\varepsilon_x, \varepsilon_y$  = dynamic strains of the circular cylinder due to drag and lift, respectively,  $\mu\text{e}$   
 $\varepsilon_{x,\text{rms}}, \varepsilon_{y,\text{rms}}$  = root-mean-square values of  $\varepsilon_x$  and  $\varepsilon_y$ , respectively,  $\mu\text{e}$   
 $\zeta_e^{(n)}$  =  $n$ th-mode effective damping ratios of a fluid-structure system,  $n=1,2,3,\dots$   
 $\zeta_s^{(n)}$  =  $n$ th-mode structural damping ratios,  $n=1,2,3,\dots$   
 $\zeta_{x,e}^{(n)}, \zeta_{y,e}^{(n)}$

- $\xi_{x,f}^{(n)}$ ,  $\xi_{y,f}^{(n)}$  =  $n$ th-mode in-line and cross-flow effective (or system) damping ratios, respectively,  $n = 1, 2, 3, \dots$
- $\xi_{x,f}^{(n)}$ ,  $\xi_{y,f}^{(n)}$  =  $n$ th-mode in-line and cross-flow fluid damping ratios, respectively,  $n = 1, 2, 3, \dots$
- $\nu$  = fluid kinematic viscosity
- $\rho$  = fluid density

### Superscript

- \* = dimensionless parameter normalized by  $d$  and  $U_\infty$  unless otherwise stated

### References

- [1] Sarpkaya, T., 1979, "Vortex-induced oscillations: A selective review," *ASME J. Appl. Mech.*, **46**, pp. 241–258.
- [2] Bearman, P. W., and Obasaju, E. D., 1982, "An experimental study of pressure fluctuations on fixed and oscillating square section cylinders," *J. Fluid Mech.*, **119**, pp. 297–321.
- [3] Weaver, D. S., and Fitzpatrick, J. A., 1988, "A review of cross-flow induced vibrations in heat exchanger tube arrays," *J. Fluids Struct.*, **2**, pp. 73–93.
- [4] Williamson, C. H. K., and Roshko, A., 1988, "Vortex formation in the wake of an oscillating cylinder," *J. Fluids Struct.*, **2**, pp. 355–381.
- [5] Parkinson, G., 1989, "Phenomena and modelling of flow-induced vibrations of bluff bodies," *Prog. Aerosp. Sci.*, **26**, pp. 169–224.
- [6] Williamson, C. H. K., and Govardhan, R., 2004, "Vortex-induced vibrations," *Annu. Rev. Fluid Mech.*, **36**, pp. 413–455.
- [7] Zhou, Y., Wang, Z. J., So, R. M. C., Xu, S. J., and Jin, W., 2001, "Free vibrations of two side-by-side cylinders in a cross-flow," *J. Fluid Mech.*, **443**, pp. 197–229.
- [8] Dwyer, H. A., and McCroskey, W. J., 1973, "Oscillating flow over a cylinder at large Reynolds number," *J. Fluid Mech.*, **61**(4), pp. 753–767.
- [9] Achenbach, E., 1968, "Distribution of local pressure and skin friction around a circular cylinder in a cross-flow up to  $Re = 5 \times 10^6$ ," *J. Fluid Mech.*, **34**(4), pp. 625–639.
- [10] Chen, S. S., 1987, *Flow-Induced Vibration of Circular Cylindrical Structures*, Hemisphere, Washington.
- [11] Higuchi, H., Kim, H. J., and Farell, C., 1989, "On flow separation and reattachment around a circular cylinder at critical Reynolds numbers," *J. Fluid Mech.*, **200**, pp. 149–171.
- [12] Mei, V. C., and Currie, I. G., 1969, "Flow separation on a vibrating circular cylinder," *Phys. Fluids*, **12**(11), pp. 2248–2255.
- [13] Nguyen, T. D., and Naudascher, E., 1991, "Vibration of beams and trashracks in parallel and inclined flows," *J. Hydraul. Eng.*, **117**(8), pp. 1056–1076.
- [14] Naudascher, E., and Wang, Y., 1993, "Flow-induced vibrations of prismatic bodies and grids of prisms," *J. Fluids Struct.*, **7**, pp. 341–373.
- [15] Chen, J. M., and Liu, C. H., 1999, "Vortex shedding and surface pressures on a square cylinder at incidence to a uniform air stream," *Int. J. Heat Fluid Flow*, **20**, pp. 592–597.
- [16] Mignolet, M. P., and Red-Horse, J. R., 1994, "ARMAX identification of vibrating structures: model and model order estimation," *Proc. of 35th Structures, Structural Dynamics, and Material Conference, AIAA/ASME*, Hilton Head, South Carolina, April 18–20, pp. 1628–1637.
- [17] Zhou, C. Y., So, R. M. C., and Mignolet, M. P., 2000, "Fluid damping of an elastic cylinder in a cross flow," *J. Fluids Struct.*, **14**, pp. 303–322.
- [18] Zhou, Y., So, R. M. C., Jin, W., Xu, H. G., and Chan, P. K. C., 1999, "Dynamic strain measurements of a circular cylinder in a cross flow using a fibre Bragg grating sensor," *Exp. Fluids*, **27**, pp. 359–367.
- [19] Jin, W., Zhou, Y., Chan, P. K. C., and Xu, H. G., 2000, "A fibre-optic grating sensor for the study of flow-induced vibrations," *Sens. Actuators, A*, **79**, pp. 36–45.
- [20] So, R. M. C., Zhou, Y., and Liu, M. H., 2000, "Free vibrations of an elastic cylinder in a cross flow and their effects on the near wake," *Exp. Fluids*, **29**, pp. 130–144.
- [21] Donnell, L. H., 1976, *Beams, Plates, and Shells*, McGraw-Hill, New York, pp. 84, 85.
- [22] Parkinson, G., and Smith, J. D., 1964, "The square prism as an aeroelastic non-linear oscillator," *Q. J. Mech. Appl. Math.*, **17**, pp. 225–239.
- [23] Okajima, A., 1982, "Strouhal numbers of rectangular cylinders," *J. Fluid Mech.*, **123**, pp. 379–398.
- [24] Knisely, C. W., 1990, "Strouhal numbers of rectangular cylinders at incidence: A review and new data," *J. Fluids Struct.*, **4**, pp. 371–393.
- [25] Zhou, Y., and Antonia, R. A., 1994, "Effect of initial conditions on structures in a turbulent near-wake," *AIAA J.*, **32**, pp. 1207–1213.
- [26] Lee, B. E., 1975, "The effect of turbulence on the surface pressure field of a square prism," *J. Fluid Mech.*, **69**, pp. 263–282.
- [27] Vickery, B. J., 1966, "Fluctuating lift and drag on a long cylinder of square cross-section in a smooth and in a turbulent stream," *J. Fluid Mech.*, **25**(3), pp. 481–494.
- [28] King, R., 1977, "A review of vortex shedding research and its application," *Ocean Eng.*, **4**, pp. 141–171.
- [29] Hasan, M. A. Z., 1989, "The near wake structure of a square cylinder," *Int. J. Heat Fluid Flow*, **10**(4), pp. 339–348.
- [30] Blevins, R. D., 1994, *Flow-Induced Vibration*, Krieger Publishing, Malabar, Florida, USA.
- [31] Granger, S., Campistron, R., and Lebet, J., 1993, "Motion-dependent excitation mechanisms in a square in-line tube bundle subject to water cross-flow: an experimental modal analysis," *J. Fluids Struct.*, **7**, pp. 521–550.
- [32] Weaver, W., Timoshenko, S. P., and Young, D. H., 1989, *Vibration Problems in Engineering Fifth Edition*, Wiley, New York, pp. 54–55, 366, 426–432, and 454–456.
- [33] Sarpkaya, T., 1978, "Fluid forces on oscillating cylinders," *J. Waterw., Port, Coastal, Ocean Div., Am. Soc. Civ. Eng.*, **104**, pp. 275–290.

# Effects of Wall Roughness on Particle Velocities in a Turbulent Channel Flow

Michael Benson  
Tomohiko Tanaka  
John K. Eaton

Department of Mechanical Engineering,  
Stanford University

*Experimental measurements using a laser Doppler anemometer (LDA) system have been performed on 150  $\mu\text{m}$  dense glass particles in a fully developed downward channel flow in air. Tests were conducted in smooth, rough development, and fully rough wall conditions with a channel Reynolds number of 13,800, corresponding to a centerline gas phase velocity of 10.5 m/s with a dilute loading of particles of 15% by mass fraction. Velocities were measured and statistics compared to see the nature of the effects of the wall roughness in a rebuilt channel facility originally used for important works including Kulick, Fessler, and Eaton, (1994, "Particle Response and Turbulence Modification in Fully-Developed Channel flow," *J. Fluid Mech.*, **277**, pp. 109–134) and Paris (2001, "Turbulence Attenuation in a Particle-Laden Channel Flow," Ph.D. thesis, Stanford University, Stanford, CA). Wall roughness has a substantial impact on gas phase mean velocities across most of the channel width, except very near the wall. The turbulence intensity of the gas phase is enhanced across the entire channel in the presence of fully rough walls. The rough walls have an even greater impact on the particle phase. Streamwise particle velocities are reduced up to 40%, and become quite uniform across the channel. Particle fluctuating velocities are nearly doubled near the channel centerplane. Profiles appear uniform, due in large part to strong transverse mixing induced by particle-wall collisions. Much of the data of Kulick and Paris is shown here to be strongly influenced by wall conditions with poorly defined roughness in the development region, followed by rapid flow recovery in a relatively smooth test section. [DOI: 10.1115/1.1891149]*

## 1 Introduction

Turbulent, particle laden shear flows in air are commonplace in a wide range of applications, including industrial conveyance processes, pulverized coal combustion, pollution control systems, fluidized beds, and the environment. Interphase exchange of mass, momentum, and energy make these flows more difficult to understand and predict than similar single-phase flows. Wall-bounded flows are even more difficult because of complex interactions of particles with nonideal wall conditions.

Documentation of the particular wall-bounded flow studied herein is extensive and dates back to the work of Kulick, Fessler, and Eaton [1], who used the same fully developed vertical down-flow channel facility studied in the present paper. They studied air flows laden with several types and sizes of fine spherical particles, each over a range of mass loadings. They found no change in the mean streamwise fluid velocities in the presence of the particles. The gas phase turbulence, however, decreased as the particle Stokes number and mass loading increased. Additionally, increases in the particle mass loading caused flattened particle velocity profiles across the channel. In a counter-intuitive finding, it was noted that particles with larger Stokes numbers had smaller mean velocity than the gas phase in the center of the channel, despite the influence of gravity. A similar effect has been observed in a few other downward pipe and channel flows, including a recent work by Caraman, Boree, and Simonin [3].

Most recently, Paris [2], continued the investigation of the same channel flow using particle image velocimetry (PIV) techniques. The same levels of gas-phase turbulence attenuation were noted as in Kulick, Fessler, and Eaton [1]. As before, measured particle velocities consistently lagged the streamwise fluid phase at the

channel centerline, a feature not supported by several numerical simulation results of the same channel, c.f. [4–8]. In addition, particle streamwise RMS velocity profiles were relatively flat, and exceeded fluid phase turbulence levels throughout the profile except near the wall.

Roughness effects have long been considered important in single-phase flows. Perry, Schofield, and Joubert [8] identified "k" and "d" type roughness, each with differing effects close to the surface. Perry, Lim, and Henbest [9] concluded that roughness effects were generally small at large distances from the surface, relative to roughness element size. Raupach, Antonia, and Rajagopalan [10] reviewed numerous rough wall experiments with similar conclusions. However, in Krogstand, Antonia, and Browne [11], significant effects were seen outside this wall region. Thus, roughness effects in single-phase flows are still a subject of some contention.

The effects of roughness in dilute particle-laden flows have been studied far less. Many recent studies of turbulence attenuation have been conducted without consideration of this potentially important condition. In an important recent work, Kussin and Sommerfeld [12] used a horizontal channel with exchangeable stainless steel wall plates to systematically study roughness effects. They used two different wall roughnesses, with particles ranging from 60  $\mu\text{m}$ –190  $\mu\text{m}$  in size and a variety of mass loadings. The higher wall roughness cases showed decreased streamwise particle mean velocities and increased particle fluctuating velocities when compared to the less rough wall cases. These changes were attributed primarily to the wall roughness increasing the frequency of interparticle and particle-wall collisions.

The present work is motivated by the poor agreement between simulations and the particle velocity measurements by Kulick, Fessler, and Eaton and Paris. These data sets are widely used as test cases for simulations attempting to predict turbulence modulation by particles, so it is important to understand why the particle mean velocity is significantly lower than expected. Kussin and Sommerfeld [12] suggested that wall roughness may play a

Contributed by the Fluids Engineering Division for publication in the JOURNAL OF FLUIDS ENGINEERING. Manuscript received by the Fluids Engineering Division May 9, 2003. Revised manuscript received December 13, 2004. Review conducted by M. Plesniak.



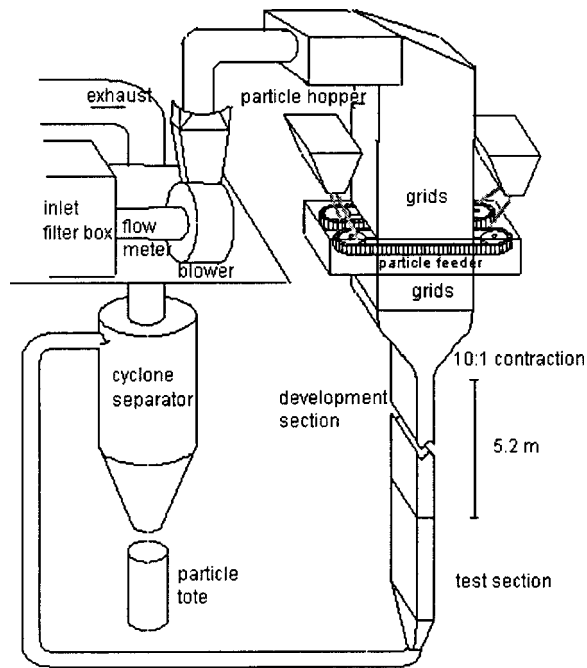


Fig. 1 Schematic of the experimental setup

significant role. The wall roughness is poorly defined in the Kulick, Fessler, and Eaton and Paris experiments. The 5 m long channel-flow development section was made of particle board which was sanded smooth. However, a layer of particles adhered to this surface making it effectively quite rough. The flow then entered the test section fabricated from smooth Plexiglas. Measurements were acquired approximately 30 cm (7.5 channel widths) downstream of the test section inlet. Therefore, the flow may still have been recovering from the effects of the rough development channel.

The objectives of this work were two fold. The first was to assess how roughness may have affected the particle-phase velocities in the Kulick, Fessler, and Eaton and Paris experiments. Experiments were conducted in which the wood development section was replaced with a smooth plexiglas channel. This was then subsequently replaced by a development channel with a well-defined roughness (the *rough development* case). The second objective was to examine the effects of roughness on the particle velocities in fully developed channel flow by extending the well-defined roughness all the way to the measurement position (the *fully rough* case).

## 2 Facility and Techniques

**2.1 Facility.** All experiments were conducted in the facility in Fig. 1. It is an open-loop, vertical, high aspect ratio, fully developed channel wind tunnel. It includes a particle feeding apparatus, a laser Doppler anemometer (LDA), and associated data acquisition and experimental control devices. Detailed descriptions of its construction and components are available in Kulick, Fessler, and Eaton [1] and Benson [14], but the critical items are briefly recounted here. The flow path begins 7.0 m above the ground floor, when ambient air is drawn from a  $0.3 \text{ m}^3$  plenum and goes through a venturi flowmeter used to monitor and control the gas phase flowrate. The flow then enters a 3700 W (5 hp) blower, exits through a diffuser into a vertical round sheet metal duct, transitions into a horizontal section that brings the cylindrical duct into a rectangular cross section oriented downward, passes through several turbulence grids, and enters the region where the particles are loaded. The glass particles are loaded uniformly across the breadth and width of this section using a system con-

sisting of a large number of drainage buckets emptying uniformly as they are pulled across the channel on belts in four locations. The particle-laden flow then passes through additional turbulence grids and enters a 10:1 contraction through a honeycomb section to reduce the particle cross-stream velocity. The flow then travels downward through 5.1 m of channel development length, with inside dimensions of  $4 \text{ cm} \times 45.7 \text{ cm}$ . This development length is constructed of smooth acrylic, replacing an earlier wooden duct used by Kulick, Fessler, and Eaton. The final 1.7 m long acrylic section of the development length, corresponding to approximately 85 channel half heights, is exchangeable, and sufficiently long to achieve fully developed flow for the Reynolds number used in this experiment Hussian and Reynolds [15]. In the smooth wall condition the final section remains acrylic. In the rough condition, a stainless steel mesh screen of wire diameter 0.25 mm and 1 mm square mesh spacing, is affixed to the inside of the 45.7 cm wide acrylic walls. Following the exchangeable section is a 63.5 cm long smooth test section, of the same inside dimensions as the rest of the channel. Glass inserts, at the center of each 4 cm side and the 45.7 cm face of the test section, provide optical access for the LDA system. Measurements were initially taken approximately half the distance down the length of the test section for comparison with Kulick, Fessler, and Eaton and Paris, and then measurements were taken at distances of 5 cm and 1 cm into the test section. Following the test section is a sheet metal contraction, transitioning the rectangular duct flow into 10 cm diameter PVC pipe, which enters a large cyclone separator. The particulate phase is extracted for weighing and reuse, and the gas phase is exhausted through the roof of the building.

**2.2 Electrostatic Effects.** Mitigation of electrostatic effects was accomplished by running static discharge wires along the length of the entire channel apparatus and grounding to structural supports at several locations along the three floors the apparatus travels. In addition, electrostatic tape was used in the vicinity of all piping transitions, where charge buildup was significant. It should be noted that these regions are downstream of the test section. While it is difficult to ensure that *all* static charge was diminished through these techniques, the relatively large glass particles have not shown preferential “sticking” to the wall sides after two years, indicating that the aerodynamic forces on the particles even deep in the boundary layer are large enough to dominate the electrostatic attraction at the walls. Only the gas-phase seeding (polydisperse fog oil droplets less than  $1 \mu\text{m}$  diameter) left deposits on the wall sides.

**2.3 (LDA) System Description and Uncertainty.** A dual beam, single component, laser Doppler anemometer (LDA) was used to measure both the particle velocities in the particle laden experiments and gas-phase tracer velocities in single phase flow. The laser was a Lexel Model 95 Argon-Ion laser operated for the initial measurements in multiline mode. For the final measurements, an etalon was installed, and the laser was operated in single-line mode at 488 nm and a power of 1 W. The transmitting optics was built from several discrete TSI Inc. (Shoreview, MN) components as described in detail by Benson [14]. The transmitting optics assembly was mounted on an optical rail, traversed in the wall normal direction by a motorized traverse system. Beams were oriented in the  $X$ - $Z$  plane to measure the streamwise velocity component and in the  $X$ - $Y$  plane to measure the wall-normal component. A TSI Model 9182 Bragg cell was included in the transmitting optics for the wall-normal measurements. The measurement volume diameter was estimated at  $60 \mu\text{m}$  for the streamwise velocity measurements and  $200 \mu\text{m}$  for the wall-normal configuration.

Side scatter collection through one of the 45.7 cm wide walls was used to minimize the length of the control volume. A Dantec Corp. (Copenhagen, Denmark) 80 mm focal length collection optics assembly was used with a photomultiplier tube. After down-mixing, the signal was processed using a TSI IFA655 Digital

**Table 1 Particle and fluid flow parameters**

Particle parameters		Fluid parameters	
Density (kg/m <sup>3</sup> )	2500	$h$	20 mm
Nominal diameter ( $\mu\text{m}$ )	150	$U_{cl}$	10.5 m/s
Number mean diameter ( $\mu\text{m}$ )	147	$Re_h$	13,800
Standard deviation of diameter ( $\mu\text{m}$ )	10.0	$U_\tau$	0.47 m/s
Mean Stokes time constant (ms)	167		

**Burst Correlator.**

Statistical uncertainty for the mean velocity was estimated using the Student-t distribution at 95% confidence interval, and the statistical uncertainty for the variance was estimated using the chi-squared distribution, also at 95% confidence. A minimum of 4000 samples were acquired for the particle phase resulting in statistical uncertainty in the mean ranging from 1.3% at the centerline to 1.6% near the wall. For the velocity variance, the statistical uncertainty varied between 0.8% and 1.1%. In the case of the gas phase statistics, over 20,000 samples were used and the statistical uncertainty was negligible. Other contributors to the overall uncertainty were the absolute uncertainty of the LDA measurements which was of the order of 1% and the repeatability and steadiness of the overall flow system. The total uncertainty was estimated to be 2.3% for the mean and 7% for the root mean square (RMS) velocity of the gas phase, and 3.6% for the mean and 13% of the rms velocity for the particle phase.

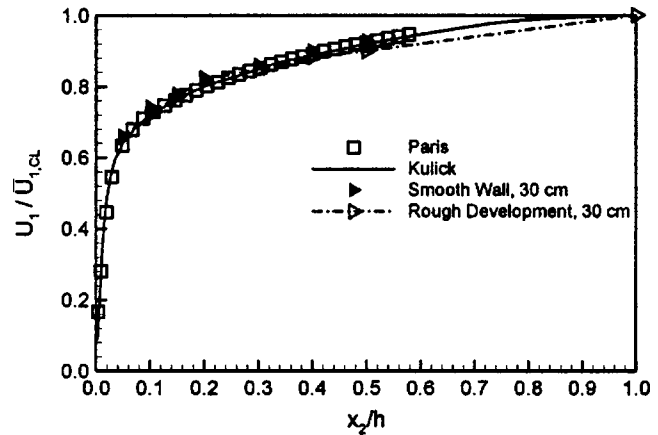
**2.4 Flow Tracer and Particle Description.** Flow tracers were generated using a ROSCO 3000 fog machine. Fog oil was vaporized and condensed as polydisperse droplets with a nominal diameter of 0.7  $\mu\text{m}$ . For the particles, 150  $\mu\text{m}$  monodisperse spherical glass beads were utilized. The glass beads were professionally sieved to obtain a narrow size distribution, with a standard deviation of 10  $\mu\text{m}$ . Pertinent particle and tracer characteristics are included in Table 1.

**3 Comparison with Kulick, Fessler, and Eaton and Paris: Rough Development Section Only**

The first experiments were designed to compare to the Kulick, Fessler, and Eaton [1] and Paris [2] experiments in which measurements were acquired approximately 30 cm downstream of the transition from the development duct. After disassembly, the original particle-board walls were found to be coated with several layers of particles producing a total roughness thickness of approximately 0.25 mm. This roughness could not be characterized precisely because of its unconsolidated nature. The 0.25 mm thick screen was selected as an analog for the roughness based solely on its thickness. Experiments were then conducted with both a smooth acrylic development section and screen roughened development section.

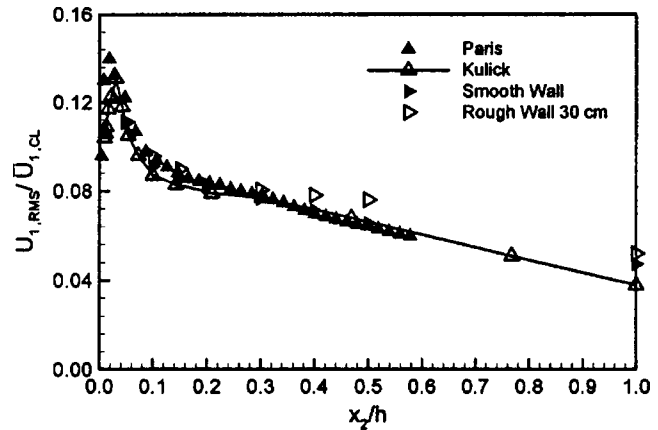
Figures 2 and 3 show the streamwise mean and RMS gas phase velocity in single phase flow. The new data for both smooth and rough development sections are in close agreement to the earlier profiles measured by Kulick, Fessler, and Eaton and Paris. This indicates that the gas phase flow recovers quickly from the effects of roughness.

The particle velocity data from Paris are nearly identical to the Kulick, Fessler, and Eaton data so only the former are shown in subsequent figures. The particle mean velocity data (Fig. 4) show good agreement between the Paris data and the new data measured with the prescribed roughness in the development section. By contrast, the particle velocities average 1.1 m/s higher across most of the channel for the case with the smooth wall development section. This is a clear indication that the rough development section in the Kulick, Fessler, and Eaton and Paris experiments caused the unexpectedly low particle mean velocities. Unlike the fluid velocity profiles, the particle velocities recover slowly after

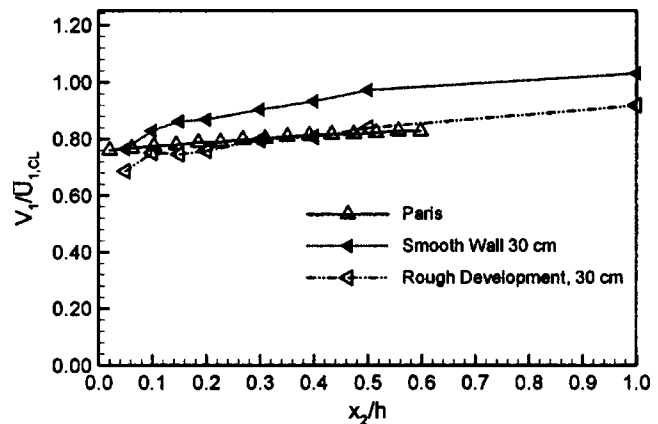


**Fig. 2 Streamwise single phase mean velocity profile, normalized by the mean gas phase centerline velocity. Smooth wall and rough development conditions are presented for comparison with Kulick, Fessler, and Eaton [1] and Paris [2] data.**

the change from rough to smooth wall. Near the wall, the smooth wall particle velocity drops to match the Paris data at the nearest measurement station to the wall. The flatter particle mean velocity



**Fig. 3 Streamwise single phase rms velocity profile normalized by the mean gas phase centerline velocity. Smooth wall and rough development conditions are presented for comparison with Kulick, Fessler, and Eaton [1] and Paris [2] data.**



**Fig. 4 Streamwise particulate phase mean velocity profile normalized by the mean gas phase centerline velocity. Smooth wall and rough development conditions are presented for comparison with Paris [2] data.**

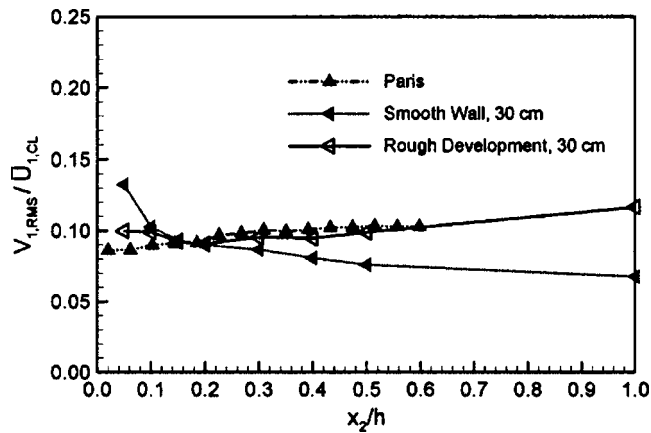


Fig. 5 Streamwise particulate phase rms velocity profile normalized by the mean gas phase centerline velocity. Smooth wall and rough development conditions are presented for comparison with Paris [2] data.

profile for the rough case is the result of higher wall-normal velocity fluctuations. Also, the new rough wall data indicate a slower particle velocity near the wall than the Paris data. This is an indication that the screen roughness causes more momentum loss for a colliding particle than the naturally formed roughness on the wood walls.

The particle RMS velocity profiles in Fig. 5 show close agreement between Paris and the present data except for a small deviation near the wall. This is likely a result of the different interactions of particles impacting the wire mesh screen versus the particle-coated inner surfaces of the particle-board wall. The smooth wall case has a lower RMS velocity near the channel centerline but rises above the rough development section results near the wall. The rise is due to the steeper particle mean velocity profile near the wall for the smooth wall case. The smaller turbulence levels near the centerline are most likely caused by reduced wall-normal particle velocities.

Overall, the present experiments show that the rough wall in the development section had almost no effect on the gas phase flow at the measurement station, but a substantial effect on the particle velocities. This confirms that the development section roughness played a significant role in the Kulick, Fessler, and Eaton and Paris experiments.

#### 4 Fully Rough Case

**4.1 Single Phase Results.** The results reported in the previous section showed that at least the single phase velocity field recovered rapidly from the results of roughness. The velocity fields of both the gas and the particle phases within the fully developed rough wall region are of interest. However, the rough wall interferes with the laser beams, so new profile data were acquired in the smooth wall section just downstream of the end of the roughness. While the smooth wall boundary condition at this location will obviously affect the near-wall velocity field, the turbulence in the outer layer and the particle velocities are probably almost the same as in the rough wall section. Most of these data were acquired at a location 5 cm downstream of the end of the roughness, but some were acquired at a location 1 cm downstream for comparison purposes. Single phase mean velocity profiles for the smooth wall, the rough development, and the fully rough cases are plotted in Fig. 6. The fully rough case includes three independently measured profiles demonstrating excellent repeatability. Two primary conclusions can be drawn from this representation. First, nearly the entire gas phase velocity profile is profoundly affected by the presence of the wall roughness. This contradicts the results of Raupach, Antonia, and Rajagopalan [10] and others,

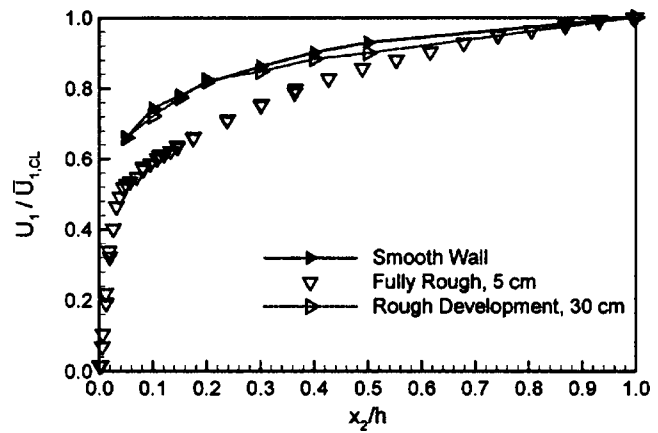


Fig. 6 Gas phase mean streamwise velocities for the smooth wall versus fully rough (5 cm) and rough development (30 cm) wall conditions. Velocities are normalized by the mean gas phase centerline velocity.

where rough wall effects are concentrated in a region extending approximately five roughness element heights away from the surface. Next, and of particular importance, is the rapid recovery exhibited by the gas phase from the wall roughness condition. Note the substantial difference between measurements 5 cm after the rough wall transitions to test section and the 30 cm location—the rough wall effects in the gas phase retain little memory of the wall roughness condition once removed. This rapid recovery at locations relatively distant from the wall condition represents an important consideration in the design of channel flow experiments where nonintrusive measurement techniques are employed. The RMS velocities of the single phase flow show similar results—wall roughness effects are evidenced by differences that are most significant from about five roughness element heights out to the channel centerline, and the single phase can rapidly recover from the perturbed wall condition. Figure 7 shows that this effect is present at more than just the centerline location. The RMS velocities of the carrier phase are substantially higher and different in shape in the rough wall case, indicating that the turbulence in the single phase both in the near-wall region and further from the wall is augmented and modified by the wall roughness condition. As the gas phase data for the rough wall were taken at the 5 cm location, it is likely that the dip exhibited in the wall region near  $x_2/h=0.1$  is influenced by the 5 cm distance traveled in the absence of the roughness condition. A probability density function (PDF) of the gas phase at the centerline condition for rough and

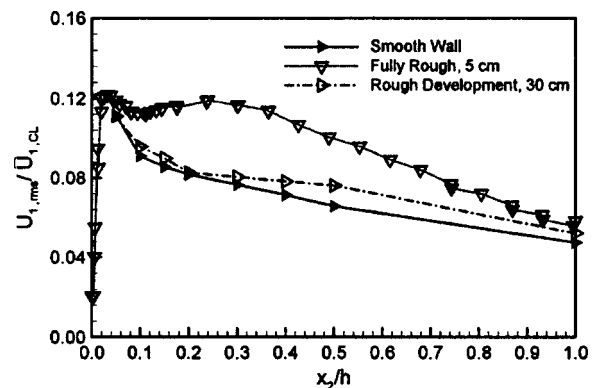


Fig. 7 Gas phase streamwise rms velocities for the smooth wall versus fully rough (5 cm) and rough development (30 cm) wall conditions. Velocities are normalized by the mean gas phase centerline velocity.

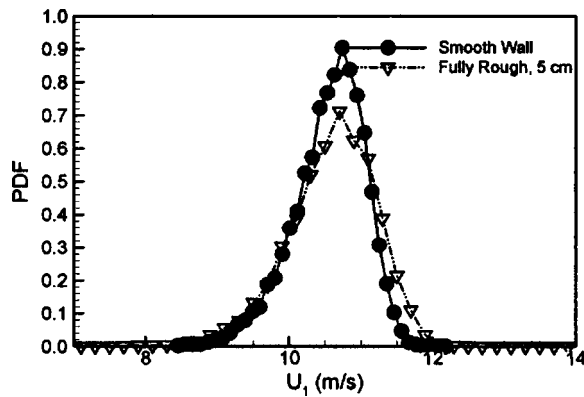


Fig. 8 Channel centerline PDF distribution for the streamwise gas phase velocity for smooth and fully rough walls

smooth walls is provided as Fig. 8, indicating that while in both cases the average centerline velocity was identical, the rough wall case had a wider range of gas phase velocities as one might expect.

**4.2 Particle Phase Results.** For the particle phase measurements, two locations in the test section—a distance of 5 cm and 1 cm from the end of the rough walls—were utilized to characterize the flow. Where possible, data from both locations are provided to show that the changes over this streamwise distance are relatively small.

The streamwise particle mean velocity profiles are shown for five different cases in Fig. 9. Here all velocities are normalized by the gas phase centerline velocity. First, excellent repeatability can be seen by comparing the two smooth wall cases. These measurements were made at two different positions in the test section with different LDA setups. Next the effect of transitioning from the rough development channel to the smooth test section can be seen clearly. The measurements at 1 cm and 5 cm downstream of the rough development section show particle velocities that are 30% to 40% slower than the smooth channel. This is due to the loss of momentum during impact with the wall and the strong cross stream mixing induced by wall collisions. The particles accelerate significantly in the smooth wall test section so they are only about 10% below the smooth wall value at a station 30 cm downstream of the rough/smooth transition.

Figure 10 shows the particle mean velocity profile for the smooth wall case compared to the single-phase gas velocity profile. Also shown is the centerline particle terminal velocity calcu-

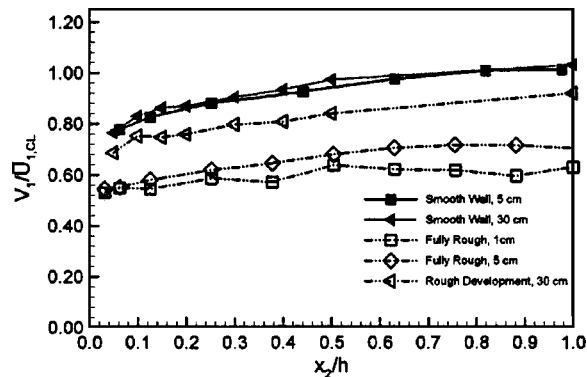


Fig. 9 Comparison of streamwise particulate phase mean velocity profiles among smooth, rough development and fully rough walls. Velocities are normalized by the mean gas phase centerline velocity.

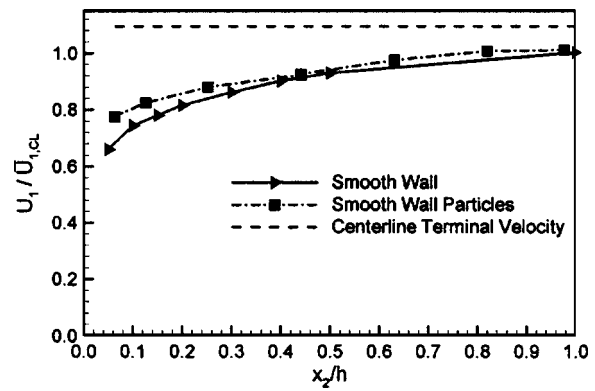


Fig. 10 Comparison of mean streamwise gas and particle phase velocity profiles for smooth walls, with particle centerline terminal velocity. Velocities are normalized by the mean gas phase centerline velocity.

lated by integrating the equation of motion for non-Stokesian particles and assuming uniform flow in the centerplane

$$\frac{dV_i}{dt} = g_i - \frac{18\mu}{\rho_p d_p^2} [1 + 0.15 \text{Re}_p^{0.687}] (V_i - U_i) \quad (1)$$

$$\text{Re}_p = \frac{\rho_f |V - U| d_p}{\mu} \quad (2)$$

The particles move faster than the flow throughout the profile. While they do not reach their predicted terminal velocity of nearly 11.5 m/s, they do have a maximum velocity at the centerline near 10.9 m/s. This indicates relatively small cross stream mixing of the particles for this smooth wall case. Further evidence of this will be shown in the following section.

Figure 11 shows rough wall cases compared to the rough wall gas phase velocity profile. The particle mean velocity profiles in this case are very flat, indicative of strong cross stream mixing. The particles move more than 40% slower than the gas near the centerline, but the profiles actually cross with the particles moving faster than the gas near the wall.

Figure 12 shows the streamwise RMS velocity profiles for the particle phase. The smooth wall particle data measured at two different locations are quite similar, again emphasizing the low experimental uncertainty of the results. The rough wall RMS velocities are everywhere significantly higher than those in the smooth wall profile, indicating that the streamwise oriented par-

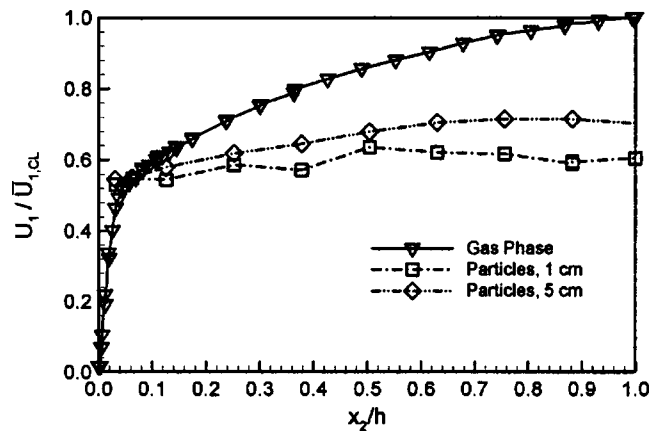


Fig. 11 Comparison of mean streamwise gas and particle phase velocity profiles for fully rough walls. Velocities are normalized by the mean gas phase centerline velocity.

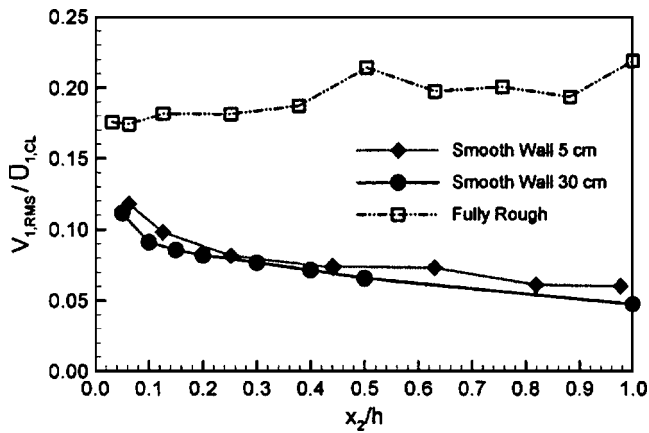


Fig. 12 Comparison of streamwise particulate phase rms velocity profiles among smooth and fully rough walls. Velocities are normalized by the mean gas phase centerline velocity.

particle trajectories are modified in the presence of the rough wall. From streamwise data alone, one can assume that the nature of the increase is due to wall collisions, the effects of which appear across the breadth of the channel. Additional insight comes from comparing the gas and particle phase data for the rough wall case alone (Fig. 13). While the gas phase rms velocities decrease toward the channel centerline, the particle phase RMS velocities increase slightly. Near the centerline the particle RMS velocity is much larger for the particles than the gas phase. This suggests that, for the rough wall case, the particles would be expected to transfer energy to the gas turbulence, an effect that is opposite of what is normally expected. Again, this is due to the strong wall-normal mixing of the particles in the rough wall case.

Figures 14 and 15 depict probability density functions for the particle phases. Figure 14, at the channel centerline, shows particles at each of the two fully rough measurement stations (1 cm and 5 cm below the end of the roughness section) with velocities ranging from near 0 to the maximum velocity for the smooth wall case. Smooth wall particles are more narrowly distributed. Figure 15 shows data in the near-wall region, at  $x_2/h=0.0315$ . Here particles in the fully rough case again show a slightly wider range of velocities, with very few traveling with speeds comparable to the smooth wall case. However, particles in the smooth wall condition, while faster than those in the rough, display a wider range of variability than at the channel centerline. In neither case are any bimodal velocity distribution effects present.

The wall-normal particle velocities were measured for additional insight into the mechanism of the energy transfers occurring

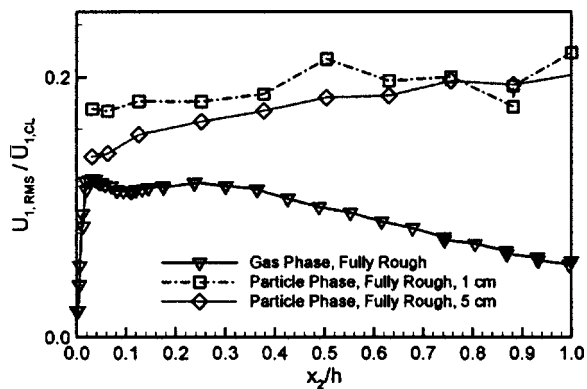


Fig. 13 Comparison of rms streamwise gas and particle phase velocity profiles for fully rough walls. Velocities are normalized by the mean gas phase centerline velocity.

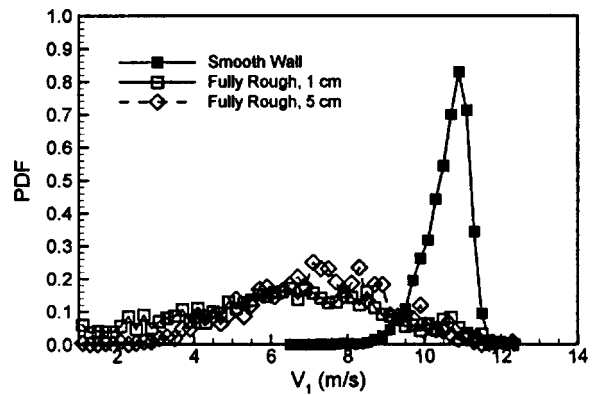


Fig. 14 Channel centerline PDF distribution for the streamwise particle phase velocity for smooth and fully rough walls

across the channel. The mean wall-normal velocities for both particle and gas phase are essentially zero across the channel. The RMS wall-normal particle velocities for the smooth and rough wall cases are shown in Fig. 16. For the smooth wall case, the wall-normal velocity fluctuations are small. This corresponds to the relatively weak wall-normal mixing evident for the smooth wall case in the streamwise particle velocity profiles. On the other hand, for the rough wall case the particle wall-normal RMS ve-

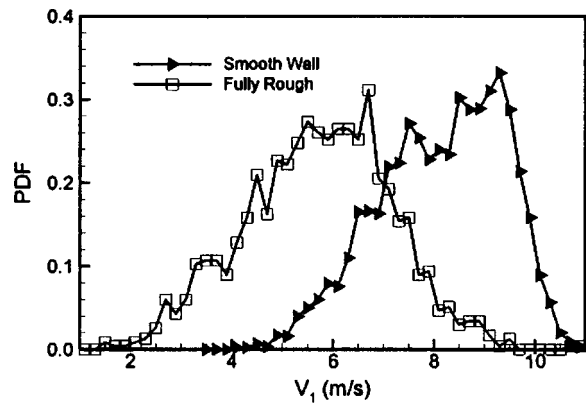


Fig. 15 Near-wall ( $x_2/h=0.0315$ ) PDF distribution for the streamwise particle phase velocity for smooth and fully rough walls

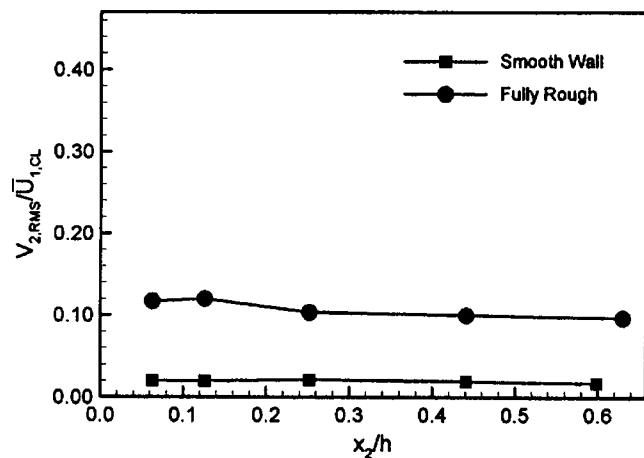


Fig. 16 Wall-normal particulate phase rms velocity for the smooth and fully rough wall conditions. Velocities are normalized by the mean gas phase centerline velocity.

locity is quite large and nearly uniform across the channel.

Because the RMS velocity component is relatively constant across the channel width, and always exceeds that of the smooth wall case, it follows that particles are impacting the wall in such a manner as to traverse the channel breadth with disparate fluctuation intensity. This is despite the relatively large velocity gradient in the gas phase in the near wall region. Likely, the particles are impacting the channel roughness elements frequently and at a variety of angles and not fully recovering their original velocity, indicating that the collisions are not specular. As particles impacting the wall slow for the loss of streamwise momentum, they increase their near-wall residence time. However, the lack of a steep velocity gradient in the near-wall region of the particle velocity profile indicates that the near-wall particles regain some energy. The only remaining mechanism is additional collisions, this time between slow and fast moving particles. If particle-particle collisions are important closer to the channel centerplane region, as discussed by several authors [7,13–16], then their effect in this experiment must be to enhance particle fluctuating velocities in the rough wall case. This result is also seen in the report by Kussin and Sommerfeld, who show RMS velocities as uniformly higher across the channel in the high roughness case [12].

## 5 Conclusions

Rough walls have a dramatic influence on the behavior of both particle and gas phases in fully developed channel flow. The gas phase profile is significantly retarded near the wall relative to the smooth wall case, and the turbulence intensity is enhanced across the entire channel. The gas flow recovers very rapidly following a rough to smooth wall transition. Nearly complete recovery of the mean velocity and turbulence profiles was observed after a distance of 7.5 channel widths.

Wall roughness effects are even stronger for the particle phase, at least due to the range of parameters studied here. The streamwise particle mean velocity was reduced up to 40% by the ordered roughness, and became quite uniform across the channel. The streamwise rms velocity was increased by up to a factor of 2 near the channel centerplane, and was quite uniform across the channel. The profile uniformity was due to the strong transverse mixing induced by particle wall collisions. The wall normal particle fluctuating velocity increased from nearly 0 to more than 12% of the centerline fluid velocity. Collisions with roughness elements were also responsible for the loss of particle streamwise momentum.

The experiments of Kulick, Fessler, and Eaton and Paris examined a case in which the flow developed in a duct with poorly defined roughness, then flowed through a smooth channel for a distance of 7.5 channel widths prior to the measurement position. The present results measured under the same conditions as Paris but using a well-defined roughness showed that the particle velocity statistics measured in the earlier experiments were a consequence of an effectively very rough wall in the development duct. However, gas phase statistics will rapidly recover from the wall roughness condition, so that for much of the data obtained in those experiments, valuable information remains.

## Acknowledgments

The United States Military Academy at West Point, NY, supported the first author in his graduate studies. The National Aeronautics and Space Administration provided financial support for this research through Grant No. NCC3-640. The authors wish to thank the reviewers for their insightful comments and assistance during preparation of this finalized manuscript. Special thanks belong also to Dr. Kulick and Dr. Paris for the use of their data. The views expressed herein are those of the authors and do not purport to reflect the position of the United States Military Academy, the United States Army, or the Department of Defense.

## Nomenclature

$\rho$	= Density
$\mu$	= Dynamic viscosity
$\varphi$	= Particle mass loading
$d$	= Diameter
$g$	= Gravitational Constant
$h$	= Channel half-width
$Re_h$	= Channel Reynolds number
$Re_p$	= Particle Reynolds number
$U$	= Fluid velocity
$V$	= Particle velocity
$x_1$	= Streamwise direction
$x_2$	= Transverse direction
$x_3$	= Spanwise direction

## Subscripts

$p$	= particle
$f$	= fluid

## References

- [1] Kulick, J. D., Fessler, J. R., and Eaton, J. K., 1994, "Particle Response and Turbulence Modification in Fully-Developed Channel Flow," *J. Fluid Mech.*, **277**, pp. 109–134.
- [2] Paris, A. D., 2001, "Turbulence Attenuation in a Particle-Laden Channel Flow," Ph.D. thesis, Stanford University, Stanford, California.
- [3] Caraman, N., Boree, J., and Simonin, O., 2003, "Effect of Collisions on the Dispersed Phase Fluctuation in a Dilute Tube Flow; Experimental and Theoretical Analysis," *Phys. Fluids*, **15**, pp. 3602–3612.
- [4] Fukagata, K., Zahrai, S., Kondo, S., and Bark, F., 2001, "Anomalous Velocity Fluctuations in Particulate Turbulent Channel Flow," *Int. J. Multiphase Flow*, **27**, pp. 701–719.
- [5] Rouson, D., 1997, "A Direct Numerical Simulation of a Particle-laden Turbulent Channel Flow," Ph.D. thesis, Stanford University, Stanford, CA; also available as Rouson, D. W. I., Abrahamson, S. D., and Eaton, J. K., Report No. TSD-101, Mechanical Engineering Department, Stanford University.
- [6] Wang, Q., and Squires, K., 1996, "Large Eddy Simulation of Particle-Laden Turbulent Channel Flow," *Phys. Fluids*, **8**, pp. 1207–1223.
- [7] Yamamoto, Y., Potthoff, M., Tanaka, T., Kajishima, T., and Tsuji, Y., 2001, "Large-Eddy Simulation of Turbulent Gas-particle Flow in a Vertical Channel: Effect of considering Inter-Particle Collisions," *J. Fluid Mech.*, **442**, pp. 303–334.
- [8] Perry, A. E., Schofield, W. H., and Joubert, P. N., 1969, "Rough-Wall Turbulent Boundary Layers," *J. Fluid Mech.*, **37**, pp. 383–413.
- [9] Perry, A. E., Lim, K. L., and Henbest, S. M., 1987, "An Experimental Study of the Turbulence Structure in Smooth and Rough-Wall Boundary Layers," *J. Fluid Mech.*, **177**, pp. 437–466.
- [10] Raupach, M. R., Antonia, R. A., and Rajagopalan, S., 1991, "Rough-wall Turbulent Boundary Layers," *Appl. Mech. Rev.*, **37**, pp. 383–413.
- [11] Krogstad, P. A., Antonia, R. A., and Browne, L. W. B., 1992, "Comparisons Between Rough and Smooth Wall Turbulent Boundary Layers," *J. Fluid Mech.*, **245**, pp. 599–617.
- [12] Kussin, J., and Sommerfeld, M., 2002, "Experimental Studies on Particle Behaviour and Turbulence Modification in Horizontal Channel with Different Wall Roughness," *Exp. Fluids*, **33**, pp. 143–159.
- [13] Tanaka, M., Maeda, Y., and Hagiwara, Y., 2002, "Turbulence Modification in a Homogeneous Turbulent Shear Flow Laden with Small Heavy Particles," *Int. J. Heat Fluid Flow*, **23**, pp. 615–626.
- [14] Benson, M., 2003, "The Effects of Wall Roughness on the Particle Velocity Field in a Fully-Developed Channel Flow," Engineer thesis, Stanford University, Stanford, California, 94305.
- [15] Hussain, A., and Reynolds, W., 1975, "Measurements in a Fully Developed Turbulent Channel Flow," *Trans. ASME*, **Dec.**, pp. 558–580.
- [16] Varaskin, A., Polezhaev, Y., and Polyakov, A., 2000, "Effect of Particle Concentration on Fluctuating Velocity of the Disperse Phase for Turbulent Pipe Flow," *Int. J. Heat Fluid Flow*, **21**, pp. 562–567.
- [17] Li, Y., and McLaughlin, J. B., 2001, "Numerical Simulation of Particle-Laden Turbulent Channel Flow," *Phys. Fluids*, **13**, pp. 2957–2967.
- [18] Boree, J., Ishima, T., and Flour, I., 2001, "The Effect of Mass Loading and Inter-Particle Collisions on the Development of the Polydispersed Two-Phase Flow Downstream of a Confined Bluff Body," *J. Fluid Mech.*, **443**, pp. 129–165.
- [19] Sheen, H., Chang, Y., and Chiang, Y., 1993, "Two-Dimensional Measurements of Flow Structure in a Two-Phase Vertical Pipe Flow," *Proc. Natl. Sci. Council, Repub. China, Part A: Appl. Sci.*, **17**, pp. 200–213.
- [20] Bendat, J., and Piersol, A., 2000, *Random Data Analysis and Measurement Procedures*, Wiley Interscience, New York.
- [21] Coleman, H., and Steele, W., 1989, *Experimentation and Uncertainty Analysis for Engineers*, Wiley, New York.

# Wind-Driven Rivulet Breakoff and Droplet Flows in Microgravity and Terrestrial-Gravity Conditions

G. McAlister

R. Ettema

J. S. Marshall

IHR—Hydroscience and Engineering, University of Iowa, Iowa City IA 52242

*A study is reported of the wind-driven breakoff of rivulets and subsequent droplet flows on a horizontal plate subject to different normal gravitational states, ranging from zero- to terrestrial-gravity conditions (1 g), and including some data for partial gravity conditions (between 0.1 g and 0.38 g). The study entailed experiments conducted in the authors' laboratory at the University of Iowa and onboard the NASA KC-135, parabolic-flight aircraft. The wind-driven rivulets exhibited a breakoff phenomenon over a broad range of flow rates, in which a "head" at the tip of the rivulet broke off periodically to form a droplet that advected down the plate. The rivulet breakoff phenomena was sensitive to the normal gravitational force acting on the plate. For instance, the frequency of rivulet breakoff was nearly an order-of-magnitude greater for the 0 g condition than for the same flow in the 1 g condition. The droplet shape and behavior were observed to be quite different between the two cases. It was furthermore found in all cases examined that wind-driven rivulet and droplet flows are markedly different from gravitationally driven flows. These differences arise primarily from the role of form drag on the droplets and on the raised ridge of the rivulet and pool flows near the moving contact line. [DOI: 10.1115/1.1881696]*

## 1 Introduction

Wind-driven flows of liquid films on a substrate are a common occurrence in aerodynamics and various vehicular problems as well as in certain regimes of two-phase pipe and duct flows. In aerodynamics, water on an airplane wing can significantly affect the surface roughness and the subsequent wing drag and overall performance [1,2]. Under freezing conditions, the impact of supercooled water on the wing precedes ice accretion, where under glaze ice conditions the water remains on the wing in liquid form for some time until freezing occurs [3–5]. Water runoff on airplane wings is also a concern following implementation of anti-icing measures, such as local surface heating, in order to avoid reformation of ice deposits [6–8]. Visual obstruction due to wind-blown water on a windshield is, of course, a problem familiar to anyone who has ever ridden in an automobile during a rainstorm. In two-phase gas-liquid pipe flow, a decrease in the liquid flow rate from that typical of the annular-flow regime results in a flow regime in which the gas fills most of the pipe and the liquid is confined to rivulets and droplets along the pipe wall, which are carried forward by the gas flow [9]. Many of these applications occur in configurations where the substrate surface may be aligned in an arbitrary direction, thus varying the relative components of the normal and tangential gravitational force. Other applications, such as gas-liquid pipe flows, are of interest for space applications, where the gravitational force may be less than in terrestrial applications or even absent entirely.

The current paper reports an experimental study of wind-driven flow of a liquid rivulet on a horizontal substrate subject to various gravitational fields ranging from microgravity to terrestrial-gravity conditions. Experiments were conducted in the authors' laboratory and onboard the NASA KC-135 parabolic-flight aircraft to achieve a range of gravitational conditions. Scaling arguments are

presented, based on consideration of the forces acting on the rivulet and detached droplets, to motivate correlations that collapse the experimental data.

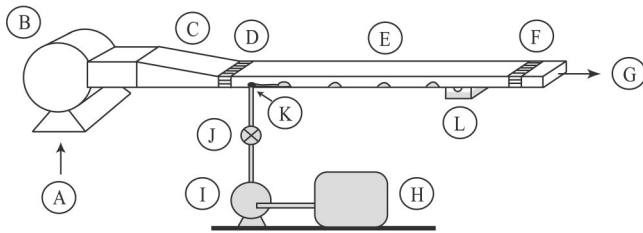
Previous experimental studies of rivulet flows focus on gravity-driven flows down inclined plates (e.g., [10]). Shear-driven rivulet flow has been examined from a computational and analytical viewpoint [5,11], but these studies employ various simplifying approximations (such as small interface slope, uniform interfacial shear stress, and steady flow), which introduce various limitations on the applicability of the model predictions. The recent paper by Myers, Liang, and Wetton [11] includes a stability analysis for splitting of shear-driven rivulets into multiple rivulets; however, this behavior was not observed in the flow regimes examined in the current study.

The current experimental study finds that wind-driven rivulets exhibit completely different behavior from that observed for gravity-driven rivulets on an inclined surface. In particular, whereas rivulets on an inclined surface progress through a series of regime changes, including droplet flow, straight rivulet, meandering steady rivulets, and oscillating rivulets, as the liquid flow rate or the plate inclination angle increases [10], wind-driven rivulets are dominated over a broad range of wind and liquid flow rates by the periodic breakoff of the rivulet tip to form a droplet, and by subsequent flow and interaction of the droplets downstream of the breakoff point. The difference between the wind- and gravity-driven rivulet flows appears to result primarily from the effects of form drag on the thicker region of the liquid film near the "head" of the rivulet.

A second general observation from the present study is that the wind-driven rivulet and droplet flows are highly sensitive to normal gravitational force. For instance, the rivulet breakoff frequency is significantly larger, up to an order of magnitude in some cases, for microgravity flows than it is for the same flow under terrestrial-gravity conditions. This difference is again coupled to the form drag and to the effect of normal gravitational force on the frontal area presented by the rivulet head region. The downstream droplet structure and dynamics are also qualitatively different for the microgravity and terrestrial-gravity conditions.

The experimental model and procedure is described in Sec. 2. Experimental results for the terrestrial (1 g) experiments are pre-

Contributed by the Fluids Engineering Division for publication in the JOURNAL OF FLUIDS ENGINEERING. Manuscript received by the Fluids Engineering Division April 13, 2004; revised manuscript received, August 23, 2004. Review conducted by J. Katz.



**Fig. 1 Sketch of the rivulet wind tunnel showing (A) air inlet, (B) blower, (C) contraction, (D) honeycomb, (E) test section, (F) honeycomb water trap, (G) air outlet, (H) collapsible water storage tank, (I) positive-displacement pump, (J) needle valve, (K) water inlet hole, and (L) water collection box.**

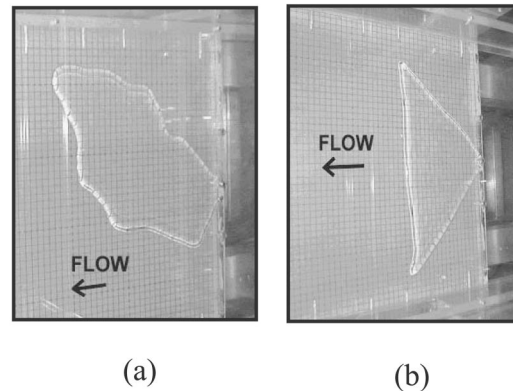
sented in Sec. 3, together with a simple model for the rivulet breakup period. Results for the microgravity and partial-gravity (between 0.1 g and 0.38 g) experiments are presented in Sec. 4. Conclusions are given in Sec. 5.

## 2 Experimental Setup

Experiments were conducted in the open-loop “rivulet wind-tunnel,” shown schematically in Fig. 1. The bottom surface of the rivulet wind tunnel consists of a flat Plexiglas sheet measuring 0.3 m wide and 1 m long. The top surface of the rivulet wind tunnel is another Plexiglas sheet mounted parallel to and at a distance of 0.05 m above the bottom surface. Airflow through these two surfaces was generated by a blower placed upstream of the channel formed by the Plexiglas plates. Blower speed is controlled by a voltage regulator. A honeycomb is placed inside the blower to help make the exit flow uniform. The maximum velocity that can be produced by the blower in the wind tunnel is 13 m/s. Wind speed was measured at different points over the width of the wind-tunnel exit using a Pitot tube and Rouse manometer. The root-mean-square variation in wind speed over the middle 75% of the wind-tunnel width measured about 2% of the mean speed.

Distilled water, used as the working fluid, is stored in a 3.8 l reservoir and pumped to the test surface using a positive-displacement pump. The liquid reservoir sides are flexible so as to allow the reservoir to collapse and avoid air or cavitation bubbles as the water is pumped out of the reservoir, which is desirable in the microgravity experiments. A positive-displacement pump is used because it is less affected by gravity than a centrifugal pump. Liquid flow rate is controlled using a precision needle valve. The liquid is injected into the test section through a 2 mm hole centered on the upstream end of the bottom Plexiglas surface of the rivulet wind tunnel. At the end of the test section, the liquid is collected in a trap through a slot in the bottom of the test surface, which is filled with a highly absorbent cloth material to capture the water. As additional measures to prevent liquid from escaping into the surroundings, a honeycomb is added at the end of the test section and a deflector shield is placed downwind of the honeycomb. The inner side of the deflector shield is covered with absorbent cloth to catch any remaining water droplets.

The microgravity experiments (zero and partial gravity) were conducted on four flights of the KC-135 aircraft, with about 40 parabolas per flight. Each parabola provided about 15 of usable microgravity conditions for testing. The test conditions were selected to provide data on as many different flow regimes as possible, and tests with each combination of wind and liquid flow conditions was repeated between three to five times in order to ensure repeatable data. The water flow was turned off between each parabola, but the airflow was left on in order to dry out the test section and clear it of residual water. The flow was filmed using digital video both from above the test section and from the side of the test section. The experimental procedure used for the terrestrial-gravity experiments was similar to that described above, with the difference that the experiment was allowed to run for a much longer period.



**Fig. 2 Photographs of experimental runs with low airflow rates: (a) large puddle spreading downstream for a very low wind speed case ( $U=4.5$  m/s); (b) fanshaped structure for a slightly higher wind speed case ( $U=6$  m/s). Both experiments are performed with a water flow rate of  $Q=5$  mL/min.**

Relative gravity data, obtained using an accelerometer, were provided by NASA. Although most tests were conducted for zero-gravity conditions, some tests were also performed for partial-gravity states, including 0.16, 0.25, and 0.38 g. The 0.16 and 0.38 g conditions correspond to the gravitational force on the Moon and on Mars, respectively.

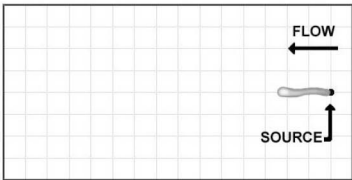
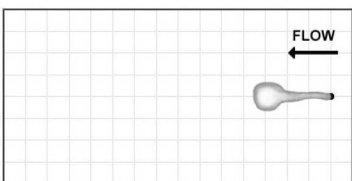
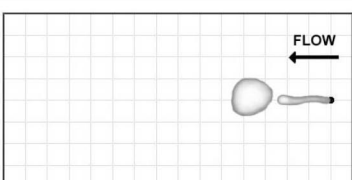
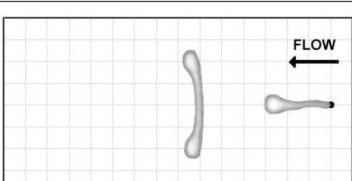
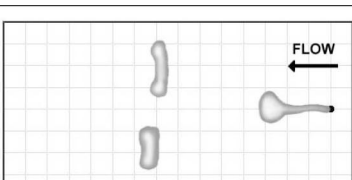
The wind speed was varied between about 7 and 12 m/s, and the width of the enlarged rivulet head (or the subsequent droplet after head detachment) varied between about 4 and 12 mm. Choosing nominal values for wind speed and droplet width of  $U=10$  m/s and  $d=8$  mm, respectively, the aerodynamic Reynolds number is  $Re=Ud/\nu_{\text{air}}=5300$ , the Weber number is  $We=\rho_{\text{air}}U^2d/\sigma=13$ , and the Bond number (in 1 g) is  $Bo=\rho_{\text{water}}gd^2/\sigma=8.6$ . For Weber and Bond numbers in this range we would expect the inertial deformation and gravitational flattening of the rivulet head and droplets to both be significant.

This flow exhibited a natural variability associated with the effect of contact angle hysteresis on the rivulet and droplet conditions. The uncertainty due to this natural flow variability is, in nearly all cases, larger than the measurement uncertainty. Details of the data uncertainty in 1 g are given in Sec. 3, which describes the specific data measured. A comprehensive uncertainty analysis was more difficult to perform for the microgravity experiments conducted on the NASA KC-135 parabolic-flight aircraft due to the limited number and short duration of the tests, particularly for the partial-gravity conditions. Checks on the performance of the experimental apparatus indicate that similar accuracies of control and measurement existed for the microgravity conditions as for the terrestrial-gravity conditions. The uncertainty in averages reported for aspects of the flow exhibiting natural variability were higher in microgravity than in 1 g, however, due to the necessity of having fewer test results over which to average the data.

## 3 Terrestrial-Gravity Results

Rivulet flow experiments under terrestrial gravity (1 g) were initially conducted for a progression of wind velocity conditions with a fixed water flow rate. At the extreme condition of zero airflow, a circular puddle of water formed and spread laterally from the inlet. For small airflow rates ( $\leq 4$  m/s) the puddle still spread from the inlet, but began to distort in shape and shift downstream of the water inlet point (Fig. 2(a)). As the wind speed increased to about 6 m/s, the water fanned out as a sheet whose width increased in a nearly linear manner with downstream distance (Fig. 2(b)), and with an approximately straight leading edge. With further increase in airflow rate, the fan angle decreased until, at about 7 m/s, a nearly straight rivulet protruded from the source location.



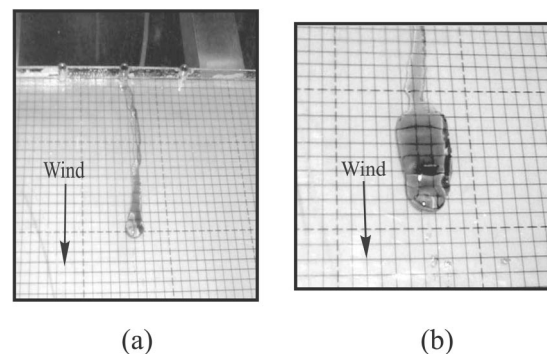
Plan View of Process	Comments
	Water comes out of the inlet hole and forms immediately into a rivulet which begins progressing downstream.
	The rivulet progression stalls and the head of the rivulet begins to increase in size as it is fed by water flowing through the rivulet.
	Aerodynamic load on the head becomes great enough to pull it away from the rivulet, forming a detached droplet.
	The droplet elongates in the direction normal to the flow forming a roller. The roller gradually elongates and stretches in the middle.
	The roller bifurcates in the middle into two smaller and slower-moving droplets, which quickly develop into smaller rollers.

**Fig. 3 Typical sequence of droplet detachment and roller development and bifurcation for the terrestrial gravity experiments**

**3.1 Rivulet Head Breakoff.** Concurrent with development of a straight rivulet emitting from the source outlet, a cyclic process occurred in which the head region at the end of the rivulet periodically broke from the rivulet and advected downstream as a detached droplet. A schematic diagram illustrating the different stages of this process is shown in Fig. 3. In the first stage of this process, water emitted from the source as a nearly straight rivulet. After a short distance, the head of the rivulet stopped progressing downstream and began to enlarge in a pool-like shape with a raised ridge at its downstream edge. After a certain time, the head broke from the rivulet to form a detached droplet.

The structure of the rivulet head close to the point of breakoff is shown in the photographs in Fig. 4. The structure close to the point of breakoff changed depending on the water and air flow rates. For some cases, such as that shown in Fig. 4, the head elongated more in the downstream direction, whereas for low flow rates the head formed a broad pool and developed a ridge of raised fluid along its downstream edge. The period of rivulet breakoff is plotted in Fig. 5(a) as a function of airflow rate for different water discharge rates. The breakoff period decreased with increase in airflow rate because higher airflow velocity caused greater drag on the rivulet head, thus requiring the head to achieve a smaller critical size at the breakoff condition. The breakoff period also decreased as the water flow rate increased, due to the fact that the

rivulet head grew faster at higher water flow rates. All breakoff period measurements are based on an average of ten measurements. The precision error of the time measurements is  $\pm 0.5$  s;



**Fig. 4 Photographs showing breakoff of a rivulet head to form a droplet in 1 g, including (a) the rivulet at a time where it has stopped progressing and is beginning to form a large head, and (b) close-up of the head about to detach from the rivulet. Grid lines have a spacing of 6 mm.**

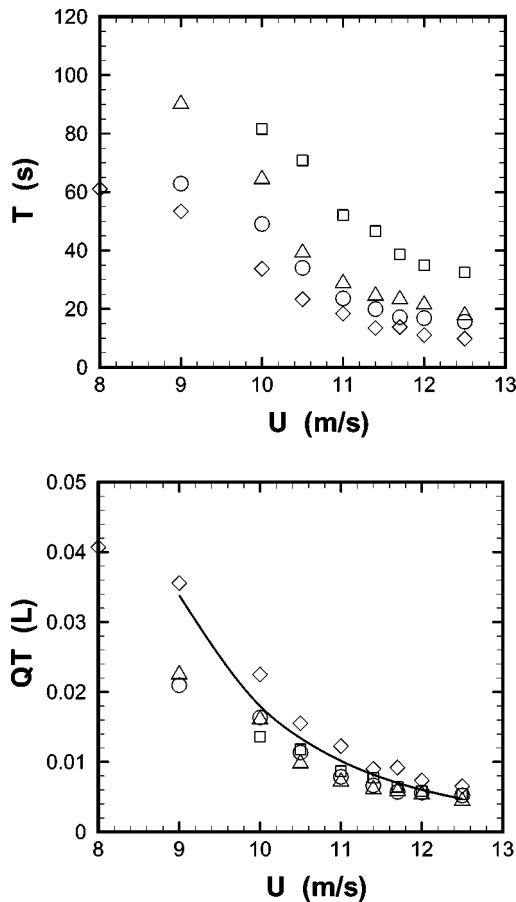


Fig. 5 Data for (a) rivulet breakup period  $T$  and (b) product of  $T$  and the water flow rate  $Q$  versus air speed  $U$  for the terrestrial gravity (1 g) case, for values of water flow rate of  $Q = 10$  ml/min (squares), 15 ml/min (triangles), 20 ml/min (circles), and 40 ml/min (diamonds). The solid line is the theoretical prediction from Eq. (6) for  $C=0.5$ .

however, the data uncertainty is controlled by the natural flow variability in rivulet breakup, which fluctuates with a standard deviation of about 20% of the mean breakup period.

The breakup of the droplet at the end of the rivulet is resisted by surface tension forces acting at the contact line due to the difference between the advancing and receding contact angles [12]. This effect has been utilized by several investigators to examine the critical condition for a droplet to stick to an inclined surface and to find the terminal velocity of droplets flowing down an inclined surface [13–17]. As the aerodynamic drag attempting to drive the stationary rivulet head forward increased, the receding and advancing contact angles approached their limiting values at zero velocity. The surface tension force thus has a maximum value, which occurs when the two contact angles have reached their limiting values, and if the driving aerodynamic exceeds this maximum value, then the rivulet head will detach from the rivulet and move forward as a droplet.

To motivate estimates for scaling the experimental data with different parameters, a simplified model for rivulet head breakup is introduced based on consideration of the different forces acting on the rivulet head. The driving force on the rivulet head is the aerodynamic drag, which is resisted by surface tension force acting along the contact line with the substrate. Close to the breakup point, the cross-sectional area of the rivulet head is much larger than that of the feeding rivulet, so the effect of the rivulet on the aerodynamic and surface tension forces on the rivulet head are neglected. For estimation of the aerodynamic force, the rivulet head is approxi-

mated as a semi-ellipsoid with semi-axis lengths  $h$  (the maximum water depth),  $b$  and  $a$ , where the latter two quantities represent, respectively, the semi-minor and semi-major axes of the elliptical area covered by the head on the substrate surface. Letting the air speed and density be denoted by  $U$  and  $\rho$ , respectively, the aerodynamic drag on the rivulet head has the form

$$F_D = \frac{1}{2} \rho U^2 \left( \frac{\pi}{2} bh \right) C_D \quad (1)$$

In Eq. (1),  $(\pi/2)bh$  is the frontal area of the rivulet head and  $C_D$  is the aerodynamic drag coefficient. We have performed numerical computations that indicate that the drag coefficient  $C_D$  for flow past a rigid hemisphere lying on a flat surface is nearly constant at a value of 0.6 for the range of the Reynolds number used in the experiments; for the current argument, it is sufficient to assume that  $C_D$  is constant.

The surface tension force on the rivulet head is approximated by

$$F_S = 2b\sigma(\cos \theta_{R,0} - \cos \theta_{A,0}) \quad (2)$$

where  $\sigma$  is the surface tension coefficient and  $\theta_{A,0}$  and  $\theta_{R,0}$  are the limits of the advancing and receding contact angles as the contact line velocity approaches zero. In writing (2), the contact angle force is projected in the streamwise direction under the simplification that the contact angle remains fixed at  $\theta_{A,0}$  all along the downstream contact line of the head and at  $\theta_{R,0}$  all along the upstream contact line. The feeding rivulet is again neglected due to its small width relative to that of the head. The transition from the advancing to the receding contact angle occurs on the sides of the head, where the projection of the contact angle force in the streamwise direction is small.

Equating the forces in (1) and (2) yields an expression for the critical water depth  $h_{crit}$  within the rivulet head for occurrence of breakup as

$$h_{crit} = \frac{8\sigma}{\pi\rho U^2 C_D} (\cos \theta_{R,0} - \cos \theta_{A,0}) \quad (3)$$

The rivulet head is continuously filled by the water flow through the rivulet until the head reaches a critical volume given by

$$V_{crit} = \frac{2\pi}{3} b_{crit} a_{crit} h_{crit} \quad (4)$$

where  $h_{crit}$  is the critical depth given by (3). The width  $2b$  and length  $2a$  of the rivulet head are functions of the depth  $h$ , as well as the water and airflow rates and the gravitational state. For instance, in zero gravity the rivulet head has a nearly hemispherical shape, so  $a \approx b \approx h$ . In terrestrial gravity experiments, the length of the rivulet head tends to be much greater than  $h$  as indicated in Fig. 4(b).

The rivulet breakup period  $T$  is the length of time required for the volume of the rivulet head to grow to the critical value (4), such that

$$QT = V_{crit}, \quad (5)$$

where  $Q$  is the liquid flow rate. If  $V_{crit}$  is assumed independent of  $Q$ , which implies that the head width is independent of  $Q$ , then the result (5) implies that the rivulet breakup period will be inversely proportional to the liquid flow rate. Substituting (3) and (4) into (5) and assuming that the rivulet head width and length are proportional to its height  $h$ , the rivulet head breakup period  $T$  is

$$T = \frac{2\pi}{3Q} \left( \frac{8\sigma}{\pi\rho U^2 C_D} \right)^3 \quad (6)$$

where the constant  $C = (a_{crit} b_{crit} / h_{crit}^2) (\cos \theta_{R,0} - \cos \theta_{A,0})^3$  depends both on the advancing and retreating contact angles and on the rivulet head shape. As suggested by the result (6), Fig. 5(b) shows that all of the experimental data for the rivulet breakup period can

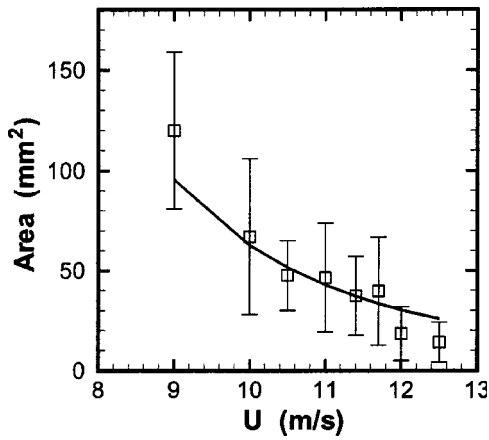


Fig. 6 Average substrate surface area covered by rivulet head at time of breakoff versus air speed for terrestrial gravity experiments. Error bars indicate the standard deviation of the data. The curve represents the theoretical prediction from Eq. (7) with  $D=3$ .

be collapsed onto one curve by plotting  $QT$  as a function of  $U$ . The expression (6) infers a data correlation of the form  $QT = \text{const} \times U^{-6}$ , which is shown in Fig. 5(b) to be in good agreement with the experimental data for 1 g flow.

The average area occupied on the substrate surface by the rivulet head at the time of breakoff is plotted in Fig. 6 as a function of the air speed. As expected, the critical head area at breakoff decreased with increase in air speed and exhibited negligible dependence on water flow rate. The error bars plotted on the data in Fig. 6 indicate the standard deviation in the measured head area, which results from natural flow variability. For low air speeds, the period of rivulet breakoff became large and the breakoff time and droplet area exhibited significantly more variability than for cases with higher air speed. An estimate for area of the rivulet head at breakoff can be obtained from the expression (3) by assuming that the area covered by the head on the substrate surface is proportional to  $\pi h_{\text{crit}}^2$ , such that

$$A_{\text{crit}} = \pi D \left( \frac{8\sigma}{\pi \rho U^2 C_D} \right)^2 \quad (7)$$

where the constant  $D$  depends only on contact angle and droplet shape. The prediction from (7) suggests a correlation of the form

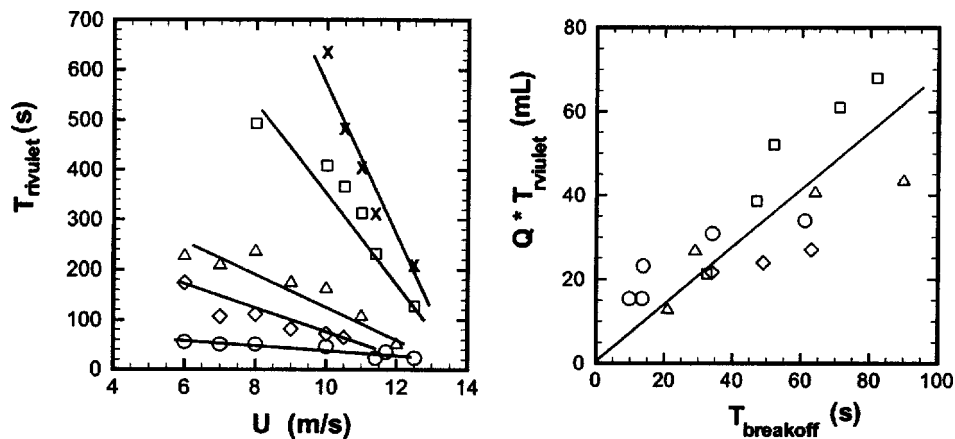
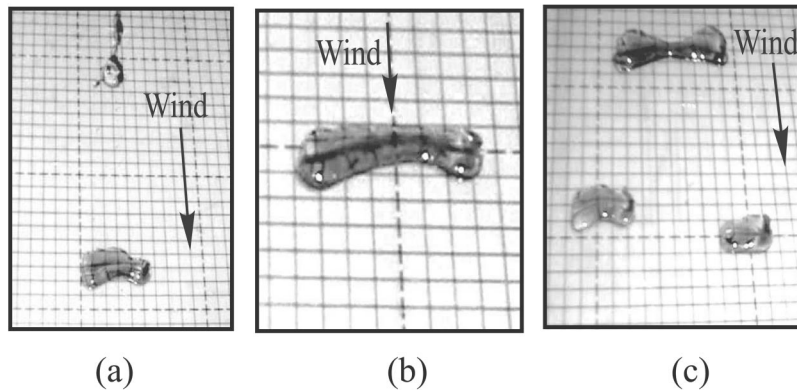


Fig. 7 (a) Average time  $T_{\text{rivulet}}$  for attached rivulet head to progress 300 mm downstream from the inlet versus air speed  $U$  for the terrestrial gravity experiments, with water flow rates  $Q=5$  ml/min (crosses), 10 ml/min (squares), 15 ml/min (triangles), 20 ml/min (circles), and 40 ml/min (diamonds). The lines are best fit to the data. (b) Correlation, showing all data, obtained by plotting as a function of rivulet breakoff period.

$A_{\text{crit}} = \text{const} \times U^{-4}$ . A data fit based on this scaling is plotted in Fig. 6 and shown to lie within the data uncertainty.

Over many cycles of rivulet head breakoff, we observe a slow creep of the location of the attached rivulet head down the test section. This downstream motion is observed to occur through a series of short discrete downstream motions of the rivulet coinciding with breakoff of the rivulet head. Two mechanisms act to aid downstream rivulet motion. In the first mechanism, the head imparts a downstream force on the feeder rivulet via surface tension at the rivulet-head attachment point, acting to drag the feeder rivulet some distance downstream as the head moves forward under the aerodynamic force. In the second mechanism, the detaching head wets the surface directly in front of the feeder rivulet, making it easier for the rivulet to move downstream. The average time for the rivulet head to progress a distance of 300 mm downstream from the source  $T_{\text{rivulet}}$  is plotted as a function of air speed for different liquid flow rates in Fig. 7(a). Because the rivulet progresses downstream only during head breakoff, the time required for the rivulet to progress a fixed distance increases as the breakoff period increases. It is shown in Fig. 7(b) that the data for rivulet creep can be collapsed by plotting  $QT_{\text{rivulet}}$  as a function of the head breakoff period  $T_{\text{breakoff}}$ . The approximately linear relationship between  $QT_{\text{rivulet}}$  and  $T_{\text{breakoff}}$  exhibited in Fig. 7(b) suggests that the rivulet springs forward by an approximately constant distance each time that the rivulet head detaches from the rivulet. Since the breakoff period decreases with increase in air speed and water discharge rate (Fig. 5), the time required for the rivulet to progress a fixed downstream distance correspondingly decreases with increase in air or liquid flow rates, as indicated in Fig. 7(a).

**3.2 Droplet Flows.** Following breakoff of the head from the rivulet, the droplet formed by the detached head rapidly elongated in the lateral direction to form a “roller” droplet. Roller formation shortly downstream of the rivulet breakoff point is shown in Fig. 8(a), and the close-up structure of the roller is shown in Fig. 8(b). The roller structure is typified by two “lobes” located on either side of the roller and has a thinner middle section. The roller is typically somewhat curved with the lobes positioned slightly downstream of the middle, due to their larger aerodynamic profile. As the roller moved downstream, it continued to elongate until a point is reached at which it bifurcated into two droplets. These offspring droplets typically continued to move downstream, although at a smaller velocity than the parent roller, and may themselves elongate to form smaller rollers. In some cases, the offspring droplets are so small that they remain fixed to the surface



**Fig. 8** Examples of downstream-propagating rollers on a horizontal surface in 1 g: (a) droplet forming a roller shortly after breakoff from rivulet, (b) close-up view of the elongated, double-lobed structure of the roller, and (c) a larger roller overtaking two smaller droplets ( $Q=15$  ml/min,  $U=11$  m/s). Grid lines have a spacing of 6 mm.

without forward movement.

In general, larger droplets have greater aerodynamic drag and therefore travel faster than smaller droplets. Because of the process of roller bifurcation, there exists sufficiently far downstream of the source a large diversity of droplet sizes and speeds. This situation gives rise to the occurrence of frequent droplet collisions, in which a larger droplet will overtake and collide with a smaller droplet. A snapshot of such a situation is shown in Fig. 8(c), where a large roller lies just upstream of two smaller droplets. Just before this photograph was taken, a roller eddy bifurcated to produce the two smaller droplets, which traveled at a slower velocity than the original roller eddy. The large second roller is moving up behind the two smaller droplets and collides with the smaller droplets just after the photograph was taken. Upon collision, the droplets coalesced, forming a single larger droplet that continued moving downstream at a yet more rapid speed. This larger droplet gradually elongated and bifurcated, providing smaller droplets and repeating the cycle. The resulting droplet flow sufficiently far downstream of the rivulet injection point was dominated by series of droplet collision, elongation, and bifurcation events that appeared to occur in a random manner.

The droplet velocity depends on the air speed and droplet size, and to a lesser extent the droplet shape. While each droplet has an approximately constant velocity, the different sizes of droplets in the 1 g experiments, caused by repeated bifurcation and collision events, led to a wide variation of droplet velocity at a given downstream location. The velocity of the initial droplet formed by breakoff of the rivulet head (prior to any bifurcation or collision events) is plotted in Fig. 9 (for all liquid flow rates) as a function of air speed. The error bars in this plot represent the standard deviation of the data. Over the range of air speeds considered, the median droplet velocity increases approximately linearly with the air speed, with a slope of about 0.006. There is little or no droplet motion observed for air speeds less than 7 m/s.

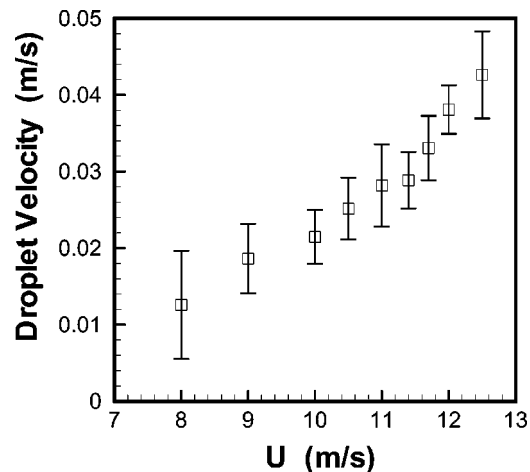
For air speeds between 7 and 10 m/s, the droplets generated by periodic breakoff of the rivulet head did not typically develop into rollers, but instead maintained a shape covering a nearly circular region of the substrate surface. At high air speeds,  $>12.5$  m/s, the separated droplets developed into rollers, but the droplets were significantly smaller than for the lower air-speed cases (see Fig. 6) and the rollers did not tend to undergo bifurcation. The generally low occurrence of roller bifurcation for high air speeds is due to the stronger effect of surface tension for these smaller size droplets. The average number of droplet bifurcations and collisions as a function of airflow rate is plotted in Fig. 10(a) and 10(b). While there is a lot of scatter in these data, we observe a specific range of airflow rates, ranging from about 10 to 12.5 m/s, over which

the flow most actively exhibits development of rollers that bifurcate and subsequently collide with other droplets. For airflow rates both higher and lower than this range, the droplet velocity is more uniform and collision of droplets is less frequent.

#### 4 Zero-Gravity and Partial-Gravity Results

**4.1 Zero-Gravity Flows.** In the terrestrial-gravity experiments described above, the normal gravitational force caused the rivulet head to expand primarily along the substrate surface, such that at the detachment point the water depth was significantly lower than the head length and width. In the zero-gravity experiments, the absence of gravitational force allowed the rivulet head shape to be set primarily by surface tension, which lead to a nearly hemispherical shape. This difference in rivulet head shape significantly increased form drag on the microgravity rivulet, in comparison to a terrestrial gravity case with the same air and water flow rates, which profoundly altered the subsequent flow behavior.

The sequence of rivulet breakoff and droplet flow for the zero-gravity cases is described in Fig. 11. A rivulet is emitted from the source, carrying the water downstream. The cross-sectional shape of the rivulet is nearly semi-cylindrical for the zero-gravity ex-



**Fig. 9** Average velocity of initial droplet versus air speed  $U$  for data with all water flow rates for the terrestrial gravity experiments. The error bars indicate the first quartile of velocity measurement around the mean.

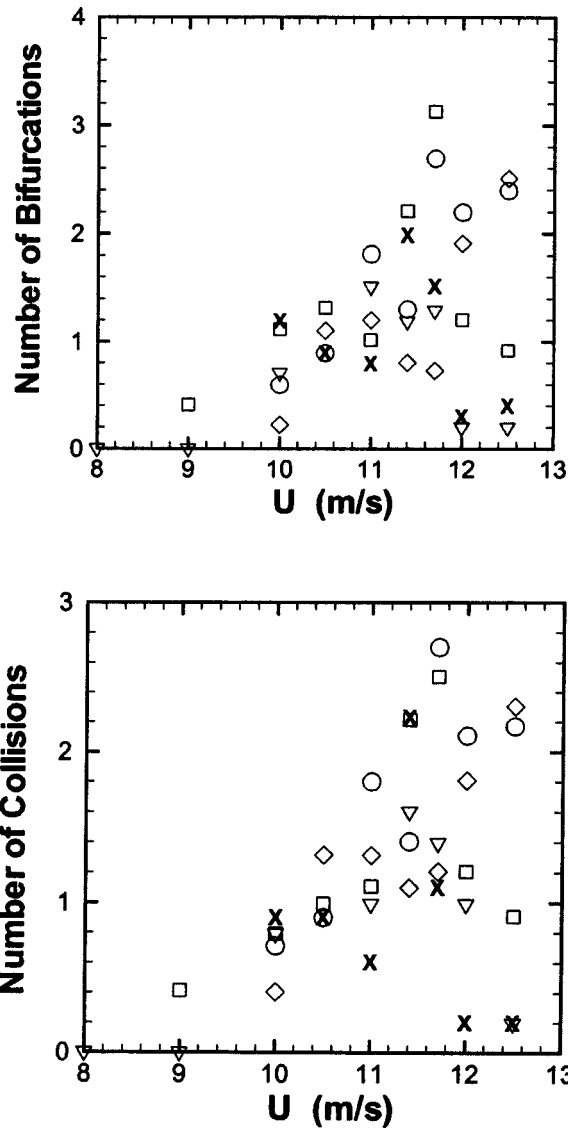


Fig. 10 Graphs of droplet bifurcations and collisions for the terrestrial gravity experiments, showing average number of times a single droplet (a) bifurcates and (b) collides with another droplet as it traverses the test surface for cases with water flow rate  $Q=5$  ml/min (crosses), 10 ml/min (squares), 15 ml/min (triangles), 20 ml/min (circles), and 40 ml/min (diamonds)

periments, whereas the rivulet is more flattened in the 1 g experiments. As in the 1 g experiments, the rivulet head stalls after a fairly short distance, after which point the head grows due to water delivered through the rivulet from the inlet. As it increases in size, the rivulet head maintains a nearly hemispherical shape. When the aerodynamic drag on the rivulet head becomes sufficiently large, the head detaches from the rivulet to form a droplet, which propagates downstream with nearly constant speed.

One of the most prominent differences between the zero and terrestrial-gravity experiments is that the rivulet breakoff frequency is nearly an order-of-magnitude greater in zero-gravity than for the same airflow and water flow rates in terrestrial gravity. The increase in breakoff frequency for the zero-gravity experiments is due to the increased form drag experienced by the rivulet head due to its elevated shape. The predictions from the scaling in Eq. (6) is indicated by the three curves in Fig. 12, corresponding to air speeds of  $U=10, 11,$  and  $12$  m/s, from bottom to top in the figure. These predictions are obtained using a value of 0.05 for the coef-

ficient  $C$  in (6), which is an order-of-magnitude smaller than the value of the coefficient in the 1 g experiments. The difference in value of  $C$  results from the fact that the rivulet head is more nearly hemispherical for the microgravity experiments, and so the ratios  $a_{\text{crit}}/h_{\text{crit}}$  and  $b_{\text{crit}}/h_{\text{crit}}$  occurring in the definition of  $C$  are much smaller than in the 1 g experiments. The experimental data exhibit much greater scatter than for the 1 g experiments, which is likely due to the noisy environment on-board the KC-135 and the greater uncertainty consequent to fewer experimental repetitions.

A plot of the maximum height of the rivulet head at the breakoff point is given in Fig. 13 as a function of airflow speed. As expected, the critical height at breakoff decreases with increase in air speed and is approximately independent of water flow rate. The result (3) yields the estimate

$$h_{\text{crit}} = \frac{8\sigma}{\pi \rho U^2 C_D} A \quad (8)$$

The scaling estimate  $h_{\text{crit}} = \text{const} \times U^{-2}$  is plotted in Fig. 13, with the empirical constant in (8) chosen as  $A=3.7$ . This prediction falls within the data scatter, although the best-fit curve to the data seems to vary more sensitively with air speed  $U$ .

In contrast to the terrestrial-gravity experiments, the detached droplets do not form rollers in the zero-gravity experiments, but instead retain an approximately hemispherical shape. The typical droplet shape is shown in a photograph in Fig. 14, where we observe two droplets that have broken off the rivulet and are propagating downstream and one droplet on the right-hand side of the figure that is just about to detach from the rivulet. Figure 15 shows the average droplet velocity for different air speeds and water flow rates. Droplets did not bifurcate in the zero-gravity experiments, and all droplets observed in a given experiment have fairly uniform size and velocity. The absence of strong velocity differences makes the occurrence of droplet collisions for the microgravity cases very rare.

Sometimes as the droplet progressed downstream, a tail of fluid formed behind the droplet's trailing edge. This tail occurred with high wind speed, was quite stable, and did not separate from the droplet. An interesting phenomenon involving this droplet tail arose when the droplet momentarily stalled on the test surface, which we refer to as "inchworm motion" due to its similarity with the motion of an inchworm. The various steps of the inchworm phenomenon are illustrated in Fig. 16, which first shows a droplet with a tail propagating on the substrate surface. The onset of the inchworm motion is typified by elongation and flattening of the front lobe of the droplet. Transport of water from the flattened front lobe into the tail section leads to formation of a large rear lobe preceded by a small front lobe at the half-cycle point. The water from the tail then suddenly sashes back to the front lobe and the droplet simultaneously lurches forward. The inchworm motion was found to be more prevalent for higher wind speeds,  $>11$  m/s, and the inchworm cycle repeated several times before the droplet returned to a steadily propagating state. The period of oscillation for the inchworm oscillation varied between 0.6 and 1, and appeared not to be particularly sensitive to the airflow or water flow rates.

**4.2 Partial-Gravity Flows.** Tests were performed with several different partial-gravity states, with 0.16 g (lunar gravity), 0.25 g, and 0.38 g (Martian gravity), and for one controlled high-gravity maneuver with 1.5 g. The rivulet behavior at partial gravity exhibits aspects of that noted above for both 0 g and 1 g. Photographs showing the rivulet and droplet from the side view for 0.38 and 1.5 g are given in Fig. 17. For 0.38 g, the droplets were similar to those observed for 0 g (see Fig. 14), with the difference that the droplets and rivulet head are noticeably flattened. However, for the 1.5 g case, with nearly the same liquid- and airflow rates, the water flattened out on the substrate surface. The more streamlined, flattened shape of the rivulet head at 1.5 g exhibited reduced aerodynamic drag compared to the micrograv-

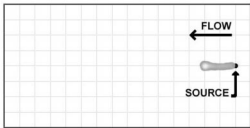
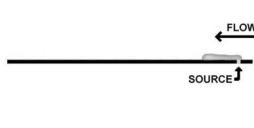
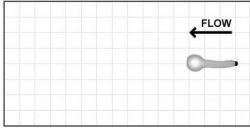

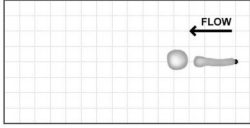

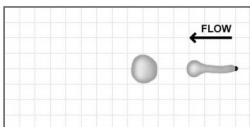

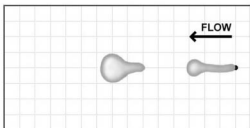

Plan View of Process	Side View of Process	Comments
		The water forms a rivulet as it exits the inlet and progresses downstream.
		As the rivulet stalls, the head increases in size. The head is approximately hemispherical.
		Aerodynamic load on the head is sufficient to overcome retarding forces and the head detaches to form a droplet.
		As the droplet progresses downstream, the water shifts slightly downstream.
		For some cases, the droplet forms a trailing tail.

Fig. 11 Typical sequence of rivulet head growth and detachment for microgravity case

ity case, and the head was not observed to break off during the period (lasting about 5) over which this enhanced gravitational state was maintained.

The rivulet breakoff period is plotted for several partial-gravity conditions in Fig. 18 as a function of water flow rate, with the air velocity maintained at 11 m/s. The shape of the curve is similar for all cases, but the breakoff period exhibits significant increase as the gravity is increased from 0 g to 0.38 g. The curves in Fig. 18 represent predictions of (6) using values for the coefficient  $C$

of 0.05, 0.07, 0.09, and 0.11. The partial-gravity data exhibit significant scatter about these curves due, at least in part, to the reduced-gravity experimental conditions.

The dynamics of the detached droplets over this range of partial-gravity conditions is similar to that observed for the microgravity state. Droplet elongation in the lateral direction, or formation of roller droplets, was not observed, nor were the droplets observed to bifurcate or collide with one another. As in the zero-

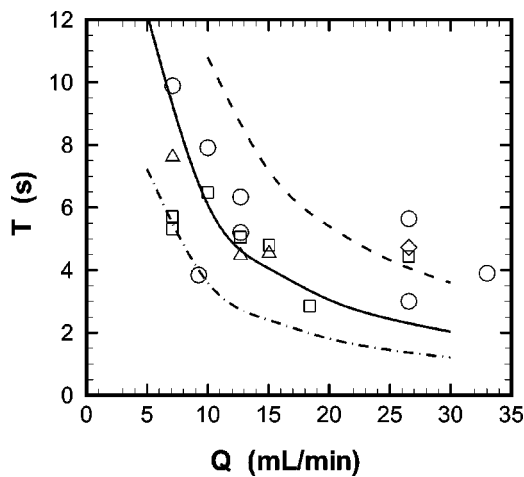


Fig. 12 Period of rivulet breakoff in microgravity versus the water discharge rate, for cases with  $Q=10.3$  ml/min (squares), 11.4 ml/min (triangles), 11.9 ml/min (circles), and 12.5 ml/min (diamonds). The curves give the theoretical predictions from Eq. (6) with  $C=0.05$  for  $U=10$  m/s (dashed), 11 m/s (solid) and 12 m/s (dashed-dotted).

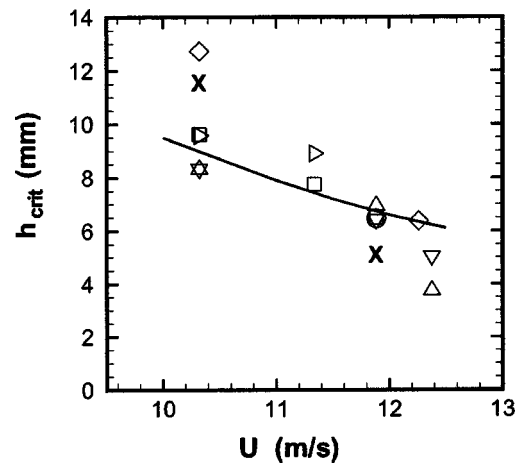


Fig. 13 The average height of the rivulet head at the breakoff time for all microgravity experiments, where  $Q=7$  ml/min (squares), 10 ml/min (triangles), 12.5 ml/min (gradients), 18.5 ml/min (right triangles), 26.5 ml/min (crosses), 33 ml/min (circles). The curve represents the theoretical prediction from Eq. (8) with  $A=3.7$ .

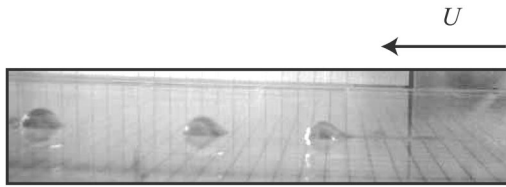


Fig. 14 Periodic shedding showing two nearly hemispherical droplets with a third about to break off from the end of the rivulet for microgravity case ( $Q=15$  mL/min,  $U=11.8$  m/s). Grid lines have a spacing of 6 mm.

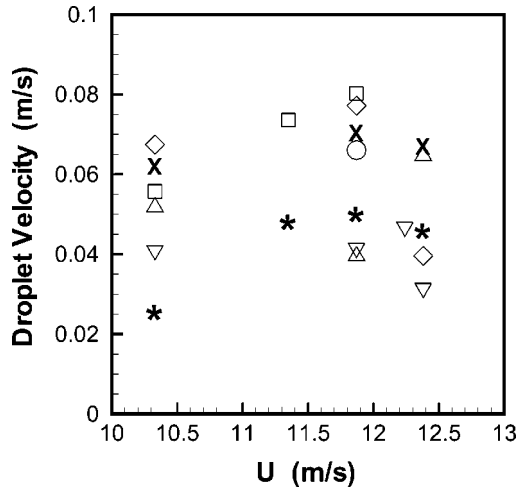


Fig. 15 Average droplet velocity versus air speed for the microgravity experiments, with  $Q=7$  ml/min (squares), 10 ml/min (triangles), 12.5 ml/min (gradients), 15 ml/min (asterisks), 18.5 ml/min (crosses), 26.5 ml/min (diamonds), and 33 ml/min (circles)

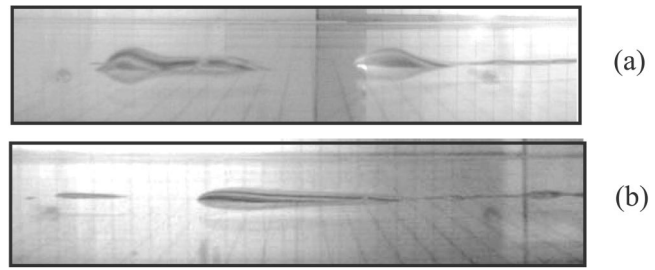


Fig. 17 Photographs of the rivulet head and detached droplets for (a) 0.38g ( $Q=10$  ml/min,  $U=11$  m/s) and (b) 1.5 g ( $Q=10$  ml/min,  $U=12.4$  m/s)

gravity tests, the droplets in these partial gravity states have a fairly uniform size and velocity in any given condition.

## 5 Conclusions

A study is reported of wind-driven rivulet breakoff and subsequent droplet flow on a horizontal surface under a variety of gravitational states, with particular focus on terrestrial-gravity (1 g) and microgravity (0 g) conditions. Large differences were observed between gravity-driven and wind-driven rivulet flows, in general, as well as between wind-driven rivulet flows under different gravitational conditions. In particular, whereas gravity-driven rivulet flows undergo a sequence of flow regimes, starting with droplet flow for small-plate inclination angles and progressing to straight rivulet flow, meandering rivulet flow, and oscillating rivulet flow as the plate inclination angle is increased, this same progression of flow regimes is not observed for wind-driven rivulet flows as the wind speed is increased. Rather, at very low wind speeds for terrestrial-gravity experiments an emitted rivulet on a horizontal plate soon forms a broad pool of liquid with slight downstream inclination. With increase in wind speed the pool adopts an interesting fan shape with nearly linear edges, where the

Plan View	Side View	Comments
		Typical zero-gravity droplet with small tail.
		The aerodynamic load on the main lobe the droplet pulls it along faster than the tail can move, creating a thin section in the middle.
		Water within droplet sloshes toward tail and droplet becomes flattened.
		Droplet forms a nearly hemispherical shape, but with most of the water in the upstream "tail" portion.
		Water sloshes back to downstream lobe, and droplet simultaneously lurches forward. The process then repeats.

Fig. 16 Typical sequence illustrating the inchworm phenomenon for microgravity droplet flows

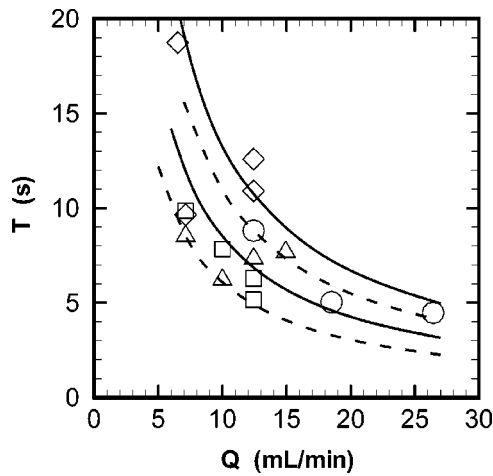


Fig. 18 Period of rivulet breakoff for partial-gravity cases as a function of water flow rate with air speed held constant at 11 m/s, for cases with 0 g (squares), 0.16 g (triangles), 0.26 g (circles), and 0.38 g (diamonds). Curves are predictions from Eq. (6) with  $C=0.05$  (lower dashed), 0.07 (upper dashed), and 0.11 (upper solid), respectively.

fan angle narrows with increase in wind speed to form a rivulet. However, the rivulet does not continue indefinitely downstream but is observed, in all cases examined, to break off into droplets after a fairly short distance. There is also a slow creep of the rivulet head downstream, where rivulet forward progression is observed to occur in steps that coincide with breakoff of the rivulet head. This rivulet breakoff regime is maintained for all higher wind speeds examined, although the dynamics of the droplets exhibits substantial variation with wind speed.

The same qualitative rivulet flow regimes are observed for the different gravitational states examined, ranging between 0 g and 1 g; however, the details of the rivulet behavior change dramatically with change in the gravitational acceleration. The most evident difference is the much smaller rivulet breakoff period, and the related smaller droplet size, as the gravitational acceleration is decreased. This decrease in breakoff period is related to the fact that under lower gravitational fields, the rivulet head has more of a raised, hemispherical shape, thus producing substantially larger form drag than the lower-profile head shape typical of higher gravitational fields. The resulting rivulet breakoff period is about an order-of-magnitude smaller for microgravity than for the terrestrial-gravity condition. A scaling argument developed by balancing form drag with surface tension force is shown to collapse the experimental data for rivulet breakoff period with different water flow rate and air speed with reasonably good accuracy for terrestrial-gravity conditions. For microgravity and partial-gravity conditions, the data exhibit great scatter about these scaling estimates, which is perhaps caused by the noisy environment onboard the KC-135 and by the greater measurement uncertainty associated with a more limited number of experimental repetitions.

The droplet dynamics downstream of the rivulet breakoff point also exhibit important differences with gravitational acceleration and with air speed. For the terrestrial gravity experiments, the droplets adopt a "roller" form, in which the droplet shape is extended in the cross-stream direction for air speeds above a critical value. There is a range of wind speeds for which these roller droplets gradually extend until they bifurcate to produce two smaller, slower-moving droplets. Droplet bifurcation creates a situation with a wide range of droplet sizes and speeds, leading to frequent droplet collisions. In this regime, the water does not pro-

ceed downstream in a single droplet, as is the case in other regimes, but rather in a stochastic sequence of droplet bifurcation and collision events.

Roller droplets and droplet bifurcation did not occur in the microgravity experiments. Instead, under certain conditions the microgravity droplets exhibit an interesting "inchworm" phenomenon, whereby the droplets progress forward in a periodic motion associated with forward and backward sloshing of the droplet mass, which appears much like the motion of an inchworm. In this inchworm motion, the droplets are stationary as the liquid mass oscillates upstream, but then they lurch forward as the liquid mass sloshes in the downstream direction. Under other conditions, the microgravity droplets progress downstream in a steady manner with a nearly hemispherical shape.

In future research, it would be of interest to repeat these experiments with several different liquids and substrate surfaces in order to better map the observed flow regimes in dimensionless parameter space. There are a number of phenomena observed for droplet flows, such as development and eventual bifurcation of roller droplets in 1 g, and the inchworm motion of microgravity droplets, which would benefit from more detailed study and modeling. It would also be of interest to examine cases where multiple rivulets are initiated at many positions on the substrate surface, such as would be the case for rivulets developing from droplet impact on a surface or from breakup of a liquid sheet.

### Acknowledgments

The authors wish to thank Charles Neiderhaus for his invaluable assistance during the microgravity experiments. Funding for this project was provided by the NASA Office of Biological and Physical Research under Grant No. NAG3-2368.

### References

- [1] Thompson, B. E., and Jang, J. 1996, "Aerodynamic Efficiency of Wings in Rain," *J. Aircr.* **33**(6), pp. 1047–1053.
- [2] Thompson, B. E., and Marrochello, M. R. 1999, "Rivulet Formation in Surface-Water Flow on an Airfoil in Rain," *AIAA J.* **37**(1), pp. 45–49.
- [3] Myers, T. G., Charpin, J. P. F., and Chapman, S. J. 2002, "The Flow and Solidification of a Thin Film on an Arbitrary Three-Dimensional Surface," *Phys. Fluids* **14**(8), pp. 2788–2803.
- [4] Myers, T. G., Charpin, J. P. F., and Thompson, C. P. 2002, "Slowly Accreting Ice Due to Supercooled Water Impacting on a Cold Surface," *Phys. Fluids* **14**(1), pp. 240–256.
- [5] Myers, T. G., and Thompson, C. P. 1998, "Modeling the Flow of Water on Aircraft in Icing Conditions," *AIAA J.* **36**(6), pp. 1010–1013.
- [6] Al-Khalil, K. M., Keith, Jr., T. G., and de Witt, K. J. 1993, "New Concept in Runback Water Modeling for Anti-Iced Aircraft Surfaces," *J. Aircr.* **30**(1), pp. 41–49.
- [7] Al-Khalil, K. M., Keith, Jr., T. G., and de Witt, K. J. 1994, "Development of an Improved Model for Runback Water on Aircraft Surfaces," *J. Aircr.* **31**(2), pp. 271–278.
- [8] Thomas, S. K., Cassoni, R. P., and MacArthur, C. D. 1996, "Aircraft Anti-Icing and De-Icing Techniques and Modelling," *J. Aircr.* **33**(5), pp. 841–854.
- [9] Hsu, Y.-Y. and Graham, R. W. 1976, *Transport Processes in Boiling and Two-Phase Systems*, Hemisphere, WA.
- [10] Schmuki, P., and Laso, M. 1990, "On the Stability of Rivulet Flow," *J. Fluid Mech.* **215**, pp. 125–143.
- [11] Myers, T. G., Liang, H. X., and Wetton, B. 2004, "The Stability and Flow of a Rivulet Driven by Interfacial Shear and Gravity," *Int. J. Non-Linear Mech.* **39**, pp. 1239–1249.
- [12] Dussan V, E. B. 1979, "On the Spreading of Liquids on Solid Surfaces: Static and Dynamic Contact Lines," *Annu. Rev. Fluid Mech.* **11**, pp. 371–400.
- [13] Dussan V, E. B. 1985 "On the Ability of Drops or Bubbles to Stick to Non-Horizontal Surfaces of Solids, Part 2. Small Drops or Bubbles Having Contact Angles of Arbitrary Size," *J. Fluid Mech.* **151**, pp. 1–20.
- [14] Dussan V, E. B., and Chow, R. T. P. 1983, "On the Ability of Drops or Bubbles to Stick to Non-Horizontal Surfaces of Solids," *J. Fluid Mech.* **137**, pp. 1–29.
- [15] Furmidge, C. G. L. 1962, "Studies at Phase Interfaces, I. The Sliding of Liquid Drops on Solid Surfaces and a Theory for Spray Retention," *J. Colloid Sci.* **17**, pp. 309–324.
- [16] Sultanovic, D., Bjerke, B., Rekestad, J., and Villalonga, K. A. 1997, "A Study of the Heat Transfer of Rivulet Flow on Inclined Plates," *Sol. Energy* **60**(3–4), pp. 221–227.
- [17] McAlister, G. 2003, "The Breakup of Sheet Flow to Rivulets and Rivulets to Droplets," M.S. thesis, University of Iowa, Iowa City.



# Numerical Study of Cavitation in Cryogenic Fluids

**Ashvin Hosangadi\***  
Principal Scientist

**Vineet Ahuja**  
Research Scientist

Combustion Research and  
Flow Technology, Inc.,  
Pipersville, PA 18947

*Numerical simulations of cavitation in liquid nitrogen and liquid hydrogen are presented; they represent a broader class of problems where the fluid is operating close to its critical temperature and thermal effects of cavitation are important. A compressible, multiphase formulation that accounts for the energy balance and variable thermodynamic properties of the fluid is described. Fundamental changes in the physical characteristics of the cavity when thermal effects become significant are identified; the cavity becomes more porous, the interface less distinct, and it shows increased spreading while getting shorter in length. The heat transfer model postulated in variants of the B-factor theory, where viscous thermal diffusion at the vapor-liquid interface governs the vaporization, is shown to be a poor approximation for cryogenic fluids. In contrast the results presented here indicate that the cavity is sustained by mass directly convecting into it and vaporization occurring as the liquid crosses the cavity interface. Parametric studies for flow over a hydrofoil are presented and compared with experimental data of Hord (1973, "Cavitation in Liquid Cryogenics II—Hydrofoil," NASA CR-2156); free-stream velocity is shown to be an independent parameter that affects the level of thermal depression.*

[DOI: 10.1115/1.1883238]

## 1 Introduction

Cavitation in cryogenic fluids generates substantial thermal effects and strong variations in fluid properties, which in turn alter the cavity characteristics. Understanding and quantifying these thermal effects are important for the design of liquid rocket turbomachinery systems that pump liquid hydrogen and liquid oxygen. Cryogenic fluid systems, however, are a subset of a broader class of problems (e.g., refrigerant systems, hot water systems such as boiler feed pumps, etc.) where the operating temperature is close to the critical temperature of the working fluid. Here, the distinction between boiling and cavitation becomes blurred and thermodynamic effects play an important role. At these operating temperatures, the ratio of liquid to vapor density is lower and consequently more liquid mass has to vaporize to sustain a cavity. Therefore evaporative cooling effects are more pronounced and result in the lowering of the mean fluid temperature in the cavitating region. Since the fluid thermodynamic properties (i.e., vapor pressure, density) are a strong function of temperature at these conditions, thermal effects suppress cavitation and lower the cavity pressure in a mean sense. Typically this results in improved mean performance of cryogenic pumps; liquid hydrogen systems being an extreme example where the pump may continue to generate head even when the fluid is boiling at the inlet. We note this is not necessarily the case when large scale flow unsteadiness is present since local temperature increases may enhance cavitation and cause flow instabilities.

To identify flow regimes where thermodynamic effects become important Brennen [2] defined two parameters:  $\Sigma(T)$  a thermodynamic parameter given by,  $\Sigma(T) = (\lambda^2 / TC_p \sqrt{\alpha_l})(\rho_v / \rho_l)^2$ , and a dynamic fluid parameter  $\Lambda$ , where  $\Lambda = \sqrt{U_\infty^2 \sigma / L}$ . Here,  $T$  is the local temperature of the fluid,  $\lambda$  is the latent heat of vaporization,  $\alpha_l$  is the liquid thermal diffusivity, and  $\rho_v$ ,  $\rho_l$  is the vapor and liquid density, respectively. Following Brennen [2], we can expect thermodynamic effects associated with boiling to dominate if  $\Sigma > \Lambda$ , and for convenience we can define a critical temperature  $T^*$ , at which  $\Sigma \approx \Lambda$ . This distinction, however, is qualitative and

for quantitative estimates of temperature and pressure depressions semiempirical correlations are required as described below.

The thermal effects of cavitation have been studied extensively by numerous researchers [1,3–6], among others. Stahl and Stepanoff [3] estimated head depression ( $\Delta H_v$ ) values due to thermodynamic effects using the so-called "B-factor" method based on a quasistatic theory where the temperature depression was estimated in terms of the ratio of the vapor volume to liquid volume taking part in the vaporization process. They provided a graph to evaluate (NPSH) corrections for hydrocarbons based on this methodology. However applying this theory was not simple since the B factor is an abstract quantity, similar to entropy in thermodynamics, and not easily estimated.

The B-factor theory was improved upon and made easier to use by Ruggeri and Moore [5] and later by Hord [1] who extended the model to include dynamic effects arising from fluid motion. They provided semiempirical correlations relating the B factor to a calibrated reference condition. An alternate but similar semiempirical procedure called the entrainment theory was given by Holl et al. [6] who directly correlated temperature depression to physical non-dimensional flow parameters. These theories postulated that the mass convection across the vapor-liquid interface was negligible and that thermal diffusion across the interface was the primary factor controlling the vaporization. Hence correlations based on Nusselt number estimates at the interface were derived and calibrated with experimental data for cavity pressure and temperature depressions. One of the key findings of our present study is that this diffusion controlled view of the cavitation process is not valid for cryogenic fluids. As we discuss later, the cavity appears to be sustained by the convection of liquid flowing across the vapor-liquid interface in the cryogenic case where the cavity spreads out substantially more and contains far less vapor than the corresponding cavity in cold water. This indicates that inviscid convective effects are more important than previously understood in the cryogenic flow regime and the rigorous treatment of "real" fluid properties essential for a correct representation of the physics.

Few numerical simulations of cavitating flows in cryogenic fluids, where thermal effects and fluid property variations have a substantial affect on the cavity development, have been reported. Cooper [7] presented simulations of liquid hydrogen pumps using a barotropic equation of state; here the energy equation was not solved but a nondimensional vaporization parameter was incorpo-

\*e-mail: hosangad@craft-tech.com

Contributed by the Fluids Engineering Division for publication in the JOURNAL OF FLUIDS ENGINEERING. Manuscript received by the Fluids Engineering Division January 20, 2004; revised manuscript received, August 15, 2004. Review conducted by G. Chahine.

rated into the barotropic equation of state to implicitly define pressure depressions due to thermal effects. Most of the recent works on numerical simulations of cavitating flows have not addressed the problem within a compressible framework and by definition neglect property variations within the liquid phase [8–10]. However, a detailed analysis of thermal damping effects on individual bubble dynamics have been reported by various researchers including Prosperetti [11], Matsumoto and Takemura [12], and Delale [13] among others. These fundamental studies analyze the impact of the heat transfer and bubble interface temperature on bubble growth and are an important component in the development of phase change models that interface with hydrodynamic formulations. However as the discussion here highlights, there is a need for more rigorous and generalized hydrodynamic frameworks to analyze extensive cavitation in “real” fluids.

The focus of this paper is on the development of a compressible framework that models generalized fluid properties over a broad range of temperatures and accounts for the thermal effects of cavitation. The vapor/liquid interface is captured as part of the solution framework and acoustic propagation in the multiphase mixture is modeled rigorously [14]. A detailed study of cavitation in liquid nitrogen and hydrogen is provided using the experiments of Hord [1] on a hydrofoil as a model problem; pressure and temperature measurements are used to validate the numerical results, and in turn numerical simulations are used to better understand the physical effects driving experimental observations. In particular, the role of variable fluid properties and thermal effects in altering the physical characteristics of the cavity is identified. These effects such as frothy cavitation zones and increased entrainment in cryogenic cavities have been observed experimentally but were not well understood. As mentioned earlier, we examine the validity of some of the key assumptions of the B-factor theory as well as the applicability of thermal equilibrium criteria for cavitation in cryogenic fluids. Since the cavitation process couples strongly with the temperature of the liquid, cavitation in cryogenic system presents a far richer spectrum of physics; parametric studies for a range of free-stream temperatures and velocities have been conducted to identify these effects.

## 2 Multiphase Equation System

The multiphase equation system is written in vector form as

$$\frac{\partial Q}{\partial t} + \frac{\partial E}{\partial x} + \frac{\partial F}{\partial y} + \frac{\partial G}{\partial z} = S + D_v \quad (1)$$

Here,  $Q$  is the vector of dependent variables,  $E$ ,  $F$ , and  $G$  are the flux vectors,  $S$  the source terms for the phase change, and  $D_v$  represents the viscous fluxes. The viscous fluxes are given by the standard compressible form of Navier-Stokes equations [15]. The vectors  $Q$ ,  $E$ , and  $S$  are given below with a detailed discussion on the details of the cavitation source terms to follow later

$$Q = \begin{pmatrix} \rho_m \\ \rho_m u \\ \rho_m v \\ \rho_m w \\ \rho_g \phi_g \\ \rho_m h_m \\ \rho_m k \\ \rho_m \varepsilon \end{pmatrix} \quad E = \begin{pmatrix} \rho_m u \\ \rho_m u^2 + P \\ \rho_m uv \\ \rho_m uw \\ \rho_g \phi_g u \\ \rho_m h_m u \\ \rho_m ku \\ \rho_m \varepsilon u \end{pmatrix} \quad S = \begin{pmatrix} 0 \\ 0 \\ 0 \\ 0 \\ m_t \\ m_t h_{fg} \\ S_k \\ S_\varepsilon \end{pmatrix} \quad (2)$$

The equations represented in the system above are in the following order in the vectors above: (1) mixture mass continuity; (2)–(4) mixture momentum (three components); (5) vapor phase mass conservation; (6) mixture energy; (7) turbulent kinetic energy, and (8) turbulent dissipation rate conservation. Here,  $\rho_m$  and  $h_m$  are the mixture density and sensible enthalpy, respectively, and  $\phi_g$  is the volume fraction or porosity of the vapor phase (note that the subscript  $g$ , as well as any references to a “gas” imply the vapor

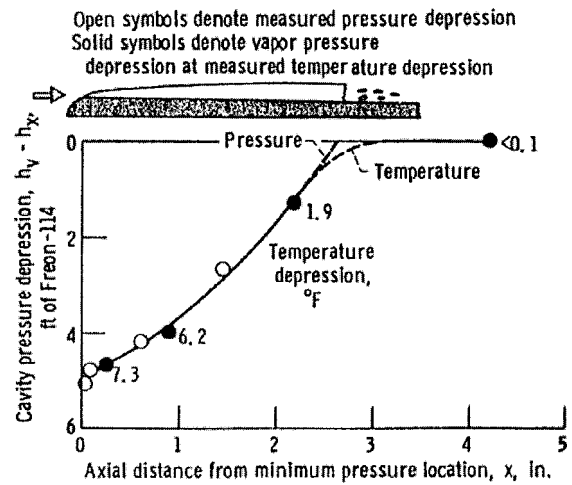


Fig. 1 Typical pressure and temperature depression within cavitating region for Freon-119 in a Venturi [Taken from [16]]

phase and not an additional noncondensable gas component). The mixture energy equation has been formulated with the assumption that the contribution of the pressure work on the mixture energy is negligible. The source term for the vapor phase arises due to cavitation where  $m_t$  is the net rate of vapor mass generation (or condensation), and the corresponding source term for the energy equation is given as  $m_t h_{fg}$  where  $h_{fg}$  is the change in enthalpy resulting from the phase change and is a function of the local fluid temperature. These phase change source terms are discussed further in Sec. 3.

The mixture density, enthalpy, and vapor porosity are related by the following relations locally in a given cell volume:

$$\rho_m = \rho_g \phi_g + \rho_L \phi_L \quad (3)$$

$$\rho_m h_m = \rho_g \phi_g h_g + \rho_L \phi_L h_L \quad (4)$$

$$1 = \phi_g + \phi_L \quad (5)$$

where  $\rho_g$ ,  $\rho_L$  are the physical material densities, while  $h_g$  and  $h_L$  are the sensible enthalpy of the vapor and liquid phase, respectively, and in general are functions of both the local temperature and pressure.

Thus far we have not made any statements defining the temperatures characterizing the liquid and vapor phases. In general, the liquid and vapor may not be in equilibrium locally and can have independent temperatures. Examination of temperature and pressure data for cavitation in Freon [16] (see Fig. 1) reveals that the saturation vapor pressure corresponding to the local fluid temperature in fact matches the local pressure measurement. This implies that the phase change process results in local thermodynamic equilibrium between the phases. The thermodynamic properties of the liquid and vapor in the cavity may now be defined by a single variable; the local saturation temperature  $T_{sat}$ . Hence, all thermodynamic properties (density, vapor pressure, viscosity, etc.) of both the liquid and the vapor phase may be generated as a tabular function of the saturation temperature. In our study here, these properties were generated from the standard thermodynamic database 12 available from National Institute of Standards and Technology (NIST) for pure fluids [17]. The thermodynamic properties of the fluid where specified using the saturation values from the table corresponding to the local temperature of the fluid.

The equation system as formulated in Eq. (1) is very stiff since the variations in density are much smaller than the corresponding changes in pressure. Therefore to devise an efficient and accurate numerical procedure we transform Eq. (1) to a pressure based form where we solve for pressure rather than density. An acoustically accurate two-phase form of Eq. (1) is first derived, fol-

lowed by a second step of time scaling or preconditioning to obtain a well-conditioned system. We begin by defining the acoustic form of density differential for the individual vapor and liquid phase as follows:

$$d\rho_g = \frac{1}{c_g^2} dP, \quad d\rho_l = \frac{1}{c_L^2} dP \quad (6)$$

Here  $c_g$  is the isothermal speed of sound  $(\partial P / \partial \rho_g)_T$  in the vapor phase, and  $c_L$  is the corresponding isothermal speed of sound in the liquid phase, which is a finite value. We note that in Eq. (6) the variation of the density with temperature has been neglected in the differential form for deriving the time-marching procedure. This assumption was made entirely for numerical convenience since it considerably simplifies the matrix algebra for the upwind flux formulation described later, at the potential expense of numerical stability in a time-marching procedure. However, more importantly, there is no impact on the accuracy since the fluid properties themselves are taken directly from the thermody-

amic data bank for each fluid based on the local temperature of the fluid which may change locally due to phase change.

Following the discussion above, the differential form of the mixture density  $\rho_m$  using Eq. (6) is written as

$$d\rho_m = (\rho_g - \rho_L) d\phi_g + \frac{1}{c_\phi^2} dP \quad (7)$$

$$\left( \frac{1}{c_\phi^2} = \frac{\phi_g}{c_g^2} + \frac{\phi_L}{c_L^2} \right)$$

Here,  $c_\phi$  is a variable defined for convenience and is not the acoustic speed  $c_m$  in the mixture, which will be defined later. Using Eq. (7), Eq. (1) may be rewritten as

$$\Gamma \frac{\partial Q_v}{\partial t} + \frac{\partial E}{\partial x} + \frac{\partial F}{\partial y} + \frac{\partial G}{\partial z} = S + D_v \quad (8)$$

where

$$\Gamma = \begin{pmatrix} \frac{1}{c_\phi^2} & 0 & 0 & 0 & (\rho_g - \rho_L) & 0 & 0 & 0 \\ \frac{u}{c_\phi^2} & \rho_m & 0 & 0 & (\rho_g - \rho_L)u & 0 & 0 & 0 \\ \frac{v}{c_\phi^2} & 0 & \rho_m & 0 & (\rho_g - \rho_L)v & 0 & 0 & 0 \\ \frac{w}{c_\phi^2} & 0 & 0 & \rho_m & (\rho_g - \rho_L)w & 0 & 0 & 0 \\ \frac{\phi_g}{c_g^2} & 0 & 0 & 0 & \rho_g & 0 & 0 & 0 \\ \frac{h_g \phi_g}{c_g^2} + \frac{h_L \phi_L}{c_L^2} & 0 & 0 & 0 & (\rho_g h_g - \rho_L h_L) & (\rho_g \phi_g C_{p,g} + \rho_L \phi_L C_{p,L}) & 0 & 0 \\ \frac{k}{c_\phi^2} & 0 & 0 & 0 & (\rho_g - \rho_L)k & \rho_m & 0 & 0 \\ \frac{\varepsilon}{c_\phi^2} & 0 & 0 & 0 & (\rho_g - \rho_L)\varepsilon & 0 & \rho_m & 0 \end{pmatrix} \quad (9)$$

and

$$Q_v = [p, u, v, w, \phi_g, T, k, \varepsilon]^T$$

The numerical characteristics of the Eq. (8) are studied by obtaining the eigenvalues of the matrix,  $[\Gamma^{-1}(\partial E / \partial Q_v)]$ . The eigenvalues of the system are derived to be

$$\Lambda = (u + c_m, u - c_m, u, u, u, u, u) \quad (10)$$

where  $c_m$  turns out to be the well-known, harmonic expression for the speed of sound in a two-phase mixture and is given as:

$$\frac{1}{c_m^2} = \rho_m \left[ \frac{\phi_g}{\rho_g c_g^2} + \frac{\phi_L}{\rho_L c_L^2} \right] \quad (11)$$

The behavior of the two-phase speed of sound as a function of the gas porosity indicates that at either limit the pure single-phase acoustic speed is recovered. However, away from the single-phase limits, the acoustic speed rapidly drops below either limit value and remains at the low level in most of the mixture regime. As a consequence, the local Mach number in the interface region can be large even in low speed flows.

To obtain an efficient time-marching numerical scheme, preconditioning is now applied to the system in Eq. (8), in order to rescale the eigenvalues of the system so that the acoustic speeds are of the same order of magnitude as the local convective velocities. This is achieved by replacing  $\Gamma$  in Eq. (8) by  $\Gamma_p$ .

$$\Gamma_p \frac{\partial Q_v}{\partial t} + \frac{\partial E}{\partial x} + \frac{\partial F}{\partial y} + \frac{\partial G}{\partial z} = S + D_v$$

where,

$$\Gamma_p = \begin{bmatrix} \frac{\beta}{c_\phi^2} & 0 & 0 & 0 & (\rho_g - \rho_L) & 0 & 0 & 0 \\ \frac{u\beta}{c_\phi^2} & \rho_m & 0 & 0 & (\rho_g - \rho_L)u & 0 & 0 & 0 \\ \frac{v\beta}{c_\phi^2} & 0 & \rho_m & 0 & (\rho_g - \rho_L)v & 0 & 0 & 0 \\ \frac{w\beta}{c_\phi^2} & 0 & 0 & \rho_m & (\rho_g - \rho_L)w & 0 & 0 & 0 \\ \frac{\phi_g\beta}{c_g^2} & 0 & 0 & 0 & \rho_g & 0 & 0 & 0 \\ \left(\frac{h_g\phi_g}{c_g^2} + \frac{h_L\phi_L}{c_L^2}\right)\beta & 0 & 0 & 0 & (\rho_g h_g - \rho_L h_L) & (\rho_g \phi_g C_{p,g} + \rho_L \phi_L C_{p,L}) & 0 & 0 \\ \frac{k\beta}{c_\phi^2} & 0 & 0 & 0 & (\rho_g - \rho_L)k & \rho_m & 0 & 0 \\ \frac{\varepsilon\beta}{c_\phi^2} & 0 & 0 & 0 & (\rho_g - \rho_L)\varepsilon & 0 & \rho_m & 0 \end{bmatrix} \quad (12)$$

Here, the parameter  $\beta$  has been introduced to precondition the eigenvalues. The modified eigenvalues of the preconditioned system are given as

$$\Lambda_p = \left( \frac{u}{2} \left( 1 + \frac{1}{\beta} \right) + c'_m, \frac{u}{2} \left( 1 + \frac{1}{\beta} \right) - c'_m, u, u, u, u, u \right) \quad (13)$$

where

$$c'_m = \frac{1}{2} \sqrt{u^2 \left( 1 - \frac{1}{\beta} \right)^2 + 4 \frac{c_m^2}{\beta}} \quad (14)$$

Equation (14) indicates that by setting  $\beta = (c_m^2 / u_p^2)$  where  $u_p = \max(u, 0.01c_m)$  the pseudoacoustic speed is of the order of  $u$  at all mixture composition values. The well-conditioned eigenvalues provide an efficient means of converging to steady-state solutions with minimal round-off and dissipation errors in the numerical flux calculation.

### 3 Viscous Transport Properties and Turbulence Model

The laminar viscosity and thermal conductivity for each phase are obtained from the NIST-12 databank as a function of the local fluid temperature. In flow regions where a two-phase mixture is present, a simplified mass-weighted mixing model, consistent with the homogenous flow model assumption of Eq. (1), is assumed

$$\begin{aligned} \mu_m^l &= \mu_g^l y_g + \mu_L^l y_L \\ k_m^l &= k_g^l y_g + k_L^l y_L \end{aligned} \quad (15)$$

Here,  $\mu_m^l$  and  $k_m^l$  are the laminar mixture viscosity and thermal conductivity, respectively, and  $y_g$  and  $y_L$  are the mass fractions of vapor and liquid, respectively. We note that the laminar viscosity in cryogenic fluids is substantially lower than that for water. Consequently, most cryogenic flows are characterized by high Reynolds numbers and turbulent conditions.

The effects of turbulent mixing are accounted for by employing a two-equation  $k$ - $\varepsilon$  model. We are justified in using a turbulence model since we are limiting our attention to mean predictions of sheet cavitation solutions where large scale unsteadiness is not

present in the cavity closure region. We recognize that for cloud cavitation problems, a more advanced unsteady, Large Eddy Simulation (LES) framework may be necessary. The turbulent viscosity is obtained by solving transport equations for the turbulent kinetic energy and its dissipation rate as follows:

$$\begin{aligned} \frac{\partial \rho k}{\partial t} + \frac{\partial}{\partial x_i} \left[ \rho u_i k - \left( \mu + \frac{\mu_T}{\sigma_k} \right) \frac{\partial k}{\partial x_i} \right] &= P_k - \rho \varepsilon + S_k \\ \frac{\partial \rho \varepsilon}{\partial t} + \frac{\partial}{\partial x_i} \left[ \rho u_i \varepsilon - \left( \mu + \frac{\mu_T}{\sigma_\varepsilon} \right) \frac{\partial \varepsilon}{\partial x_i} \right] &= C_1 f_1 P_k - C_2 f_2 \rho \varepsilon + S_\varepsilon \end{aligned} \quad (16)$$

$$P_k = \tau_{ij} \frac{\partial u_i}{\partial x_j}, \quad \tau_{ij} = -\frac{2}{3} \rho k + 2 \mu_T * \left( S_{ij} - \frac{1}{3} \frac{\partial u_k}{\partial x_k} \delta_{ij} \right),$$

$$\mu_T = C_\mu f_\mu \rho \frac{k^2}{\varepsilon}$$

where,  $\sigma_k$ ,  $\sigma_\varepsilon$ ,  $C_1$ , and  $C_2$  are the modeling constants, and  $f_1$ ,  $f_2$ ,  $f_\mu$  are empirical modeling functions to account for low Reynolds number (near wall). (They equal unity in the high Reynolds number form.)

Low Reynolds number effects in the near wall are accounted for by using an extension of the near wall model of So et al. [18]. This model has been shown to reproduce the near wall asymptotic relations for the Reynolds stress and kinetic energy accurately. In this model, the damping functions,  $f_1$ ,  $f_2$ ,  $f_\mu$ , are defined as follows:

$$f_1 = 1.0 - \exp \left[ - \left( \frac{\text{Re}_t}{40} \right)^2 \right]$$

$$f_2 = 1 - \frac{2}{9} \exp \left[ - \left( \frac{\text{Re}_t}{6} \right)^2 \right]$$

$$S_\varepsilon = \frac{1}{4} c_3 \mu_L \left[ \left( \frac{\partial k^{1/2}}{\partial x} \right)^2 + \left( \frac{\partial k^{1/2}}{\partial y} \right)^2 + \left( \frac{\partial k^{1/2}}{\partial z} \right)^2 \right]$$

and

$$\text{Re}_\tau = \frac{\rho k^2}{\mu_L \varepsilon}$$

$$f_\mu = (1 + 4 \text{Re}_\tau^{-3/4}) \tanh\left(\frac{\text{Re}_k}{125}\right)$$

where

$$\text{Re}_k = \frac{\rho \sqrt{k} y}{\mu} \quad (17)$$

The constants for this model are given as follows:

$$\begin{aligned} c_\mu &= 0.09, & \sigma_k &= 1.4, & \sigma_\varepsilon &= 1.4, \\ c_1 &= 1.44, & c_2 &= 1.92, & c_3 &= 2.9556 \end{aligned} \quad (18)$$

This model has been tested for a number of standard turbulence test cases to verify that it gives correct boundary layer growth and reattachment length for recirculating flows. We have also applied this model to cavitation in water and have obtained good results for the mean cavity length [14]. We note that the cases reported here did not exhibit large scale unsteadiness in the cavity closure region and our focus was on the prediction of mean cavity solutions in the absence of highly unsteady cloud cavitation in the wake. The use of a Reynolds Averaged Navier-Stokes (RANS) methodology for the latter situation of cloud cavitation is less justifiable and more suited for a LES analysis where the flow dynamics is not damped by large values of “turbulent” eddy viscosity. However, we do note that there are other efforts reported in the literature where a variety of turbulence models have been evaluated for unsteady cavity simulations [19].

The net viscosity and thermal conductivity are given as the sum of the laminar and turbulent contributions

$$\begin{aligned} \mu &= \mu_m^l + \mu_T \\ k &= k_m^l + \frac{\mu_T \cdot C_{Pm}}{\text{Pr}_T} \end{aligned} \quad (19)$$

The turbulent Prandtl number was specified to be 0.9 for the calculations presented here. As we shall discuss later in Sec. 6.0, the leading edge temperature depression was found to be quite insensitive to the turbulent Prandtl number probably because the temperature gradients were not substantial at the outer cavity edge.

#### 4 Numerical Procedure Overview

The multiphase formulation derived in the previous section has been implemented within a three-dimensional unstructured code CRUNCH CFD® [20]. The CRUNCH CFD® code has a hybrid, multielement unstructured framework, which allows for a combination of tetrahedral, prismatic, pyramidal, and hexahedral cells. The grid connectivity is stored as an edge-based, cell-vertex data structure where a dual volume is obtained for each vertex by defining surfaces, which cut across edges coming to a node. An edge-based framework is attractive in dealing with multielements since dual surface areas for each edge can include contributions from different element types making the inviscid flux calculation “grid transparent.”

The integral form of the conservation equations are written for a dual control-volume around each node as follows:

$$\Gamma_p \frac{\Delta Q_v V}{\Delta t} + \int_{\partial\Omega_i} F(Q_v, n) ds = \int_{\Omega_i} S dV + \int_{\partial\Omega_i} D(Q_v, n) ds \quad (20)$$

The inviscid flux procedure involves looping over the edge list and computing the flux at the dual face area bisecting each edge. A Riemann problem is solved for using higher-order reconstructed values of primitive variables at the dual face. Presently a second-order linear reconstruction procedure (following Barth and Linton

[21]) is employed to obtain a higher-order scheme. We note that the inviscid flux as outlined above is grid transparent since no details of the element type are required in the flux calculation.

The Riemann problem at the dual face is computed with a Roe-averaged, flux-differenced solver, which defines the flux  $F_m$  as

$$\begin{aligned} F_m &= \frac{1}{2} [F(Q_m^-, \vec{n}_{oi}) + F(Q_m^+, \vec{n}_{oi}) + \Delta F^-(Q_I^m, \vec{n}_{oi}) \\ &\quad + \Delta F^+(Q_I^m, \vec{n}_{oi})] \end{aligned} \quad (21)$$

where  $\vec{n}_{oi}$  is the vector area of the dual face crossing edge  $\vec{e}_{oi}$ , and the subscript “I” denotes Roe-averaged variables. The flux differences  $\Delta F^-$  and  $\Delta F^+$  are given as

$$\Delta F^+(Q_I^m, \vec{n}_{oi}) = \frac{1}{2} (R_I^m (\Lambda + |\Lambda|)_I L_I^m) (Q_m^+ - Q_m^-) \quad (22)$$

$$\Delta F^-(Q_I^m, \vec{n}_{oi}) = \frac{1}{2} (R_I^m (\Lambda - |\Lambda|)_I L_I^m) (Q_m^+ - Q_m^-)$$

Here,  $R$  and  $L$  are, respectively, the right and left eigenvector matrices, while  $\Lambda$  is the diagonal eigenvalue matrix. The Roe averaged velocities and scalars are defined as

$$y_I = \frac{y^+ \sqrt{\rho^+} + y^- \sqrt{\rho^-}}{\sqrt{\rho^+} + \sqrt{\rho^-}}, \quad \{y \in (u, v, w, T, k, \varepsilon)\} \quad (23)$$

while, the volume fraction  $\phi_g$  is defined by doing a simple arithmetic average

$$\phi_{g,I} = \frac{1}{2} (\phi_g^+ + \phi_g^-) \quad (24)$$

This average value of the  $\phi_g$  is used to define the speed of sound of the mixture at the dual face.

For efficient computations, a parallel framework for distributed memory systems has been implemented, along with a time-marching implicit solution procedure. The sparse implicit matrix is derived by doing an Euler explicit linearization of the first-order flux, and a variety of iterative sparse matrix solvers, e.g., Generalized Minimum Residual (GMRES), symmetric Gauss-Seidel procedure, are available in the code.

#### 5 Cavitation Source Terms

Development of numerical models for cavitation phase change is an area of continuing research and we provide a brief review. For the purposes of our discussion here, these models are classified into the following two categories: (a) A bubbly framework using the Rayleigh-Plesset equation and (b) continuum formulation solving for vapor phase transport. There have been numerous numerical studies using the bubbly closure model [8,9,22]. While there are significant differences between these studies in the details of their formulation, they model the phase change in a similar fashion; the flow field is seeded with bubbles and the change in bubble mass (and therefore the mixture density in each cell) is obtained from the Rayleigh-Plesset equations. The advantage of this formulation is that a physical model describes the cavitation phase change. However, the *key limitation* of these studies arises from their implicit restriction that the mixture be “dilute,” i.e., the gas void fraction is negligibly small. For instance, Kubota et al. [8] define mixture density as  $\rho_m = (1 - \phi_g) \rho_l$  which neglects the vapor phase. When  $\phi_g \approx 1$ , the conservation equations for the mixture become singular. This is a severe restriction. In particular, when extensive cavitation occurs the vapor clouds are dense and the spatial extent of each distinct cloud large. This requires the numerical resolution of the vapor phase mass and momentum within the cloud and a more complete definition of the mixture density.

The second approach is a continuum formulation that is applicable to dense cavitating flow [10,14,23,24]. Here, a separate equation for the transport of the gas phase is solved for and there is no restriction on the volume fraction of the gas-phase being small. The cavitation process is modeled as a phase change source term with a rate equation for phase change based on the local pressure. While the works referenced above use different formu-

lations to specify this rate of phase change, they are similar in that they do not integrate the cloud bubble dynamics, since neither the radius nor the number density of the bubbles in the vapor cloud is computed. Hence, the specified rate of vaporization and condensation becomes an ad hoc numerical parameter. We note that barotropic formulations (e.g., Song and Qin [25]) are a subset of this class of models under the assumption of an infinitely fast rate of phase change.

The continuum formulations listed above provide good results for mean cavity solutions of sheet cavitation problems where large scale unsteadiness is not present. For steady attached cavitation cases, this simplified model may be adequate since the vaporization occurs only over a small region at the interface of the vapor and liquid zone. Therefore for cases where the reentrant jet in the cavity closure region does not lead to shedding of the vapor cloud, the vaporization and condensation zone are well defined and the cavitation time scales and the fluid time scales do not interact in a significant manner. This is obviously not the case for cloud cavitation where a far more complex and dynamic interaction between the cavitation process and the hydrodynamics is evident and the more rigorous bubbly model would need to be integrated within this framework. For the present study, since our focus of interest is on the mean solution of quasisteady sheet cavitation problems we implement this simplified cavitation model. As our results will indicate, this model performed well for both liquid nitrogen and liquid hydrogen over a range of flow conditions and accurately resolved the effects of temperature gradients and fluid property variation on the evolution of the cavity.

In the present effort, the cavitation source term is defined via a simplified nonequilibrium, finite rate form as follows:

$$m_i = K_f \rho_L \phi_L + K_b \rho_g \phi_g \quad (25)$$

where the constant  $K_f$  is the rate constant for vapor being generated from liquid in a region where the local pressure is less than the vapor pressure. Conversely,  $K_b$  is the rate constant for reversion of vapor back to liquid in regions where the pressure exceeds the vapor pressure. Here, the rate constants are specified using the form given by Merkle et al. [26].

$$K_b = \begin{cases} 0 & p < p_v \\ \frac{1}{\tau_b} \left( \frac{Q_\infty}{L_\infty} \right) \left[ \frac{p - p_v}{\frac{1}{2} \rho_\infty Q_\infty^2} \right] & p > p_v \end{cases} \quad (26)$$

$$K_f = \begin{cases} 0 & p > p_v \\ \frac{1}{\tau_f} \left( \frac{Q_\infty}{L_\infty} \right) \left[ \frac{p - p_v}{\frac{1}{2} \rho_\infty Q_\infty^2} \right] & p < p_v \end{cases}$$

$\tau_f$  = Time constant for vapor formation

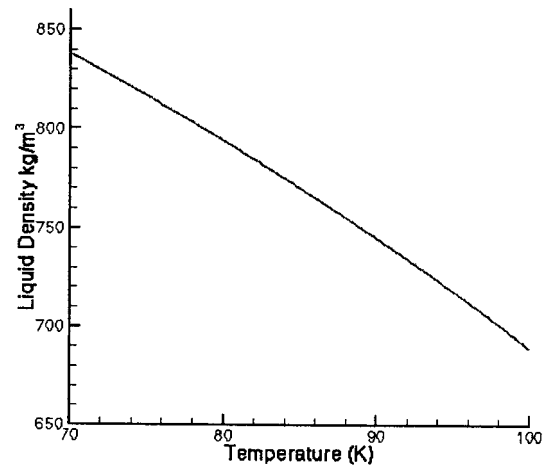
$\tau_b$  = Time constant for liquid reversion

$$\text{Cavitation Number} = \frac{p_\infty - p_v}{\frac{1}{2} \rho_\infty Q_\infty^2}$$

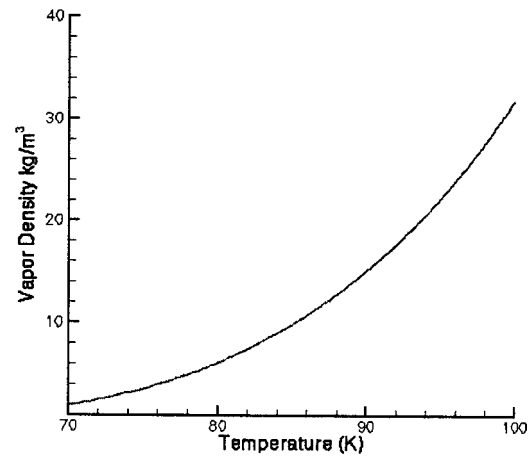
For the present study the baseline vaporization and condensation rate parameters were set at 0.01 s. The sensitivity of the cavity solution to the rate constants has been evaluated in Sec. 8.1.

## 6 Impact of Thermal Effects on Cavity Characteristics

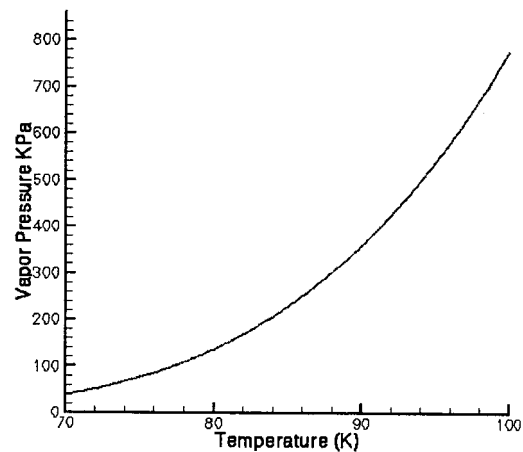
To understand the impact of thermal effects at operating temperatures close to the critical temperature of the fluid, we analyze cavitation in liquid nitrogen. The critical temperature of nitrogen is 126.19 K and the triple point is at 63.15 K. The variation of nitrogen properties along the saturation line for liquid and vapor densities as well as the vapor pressure are shown in Fig. 2 for an operating range of 70–100 K. We observe that over this operational range, the liquid nitrogen density varies from approximately 840–680 kg/m<sup>3</sup>, while the vapor pressure and correspondingly the vapor density vary by more than order of magnitude (2–34 kg/m<sup>3</sup>



(a)



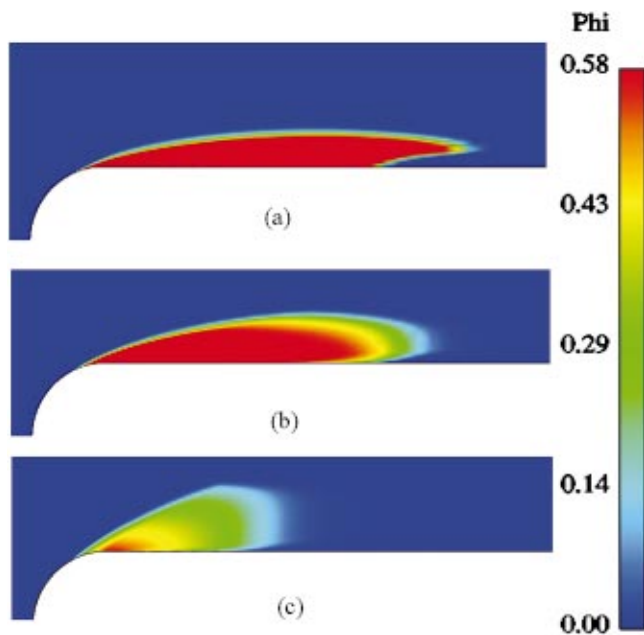
(b)



(c)

**Fig. 2 Saturation properties of nitrogen as a function of temperature: (a) liquid nitrogen density; (b) vapor density; (c) vapor pressure**

for vapor density). In fact at a representative temperature of 89 K, the slope of vapor pressure indicates a 16 KPa increase for a 1 K change in temperature, while the ratio of liquid to vapor density is only around 50. In contrast, the liquid to vapor density ratio for water at 298 K is of the order of 40,000. As discussed earlier, it is the combination of rapid vapor pressure variation and low liquid



**Fig. 3 Sensitivity of vapor volume fraction in liquid nitrogen cavity to heat of vaporization: ( $U_\infty=20$  m/s,  $T_\infty=89$  K,  $K_c=0.2$ )—(a) isothermal cavitation; (b) heat of vaporization= $0.1 \cdot h_{fg}$ ; (c) cryogenic cavitation**

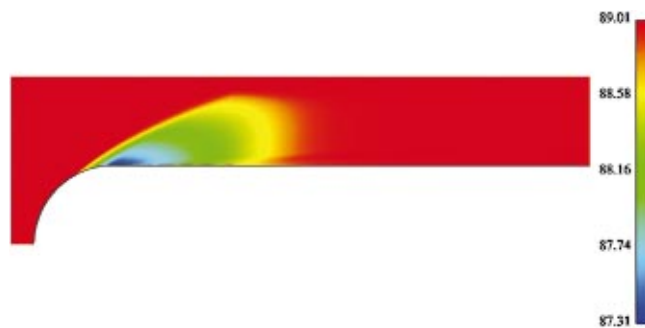
to vapor density ratio that generates substantial thermodynamic effects due to cavitation. As we shall see below, this fundamentally alters the nature of the cavity.

To demonstrate thermal effects on the cavity, we model flow over a quarter-caliber headform with a diameter of one inch, with the free-stream liquid nitrogen temperature at 89 K, and a velocity of 20 m/s. The freestream pressure is 360 KPa, which corresponds to a cavitation number of 0.2. The Reynolds number based on the diameter of 1 in. of the headform is  $3.6 \times 10^6$ . The high Reynolds number despite a small length scale of 1 in. highlights the fact that viscosity values are substantially lower in cryogenic fluids and the flow is fully turbulent even for sub-scale geometries.

The effect of evaporative cooling at these conditions is deduced by artificially altering the heat of vaporization for liquid nitrogen while keeping all other thermodynamic properties identical to that provided by the NIST databank. Figure 3 shows the vapor volume fraction in the cavity for the following three different heat of vaporization factors: (1) isothermal, (2)  $h_{\text{vap}}=0.1 \cdot h_{fg}$ , (3)  $h_{\text{vap}}=h_{fg}$  where  $h_{fg}$  is the latent heat of vaporization obtained from the databank for the local flow temperature. There is a distinct change in the character of the cavity as thermal effects become larger. For the isothermal case, a sharp and distinct cavity is obtained with vapor volume fraction in the cavity being near unity. As the thermal effects become pronounced the cavity interface becomes less sharp and the volume fraction of vapor in the cavity drops dramatically; for the correct heat of vaporization, the volume fraction at the leading edge is approximately 0.5 with the volume fraction in the interior being even smaller.

The temperature field for the simulation with full thermal effects (Case 3 of Fig. 3) is shown in Fig. 4. The largest temperature depression is close to the leading edge of the cavity where the temperature has been reduced to 87.3 K from the free-stream value of 89 K. This also indicates that the bulk of the vaporization is occurring near the leading edge with subsequent vaporization downstream along the interface being suppressed due to the temperature depression at the leading edge.

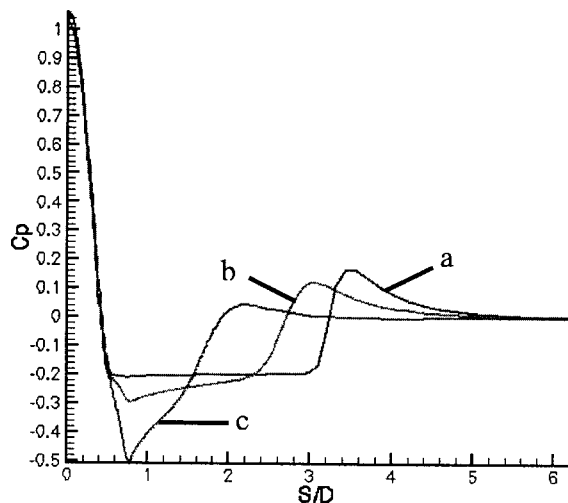
The dramatic change in the shape of the cavity due to thermal effects is also evident from both Figs. 3 and 4: the cavity length becomes smaller while the interface itself spreads out more caus-



**Fig. 4 Temperature variations in liquid nitrogen cavity ( $U_\infty=20$  m/s,  $T_\infty=89$  K,  $K_c=0.2$ )**

ing larger entrainment of liquid. These effects have been observed experimentally. Sarosdy and Acosta [27] compared cavitation in water and Freon for identical B factors and noted that the cavity in Freon was “frothy” as opposed to the “glassy” cavity in water. Furthermore, they also observed the change in cavity shape (i.e., shorter but with increased spreading) between the Freon and water cases as indicated by our results here. We conjecture that the frothiness may be attributed to the lower volume fraction in the cavity that reduces the density difference. The lower volume fraction also raises the mixture density within the cavity and the oncoming liquid experiences a much smaller gradient at the vapor interface. Consequently, the flow does not turn quite as rapidly and the low pressure field extends out further radially yielding a cavity with a larger spread.

The pressure profiles on the head-form surface are plotted in Fig. 5 for the three cases discussed above. For the isothermal case, the pressure in the cavity is at a constant value given by the free-stream cavitation number. With increasing thermal effect there is depression at the leading edge due to local temperature drop and a gradual relaxation back to the freestream value as the temperature rises in the aft region of the cavity where vapor condenses back to liquid. Interestingly, the pressure rise in the cavity closure region is a lot slower in the cryogenic case compared to the isothermal case even though the condensation rate value is unchanged. The cavity closure region experiences smaller gradients in the mixture density due to the reduced vapor content of the cavity. This weakens the reentrant jet thereby allowing the vapor phase to continue being convected downstream and providing a



**Fig. 5 Pressure coefficient on head-form surface as a function of heat of vaporization ( $U_\infty=20$  m/s,  $T_\infty=89$  K,  $K_c=0.2$ ) heat of vaporization factor: (a)=0; (b)=0.1; (c)=1.0**

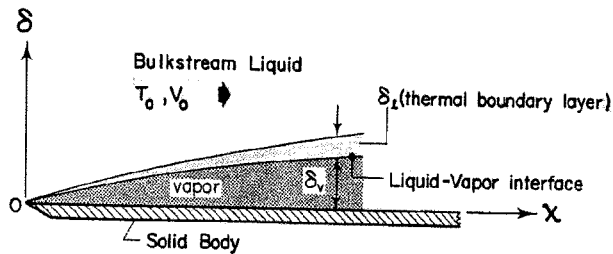


Fig. 6 Heat transfer model for dynamic variants of B-factor theory—[Figure taken from Report by Hord [1]]

slower pressure recovery. Thus, we find that the hydrodynamic response to the temperature variations resulting from phase change has a profound impact on the global evolution of the cavity. Quantitative validation of both the leading edge pressure and temperature depressions as well as the recovery of temperature and pressure in the closure region is provided in Sec. 8.

**7 Comparison of B-Factor Theory With Simulations**

We examine some of the basic assumptions postulated in the dynamic variant of the B-factor theory given by Hord [1] and compare them to our simulations. In Fig. 6, the heat transfer model that forms the basis for this theory is shown in schematic form. The primary assumption is that liquid flows over the cavity as if it were a solid body i.e., the vapor-liquid surface is a limiting streamline and no convection of liquid mass is occurring across this interface. Consequently, the primary factor governing the vaporization is the viscous diffusion of energy across vapor-liquid interface, which sustains the continuous vaporization of the liquid. Hence, the B factor may be defined as follows:

$$B = V_v / V_l = \int_0^x \delta_v dx / \int_0^x \delta_t dx \quad (27)$$

where  $\delta_v$  and  $\delta_t$  are vapor-liquid interface and thermal boundary layer thickness, respectively. Assuming that the liquid-vapor interface has a parabolic shape ( $\delta_v \approx x^p$ ) and employing a correlation for Nusselt number to define the thermal boundary layer ( $\delta_t \approx x \cdot Re_x^{-m} \cdot Pr^{-n}$ ) the B factor is defined as

$$B \approx x^{p-1} Re_x^m Pr^n \quad (28)$$

where the coefficients  $p, m, n$ , are determined by correlating the expression with experimental data. We note that the expression in Eq. (28) is not a nondimensional expression but rather reflects the parameters chosen by Hord to calibrate the B factor versus a reference value. The important point reinforced by Eq. (28) is that viscous coefficients such as the Reynolds number and Prandtl number are the critical parameters governing vaporization, and *convection of liquid mass across the interface is neglected* by definition. It is the validity of this basic premise that interests us.

To compare our results with the B-factor theory, we plot particle traces of the liquid streamlines in Fig. 7 for the isothermal case ( $h_{vap}=0.0$ ), and the cryogenic case ( $h_{vap}=h_{fg}$ ), respectively. For the isothermal case [Fig. 7(a)], where there is a large jump in mixture density across the vapor-liquid interface, the bulk of the oncoming liquid skirts the vapor-liquid interface and flows around it. In fact the vapor-liquid interface behaves like a limiting streamline and the isothermal cavity case is reasonably consistent with the model postulated in the B-factor theory.

The vaporization dynamics for the cryogenic case [Fig. 7(b)] is entirely different from the isothermal case and the B-factor heat transfer model breaks down for this case. Since the interface spreads out further and because the cavity is more porous, the liquid streamlines flow into the cavity. A small fraction of the liquid is locally vaporized as it convects into the cavity with the vaporization being driven by the difference between the local

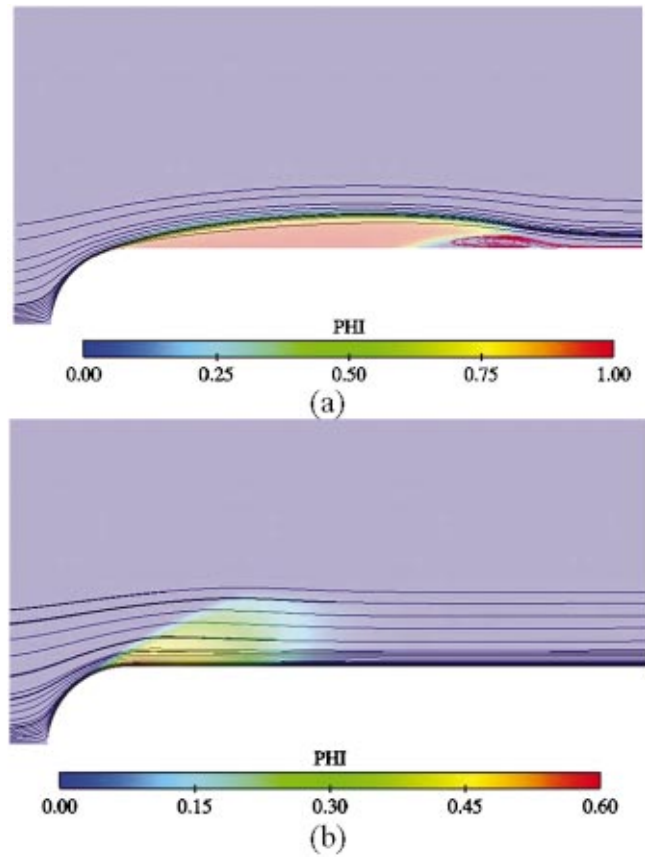


Fig. 7 Fluid streamlines and their interaction with the cavity for (a) isothermal cavity and (b) cryogenic cavity

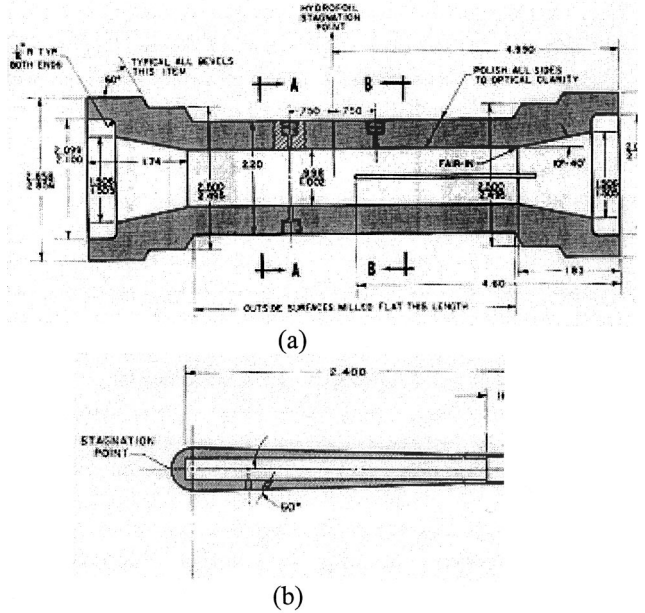


Fig. 8 Details of tunnel geometry and hydrofoil used by Hord (Ref. [1]) [Figure taken from Hord's report]: (a) tunnel geometry; (b) quarter caliber hydrofoil with a tapered diffuser



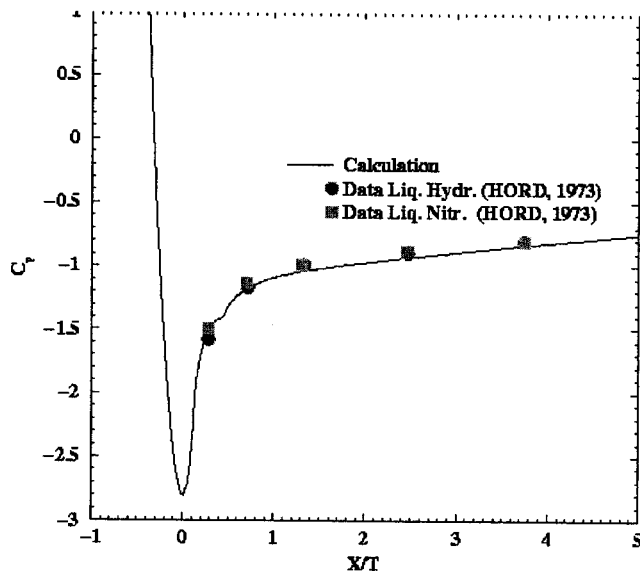


Fig. 9 Pressure coefficient for noncavitating flow over hydrofoil

pressure and the saturation vapor pressure corresponding to the local temperature. While the viscous thermal diffusion does affect the local temperature via heat conduction, it is by no means the limiting factor in determining vaporization. Indeed, in the cryogenic case, the convective mass flux (i.e., fluid velocity) and the resulting pressure field from the multiphase hydrodynamics takes precedence.

The sensitivity of the cavity to both the turbulent Prandtl number as well as the cavitation vaporization and condensation rates was assessed. The turbulent Prandtl number was changed from 0.09 (the default value used for all calculations shown here) to 0.18 as well as 0.04. However, no noticeable change in the cavity was observed probably because the primary turbulence growth is within the boundary layer at the body and not at the vapor interface. The effect of the cavitation phase change rates was also assessed. Results are shown later in Sec. 8.1 for a slightly different geometry at three different rate constants. The leading edge temperature and pressure depression show no change at all despite the large variation in the phase change rates. As we discuss in detail in Sec. 8.1, for a given fluid and a given flow geometry, the primary factor controlling leading edge temperature depression

Table 1 Run conditions for liquid nitrogen cases

Run number	Free-stream temp. (K)	Free-stream vel. (M/S)	Cavitation number
289C	88.64	23.5	1.55
290C	83.06	23.9	1.70
293A	77.64	24.0	1.75
294F	77.94	9.8	1.78

appears to be free-stream velocity with the fluid temperature and cavitation number having a secondary effect. These results are all consistent with the cavitation physics being a convection dominated phenomenon in cryogenic flows and the temperature gradients were being small except near the wall.

## 8 Simulations of Cavitating Hydrofoil

Simulations of experiments by Hord [1] on a cavitating hydrofoil for both liquid nitrogen and liquid hydrogen are presented. Detailed pressure and temperature measurements in these experiments are used to validate the numerical results. In addition we have sorted the large number of experimental measurements and generated a database of appropriate test points that can be used for parametric evaluation of cavity response to variations in freestream pressure, temperature and velocity.

Hord [1] performed subscale tests in a blow-down tunnel; details of the tunnel and the hydrofoil geometry are given in Fig. 8. The tunnel width is 1 in. while the hydrofoil width is 0.312 in. Since considerable blockage effects are present it became necessary to model details of the tunnel geometry in the simulations reported. To verify that these tunnel interaction effects were being correctly modeled we performed single-phase, noncavitating simulations and have compared it to Hord's noncavitating data in Fig. 9. Excellent agreement is obtained; note that the pressure coefficient only recovers to  $-0.8$  (as opposed to zero in a flow without blockage) at the exit of computation due to blockage. Furthermore, the single-phase solution appears insensitive to Reynolds number variations since both liquid hydrogen and nitrogen data points show identical pressure profiles.

The numerical grid for the solution consisted of approximately 100,000 grid points for a multiblock hexahedral grid; there were approximately 300 points along the body of the hydrofoil and there were approximately 120 points normal to the hydrofoil in the region between it and the tunnel wall. The boundary conditions imposed were mass flux and free-stream temperature at the inflow boundary along with free-stream turbulence values. At the

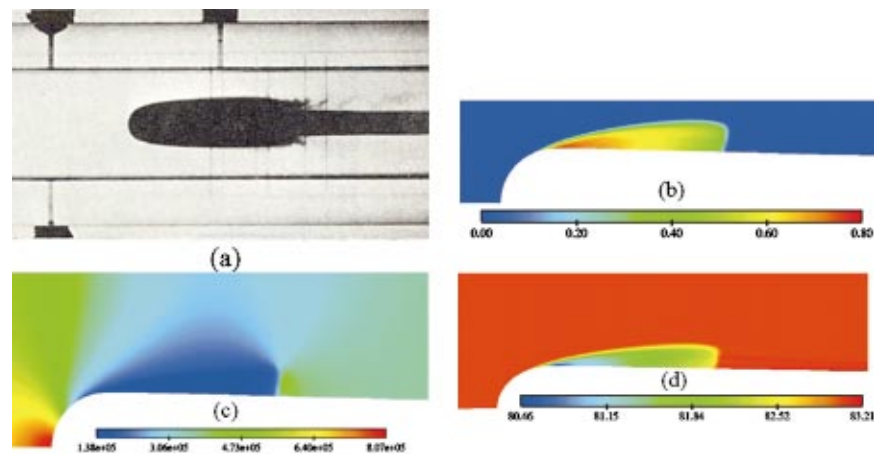


Fig. 10 Cavitating flowfield in liquid nitrogen for hydrofoil geometry: (a) flow visualization taken from Hord (Ref. [1]); (b) computed vapor volume fraction; (c) computed pressure field; (d) computed temperature field

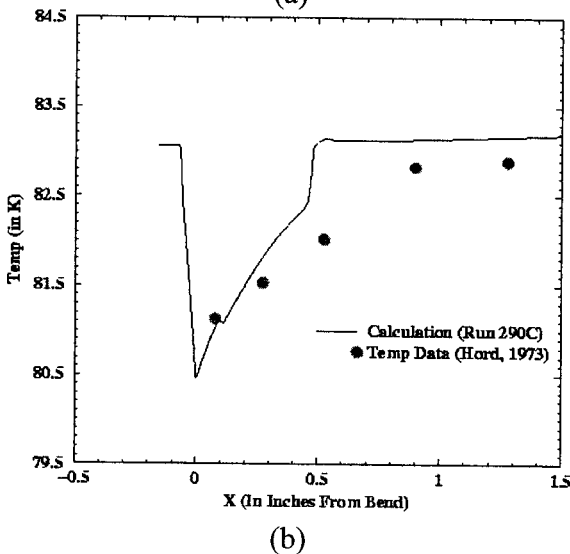
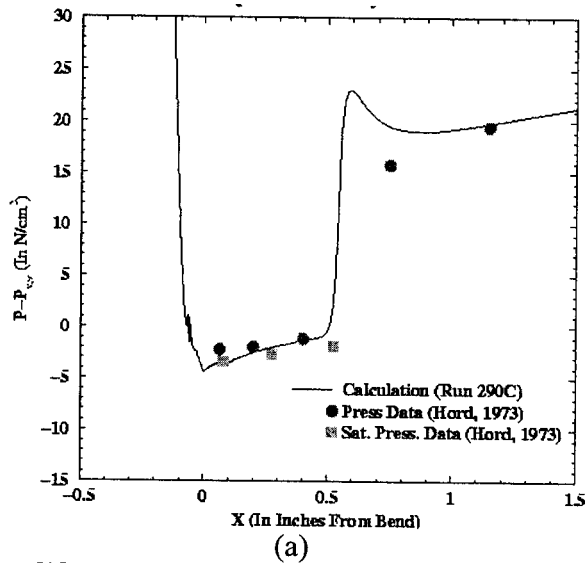


Fig. 11 Computed pressure and temperature depression in liquid nitrogen compared with experimental data of Hord (Ref. [1]) ( $U_\infty = 23.9 \text{ m/s}$ ,  $T_\infty = 83.06 \text{ K}$ ,  $K_c = 1.70$ )

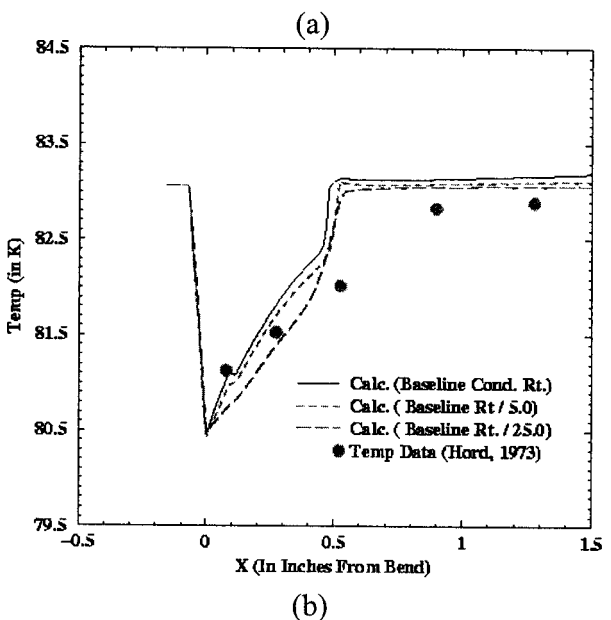
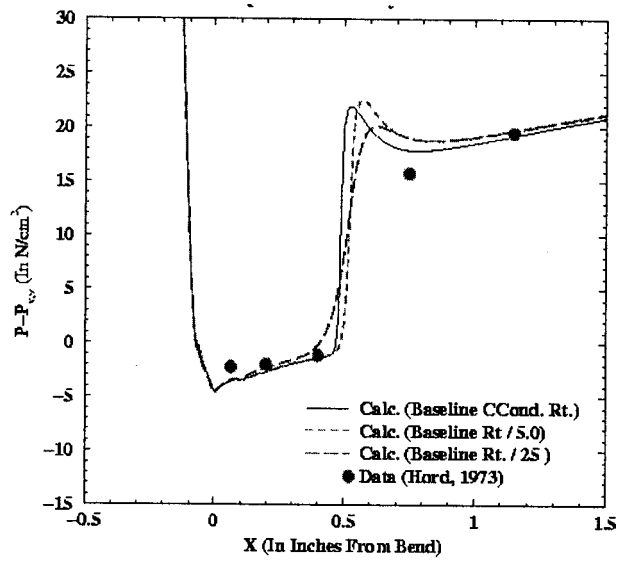


Fig. 12 Sensitivity of pressure and temperature depression to vaporization and condensation rates

outflow a backpressure was imposed. The grid was decomposed over 16 processors and solutions were obtained on a Linux PC cluster.

**8.1 Cavitation in Liquid Nitrogen.** Simulations at four different tunnel conditions (see Table I) are simulated as part of a parametric study. The first three calculations (Runs 289C, 290C, and 293A) were done at a nominally similar freestream velocity of 24 m/s but at different free-stream temperatures and free-stream cavitation numbers [free-stream cavitation number is  $K_c = (P_\infty - P_{v,\infty}) / (0.5 \cdot \rho_\infty U_\infty^2)$ ] to ascertain if leading edge pressure depression is a strong function of free-stream cavitation number at a given dynamic head. The last two calculations (Runs 293A and 294F) were chosen because they have similar free-stream temperatures and cavitation numbers but different velocities. Note that the labels given to the different tunnel conditions are taken directly from the nomenclature in Hord's report.

The general characteristics of the cavitating hydrofoil flowfield are shown in Figs. 10(a)–10(d) for tunnel conditions corresponding to Run 290C (Table I). The vapor volume fraction [Fig. 11(b)] is qualitatively compared with a typical flow visualization [Fig. 10(a)] of the flow. While the overall shape and features of the

cavity appear to be similar, we note however, that the flow conditions at which this visualization was done are not reported in Hord's report and the comparison of cavity shape is only qualitative at best. It is also clear that the numerical simulations are not capturing the unsteady features in the cavity closure region. This appears to be due to the RANS turbulence model employed; the model yields large turbulence viscosity values that dissipate the reentrant jet. Unsteady LES calculations will be required to further examine this issue. The computed pressure field [Fig. 10(c)] indicates strong interaction between the cavity and the tunnel wall, which is expected due to the relative scales of the geometry. Figure 10(d) shows the temperature profile in the cavity. The strong temperature depression at the leading edge of the cavity is evident with the gradual temperature recovery due to condensation in the rear of the cavity; this is similar to the headform result shown earlier in Fig. 4.

The quantitative comparisons of pressure and temperature depression in the cavity with experimental data are shown in Fig. 11 for Run 290C at a free-stream temperature of 83.06 K, velocity of 23.9 m/s, and cavitation number of 1.70. Note that the pressure

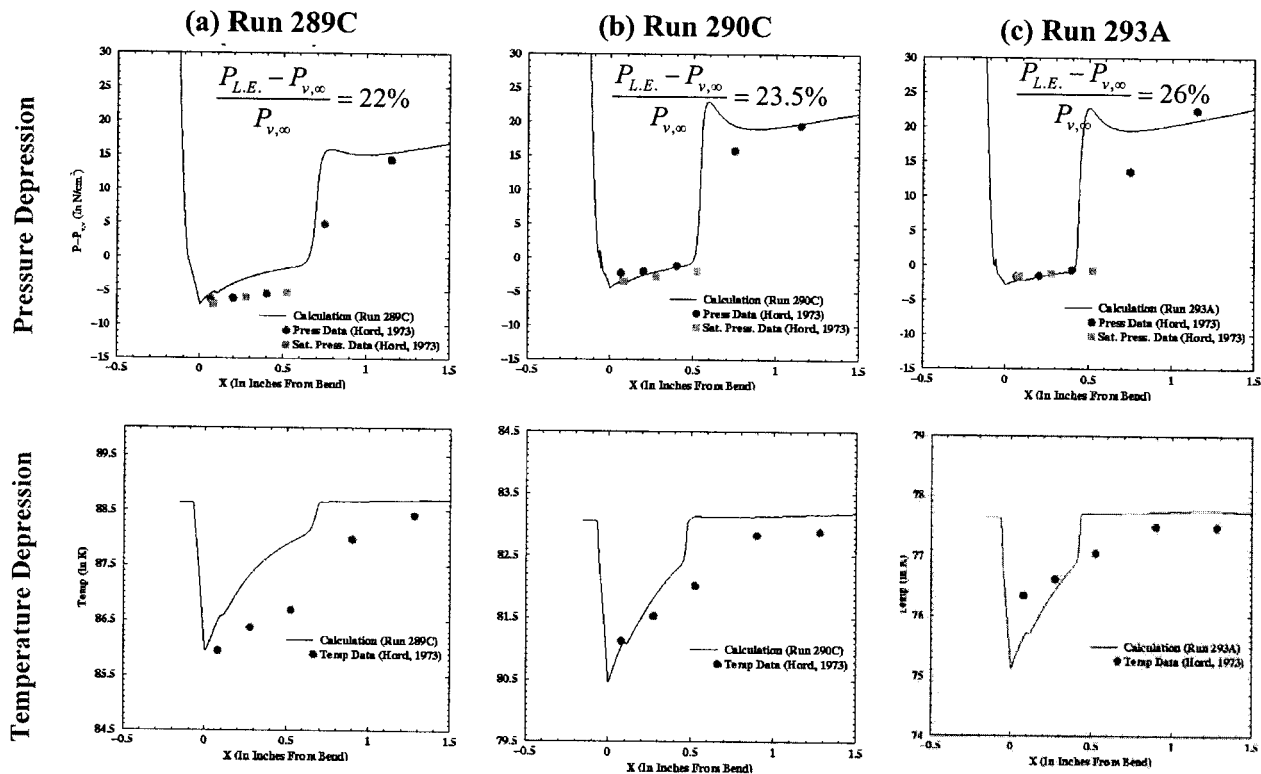


Fig. 13 Comparison of pressure and temperature depressions in liquid nitrogen as a function of freestream pressure and temperature conditions at similar freestream velocities. (Conditions given in Table I.)

depression values plotted are  $(P - P_{v,\infty})$  where  $P$  is the local pressure, and  $P_{v,\infty}$  is the free-stream vapor pressure. If no thermal effects are present this value would be zero in the cavity (assuming absence of non-condensable gas), while values below zero in the cryogenic case indicate pressure depression due to thermal effects. The comparison of the pressure depression in Fig. 11(a) indicates excellent overall comparison with data in the front portion of the cavity and the simulations are within the instrumentation error bar of  $0.69 \text{ N/cm}^2$ . The predicted cavity length is reasonably close to the experimental value of 0.748 although we note that the cavity length shows larger errors in other cases modeled. The leading edge pressure depression of approximately  $5 \text{ N/cm}^2$  is a 23.5% reduction in pressure relative to the free-stream vapor pressure. It further illustrates why thermal effects have a substantial impact on the performance of cryogenic pumps. The experimental data plotted includes both the actual pressure measured (symbol: circle) as well as the saturation pressure values (symbol: square) corresponding to the local temperature measurements. The close match between the actual pressure and saturation pressure values indicates that the thermodynamic equilibrium within the cavity is a valid assumption for liquid nitrogen flows.

The experimental measurements of temperature within the cavity are compared with the numerical predictions in Fig. 11(b). Good comparison is obtained for the leading edge temperature depression of approximately 2.5 K; the instrumentation error given for the chromel-gold thermocouples is 0.20 K and the computed results are within the uncertainty of the experiments in the front portion of the cavity. The temperature recovery slope within the cavity compares well with measured profile. However, the temperature rise in the cavity closure region shows differences; the computed solution recovers to the free-stream value more quickly than does the data, which does not quite fully recover to the free-stream value. The discrepancy in the cavity closure region was investigated further by evaluating the effect of vaporization and condensation rates on the temperature recovery. Figure 12 shows the pressure depression and temperature profiles for three phase change rates: the baseline rate used for Fig. 11, baseline

rate/5, and baseline rate/25.0. Note that both the vaporization and condensation rates were changed by equal amounts. On examining Fig. 12, it is striking that even a large variation of phase change rates had absolutely no impact on the leading edge pressure and temperature. The condensation rate does affect the temperature and pressure recovery particularly in the closure region. However, here again the overall cavity length appears to be unchanged with the primary effect being that temperature recovery is slower within the cavity. The sharper recovery in temperature at the cavity closure appears to be controlled by the reentrant jet and is not very sensitive to the phase change rates. In any case, the experimental temperature profile in the cavity closure is not obtained and this issue may point to the need for unsteady LES simulation to further investigate unsteady temperature fluctuations in the closure region which might yield a slower temperature recovery for the mean profile.

A parametric study of cavitation response at three different free-stream temperature and pressure conditions, but at a similar velocity of 24 m/s is examined. In Fig. 13, we compare simulations at tunnel conditions of Runs 289C, 290C, and 293A from Table I. The free-stream cavitation numbers are 1.55, 1.7, and 1.75, respectively, therefore the corresponding cavity lengths decrease with the increasing cavitation numbers. There is also a large variation in freestream temperature (from 77.6 to 88.6 K) that entails substantial differences in fluid properties. The comparison between the simulations and experimental results, particularly the leading edge value, continue to be good over the range of cavity lengths. The key point to note is that despite the different cavity lengths and thermodynamic properties, there are only minor differences in the leading edge pressure depression; the pressure depression as a percentage of free-stream vapor pressure ranges only from 22% for the largest cavity to 26% for the smallest cavity.

In contrast to the results above, the leading edge pressure and temperature depressions show dramatic variation with the free-stream velocity (or dynamic head) while keeping other parameters

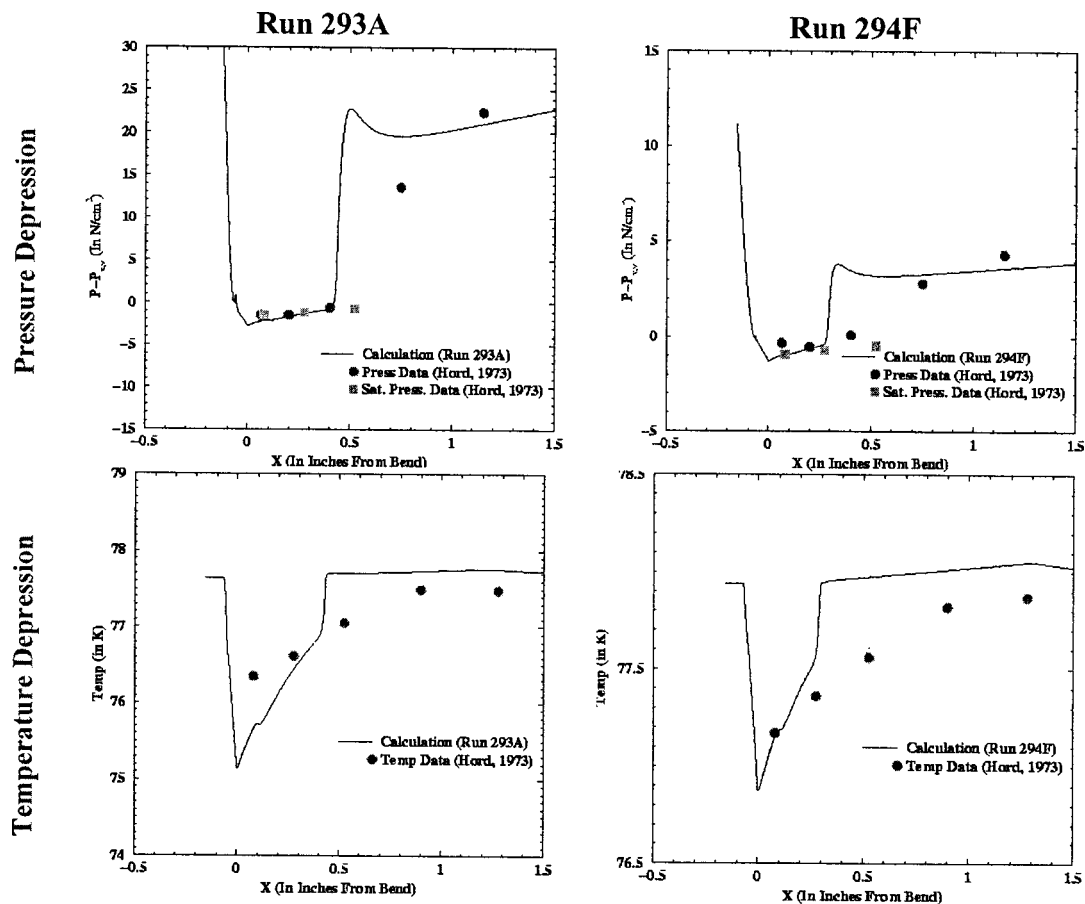


Fig. 14 Sensitivity of pressure and temperature depression in liquid nitrogen to changes in freestream velocity

the same. To illustrate this effect, we compare simulations for Run 293A and Run 294F in Fig. 14. The free-stream velocity for the two cases is 24 and 9.8 m/s, respectively. However, the temperature ( $=77$  K) and, more importantly, the cavitation number ( $=1.7$ ) are the same for the two runs. The temperature and pressure depression (as a ratio of freestream vapor pressure) levels are observed to scale with the free-stream dynamic head. At the larger velocity of 24 m/s, the temperature depression is about 2.5 K while it is less than 1 K at the lower velocity of 9.8 m/s. The pressure depressions (as a ratio of free-stream vapor pressure) show the corresponding differences as well with the pressure depression being 26% for the higher velocity case, while only being 12% at the lower velocity.

The variation of pressure depression with fluid velocity can be qualitatively explained by defining a quantity  $K_{c,\min}$ , which is the minimum cavitation number at the leading edge of the cavity and is given as

$$K_{c,\min} = (P_\infty - P_{\min}) / (0.5 \cdot \rho_\infty U_\infty^2) \quad (29)$$

This can be rearranged to give the following expression for pressure depression,  $\Delta P_v = P_{v,\infty} - P_{\min}$ , at the leading edge:

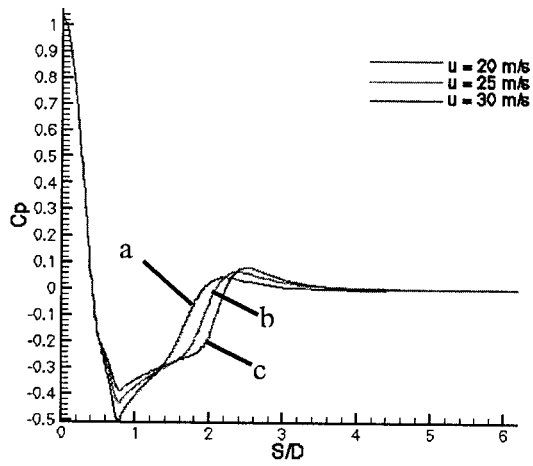
$$\Delta P_v = (K_{c,\min} - K_c) * 0.5 \rho_\infty U_\infty^2 \quad (30)$$

where  $K_c$  is the free-stream cavitation number. For two cavities to be self similar in cryogenic fluids, both  $K_{c,\min}$  and  $K_c$  have to match, and the pressure depression  $\Delta P_v$  at the leading edge varies proportionally with the dynamic head to preserve the value of  $K_c$ . The value of  $K_{c,\min}$  is computed for Run 293A and 294 F to be 1.88 and 2.1, respectively. This indicates that the two flows are not similar and that the lower velocity case (Run 294F) in fact experiences larger thermal depression as a *proportion of its dynamic*

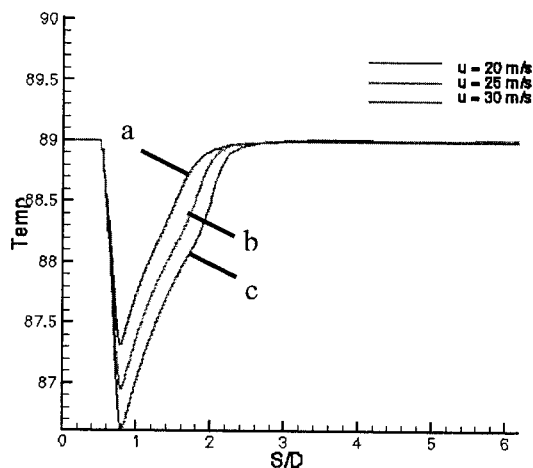
*head*. Paradoxically, this is the reverse of the trend when pressure depression is normalized by the freestream dimensional vapor pressure i.e.,  $\Delta P_v / P_{v,\infty}$  has the opposite trend as  $\Delta P_v / 1/2 \rho_\infty U_\infty^2$ .

The influence of free-stream velocity as an independent parameter controlling cavity characteristics is confirmed by doing a more carefully controlled parametric study for the free head-form geometry that was described in the previous section. The freestream cavitation number is maintained at 0.2, the free-stream temperature at 89 K, and the solution computed at the following three free-stream velocities: (a) 20 m/s, (b) 25 m/s, and (c) 30 m/s. The pressure coefficients and temperature distributions on the surface are plotted in Fig. 15. The increased thermal depression as a proportion of the dynamic head is indicated by the decreasing value of ( $K_{c,\min} = -C_p$ ) at higher velocities: 0.5, 0.43, and 0.39 for cases (a), (b), and (c), respectively. The larger leading edge temperature drop, *in absolute terms*, at higher velocities may seem contradictory at first. However, this is misleading since the net thermal depression effect on the flow is still smaller for the much larger value of dynamic head. Consequently, the cavity lengths and volume become larger with increasing velocity (or lower relative thermal depression), which is quite apparent from Fig. 15. We hypothesize that the strong effect of free-stream velocity is indicative of the vaporization process in cryogenic cavities. As discussed earlier, mass is convected into the cavity and the liquid vaporizes as it crosses the vapor-liquid interface. Therefore, altering the mass influx across the vapor-liquid interface appears to have a first-order impact on the cavitation process.

**8.2 Cavitation in Liquid Hydrogen.** Simulations of the cavitating hydrofoil in liquid hydrogen are examined. The triple point of hydrogen is 13.957 K and the critical temperature is



(a)

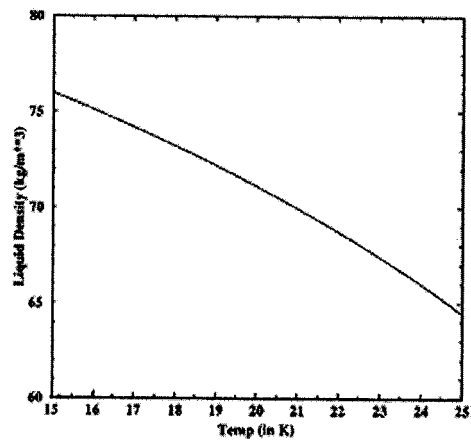


(b)

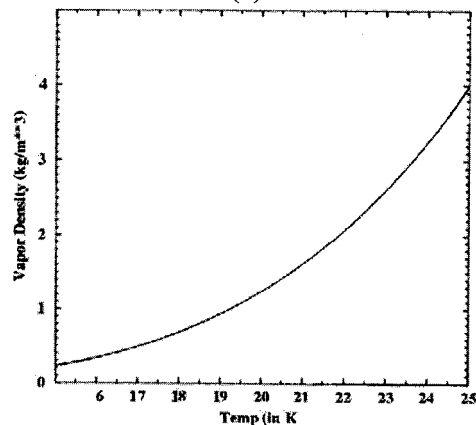
**Fig. 15 Pressure coefficient and temperature distribution on headform as a function of freestream velocity; (a)  $U_\infty = 20$  m/s, (b)  $U_\infty = 25$  m/s, (c)  $U_\infty = 30$  m/s**

33.19 K. Therefore, the entire operational range of liquid hydrogen systems is only about 19 K. The saturation properties of hydrogen are plotted in Fig. 16. While the general trend of variations is similar to liquid nitrogen, the magnitude of the variations is much larger, e.g., the slope of vapor pressure variation is about twice as high as liquid nitrogen (approximately 30 KPa/K as compared to 16 KPa/K for liquid nitrogen). Hence thermal effects are more pronounced in hydrogen. The extremely narrow temperature range and strong variations in properties poses a severe test for diagnostic techniques and numerical procedures alike. For instance, the thermocouple error bar of 0.20 K reported by Hord [1] has a relatively larger impact on measurements in liquid hydrogen than for liquid nitrogen. The comparisons shown below reflect these difficulties.

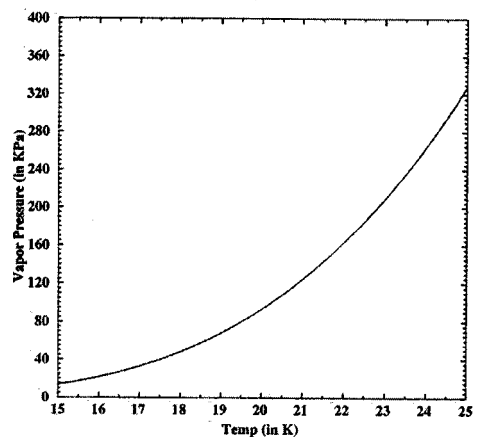
Cavitation in liquid hydrogen was investigated for a range of conditions and our experience is that the trends are in general similar to what was discussed for liquid nitrogen. However, examination of Hord's data indicates the possibility of thermal equilibrium beginning to break down and we focus on this issue here. To investigate this three different tunnel conditions were simulated (see Table II) with increasing cavity lengths; the free-stream temperatures were similar (20 K) but the velocities and cavitation number were different. The comparisons of the pressure and temperature profiles are shown in Fig. 17. The leading edge tempera-



(a)



(b)



(c)

**Fig. 16 Saturation properties of liquid hydrogen as a function of temperature**

ture and pressure depressions continue to be predicted very well. However, temperature profiles inside the cavity and particularly in

**Table 2 Run conditions for liquid hydrogen cases**

Run number	Free-stream temp. (K)	Free-stream vel. (M/S)	Cavitation number
247B	20.69	65.2	1.68
249D	20.70	58.1	1.57
231C	20.63	51.4	1.34

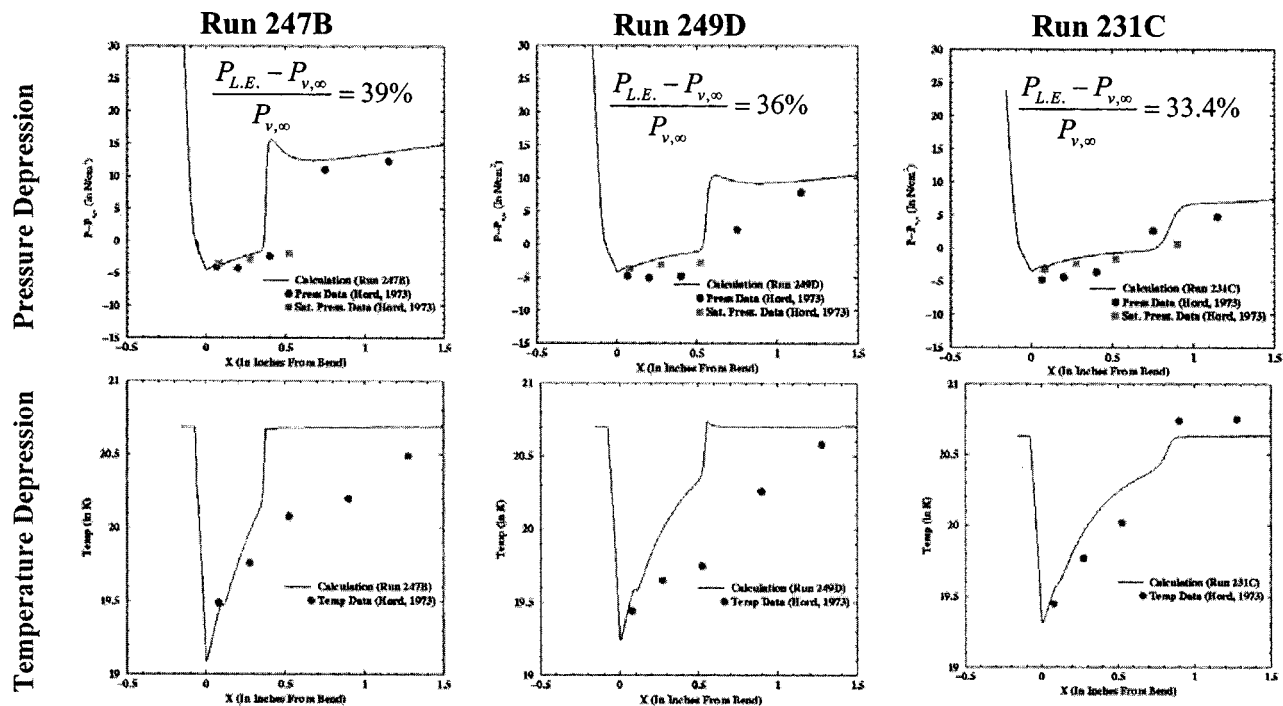


Fig. 17 Pressure and temperature depression in liquid hydrogen cavities for different freestream conditions. Conditions given in Table II.

the closure regions are more inconsistent and showing larger differences perhaps indicating more significant unsteadiness in the flowfield. Note that due to increased thermal effects the mean level of pressure depression is much higher—around 35% as compared to 25% for the liquid nitrogen calculations.

A detailed comparison of the pressure profiles shows excellent comparison with the saturation pressure values, which is consistent with the thermal equilibrium assumption of the numerical formulation. However, the saturation pressure levels and the actual pressure measurements show a distinct (if relatively minor) difference consistently for all three cases simulated. This indicates that thermal equilibrium may be beginning to break down in these cases. We observe that all the liquid hydrogen runs were done at velocities greater than 50 m/s, which is roughly twice that of the liquid nitrogen runs. Given the strong dependence of the temperature depression on the free-stream velocity it is possible that non-equilibrium effects start having a more pronounced impact. Perhaps more accurate unsteady data as well as unsteady numerical simulations will be required to continue further investigations into this issue.

## 9 Summary

A numerical study of cavitation in cryogenic fluids, which operate close to their critical temperatures, is presented. The energy equation for the mixture is solved in conjunction with the mass and momentum conservation, and the evaporative cooling effects of cavitation are accounted for. The formulation is based on a thermal equilibrium assumption between the vapor and liquid in the cavitating region; fluid thermodynamic properties are specified along the saturation line as a function of temperature using the NIST-12 data bank.

Variable fluid properties and temperature effects of cavitation were shown to substantially alter the nature of the cavity. As thermal effects become more significant, the cavity becomes more porous with reduced vapor content (experimentally visualized as being frothy) and the interface between the vapor and liquid is

less distinct. The cavity shape shows a substantial change; the cavity becomes shorter but spreads out more as thermal effects increase.

The smaller density differences across the vapor-liquid interface and the increased spreading of the cavity alter the hydrodynamics in a cryogenic fluid. The cavity is sustained by mass directly being convected into the cavity with the liquid vaporizing as it travels across the vapor-liquid interface. In particular, the heat transfer models postulated in the B-factor model variants (e.g., Hord, [1]) are a poor approximation since they postulate mass diffusion into the cavity controlled by the heat transfer through the thermal boundary layer. They specifically neglect substantial mass convection into the cavity and treat the vapor-liquid interface as an internal boundary. In contrast, our results indicate that convective phenomena that governs that mass flux across the vapor-liquid interface is the primary factor controlling the cavity evolution and that viscous diffusion on a macroscopic scale at the interface has a negligible effect on the temperature and pressure depression.

The experiments by Hord [1] for a cavitating hydrofoil in liquid nitrogen/hydrogen are simulated, and the measurements used as a database to both better understand and validate numerical observations. For a given free-stream velocity, leading edge temperature and pressure depression were found to be relatively insensitive to variations in both free-stream temperature as well as pressure. In contrast, the cavity solutions showed strong sensitivity to free-stream velocity for a fixed temperature and cavitation number. As velocity increases, the cavity becomes longer and has a higher vapor content. Thermal depression is enhanced at lower velocities; the values of leading edge pressure depression normalized by free-stream dynamic head become larger at lower velocities. Free-stream velocity is conclusively shown to be an independent parameter governing the cavitation solution. This is consistent with the convection dominated model of vaporization that we have postulated.

The validity of thermal equilibrium was evaluated for both liquid nitrogen and hydrogen. Thermal equilibrium appears to be a

valid assumption for liquid nitrogen at least over the range of velocities investigated for the hydrofoil. However for liquid hydrogen flows over the hydrofoil there was a distinct, but small, difference between the saturation pressure and physical pressure measurement indicating the possibility of nonequilibrium effects. It is unclear at this point if these nonequilibrium effects are solely a function of fluid thermodynamic properties or whether the velocity of the fluid also plays a role.

## Acknowledgments

The authors acknowledge funding for this work through a SBIR program under Contract No. NAS8-02098 funded by NASA Marshall Space Flight Center. The contract monitor is Dr. Dan Dorney. The technical inputs provided by Dr. Dan Dorney and Robert Garcia are gratefully acknowledged. The authors would also like to thank Dr Paul Cooper. His insights into this problem, going back to his pioneering work in the 1960s, were invaluable to our effort.

## References

- [1] Hord, J., 1973, "Cavitation in Liquid Cryogenics II—Hydrofoil," NASA CR-2156.
- [2] Brennen, C. E., 1995, *Cavitation and Bubble Dynamics*, Oxford University, New York.
- [3] Stahl, H. A., and Stepanoff, A. J., 1956, "Thermodynamic Aspects of Cavitation in Centrifugal Pumps," *Trans. ASME*, **78**, pp. 1691–1693.
- [4] Salemann, V., 1959, "Cavitation and NPSH Requirements of Various Liquids," *ASME J. Basic Eng.*, **81**, pp. 167–180.
- [5] Ruggeri, R. S., and Moore, R. D., 1969, "Method for Prediction of Pump Cavitation Performance for Various Liquids, Liquid Temperature, and Rotation Speeds," NASA, TN, D-5292.
- [6] Holl, J. W., Billet, M. L., and Weir, D. S., 1975, "Thermodynamic Effects on Developed Cavitation," *ASME J. Fluids Eng.*, **97**(4), pp. 507–516.
- [7] Cooper, P., 1967, "Analysis of Single and Two-Phase Flows in Turbopump Inducers," *J. Eng. Power*, **89**, pp. 577–588.
- [8] Kubota, A., Kato, H., and Yamaguchi, H., 1992, "Cavity Flow Predictions Based on the Euler Equations," *J. Fluid Mech.*, **240**, pp. 59–96.
- [9] Colonius, T., d'Auria, F., and Brennen, C. E., 2000, "Acoustic Saturation in Bubbly Cavitating Flow Adjacent to an Oscillating Wall," *Phys. Fluids*, **12**(11), pp. 2752–2761.
- [10] Singhal, A. K., Athavale, M. M., Li, H., and Jiang, Y., 2002, "Mathematical Basis and Validation of the Full Cavitation Model," *ASME J. Fluids Eng.*, **124**(3), pp. 617–624.
- [11] Prosperetti, A., 1991, "The Thermal Behavior of Oscillating Gas Bubbles," *J. Fluid Mech.*, **222**, pp. 587–616.
- [12] Matsumoto, Y., and Takemura, F., 1994, "Influence of Internal Phenomena on Gas Bubble Motion (Effects of Thermal Diffusion, Phase Change on the Gas-Liquid Interface and Mass Diffusion Between Vapor and Non-Condensable Gas in the Collapsing Phase)," *JSME Int. J., Ser. B*, **37**(2), pp. 736–745.
- [13] Delale, C. F., 2002, "Thermal Damping in Cavitating Nozzle Flows," *ASME J. Fluids Eng.*, **124**(4), pp. 969–976.
- [14] Ahuja, V., Hosangadi, A., and Arunajatesan, S., 2001, "Simulations of Cavitating Flows Using Hybrid Unstructured Meshes," *ASME J. Fluids Eng.*, **123**, pp. 331–340.
- [15] Hosangadi, A., Lee, R. A., Cavallo, P. A., Sinha, N., and York, B. J., 1998, "Hybrid, Viscous, Unstructured Mesh Solver for Propulsive Applications," AIAA-98-3153, AIAA 34th JPC, Cleveland, OH (34th AIAA/ASME/SAE/ASEE Joint Propulsion Conference & Exhibit, Cleveland, OH, July 13–15, 1998).
- [16] Ruggeri, R. S., and Moore, R. D., 1968, "Prediction of Thermodynamic Effects of Developed Cavitation Based on Liquid-Hydrogen and Freon-114 Data in Scaled Venturis," NASA TN, D-4387.
- [17] Lemmon, E. W., McLinden, M. O., Peskin, A. P., and Friend, D. G., 2000, "Thermodynamic and Transport Properties of Pure Fluids and Mixtures (NISIR12)," *NIST: Standard Reference Data Program National Institute of Standards and Technology*, 100 Bureau Dr., Stop 2310 Gaithersburg, MD 20899-2310.
- [18] So, R. M. C., Sarkar, A., Gerodimos, G., and Zhang, J., 1997, "A Dissipation Rate Equation for Low Reynolds Number and Near-Wall Technique," *Theor. Comput. Fluid Dyn.*, **9**, pp. 47–63.
- [19] Coutier-Delgosha, O., Fortes-Patella, R., and Reboud, J. L., 2003, "Evaluation of the Turbulence Model Influence on the Numerical Simulations of Unsteady Cavitation," *ASME J. Fluids Eng.*, **125**(1), pp. 38–45.
- [20] Hosangadi, A., Lee, R. A., York, B. J., Sinha, N., and Dash, S. M., 1996, "Upwind Unstructured Scheme for Three-Dimensional Combusting Flows," *J. Propul. Power*, **12**(3), pp. 494–503.
- [21] Barth, T. J., and Linton, S. W., 1995, "An Unstructured Mesh Newton Solution for Compressible Fluid Flow and Its Parallel Implementation," AIAA-95-0221, 33rd AIAA Aeospace Sciences Mtg., Reno, NV, January 9–12, 1995.
- [22] Chen, Y., and Heister, S. D., 1996, "Modeling Hydrodynamic Nonequilibrium in Cavitating Flows," *ASME J. Fluids Eng.*, **118**, pp. 172–178.
- [23] Venkateswaran, S., Lindau, J. W., Kunz, R. F., and Merkle, C. L., 2002, "Computation of Multiphase Mixture Flows With Compressibility Effects," *J. Comput. Phys.*, **180**, pp. 54–77.
- [24] Senocak, I., and Shyy, W., 2002, "A Pressure-Based Method for Turbulent Cavitating Flow," *J. Comput. Phys.*, **176**, pp. 363–383.
- [25] Song, C. S. S., and Qin, Q., 2001, "Numerical Simulations of Unsteady Cavitating Flows," *Proceedings of the Fourth International Symposium on Cavitation*, Pasadena, CA, California Institute of Technology, Pasadena, California, 20–23 June, 2001.
- [26] Merkle, C. L., Feng, J. Z., and Buelow, P. E. O., 1998, "Computational Modeling of the Dynamics of Sheet Cavitation," *Proceedings of the 3rd International Symposium on Cavitation*, Grenoble, France, Proceedings 3rd International Symposium on Cavitation, Grenoble, France, April 7–9, 1998.
- [27] Sarosdy, L. R., and Acosta, A. J., 1960, "Note on Observations of Cavitation in Different Fluids," Paper No. 60-WA-83, ASME Winter Annual Meeting, New York, November 27–December 2, 1960.

# Cavitation Properties of Oils Under Dynamic Stressing by Tension

P. R. Williams

R. L. Williams

Centre for Complex Fluids Processing,  
School of Engineering,  
University of Wales Swansea, Singleton Park,  
Swansea SA2 8PP, UK

*We report measurements of the effective tensile strength  $F_c$  of commercial “multigrade” oils (in the SAE viscosity grades 5W-30 and 10W-40) over a range of temperatures  $T$ , which are representative of those encountered under their normal operating conditions (in the range  $20^\circ\text{C} \leq T \leq 140^\circ\text{C}$ ). Also reported are the values of  $F_c$  that are obtained for Newtonian silicone oils over a range of shear viscosities. In the experiments reported herein, samples of liquid are subjected to dynamic stressing by a pressure-tension cycle, this being a feature of the conditions experienced by a lubricant within a dynamically loaded journal bearing and the method used to estimate  $F_c$  avoids reliance on direct measurements of substantial dynamic tensions using conventional pressure transducers. [DOI: 10.1115/1.1881692]*

*Keywords:* Effective Tensile Strength, Cavitation, Cavitation Threshold, Dynamic Stressing

## 1 Introduction

The term “cavitation” usually refers to the formation of bubbles in a liquid when it experiences “negative pressure,” or tension. If the tension exceeds a liquid’s cavitation threshold or effective tensile strength  $F_c$ , at that temperature [1,2] it changes irreversibly into a two-phase system of liquid and a mixture of vapor and dissolved gas, the latter appearing as cavitation bubbles.

During the flow of an oil within a dynamically loaded journal bearing, the lubricant may experience wide ranges of temperature and pressure. In such a situation, the effective tensile strength of an oil is an important consideration in the assessment of flow boundary conditions within fluid film bearings, their load bearing capacity, and the cavitation damage potential of liquids [1–8]. The subambient pressures that give rise to cavitation in lubricating films may be either *gaseous* or *vaporous*: the former may arise due to ventilation from the surrounding atmosphere or by the dissolution of gases, whereas vaporous cavitation results if the pressure in a lubricant falls to (or below) its vapor pressure. It is the latter phenomenon (which may occur in the dynamic loading of engine bearings) that is the subject of the present paper.

Homogeneous nucleation theory predicts that the formation of vapor bubbles requires large tensions, some 1.3 kbar for water [9]. Cavitation in common engineering liquids, such as lubricants, usually involves heterogeneous nucleation at lower tensions, and in the absence of an adequate theory, it is necessary to *measure* the cavitation threshold of such liquids. To be of engineering relevance, such measurements (which are necessarily of the liquid’s “effective” tensile strength) must be made under pertinent conditions. These can involve enormous rates of negative pressure development ( $>1 \text{ bar}/\mu\text{s}$ ) and a wide range of temperatures ( $<150^\circ\text{C}$  in the case of some motor oils).

Addressing such issues in rigorous experiments is difficult and an important motivation in the present work is the fact that no single technique has previously been established as a reliable means of measuring cavitation thresholds under conditions of engineering relevance. Moreover, scant reliable data exists concerning the temperature dependence of the tensile strength of engi-

neering liquids, such as lubricants, under dynamic stressing. In the case of water, the most commonly encountered liquid in engineering flows, studies under dynamic stressing have produced disturbingly large discrepancies between theoretical and experimental values of  $F_c$  [10,11], and in the case of multigrade oils, there is a paucity of data concerning the temperature dependence of  $F_c$  under appropriate conditions of dynamic stressing [12,13]. The main purpose of this paper is to report on experiments in which such measurements have been made.

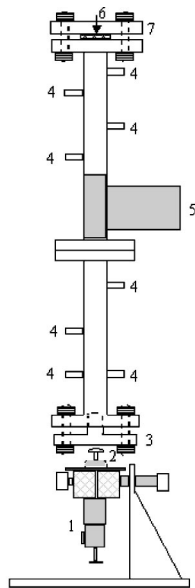
**1.1 Previous Related Work.** One of the few previously reported studies of the temperature dependence of  $F_c$  under dynamic stressing involved experiments in which a pressure pulse is generated in a column of liquid by a bullet striking a piston at the base of column [10]. The pulse is reflected at the free surface as tension, and by varying the peak pressure  $P$  in the incident pulse (using different combinations of bullet power and piston length) the values of  $P$  and peak tension  $F$  of the reflected pulse are recorded. The  $(F, P)$  curve shows a limiting value that provides an estimate of the liquid’s tensile strength  $F_c$ .

In this “Bullet-Piston” (B-P) experiment, cavitation results from a single tension pulse whose characteristics are relevant to cavitation in engineering flow situations, estimates of the rates of tensile stress development in oils within engine bearings being commensurate with those in B-P work (50–100  $\mu\text{s}$ ). Despite these desirable features, the B-P technique has suffered serious drawbacks.

First, the means by which  $P$  is varied (using different combinations of piston mass, piston length and bullet momentum) necessitates frequent dismantling of the apparatus and removal of the liquid; this alters the liquid’s nucleation state and is inconvenient for work at high and low temperatures. More seriously, the values of  $F_c$  resulting from previous B-P work are anomalously low, by at least an order of magnitude in the case of water. For the latter reason, B-P work was little reported after the mid-1970s, but more recent work involving a development of the technique has established that its apparent unreliability was due to deficiencies in transduction rather than any inherent limitation [11,14]. This recent work eschews conventional measurements of dynamic negative pressures (which rely on transducers designed for positive pressures) and has the benefit of allowing dynamic tensions to be varied while the liquid remains in situ. The present paper re-

Contributed by the Fluids Engineering Division for publication in the JOURNAL OF FLUIDS ENGINEERING. Manuscript received by the Fluids Engineering Division August 11, 2003; revised manuscript received, October 29, 2004. Review conducted by H. Johari.





- 1 Magnum model 7000 captive bolt stun gun
- 2 Mushroom-headed cosh
- 3 Steel piston
- 4 Transducer ports
- 5 Support arm
- 6 Sealing gasket
- 7 Sealing flange

Fig. 1 Schematic of the B-P apparatus

ports the use of this new, improved technique in measurements of the cavitation threshold of multigrade lubricants over a range of temperatures.

## 2 Experimental

The B-P apparatus used in the present work (see Figs. 1 and 2) consists of a cylindrical stainless steel tube (length 1.4 m and internal diameter 0.0243 m), which is closed at its lower end by a piston (#3). The piston is coupled to the projecting face of a Magnum Model 7000 captive-bolt stun gun (Shelby and Vokes, UK), whose action generates a pressure pulse in a column of liquid within the tube. The duration of the pressure (and tension) pulses is typically 200–500  $\mu$ s, with a rise time to peak amplitude of 50–100  $\mu$ s. The characteristic time of these pulses is an important feature of the B-P technique in terms of its application to lubrication within a dynamically loaded journal bearing. One example of the relevance of the B-P technique to this area is evident from a

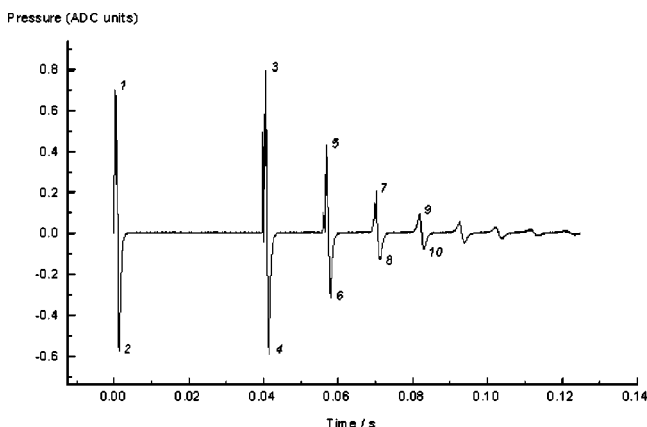


Fig. 2 The B-P apparatus (with heating jacket removed)

rheological study of multigrade oils in an extensional flow field conducted by Gupta et al. [15]. In an attempt to relate their results to the performance of oils at engine operating conditions, the latter workers estimated the maximum rates of extensional deformation experienced by an oil within the main front bearing of a typical automobile engine. For engine speeds between 2000 and 6000 rpm, the characteristic times corresponding to these extension rates are commensurate with the time scales of stressing associated with the action of the present B-P apparatus (200–500  $\mu$ s).

In the present apparatus, pressure changes within the liquid in the tube were monitored using two dynamic pressure transducers (Kistler 603B, Kistler UK) mounted in mechanically insulated ports in the tube wall, the positions of the transducers above the face of the piston being 33.6 and 77.8 cm. The 603B, which has a short rise time (1  $\mu$ s), a high natural frequency (>450 kHz), and a 200 bar range, has been used in other cavitation studies [16]. The 603B transducer outputs were sampled at 1 MHz by 12-bit analog-to-digital converters (ADCs) in a Microlink 4000 transient recorder (Biodata, UK). In addition, a KP-136 hydrophone (Ktech Corp., USA) was used. The output from the KP-136 was connected via BNC connectors and RF coaxial cables to a Gage 8012A, 12-bit ADC (Gage Inc., Can.) and converted to pressure in the following way.

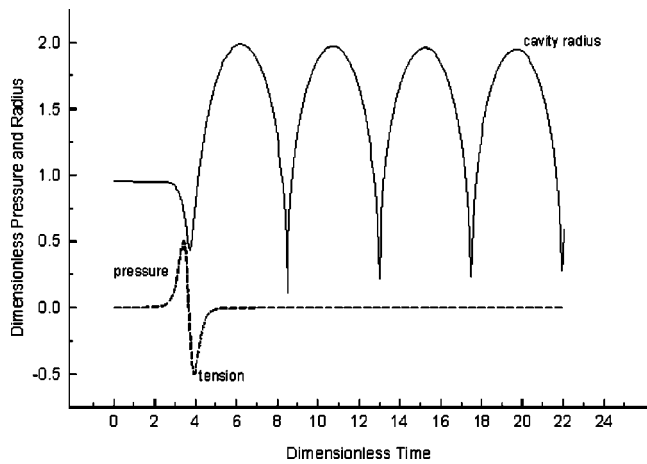
Assuming one-dimensional planar shock propagation normal to the transducer's active area, the pressure (kbar) is related to the charge/active area,  $x(\mu C/cm^2)$ , of the transducer as follows, after calibration by Sandia National Laboratories, USA ([www.sandia.gov/psl/](http://www.sandia.gov/psl/)):

$$\text{Pressure (kbar)} = ax + bx^2 + cx^3 + dx^4 + ex^5 + fx^6$$

where  $a=4.2695164$ ;  $b=12.413068$ ;  $c=-13.229975$ ;  $d=8.7742958$ ;  $e=-2.6080845$ ;  $f=0.27130771$ ; and  $x=CV/A$ , where  $C$  is the total capacitance of the recording circuit (comprising transducer (41 pF)+lead(178 pF)+CS8012A charge amplifier input (25 pF) to give a total of 0.000244  $\mu$ F);  $V$  is the voltage output and  $A$  is the active area of the transducer (0.0905  $cm^2$ ).

The upper steel flange connects the tube to (i) a high-pressure steam line; (ii) a vacuum line, and (iii) a regulated static pressure line, the latter being connected by a valve to an oxygen-free nitrogen supply and a pressure gage. The lower flange houses the piston, which, when removed, provides a connection to a steam condensation system and a liquid drain point. Prior to experiments, superheated (110°C) steam is blown through the tube. Periodically, steel plugs which are screwed into the transducer ports in the tube walls and whose ends are mounted flush with the inner tube wall, were removed for inspection and replaced. The walls of the open tube were subsequently heated and allowed to dry at 100°C. Following this procedure the tube was allowed to cool prior to being refilled to the required depth with a fresh sample of liquid, which was subsequently heated to the test temperature. The liquid was then thoroughly degassed in situ by connecting the upper flange to a vacuum line (-1 bar). The temperature of the liquid in the range 20–140°C was regulated by means of a 3 m heating tape (100 w/m at 230 V) and an Armourflex-laged (IPS Ltd., UK) insulating jacket wrapped around the tube's external surface. The temperature at the tube's inner surface was measured using three flush-mounted thermocouples (Jenway, UK).

In the present work, dynamic stressing experiments were conducted on samples of degassed deionized water, commercial multigrade motor oils in the 10W-40 (for petrol and diesel engines: API SJ/CF, ACEA A3/B3-98, and API CF, ACEA B3-98, respectively) and 5W-30 (for petrol engines: API SJ/CF, ACEA A3/B3/B4-98) categories, and a series of silicone oils (Dow Corning 200, BDH Chemicals, UK), the latter having kinematic viscosities in the range 1–350 cS. In each experiment, the free surface was 0.945 m above the face of the piston at the base of the liquid column. All samples were degassed in situ for 90 min prior to measurements. In the case of the oil samples, the degassing pro-



**Fig. 3** A typical pressure record obtained from a 603B transducer in an experiment on silicone oil. The pressure transducer output is in ADC units, positive values of which correspond to positive pressure and vice versa. The record contains the primary (1-2) and secondary pressure-tension cycles (3-4, 5-6, etc.).

cedure was conducted at a temperature of 90 °C due to their relatively high shear viscosity, the samples being subsequently brought to the requisite test temperature. The shear viscosity of the liquids was measured using an ARES controlled-strain rheometer (Rheometric Sci., USA) fitted with a cone-and-plate geometry.

### 3 Results

**3.1 Primary and Secondary Pressure-Tension Cycles.** The main features of a typical pressure record obtained from a 603B transducer in an experiment on a sample of silicone oil (shear viscosity 1 cS) are shown in Fig. 3, in which the data are presented in terms of transducer output in unscaled analog-to-digital convertor (ADC) units (positive values correspond to positive pressure and vice versa). A pressure pulse (feature 1 in Fig. 3) is followed immediately by a tension pulse (feature 2) and the cycle

1-2 is referred to herein as the “primary” pressure-tension cycle. Thereafter, the record comprises “secondary” pressure-tension cycles (3-4, 5-6, etc.), which are associated with cavitation activity (subsequent bubble rebound-collapse cycles) and the reflection of pressure waves from the free surface of the liquid column [17].

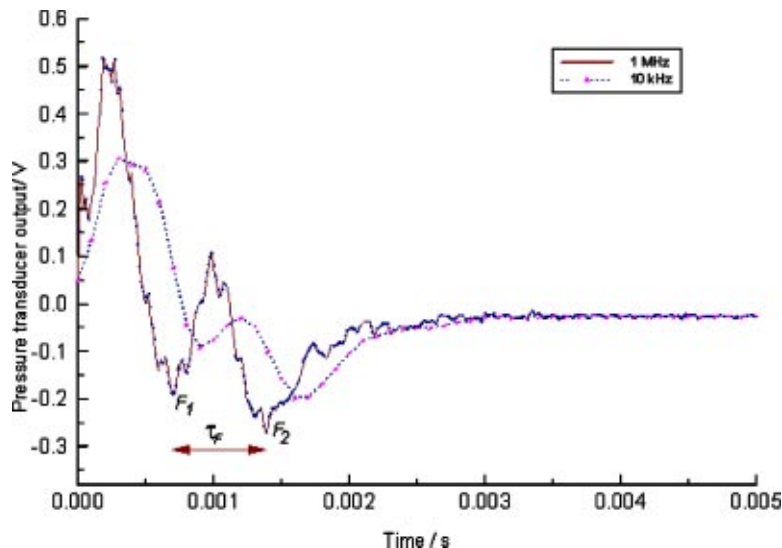
That the response of a bubble nucleus to a single pressure-tension cycle, such as that generated in the present experiments, can result in several cycles of cavitation activity, which may be illustrated as follows. We begin by considering the collapse of a cavity in a large mass of incompressible liquid, in which case the cavity boundary  $R(t)$  obeys the relation

$$R \frac{d^2 R}{dt^2} + \frac{3}{2} \left( \frac{dR}{dt} \right)^2 = \frac{1}{\rho_l} \left( P_b - \frac{2\sigma}{R} - P_\infty + \frac{4\mu}{R} \frac{dR}{dt} \right) \quad (1)$$

in which  $\rho$  is the liquid density and  $p_\infty$  is the pressure in the liquid at a large distance from the bubble. The generalized Rayleigh-Plessett equation (Eq. (1)) includes the effects of surface tension  $\sigma$  and shear viscosity  $\mu$ , and the pressure in the gas at the bubble wall  $p_i$  (and  $p_\infty$ ) may be a function of time [18]. Figure 4 shows the result of an integration of Eq. (1) (using a fourth-order adaptive Runge-Kutta method) in which  $p_\infty(t)$  is chosen to represent a primary pressure-tension cycle, such as 1-2 in Fig. 3. The representative values of  $\sigma, \mu, \rho$ , and  $p_i$  are taken to be those of water at 20°C [19], the vapor pressure of the liquid at this temperature representing  $p_i$  and the initial radius of the cavity (at rest) being 10  $\mu\text{m}$ . The resulting change in the cavity radius  $R(t)$  in response to the primary pressure-tension cycle involves a series of oscillatory cycles of bubble growth followed by rapid collapse and rebound, as shown in Fig. 4, in which time is made dimensionless by the appropriate value of the Rayleigh collapse time  $\tau$  [20], where

$$\tau = 0.915 R_m \left( \frac{\rho}{p_0 - p_v} \right)^{1/2} \quad (2)$$

and the cavity radius is represented by  $R/R_m$ , where  $R_m$  is the initial radius of the cavity (note that the pressure  $p_0$  is atmospheric pressure, the values of pressure in the primary cycle being made dimensionless by the peak pressure  $P$  in the incident pulse). In the corresponding experiments, the hydrodynamic pressure variation



**Fig. 4** Results of a numerical integration of Eq. (1) illustrating the response of a cavity nucleus (initially at rest) to a pressure variation that represents the primary pressure-tension cycle generated in the experiments. The resulting change in cavity radius involves several oscillatory cycles of gradually diminishing amplitude and period.

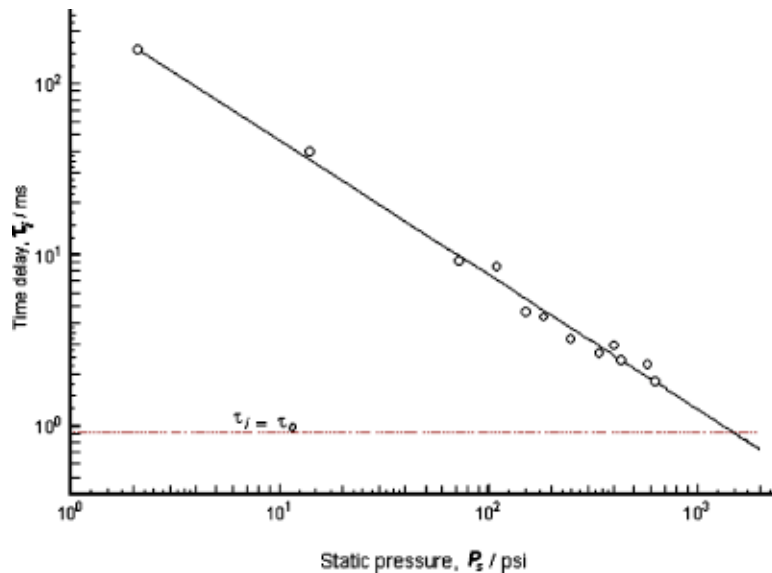


Fig. 5 Results of experiments on degassed, deionized water. The pressure-tension cycles were recorded using the KP-136 at a sampling rate of 1 MHz (solid line). The pulses  $F_1$  and  $F_2$  recorded at 1 MHz appear as a single tension pulse at a (simulated) 10 kHz sampling rate.

produced about the oscillating cavitation bubble(s) is recorded as the secondary pressure-tension cycles shown in pressure records, such as Fig. 3

### 3.2 Measurements of Liquid Tensile Strength in the B-P Apparatus.

**3.2.1 Experiments Involving the KP-136 Hydrophone.** An initial series of experiments was conducted on samples of degassed deionized water that were obtained from a two-stage, reverse-osmosis, ion-exchange purification system (Elga, UK) incorporating a carbon filter (for organics), a “nuclear grade” deionization stage, and a final membrane filter (0.2  $\mu\text{m}$ ). In these experiments the length of the liquid column was 0.95 m, the position of the free surface being 61.4 cm above the location of a KP-136 hydrophone. A typical record of dynamic pressures within the water is shown in Fig. 5 in terms of the KP-136’s voltage output, which was recorded at a sampling rate of 10 MHz (solid line). The corresponding record obtained at a simulated 10 kHz sampling rate is also shown, this sampling rate corresponding to that employed in previous B-P work. Note that the pulses  $F_1$  and  $F_2$  recorded at 10 kHz appear as a *single*, broad tension pulse, which corresponds to descriptions of this feature in previous B-P work. The upward-traveling pressure pulse is reflected at the free surface as a downward-traveling tension pulse  $F_1$ . This is followed, after a time  $\tau_F$  by an upward-traveling tension pulse  $F_2$  due to reflection from the face of the piston [11]. Using the relationship given above for the calibration of the KP-136 hydrophone, the maximum dynamic tension sustained by degassed, deionized water at 20°C was found to be 90 bar ( $\pm 5$  bar).

**3.2.2 Experiments Involving the Application of a Regulated Static Pressure.** As explained above, the B-P technique used in previous work has the disadvantage that the means by which  $P$  is varied (using different combinations of piston mass, piston length, and bullet momentum) necessitates frequent dismantling of the apparatus and removal of the liquid. This was overcome in the present work by a new method, which allows  $F_c$  to be estimated with the same liquid sample remaining in situ throughout.

This method involves regulating a static pressure  $P_s$  in the space above the liquid column,  $P_s$  being increased gradually in a series of dynamic stressing experiments. From the dynamic pres-

sure records obtained in these experiments a record is made of the time delay  $\tau_i$  between the peak incident pressure (corresponding to 1 in Fig. 3) and the first pressure pulse arising from cavitation bubble collapse (corresponding to 3 in Fig. 3). It is useful to recall here that, under tension, cavitation bubbles grow from preexisting nuclei within the liquid and eventually collapse and rebound, emitting a pressure wave into the liquid as they do so. Hence the interval  $\tau_i$ , which encompasses the attainment of maximum cavity radius and its subsequent decrease to a minimum value, is reduced by increasing  $P_s$  ( $\tau_i$ , therefore, provides a convenient measure of cavitation activity).

The B-P experiment involves the transmission of a pulse of tension by the liquid to the face of the piston, and that cavitation may result from this pulse. It follows that, in the case of experiments in which cavitation activity is detected, the magnitude of the tension transmitted by the liquid is sufficient to result in the development of a transient net negative pressure in the presence of a background static pressure  $P_s$ . Thus an estimate of the magnitude of tension capable of being transmitted by the liquid can be obtained from a knowledge of  $P_s$ .

The results of such experiments on degassed, deionized water are shown in Fig. 6, in which  $\tau_i$  is plotted as a function of  $P_s$  (absolute, in psi) and from which  $F_c$  is estimated in the following way. The time delay  $\tau_0$  between pulses corresponding to 1 and 2 in Fig. 3 represents the time required for the upward-traveling pressure wave to return, as tension, to the lower transducer’s location: it also represents the smallest time interval for which a cavity growth-collapse cycle could occur given that a bubble would have to grow and collapse infinitely quickly in order that  $\tau_i = \tau_0$ . Thus  $F_c$  is estimated by extrapolation of the data in Fig. 5 to that pressure  $P_s$  at which  $\tau_i = \tau_0$ , this condition representing the complete suppression of cavitation. This procedure yields a value of  $F_c$  of 96 bar ( $\pm 5$  bar), in good agreement with the maximum value of 90 bar ( $\pm 5$  bar) recorded by the KP-136 hydrophone.

It is clearly appropriate to compare our results to values obtained by other dynamic stressing techniques that do not rely on the direct measurement of negative pressures using pressure transducers. Such a technique has been reported by Marston and Unger [21] and involved a compressive pulse of duration 1.7  $\mu\text{s}$  that was reflected at a flexible membrane to create a pulse of tension in the liquid. Their values of  $F_c$  (100–110 bar) for degassed, distilled

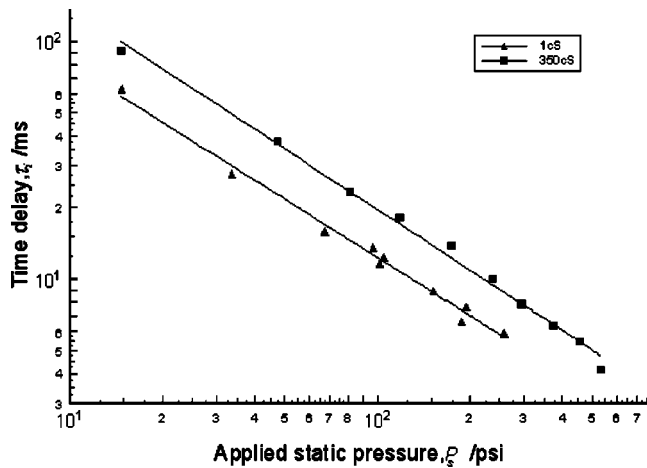


Fig. 6 The time interval  $\tau_i$  as a function of applied static pressure  $P_s$  (in psi) for degassed, deionised water. Also shown is the value of the time interval  $\tau_0$  used to estimate  $F_c$ .

water are in good agreement with the results of the present work, which yield a value of 96 bar ( $\pm 5\%$ ). Our slightly lower value may be attributed to the longer time of stress development involved in the present work (50–100  $\mu$ s rather than 1–2  $\mu$ s). It is well established that in work involving the dynamic stressing of liquids by tension, the higher the rate of stress development, the higher the value of  $F_c$  obtained [12].

Very few studies of the dependence of  $F_c$  on shear viscosity  $\mu$  have been conducted but, among the work reported, pulse reflection methods have figured prominently, the B-P experiment being the most widely employed. Bull [22] and Couzens and Trevena [23] reported that their results could be represented by an expression of the form  $F_c \propto \mu^n$ , the value of  $n$  being 0.2 in the former study, whereas the latter workers reported a value of 0.1. In work involving a pulse reflection technique, Carlson and Levine [24] reported a power-law relationship for samples of glycerol whose viscosity was varied by changing the test temperature, the value of  $n$  found in their work being 0.3. In the light of the different results found in the aforementioned studies, experiments were conducted using the B-P apparatus on a range of Newtonian silicone oils (Dow Corning 200 series, BDH Chemicals, UK) of different shear viscosities (1, 50, 100, and 350 cS). For the sake of clarity, the results obtained in experiments on two silicone oils (viscosity 1 and 350 cS, respectively) are shown in Fig. 7, and the values of  $F_c$  obtained for the series of oils are shown in Table 1. The results may be represented by an expression of the form  $F_c \propto \mu^n$ , where  $n=0.09$  ( $\pm 0.005$ ). This finding corresponds closely to that ( $n=0.1$ ) reported by Couzens and Trevena [23] for silicone oils, in a similar viscosity range (although the absolute values of  $F_c$  found in the present work are significantly higher).

The relation  $F_c \propto \mu^{0.2}$  obtained by Bull [22] in pulse reflection work on samples of water, olive oil, glycerol, and syrup has been attributed as due more to a coincidental distribution of nuclei in these different liquids than to other, more basic features of cavitation [25]. In view of the agreement found between the results of the present study and those of Couzens and Trevena [23], it is noteworthy that both involved a series of silicone oils with a range of viscosities, rather than a range of different fluids, with different viscosities, as in the work of Bull [22].

We now turn to the results obtained in experiments on samples of commercial multigrade oils (10W-40 petrol, 10W-40 diesel, and 5W-30 petrol), which were conducted at various temperatures  $T$  in the range  $20^\circ\text{C} \leq T \leq 140^\circ\text{C}$ . The values of  $\tau_i$  recorded over a range of pressures  $P_s$  at two temperatures (20 and  $90^\circ\text{C}$ , respectively) are shown in Fig. 8–10 for the different oils. A total of five sequential repeat dynamic stressing measurements were made at

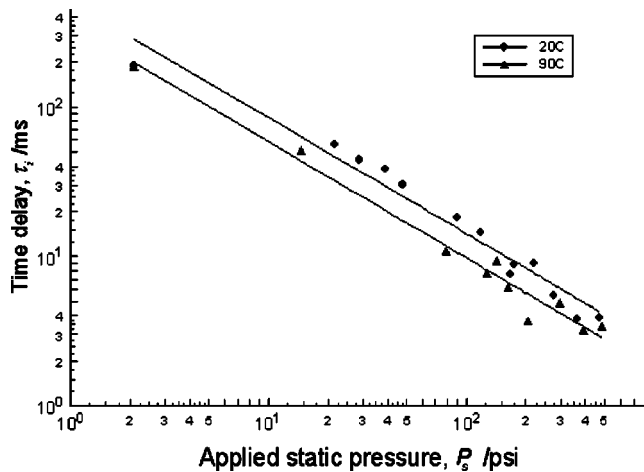


Fig. 7 The time interval  $\tau_i$  as a function of applied static pressure  $P_s$  (in psi) for two silicone oils of different shear viscosities (1 and 350 cS)

each value of the applied static pressure at each temperature, which procedure established the repeatability of the results as being within  $\pm 5\%$  of the values reported herein, the average values being indicated by the height of the symbols. An example of the pressure record obtained in an experiment at a temperature of  $120^\circ\text{C}$  (background static pressure atmospheric) is shown in Fig. 11.

We attempt to set these findings in the context of *vaporous* rather than *gaseous* cavitation phenomena, although the latter represent an important (possibly dominant) feature of oil cavitation. Our reasons for choosing to study degassed liquids in the present work are to introduce a new technique in lubricant cavitation testing and to explain its operation and the analysis of results. In so doing it is important to compare the results of measurements made

Table 1 Tensile strength  $F_c$  for Dow Corning® 200 silicone oils at  $20^\circ\text{C}$

Shear viscosity of oil (cS)	$F_c$ (bar)
1	69
50	72
100	81
350	125

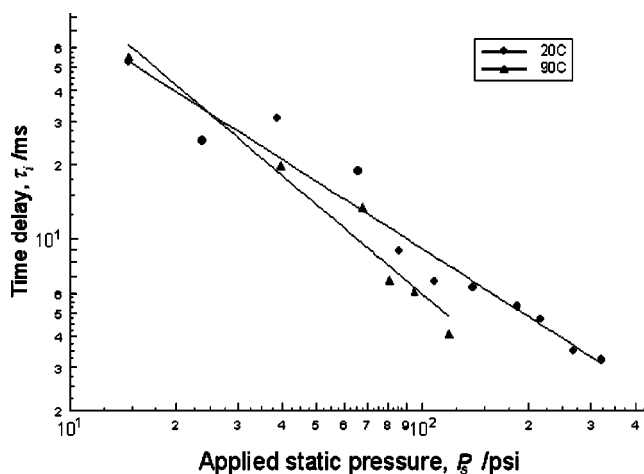


Fig. 8 The time interval  $\tau_i$  as a function of applied static pressure  $P_s$  (in psi) for SAE 10W-40 petrol oil at two temperatures,  $20^\circ\text{C}$  and  $90^\circ\text{C}$

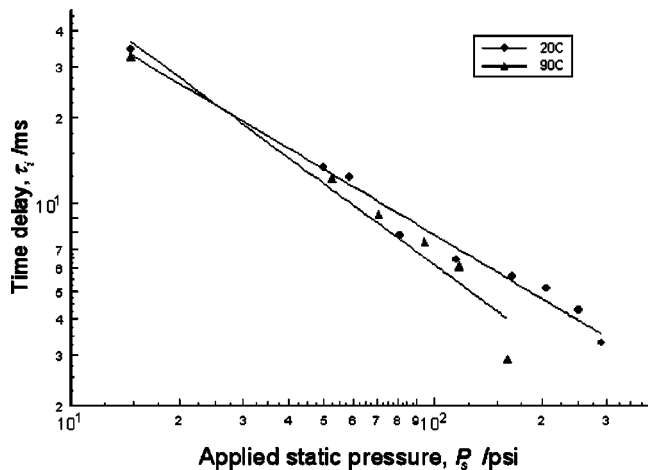


Fig. 9 The time interval  $\tau_i$  as a function of applied static pressure  $P_s$  (in psi) for SAE 10W-40 diesel oil at two temperatures, 20°C and 90°C

on oil samples with those made on other liquids, some of which have also been studied by other related techniques. In order to facilitate a meaningful basis for such comparisons the provision of degassed samples provides a convenient “baseline,” given the well-documented dependence of  $F_c$  on the presence of permanent gas bubbles within a liquid [11]. Our aim is to explain how the B-P apparatus enables the cavitation response of a lubricant to an alternate pressure-tension cycle to be investigated over an appropriate range of temperature (such a technique has been lacking in cavitation research until now) and to establish that the resulting values of  $F_c$  provide reliable, upper-bound estimates for the lubricant’s tensile strength, these being particularly valuable in the case of comparisons of  $F_c$  at different temperatures (and hence gas solubilities).

As can be seen from Tables 2–4, at 20°C samples of the degassed motor oil are capable of sustaining a substantial transient tension ( $\geq 59$  bar), the corresponding values being 180 bar for 10W-40 (petrol engine oil), 80 bar for 5W-30 (petrol engine oil), and 59 bar for 10W-40 (diesel engine oil). Moreover, even at the highest test temperature attained for the 10W-40 (petrol engine) sample (140°C), the oil was capable of sustaining a transient tension of 10 bar. If the repeated application of tension (due to bearing action) to the recirculating oil were to progressively denude it

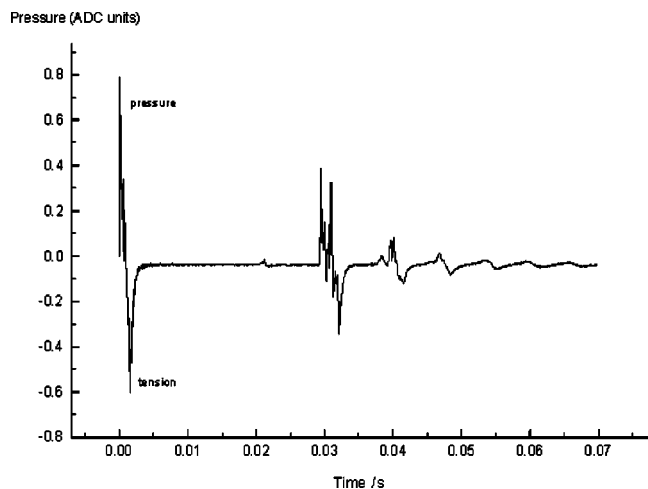


Fig. 10 The time interval  $\tau_i$  as a function of applied static pressure  $P_s$  (in psi) for SAE 5W-30 petrol oil at two temperatures, 20°C and 90°C



Fig. 11 Pressure record obtained in the dynamic stressing of an SAE 10W-40 petrol oil at 120°C and atmospheric pressure

of nuclei, then our findings suggest that during an engine’s

Table 2 Viscosity and tensile strength data for 10W-40 petrol oil at various temperatures

Temperature (°C)	$F_c$ (bar)	Viscosity (Pa s)
20	180	0.26
30	113	0.12
50	92	0.05
90	48	0.014
110	38	0.0096
140	30	N/A

**Table 3 Viscosity and tensile strength data for 10W-40 diesel oil at various temperatures**

Temperature (°C)	$F_c$ (bar)	Viscosity (Pa s)
20	59.4	0.227
40	51	0.073
70	28.9	0.022
90	22.2	0.012

“warming-up” period, prior to the attainment of its normal operating temperatures following a cold start, the lubricant may be substantially resistant to (vaporous) cavitation. This may have serious consequences in terms of the load-carrying capacity of fluid-film bearings, given the stabilizing influence of cavitation on journal dynamics [26,27], e.g., in the absence of cavitation it is well established that a journal exhibits half-speed whirl for a constant viscosity lubricant; under fullfilm conditions the journal’s trajectory spirals toward the bearing and, as it does so, the angular velocity of the path approaches half-speed whirl, resulting in zero load-bearing capacity and, ultimately, failure of the bearing [8,28].

The trend of the data suggests far lower (and possibly negligible) levels of  $F_c$  at temperatures in excess of 150°C. This leads us to speculate that the eventual attainment of normal operating temperatures may correspond to an inability of the lubricant to resist vaporous cavitation.

We now turn to consider another aspect of the data in Table 2, which may be represented by an expression of the form  $F_c \propto \mu^n$  (as is the case for the silicone oils), with  $n=0.43$ . This value of  $n$  is substantially greater than that obtained for the silicone oils or other Newtonian fluids in related studies [12]. We emphasize that the study of Newtonian glycerol samples reported by Carlson and Levine [24] is relevant to the present work insofar as it involved measurements of  $F_c$  by dynamic stressing, in which the reflection principle was used to convert a pressure pulse into a tension pulse and in which the liquid’s viscosity was varied by changing its temperature (as in the case of the present work involving motor oils). However, the value of  $n$  found in that work [24], in which the rate of tensile stress development is approximately  $10^4$  times higher than in the present work, is lower ( $n=0.3$ ) than in the case of our result for the 10W-40 petrol motor oil but is similar to that achieved for the 10W-40 (diesel) oil ( $n=0.34$ , from Table 3). The value of  $n=0.22$  for the 5W-30 (petrol) oil (from Table 4) is comparable to that obtained by Bull [22], however all  $n$  values are higher than the  $n=0.1$  value for the Newtonian fluids reported by Couzens and Trevena [23] and the  $n=0.09$  determined herein for silicone oils. The differences in  $n$  values for the motor oils studied may reflect differences in formulation in terms of the type of polymer additives and their relative concentrations in oil treatments, but it is interesting to speculate on the possible influence of the extensional viscosity  $\eta_E$  in these results.

Rheological studies of multigrade oils [29], including work at elevated pressures [30], have confirmed that samples of commercial multigrade oils may exhibit an enhanced resistance to extensional deformation, with values of the Trouton ratio,  $Tr(=\eta_E/\mu)$ , in excess of that value (3) expected for a Newtonian fluid. Many cavitation techniques (including that used in the present work) yield estimates of  $F_c$  based on the detection of pressure waves

**Table 4 Viscosity and tensile strength data for 5W-30 petrol oil at various temperatures**

Temperature (°C)	$F_c$ (bar)	Viscosity (Pa s)
20	80.5	0.131
40	59	0.047
70	50	0.016
90	44	0.009

resulting from the dynamics of cavitation bubbles in a liquid when it is subjected to an imposed pressure variation. But the growth and collapse of a bubble in a liquid is associated with the production of an extensional flow [31] and thus, for liquids exhibiting a high value of  $Tr$ , the extensional viscosity  $\eta_E$  may influence estimates of  $F_c$ . Rheological studies of commercial multigrade oils have established that such liquids display a high extensional viscosity [30] which, in the context of the present work, would be expected to increase the estimated value of  $F_c$  by increasing  $\tau_i$  (due to the fact that the latter parameter encompasses both the time required for the growth and the collapse of cavitation bubbles). Moreover, cavitation bubble oscillation in liquids with high values of  $Tr$  may be expected to produce pressure waves of significantly lower amplitudes than in their Newtonian counterparts. That this is so may be seen from basic hydrodynamic theory, in which the generalized Bernoulli equation predicts that the pressure variation  $\Delta P$  about an oscillating bubble will vary as  $\Delta P \propto d^2V/dt^2$ , where  $V$  is the volume of the bubble. Thus higher levels of applied tension may be required to stimulate detectable levels of acoustic emission in liquids with high  $Tr$ . These higher levels of tension would result in higher estimates of  $F_c$  and would support the idea mooted by Berker et al. [4] in their study of the effect of polymer on flow in journal bearings of some “mitigating effects” of viscoelasticity on cavitation.

#### 4 Concluding Remarks

The salient features of the work reported in this paper are as follows. It describes a technique in which lubricants (and other common engineering liquids) may be subjected to dynamic stressing by pulses of tension, at temperatures representative of those encountered in their normal operation. It is important to note that the present work does not represent an attempt to recreate the complicated flow field experienced by a lubricant within a bearing, this being a mixture of shear and extensional flow [15]; rather, it is concerned solely with isolating, for separate detailed study, the effects (nonetheless important) of subjecting a liquid to a pressure-tension cycle (which is also a feature experienced by a lubricant during its passage through a bearing). Also reported are values of  $F_c$  for degassed samples of several commercial multigrade oils which, as far as we are aware, are the first of their kind to be reported for these lubricants at elevated temperatures. The results obtained suggest that further experiments should now be conducted using this technique in order to study the effect(s) of the presence of dissolved (permanent) gases in the cavitation of lubricants under dynamic stressing by pulses of tension. Such work is planned, and the results will be communicated in a future paper.

#### Nomenclature

- $F_c$  = tensile strength (cavitation threshold) of liquid
- $F$  = peak negative pressure (tension)
- $P$  = peak incident pressure
- $\rho$  = fluid density
- $R$  = cavity radius
- $R_m$  = maximum cavity radius
- $p_i$  = internal pressure of cavity
- $p_\infty$  = bulk liquid pressure
- $p_0$  = atmospheric pressure
- $\sigma$  = surface tension
- $n$  = power-law index
- $\Delta P$  = hydrodynamic pressure variation
- $P_s$  = applied static pressure
- $Tr$  = Trouton ratio
- $\tau$  = Rayleigh collapse time
- $\tau_i$  = time delay between initial pressure wave and first cavitation pressure peaks
- $\tau_0$  = minimum time delay in the experiments
- $\mu$  = zero-shear viscosity

$\eta_E$  = extensional viscosity  
 $V$  = bubble volume

## References

- [1] Braun, M. J., and Hendricks, R. C., 1984, "An Experimental Investigation of the Vaporous/Gaseous Cavity Characteristics of an Eccentric Journal Bearing," *ASLE Trans.*, **27**, pp. 1–14.
- [2] Savage, M. D., 1977, "Cavitation in Lubrication-Part 1: On Boundary Conditions and Cavity-Fluid Interfaces" *J. Fluid Mech.* **80**, pp. 743–755.
- [3] Dowson, D., and Taylor, C. M., "Cavitation in Bearings," *Annu. Rev. Fluid Mech.* 1979, **11**, 35–66.
- [4] Berker, A., Bouldin, M. G., Kleis, S. J., and Van Arnsdale, W. E., 1995, "Effect of Polymer on Flow in Journal Bearings," *J. Non-Newtonian Fluid Mech.* **56**, pp. 333–347.
- [5] Floberg, L., 1972, "Lubrication of Two Rotating Cylinders at Variable Lubricant Supply With Special Reference to the Tensile Strength of the Liquid Lubricant," *ASME-ASLE Conf.*, New York, Paper No. 72-Lub. 2.
- [6] Elrod, H. G., 1981, "A Cavitation Algorithm," *ASME J. Lubr. Technol.* **103**, pp. 350–354.
- [7] Brewster, D. E., 1986, "Theoretical Modeling of the Vapor Cavitation in Dynamically Loaded Journal Bearings," *ASME J. Tribol.* **108**, pp. 628–638.
- [8] Gwynllyw, D. Rh., Davies, A. R., and Phillips, T. N., 1996, "On the Effects of a Piezoviscous Lubricant on the Dynamics of a Journal Bearing," *J. Rheol.* **40**, pp. 1239–1266.
- [9] Skripov, V. P., 1974, *Metastable Liquids*, Wiley, New York.
- [10] Sedgewick, S. A., and Trevena, D. H., 1976, "Limiting Negative Pressure of Water Under Dynamic Stressing," *J. Phys. D* **9**, pp. 1983–1990.
- [11] Williams, P. R., and Williams, R. L., 2000, "On Anomalously Low Values of the Tensile Strength of Water," *Proc. R. Soc. Edinburgh, Sect. A: Math. Phys. Sci.* **456**, pp. 1321–1332.
- [12] Trevena, D. H., 1987, *Cavitation and Tension in Liquids*, Adam Hilger, Bristol.
- [13] Joseph, D. D., 1998, "Cavitation and the State of Stress in a Flowing Liquid," *J. Fluid Mech.* **366**, pp. 367–378.
- [14] Williams, P. R., and Williams, R. L., 2002, "Cavitation of Liquids Under Dynamic Stressing by Pulses of Tension," *J. Phys. D* **35**, pp. 2222–2230.
- [15] Gupta, R. K., Chan, R. C., and Deysarkar, A. K., 1990, "Flow of Multigrade Motor Oils in an Extensional Flow Field," *J. Rheol.* **34**, pp. 1373–1386.
- [16] Tomita, Y., and Shima, A., 1986, "Mechanisms of Impulsive Pressure Generation and Damage Pit Formation by Bubble Collapse," *J. Fluid Mech.* **169**, pp. 535–564.
- [17] Barrow, M. S., Bowen, W. R., Hilal, N., Al-Hussany, A., Williams, P. R., Williams, R. L., and Wright, C. J., 2003, "A Study of the Tensile Properties of Thin Fluid Films in an Atomic Force Microscope," *Proc. R. Soc. Edinburgh, Sect. A: Math. Phys. Sci.* **459**, pp. 2885–2908.
- [18] Plessett, M. S. and Prosperetti, A., "Bubble Dynamics and Cavitation," *Annu. Rev. Fluid Mech.* 1977, **9**, pp. 145–185.
- [19] Bolz, R., and Tuve, G., (Eds.) 1973, *CRC Handbook of Tables for Applied Engineering Science*, 2nd Edition, CRC Press, Boca Raton, FL.
- [20] Rayleigh, L., 1917, "On the Pressure Developed in a Liquid During the Collapse of a Spherical Cavity," *Philos. Mag.* **34**, pp. 94–98.
- [21] Marston, P. L., and Unger, B. T., 1986, "Rapid Cavitation Induced by the Reflection of Shock Waves," in *Shock Waves in Condensed Matter*, Plenum, New York, pp. 401–405.
- [22] Bull, T. H., 1956, "The Tensile Strengths of Liquids Under Dynamic Loading," *Philos. Mag.* **8** pp. 153–165.
- [23] Couzens, D. C. F., and Trevena, D. H., 1974, "Tensile Failure of Liquids Under Dynamic Stressing," *J. Phys. D* **7**, pp. 2277–2287.
- [24] Carlson, G. A., and Levine, H. S., 1975, "Dynamic Tensile Strength of Glycerol," *J. Appl. Phys.* **46**, pp. 1594–1601.
- [25] Hsieh, D. Y., 1970, "Bubble Growth in a Viscous Liquid Due to a Transient Pulse," *ASME J. Basic Eng.* **92**, pp. 815–818.
- [26] Li, X. K., Gwynllyw, D. Rh., Davies, A. R., and Phillips, T. N., 2000, "On the Influence of Lubricant Properties on the Dynamics of Two-Dimensional Journal Bearings," *J. Non-Newtonian Fluid Mech.* **93**, pp. 29–59.
- [27] Brindley, J., Elliott, L., and McKay, J. T., 1983, "The Role of Cavitation in Whirl Instability in a Rotor Bearing," *ASME J. Appl. Mech.* **50**, pp. 877–890.
- [28] Cameron, A., 1981, *Basic Lubrication Theory*, Ellis Horwood, London.
- [29] Barrow, M. S., Brown, S. W. J., Cordy, S., Williams, P. R., and Williams, R. L., 2004, "Rheology of Dilute Polymer Solutions and Engine Lubricants in High Deformation Rate Extensional Flows Produced by Bubble Collapse," *ASME J. Fluids Eng.* **126**, pp. 162–169.
- [30] Binding, D. M., Couch, M. A., and Walters, K., 1999, "The Rheology of Multigrade Oils at Elevated Pressures," *J. Non-Newtonian Fluid Mech.* **87**, pp. 155–164.
- [31] Pearson, G., and Middleman, S., 1977, "Elongational Flow Behaviour of Viscoelastic Liquids: Part 1. Modelling of Bubble Collapse," *AIChE J.* **23**, pp. 714–721.

# Computational Analysis of Pressure and Wake Characteristics of an Aerofoil in Ground Effect

Stephen Mahon

Xin Zhang

Aerospace Engineering, School of Engineering Sciences, University of Southampton, Southampton SO17 1BJ, UK

*The pressure and wake of an inverted cambered aerofoil in ground effect was studied numerically by solving the Reynolds-averaged Navier-Stokes equations. Efforts were focused on the setting up of an accurate numerical model and assessing the abilities of various turbulence models in capturing major physical features associated with the flow, such as surface pressure distribution, separation, level of downforce, and wake. A number of ride heights were studied covering various force regions. Surface pressures, sectional forces, and wake characteristics were compared to experimental data. The  $k-\omega$  SST and Realizable  $k-\epsilon$  turbulence models were found to offer good overall simulations, with the  $k-\omega$  SST performing better for the surface pressure and the Realizable  $k-\epsilon$  better for the wake. The simulations at various ride heights correctly captured the trends in flow-field variations with ride height. The surface pressures, wake flow field, and region of separation on the suction surface of the aerofoil, at lower ride heights, were all modeled accurately. [DOI: 10.1115/1.1891152]*

## 1 Introduction

Aerodynamics of wings in ground effect has applications to high-performance racing cars. The understanding of flow physics is a relatively recent experience led by wind tunnel model experiments. Despite efforts by various workers, there remain a number of areas deserving further attention [1]. Because of the high cost of wind tunnel model tests, numerical modeling of the flow should be developed and the best practice assessed.

Computational investigations into inverted wings in ground effect started in the 1980s. The earliest work was done by Katz [2] in which a single-element wing in ground effect was modeled using a panel method. Ground effect was modeled using the image-plane method. The method does not take into account viscous effects, and as a result, no downforce reduction at low ride heights was observed.

In engineering applications, numerical solutions of Reynolds-averaged Navier-Stokes (RANS) equations, often in steady state, are generally obtained. The work by Ranzenbach and Barlow [3,4] studied two-dimensional (2D) aerofoils in ground effect. In Ref. [3], a NACA 0015 aerofoil at zero angle of attack was studied. The Reynolds number based on the chord was  $1.5 \times 10^6$ . A RANS solution was sought with the effect of turbulence modeled by a variant of the  $k-\epsilon$  model. The multiblock fully structured grids contained a total of 20,000–30,000 grid points. Force coefficients were compared to tests. In Ref. [4], a cambered airfoil (NACA 4412) was employed. Again the angle of attack was zero and the Reynolds number was  $1.5 \times 10^6$ . In all cases the ground was stationary, thus, producing a ground boundary layer and an inaccurate ground plane simulation. The downforce compared well to experimental data, obtained by Ranzenbach and Barlow, for a stationary ground case. The results indicated a sharp reduction in downforce at ride heights of the order of 0.05 of the chord. Because of the presence of a thick ground boundary layer, this phe-

nomena, referred to as the force-reduction phenomena, was attributed to the merging of the aerofoil and ground boundary layers.

Recently in a series of studies into an inverted wing in ground effect, Zerihan and Zhang [1] and Zhang and Zerihan [5] highlighted major physical features of wings in ground effect. A study was performed in order to establish a numerical model [6]. The method used solutions of Reynolds-averaged Navier-Stokes equations with turbulence modeled by the Spalart-Allmaras model [7] and the  $k-\omega$  SST model [8]. Fully structured grids were used containing up to 30,000 grid points. The results were compared to measured surface pressures and velocities taken at the center of a wing span in ground effect. Major features of the flow were captured. The results yielded good qualitative trends for the aerodynamic performance, using the one-equation model when the surface pressures were compared at different ride heights. In general, the wake thickness was predicted reasonably well in the region near the trailing edge. Further downstream, the wake was predicted to be thicker than that found in the experiments, with reduced velocities. A boundary layer along the ground plane, indicated by the experimental results, was predicted well using the one-equation model, but was significantly too thick using the two-equation model. In all cases a moving ground was simulated.

In another study, Lawson et al. [9] conducted a numerical study of a GA(W)-1 aerofoil in ground effect through solutions of the RANS equations on a fully structured grid. The total number of grid points were 48,500. Turbulence was modeled by the Spalart-Allmaras model [7]. The computational results were compared to experimental surface pressures and particle image velocimetry (PIV) images obtained with a finite wing. A moving ground was simulated in all computational and experimental cases. The agreement between the experimental and computational data was poor because of different values of freestream velocity employed in the experimental and computational studies, thus assuming zero scaling effects. Although the surface pressures were presented, the computational force variations with ride height were not.

The computational studies conducted thus far have contributed to the general understanding of flow physics and, in some cases, supported critical experimental observations. However, few numerical simulations have obtained entirely satisfactory prediction with a moving ground. Agreement with measurements vary

Contributed by the Fluids Engineering Division for publication in the JOURNAL OF FLUIDS ENGINEERING. Manuscript received by the Fluids Engineering Division January 21, 2004. Revised manuscript received September 27, 2004. Review conducted by H. Johari.



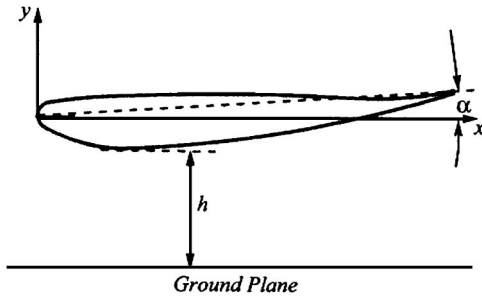


Fig. 1 Definition of the terms and coordinate system

among various studies. The differences can be attributed to various factors, chief among them are type of grid, grid resolution, and turbulence models employed with the RANS simulation. However, there have been no comparative studies between the performance of different turbulence models. The current study aims to investigate the influence of individual turbulence models, using a RANS simulation and wind-tunnel measurements. Although the flow field of a wing in ground effect is inherently three-dimensional, the center-span flow field has been shown to be quasi-two-dimensional [1]. Within this study only two-dimensional cases will be considered in order to decompose the complex flow field generated by a wing in ground effect and obtain a correct computational method without the additional considerations of wing-tip vortices. The focus of this investigation is on both pressures and the wake flow field, since practice dictates that other aerodynamic components follow the front wing of a racing car.

## 2 Numerical Method

**2.1 Aerofoil Geometry and Flow Condition.** The aerofoil used in this investigation is a derivative of the LS(1)-0413 MOD profile. A detailed listing of the profile can be found in Zerihan [10]. The aerofoil is inverted such that the suction surface is closest to the ground. The chord  $c$  and incidence  $\alpha$  of the aerofoil are 223.4 mm and +3.6 deg, respectively. The profile possesses a finite trailing edge of  $0.007c$ . The ride height  $h$  is defined as the vertical distance between the lowest point on the suction surface of the aerofoil and the ground plane. The origin of the coordinates is at the leading edge of the aerofoil (Fig. 1). Incidence, defined as the angle between the chord of the aerofoil and the horizontal, is positive for a nose-down rotation.

All computations were performed at a Reynolds number of  $4.6 \times 10^5$ , with a freestream velocity of 30 m/s. These conditions correspond to the experimental conditions [1,5].

**2.2 Governing Equations.** Simulations were performed using a RANS solver and were calculated on a linux-based cluster. The numerical solver was set up in a steady-state 2D segregated configuration, which utilized an implicit formulation. In such a configuration solutions at each iteration were obtained by solving the Reynolds-averaged Navier-Stokes equations

$$\frac{\partial \bar{u}_j}{\partial x_j} = 0 \quad (1)$$

$$\frac{\partial}{\partial t}(\rho \bar{u}_i) + \frac{\partial}{\partial x_j}(\rho \bar{u}_i \bar{u}_j) = -\frac{\partial \bar{p}}{\partial x_i} + \frac{\partial}{\partial x_j}(\bar{\tau}_{ij} - \overline{\rho u'_i u'_j}) \quad (2)$$

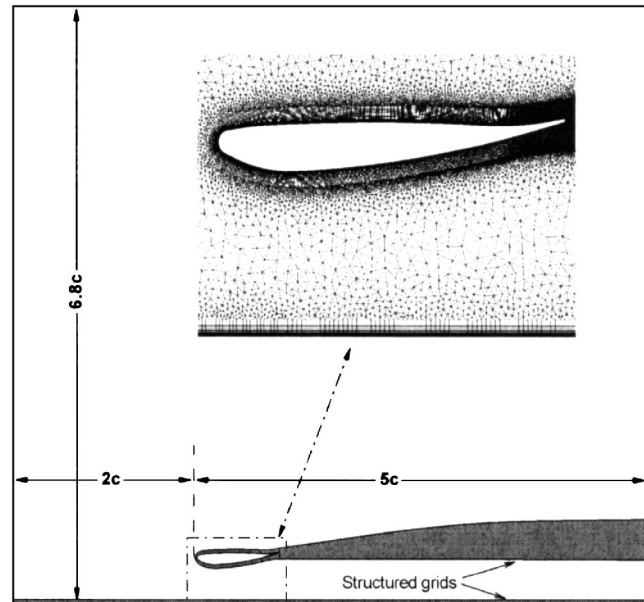


Fig. 2 Schematic of computational domain

$$\frac{\partial}{\partial t}(\rho c_p \bar{T}) + \frac{\partial}{\partial x_j}(\rho c_p \bar{T} \bar{u}_j) = \frac{\partial \bar{p}}{\partial t} + \bar{u}_j \frac{\partial \bar{p}}{\partial x_j} + u'_j \frac{\partial p'}{\partial x_j} + \frac{\partial}{\partial x_j} \left( k \frac{\partial \bar{T}}{\partial x_j} - \rho c_p \overline{T' u'_j} \right) + \bar{\Phi} \quad (3)$$

where

$$\bar{\tau}_{ij} = \mu \left( \frac{\partial \bar{u}_i}{\partial x_j} + \frac{\partial \bar{u}_j}{\partial x_i} \right) \quad (4)$$

and

$$\bar{\Phi} = \overline{\tau_{ij} \frac{\partial u_i}{\partial x_j}} \quad (5)$$

An upwind discretization scheme was used for all flow variables, which yielded second-order spatial accuracy. The SIMPLEC pressure-velocity coupling algorithm was used. To aid the rate of convergence V-Cycle and flexible multigrid schemes were used for pressure and momentum, respectively.

The criteria for convergence was specified using the sectional forces of the aerofoil, in particular,  $C_L$ . Typically, simulations were run until steady-state values of downforce and drag were observed.

**2.3 Turbulence Models.** The six turbulence models investigated are the one-equation Spalart-Allmaras model [7], the standard  $k-\epsilon$  model [11], the standard  $k-\omega$  model [12], the  $k-\omega$  SST model [8], the  $k-\epsilon$  RNG model [13], and the Realizable  $k-\epsilon$  model [14]. Enhanced wall treatments are used with the  $k-\epsilon$  model and corresponding variants.

**2.4 Computational Grids.** A multiblock hybrid grid design was used, containing both structured and unstructured blocks. At various ride heights, the relative grid topology and structure were maintained. A schematic of the computational domain and grid is shown in Fig. 2. To capture the boundary layer of the aerofoil accurately, a hyperbolically extruded structured grid was used. A conventional structured block was used to capture the ground boundary layer. A separate structured block was positioned directly downstream of the aerofoil with the purpose of capturing the wake. The remainder of the computational domain was unstructured and refined in areas of importance. Within the ground

and aerofoil boundary layer blocks the initial cell spacing, normal to the wall, was set such that  $y^+ \approx 1$ . The exact number of cells vary according to the ride height. Typically the grids contained of the order of 350,000 cells with the majority of those located toward the trailing edge of the aerofoil and within the wake block.

The boundary conditions were configured to replicate the experimental conditions. The upstream boundary was modeled using a velocity inlet boundary condition. The corresponding inlet velocity was set at 30 m/s in a positive streamwise direction with a uniform vertical distribution. The downstream boundary was modeled using a pressure-outlet boundary condition. The gage pressure was set at zero. The height of the upper edge of the domain above the simulated ground plane corresponded to the height of the wind-tunnel test section. A slip wall boundary condition was imposed on the upper edge therefore imposing a zero cross-flow condition and removing the requirement of additional boundary layer resolution. This formulation was set in order to replicate the experimental conditions imposed by the roof of the wind-tunnel test section.

The aerofoil and ground plane were modeled as solid walls with a no-slip condition enforced. In addition, the ground surface was provided with a translational velocity equal to free stream. In order to model the transition of the aerofoil boundary layers to turbulent, a laminar zone was used within the boundary layer domain, extending downstream from the leading edge to  $x/c = 0.1$ , in accordance with the experimental data [1]. The streamwise location of the aerofoil is shown in Fig. 2 and was set as a result of a sensitivity study, which was performed prior to conducting the final simulations.

Initial levels of turbulence within the flow were prescribed via values of turbulence intensity and turbulent viscosity ratio. The freestream turbulence intensity level within the  $2.1 \text{ m} \times 1.7 \text{ m}$  wind tunnel facility is 0.3% at a freestream velocity of 30 m/s. A turbulent viscosity ratio of 10 was used. Further details concerning the design of the moving ground facility within the  $2.1 \text{ m} \times 1.7 \text{ m}$  wind-tunnel facility may be found in the work of Burgin et al. [15].

Fine grids were used in this study to isolate other features of the numerical simulation. A grid sensitivity study was performed at a ride height of  $h/c = 0.224$ . Three grids were constructed: a coarse grid of 250,000 cells, a medium grid of 350,000 cells, and a fine grid of 450,000 cells. The medium grid was the one eventually used in the study. The variations in grid density were focused in the wing boundary layer block and wake block. Turbulence was modeled with the Realizable  $k-\varepsilon$  model. The surface pressures and wake profiles at  $x/c = 1.2$  are presented in Fig. 3. Very little variation in the results was observed.

### 3 Results and Discussion

**3.1 Turbulence Models.** A quantitative study of turbulence models was conducted. Two cases were selected ( $h/c = 0.224$  and  $0.09$ ).  $h/c = 0.224$  represents a typical flow condition where the ride height of the aerofoil is in the force enhancement region [1], but separation is starting to appear on the suction surface near the trailing edge. At  $h/c = 0.09$  a large separation region is present on the suction surface. The suitability of each turbulence model was quantitatively assessed using the surface flow features and wake characteristics.

At  $h/c = 0.224$  (Fig. 4(a)), all the turbulence models captured the general features of the surface pressures. The leading edge stagnation pressure ( $C_{p_{\text{stag}}}$ ) was accurately predicted at 1.00 by all the turbulence models at  $x/c = 0.003$  on the pressure surface. Discrepancies were observed in the prediction of the suction peak ( $C_{p_{\text{suc}}}$ ) and subsequent pressure recovery along the suction surface. The term *suction peak* refers to the value of maximum suction. No single turbulence model captured the entire surface pressure distribution perfectly. However, specific features were captured accurately with various models. At this ride height

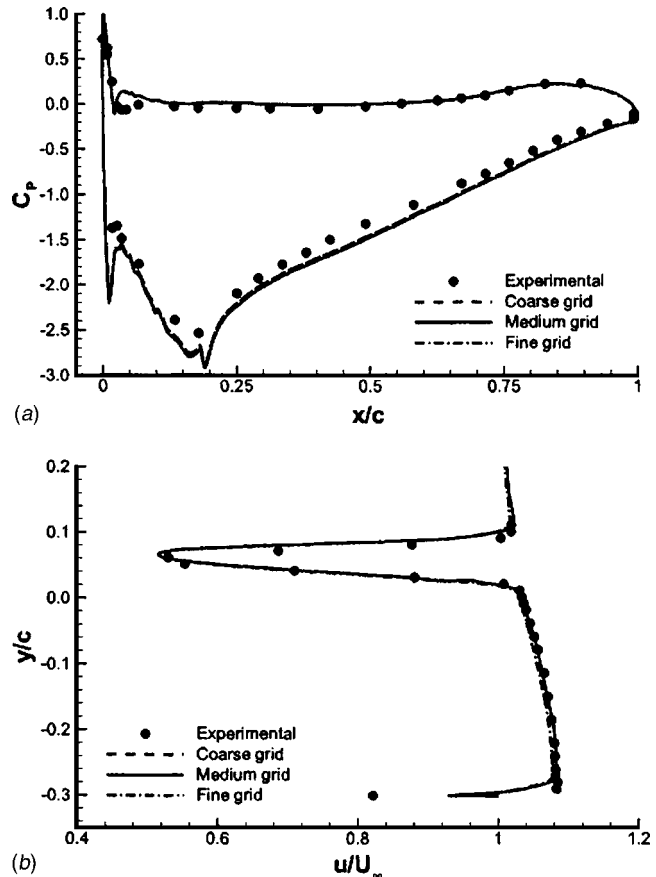


Fig. 3 Effect of grid density: (a) surface pressure distributions and (b) wake profiles at  $x/c = 1.2$

(0.224c) the surface pressures were most accurately predicted with the  $k-\omega$  SST model. The quantitative features of the surface pressures predicted by each turbulence model are listed in Table 1.

Comparisons between the numerical and experimental wake data at  $x/c = 1.2$  are also presented in Fig. 4(b). The experimental wake profile was measured by Zhang and Zerihan [5] using the laser Doppler anemometry (LDA) technique in a separate wind-tunnel study. Unlike the surface pressures a wide variation in the prediction of the wake profile was observed. It may be noted that toward the ground plane the nondimensional velocity ( $u/U_\infty$ ) decreases to approximately 0.89 then sharply increases to a value of unity. Since the ground plane is provided with a freestream velocity this trend seems incorrect. However, it must be remembered that the aerofoil generates an adverse streamwise pressure gradient because of the recovery of the flow beneath the suction surface. This, in turn, generates a boundary layer along the ground plane originating from a streamwise location corresponding to the suction peak. The resulting ground boundary layer velocity profile is present at all ride heights and is accordingly present in all the computational wake profiles.

The standard  $k-\varepsilon$  model failed to capture the vertical location of the lower boundary of the wake ( $\delta_{\text{bottom}}$ ) and the corresponding velocity recovery, resulting in an unrealistic velocity profile. The standard  $k-\omega$ ,  $k-\omega$  SST, and Spalart-Allmaras models all captured the velocity deficit ( $u_{\text{min}}$ ) accurately, however, they failed to accurately predict the velocity recovery at the lower wake boundary. The  $k-\varepsilon$  RNG and Realizable  $k-\varepsilon$  models provided accurate predictions of the lower boundary, however, the  $k-\varepsilon$  RNG model underpredicted the velocity deficit. The most accurate prediction of the wake profile was obtained with the Realizable  $k-\varepsilon$  model,

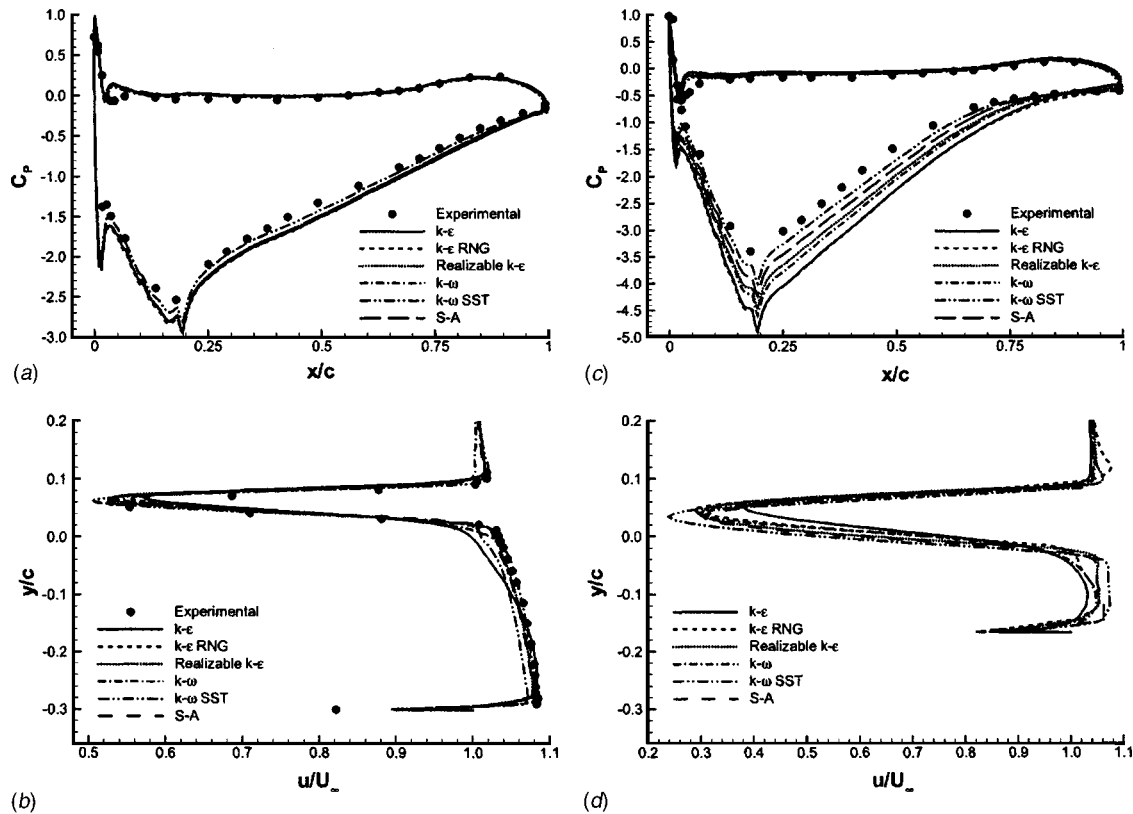


Fig. 4 Effects of turbulence models: (a) surface pressures at  $h/c=0.224$ , (b) wake profiles at  $x/c=1.2$  for  $h/c=0.224$ , (c) surface pressures at  $h/c=0.09$ , and (d) wake profiles at  $x/c=1.2$  for  $h/c=0.09$

which correctly predicted the velocity deficit, wake thickness, and corresponding boundaries. Table 2 lists quantitative data concerning the wake profiles predicted by each turbulence model.

At  $h/c=0.09$  (Fig. 4(c)), separation occurs well ahead of the trailing edge and poses an additional challenge to the numerical model. The surface pressures again suggest that the  $k-\omega$  SST model gives the best prediction, with the variation between turbulence models observed at the higher ride height amplified. There

are no wake measurements at this height, but we note that the variations between the turbulence models were similar to those observed at the higher ride height (Fig. 4(d)).

**3.2 Surface Pressures.** We now proceed to investigate the effect of ride height, using the  $k-\omega$  SST and the Realizable  $k-\epsilon$  models. Calculations were performed at  $h/c=0.448, 0.313, 0.224, 0.179, 0.134, 0.112,$  and  $0.09$ . Quantitative data concerning the general flow field, surface pressures, wake characteristics, and sectional forces was extracted.

The calculated surface pressures and the experimentally measured values are shown in Fig. 5. Only two heights are included for clarity. The agreement between the computational and experimental pressures on the pressure surface of the aerofoil was good. The leading edge stagnation point was accurately predicted at  $x/c=0.003$  for all ride heights with both turbulence models. As the ride height was reduced, discrepancies were observed in the pressure surface pressures between  $x/c=0.024$  and  $0.134$ , where the pressures were overpredicted. This was attributed to a spike in the curvature of the aerofoil at  $x/c=0.016$ , which resulted in a

Table 1 Surface pressure information for various turbulence models,  $h/c=0.224$

Turbulence model	$C_{P_{suc}}$	$x/c$ at $C_{P_{suc}}$
Experimental	-2.53	0.18
Spalart-Allmaras	-2.92	0.19
Standard $k-\omega$	-2.92	0.19
$k-\omega$ SST	-2.81	0.19
Standard $k-\epsilon$	-2.94	0.19
$k-\epsilon$ RNG	-2.97	0.19
Realizable $k-\epsilon$	-2.92	0.19

Table 2 Wake information for various turbulence models at  $x/c=1.2$  and  $h/c=0.224$

Turbulence model	$u_{min}/U_\infty$	$y/c$ at $u_{min}$	$y/c$ at $\delta_{top}$	$y/c$ at $\delta_{bottom}$	$\delta_{99}/c$
Experimental	0.53	0.06	0.09	0.02	0.07
Spalart-Allmaras	0.55	0.07	0.10	0.02	0.08
Standard $k-\omega$	0.53	0.07	0.10	0.01	0.09
$k-\omega$ SST	0.51	0.06	0.09	0.02	0.07
Standard $k-\epsilon$	0.57	0.07	0.10	0.01	0.09
$k-\epsilon$ RNG	0.56	0.07	0.10	0.02	0.08
Realizable $k-\epsilon$	0.53	0.07	0.09	0.02	0.07

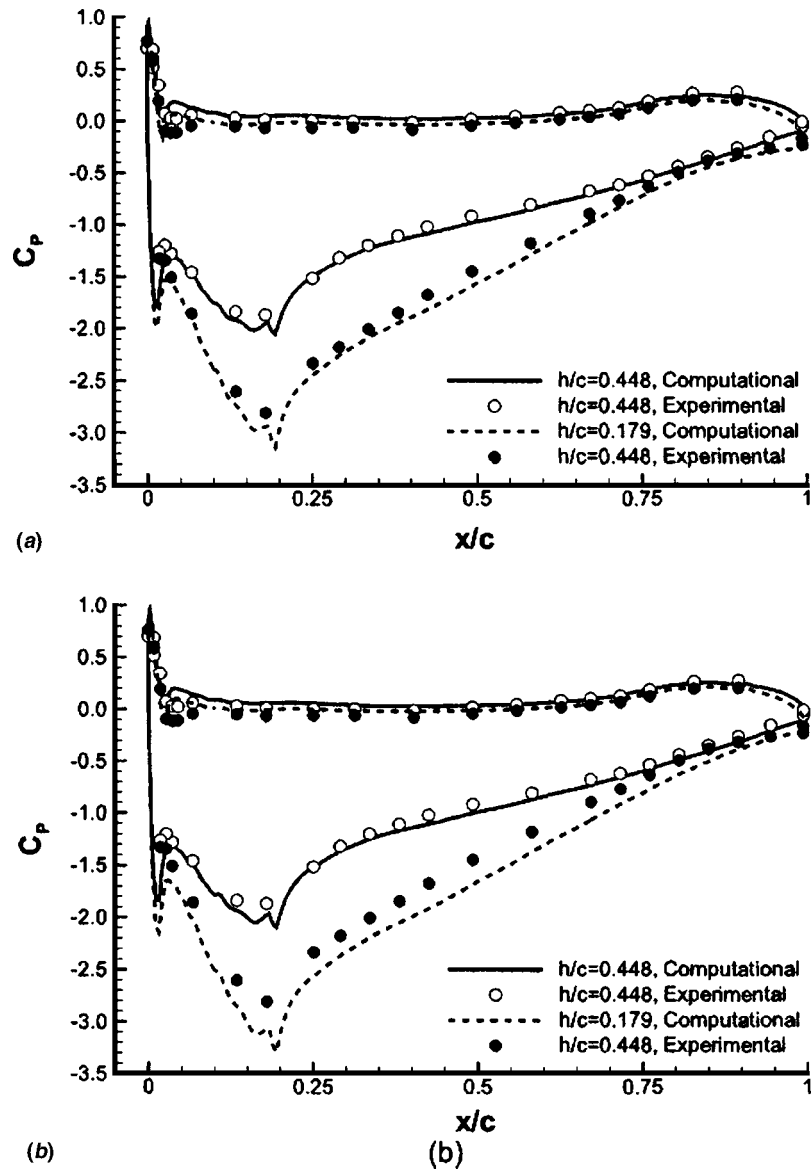


Fig. 5 Surface pressures at various ride heights: (a)  $k-\omega$  SST model and (b) Realizable  $k-\epsilon$

sudden deceleration in the flow. The experimental data illustrated a gradual increase in  $C_p$  within this region, possibly because of the spike in curvature being absent, due to manufacturing techniques.

The suction surface pressures were slightly overpredicted with the overprediction increasing with decreasing ride height. A suction spike was observed at  $x/c = 0.013$ , the magnitude of which increased as the simulated ride height was reduced. This leading edge suction spike was not observed in the experiment because of the discrete nature of the surface pressure data. Directly downstream of the the leading edge suction peak, a decrease in suction was observed at  $x/c = 0.023$ . The curvature of the airfoil at this location was discontinuous, resulting in a region of decelerated flow. Disturbances in the suction surface pressures between  $x/c = 0.033$  and  $x/c = 0.180$  were observed, corresponding to yet more discontinuities in the curvature.

The suction surface peak was consistently observed at  $x/c = 0.190$ , increasing in magnitude with decreasing ride height. The suction peak was overpredicted for all ride heights. Downstream of the suction peak existed a region of pressure recovery extending to the trailing edge. The rates at which the pressures recovered

along the suction surface were accurately captured for all nondimensional ride heights with the  $k-\omega$  SST model. The Realizable  $k-\epsilon$  model, however, overpredicted the pressure recovery rate at  $h/c = 0.09$  resulting in an inaccurate finite pressure difference at the trailing edge.

Overall the  $k-\omega$  SST model gives a better prediction at all heights, especially lower ride heights mainly in the pressure recovery region on the suction surface. The pressures on the pressure surface experience relative small variations over the range of heights.

**3.3 Sectional Forces.** The sectional forces generated by the airfoil at various ride heights are shown in Fig. 6. The predicted downforce is compared to the sectional values measured experimentally. The overall trend in downforce variation was captured most accurately with the  $k-\omega$  SST model. The Realizable  $k-\epsilon$  model overpredicted the downforce at all ride heights and failed to accurately predict the stall of the airfoil. There is a marked improvement with the  $k-\omega$  SST model because of better prediction of the pressure recovery process. As mentioned previously, the suction surface pressures were overestimated for all ride heights,

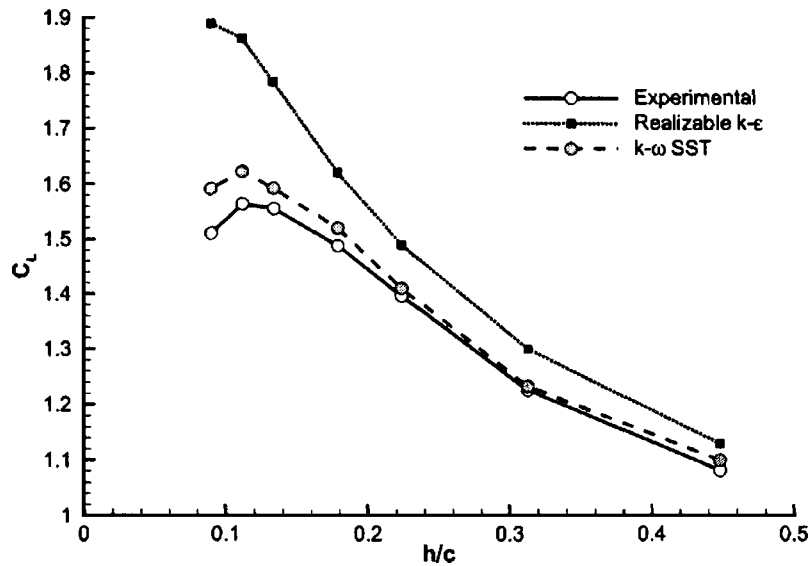


Fig. 6 Sectional forces at various ride heights

accordingly the calculated values of downforce were also overestimated. This feature is particularly acute near the maximum downforce ride height. The largest discrepancy occurs at the maximum force height of  $h/c=0.112$ . At this ride height the value of downforce ( $C_L$ ) predicted by the  $k-\omega$  SST model is 2% greater than the measured value and for the Realizable  $k-\epsilon$  model 19% greater. The reduction in downforce at  $h/c=0.09$  due to the aerofoil stalling [1] was correctly predicted with the  $k-\omega$  SST model whereas the Realizable  $k-\epsilon$  failed to predict the stall.

**3.4 Flow Between Aerofoil and Ground.** Figure 7 presents line contours of nondimensional streamwise velocity ( $u/U_\infty$ ) for  $h/c=0.448$  and  $0.09$ . The contours for  $h/c=0.448$  show a slightly accelerated flow beneath the aerofoil and a thin wake. A small region of recirculation was observed directly downstream of the finite trailing edge. Decreasing the ride height caused the flow beneath the wing to become increasingly accelerated with maximum values of  $u/U_\infty=2.0$  achieved at  $h/c=0.09$ .

The contours of  $u/U_\infty$  indicated that the flow located between

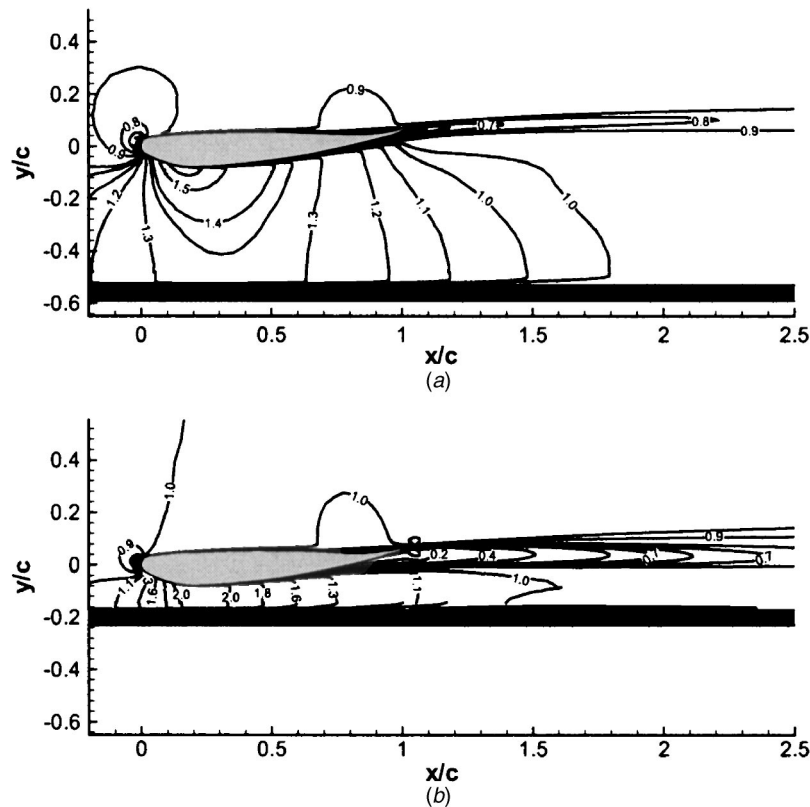


Fig. 7 Contours of  $u/U_\infty$  with the Realizable  $k-\epsilon$  model: (a)  $h/c=0.448$  and (b)  $h/c=0.09$

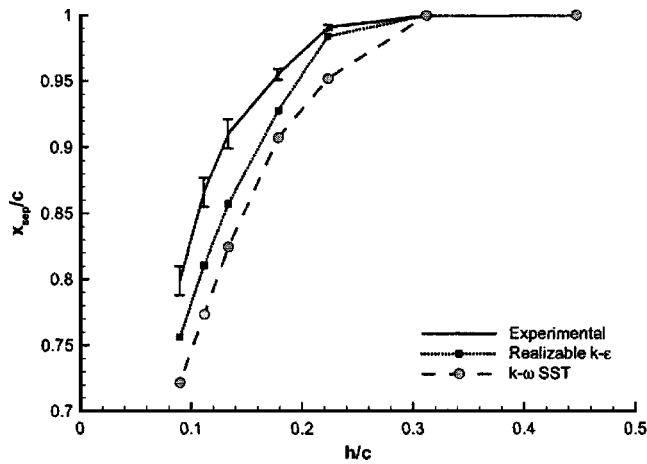


Fig. 8 Streamwise location of separation for various ride heights

the lower boundary of the wake and ground possessed higher than freestream values of velocity. This region of flow was seemingly constrained by the lower boundary of the wake, forming a wall jet. Decreasing the ride height caused the wall jet to become increasingly accelerated, a trend that was observed experimentally [5].

Figure 8 shows the streamwise location of separation ( $x_{sep}/c$ ) on the suction surface of the aerofoil. The measured values for a wing with free transition [1] are also included since values with fixed transition were not available. The location of separation moved upstream along the suction surface as the ride height was decreased, a trend that was observed in both experiment and computation. This was a direct result of the pressure gradient beneath the aerofoil becoming increasingly adverse as the ride height was reduced. When compared to the experimental separation locations the computed values were overpredicted for all ride heights even though the surface pressures indicated good agreement. This overprediction was attributed to the difference in the location of transition on the suction surface of the aerofoil between the experimental and computational data. Transition was found to occur naturally at  $x/c=0.3$  to  $0.35$  [1], whereas, within this study and for all other experimental data, transition was fixed at  $x/c=0.1$ . Accordingly, the suction surface boundary layer will be thicker at a fixed streamwise location for the fixed transition case, therefore, more prone to separation. A quantitative comparison concerning the location of separation can therefore not be made because of the difference between experimental and computational setup.

**3.5 Wake Flow Field.** The turbulent wake downstream of the aerofoil is seen in Fig. 7. The size of the wake increases as the ride height is reduced. The development of the wake is constrained by the ground. As the ride height is reduced and the wall jet is formed by the boundary layer separation on the suction surface and the ground, the lower boundary of the wake changes. The velocity deficit in the wake increases as the ride height is reduced. Further downstream the velocity deficit was slowly recovered, which is accompanied by an increase in the thickness of the wake.

Figure 9 shows the profiles of relative streamwise velocity, tangential to the ground plane at a streamwise locations of  $x/c=1.2$ . Only three ride heights are included in the figure, corresponding to ride heights with available experimental data. A summary of the prediction is given in Table 3.

Unlike the surface pressure prediction where the  $k-\omega$  SST model gives the best prediction, the Realizable  $k-\epsilon$  model produces the most accurate prediction of the wake profile. Both turbulence models accurately predicted the velocity deficit within the ground boundary layer, associated thickness, and the thickening

thereof with reducing ride height. The velocity deficit within the wake and top wake boundary were also predicted well by both models, however, discrepancies were observed within the prediction of the lower wake boundary. The  $k-\omega$  SST model underpredicted the rate of velocity recovery toward the lower wake boundary, resulting in a slightly inaccurate prediction of the lower wake boundary, and an overprediction in the wake thickness. The Realizable  $k-\epsilon$  model accurately predicted the lower wake boundary and the corresponding rate of velocity recovery. Accordingly the wake thickness was accurately predicted by the Realizable  $k-\epsilon$  model.

#### 4 Further Comments

Accurate, realistic steady-state computations of an inverted aerofoil in ground effect were obtained, quantifying the effects of grid resolution, turbulence model, and ride height. A strong dependence of the surface pressures over the suction surface of the aerofoil on ride height was observed. The channel created between the suction surface of the aerofoil and the ground plane resembles a Venturi nozzle. The flow entering between the leading edge and the ground plane is therefore initially accelerated until the throat of the nozzle (the lowest point on the aerofoil suction surface), then decelerated underneath the downstream section of the aerofoil. The rate of acceleration and deceleration is dependent on the shape of the nozzle and hence the ride height, with low ride heights generating greater velocities. The surface pressures illustrate this process with reductions in ride height generating suction surface pressures of greater magnitude, while the pressure surface pressure remain relatively constant. The streamwise location of the suction peak was independent of ride height at  $x/c=0.190$ , corresponding to the throat of the channel and, therefore, the location of highest velocity. The surface pressures obtained in the study show improvement over earlier efforts. The  $k-\omega$  SST model was found to offer the best prediction of the surface pressures over the entire range of ride heights, from the force-enhancement region to force-reduction region [1].

At high ride heights the accelerated flow underneath the aerofoil could recover to a freestream value prior to the aerofoil trailing edge. Reducing the ride height created a velocity recovery rate, which could not be physically achieved. Therefore, a flow that possessed a greater-than-freestream value of velocity such that  $\bar{u}/U_\infty > 1.0$ , was generated, i.e., a wall jet.

The flow beneath the aerofoil exists into a region constrained by the ground plane and the lower wake boundary. Unlike the surface pressures and sectional forces the Realizable  $k-\epsilon$  model was found to produce the best prediction of the wake flow. A jet flow between the lower boundary of the wake and the ground plane was observed, especially at low ride heights ( $h/c=0.09$ ). It is well documented that flows with large mean strain rates, such as jets, are difficult to model using turbulence models. The method adopted by the Realizable  $k-\epsilon$  model is to calculate the eddy viscosity locally therefore allowing the model to remain realizable even in regions of large mean strain rates. Shih et al. [14] has shown that this modification results in a much improved simulation of jet flows, in particular, the spreading rates. It could, therefore, be hypothesized that improved simulations of the ground jet flow resulted in improved simulations of the lower boundary of the wake and hence the entire wake flow.

It was noted that the thickness of the wake increased as the ride height decreased. However the transverse location of the upper boundary of the wake remained constant at  $y/c \approx 0.15$ , i.e., the transverse location of the lower boundary of the wake decreases with ride height. It has been shown that as the ride height is decreased, the magnitude of the wall jet increases. It is felt that the downward translation of the lower wake boundary with decreasing ride height is linked to the strength of the wall jet, however, conclusions cannot be drawn without further investigation.

The numerical investigations conducted were two-dimensional, whereas in reality the flow field generated by a wing in ground

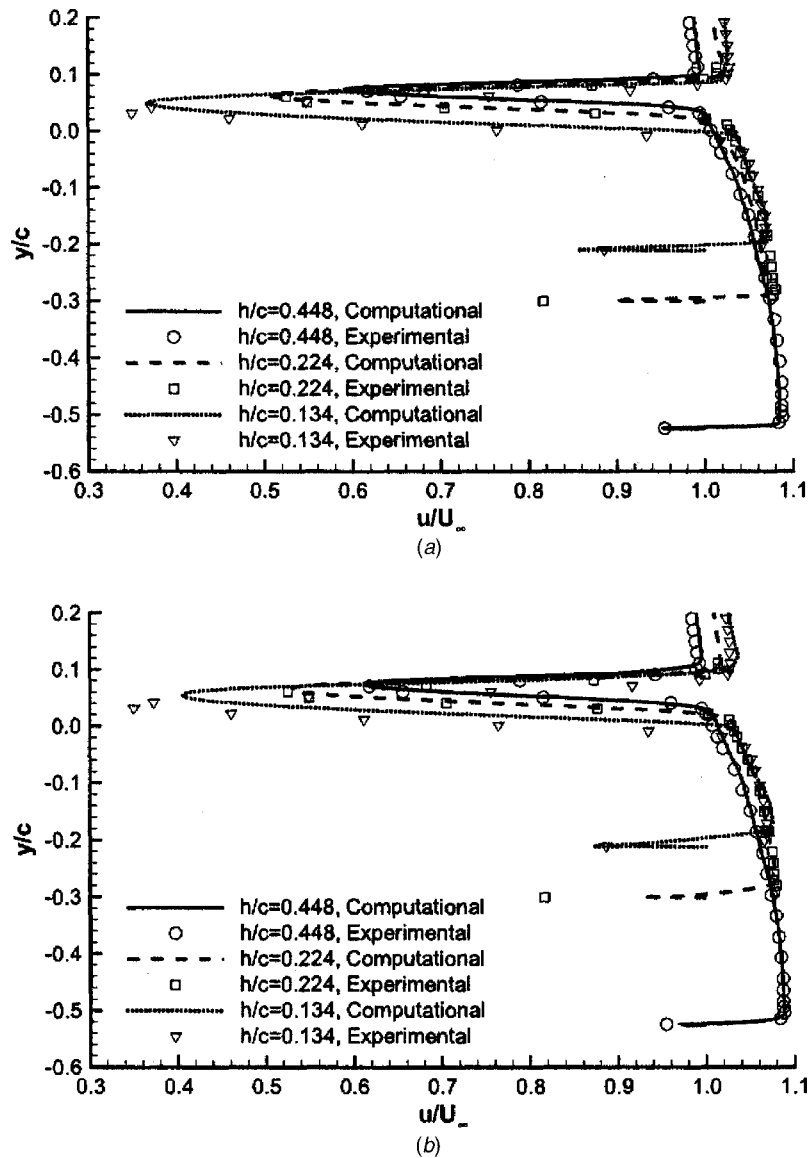


Fig. 9 Wake profiles at  $x/c=1.2$ : (a)  $k-\omega$  SST and (b) Realizable  $k-\epsilon$

effect is intrinsically three-dimensional. Within this study the performance of each turbulence model was based on the two-dimensional values of surface pressures and wake flow field. Within a three-dimensional case, the performance of numerical schemes will, in addition, be based on the predictive capability concerning the wing tip vortices. More complex schemes, such as large eddy simulation (LES) and detached eddy simulation (DES),

may therefore be more suited to the situation of a wing in ground effect due to the good predictive capabilities concerning vortical flows.

Table 3 Wake information for various ride heights at  $x/c=1.2$

$h/c$	Expt/CFD	$u_{\min}/U_{\infty}$	$y/c$ at $u_{\min}$	$y/c$ at $\delta_{\text{top}}$	$y/c$ at $\delta_{\text{bottom}}$	$\delta_{99}/c$
0.448	Expt	0.617	0.071	0.103	0.032	0.071
	Real $k-\epsilon$	0.613	0.074	0.110	0.004	0.106
	$k-\omega$ SST	0.591	0.073	0.099	0.037	0.062
0.224	Expt	0.525	0.061	0.090	0.022	0.068
	Real $k-\epsilon$	0.529	0.065	0.098	0.024	0.074
	$k-\omega$ SST	0.507	0.063	0.091	0.022	0.069
0.134	Expt	0.350	0.031	0.082	-0.016	0.098
	Real $k-\epsilon$	0.405	0.054	0.094	0.004	0.090
	$k-\omega$ SST	0.367	0.049	0.085	-0.001	0.086

## 5 Conclusion

A numerical investigation into an aerofoil in ground effect was undertaken. The effects of turbulence model, grid density, and ride height were all investigated, and the following conclusions may be drawn:

1. The two-dimensional flow field generated by an inverted aerofoil in ground effect can be accurately modeled by solving the Reynolds-averaged Navier-Stokes equations.
2. The most accurate predictions of the surface pressures and sectional forces were obtained with the  $k-\omega$  SST turbulence model.
3. The most accurate predictions concerning the wake flow field, in particular, the lower wake boundary, were obtained with the Realizable  $k-\varepsilon$  turbulence model. The formulation of this turbulence model provided improved predictions of the wall jet and hence improved simulations of the lower wake boundary.

## Acknowledgments

The authors would like to thank BARf1 for their continuing support and help. In particular, the authors would like to thank Jonathan Zerihan and Willem Toet for their input and technical discussion.

## Nomenclature

$c$	= chord
$C_L$	= sectional lift coefficient, $L/q_\infty c$
$C_p$	= coefficient of pressure, $(p-p_\infty)/q_\infty$
$C_{p\text{stag}}$	= coefficient of pressure at the leading edge stagnation point
$C_{p\text{suc}}$	= coefficient of pressure at maximum suction
$h$	= ride height
$L$	= lift, positive indicates downforce i.e. force in a negative $y$ direction
$p$	= static pressure
$q_\infty$	= dynamic head, $\frac{1}{2}\rho U_\infty^2$
$t$	= time
$u, v, w$	= streamwise, traverse and spanwise velocity components
$\bar{u}$	= mean streamwise velocity at $x/c=1$ between the lower trailing edge and the ground plane
$u_{\text{min}}$	= minimum $u$ velocity component in wake
$U_\infty$	= freestream velocity

$x, y$  = Cartesian coordinates,  $x$  positive downstream,  $y$  positive upward  
 $x_{\text{sep}}$  = suction surface separation point  
 $y^\dagger$  = nondimensional length,  $yU_\tau/\nu$

## Greek Symbols

$\alpha$	= incidence of aerofoil, positive for a nose down rotation
$\delta_{\text{bottom}}$	= bottom of wake thickness
$\delta_{\text{top}}$	= top of wake thickness
$\delta_{99}$	= wake thickness as measured by 99% displacement thickness
$\mu$	= viscosity
$\rho$	= density

## Subscripts

$\infty$  = freestream

## References

- [1] Zerihan, J. D. C. and Zhang, X., 2000, "Aerodynamics of a Single Element Wing in Ground Effect," *J. Aircr.* **37**(6), pp. 1058–1064.
- [2] Katz, J., 1985, "Calculation of the Aerodynamic Forces on Automotive Lifting Surfaces," *ASME J. Fluids Eng.* **107**, pp. 438–443.
- [3] Ranzenbach, R. and Barlow, J. B., 1994, "Two-Dimensional Airfoil in Ground Effect, An Experimental and Computational Study," SAE Paper No. 94-2509.
- [4] Ranzenbach, R. and Barlow, J., 1996, "Cambered Airfoil in Ground Effect: An Experimental and Computational Study," SAE Paper No. 96-0909.
- [5] Zhang, X. and Zerihan, J. D. C., 2003, "Off-Surface Aerodynamic Measurements of a Wing in Ground Effect," *J. Aircr.* **40**(4), pp. 716–725.
- [6] Zerihan, J. D. C. and Zhang, X., 2001, "A Single Element Wing in Ground Effect: Comparisons of Experiments and Computation," AIAAPaper 2000-0423, pp. 1–12.
- [7] Spalart, P. R. and Allmaras, S. R., 1992, "A One-Equation Turbulence Model for Aerodynamic Flows," AIAA Paper No. 92-0439.
- [8] Menter, F. R., 1994, "Two-Equation Eddy-Viscosity Turbulence Models for Engineering Applications," *AIAA J.* **32**(8), pp. 1598–1605.
- [9] Lawson, N. J., Knowles, K., Hart, R. J. E., Wray, J. N., and Eyles, J. M., 2002, "An Experimental Investigation Using PIV of the Underflow of a GA(W)-1 Aerofoil Section in Ground Effect," *Proc. of the 4th MIRA International Vehicle Aerodynamics Conference, 16-17 October*, MIRA, Warwick, pp. 1–14.
- [10] Zerihan, J. D. C., 2001, "An Investigation Into the Aerodynamics of Wings in Ground Effect," Ph.D. thesis, University of Southampton, Southampton, UK.
- [11] Launder, B. E. and Spalding, D. B., 1974, "The Numerical Computation of Turbulent Flows," *Comput. Methods Appl. Mech. Eng.* **3**, pp. 269–289.
- [12] Wilcox, D. C., 1988, "Multiscale Models for Turbulent Flows," *AIAA J.* **26**(11), pp. 1311–1320.
- [13] Yakhot, A. and Orszag, S., 1986, "Renormalisation Group Analysis of Turbulence: I Basic Theory," *J. Sci. Comput.* **1**(1), pp. 1–51.
- [14] Shih, T-H, Liou, W. W., Shabbir, A., Yang, Z., and Zhu, J., 1995, "A New  $k-\varepsilon$  Eddy Viscosity Model for High Reynolds Number Turbulent Flows," *Comput. Fluids* **24**, pp. 227–238.
- [15] Burgin, K., Adey, P. C., and Beatham, J. P., 1986, "Wind Tunnel Tests on Road Vehicle Models Using a Moving Belt Simulation of Ground Effect," *J. Wind. Eng. Ind. Aerodyn.* **22**, pp. 227–236.



# Experimental and Numerical Investigation of the Flow Field in the Tip Region of an Axial Ventilation Fan

Xiaocheng Zhu  
e-mail: zhxc@sjtu.edu.cn

Wanlai Lin  
e-mail: wllin@sjtu.edu.cn

Zhaohui Du  
e-mail: zhdu@sjtu.edu.cn

School of Mechanical Engineering, Shanghai Jiaotong University, Shanghai, 200030, China

*The tip leakage flow in an axial ventilation fan with various tip clearances is investigated by experimental measurement and numerical simulation. For a low-rotating-speed ventilation fan with a large tip clearance, both experimental measurement and numerical simulation indicate that the leakage flow originating from the tip clearance along the chord rolls up into a three-dimensional spiral structure to form a leakage flow vortex. The mixing interaction between the tip leakage flow and the main flow produces a low axial velocity region in the tip region, which leads to blockage of the main flow. As the tip clearance increases, the tip leakage flow and the reverse flow become stronger and fully developed. In addition, the position of the first appearance of the tip leakage vortex moves further downstream in a direction parallel to the mid chord line.*

[DOI: 10.1115/1.1881654]

## 1 Introduction

A ventilation fan used in HVAC (heating, ventilation, and air conditioning) industry has characteristics of a low pressure rise and a low rotating speed. In addition, the tip clearance for a ventilation fan usually is quite large in order to maintain safe operation and reduce manufacturing cost. The flow in the tip region of an axial ventilation fan with a tip clearance is quite complex. The interaction of the leakage flow, the boundary flow at the casing wall, and the boundary flow around the blade introduce three-dimensionality to the flow. Therefore, it is very difficult to experimentally measure and numerically predict the detail flow field [1]. It has been found that the flow in the tip region has a big impact on the fan performance and stability [2]. At the present time, little research work has been done in this area. Most investigations of tip clearance flow have concentrated on gas turbine compressors, which have a high pressure rise, a high rotating speed, and a relatively small tip clearance.

Due to the relative rotation between the blade and the casing wall, it is very difficult to measure the flow field in the tip clearance region and inside the rotor. Some measurements were focused on cascades or downstream of the rotor [3–5]. Lakshminarayana et al. [6,7] measured the flow field in the tip region of a compressor using a triaxial hot wire probe, which rotated with the rotor. The probe is intrusive, and it is quite complex to have the probe rotating with the rotor. Inoue et al. [8] first measured the flow field downstream of the rotor with a hot wire probe. A vortical structure of the tip leakage flow was reported. The general structure of the tip clearance flow in the tip clearance was then measured, using a hot wire probing into the tip clearance by his group [9]. However, the flow field inside the rotor was still not acquired.

The laser Doppler velocimeter (LDV) system provides a useful nonintrusive tool. In 1973, it was first employed to measure the flow field in turbomachinery by Wisler and Mossey [10]. More recently LDV systems have been widely used to measure the flow field in turbomachinery. Murthy and Lakshminarayana [11] acquired the 2D flow field in the tip region of an axial compressor using a single-channel LDV system. Stauter [12] measured the three-dimensional velocity flow field in a two-stage axial com-

pressor using a three-dimensional LDV system. The vortical motion of the tip leakage flow vortex at several axial locations was examined from different angles.

Numerical and theoretical analyses are valuable tools for investigating tip leakage flow. A theoretical model that considers a vortex core as a rotating solid body was developed by Lakshminarayana [13]. Chen et al. [14] provided a similar model to describe the trajectory of the leakage vortex. Based on the model, the locus of the tip vortex trajectory inside the passage does not depend on the size of the tip clearance region. Storer and Cumpsty [15] showed that the mixing between the leakage flow and the main flow is the cause of the loss due to the tip clearance. The loss can be predicted from the angle between the leakage flow and the main flow. Other simplified models were derived by Denton [16] to obtain overall flow structure of the tip leakage flow.

With the development of computer technology in the past two decades, CFD (computational fluid dynamics) has become popular in the modeling of a detailed flow field of the tip clearance region. Hah [17] simulated the flow field of axial turbomachinery with a tip clearance. The grid in the tip region had the same grid topology structure as those in the main flow. A sharp edge of blade tip was modeled. Using a similar grid topology, Dawes [18] simulated the flow field of a transonic compressor rotor with a round blade tip. An improved grid topology in which the embedded tip clearance grid is different from that in the main flow region was proposed to provide an accurate modeling of the tip clearance region [19].

In this research, the performance and detailed flow field of an axial ventilation fan with three different tip clearances are tested and measured at the Turbomachinery Laboratory of Shanghai Jiaotong University, using a three-dimensional phase Doppler anemometer (PDA) technology. The test fan is designed by Emerson Electric Corporation (USA). The numerical analysis of the tip clearance flow by commercial software CFX-TASCFLOW is conducted. An embedded grid for the tip clearance region, which is different from the major grid of the fan rotor, is employed. The structure of the tip leakage flow at various tip clearances is investigated by the detailed analysis and comparison of experimental and CFD results. Understanding the detailed flow pattern in the tip clearance region will help engineers improve the design of an axial ventilation fan.

Contributed by the Fluids Engineering Division for publication in the JOURNAL OF FLUIDS ENGINEERING. Manuscript received by the Fluids Engineering Division July 8, 2003; revised manuscript received, December 28, 2004. Review conduct by J. Lee.

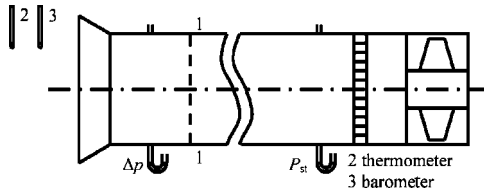


Fig. 1 General schematic of the fan performance test

## 2 Test Facility

The experimental facility is arranged based on Chinese National Standard GB1236-2000 (Test Methods of Aerodynamic Performance for Fans). This standard is equivalent to ISO5801 (1997E), as shown in Fig. 1. Based on this arrangement, the inlet flow can be kept steady and uniform. The flow rate can be adjusted easily at a range of 0–2.5 m<sup>3</sup>/s. The cone shape inlet is used to measure the flow rate. The experiment measurement data will be corrected to 300 K and 101325 Pa. The static pressure is measured by a micromanometer with a resolution of 0.5 Pa. The pressure difference between the inlet and outlet sections is <300 Pa, so the density and temperature of the air can be considered as constant values.

The rotor has six blades. The diameter of rotor is 457 mm, and the ratio of hub and tip diameter of the fan is 0.33. The average blade span  $h$  is 152.4 mm.  $h$  is used for the normalization of the tip clearance  $\tau$  and the radial distance  $r$ . The rotor is driven by a 1 kW motor. The design rotation speed of the fan is 1800 rpm, and the design flow rate is 1.88 m<sup>3</sup>/s. Table 1 gives the chord length  $C$ , the stagger angle  $\lambda$ , and the solidity  $C/S$  of the fan blade at three radial positions. Because the normalized tip clearance  $t$  for a ventilation fan can be up to 5%, three normalized tip clearances of 0.66%, 1.98%, and 3.96% were selected for this research. The tip clearance of the blade along the circumferential direction is quite uniform with a maximum variation of less than 0.1% of the blade span  $h$ .

The geometry shape of the blade is shown in Fig. 2, which is also the grid structure used in the numerical simulation. At the beginning, the casing wall was made of a transparent Plexiglass. However, it was difficult for the laser beam to transmit through

Table 1 Main blade geometry parameters

	Blade root	Mid span	Blade tip
$R$	0	0.5	1
$C$ (mm)	87.10	94.53	87.10
$\lambda$ (deg)	41.89	60.52	71.39
$C/S$	1.092	0.546	0.364

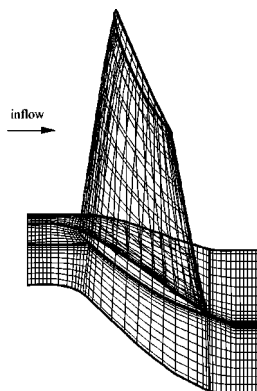


Fig. 2 General geometry shape of the blade

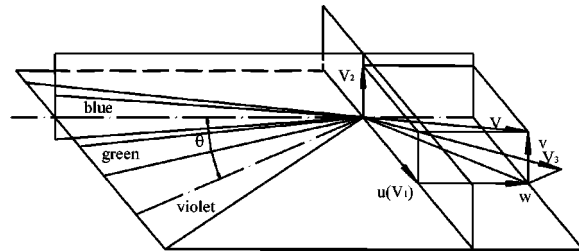


Fig. 3 Velocity-component definitions

this casing wall, probably because the casing was too thick and the refraction index of the Plexiglass was not appropriate. Therefore, an optics glass window was employed to transmit the laser beam into the rotor passage. The optics glass window is 296 mm long, 18 mm wide, and 1 mm thick.

**2.1 PDA System.** A three-color Dantec Dual-PDA system was employed to acquire the flow information of the seeding particle. A PDA system cannot only measure the velocity but also the diameter of the seeding particle. In this experiment, only the velocity information was of interest, so a PDA system is equivalent to a LDV (laser Doppler velocimeter) system.

A PDA system consists of a laser source, transmitting optics, receiving optics, and a signal processor. Due to the geometry configuration of the fan, a three-dimensional orthogonal PDA system cannot be used. A green light ( $\lambda=514.50$  nm) beam and a blue light ( $\lambda=488.00$  nm) beam in one optical rail are introduced into the flow field to directly sample the axial and tangential components of the velocity. This optical rail is perpendicular to the casing wall. A violet light ( $\lambda=476.50$  nm) beam is arrayed in another optical rail with an angle away from the perpendicular direction to get the radial component of the velocity. The radial velocity component can be calculated from the following formulation (as shown in Fig. 3):

$$\begin{aligned} u &= V_1 \\ v &= V_2 \end{aligned} \quad (1)$$

$$w = V_3/\sin \theta - V_1/\tan \theta$$

It is shown in the Eq. (1) that sine and tangent terms are critical in determining the accuracy of the velocity component  $w$ . Based on experience,  $\theta$  is adjusted to about 30 deg to maintain the sensitivity to the radial velocity. A flow unit (Dantec), which has a high-resolution control valve and a series of Laval nozzles (a range of 0.02–300 m/s), is used to determine the velocity accuracy. The seeding particle follows the flow from the flow unit. The difference between the measured velocity of the seeding particle and the flow velocity from the flow unit is <0.2 m/s for the flow velocity <30 m/s. In other words, the uncertainty of the measured velocity is <0.2 m/s when the flow velocity is <30.0 m/s.

To resolve the direction ambiguity, one of two crossing beams is adjusted to pass through a Bragg Cell, through which the frequency is shifted to 40 MHz. A signal processor interfaced with a computer provides an on-line data processing capability. An autocorrelation technique is used to process the Doppler signal. When all three-color beams pass through a hole with a diameter of 0.2 mm, these three velocity components are measured simultaneously at the same point. The measured volume is 0.4 mm  $\times$  0.2 mm  $\times$  0.2 mm.

The transmitting and receiving optics of the PDA system are mounted on a three-axial traverse system with a calibration factor of 80 pulse/mm (Dantec). The axial position and radial position of the measurement are determined by the traverse system, which can be controlled by the software SIZEWARE of the PDA system. The velocity components are measured at a random circumferen-

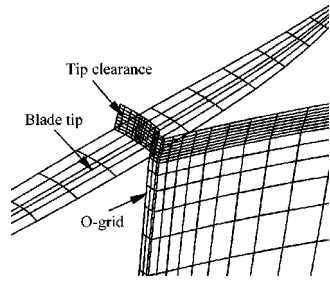


Fig. 4 Computation grid for the fan

tial position. To determine a circumferential position, a sign from the shaft encode (3600 pulses per revolution, clocking 1 pulse per revolution triggering) is recorded with the velocity data. All laser anemometer results are based on the velocity distribution across an averaged blade passage, which is calculated by an ensemble-averaged measurement acquired in each individual blade passage. A blade passage is discretized into 120 bins.

The seeding particles from a water humidifier are injected into the flow 300 mm upstream of the rotor inlet. The diameter of the seeding particles is about 1–5  $\mu\text{m}$ . Based on our measurements the seeding particles follow the flow within an acceptable degree of error.

### 3 Computational Procedure

The commercial CFD software CFX-TASCFLOW 2.09 is used to solve Reynolds averaged Navier-Stokes equations. CFX-TASCFLOW uses a modified finite volume method, which retains much of the geometric flexibility for a finite element method as well as the conservation properties of a finite volume method. The Multigrid solver used in CFX-TASCFLOW is an algebraic multigrid method (AMG) based on the additive correction multigrid (ACM) strategy, which has been found to be quite robust.

CFX-TURBOGRID 1.4 is employed to generate a grid, and a general multiblock grid template is used. An O-grid is created around the blade and an H-grid is used in the blade passage. The computation domain consists of 13 blocks of grids. Six of them are in the blade passage, four of them are around the blade, and the remaining three blocks are in the tip clearance region. The grids in the tip clearance are embedded in the O-grid (as shown in Fig. 4). Four grids with a grid number of 134, 056, 225, 126, 281, 176, and 343,096 are created, respectively, to investigate the grid independence of the CFD modeling. Figure 5 shows the global performance from CFD modeling at the normalized tip clearance of 1.98%. The static pressure and static efficiency at different grid numbers are presented to show the grid independence of numerical simulation. Because it is very difficult for a CFD calculation to converge at a small flow rate, only results at three different flow rates near the design flow rate are given. It is founded that the grid number of 225,126 is fine enough to generate a grid-independent

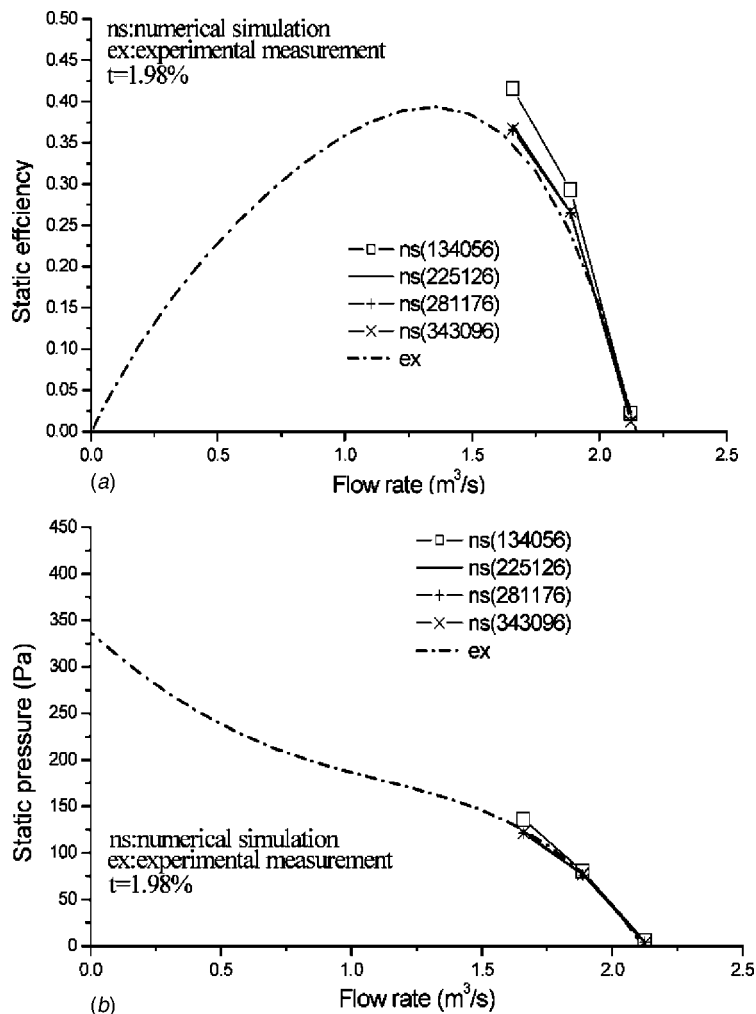


Fig. 5 (a) Static efficiency at different grid number and (b) static pressure rise at different grid number

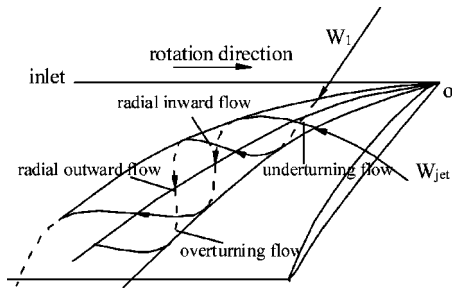


Fig. 6 Model of tip leakage vortex

solution. Therefore, the result from this grid will be analyzed and discussed in this paper. In the tip region of this grid, there are nine cells along the radial direction, 47 cells along the circumferential direction, and 25 cells between the leading edge and trailing edge.

Based on the experimental conditions, the boundary conditions are defined as the following: a mass flow rate per blade passage is

specified over the entire inlet area. An averaged outlet static pressure over the outlet area is applied as the outlet boundary condition. The inlet section is at an axial position, which is about 300% of the blade chord before the blade leading edge, and the outlet section lies about 500% of the blade chord after the blade trailing edge. The casing wall is absolutely stationary, while the hub and the blade surfaces are rotating. The walls are considered as hydraulically smooth. The standard  $k-\epsilon$  turbulence model with a standard wall function is employed in the modeling. The convergence condition is set as such that the maximum residual must be less than  $10^{-4}$ .

#### 4 Results and Discussions

In general, the leakage flow from the tip clearance has a chance to roll up into a discrete vortex (as shown in Fig. 6). The overturning, underturning, and radial inward and outward flow induced by the tip leakage vortex are illustrated in Fig. 6.

The data are acquired at the design condition for both CFD and experiment. The global performance of the fan is presented in Fig. 7. To identify the leakage flow, the relative velocity vector and

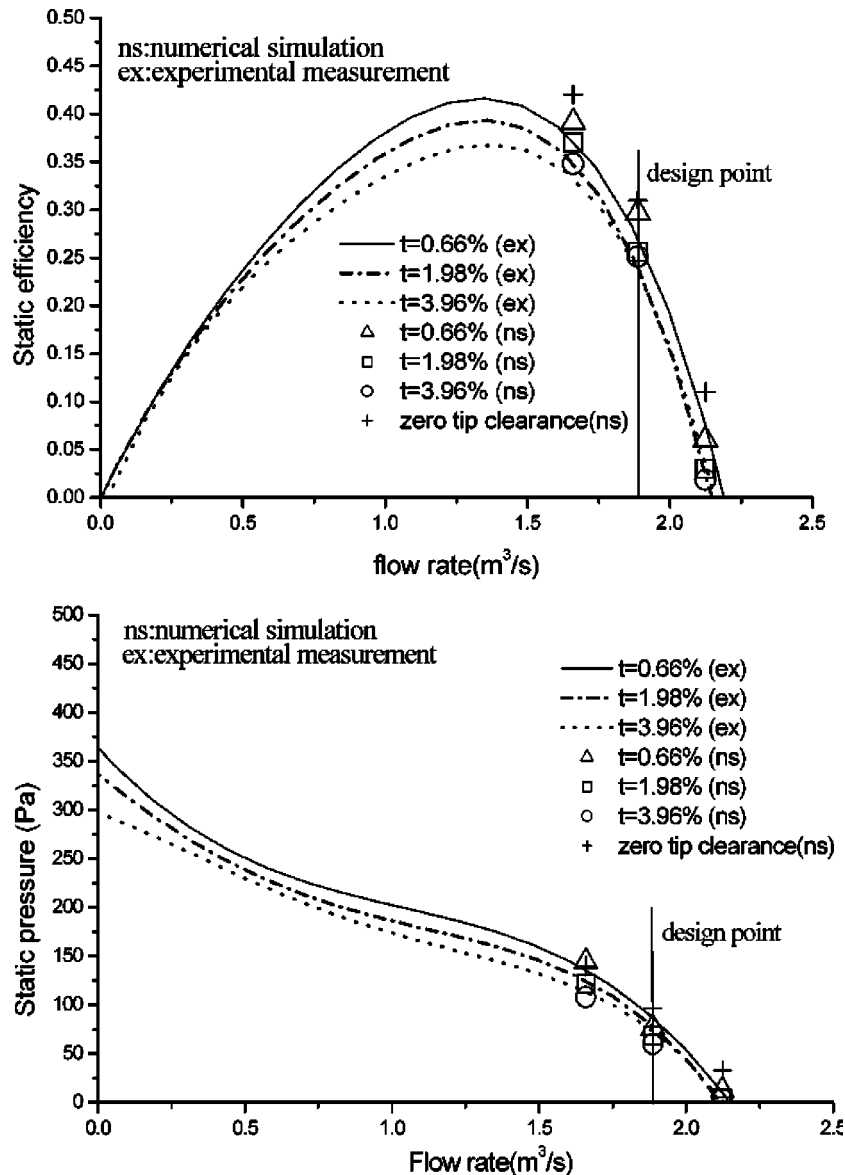


Fig. 7 (a) Static efficiency at different flow rate and (b) Static pressure rise at different flow rate

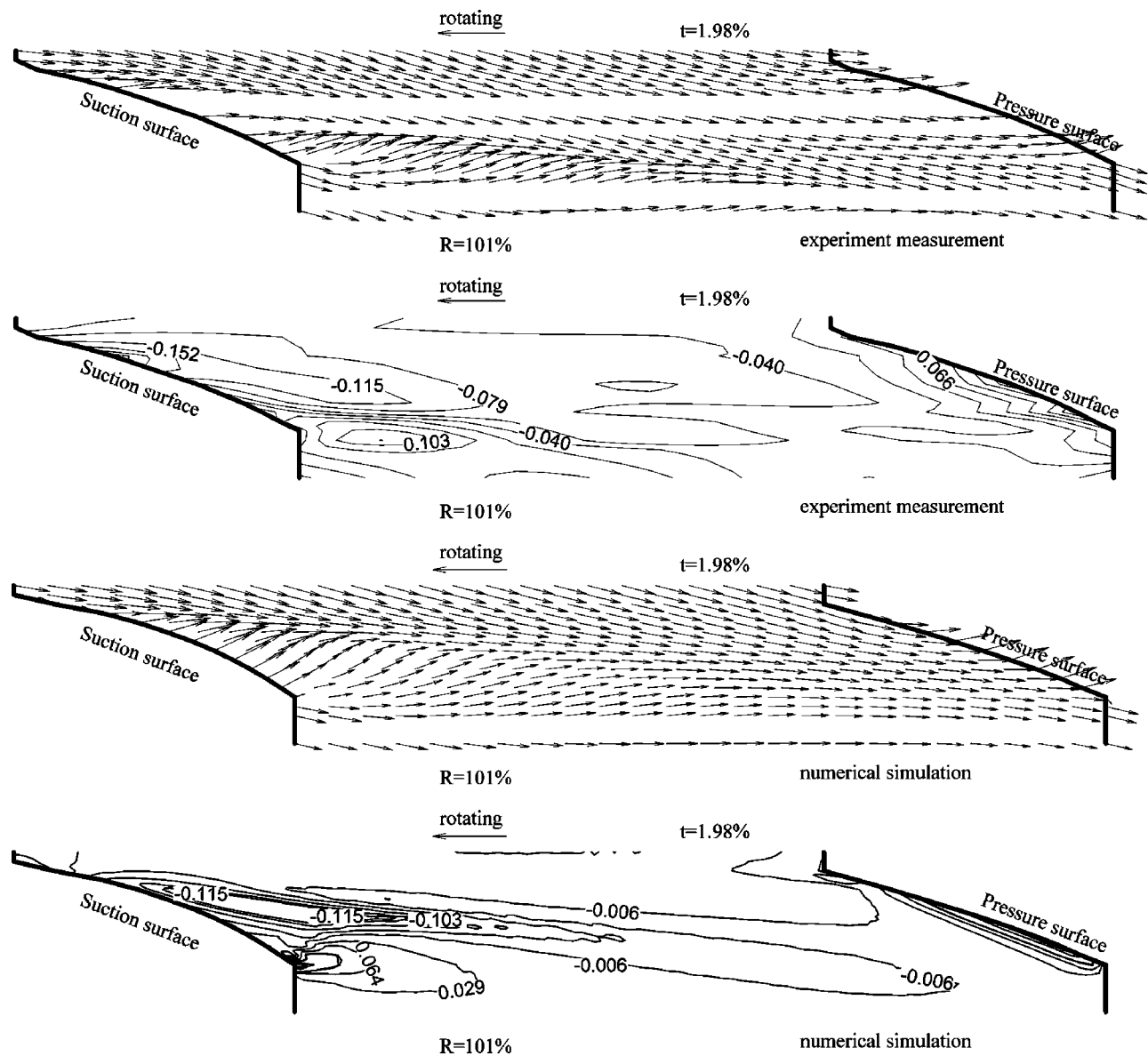


Fig. 8 Relative velocity vector and radial velocity contour in the blade-to-blade surface at  $R=101\%$  blade span for the normalized tip clearance of 1.98%

radial velocity contour in the blade-to-blade surface for the normalized tip clearance of 1.98% is given in Fig. 8. At the normalized tip clearance of 1.98%, the secondary flow, total velocity contour, and axial velocity contour on the surface at 100% axial chord after the leading edge are illustrated in Fig. 9 to get the overall structure of the tip leakage vortex.

The secondary flow vectors are shown in Figs. 10 and 11 in order to illustrate the vortical motion of the tip leakage flow. To quantitatively present the effect of different tip clearances, Fig. 12 shows the distribution of the pressure coefficient on the suction and the pressure surfaces of the fan blade. Furthermore, the radial variation of the mass-averaged axial velocity and flow angle are presented in Figs. 13 and 14.

For the experimental measurement, an ensemble-averaged velocity is employed to show the steady flow of the tip leakage flow.

**4.1 Global Performance of Fan.** The global performances of the fan at three different tip clearances are shown in Fig. 7. In the plot, a fan static pressure is defined as the fan total pressure rise

less the fan velocity pressure. It can be calculated by subtracting the inlet velocity pressure from the static pressure difference, as shown in the following:

$$SP = \bar{P}_{\text{outlet}} - \bar{P}_{\text{inlet}} - \frac{\rho \bar{V}_{\text{inlet}}^2}{2g} \quad (2)$$

In the experiment, the inlet static pressure is measured directly (as shown in Fig. 1). The outlet static pressure is the atmosphere pressure.

The static efficiency of a fan is defined as

$$\eta_{SP} = \frac{Q \times SP}{P} \quad (3)$$

where  $Q$  and  $SP$  are flow rate and static pressure, respectively, and  $P$  is the shaft power.

Both experiment and CFD show that the fan static pressure and static efficiency drop as the tip clearance increases. An increase in

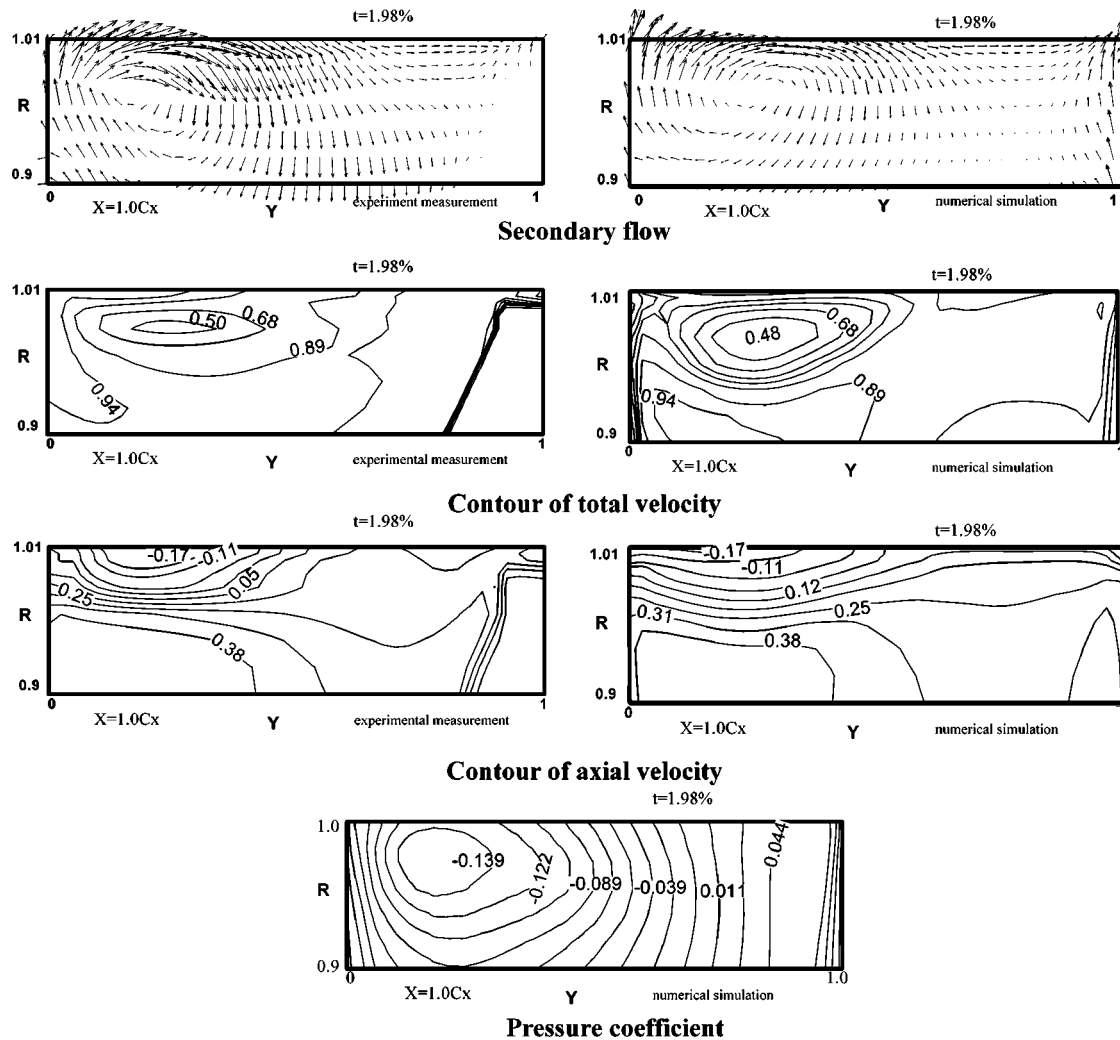


Fig. 9 Secondary flow, contour of axial velocity, and total velocity on the surface 100% axial chord location after the leading edge for the normalized tip clearance of 1.98%

the tip clearance leads to a stronger leakage flow and a stronger reverse flow, which attribute to a larger energy loss, as further illustrated in the following sections. In CFD modeling, there is no mechanical transfer loss (such as bearing), which is included in the experimental measurement. Therefore, the static efficiency from CFD is slightly higher than those from the experiment, as shown in Fig. 7.

**4.2 Flow in the Blade-to-Blade Surface.** At the normalized tip clearance of 1.98%, the relative flow vector and radial velocity contour in the blade-to-blade surface of 101% blade span are shown in Fig. 8. The relative vectors consist of an axial velocity component and a relative tangential velocity component. A positive radial velocity is defined as a radial outward flow, from the hub to the casing wall. Likewise, a negative radial velocity is a radial inward flow.

Overall, the flow field from CFD and experiment are in good agreement. It is shown from the relative velocity directions that there is an effect of the tip leakage flow at a normalized tip clearance of 1.98%. From the relative velocity vector direction, the leakage jet flow is weak near the leading edge and becomes stronger in the downstream direction. At the exit of the rotor, the axial reverse flow has appeared. Due to the relative motion between the casing wall and the rotor, the affected region of the leakage flow is far away from the suction surface.

In the affected region of leakage flow, the radial velocity turns from the radial outward flow to radial inward flow along the pitch-

wise direction; this is consistent to the rollup direction with tip leakage vortex. Up to 50% chord, there are large radial inward flows near the suction surface, which is induced by the blockage of the tip leakage vortex.

**4.3 Flow on the Surface at 100% Axial Chord Location After the Leading Edge.** The trailing edge of the blade lies on the surface at 100% axial chord after the leading edge, which is bounded by the suction surface ( $Y=0$ ) at the left-hand side, and the pressure surface ( $Y=1$ ) at the right-hand side. In the radial direction, it is shown from 90% of the blade span to the casing wall. The blank areas near the pressure side of the blade in the experimental measurement of Fig. 9 correspond to the areas that cannot be measured by a laser probe.

Based on experimental data and numerical simulation, the secondary flow vector, the contours of the total relative velocity, and the contours of axial velocity component on the surface at 100% axial chord location are shown in Fig. 9. The contour value is also normalized by the rotating speed of the blade tip. The total velocity is defined as follows:

$$V = \sqrt{u^2 + v^2 + w^2} \quad (4)$$

The secondary flow field is defined as the projection of the velocity field at the exit angle of the blade tip. The vector consists of a radial velocity component and a velocity component that is perpendicular to the exit angle of the blade tip. The whole discrete

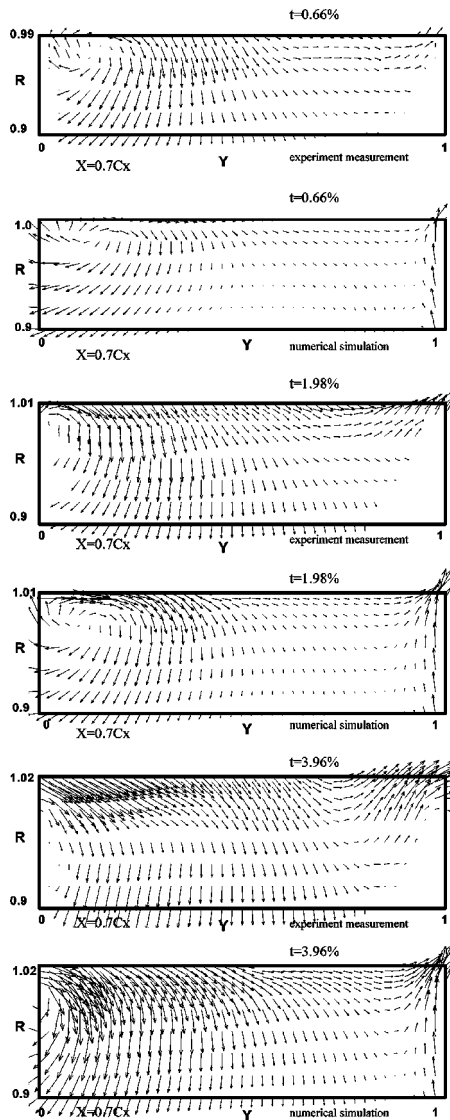


Fig. 10 Secondary flow field at 70% axial chord location

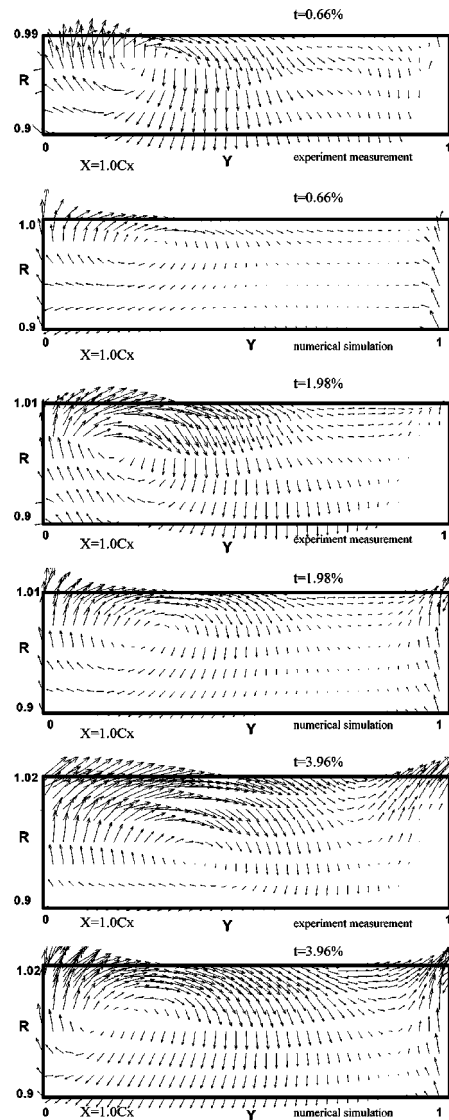


Fig. 11 Secondary flow at 100% axial chord location

tip leakage vortex can be clearly observed in Fig. 9. Besides the distributions of the radial inward and outward velocities, the underturning near the tip region and the overturning near 90% blade span region can also be shown in the secondary flow field.

Overall the secondary flow provided by both experiment and CFD are quite consistent. From both experimental data and numerical simulation, the mixing region occupies almost half of the passage in the tip region. Both experiment and CFD show a similar flow structure for the total velocity, though experiment shows a smaller zone of a low total velocity. This discrepancy is possibly caused by the ensemble-averaged method used in the process of the experimental data and caused by the standard  $k-\epsilon$  turbulence model with standard wall functions in the CFD simulation.

The contours of the axial velocity at the same chord location are also shown in Fig. 9. The axial velocity is not uniform. The reverse flow appears in the tip region for both experimental data and numerical simulation. The low axial velocity means the blockage of the incoming through flow.

From the numerical simulation, the pressure coefficient on the surface at the same axial location is also illustrated. The low-pressure zone coincides with the center of the tip leakage vortex. This means that the mixing interaction between the tip leakage flow and the main flow contributes to the energy loss.

#### 4.5 Secondary Flow. Figures 10 and 11 show the secondary

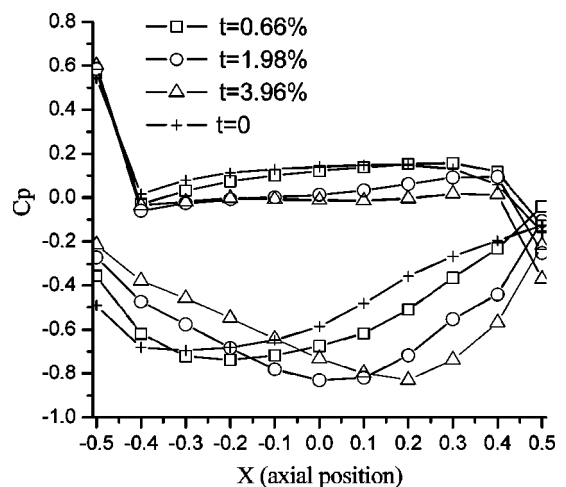


Fig. 12 Distribution of the pressure coefficient at the 99% of the blade span (numerical simulation)

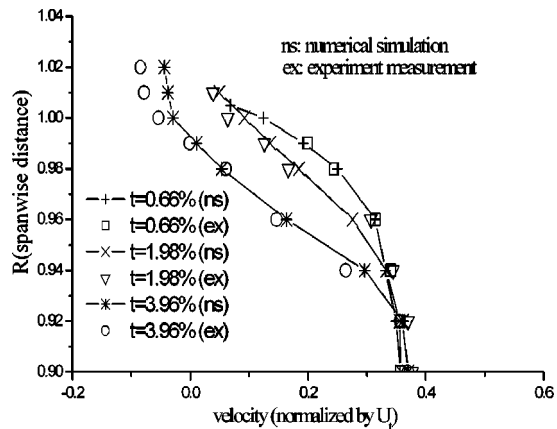


Fig. 13 Radial variation of mass averaged axial velocity ( $X=1.20Cx$ )

flow field at two different axial locations. They are shown on surfaces at 70% and 100% axial chord after the leading edge of the fan blade, respectively.

At 70% axial chord location ( $X=0.7Cx$ ), vortical motions are observed at three different tip clearances. However, the vortical motion does not appear as a vortex at the largest tip clearance ( $t=3.96\%$ ). This phenomenon demonstrates that a leakage vortex will be formed at a distance further downstream when the tip clearance is increased, as shown in Fig 11. Figure 11 shows the secondary flow field at 100% axial chord location ( $X=1.0Cx$ ). The plots show a significant vortical motion, and there are vortex centers at all three tip clearances. The centers of the vortices move toward the pressure side of the blade due to the rotation of the blade.

Overall the secondary flow provided by both experiment and CFD are quite consistent. It is noted that at smaller tip clearances ( $t=0.66\%$  and  $t=1.98\%$ ), the vortex centers provided by both measurement and CFD modeling are quite close. While at a larger tip clearance ( $t=3.96\%$ ), CFD predicts a position of vortex center that is closer to the suction surface of the blade than the position from the experimental measurement, as shown in Fig. 11. In other words, the leakage flow predicted from CFD migrates toward the pressure surface more slowly than that measured by the experiment. This may be explained by the fact that a standard  $k-\epsilon$  model with a wall function is not adequate for the prediction of turbulent boundary layers with unsteady and separated flows, etc. [20]. In addition, the tip clearance flow with a tip vortex of an axial flow fan is an unsteady and separated flow in a rotating frame.

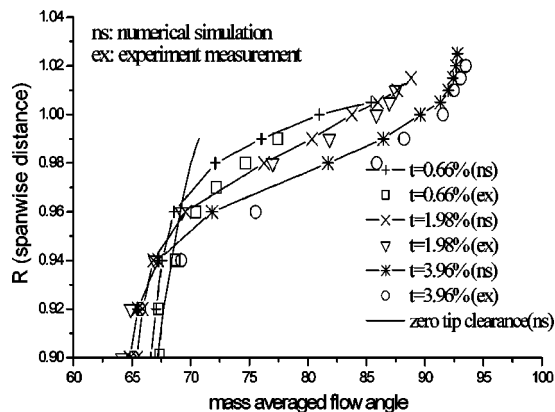


Fig. 14 Radial variation of mass-averaged flow angle ( $X=1.20Cx$ )

**4.6 Blade Pressure Distribution at 99% Blade Span.** The tip leakage flow is induced by the pressure difference between the pressure and suction surfaces of the fan blade near the tip region. Figure 12 shows the distribution of the pressure coefficient on the blade surfaces from CFD modeling. The definition of the pressure coefficient is given in the formulation

$$C_p = \frac{(p - p_1)}{1/2\rho U_t^2} \quad (5)$$

Due to the blockage of the tip leakage vortex, the pressure coefficient on the suction surface side near the leading edge increases with the tip clearance. Except near the leading edge, the pressure coefficient on the suction side drops substantially when the tip clearance is increased from 0 to 0.66% of the blade span, while the values on the pressure side remain almost unchanged. This means that at a small tip clearance ( $t=0.66\%$ ) only the flow field near the suction surfaces of the blade has been disturbed because of the tip leakage vortex. As the tip clearance increases to 1.98% and 3.96% of the blade span, respectively, the flow near the pressure side begins to be disturbed by the leakage vortex. The corresponding pressure coefficient at the pressure side also decreases. At the same time, the minimum pressure at the suction side moves downstream. This is consistent with the movement of vortex centers shown in Figs. 10 and 11.

**4.7 Radial Variation of Mass Averaged Axial Velocities and Flow Angles.**

The radial variations of mass-averaged axial velocities and flow angles at an axial position, which is 20% of the axial chord length after the trailing edge of the blade, are given in Figs. 13 and 14, respectively. The presence of the tip leakage flow results in a low axial velocity in the tip region. As the tip clearance is increased, the axial velocity decreases in the tip region. A lower axial velocity increases the flow blockage and reduces the global flow rate. This also contributes to the decline of the global performance as the tip clearance increases. Judging from the velocity triangle, a lower axial velocity leads to the underturning of the flow shown in Fig. 12.

The effect of the tip leakage flow on the averaged flow angle  $\beta$  is shown in Fig. 14. The flow angle distribution is consistent with the rotation of the tip leakage vortex. Both experimental measurement and numerical simulation show that the flow underturning is confined to the tip region, and the overturning happens at a lower blade span region when the tip clearance increases. There is a critical span position of about 94% for the flow underturning and overturning. At the smallest tip clearance ( $t=0.66\%$ ) the overturning at a lower span region is quite small as the flow angle is close to the values at a zero tip clearance. However, both CFD modeling and experiment show a substantial underturning in the tip region. This means that the flow field in a lower span region is almost unaffected when the tip clearance is small, whereas the flow field in the tip region has been disturbed greatly even at a small tip clearance. As the tip clearance is increased from 0.66% to 1.98% of the blade span, there is a jump of the flow overturning in a lower span region, which indicates that the flow field in the lower span region has begun to be disturbed at this tip clearance. The global performance drops substantially as shown in Fig. 7(a). When the tip clearance is further increased from  $t=1.98\%$  to  $t=3.96\%$ , the underturning in the tip region increases greatly, whereas the overturning in a lower span region does not change a lot. The corresponding static efficiency and static pressure also remain close, which may explain the existence of an optimal tip clearance for the drop in static efficiency. At the same time, it demonstrates that the most important region for the energy transfer efficiency is the region below 94% of the blade span, as shown in Figs. 7 and 14.

A flow angle of  $>90$  deg means that there is a reverse flow in that region due to the existence of the leakage vortex. As the tip



clearance increases, more reverse flow is observed near the tip clearance region as shown in Fig. 14. More reverse flow means more energy loss at a larger tip clearance.

## 5 Conclusion

A three-dimensional velocity flow field in the tip region of an axial ventilation fan with three different clearances has been measured with a PDA system and predicted by CFD. The corresponding global performance of the fan is also obtained. Based on the measurement data and numerical simulation results, the following conclusions can be drawn for low-speed and low-pressure axial flow fans:

1. The global performance and the general structure of the tip leakage flow from both experiment and numerical simulation are in good agreement. The global performance (static pressure and static efficiency) decreases as the tip clearance increases.
2. The leakage flow originating from the tip clearance rolls up into a spiral to form a leakage vortex. The magnitude and intensity of the tip leakage vortex grow as the tip clearance is increased, and the first appearance position of the tip leakage vortex moves further downstream along the chord.
3. The mixing interaction between the tip leakage flow and the main flow produces a low axial velocity region. This leads to flow loss and blockage of the main flow in the tip region. There are underturning zones near and in the blade tip region and overturning zones in a lower span region with a critical span-wise position of about 94%.
4. As the tip clearance increases, a reverse flow appears. More reverse flow at a larger tip clearance leads to a larger energy loss.

This research involves an unsteady and a separated tip clearance flow. This is the essential reason for the discrepancy between PDA experiment and CFD. In the next research stage, PIV (Particle Image Velocimetry) system will be employed to investigate the unsteady flow of the tip leakage flow.

## Acknowledgments

The authors acknowledge the financial support for this work and the permission to publish this paper by the administration of Emerson Electric Corporation (USA). Also, this work is a part of Project Nos. 50406017 and 5017603 supported by National Natural Science Foundation of China.

## Nomenclature

$C$	= chord length, mm
$Cx$	= axial chord length, mm
$Cp$	= static pressure coefficient
$h$	= average blade span, mm
$N$	= blade number (6)
$P$	= shaft power, W
$\bar{P}_{inlet}$	= mass-averaged inlet static pressure, Pa
$\bar{P}_{outlet}$	= mass-averaged outlet static pressure, Pa
$Q$	= flow rate, m <sup>3</sup> /s
$r$	= radius, mm
$R$	= normalized radius ( $r/h$ ).
$S$	= pitch $2\pi r/N$ , mm
$SP$	= fan static pressure, Pa
$t$	= normalized tip clearance ( $\tau/h$ ).
$u$	= axial velocity component, m/s
$U_t$	= blade-tip speed (43.25 m/s), m/s
$v$	= tangential velocity component, m/s
$V_1, V_2, V_3$	= velocity components which are perpendicular to the beam bisectors in the planes of the beams, m/s

$V$	= flow velocity, total velocity, m/s
$\bar{V}_{inlet}$	= mass-averaged inlet velocity, m/s
$w$	= radial velocity component, m/s
$x$	= axial distance from rotor leading edge, mm
$X$	= normalized distance ( $x/Cx$ )
$y$	= tangential distance from the suction surface, mm
$Y$	= normalized tangential distance by the local blade spacing, $Y=0$ on the suction surface. $Y=1$ on the pressure surface.
$\beta$	= relative air flow angle measured from the axial direction, deg
$\theta$	= interaction angle, the angle between bisector of the green laser beam and the violet laser beam, deg
$\lambda$	= stagger angle; the angle between the chord line and the axial direction, deg
$\eta_{SP}$	= static efficiency of a fan
$\rho$	= density, kg/m <sup>3</sup>
$\tau$	= tip clearance, mm

## References

- [1] Takur, S., Lin, W. L., Wright, J., Wang, S. Y., and Ron, L. Y., 2000, "Computational Modeling of Low Pressure Fan," ASME Paper No. 2000-GT-621, Munich, Germany.
- [2] Wisler, D. C., 1985, "Loss Reduction in Axial-Flow Compressor Through Low-Speed Model Testing," ASME J. Turbomach., **107**, pp. 354–363.
- [3] Kang, S., and Hirsch, C., 1993, "Experimental Study on the Three Dimensional Flow Within a Compressor Cascade With Tip Clearance: Part I-Velocity and Pressure Fields," ASME J. Turbomach., **115**, pp. 435–443.
- [4] Kang, S., and Hirsch, C., 1993, "Experimental Study on the Three Dimensional Flow Within a Compressor Cascade With Tip Clearance: Part II-The Tip Leakage Vortex," ASME J. Turbomach., **115**, pp. 444–452.
- [5] Hunter, I. H., and Cumpsty, N. A., 1982, "Casing Wall Boundary-Layer Development Through an Isolated Compressor Rotor," ASME J. Eng. Power, **104**, pp. 805–818.
- [6] Lakshminarayana, B., Davino, R., and Pouagare, M., 1982, "Three Dimensional Flow Field in the Tip Region of a Compressor Rotor Passage—Part I: Mean Velocity Profiles and Annulus Wall Boundary Layer," ASME J. Eng. Power, **104**, pp. 760–771.
- [7] Lakshminarayana, B., Davino, R., and Pouagare, M., 1982, "Three Dimensional Flow Field in the Tip Region of a Compressor Rotor Passage—Part II: Turbulence Properties," ASME J. Eng. Power, **104**, pp. 772–781.
- [8] Inoue, M., Kuroumaru, M., and Fukuhara, M., 1986, "Behavior of Tip Leakage Flow Behind an Axial Compressor Rotor," ASME J. Turbomach., **108**, pp. 7–15.
- [9] Inoue, M., and Kuroumaru, M., 1989, "Structure of Tip Clearance Flow in an Isolated Axial Compressor Rotor," ASME J. Turbomach., **111**, pp. 250–256.
- [10] Wisler, D. C., and Mossey, P. W., 1973, "Gas Velocity Measurements Within a Compressor Rotor Passage Using the Laser Doppler Velocimeter," ASME J. Eng. Power, **95**(2), pp. 91–97.
- [11] Murthy, K. N. S., and Lakshminarayana, B., 1986, "Laser Doppler Velocimeter Measurement in the Tip Region of a Compressor Rotor," AIAA J., **24**(5), pp. 807–814.
- [12] Stauter, R. C., 1993, "Measurement of the Three-Dimensional Tip Region Flow Field in an Axial Compressor," ASME J. Turbomach., **115**, pp. 468–476.
- [13] Lakshminarayana, B., 1970, "Methods of Predicting the Tip Clearance Effects in Axial Flow Turbomachinery," ASME J. Basic Eng., **92**, pp. 467–482.
- [14] Chen, G. T., Greitzer, E. M., Tan, C. S., and Marble, F. E., 1991, "Similarity Analysis of Compressor Tip Clearance Flow Structure," ASME J. Turbomach., **113**, pp. 260–271.
- [15] Storer, J. A., and Cumpsty, N. A., 1994, "An Approximate Analysis and Prediction Method for Tip Clearance Loss in Axial Compressors," ASME J. Turbomach., **116**, pp. 648–656.
- [16] Denton, J. D., 1993, "Loss Mechanisms in Turbomachines," ASME J. Turbomach., **115**, pp. 621–656.
- [17] Hah, C., 1986, "A Numerical Modeling of Endwall and Tip-Clearance Flow of an Isolated Compressor Rotor," ASME J. Eng. Gas Turbines Power, **108**, pp. 15–21.
- [18] Dawes, W. N., 1987, "A Numerical Analysis of the 3-D Viscous Flow in a Transonic Compressor Rotor and Comparison With Experiment," ASME J. Turbomach., **109**, pp. 83–90.
- [19] Von Zante, D. E., 1999, "Recommendations for achieving Accurate Numerical Simulation of Tip Clearance Flow in Transonic Compressor Rotors," *International Gas Turbine and Aeroengine Congress and Exhibition*, Indianapolis.
- [20] Patel, V. C., Rodi, W., and Scheuerer, G., 1984, "Turbulence Models for Near-Wall and Low Reynolds Number Flows: A Review," AIAA J., **23**(9), pp. 1308–1319.

# Periodic Velocity Measurements in a Wide and Large Radius Ratio Automotive Torque Converter at the Pump/Turbine Interface

S. O. Kraus

R. Flack

A. Habsieger

G. T. Gillies

Mechanical and Aerospace Engineering,  
University of Virginia,  
Charlottesville, VA 22903-2442  
e-mail: rdf@virginia.edu

K. Dullenkopf

Institut für Thermische Strömungsmaschinen,  
Universität Karlsruhe,  
Karlsruhe, Germany 76131

*The unsteady flow field due to blade passing at the pump/turbine interface of a torque converter was studied. The current geometry is wide and has a large outer to inner radius ratio. A laser velocimeter was used to measure the periodic velocity components at four operating conditions determined by the speed ratios between the turbine and pump of 0.065 (near stall), 0.600, 0.800, and 0.875 (coupling point). The flow fields at the pump exit and turbine inlet planes were visualized and are presented. Using instantaneous pump and turbine blade positions with the velocity data, animations ("slow-motion movies") are generated to effectively visualize and understand the unsteady behavior. The turbine inlet flow was markedly periodic due to the exiting jet/wake from the upstream pump passage; however, the pump exit flow field showed little dependence on the turbine blade positions. The highest unsteadiness was seen for the highest speed ratios. Four "shots" from the sequences of one cycle for all speed ratios and each plane are presented herein. The results are also compared to unsteady results for a previously examined torque converter with a small radius ratio to determine the effect of parametric geometric changes on the flow field. Generally, the unsteady velocity fields show no significant difference for the two geometries—the trends are the same. [DOI: 10.1115/1.1891150]*

## 1 Introduction

An automotive torque converter is a very complex "mixed flow" hydrodynamic turbomachine with three independent components that govern the internal flow field. The flow has significant radial, tangential, and axial velocity components. The pump energizes the working oil and is connected to the engine. This pump operates similarly to a conventional centrifugal pump. The radial pump blades accelerate the flow in the radial and tangential directions thereby imparting kinetic and potential (pressure) energy into the flow. The turbine drives the transmission shaft. The turbine operates like a radial inflow turbine and absorbs the fluid energy. The function of the stator is to redirect the flow exiting the turbine to have an ideally incidence free flow into the pump at a specifically designed turbine/pump angular speed ratio. The stator also acts as a torque reactor at low pump/turbine speed ratios (allowing for torque amplification), thus differentiating the torque converter from the conventional fluid coupling. The pump and turbine rotate at different speeds, while the stator is either locked or allowed to rotate freely which depends on the application. Due to the interaction of the pump, turbine, and stator blades, the flow field in the torque converter is highly periodic at the interfaces.

Furthermore, a torque converter should operate efficiently at both on-design and off-design conditions. However, the flow field changes drastically over the typical operating range; namely, incidence angles at the element interfaces can change drastically as the pump/turbine speed ratio increases from zero to unity. Blade slip can also be a problem as in any turbomachine. These two effects also demonstrate periodicity.

## 2 Previous Studies

A number of papers have been published over the past decade on internal flows in torque converters. Whitehead and Flack [1]

and Claudel [2] effectively review the literature for average flow fields. Only the more relevant work will be summarized here.

Browarzik [3] used hot-film anemometry to investigate the unsteady rotor/rotor interaction in the region between the pump exit and turbine inlet. A large wake region at the pump exit near the core-suction side was found which was unaffected by the instantaneous position of the turbine.

Marathe and Lakshminarayana [4] measured pressures at the exit of a torque converter stator and turbine by using a fast response five-hole probe and embedded transducers in the stator vanes. Large secondary flows were observed at the stator exit. Also, the separated flow near the stator shell side was observed.

Marathe and Lakshminarayana [5] also obtained average and unsteady pressure and velocity data upstream and downstream of a torque converter pump using the high frequency response five-hole probe. Separation zones were found near the core at the 0.800 speed ratio and at the shell at the 0.065 speed ratio.

Dong et al. [6] studied the flow fields at the exit of the torque converter pump and turbine. Four zones were found in the pump exit flow: free stream flow, blade wake flow, core-suction corner separation, and mixing zone. A fully developed turbine exit flow was found with small velocity gradients in the radial direction. At the turbine core a separation region with high unsteadiness was found.

Brun and Flack [7] developed the fundamental principles to organize data with discrete sampling so that the effects of the pump exit and turbine inlet blade positions on the unsteady flow field and performance parameters in the pump exit and turbine inlet planes could be determined. Brun et al. [8] and Brun and Flack [9] then employed a 230-mm-diam torque converter geometry entirely machined from Plexiglas™ and a laser velocimeter to obtain detailed periodic velocity profiles in the pump exit and turbine inlet, respectively.

Whitehead and Flack [1] and Christen et al. [10] utilized the same setup to test a series of three 245-mm-diam and 75-mm-wide automotive torque converters with small radius ratios in

Contributed by the Fluids Engineering Division for publication in the JOURNAL OF FLUIDS ENGINEERING. Manuscript received by the Fluids Engineering Division September 11, 2003. Revised manuscript received December 9, 2004. Review conducted by J. Lee.

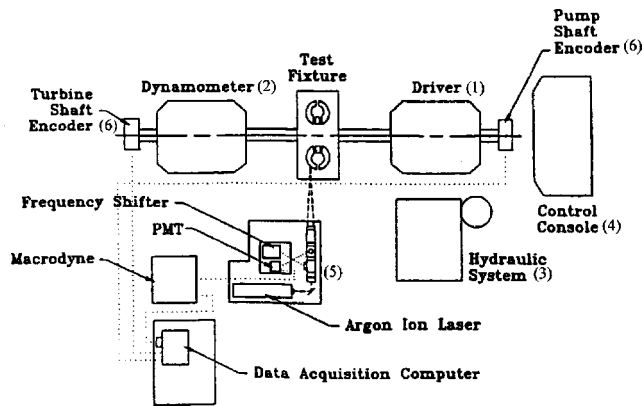


Fig. 1 Torque converter and laser velocimeter system

which pump and turbine blade angles varied. Limited unsteady measurements were taken for 0.065, 0.600, and 0.800 speed ratios at the pump/turbine interface.

### 3 Motivations of the Current Research

Great strides have been made in CFD. However, as applied to the complex torque converter, the analysis has not yet developed to a level permitting design solely from computational results. This is especially true for unsteady predictions, for which quasi-steady approaches are often used. Experimental unsteady velocity distributions and pressure data for the internal flow are needed to verify computational results. Benchmark velocity data over a wide range of geometries are needed to understand the flow mechanics and to verify CFD predictions. Furthermore, a basic understanding of periodic mixed-flow behavior is timely for industries outside of the automotive industry, including such industries as compressors.

### 4 Particular Objectives

For this paper, a laser velocimeter (LV) was used to measure periodic velocity components in the pump exit and turbine inlet of an automobile torque converter with a larger radius ratio than previously studied and at four speed ratios. From the velocity data, flow non-uniformities and secondary flows were determined. The data presented herein complements earlier data in that the designs are different and can be used for further verification and testing of theoretical models over a wider envelope of geometries as well as speed ratios. Furthermore, the data have been organized herein so that the complexities of the unsteadiness are easily observed from visualization. The velocities are compared to results from previous studies.

### 5 Experimental Facility

The same basic experimental facility described in Whitehead and Flack [1] and Claudel [2] was used for this research.

**5.1 Torque Converter Rig.** A schematic of the experimental setup is presented in Fig. 1. The rig consists of: (1) an input dynamometer (driver) to power the torque converter pump, (2) an eddy current dynamometer to load the turbine, (3) a hydraulic system to cool, pressurize, and lubricate the rig, (4) a control unit to adjust shaft speeds and torques, (5) LV system to measure velocities, and (6) shaft encoders to correlate the LV data with the pump and turbine angular positions.

The input dynamometer, which controls the pump speed, is a 20 kW unit and the output dynamometer, which controls the turbine speed, is a 130 kW capacity unit. Both dynamometers control the shaft speeds with 1 rpm.

The torque converter was constructed of Plexiglas so that all locations in the flow field could be measured. The index of refraction of Plexiglas is nominally 1.490. Shell-Flex 6212 oil, which

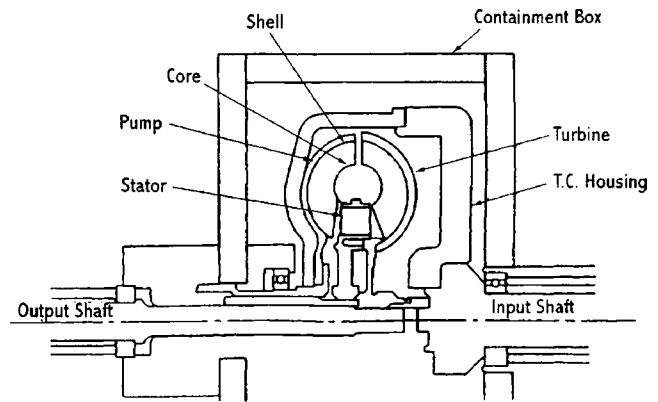


Fig. 2 Cross-sectional view of torque converter showing containment box, components, and dimensions

has a matching index of refraction of 1.489 at 25 °C, was used to reduce undesired laser beam refraction and scattering. The density of the oil at 25 °C is 899 kg/m<sup>3</sup> and the viscosity is 1.98 and 1.29 × 10<sup>-3</sup> kg/m s at 25 and 40 °C, respectively. The entire torque converter is in a rectangular oil-filled Plexiglas containment box as shown in Fig. 2 to minimize the effects of wall curvature on the LV measurements. Important dimensions are also shown in Fig. 2. In particular the inner radius width of this converter is 55.3 mm compared to 62.3 mm previously tested by Whitehead [11] and Flack and Whitehead [12].

In Fig. 3 the pump and turbine geometries are shown. Blades are 1.1 mm thick; the shells are 2.67 mm thick. The component blade angles and numbers are presented in Table 1. The geometries UE, QD, and UQ (GM notation) are for the current effort. The geometries NW, LC, NL were used by Whitehead [11]. Blade angles are nearly identical for the two geometries. All angles are relative to the axial direction. At the mid-plane the pumps had strictly radial blades. The torque converter cylindrical coordinate system is defined as follows: axial—along the torque converter shaft, tangential—in the torque converter rotational direction, and radial—perpendicular to the shaft.

The torque converter was studied in detail for four turbine to pump rotational speed ratios. The operating conditions are presented in Table 2.

**5.2 Laser Velocimeter System.** The system is a one-directional dual beam back-scatter frequency shifted LV. A one-directional system was used. Perfect probe volume overlapping with a two-directional multi-beam system was impossible due to the small difference of index of refraction between the oil and Plexiglas and the curvature of the components.

The entire optical assembly (transmitting and receiving optics) was mounted on a mill table. The probe volume location (measurement point) was traversed in the torque converter in all three

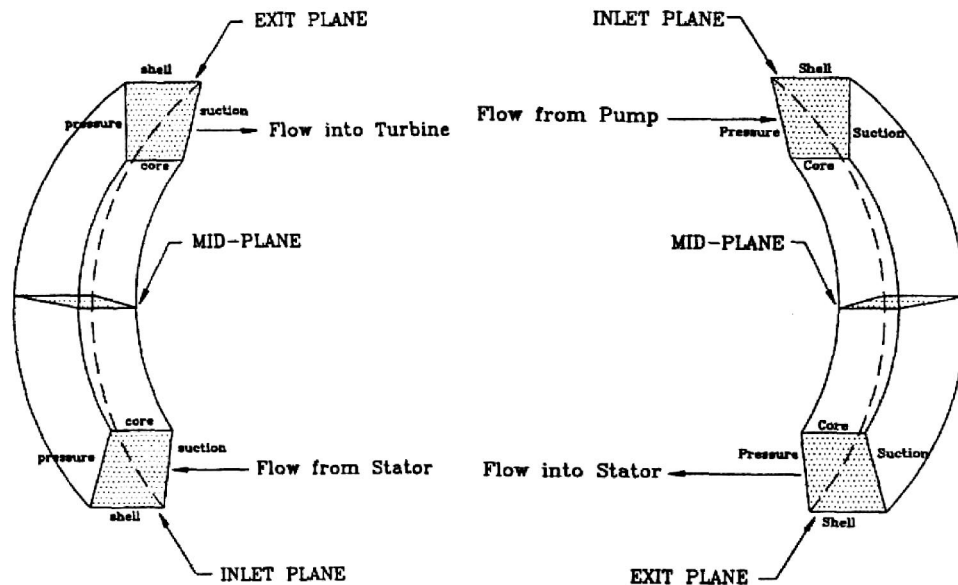


Fig. 3 Pump and turbine passage geometries

directions using the mill bed and a digital readout for precise location of the probe volume. The resulting uncertainty in position of the digital readout was 0.005 mm in any direction.

A 2 W argon-ion laser operating at 514.5 nm was used. All three velocity components were obtained by rotating the beam splitter and realigning the optics for each component. The effective probe volume is 72  $\mu\text{m}$  in diameter and 793  $\mu\text{m}$  long. Aluminum coated styrene particles 9  $\mu\text{m}$  in diameter were seeded into the flow; the density of the particles approximated the density of the oil. The scattered light was focused into a photomultiplier tube (PM tube). Output signals of the PM tube were amplified, bandpass filtered, and transmitted to a signal processor.

The signal processor is a burst type processor with a minimum threshold and a 5/8 count comparator to validate the Doppler signal. Each valid Doppler signal was recorded with a dedicated microcomputer (Fig. 1). The instantaneous angular position of the pump and turbine were measured for each valid velocity signal using 9 bit (1024 circumferential positions) shaft encoders on the pump and turbine shafts (Fig. 1).

Due to the small difference of index of refraction, the uncertainty of the probe volume position varied depending on the number of interfaces the laser beams traversed. For the pump exit and turbine inlet planes the uncertainty of the probe volume location

was 0.2 mm in the direction of the length of the probe volume.

Uncertainties in measured velocities are due to the clock in the digital processor, uncertainties in the beam crossing angle, and the finite number of samples used to approximate the true distribution and the uncertainty is typically  $\pm 0.05$  m/s. Furthermore, uncertainties in position translate to uncertainties in the velocity when velocity gradients are present. The total uncertainty due to the combination of these effects is typically 0.07 m/s.

**5.3 Periodic Measurement Procedure.** For measurements of the interactions between the pump exit and turbine inlet flow field, the stator was considered to have no influence, because it was either far up or downstream, as was demonstrated by Brun et al. [8]. Also, because in the pump and turbine the blade passages of the elements are geometrically identical, a flow cycle in a passage is not only periodic over one total relative revolution of the opposite element, but also at the blade passing frequency of the opposite element. Now because the LV system takes data samples randomly over the entire 360° of the blade cascade of the pump/turbine (and not continuously in the same passage), the samples must be superimposed and averaged to obtain one representative blade passage during post-processing. Furthermore, they must be ordered into subgroups according to their position relative to the opposite element passage, so that the blade passing frequency is included in that data.

Ten core to shell positions were accessed and 30 000 samples per position were collected in each plane. Core to shell measurement locations were determined by using accurate reference points in the torque converter and the known dimensions. The grid-resolution was determined in the circumferential direction by the resolution of the shaft encoders. The resolution of the pressure-suction direction in the measurement grid depends on the shaft-encoder resolution and the number of passages. With an encoder resolution of 1024 and 32 passages for the pump and 36 for

Table 1 Torque converter geometries

Component	Inlet blade angle	Exit blade angle	No. blades
NW pump	-30.0°	30.0°	32
UE pump	-29.9°	29.9°	32
LC turbine	61.4°	-63.0°	36
QD turbine	60.0°	-60.0°	36
NL stator	27.0°	70.0°	17
UQ stator	41.6°	55.1°	14

Table 2 Test conditions

Speed ratio (SR)	Pump speed (rpm)	Turbine speed (rpm)	Stator speed (rpm)
0.065	800	52	0
0.600	1100	660	0
0.800	1100	880	0
0.875	1100	962	0

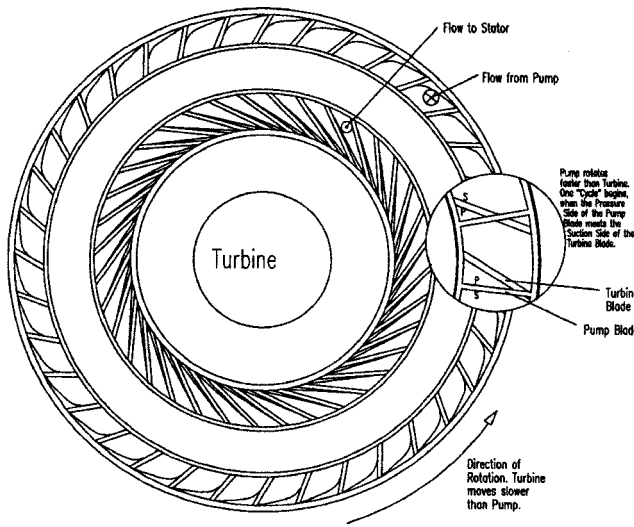


Fig. 4 Turbine inlet plane for one instantaneous pump position

the turbine, this led to 32 separate measurement points in the circumferential direction of the pump passage and 28 separate measurement points in the circumferential direction of the turbine passage. Thus, the pump data for the rotating planes were resolved into a  $32 \times 10$  measurement grid for the flow field for the rotating coordinate system. The turbine data for the rotating planes were resolved into a  $28 \times 10$  measurement grid.

Furthermore, one complete flow cycle in the measured passage is explained as the “sweeping-by” of a blade passage of the opposite element whose interaction is important (namely, Fig. 4). For example, each of the 32 pressure-to-suction locations in the pump passage encounters 28 different flow situations as one turbine passage sweeps by. This is referred to as the  $\Delta$  periodic position. The pump data consists of 28  $\Delta$  periodic positions, while the turbine data consists of 32  $\Delta$  periodic positions.

After collection, the data were post-processed into the measurement grid (displaying the velocity flow field), and ordered into temporal subgroups according to their relative periodic position to the opposite element. The velocity grid is thus generated 28 times for periodic measurements in the pump passage (and 32 times for measurements in the turbine passage) for each complete flow cycle. Data are presented in this paper as typical instantaneous flow fields for different relative blade positions. Lastly, since more than 30 000 valid velocity samples were collected for each of the measured core-to-shell positions, more than 50 valid velocity samples resulted for each of the time resolved measured grid po-

sitions. Thus, sufficient samples were used for a high confidence in the calculated velocities at every geometric and temporal position.

## 6 Results

In this paper, the pump/turbine interface was examined by analyzing the interdependencies in the through flow velocity component. The fluctuations in the flow field can have significant influence on the performance of the torque converter largely due to unsteady incidence angles to the component blades. Therefore, the unsteady, or periodic flow field at the pump exit and turbine inlet at four different operating conditions for the current torque converter are presented. The speed ratio, 0.065 (near stall), 0.600, 0.800, and 0.875 (coupling point) again determined these operating conditions. The turbine, located directly downstream of the pump, rotates at a lower angular speed than the pump. The turbine inlet is located 3.28 mm downstream of the pump exit. Consequently, as will be shown, the turbine has a slight upstream influence on the pump. On the contrary the pump has a significant effect on the turbine inlet flow field, as the non-uniform pump exit flow is directly forced into the turbine passages. To create the data presented herein, a visualization of the transient flow field was created by setting up an animation of the 28 different pump situations and 32 discrete turbine flow situations. Due to the wealth of data, only typical velocity contours are presented herein: 0%, 25%, 50%, and 75% relative pump/turbine positions. These animations were created using the Tecplot 8.0 commercial plotting package and can be viewed using the Tecplot movie player “Framer” (copyright 1991–1998 Amtech Engineering, Inc.) that supports the presentation of a file format called Rastermetafile (.rm). This format was originally developed by NASA and allows the combination of separate images within one file. The visual animations provide smooth transitions between the relative pump/turbine positions.

**6.1 Pump Exit Plane—Turbine Influence.** In order to present the interaction between pump and turbine within this paper four distinct and representative relative positions between pump and turbine blades were chosen for the sake of brevity. These were at 0% (same as 100%), 25%, 50%, and 75% of the total flow cycle, respectively. The 0% flow cycle position is defined as when the shell corner of the turbine’s pressure side coincides with the suction side of the pump.

As seen in Fig. 5, the turbine blade shows only moderate influence on the pump exit contour plot for  $SR=0.065$ . The average high velocity region covers almost 50% of the suction to pressure distance along the shell side. Only a very small velocity gradient is observed toward the suction side. The location of the downstream sweeping by turbine blade causes only a slight reduction of through flow velocity at the pump exit, exactly “in front” of the

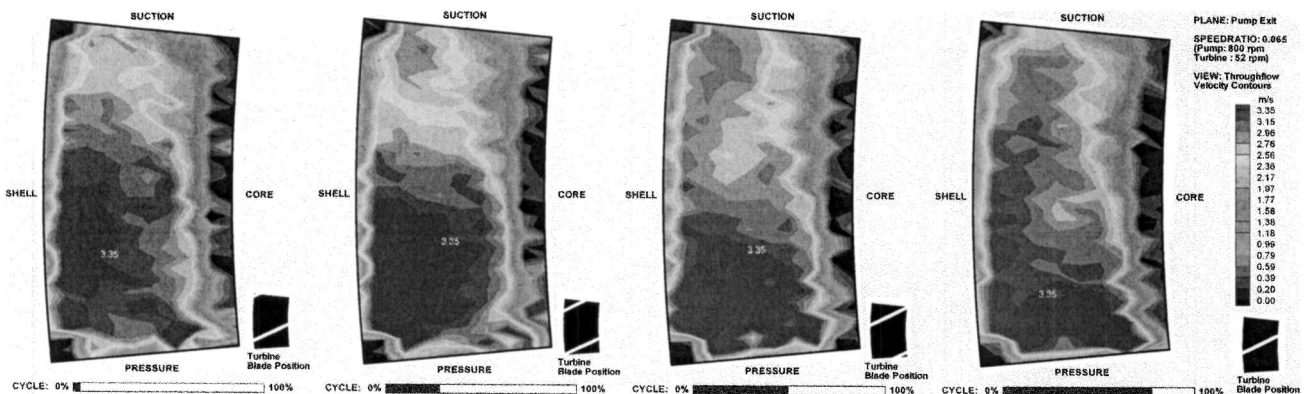


Fig. 5 Pump exit plane,  $SR=0.065$

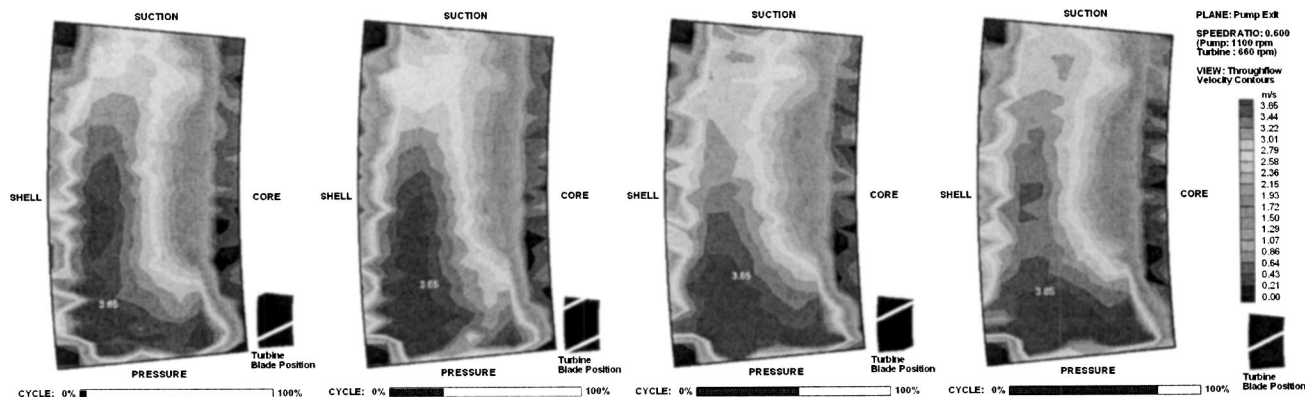


Fig. 6 Pump exit plane, SR=0.600

pressure side of the turbine blade that moves into the pump flow passage. The turbine blade can be seen as an obstacle downstream of the flow passage. The disturbance has to travel upstream against the main flow. At the 25% and 50% flow cycle positions one can see that the high velocity flow area splits into two regions separated by a zone of lower velocity. The turbine blade loses its influence with decreasing distance to the pump pressure side. At the 75% flow cycle position this is already evident and continues until the end of the flow cycle. This is due to the fact that the highest velocity values are found on the pump pressure side. The upstream traveling disturbances are much less effective here as compared to the lower velocity area close to the suction side.

The same effect of the turbine blade as observed at the 0.065 speed ratio can be found at the 0.600 speed ratio, depicted in Fig. 6. However, a significant difference can be seen due to the average velocity distribution at this speed ratio. The area of high velocity decreases with increasing speed ratio; it is in general moving closer to the shell side of the passage, although the suction to pressure distribution is still very similar to the 0.065 speed ratio. The velocity deficit caused by the sweeping by turbine blade is again seen particularly in the suction half of the pump passage and loses intensity with decreasing distance to the pressure side and increasing proximity of the high velocity jet at the pressure surface. In the animation of the flow cycle one can clearly observe how the turbine blade therefore creates an oscillating movement of the high velocity region in suction to pressure direction. Namely, the moved jet area spreads out again in direction of the suction side as soon as the turbine blade has passed by in every flow cycle.

As presented in Fig. 7, only marginal differences can be seen between the 0.600 and the 0.800 speed ratio. Since in general the high velocity area further decreases, moving in the pressure direc-

tion, and the jet is located very close to the pressure side, the influence of the turbine blade can primarily be seen from the suction side to about 80% of the suction to pressure distance. At the present speed ratio again the upstream traveling disturbances result in a local velocity reduction occurring at the pressure side of the turbine blade. This causes a periodic pushing back of the high velocity area toward the pressure side followed by a slight acceleration on the suction side of the turbine blade having passed. Again the flow area close to the pressure side remains relatively steady over the flow cycle.

The turbine inlet blades lose their influence at the 0.875 speed ratio. There is only a very small high velocity jet remaining close to the pump pressure surface. A wide area of moderate through flow velocity, where no velocity reductions or accelerations can be seen over the flow cycle, dominates the passage. Figure 8 depicts this cycle again at four different relative pump/turbine positions.

**6.2 Turbine Inlet Plane—Pump Influence.** Analogous to the visualization of the influence of the turbine blades on the pump exit through flow contour, the unsteadiness of the turbine through flow velocity field is presented. Again, four representative, discrete relative pump/turbine positions were chosen to depict the transient flow in this paper: 0% (or 100%), 25%, 50%, and 75% of the total flow cycle. The 0% flow cycle position is defined as when the pressure side of the pump passage coincides with the suction side of the turbine shell edge. As the pump exit is positioned only 3.28 mm upstream of the turbine inlet, the pump shows a significant effect on the turbine inlet flow field as shown on the following contour plots.

The least influence of the pump exit on the turbine inlet can be found at the 0.065 speed ratio, as depicted in Fig. 9. The velocity distribution in the pump exit at any time is essentially the instan-

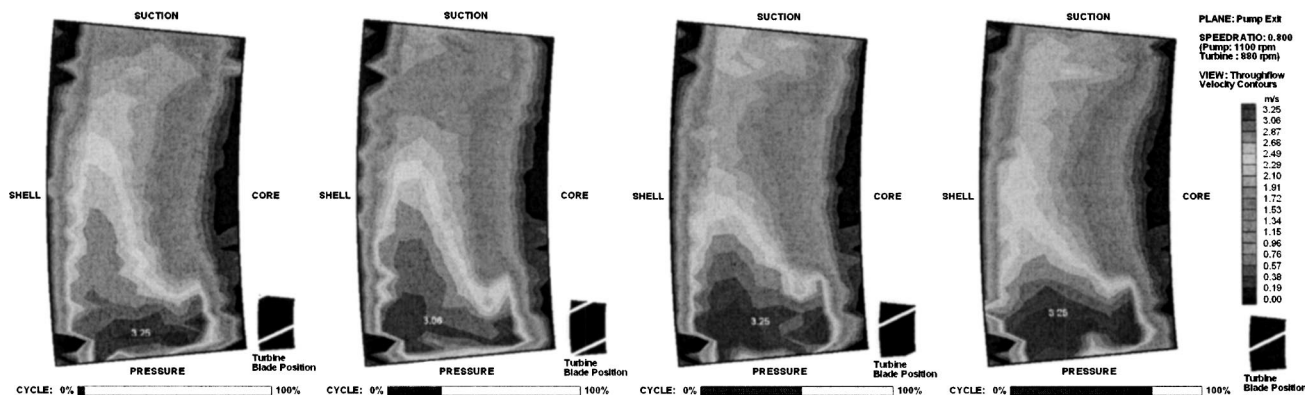


Fig. 7 Pump exit plane, SR=0.800

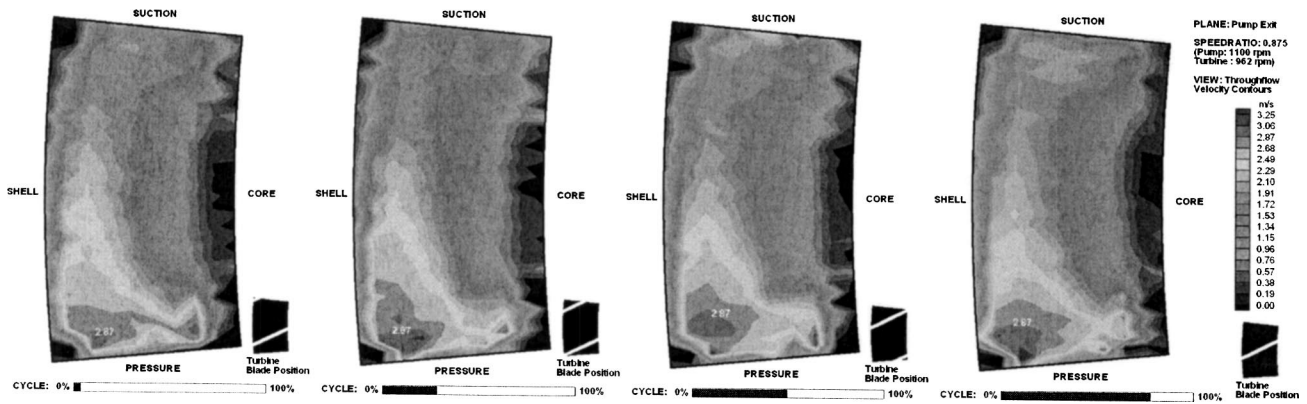


Fig. 8 Pump exit plane, SR=0.875

taneous inlet condition to the turbine. Therefore the contour plot in the turbine inlet clearly resembles the flow contours of two neighboring pump exit passages, divided by the pump blade. The pump blade at the 0.065 speed ratio can be detected as a velocity deficit or wake within the large high velocity area along the shell stretching out from the suction to the pressure side. This velocity deficit is due to the lower velocity region on the suction side of the pump blade. Because a high velocity area covering about 90% of the pressure to suction direction dominates the pump exit plane, the flow in the turbine inlet accelerates again quickly after the pump blade has passed. No influence of the pump blades can be seen in the low velocity area along the core side of the turbine

inlet.

The same influence as observed at the 0.065 speed ratio can be found at the 0.600 speed ratio as shown in Fig. 10. At this speed ratio, the contour of the through flow field is still very similar to the one at the 0.065 speed ratio although the high velocity area does not reach as far to the suction side. This is the reason for the wider band of velocity disturbance one can see sweeping through the turbine inlet contour plot. The cause for this drastic influence of the pump blades is again the fact that the pump passages force the flow into the turbine inlet passages regardless of the relative position between pump and turbine, retaining the suction to pres-

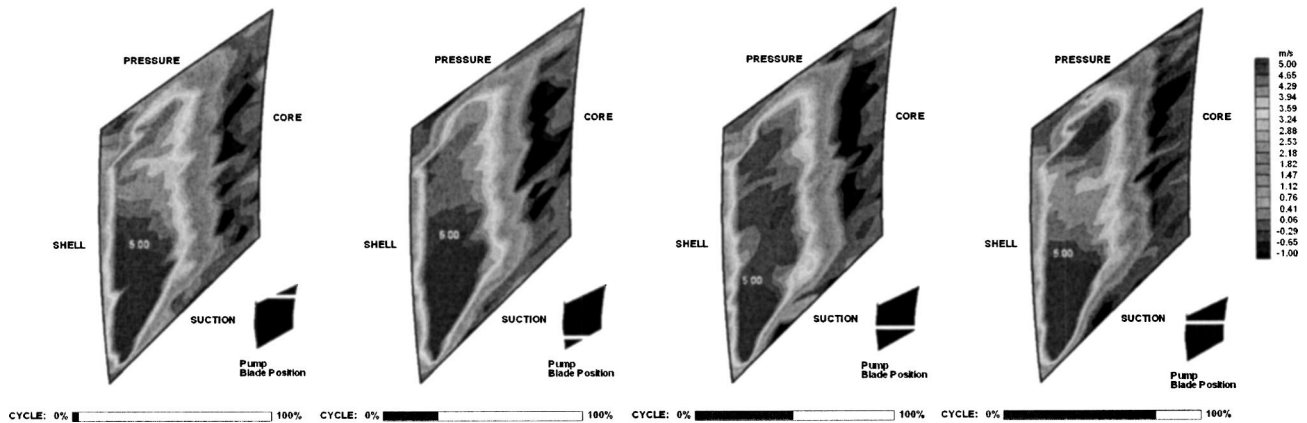


Fig. 9 Turbine inlet plane, SR=0.065

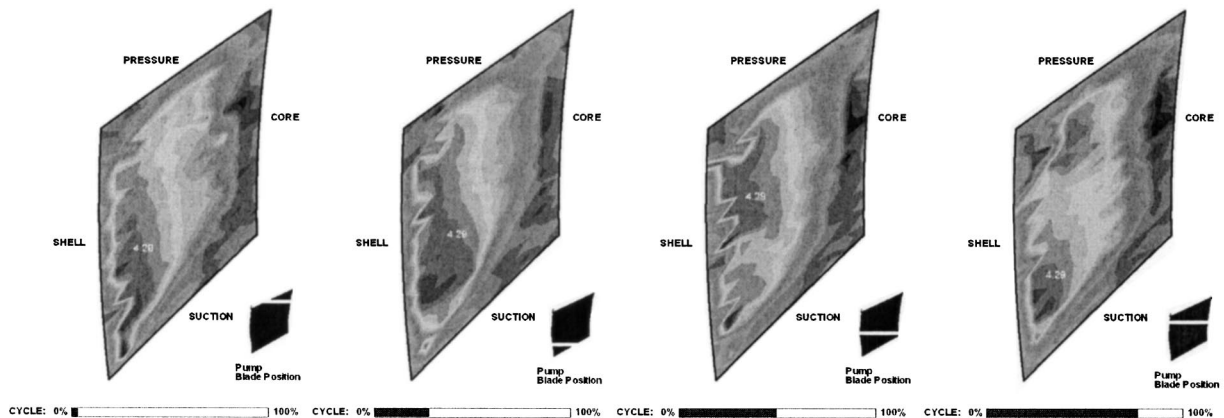


Fig. 10 Turbine inlet plane, SR=0.600

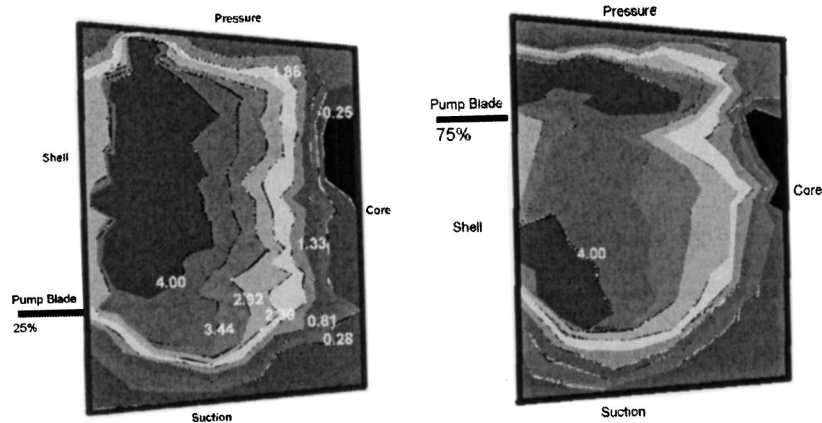


Fig. 11 Turbine inlet plane from Whitehead [11],  $SR=0.600$  (scales in m/s)

sure velocity distribution within the pump exit planes. As already seen, no influence of the pump blades along the core side of the turbine inlet plane within the low velocity region is seen.

In Fig. 11 two typical excerpts from the periodic sequence for the NL torque converter are shown for the turbine inlet for  $SR=0.600$  from Whitehead [11]. These compare to Figs. 10(b) (25% cycle) and 10(d) (75% cycle) for the current geometry. The general flow field shapes are approximately the same. For example, at 75% cycle, two jets are seen—one near the pressure shell corner and the other along the shell at about 30% pressure surface-to-suction surface position. Also, at 25% cycle, only one jet is seen, directly above the pump pressure surface for both geometries. Because of the great similarity of the flow fields at other speed ratios, and because the previous studies were not extensive, more such figures for NL are not presented for the sake of brevity.

With increasing speed ratio also the influence of the pump exit on the turbine inlet grows. Figure 12 depicts the excerpts of the flow cycle for  $SR=0.800$ . With increasing speed ratio, the flow in the pump is more and more forced against the shell side of the passages; the separation area on the core side grows. This effect causes the curved shape of the through flow contours in the pump passages. Namely, for larger speed ratios the flow is less uniform in the pump exit than for lower speed ratios. Only on the pressure and suction side of the pump passages positive flow covers up to 90% of the shell to core length. As the flow exiting the pump now passes the turbine passages the high velocity jet sweeps through the turbine inlet plane from the suction/shell corner toward the pressure side. The closer the pump and turbine blades get the more the pump forces the fluid within the jet, in front of the pump pressure side, into the pressure/core corner as is seen at the 75%

flow cycle position and in the animation. The flow on the suction side of the pump blade only accelerates slowly again following the velocity distribution of the pump exit planes. In another description, a high velocity region begins in the suction-shell corner, moves toward the pressure surface and eventually forms two high velocity jets in the turbine inlet plane before the high velocity in the pressure-core corner dissipates and the cycle begins again.

In Fig. 13 a typical series of snapshots of the blade-to-blade profiles are shown at the 50% core-to-shell position for different relative pump and turbine positions for  $SR=0.800$ . For comparison, in Fig. 14 a similar series of profiles are shown from Whitehead [11]. In general, the shapes of the profiles are similar and they vary similarly for different pump/turbine positions. Namely, as the percent cycle increases, the jet progresses from the turbine suction surface to the pressure surface for both geometries.

The pump influence at the 0.875 speed ratio as presented in Fig. 15 can be seen as an amplification of the effects described at the 0.800 speed ratio. Due to the increased speed ratio, the waist of the positive flow area in the middle of the pump exit plane has decreased further and only a small high velocity jet remained close to the pump pressure surface. The influence on the turbine velocity distribution is primarily seen in the jet that sweeps through the turbine inlet plane from the suction/shell to the pressure/core corner. At the present speed ratio this jet is only a small, isolated flow area being forced into the turbine inlet. The flow acceleration following the pump suction side is only moderate as the velocity gradient of the pump exit plane in suction to pressure direction is very small over about 75% of the suction to pressure length.

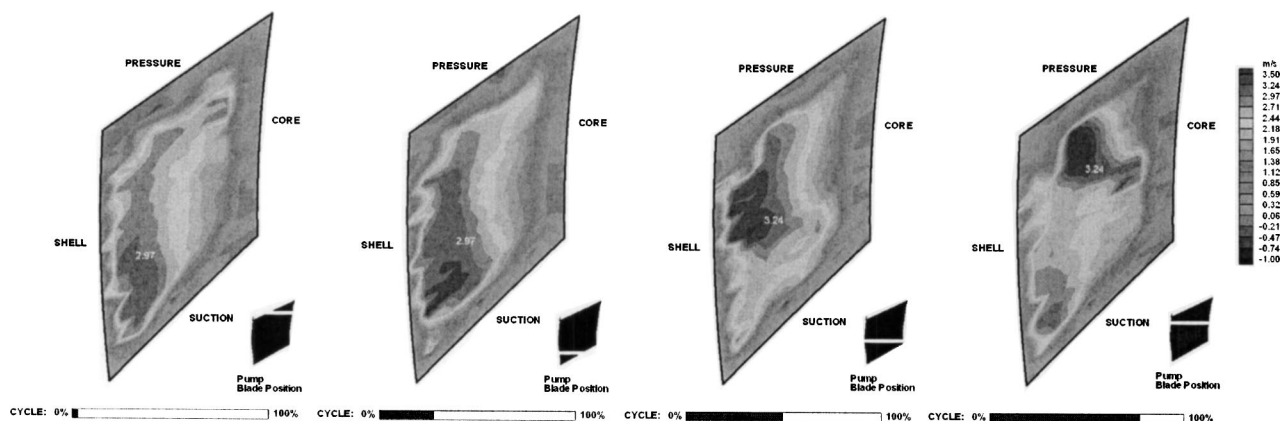


Fig. 12 Turbine inlet plane,  $SR=0.800$



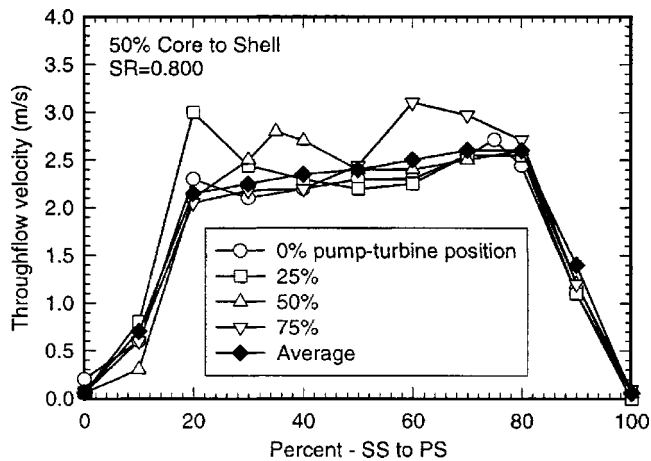


Fig. 13 One typical variation of turbine inlet blade-to-blade profile

For comparison, the time averaged velocity contours are presented in Fig. 16 for the turbine inlet for the four speed ratios. Transverse or secondary flows are included on the plots.

The fact that the pump influence on the periodicity in the tur-

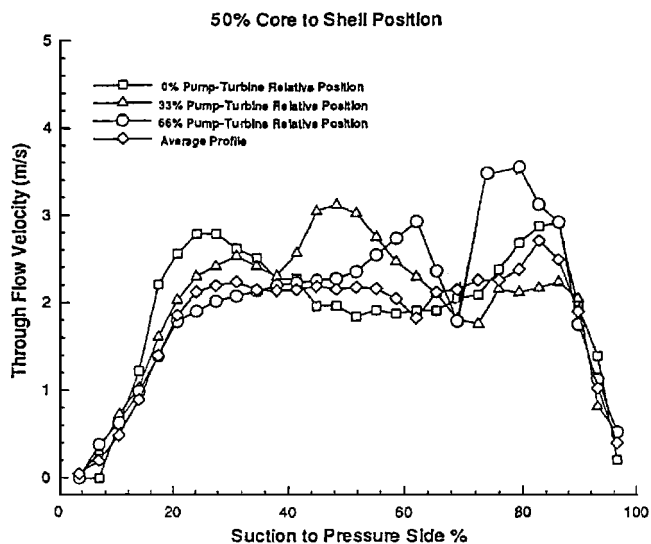


Fig. 14 Variation of turbine inlet blade-to-blade profile From Whitehead [11], SR=0.800

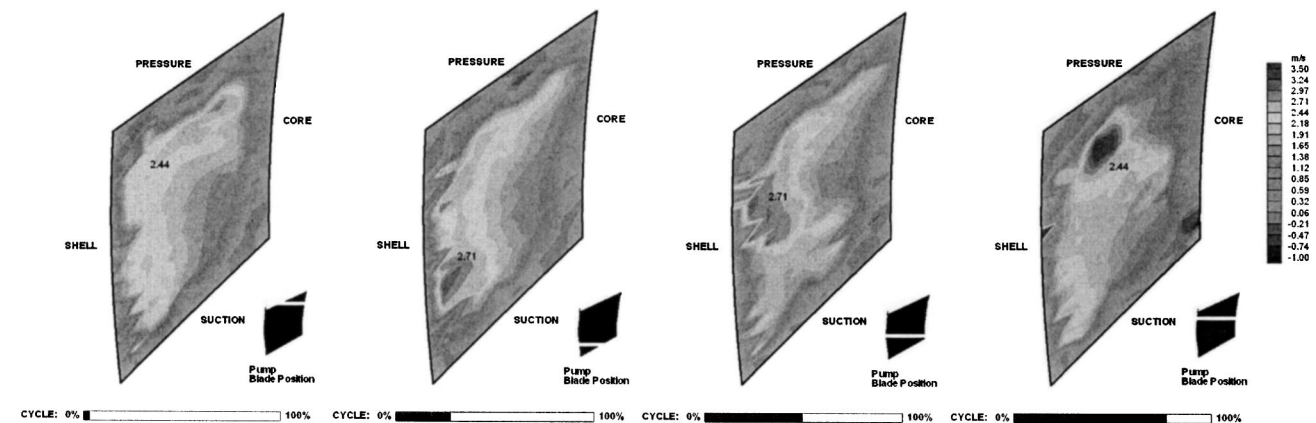


Fig. 15 Turbine inlet plane, SR=0.875

bine increases with speed ratio can be explained as follows. As the speed ratio increases the internal mass flow decreases in both pump and turbine. As a result, in the pump, the momentum flux decreases and pressure at the pump exit increases, resulting in more likelihood of separation. The general behavior is very much like the flow in a conventional centrifugal pump at part flow.

## 7 Summary

The flow field at the pump/turbine interface of a torque converter was studied using laser velocimetry for four turbine/pump speed ratios: 0.065 (near stall), 0.600, 0.800, and 0.875 (coupling point). The data presented herein represent the most complete set of periodic torque converter data available. The current geometry is wide and has the largest outer to inner radius ratio studied to date. The flow fields at the pump exit and turbine inlet planes were visualized and are presented. Instantaneous pump and turbine blade positions with the velocity data were used to generate animations to effectively visualize and understand the periodic behavior. The turbine inlet flow was markedly periodic due to the exiting jet/wake from the upstream pump passage. On the other hand, the pump exit flow field showed little dependence on the turbine blade positions. The greatest periodicity was seen for the highest speed ratios, due to reduced momentum flux in the pump and resulting increased velocity non-uniformity in the pump exit. The results were also compared to unsteady results for a geometrically different and previously examined torque converter to determine the effect of radius ratio on the periodic flow field. In general the unsteady velocity fields show no significant difference for the two geometries; namely, the trends are the same.

## Acknowledgments

General Motors Corporation Powertrain Division primarily sponsored this research. The authors wish to express their gratitude to D. Maddock for his expertise and the technical and hardware support. The research was also supported in part by the Rotating Machinery and Controls Laboratory at the University of Virginia.

## References

- [1] Whitehead, L. D., and Flack, R. D., 1999, "Velocity Measurements in an Automotive Torque Converter, Part I - Average Pump Measurements," *STLE Tribol. Trans.*, **42**, pp. 697-706.
- [2] Claudel, W. D., 1997, "A Comparison of the Internal Flow Fields of Three Automotive Torque Converter Pumps using Laser Velocimetry," M.S. thesis, University of Virginia, Charlottesville, Virginia.
- [3] Browarzik, V., 1994, "Experimental Investigation of Rotor/Rotor Interaction in a Hydrodynamic Torque Converter using Hot Film Anemometry," *39th International Gas Turbine and Aeroengine Congress and Exposition*, The Hague, The Netherlands, June 13-16, ASME Paper No. 94-GT-246.
- [4] Marathe, B. V., and Lakshminarayana, B., 1995, "Experimental Investigation of Steady and Unsteady Flow Field Downstream of an Automotive Torque

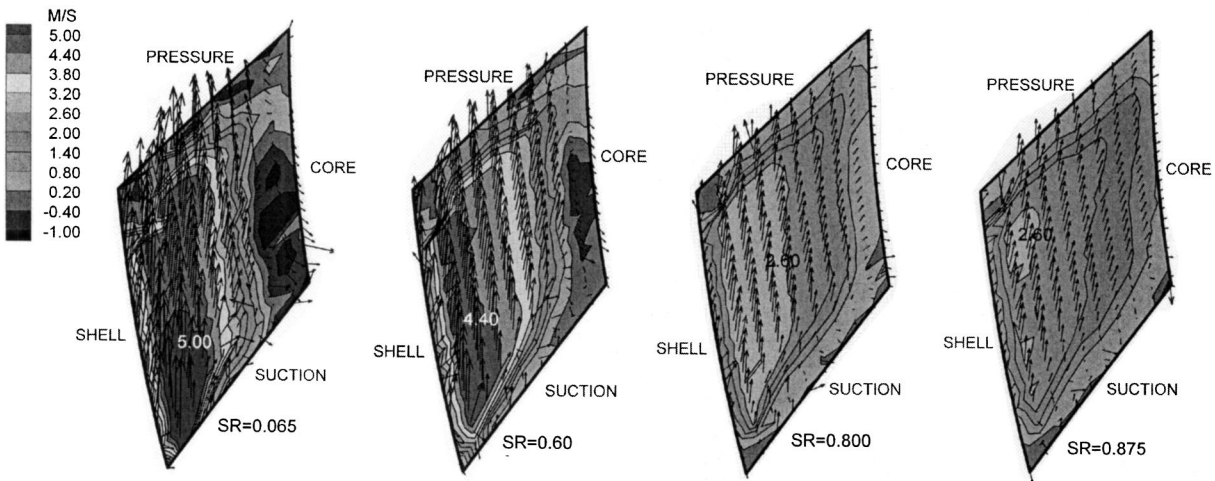


Fig. 16 Time-averaged turbine inlet plane velocities

- Converter Turbine and Stator," *Int. J. Rotating Mach.*, **2**, pp. 67–84.
- [5] Marathe, B. V., and Lakshminarayana, B., 1997, "Experimental Investigation of Steady and Unsteady Flow Field Upstream and Downstream of an Automotive Torque Converter Pump," *1997 ASME Fluid Engineering Division Summer Meeting*, Vancouver, June 22–26, ASME Paper No. FEDSM97-3353.
- [6] Dong, Y., Lakshminarayana, B., and Maddock, D. G., 1997, "Steady and Unsteady Flow Field at Pump and Turbine Exit of a Torque Converter," *1997 ASME Fluid Engineering Division Summer Meeting*, Vancouver, June 22–26, ASME Paper No. FEDSM97-3351.
- [7] Brun, K., and Flack, R. D., 1994, "A Method to Measure Periodic Velocity Fields in Multi-Element Turbomachines with Discrete Sampling," *Meas. Sci. Technol.*, **5**, pp. 418–425.
- [8] Brun, K., Flack, R. D., and Gruver, J. K., 1996, "Laser Velocimeter Measurements in the Pump of a Torque Converter, Part II - Unsteady Measurements," *J. Turbomach.*, **118**, pp. 570–577.
- [9] Brun, K., and Flack, R. D., 1997, "Laser Velocimeter Measurements in the Turbine of an Automotive Torque Converter, Part II - Unsteady Measurements," *J. Turbomach.*, **119**, pp. 655–662.
- [10] Christen, B., Gruber, M., Hotho, M., and Flack, R. D., 1999, "Effect of Pump Exit Angle on the Unsteady Flow at the Pump Turbine Interface of an Automotive Torque Converter," *3rd ASME-JSME Joint Fluids Engineering Conference*, San Francisco, CA, July 18–23, ASME Paper No. FEDSM99-6995.
- [11] Whitehead, L. D., 1995, "A Comparison of the Internal Flow Fields of Two Automotive Torque Converters using Laser Velocimetry," M.S. thesis, University of Virginia, Charlottesville, Virginia.
- [12] Flack, R. D., and Whitehead, L. D., 1997, "Unsteady Velocities at the Pump-Turbine Interface of an Automotive Torque Converter," *Proc. 7th International Conference on Laser Anemometry*, Karlsruhe, Germany, September 8–11, pp. 263–270.

# Slip Factor for Centrifugal Impellers Under Single and Two-Phase Flow Conditions

José A. Caridad

Frank Kenyery

Laboratorio de Conversión de Energía Mecánica,  
Universidad Simón Bolívar, Caracas, Venezuela

*Throughout the history of turbomachines investigators have tried to develop reliable methods for prediction of centrifugal pump behavior. Among the parameters available to estimate the performance of this kind of machine is the slip factor. In spite of being regarded as a variable of great significance in the analysis of turbomachinery, there seem to be a misconception regarding its concept and application. Indeed, empirical correlations have been widely used to estimate the slip factor, even in the case of two-phase flow applications, where it has not been investigated. Moreover, these correlations provide a constant value of the slip factor for a given impeller only at the best efficiency point, which is an important restriction to the pump performance prediction, considering that slip factor varies with the pump flow rate. In this study, three-dimensional computational fluid dynamics simulations were carried out on an impeller of known geometry ( $N_S = 1960$ ) from which values of slip factor were calculated for both single- and two-phase flow (water and water-air). These results include curves of the slip factor as a function of the specific capacity and the gas-void fraction. Additionally, results for the slip factor in the case of single-phase flow (water) are given for various centrifugal impellers ( $N_S = 1157, 1447, 1612, \text{ and } 3513$ ) in order to illustrate the influence of the flow rate on this parameter. Finally, based on the numerical results, a methodology for prediction of the pump head is presented. Excellent agreement with experimental results has been found. This paper attempts to contribute to a better understanding of the fluid dynamics within centrifugal pump impellers and to shed more light on the path that prediction models should follow in the future. [DOI: 10.1115/1.1891153]*

## 1 Introduction

Euler's equation ( $H_{T\infty}$ ) constitutes the basic relationship for the analysis of any kind of turbomachinery. It is obtained by applying the principle of angular momentum to a mass of flow passing through a rotor, assuming perfect flow conduction

$$H_{T\infty} = \frac{U_2 V_{U2}}{g} \quad (1)$$

or, equivalently,

$$H_{T\infty} = \frac{U_2}{g} (U_2 - V_{M2} C t g \beta_2). \quad (2)$$

Even though this equation is based on a hypothesis of a one-dimensional point of view, inviscid flow, and steady state, it is considered as an important parameter for the design and prediction of the pumps performance.

Centrifugal pumps are rotodynamic machines that impart energy to a fluid by means of the change of its kinetics momentum. Moreover, Euler's equation represents the theoretical head that a certain pump is able to produce for a given configuration of the impeller.

Unfortunately, to satisfy the perfect "flow conduction" hypothesis it would be necessary to have an infinite number of blades, which has no practical sense because of the increase of the hydraulic losses. Given that, in industrial pumps, the flow deviates from the path imposed for the blades, leaving the impeller with an angle  $\beta'_2$  less than the constructive angle of the blades  $\beta_2$  (see Fig. 1). Therefore, the theoretical head of the impeller ( $H_{T\infty}$ ) dimin-

ishes to  $H_T$  (theoretical head for a finite number of blades). This phenomenon gives rise to the concept known as slip factor, which is defined as follows:

$$\varepsilon_z = \frac{H_T}{H_{T\infty}} \quad (3)$$

where

$$H_T = \frac{U_2}{g} (U_2 - V_{M2} C t g \beta'_2) \quad (4)$$

Much has been written concerning the slip factor, nevertheless, it seems to remain misunderstood with regards to its concept and application, particularly in the case of centrifugal pumps handling two-phase mixtures. As a matter of fact, most of the models published thus far, attempting to predict the phenomenon, do not take into account this parameter. On the other hand, those that have included it into the analysis consider the slip factor the same for single- and two-phase flow and, besides, an independent variable of the pump flow rate. These misconceptions can lead to significant errors in the prediction of the performance of centrifugal pumps and, as a consequence, the analytical models developed to date have not accomplished satisfactory results.

## 2 Previous Work

**2.1 Slip Factor.** First attempts to estimate slip factors were entirely theoretical. Perhaps the most accepted of these works was developed by Busemann [1], who obtained values of the slip factor by means of potential flow analysis. However, the flow within a centrifugal pump impeller near the walls is far from potential, and this analysis could result in bad approximations.

On the other hand, Pfeleiderer [2] developed a method to calculate the slip assuming a uniform distribution of the pressure around the blade. This method was strongly influenced by the type

Contributed by the Fluids Engineering Division for publication in the Journal of Fluids Engineering. Manuscript received by the Fluids Engineering Division February 18, 2004. Revised manuscript received October 12, 2004. Review conducted by Y. Tsujimoto.

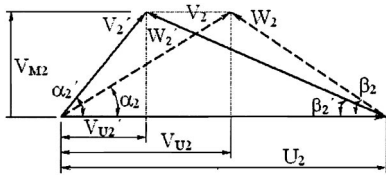


Fig. 1 Impeller discharge velocity diagrams

of diffuser. Another well-known expression for calculating the slip factor is provided by Stodola [3], who assumed a rotating cylinder of fluid at the end of the interblade channel as the cause of the slippage. Later, Stanitz [4] proposed a slip factor correlation derived from the results of two-dimensional fluid flow solutions. Even though there are some results for backward-curved vanes, most of the work is related to radial blades.

As early as 1967, Wiesner [5] carried out a comprehensive review of the literature available up until that time regarding the slip factor. In this classical paper, Wiesner concluded that the method of Busemann was still the most accurate. Furthermore, the author proposed a correlation fitting the Busemann data extremely well up to a limiting inlet-to-outlet impeller radius ratio. All the same, an empirical correction factor for conditions beyond this limiting radius factor was presented. Several other investigators have studied the slip factor on turbomachines; however, we consider those mentioned above as the most representative.

In spite of its highly empirical origin, Wiesner's correlation has maintained great acceptance among researchers aiming to predict the performance of centrifugal pumps. Nevertheless, there are some details not clearly stated in these papers and commonly disregarded by most of the investigators. These details could be summarized as follows:

- The slip factor does not represent a hydraulic loss. It just stands for a reduction in the capability of the pump to transfer energy.
- The slip factor is by no means a constant for a given impeller. In fact, it rises as the flow is reduced.
- The slip factor for two-phase conditions has not been investigated thus far.

**2.2 Performance Prediction of Centrifugal Pumps Under Two-Phase Flow Conditions.** Performance prediction of centrifugal pumps handling two-phase mixtures has been an active area of research in both the nuclear and petroleum industries. The nuclear industry is concerned with the loss of coolant accidents (LOCA) in nuclear reactors due to safety purposes. In such accidents, the reactor centrifugal pumps need to handle two-phase mixtures because of a rapid depressurization of the coolant. As for the petroleum industry, fair amounts of gas are entrained in the oil handled by electric submersible pump applications.

In both cases, the pump undergoes a decrease in the head de-

livered, which must be estimated. Thus, developing analytical methods to determine the performance of pumps operating under two-phase flow conditions is a matter of prime interest.

Several investigators [6–11] have undertaken this task with limited success. Although there are some prediction models including the slip factor in the analysis [6,7,10], this parameter is assumed to be not just constant but equal for one- and two-phase flow cases. Given that, the results obtained from these studies are neither satisfactory nor reliable. Needless to say, the models that have overlooked the slip factor lack physical meaning and are fortunate, indeed, to produce any useful result.

### 3 Slip Factor Under Two-Phase Flow Conditions

**3.1 Problem Formulation.** In order to predict the behavior of the slip factor, three-dimensional (3D) computational fluid-dynamics (CFD) two-phase flow (water/air) simulations were conducted in a centrifugal impeller with a specific speed  $N_S=1960$ . Liquid flow rate, gas-void fraction (GVF), and bubble diameter were chosen as independent variables. The geometry of the impeller is the same as that tested by Añez [12].

Based on a two-fluid model, the momentum equations (Navier-Stokes) coupled with the continuity equation were solved using a commercial CFD package, which employs the finite-volume technique.

Given the symmetry of the problem, the computational domain of flow consisted of a single blade-to-blade passage. Total pressure (static plus dynamic) at the inlet and mass flow at the outlet were chosen as boundary conditions, according to recommendations for centrifugal impellers [13]. With regard to turbulence modeling, the multiphase version of the standard  $\kappa-\epsilon$  model was implemented. Additional details in relation to assumptions, mesh analysis, and mathematical models can be found in Refs. [13,14].

**3.2 Procedure.** From the simulations, the actual relative fluid angle  $\beta'_2$  (based on mass average) was obtained. Thus, the theoretical head for a finite number of blades and the slip factor were calculated by means of Eqs. (3) and (4), respectively, for the whole range of liquid flow and gas-void fraction. In order to illustrate the influence of the liquid flow rate on the slip factor, the previous procedure was repeated for another four centrifugal pump impellers ( $N_S=1157, 1447, 1612, \text{ and } 3513$ ) in the case of single-phase flow. Details of the above-mentioned impellers are summarized in Table 1.

### 3.3 Numerical Results.

**3.3.1 Change of Slip Factor Under Two-Phase Flow Conditions.** Results for the slip factor as a function of the specific capacity ( $\Phi$ ) for different values of the gas-void fraction can be seen in Fig. 2. The dashed curve corresponds to single-phase flow, whereas the solid curves correspond to GVF values of 10%, 15%, and 17%. The bubble diameter was set to 0.1 mm, as will be substantiated in Sec. 4.

All the curves depict the same tendency, namely, the slip factor

Table 1 Characteristics of the simulated impellers

$N_S$	$N$ (RPM)	$N_B$	$A_2(\text{cm}^2)^a$	$D_2/D_1$	$\beta_2(^{\circ})$	$\Phi_{BEP} \times 10^{+03}$
1157	1450	4	217	2.69	24	7.65
1447	1450	5	341	2.54	28	12.92
1612	1270	7	322	3.07	26.6	14.15
1960	3000	7	25	2.22	30	16.08
3513	1480	5	620	2.10	32.5	43.32

<sup>a</sup> $A_2=(\pi \cdot D_2 - N_B \cdot Th) \cdot b_2$

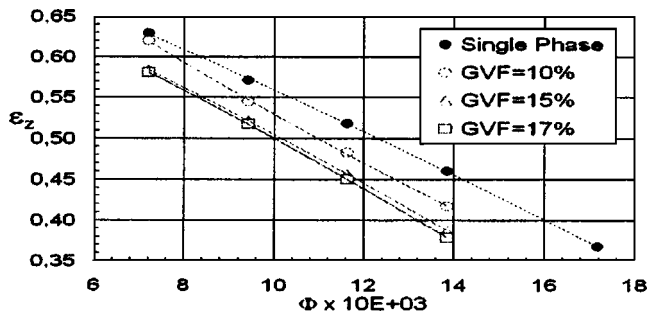


Fig. 2 Slip factor for different GVF as a function of the specific capacity ( $N_S=1960$ )

decreases almost linearly with specific capacity. On the other hand, it is shown that the slip factor is also influenced by the GVF. In fact, this parameter diminishes as the GVF increases.

An alternative option to represent the slip-factor significance is by means of Euler's theoretical heads ( $H_{T\infty}$  and  $H_T$ ). Figure 3 shows the tendencies of  $H_T$  for the same conditions as in Fig. 2, where the curve of  $H_{T\infty}$  (dashed line) is included for reference purposes.

As it was pointed out before, the theoretical head for a finite number of blades does not represent a hydraulic loss but rather a diminution in the capacity of the pump for transferring energy. From Fig. 2 it can be seen that the higher the GVF, the lower the capacity of the pump to develop head (for a constant specific capacity). Therefore, the presence of gas entrained in the fluid handled by the pump affects the fluid dynamic within the impeller in such a way that the kinetic momentum change of the fluid is impaired.

Thus, implementation of slip-factor results from single-phase data to analyze the behavior of centrifugal pumps handling two-phase flow is incorrect. Further investigations are in order.

**3.3.2 Effect of Flow Rate on the Slip Factor.** Curves of the slip factor as a function of the specific capacity for different values of  $N_S$  are presented in Fig. 4. The slip factor rises almost linearly as  $\Phi$  is reduced. This tendency is repeated in the four impellers analyzed. In this way, the fluid deviates less and less from the blades as the flow rate diminishes. On the other hand, even in the case of the nominal flow rate, values for the slip factor produced by correlations could have errors as large as 52% as is illustrated in Table 2.

**3.3.3 Fundamental Variables.** Computational fluid dynamics can be used successfully in the analysis of the complex flow inside pumps. Indeed, the results obtained from the simulations enable the calculation of fundamental variables, such as slip factor, hydraulic losses, and efficiency, among others.

Caridad [14] and Bastardo [15] implemented CFD tools to char-

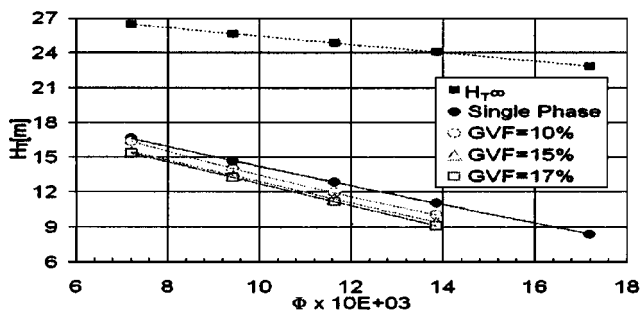


Fig. 3 Theoretical head for different GVF as a function of the specific capacity ( $N_S=1960$ )

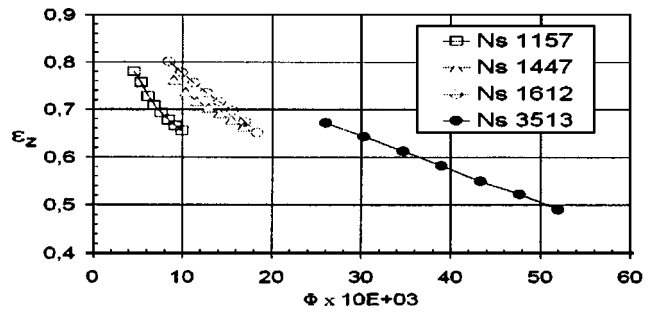


Fig. 4 Slip factor for different specific speeds as a function of the specific capacity

acterize the impeller and the diffuser of a particular electric submersible pump ( $N_S=1960$ ), respectively. Bastardo also took advantage of the symmetry of the problem and simulated a single blade-to-blade passage.

Following the methodology described in the Secs. 3.1 and 3.2, the slip factor was obtained as a function of the specific capacity for different gas-void fractions (Fig. 2). Additionally, the impeller hydraulic losses were calculated as follows:

$$Z_R = H_T - H_R \quad (5)$$

where

$$H_R = (1-x) \left( \frac{P_2 - P_1}{\gamma} + \frac{V_2^2 - V_1^2}{2g} \right)_L + x \left( \frac{P_2 - P_1}{\gamma} + \frac{V_2^2 - V_1^2}{2g} \right)_G \quad (6)$$

Figure 5 shows the rotor hydraulic losses as a function of  $\Phi$ . The results are presented for different gas-void fractions (including single-phase flow). The general tendency is that the hydraulic losses vary approximately as the square of the specific capacity. This behavior could be explained by the increase of the slippage—the difference between the velocities of the liquid and the gas—as the GVF increases.

On the other hand, Bastardo obtained the hydraulic losses in the diffuser. It is important to mention that the outlet conditions of the rotor were used as the inlet conditions of the diffuser.

The hydraulic losses of the diffuser ( $Z_D$ ) as a function of the specific capacity are presented in Fig. 6, in the case of single-phase flow and two different GVF, namely, 10% and 15%. Contrary to the expected, the hydraulic losses for single-phase flow

Table 2 Values of the slip factor obtained from correlations for the impellers studied (Reference: simulations)

$N_S$	Weisner [5]	Stodola [3]	Stanitz [4]	Ref.
1156	0.758	0.681	0.505	0.693
Error(%)	9	2	27	-
1447	0.778	0.705	0.604	0.703
Error(%)	10	0	14	-
1612	0.829	0.799	0.717	0.716
Error(%)	14	10	0	-
1960	0.819	0.776	0.717	0.395
Error(%)	52	49	45	-
3513	0.762	0.662	0.604	0.550
Error(%)	28	17	9	-

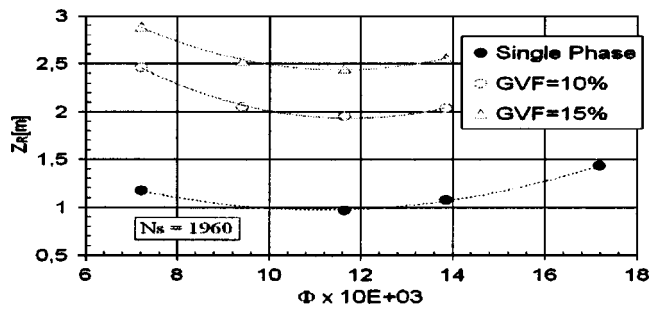


Fig. 5 Hydraulic losses of the impeller for different GVF as a function of the specific capacity

are larger than in the case of GVF=10% and 15%, for the whole range of liquid flow rates studied. As Bastardo pointed out, this result arises from the fact that each gas-void fraction has associated a different flow incidence angle upon the diffuser, for a given specific capacity.

In fact, the flow incidence angle corresponding to higher gas-void fractions results in a diminution of the size of the flow recirculation obtained in the suction side of the diffuser, which is the main cause of hydraulic losses in the diffuser. For more details, see Ref. [15].

#### 4 Performance Prediction by Means of the Slip Factor

Based on the results described previously, it is possible to predict the pump head  $H_P$  for the whole stage (rotor plus diffuser). It is worth mentioning that this methodology is valid for single- and two-phase flow.

The procedure is as follows:

- The  $H_T$  is calculated from Eqs. (2) and (3), and Fig. 2.
- The impeller head  $H_R$  is determined from Eq. (6) and Fig. 5.
- The pump head  $H_P$  is estimated by means of Eq. (7) and Fig. 6,

$$H_P = H_R - Z_D. \quad (7)$$

Thus,  $H_P$  is predicted based on geometrical variables and CFD simulations. Figures 7–9 show the results as a function of the specific capacity for gas-void fractions corresponding to 0 (single-phase), 10% and 15%. For comparison purposes, these figures also include the experimental data taken from Añez [12], who tested the same pump as used in this study.

Figure 7 shows that the predicted head via numerical simulation (corresponding to single-phase flow) compares favorably to the experimental data. As for GVF=10% the agreement is excellent. This justifies the assumption of 0.1 mm as the bubble diameter of the gassy phase.

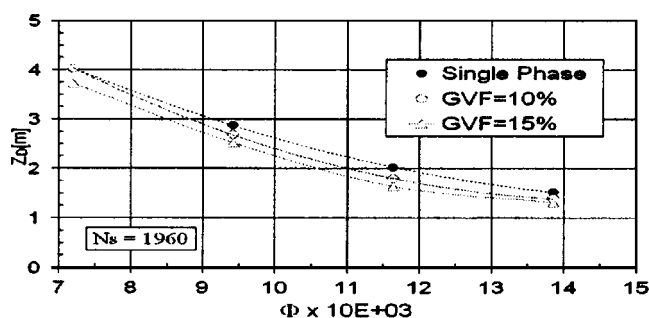


Fig. 6 Hydraulic losses of the diffuser for different GVF as a function of the specific capacity

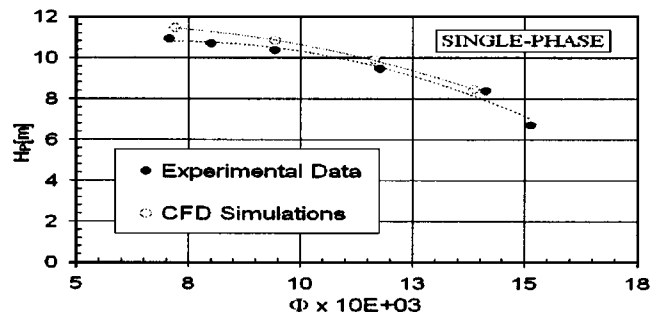


Fig. 7 Comparison between numerical simulations and experimental results for different gas-void fractions ( $N_S=1960$ )

Regarding Fig 9 (GVF=15%), the comparison is also good. However, for larger specific capacities, the simulations tend to overpredict the pump head. This tendency is expected as larger gas-void fractions should correspond to larger bubble diameters and, hence, larger hydraulic losses. Thus, for GVF=15% the proper bubble diameter should be greater than 0.1 mm.

#### 5 Analysis

Accurate modeling of the turbomachinery performance is challenging. Complicated geometry, secondary flows, and multiphase flow, among other variables, have forced the inclusion of experimental parameters to validate the models. Furthermore, the lack of understanding of the fluid dynamics inside a centrifugal pump impeller is the main obstacle for developing accurate prediction tools.

Slip factor is not an exception to these shortcomings. Even though a constant value of the slip factor can hold certain validity for radial blade impellers (where, theoretically, the head is not a function of the flow rate), investigators have been using empirical correlations excessively for a large range of diameters and blade angles.

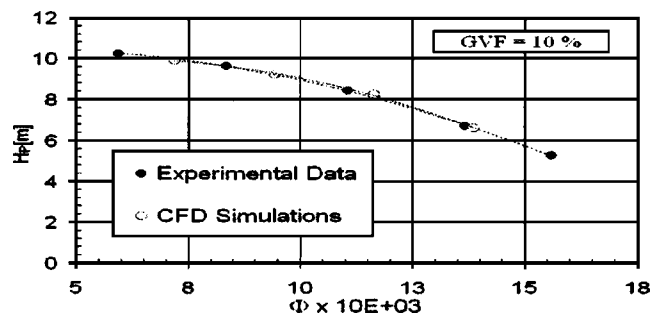


Fig. 8 Comparison between numerical simulations and experimental results for different gas-void fractions ( $N_S=1960$ )

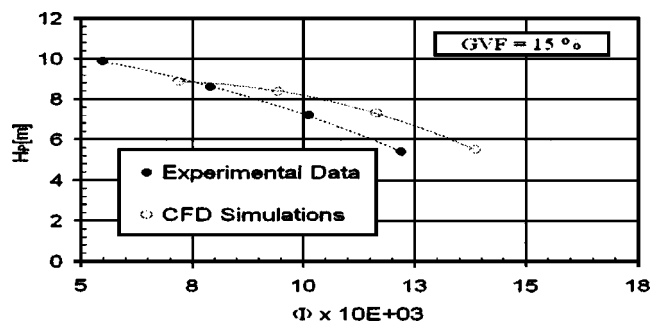


Fig. 9 Comparison between numerical simulations and experimental results for different gas-void fractions ( $N_S=1960$ )

From the results stated above, it is clear that considering the slip factor constant for the whole operation range of the pump is a remarkable mistake. Moreover, the fluid dynamics of single-phase flow is quite different from that corresponding to two-phase flow. Therefore, new approaches to estimate slip factor for centrifugal pumps need to be developed.

This work does not attempt to develop a new correlation for the slip factor but aims to clear up some misunderstanding with respect to its application. Likewise, the presented methodology could be used as a trend to follow for subsequent models.

Even though the pump head prediction was possible for the presented case, there remains several uncertainties, particularly concerning the bubble diameter. Thus, further investigations are necessary in order to establish the variation of this variable along centrifugal pumps as a function of gas-void fraction, rotational speed, suction pressure, and specific speed. Needless to say, there is much to be done to achieve a complete characterization of turbomachines.

To the authors' knowledge, there have been no serious attempts to estimate the slip factor for many years. Computational fluid dynamics (CFD) emerges as the most appropriate tool to undertake this task. Indeed, CFD permits the understanding of the flow physics, which, in turn, is the first step for accurate and reliable models. Besides, analytical model trends in the future should rely on flow physics rather than on empirical correlations, thus, expressions such as Weisner's have to be avoided in order to obtain satisfactory results in the prediction of centrifugal pump performance.

## 6 Conclusions and Recommendations

The slip factor for a centrifugal pump impeller handling two-phase flow was estimated by means of 3D-CFD numerical simulations. Additional simulations were carried out for another four impellers (single-phase flow).

On the other hand, a methodology is proposed in order to achieve the prediction of centrifugal pumps. The results obtained are summarized below:

- Slip factor is strongly influenced by the liquid flow rate and the gas-void fraction. Thus, for a constant GVF, slip factor increases as the flow rate diminishes. For a constant liquid flow rate, the slip factor drops as the GVF increases.
- Analytical models developed thus far have applied the slip-factor concept erroneously.
- On the other hand, there are some other models that have overlooked the slip. As for these, thorough revisions need to be done.
- New approaches need to be developed in order to investigate the behavior of the slip factor for two-phase flow conditions.
- Computational fluid dynamics can be used not just to estimate the slip factor but as a tool for designing and prediction of turbomachinery performance.
- The prediction methodology proposed has proved to produce useful results and can be the starting point of new characterization models to be developed.
- Further research is necessary in order to investigate the behavior of the bubble diameter in centrifugal pumps.
- Empirical correlations need to be disregarded in the future. Instead, the understanding of the physical mechanism of the phenomenon (via CFD) will lead to more reliable and accurate models.

## Nomenclature

$A$	= area
$b$	= impeller width
ESP	= electric submersible pump
$D$	= impeller diameter
$g$	= acceleration of gravity
GVF	= gas void fraction

$H$	= head
$N$	= rotational speed (rpm)
$Nb$	= number of blades of the impeller
$N_S$	= specific speed of the impeller
$P$	= pressure
$Q$	= flow rate
$Th$	= blade thickness
$U$	= tangential velocity
$V$	= flow velocity
$W$	= relative velocity
$x$	= mixture quality
$Z$	= hydraulic losses
$\alpha$	= absolute flow angle
$\beta$	= relative flow angle
$\varepsilon_Z$	= slip factor
$\kappa$	= turbulence kinetics energy.
$\varepsilon$	= energy dissipation rate
$\gamma$	= Specific Weight.
$\Phi$	= specific capacity $(Q/\omega D_2^3)$ (adimensional parameter)
$\omega$	= angular velocity

## Subscript

BEP	= best efficiency point
$D$	= diffuser
$G$	= gas
$L$	= liquid
$M$	= meridional component
$P$	= pump
$R$	= relative to the impeller
$T$	= theoretical for a finite number of blades
$T^\infty$	= theoretical for an infinite number of blades
$U$	= tangential component
1	= impeller inlet condition
2	= impeller outlet condition

(Prime values denote variables with slip considered.)

## References

- [1] Bussemann, A., 1928, "Das Förderhöhenverhältniss radialer Kreiselpumpen mit logarithmischspiralen Schaufeln," *Z. Angew. Math. Mech.* **8**, pp. 372–384.
- [2] Pfeleiderer, C., 1924, *Die Kreiselpumpen für Flüssigkeiten und Gase*, 1st Edition, Springer, Berlin, pp. 937.
- [3] Stodola, A., 1927, *Steam and Gas Turbines*, McGraw-Hill, NY.
- [4] Stanitz, J. D., 1952, "Some Theoretical Aerodynamic Investigations of Impellers in Radial and Mixed Flow Centrifugal Compressors," *Transactions of ASME* **74**, pp. 473–497.
- [5] Wiesner, F. J., 1967, "A Review of Slip Factors for Centrifugal Impellers," *ASME Journal of Engineering for Power*, **89**, pp. 558–572.
- [6] Minemura, K., Murakami, M., and Katagiri, H., 1985, "Characteristics of Centrifugal Pumps Handling Air-Water Mixtures and Size of Air Bubbles in Pump Impellers," *Bull. JSME* **28** (244), pp. 2310–2318.
- [7] Minemura, K., Uchiyama, T., Shoda, S., and Egashira, K., 1998, "Prediction of Air-Water Two-Phase Flow Performance of a Centrifugal Pump Based on One-Dimensional Two-Fluid Model," *J. Fluids Eng.* **120**, pp. 327–334.
- [8] Noghrehkar, G. R., Kawagi, M., Chan, A., Nakamura, H., and Kukita, Y., 1995, "Investigation of Centrifugal Pump Performance Under Two-Phase Flow Conditions," *J. Fluids Eng.* **117**, pp. 129–137.
- [9] Furuya, O., 1985, "An Analytical Model for Prediction of Two-Phase (Non-condensable) Flow Pump Performance," *J. Fluids Eng.* **107**, pp. 139–147.
- [10] Sachdeva, R., Doty, D. R., and Schmidt, Z., 1994, "Performance of Electric Submersible Pumps in Gassy Wells," *SPE Paper No. 22767*.
- [11] Zakem, S., 1980, "Analysis of Gas Accumulation and Slip Velocity in a Rotating Impeller," *Proc. of ASME Cavitation and Polyphase Forum, ASME, NY*, pp. 32–34.
- [12] Añez, D., Kenyery, F., Escalante, S., and Teran, V., 2001, "ESP's Performance with Two-Phase and Viscous Flow," *Proc. of ETCE 2001, Petroleum Production Technology Symposium, ASME, Houston, Feb. 4–7*, pp. 1–9.
- [13] AEA Technology, 1997, "CFX 4.3 Solver" (*User manual for the Computational Fluid Dynamics Software CFX-4.3*) CFX Int., Oxfordshire, UK.
- [14] Caridad, J. and Kenyery, F., 2002, "CFD Analysis of Electric Submersible Pumps (ESP) Handling Two-Phase Mixtures," *ASME Journal of Energy Resources Technology* **126**, pp. 99–104.
- [15] Bastardo, R., 2003, "Simulación Numérica del Flujo Bifásico Líquido-Gas en el Difusor de una Bomba Centrífuga Multietapa," M.S. thesis (in Spanish), Universidad Simón Bolívar, Venezuela.

# Experimental Analysis on Tip Leakage and Wake Flow in an Axial Flow Fan According to Flow Rates

C.-M. Jang<sup>1</sup>

Senior Researcher, Fire & Engineering Services  
Research Department, Korea Institute of  
Construction Technology, 2311, Dachwa-dong,  
Goyang-Si, 411-712, Korea  
e-mail: jangcm@kict.re.kr

D. Sato

T. Fukano

Department of Mechanical Science and  
Engineering, Kyushu University, 6-10-1,  
Hakozaki, Higashi-Ku, Fukuoka, 812-8581, Japan

*The flow characteristics in the blade passage and in the wake region of a low-speed axial flow fan have been investigated by experimental analysis using a rotating hot-wire sensor and a five-hole probe for design and off-design operating conditions. The results show that the tip leakage vortex is moved upstream when the flow rate is decreased, thus disturbing the formation of wake flow near the rotor tip. That is, the tip leakage vortex interfaces with the blade suction surface and results in high velocity fluctuation near the blade suction surface. From axial velocity distributions downstream of the fan rotor, large axial velocity decay near the rotor tip is observed at near-stall condition, which results in a large blockage compared to that at the design condition. Finally, the wake flow downstream of the rotor blade is clearly measured at the design and off-design conditions. However, the trough of the high velocity fluctuation due to Karmann vortex street in the wake flow is observed at a higher flow condition than the design flow rate. [DOI: 10.1115/1.1881695]*

## 1 Introduction

The present study is focused on the understanding of a detailed vortical flow and a wake flow inside blade passage and downstream of a low-speed axial flow fan operating at design and off-design conditions. The vortical flow in axial turbomachines has been studied by many researchers by experiments and numerical simulations [1–5]. Murthy and Lakshminarayana [2] studied the trajectory of a tip leakage vortex in an axial compressor rotor according to flow rates using LDV measurements. Inoue and Kuroumaru [4] showed the distinctive feature of the rolling-up of a tip leakage vortex of an axial compressor rotor tip: a leakage jet flow entering from the pressure side to the suction side of the blade interfaces with the incoming through flow. Foley and Ivey [5] reported the behavior of a tip leakage flow in a multistage compressor rotor downstream of the rotor and the stator using a pitot tube and LDV measurements. Throughout most of the experimental studies on axial turbomachines, it is found that the tip leakage vortex has an important role on performance and noise generation.

Fukano et al. [6] tried to measure a periodic velocity fluctuation downstream of the trailing edge of a rotating flat-plate blade using a hot-wire sensor. They showed the periodic velocity fluctuation due to Karman vortex street downstream of the rotating flat-plate blade. Fukano et al. [7] also reported the generation mechanism of the tip clearance noise in an axial flow fan by measuring the real-time velocity fluctuation with rotating hot-wire probe sensors. They showed that the increase in noise at a lower flow rate than the design condition is caused by an interference between a tip leakage vortex and an adjacent blade surface. Recently, the authors also studied the characteristics of vortical flow structure and velocity fluctuation in an axial flow fan having two different tip clearances with the help of numerical simulation and experimental analysis [8]. They showed that an enlarged vortical flow producing at a larger tip clearance induces the acceleration of through flow, thus resulting in the increase of broadband (turbulent) noise.

In the present study, detailed measurements of vortical flow

inside blade passage and wake flow in an axial flow fan designed recently have been performed by using a hot-wire sensor rotating with the fan rotor at design and off-design operating conditions. Three-dimensional velocities upstream and downstream of the fan rotor obtained by a five-hole probe were analyzed by comparing the values of the designed fan. In addition, a velocity fluctuation due to Karmann vortex street downstream of the fan rotor was measured in relation to the formation of the tip leakage vortex according to the flow rates (at a design and off-design operating conditions).

## 2 Axial Flow Fan and Experimental Methods

**2.1 Axial Flow Fan.** A low-pressure axial flow fan having 2 mm tip clearance (1.5% tip chord) was introduced to analyze the tip leakage vortex and the wake flow for a design and off-design flow rates. In the design of the fan rotor, velocity distributions upstream and downstream of the fan rotor were calculated by a streamline curvature equation. Figure 1 shows the calculated streamlines on a meridional plane. The streamlines are shown at 11 radial positions, which have a constant flow rate at each interval of the streamlines. NACA 65 series profile sections designed by a free vortex operation were adopted for the present fan design. A blade camber and an angle of attack as shown in Fig. 2 were obtained by using a Carpet plot. The detailed design specifications of the rotor blade at three radial positions are summarized in Table 1. To avoid a loss production due to flow separation on the rotor blades, an equivalent diffusion ratio defined by Lieblein  $D_{eq}$  was evaluated. The definition of  $D_{eq}$  used in the present calculation is

$$D_{eq} = \frac{\cos \beta_2}{\cos \beta_1} \left[ 1.12 + 0.61 \frac{\cos^2 \beta_1}{\sigma} (\tan \beta_1 - \tan \beta_2) \right] \quad (1)$$

where  $\beta_1$ ,  $\beta_2$ , and  $\sigma$  denote inlet flow angle, outlet flow angle, and solidity, respectively.

As shown in Table 1, the  $D_{eq}$  has value below 2.0, which is critical to produce a large loss rapidly on the rotor blades. The fan has a design flow coefficient  $\Phi$  (mean axial velocity divided by rotor tip speed) of 0.41 and a design pressure rise coefficient  $\Psi_t$  (total pressure rise divided by dynamic pressure at rotor tip) of 0.3 with the rotational speed of the fan rotor of 1000 rpm and the

<sup>1</sup>Corresponding Author.

Contributed by the Fluids Engineering Division for publication in the JOURNAL OF FLUIDS ENGINEERING. Manuscript received by the Fluids Engineering Division April 9, 2004; revised manuscript received, October 16, 2004. Review conducted by J. Lee.



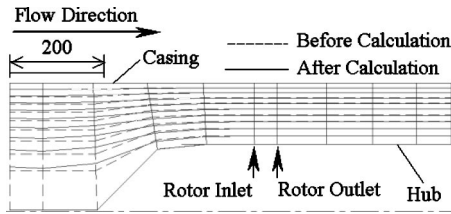


Fig. 1 Meridional streamlines for the design of an axial flow fan (mm)

number of blade of 9. Figure 3 shows the sectional view of the rotor blades for 11 radial positions. The origin of a coordinate represents the position of a blade stacking. The three-dimensional (3D) solid modeling of the designed rotor was performed using the three-dimensional blade surface data. The prototype of the rotor blades was made by rapid prototyping techniques with stereolithography (SLA).

Figure 4 shows the total pressure rise  $\Psi_t$  and the sound pressure level (SPL) plotted against the flow rate of the test fan. The total pressure rise was determined using the three-dimensional velocities and static pressure upstream and downstream of the fan rotor obtained by the five-hole probe. In the figure, a closed triangle indicates the design value. It is noted that the design value corresponds well to that obtained by the experimental measurement. The SPL was measured at 1 m upstream from the test fan. The SPL is rapidly increased at lower flow conditions than the peak total pressure as shown in Fig. 4. It is noted that the SPL has a minimum value at the design flow rate. The authors reported that the rapid increase of the SPL is caused by the interference between a tip leakage vortex and an adjacent blade pressure surface [7]. Reynolds number based on the rotor tip speed and the rotor tip chord length is  $1.1 \times 10^5$ .

In the present study, the characteristics of a three-dimensional vortical flow inside blade passage and downstream of the rotor blades have been analyzed by experimental measurements using a hot-wire sensor rotating with the rotor blades at three off-design

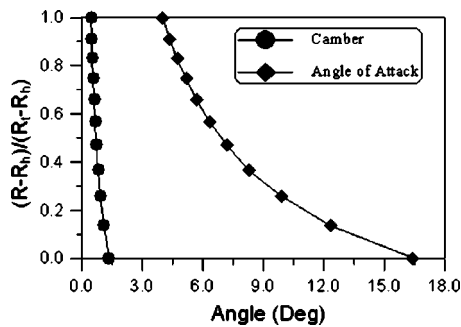


Fig. 2 Distribution of design parameters obtained from the Carpet plot

Table 1 Design specifications of axial fan rotor

	Hub	Near midspan	Tip
Radius (mm)	150.0	230.0	287.5
Chord length (mm)	138.0	132.0	131.0
Camber	1.36	0.69	0.5
Solidity	1.32	0.83	0.65
Max. thick/chord (%)	10.0	8.8	8.0
Stagger angle (deg)	35.3	56.5	63.9
Inlet Flow angle (deg)	51.74	62.83	67.91
Outlet Flow angle (deg)	26.13	55.03	64.03
Equivalent diffusion ratio	1.82	1.5	1.36

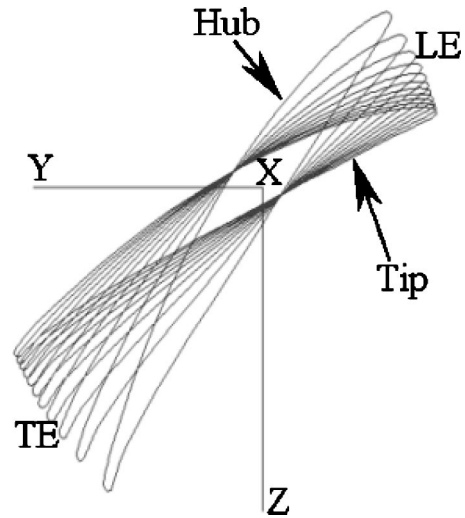


Fig. 3 Blade profile of the designed axial flow fan

operating conditions ( $\Phi=0.28, 0.31, \text{ and } 0.47$ ) as well as at the design condition ( $\Phi=0.41$ ) as shown in the performance curve of Fig. 4.

## 2.2 Experimental Apparatus and Measuring Procedure.

The schematic view of an experimental setup is shown in Fig. 5. It was an open-loop facility having inner duct diameter of 0.579 m. A bell-mouth inlet, a fan rotor, and a fan-driving motor connected by a belt were installed in a circular duct. The downstream end of the section shown in Fig. 5 was connected to an outlet duct followed by a damper and a booster fan. The distance between the

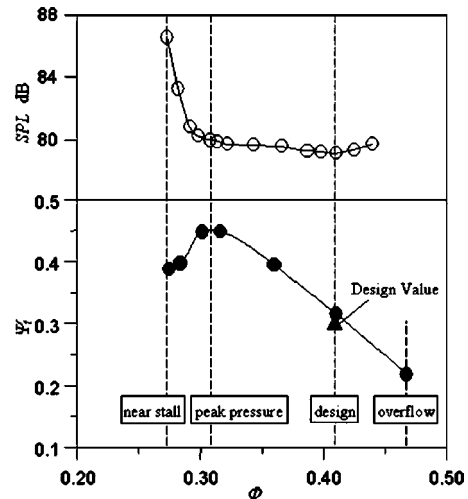


Fig. 4 Sound pressure level and total pressure rise

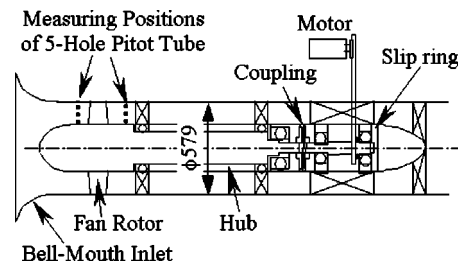


Fig. 5 Schematic view of experimental setup (mm)

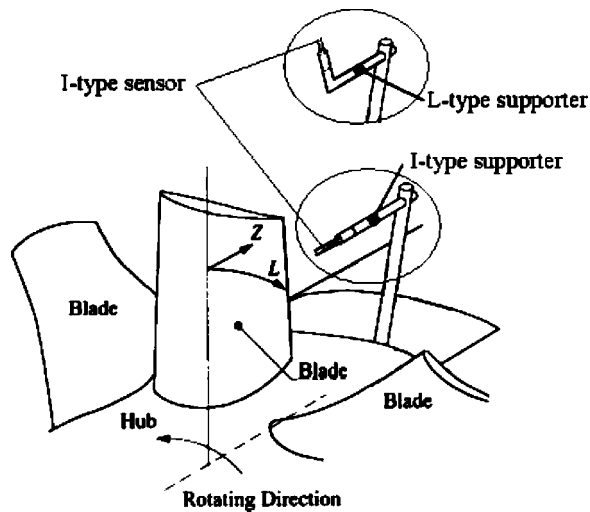


Fig. 6 Test blade measuring system

bell-mouth inlet and the test fan was 0.43 m.

The schematic view of a measuring system is shown in Fig. 6. A hot-wire sensor rotating with the fan rotor was introduced for the present study to obtain relative velocity and velocity fluctuation inside and downstream of the fan rotor. Two kinds of supporter, I-type and L-type, as shown in Fig. 6, were introduced. The I-type and L-type supporters are used to measure the flow velocity near the blade pressure and suction surfaces, which will be described in more detail later. The I-type sensor of the hot-wire probe was a tungsten filament wire of  $5\ \mu\text{m}$  dia. The wire of the probe sensor was set parallel to the radial direction of the rotor blades. The probe was controlled by a three-dimensional traversing system (i.e., radial, axial, and rotational direction) installed inside of the hub with traverse resolution of 0.3 mm. The maximum traversing span of the traversing system in radial, axial, and tangential directions was 45 mm, 60 mm, and 50 deg (45 deg for one blade passage), respectively. The real-valued velocity fluctuations were measured by using a constant-temperature hot-wire anemometer and interfacing technique with an on-line computer. The output from the hot-wire sensor was carried from a rotating frame to a stationary frame through a Michigan Scientific Corporation mercury slip-ring unit installed inside of the hub as shown in Fig. 5.

The relative velocity and the velocity fluctuation inside and downstream of the rotor blades were measured by moving probe and determined by a constant-temperature hot-wire anemometer and an averaging technique with an on-line computer. The calibration of the hot-wire probe was performed by detaching the rotor blade from the test fan and by measuring the tangential velocity for the four different rotational frequencies: 300, 600, 900, and 1200 rpm. The mean standard errors of the tangential velocity keep below 1% for the velocities greater than 1 m/s. In addition, the magnitude of the deformation of the probe supporter caused by the rotor rotation was calibrated prior to the experiments. Ensemble-averaged values of the velocity and the velocity fluctuation were obtained using 6000 sample data at each measuring position acquired at a sample rate of 10,000 Hz for a total sample period of 0.6 s. The sample data and the sample rate were determined by preliminary experiments to minimize the experimental uncertainty. Over the blade passage, the uncertainty of the velocity component was lower than 5.0% based on the time-averaged velocity.

Three-dimensional velocity distributions upstream and downstream of the fan rotor were measured using a five-hole probe. The head diameter and hole diameter of the probe are 3.6 and 0.7 mm, respectively. The calibration of the five-hole probe was

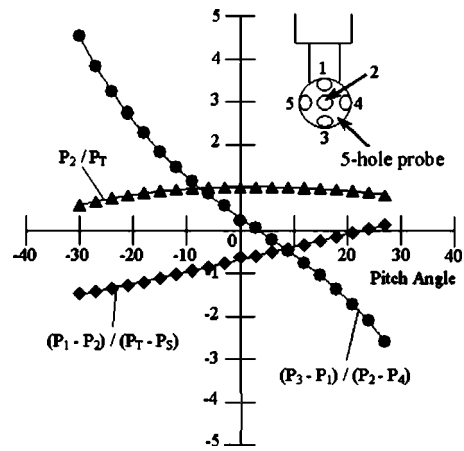


Fig. 7 Calibration curves of five-hole probe

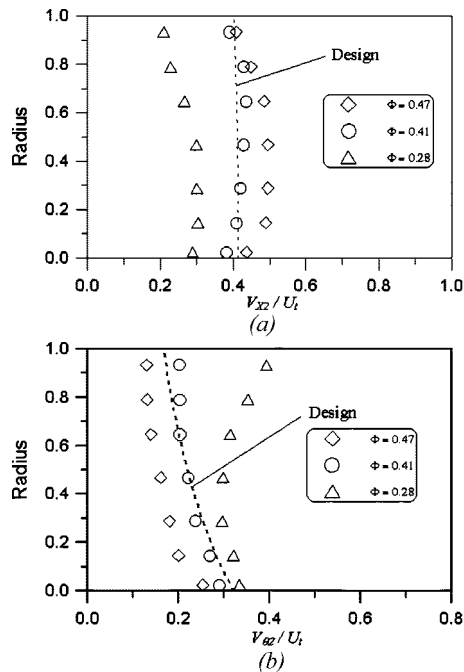
performed in a wind tunnel having the potential core diameter of 50 mm. The probe was calibrated over a pitch angle range of  $\pm 30$  deg using 3 deg increments. A jet velocity in the potential core was 20 m/s, and a calibration curve is shown in Fig. 7. In Fig. 7,  $P_1-P_5$  are pressures obtained from the five-hole probe. Total pressure  $P_T$  and static pressure  $P_S$  were determined by a standard pitot tube, which was set in the potential core of the wind tunnel. Throughout the three repeated measurements, the errors keep below 1% for the three parameters. The five-hole probe was used to measure the three dimensional velocities upstream and downstream of the fan rotor. For the careful measurements of the velocities, measuring time took at least 10 min per one position. The maximum error showed near the casing due to the flow distortion resulted from the interference between the casing wall and the probe head. The maximum uncertainty of the velocity component was about 5.0% based on the time-averaged velocity.

### 3 Results and Discussion

**3.1 Flow Characteristics Upstream and Downstream of the Fan Rotor at a Design and Off-Design Operating Conditions.** The three-dimensional velocity distributions upstream and downstream of the fan rotor were analyzed and compared to the design data at the design and off-design operating conditions.

Figure 8 shows the distribution of axial and tangential velocity for the design ( $\Phi=0.41$ ) and two off-design conditions ( $\Phi=0.28$  and 0.47), which were measured downstream of the rotor and obtained using the five-hole probe. The distance between the rotor trailing edge and the head of the probe was 200 mm (150% tip chord) as shown in Fig. 5. In the figure, the horizontal axis represents an axial velocity  $V_{x2}$  and a tangential (circumferential) velocity  $V_{\theta 2}$  normalized by the tangential velocity of the rotor tip  $U_t$ . The radius shown in the vertical axis is a nondimensional value i.e., 0.0 and 1.0 indicates the blade hub and tip, respectively. In the figure, the dashed line denotes the design value. As shown in Fig. 8, experimental data of the axial and tangential velocities are in good agreement with the design values. High axial velocity decay is observed above 50% span at near stall condition ( $\Phi=0.28$ ). This implies that the low-velocity region is rapidly increased near the rotor tip, thus resulting in large blockage. The increase in tangential velocity near the rotor tip also corresponds to the large blockage effect at near stall condition. It can be considered that the rapid increase of the SPL at near-stall condition, shown in Fig. 4, has a close relation with the larger blockage near the rotor tip.

Figure 9 shows the distribution of a relative inlet and an outlet flow angle for the design condition upstream and downstream of the fan rotor. The measuring position for the inlet flow angle was

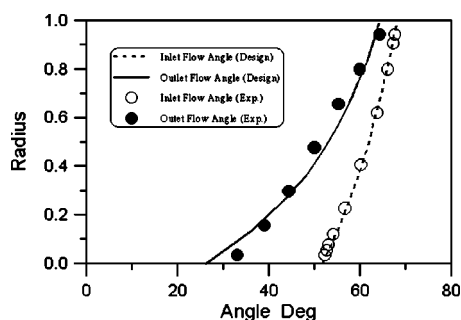


**Fig. 8** Distribution of an axial velocity and a tangential velocity downstream of the fan rotor: (a) axial velocity (b) tangential velocity

55 mm (42% tip chord) upstream from the leading edge of the fan rotor. As shown in Fig. 9, the inlet and outlet flow angles obtained by the flow measurement correspond well to the design ones. This means that the performance of the axial flow fan has almost the same value compared to the design one.

**3.2 Measurement of the Tip Leakage Vortex by Using a Rotating Hot-Wire Sensor at the Design and Off-Design Conditions.** The vortical flow in the blade passage and downstream of the fan rotor was analyzed by experimental measurements using a hot-wire sensor rotating with the rotor blade at three off-design conditions ( $\Phi=0.28$ ,  $0.31$ , and  $0.47$ ) and at the design condition ( $\Phi=0.41$ ) as well.

Figure 10 shows the contour of relative velocity on the plane of the 96% span at the design and three off-design conditions, which is a perspective view from the casing. Two measuring regions, A and B as shown in Fig. 10(a), are positioned on the blade pressure and suction sides. The L-type supporter shown in Fig. 6 is used for measuring the region A, and the I-type supporter is for the region B. The interval of measuring positions of the hot-wire sensor is about 3 mm for both axial and tangential directions. The minimum measuring distance from the blade surfaces is about



**Fig. 9** Distribution of relative flow angle upstream and downstream of fan rotor at the design operating condition

9 mm. The measuring positions upstream and downstream in the axial direction are 27% and 121% of axial chord from the leading edge, respectively. The relative velocity  $V_{at}$  obtained by hot-wire sensor is defined and normalized by the tangential velocity of the blade tip

$$V_{at} = \frac{\sqrt{V_a^2 + V_t^2}}{U_t} \quad (2)$$

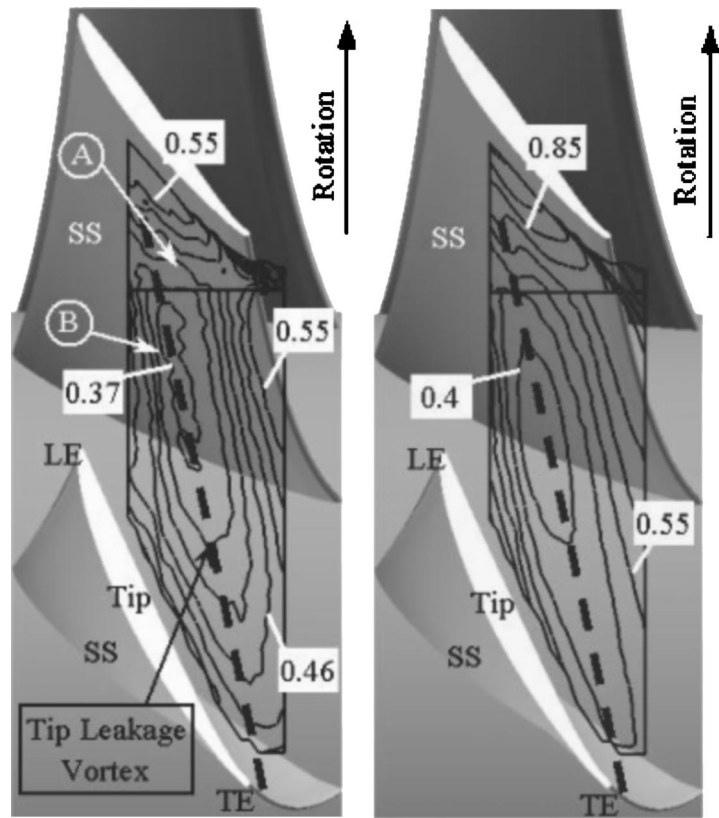
where  $V_a$  and  $V_t$  denote local axial velocity and tangential velocity, respectively. The plane of the 96% span is selected because most of the vortical centers of the leakage vortex are distributed near the 95% span as shown in Fig. 14, which will be discussed later. As shown in Fig. 10, the trough having a low velocity is clearly observed at all flow rates. The authors also showed that the low-velocity region in the blade passage of the axial flow fan corresponds to the leakage vortex [7,8]. The dashed line in Fig. 10 indicates the trajectory of the vortical center of the leakage vortex. At  $\Phi=0.28$  and  $0.31$ , it is shown that the leakage vortex interferes with the adjacent blade pressure surface. However, the leakage vortex at  $\Phi=0.47$  is moved close to the blade suction surface, which results in the interference with the suction surface. At the design condition, the leakage vortex formed on suction side grows in the downstream direction without interference with the adjacent blade surface as shown in Fig. 10(c).

Figure 11 shows the trajectories of the vortical center of the leakage vortex, which are the perspective view from the casing. It is found that the leakage vortex is moved upstream as the flow rate is decreased, thus resulting in interference with the adjacent pressure surface. This is generally acknowledged as described by Murthy and Lakshminarayana [2] and Inoue et al. [4] in an axial compressor rotor.

Figure 12 shows the contour of the velocity fluctuation on the plane of the 96% span, which is shown in the same manner as that in Fig. 10. At  $\Phi=0.28$  and  $0.31$ , where the leakage vortex interferes with the adjacent pressure surface as shown in Fig. 10, a high velocity fluctuation is observed upstream of the leakage vortex and also near the suction surface. It can be considered that the high velocity fluctuation is caused by the interference between the leakage vortex and the main flow due to a large variation of the leakage vortex in time. This also results in high velocity fluctuation on the adjacent pressure surface, thus increasing noise at a lower flow condition than at the design flow rate as shown in Fig. 4 [7]. High velocity fluctuation is shown around the vortical center of the leakage vortex at the design ( $\Phi=0.41$ ) and the overflow condition ( $\Phi=0.47$ ). It is noted that the high velocity fluctuation is observed close to the suction surface at  $\Phi=0.47$  as shown in Fig. 12(d). From distributions of the velocity fluctuation, the maximum magnitude of the velocity fluctuation at the design flow rate is relatively low as compared to that at the off-design conditions.

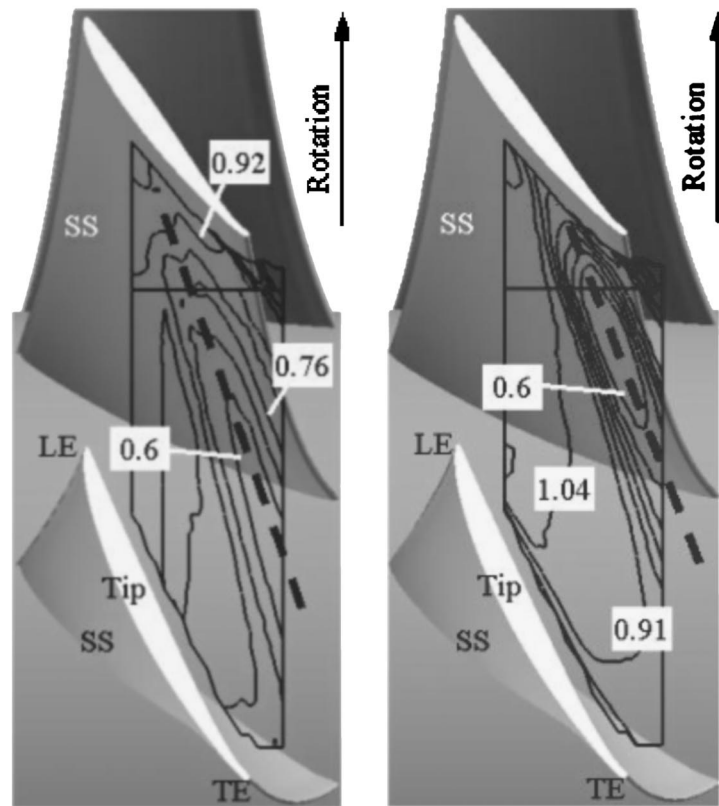
To clearly understand the distribution of the relative velocity and the velocity fluctuation in the leakage vortex, quasi-orthogonal planes to the leakage vortex are introduced.

Figure 13 shows the contour of the relative velocity and the velocity fluctuation on the quasi-orthogonal planes to the leakage vortex at the design condition ( $\Phi=0.41$ ). The positions of five quasi-orthogonal planes to the leakage vortex are shown in Fig. 13(a). The axial position from the leading edge is located between 27% and 121% axial tip chord. From the distribution of the relative velocity as shown in Fig. 13(b), the vortical flow due to the leakage vortex can be observed clearly. The vortical flow is formed at the low-velocity region, and it is surrounded by the main flow. The vortical center is determined by a position having minimum relative velocity at each plane and indicated by + as shown in Figs. 13(b) and 13(c). A dashed line in Fig. 13(a) is obtained by using the vortical center of the quasi-orthogonal planes. It is found that the high velocity fluctuation is mainly observed in the interference region between the leakage vortex



(a)

(b)



(c)

(d)

Fig. 10 Contour of relative velocity on the plane 96% span: (a)  $\Phi=0.28$ , (b)  $\Phi=0.31$ , (c)  $\Phi=0.41$ , and (d)  $\Phi=0.47$

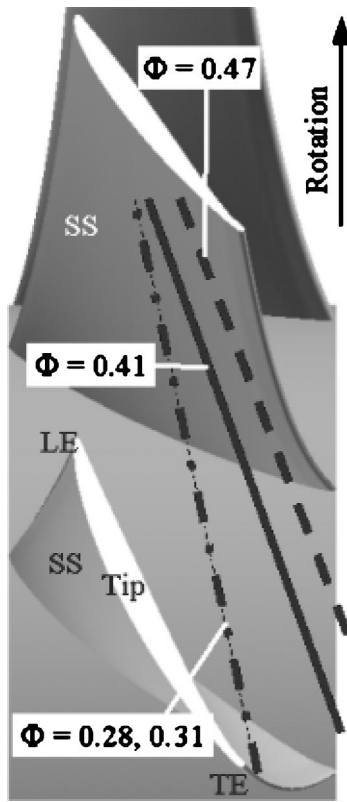


Fig. 11 Trajectory of the vortical center of the tip leakage vortex

and the main flow.

Figure 14 shows the radial position of vortical center of the leakage vortex. The horizontal axis represents the axial chord normalized by the axial tip chord ( $=57.6$  mm) from the leading edge at the rotor tip. The axial chord of 1 means the trailing edge at the rotor tip. The radial position of vortical center is distributed between 94% and 96% span in the present axial flow fan having 2 mm tip clearance.

**3.3 Effect of the Tip Leakage Vortex on the Wake Flow at the Design and Off-Design Conditions.** As mentioned in Sec. 3.2, the tip leakage vortex interferes with the adjacent blade surfaces at the design and off-design operating conditions. In the following, the effect of the leakage vortex on the wake flow will be discussed at the design and off-design conditions.

Figure 15 shows the experimental grid of the hot-wire sensor. This is used to measure the relative velocity and the velocity fluctuation in the wake region. The measuring area in the radial direction is distributed from 42% span to 98% span. The interval of each measuring position of the hot-wire sensor is 3 mm for the spanwise direction. The axial distance between the blade trailing edge and the first measuring line from the rotor is 3 mm.

Figure 16 shows the contour of relative velocity and velocity fluctuation in the wake region. The measuring plane is located 3 mm downstream from the trailing edge of the rotor in the axial direction. Near the 95% span on the blade pressure side, high velocity fluctuation is observed at the peak pressure condition ( $\Phi=0.31$ ) due to the interference between the leakage vortex and the pressure surface. This phenomenon was also observed in an axial flow fan having a different blade shape [7]. In [7] the high velocity fluctuation induces high pressure fluctuation on the blade surface, which has considerable effect on the noise generation in an axial flow fan operating at a lower flow condition than that at the design flow rate. At the overflow condition ( $\Phi=0.47$ ) where the leakage vortex interfaces with the blade suction surface as

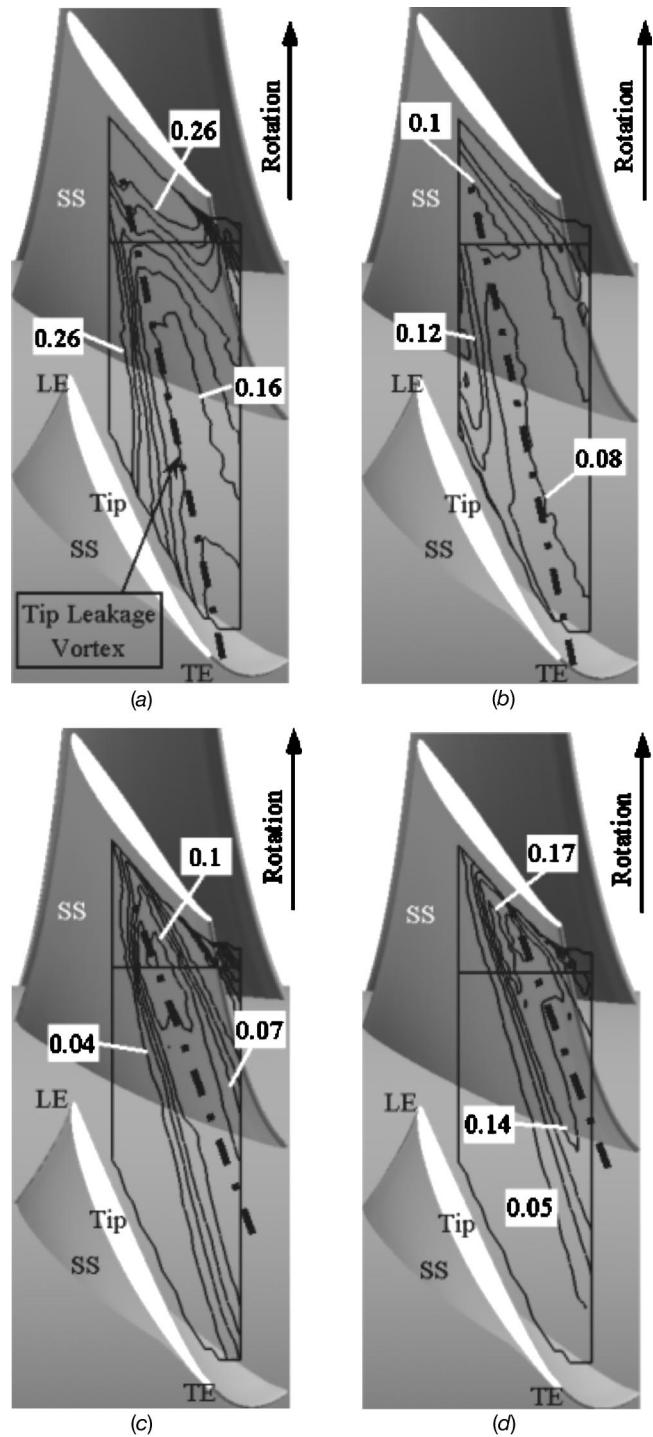


Fig. 12 Contour of velocity fluctuation on the plane 96% span (a)  $\Phi=0.28$ , (b)  $\Phi=0.31$ , (c)  $\Phi=0.41$ , and (d)  $\Phi=0.47$

shown in Fig. 10(d), relatively high velocity fluctuation is distributed near the blade suction side of the rotor tip. The high velocity fluctuation is observed only behind the blade trailing edge at the design condition ( $\Phi=0.41$ ).

In Fig. 16(a), a low relative velocity is distributed along the blade trailing edge above the design flow rate ( $\Phi=0.41, 0.47$ ). However, the low relative velocity region distributed along the blade trailing edge is decreased to the rotor tip direction and vanished near the rotor tip where the high velocity fluctuation is formed at the peak pressure condition ( $\Phi=0.31$ ). This can be considered as the leakage vortex has disturbed the formation of

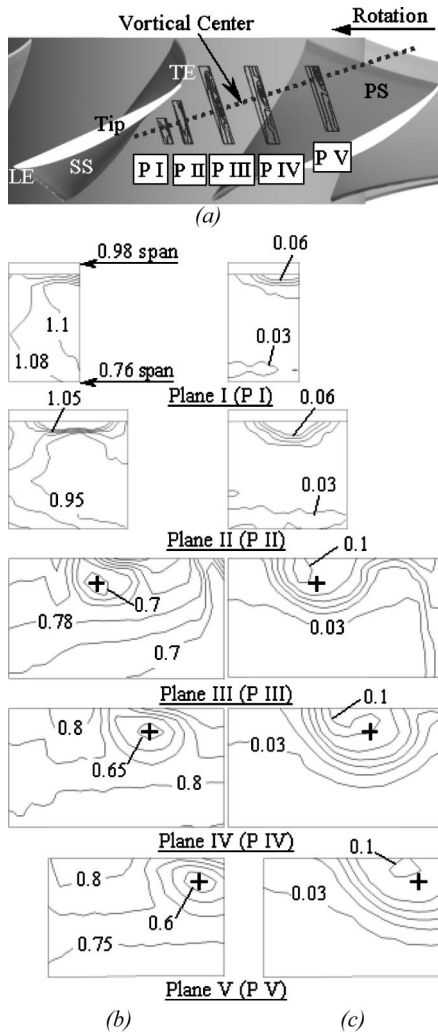


Fig. 13 Contour of relative velocity and velocity fluctuation on the quasi-orthogonal plane to the tip leakage vortex ( $\Phi=0.41$ ): (a) positions of the quasi-orthogonal planes to the tip leakage vortex, (b) relative velocity, and (c) velocity fluctuation

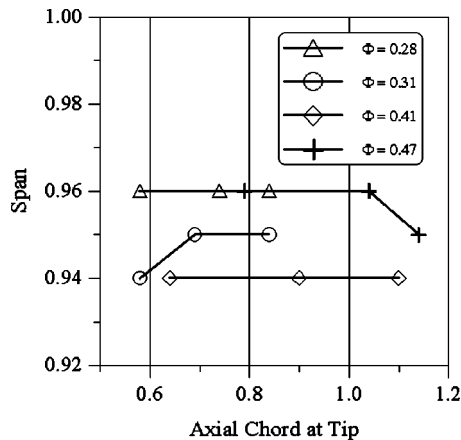


Fig. 14 Radial positions of the vortical center of a tip leakage vortex

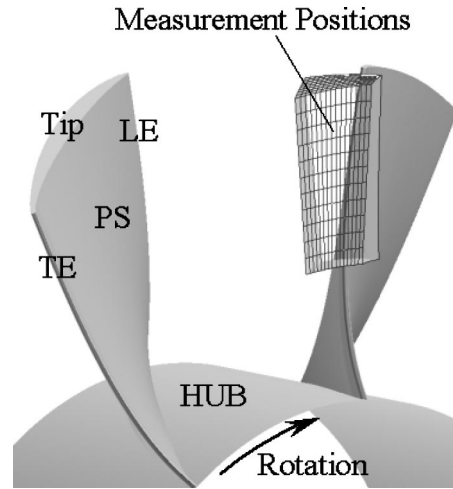


Fig. 15 Perspective view of experimental grid in the wake region

the wake flow downstream of the rotor tip.

Contours of the relative velocity and the velocity fluctuation on the plane of 68% span downstream of the rotor at the design and the overflow conditions ( $\Phi=0.31, 0.41, \text{ and } 0.47$ ) are shown in Figure 17, which are the perspective view from the rotor tip to the hub. The minimum and maximum axial distance downstream of the trailing edge of the rotor blades is 3 and 30 mm, respectively. As shown in Fig. 17(a), the wake flow is clearly observed downstream of the rotor blade. The dashed line in Fig. 17 indicates the

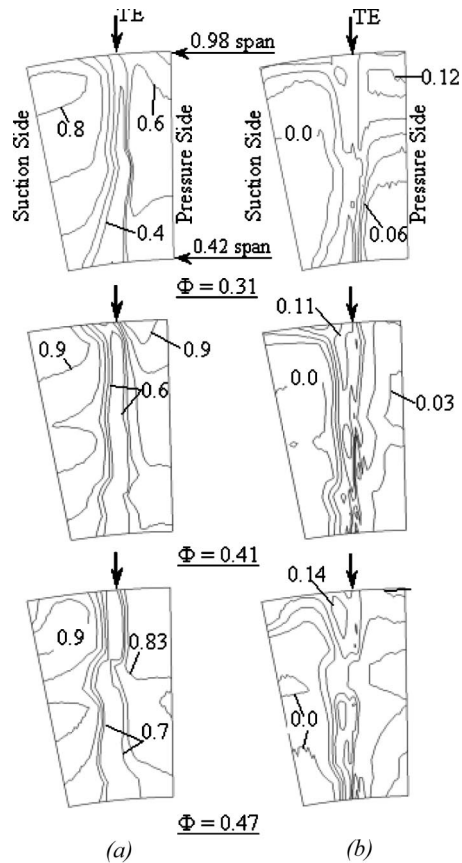
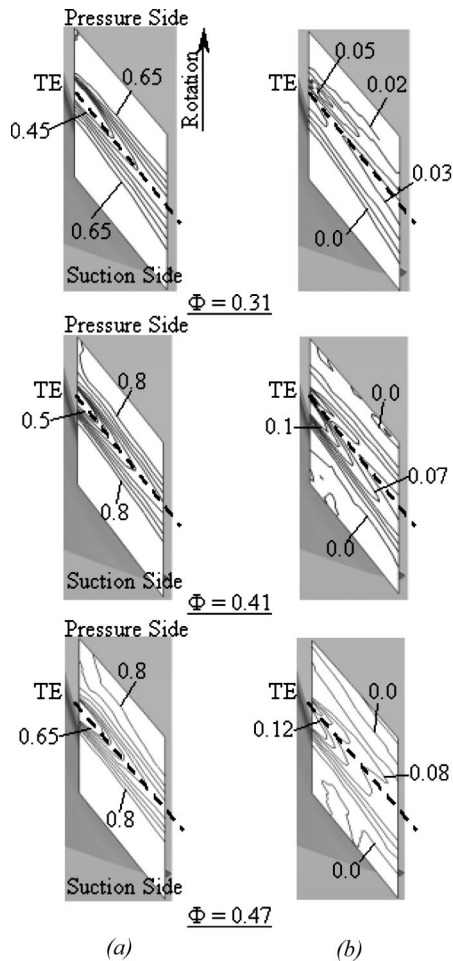


Fig. 16 Contour of relative velocity and velocity fluctuation in the wake region: (a) relative velocity and (b) velocity fluctuation



**Fig. 17 Contour of relative velocity and velocity fluctuation on the plane of 68% span in the wake region: (a) relative velocity and (b) velocity fluctuation**

position of the trough of the wake flow. The trough of the high velocity fluctuation is observed at both sides of the trough of the wake flow excepting the flow condition of  $\Phi=0.31$  as shown in Fig. 17(b). It is noted that the trough of the velocity fluctuation results from Karmann vortex street. In the present axial flow fan, Karmann vortex street is clearly observed at design flow rate and above throughout the flow measurement with the rotating hot-wire sensor.

#### 4 Conclusion

The validity of the blade design is analyzed by measuring the three-dimensional velocities upstream and downstream of the fan rotor using a five-hole probe. In addition, detailed measurements of the vortical flow and the wake flow in an axial flow fan have been performed by using a rotating hot-wire probe sensor for the design and three off-design operating conditions. The results are summarized as follows:

1. By comparing the inlet and outlet flow angles obtained by using a five-hole probe, the validity of the design of the present fan rotor can be confirmed. A massive decay in axial velocity near the rotor tip is observed at near-stall condition, which results in a large blockage as compared to that at the design condition.
2. The tip leakage vortex is moved upstream when the flow rate is decreased, thus disturbing the formation of wake flow near the rotor tip. The tip leakage vortex interfaces with the blade suction surface as the flow rate is increased, which results in high velocity fluctuation near the blade suction surface.
3. The investigation of the relative velocity and its fluctuation on quasi-orthogonal planes to the tip leakage vortex is very useful to understand the nature of a vortical flow: that is, the vortical center of a leakage vortex and the distribution of high velocity fluctuation with related to the position of vortical flow. Although the high velocity fluctuation region is moved upstream and enlarged as the flow rate is decreased, the radial position of the vortical center of the tip leakage vortex is changed only 2% span compared to that at the design flow rate.
4. The wake flow downstream of the rotor blade is clearly measured at the design and off-design conditions by using a rotating hot-wire sensor. However, the trough of the high velocity fluctuation due to Karmann vortex street is observed at design flow rate and above.

#### Acknowledgment

The authors are grateful to Prof. Hayashi of Nagasaki University in Japan. He gave us the precious comments on the present experiments, especially in the velocity measurement upstream and downstream of the fan rotor using a five-hole probe.

#### References

- [1] Fukano, T., Takamatsu, Y., and Kodama, Y., 1986, "The Effects of Tip Clearance on the Noise of Low Pressure Axial and Mixed Flow Fans," *J. Sound Vib.*, **105**, pp. 291–308.
- [2] Murthy, K. N. S., and Lakshminarayana, B., 1986, "Laser Doppler Velocimeter Measurement in the Tip Region of a Compressor Rotor," *AIAA J.*, **24**(5), pp. 807–814.
- [3] Hah, C., 1986, "A Numerical Modeling of Endwall and Tip-Clearance Flow of an Isolated Compressor Rotor," *ASME J. Eng. Gas Turbines Power*, **108**, pp. 15–21.
- [4] Inoue, M., and Kuromaru, M., 1989, "Structure of Tip Clearance Flow in an Isolated Axial Compressor Rotor," *ASME J. Turbomach.*, **111**, pp. 250–256.
- [5] Foley, A. C., and Ivey, P. C., 1996, "Measurement of Tip-Clearance Flow in a Multistage Axial Flow Compressor," *ASME J. Turbomach.*, **118**, pp. 211–217.
- [6] Fukano, T., Saruwatari, H., Hayashi, H., Isobe, H., and Fukuhara, M., 1995, "Periodic Velocity Fluctuation in the Near Wake of a Rotating Flat-Plate Blade and Their Role in the Generation of Broadband Noise," *J. Sound Vib.*, **181**, pp. 53–70.
- [7] Fukano, T., Nobuyoshi, O., and Jang, C.-M., 2003, "Axial Flow Fan Noise Generated by the Interaction Between Tip Leakage Flow and an Adjacent Rotor Blade," *Trans. JSME*, **69**(685), pp. 2010–2016 (in Japanese).
- [8] Jang, C.-M., Fukano, T., and Furukawa, M., 2003, "Effects of the Tip Clearance on Vortical Flow and Its Relation to Noise in an Axial Flow Fan," *JSME Int. J., Ser. B*, **46**(3), pp. 356–365.

# Hydrodynamic Design of Rotodynamic Pump Impeller for Multiphase Pumping by Combined Approach of Inverse Design and CFD Analysis

**Shuliang Cao**

Professor  
Department of Thermal Engineering,  
Tsinghua University,  
Beijing 100084, P. R. China  
e-mail: caoshl@mail.tsinghua.edu.cn

**Guoyi Peng<sup>1</sup>**

Assistant Professor  
Department of Mechanical Systems Engineering,  
Toyama Prefectural University,  
5180 Kurokawa, Kosugi-machi,  
Toyama 939-0398, Japan  
e-mail: Peng@pu-toyama.ac.jp

**Zhiyi Yu**

Doctoral Candidate  
Department of Thermal Engineering,  
Tsinghua University,  
Beijing 100084, P. R. China

*A combined approach of inverse method and direct flow analysis is presented for the hydrodynamic design of gas-liquid two-phase flow rotodynamic pump impeller. The geometry of impeller blades is designed for a specified velocity torque distribution by treating the two-phase mixture as a homogeneous fluid under the design condition. The three-dimensional flow in the designed impeller is verified by direct turbulent flow analysis, and the design specification is further modified to optimize the flow distribution. A helical axial pump of high specific speed has been developed. To obtain a favorable pressure distribution the impeller blade was back-loaded at the hub side compared to the tip side. Experimental results demonstrate that the designed pump works in a wide flow rate range until the gas volume fraction increases to over 50% and its optimum hydraulic efficiency reaches to 44.0% when the gas volume fraction of two-phase flow is about 15.6%. The validity of design computation has been proved. [DOI: 10.1115/1.1881697]*

## 1 Introduction

With developing of petroleum industry and depleting of petroleum resources the exploitation of oilfields in remote locations, such as sandy wastes and underwater grounds, comes to be a real demand and the transportation of multiphase products of oil and accompanied natural gas becomes work with much challenge. A multiphase production system requires transporting multiphase fluids of petroleum products from the producing well to a distant processing facility. Conventionally the mixture of oil, water, and gas are separated into the oil and the natural gas and then pumped and compressed through separate pipelines, respectively. In many cases, the natural gas was flared off since its value had not been recognized for a long time. In order to exploit and utilize the depleting energy source more efficiently, the new technology of multiphase transporting has attracted much attention. In a multiphase transporting system the mixture of multiphase fluids is pumped simultaneously, and only one multiphase pipeline is needed. So, the cost of a multiphase transporting facility is only about 70% of a conventional separate transporting facility by eliminating separation equipment and extra pipelines [1]. However, the key equipment of multiphase pumps for multiphase transporting does operate less efficiently than conventional pumps and compressors.

Multiphase pumps developed for gas-liquid multiphase flow in the petroleum industry may be mainly classified into two broad categories of the displacement and the rotodynamic pumps. Displacement pumps, such as the screw pump, are particularly adept at handling multiphase flow of high gas volume fraction and remain functional even at the gas volume fraction of 95%. However, their manufacturing is required to be very accurate to guarantee the volume of the pumping chamber. This type of pump is sensitive to sand particles contained in working fluids and easy to be

eroded in high sand production rates. Its volume flow rate is comparatively small. Rotodynamic pumps work by transferring the mechanical input into the kinetic energy of working fluids that is then converted into working pressure. Early multiphase rotodynamic pumps were developed based on the electric submersible centrifugal pump. With great improvements in the geometry structure of impellers, a kind of multistage helico-axial pump was developed by the Poseidon group (IFP, Total and Statoil). The pump includes a series of pump stages each of that consists of a rotational impeller and a stationary diffuser. This configuration is akin to the hybrid of a pump and a compressor. Each impeller delivers a pressure boost with an interstage diffuser acting to homogenize and redirect flow into the next impeller. This interstage mixing prevents the separation of the gas-liquid mixture and enables a stable pressure-flow characteristic. It can also provide a large flow rate. As the impeller tip clearance is sufficient to allow passing of small sand particles, this kind of pump is applicable to multiphase flow containing small sand particles, and the manufacturing requirement is not so strict.

Although the helico-axial pump shows a great advantage to multiphase pumping, its hydrodynamic design is still difficult work. Unlike the single-phase pumps and compressors, there is no generalized model directly applicable to the hydraulic design of multiphase impeller blades. Rotodynamic multiphase pumps were usually developed empirically case by case, and a better impeller of good performance is usually selected through experiments of many designed impellers. This process is very time-consuming and costly. The accelerated production development is depriving the designer of time to carry out so many trial designs and selecting experiments for a particular case. A practical method calculating the blade geometry theoretically is desired to expedite the hydraulic design of multiphase impeller.

On the other hand, with advancing of computation technology and rapidly increasing of computing capacity, computational fluid dynamics (CFD) gets to be used as a common tool of flow analysis in turbomachinery [2,3]. Some numerical methods for modeling of two-phase flow in simple form, such as homogenous bubbly flow [4,5], were developed with efforts, and it becomes possible to calculate the gas-liquid two-phase flow in turboma-

<sup>1</sup>Corresponding author.

Contributed by the Fluids Engineering Division for publication in the JOURNAL OF FLUIDS ENGINEERING. Manuscript received by the Fluids Engineering Division May 18, 2004; revised manuscript received October 1, 2004. Review conducted by Y. Tsujimoto.



chinery under certain simplifications. However, the direct flow analysis of CFD does not directly propose a blade geometry generating favorable flow pattern. Although it is possible to seek a feasible blade geometry by iterative use of CFD code for different geometries, the so-called direct method is inefficient for the difficulty to define a good relation of blade geometry modification and flow field features. The other way of turbomachinery design is so-called inverse method by which corresponding blade geometry is calculated theoretically from specifications of required flow field features given as input. For the difficulty of inverse problem, the real viscous flow is usually simplified into an inviscid one considering the fact that the effect of fluid viscosity mainly dominates in a thin layer near to solid boundaries in actual machines. Existing practical inverse models may be mainly classified into two categories of quasi-three-dimensional (Q3D) and fully three-dimensional (F3D) methods. The Q3D methods calculate three-dimensional flow in turbomachinery blades by iterative computations of a mean hub-to-tip ( $S_{2m}$ ) stream surface and a serious symmetric blade-to-blade ( $S_1$ ) stream surface based on Wu's theory of two-type stream surfaces [6,7]. For its reliability the Q3D theory were applied to various types of turbomachinery and came into wide use in engineering practice [8,9]. The F3D methods calculate three-dimensional flow in turbomachinery by superposition of a circumferential mean flow and a circumferentially periodic flow in which the function of blade is replaced by a blade-bound vortex [10–12]. The F3D theory takes account of the effect of a circumferential flow twist that is neglected in the Q3D theory, but its convergence is relatively slow near the blade ends where the normal gradient of swirl velocity is often great. Compared to the F3D inverse model, the Q3D inverse model has a feature of quick convergence, and its accuracy is acceptable to engineering practice since the circumferential twist of flow in hydraulic machinery is very small.

The inverse method calculates the geometry of blades according to a certain design specification of flow field features. However, it is not easy to define a well-posed design specification. Especially for the multiphase gas-liquid two-phase flow pump, the gas phase and liquid phase may separate, depending on pressure and velocity distributions. The head and the efficiency of a multiphase pump may decline and even the pump may be unable to work for the influence of stagnant air bubbles. The inverse computation of multiphase pump impeller should consider the gas-liquid fluid separation and the gas blockage carefully, but it is not clear what type of design specification is most suitable. To solve this problem a combined approach of inverse method and direct flow analysis is proposed in this paper for the hydrodynamic design of multiphase rotodynamic pump impeller. The geometry of impeller blades is designed for a specified velocity torque distribution on a given meridional geometry by the Q3D inverse method, and the three-dimensional flow in the designed impeller is verified by direct CFD analysis employing RANS equations and the  $k-\varepsilon$  turbulence model. Based on the flow analysis, the design specification of velocity torque distribution is further modified to obtain a favorable flow distribution. A high specific-speed helical axial pump impeller for gas-liquid two-phase flow pumping was designed by applying the approach. The impeller blade was back-loaded at the hub side to optimize the pressure distribution in consideration of the problem of gas blockage. The performance of the designed pump was investigated experimentally. Experimental results demonstrate that the designed pump stage has a maximum hydraulic efficiency of 44.0% when the gas volume fraction of two-phase fluid mixture is about 15.6%, and it works in a wide flow rate range until the gas volume fraction increases to over 50.0%.

## 2 Numerical Approach of Multiphase Impeller Design

**2.1 Modeling of Gas-Liquid Two-Phase Flow.** The numerical approach for inverse design of multiphase pump consists of a

Q3D inverse computation and a direct 3D viscous flow analysis. Under the design working condition, it is assumed that the gas phase disperses in liquid phase uniformly in the form of small bubbles and the gas-liquid two-phase fluid mixture is treated as a homogeneous pseudo-single phase medium. As in the petroleum industry the content of gas included in the gas-liquid mixture is defined by GOR, the ratio of gas associated to per volume of liquid

$$\text{GOR} = Q_{g0}/Q_l \quad (1)$$

where  $Q_{g0}$  denotes the volumetric flow rate of gas-phase medium under the standard atmospheric pressure denoted by  $p_0$ . In consideration of its compressibility the volume flow rate of gas phase may be given as follows under a certain working pressure based on the assumption of ideal adiabatic gas

$$Q_g = Q_{g0}(p_0/p)^{1/\gamma} \quad (2)$$

where  $\gamma$  denotes the specific heat ratio of working gas. For describing the two-phase mixture, an average volume fraction of gas medium is then defined as follows:

$$\text{GVF} = Q_g/Q \quad (3)$$

where  $Q = Q_g + Q_l$ . According to the relation of Eq. (2) we understand that GVF decreases with the increase of working pressure under a certain gas ratio to per volume of liquid phase. As the working pressure in a multistage pump increases gradually from the first stage to the last stage, the gas volume fraction varies with the working pressure in different pump stages. The variation should be considered in hydrodynamic design of different certain pump stages. In a given pump stage the working pressure varies also from the inlet to the outlet, but the pressure difference is not so great in the case of helical axial impeller to be concerned. The variation of gas volume fraction within a pump stage is very small and may be neglected. So, the gas volume fraction under the suction pressure of the pump stage is adopted as the mean gas volume fraction of representative, and the mean density of multiphase medium is then defined by the mean gas volume fraction

$$\rho = \rho_l(1 - \text{GVF}) + \rho_g \text{GVF} \quad (4)$$

The mean viscosity coefficient of gas-liquid mixture is estimated by following relation [13]

$$\mu = (1 - \text{GVF})(1 + 2.5\text{GVF})\mu_l + \text{GVF}\mu_g \quad (5)$$

Although the gas phase included in the two-phase fluid mixture is compressible its influence is significant mainly in the transitional process of pump working when the flow field varies sharply. With the aim to develop a practical approach for the hydrodynamic design of multiphase impeller the present design computation is concentrated on the steady flow under the design working condition, where a local sharp variation of flow field should be restrained to prevent two-phase flow separation. In addition, the relative flow velocity in the impeller is far lower than the speed of sound. So, the influence of compressibility becomes very small and negligible under the design condition. The two-phase flow is treated to be incompressible in the hydraulic design computation of multiphase impeller in consideration of engineering practices.

**2.2 Inverse Design Method.** Figure 1 shows the schematic diagram of the helical axial pump stage to be concerned, where a right-handed cylindrical coordinate system rotating with the impeller is denoted by  $(r, \theta, z)$ . The pump stage unit consists of an impeller to boost the working fluid and a diffuser to convert the kinetic energy into pressure. When the fluid mixture passes through the impeller, it is speeded up and its angular momentum increases for the effect of centrifugal forces generated by the rotational impeller. This momentum is then converted into pressure energy when the flow is slowed down and redirected through the stationary diffuser. As the flow through the pump is constrained into a narrow passage in the radial direction, the twist of  $S_1$  stream

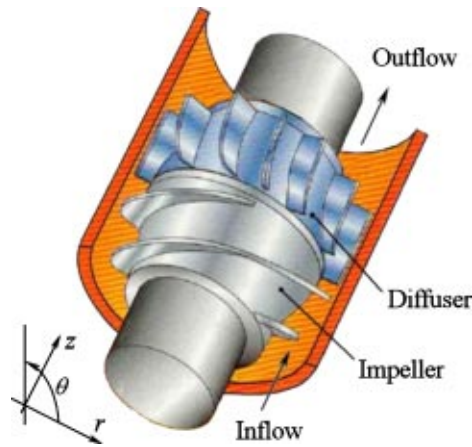


Fig. 1 Schematic diagram of helical axial pump stage

surfaces in the circumferential direction is thought to be very small. Therefore, the impeller was designed with the Q3D inverted model proposed by Peng et al. [14]. In the inverse model the 3D flow is calculated by iteration computation of the mean  $S_{2m}$  surface and a series of axisymmetric flow on  $S_1$  surfaces. The interaction of the impeller and the following diffuser is taken into account also by simultaneous computation of the mean  $S_{2m}$  flow through the impeller and the diffuser. The shape of the blade mean surface (chamber) is calculated by integration of a first-order differential equation for blade geometry design along meridional streamlines. Then, the blade geometry of pressure and suction surfaces is determined according to the distribution of blade thickness that is given as input data.

Except basic working parameters of pump impeller the input data of design specifications includes: (a) geometry of flow passage, (b) velocity distribution at the inlet, (c) meridional geometry of blade, (d) blade stacking condition, (e) blade thickness distribution, (f) blade number, and (g) velocity torque distribution. Among these design specifications, the velocity torque distribution is the most important one for controlling of 3D flow. The geometry of flow passage and the blade number are specified referring to the existing knowledge basis of statistical data, and the inlet velocity distribution is calculated according to the volumetric flow rate and geometry of flow passage. The blade thickness and stacking condition are determined in consideration for requirements of structural strength and manufacturing technology.

The design specification of velocity torque distribution is directly relative to the blade loading, which is defined to be the pressure difference across the blade by the following equation [15]:

$$p_p - p_s = (2\pi/N_b)\rho W_{mb}\partial(V_{\theta r})/\partial m \quad (6)$$

where  $p_p$  and  $p_s$  denote pressures on the pressure and suction sides of impeller blade, respectively.  $W_{mb}$  is the meridional component of mean relative velocity on the blade and  $V_{\theta}$ , the circumferential component of mean absolute velocity.  $V_{\theta r}$  is called velocity torque (or swirl velocity) here. Its distribution is defined along meridional streamlines with the following formula:

$$V_{\theta r} = (V_{\theta r})_{0,i} + f_i(m)\Delta(V_{\theta r}) \quad (7)$$

where the subscript 0 denotes the blade inlet and  $i$  does a streamline.  $\Delta(V_{\theta r})$  denotes the variation of velocity torque from the leading edge to the trailing edge, and it is determined by the energy conservation as follows:

$$\Delta(V_{\theta r}) = \eta\Delta P/(\omega\rho) \quad (8)$$

in which  $\Delta P$  denotes the pressure increase from the inlet to the outlet of the pump stage to be designed.

$f_i(m)$  included in Eq. (7) is a dimensionless distribution func-

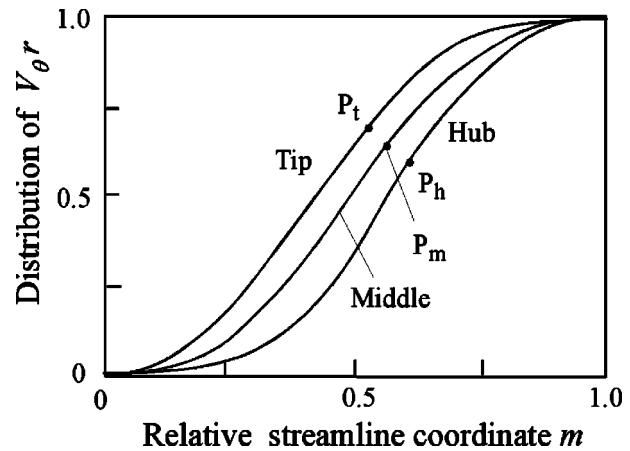


Fig. 2 Velocity torque distribution along streamlines

tion of which  $0 \leq f_i(m) \leq 1$  [16]. It is given that  $f_i(m)=0$  at  $m=0$  (the leading edge) and  $f_i(m)=1.0$  at  $m=1.0$  (the trailing edge). Concerning the velocity torque distribution, its derivative in the streamline direction should be zero at the trailing edge in order to satisfy the Kutta-Joukowski condition. At the blade leading edge, the flow attacking angle is dependent on the velocity torque distribution, and its derivative in the streamline direction should be zero for a no-incidence inflow. On this consideration the  $V_{\theta r}$  distribution is specified along streamlines with the distribution function. In order to adjust the distribution function an inner location denoted as  $P_i$  is further adopted, so that  $f_i(m_{P_i})=f_{P_i}$ , where  $f_{P_i}$  is a dimensionless parameter and  $m_{P_i}$  denotes the relative streamline coordinate of  $P_i$ . Thus, the distribution function is described by a fourth-order polynomial in the streamline direction whose parameters are simply determined with above five constraints. In the span direction a quadratic function is adopted to describe the distribution of inner locations on every streamline, and the quadratic function is determined by three inner locations at the hub, the midspan, and the tip streamlines. Figure 2 shows the dimensionless distribution of velocity torque specified for the hydraulic design of helical axial impeller, where  $P_h$ ,  $P_m$ , and  $P_t$  are inner locations at the hub, the midspan, and the tip streamlines, respectively. Three design parameters (at inner locations  $P_h$ ,  $P_m$ , and  $P_t$ ) are used to define the distribution function in the inverse computation.

According to the above we know that the mean density of working fluid mixture serves as an important parameter to determine the design specification of blade loading. As shown in Eq. (4) the mean density is a dependent variable of the gas volume fraction. So, the blade loading is dependent on the mean gas volume fraction of working fluid mixture given at the suction pressure and the design specification of velocity torque distribution should be adjusted accordingly in the design computation of different pump stages.

**2.3 CFD Analysis Method.** As mentioned previously the gas-liquid two-phase flow is treated as homogeneous pseudo-single-phase fluid media and the influence of compressibility is thought to be negligible under the design condition. So, the relatively steady Reynolds averaged Navier-Stokes (RANS) equations for incompressible flow are employed to evaluate the 3D viscous flow under the design working condition. The temperature of working fluid is assumed to be constant, and the conservation equation of energy is removed from a set of governing equations. The conservation equations of mass and momentum are written as follows in vector form:

$$\nabla \cdot (\rho\mathbf{w}) = 0 \quad (9)$$

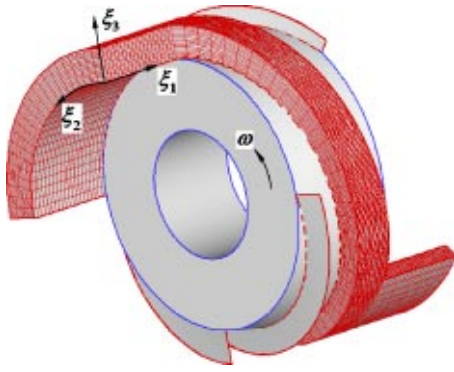


Fig. 3 Computation domain and body-fitted computational grid (203×41×15) for flow analysis

$$\nabla \cdot (\rho \mathbf{w} \mathbf{w} - \boldsymbol{\tau}) = -\nabla p - 2\rho \boldsymbol{\omega} \times \mathbf{w} + \rho \boldsymbol{\omega}^2 \mathbf{r} \quad (10)$$

where  $\boldsymbol{\tau}$  denotes the viscous stress tensor concerning fluid viscosity as well as turbulence viscosity. Its components are written in following form:

$$\tau_{ij} = 2\mu s_{ij} - \overline{\rho w'_i w'_j} \quad (11)$$

where  $i, j=1, 2, 3$  represent three directions of a relative Cartesian coordinate system  $(x_1, x_2, x_3)$  rotating with the impeller.  $s_{ij}$  denotes the strain tensor.  $-\overline{\rho w'_i w'_j}$  represents the turbulent Reynolds stresses due to turbulent motion, which is linked to the mean velocity field via a turbulence model. As the Reynolds number of flow through the impeller to be concerned is as high as the order of  $10^4-10^5$ , the standard  $k-\varepsilon$  turbulence model [17] for high Reynolds number turbulent flow is adopted to take account of the turbulence effect. The turbulent Reynolds stress tensor is given in following form:

$$-\overline{\rho w'_i w'_j} = 2\mu_t s_{ij} - \frac{2}{3}\rho k \delta_{ij} \quad (12)$$

where  $\mu_t$  is the turbulent viscosity given as follows:

$$\mu_t = C_\mu \rho k^2 / \varepsilon \quad (13)$$

in which  $C_\mu$  is an empirical coefficient. The turbulence energy and the turbulence dissipation rate are computed by solving the following conservation equations:

$$\nabla \cdot (\rho \mathbf{w} k - (\mu + \mu_t / \sigma_k) \nabla k) = \mu_t D - \rho \varepsilon \quad (14)$$

$$\nabla \cdot (\rho \mathbf{w} \varepsilon - (\mu + \mu_t / \sigma_\varepsilon) \nabla \varepsilon) = C_{\varepsilon 1} \frac{\varepsilon}{k} \mu_t D - C_{\varepsilon 2} \rho \frac{\varepsilon^2}{k} \quad (15)$$

where the turbulent production rate  $D=2s_{ij} \cdot \nabla \mathbf{w}$ . The empirical coefficients included in the turbulence model are assigned as  $C_\mu=0.09$ ,  $\sigma_k=1.0$ ,  $\sigma_\varepsilon=1.3$ ,  $C_{\varepsilon 1}=1.44$ , and  $C_{\varepsilon 2}=1.92$ .

Considering the geometry structure of pump impeller a right-handed body fitted coordinate system  $(\xi_1, \xi_2, \xi_3)$  is adopted. As shown in Fig. 3 three coordinates  $\xi_1$ ,  $\xi_2$ , and  $\xi_3$  are defined in the streamline direction from the inlet to the outlet, the circumferential direction from the pressure surface to the suction surface, and the radial direction from the hub to the tip, respectively. Equations (9), (10), (14), and (15) are then transferred into differential equations in the body-fitted system and expressed into following generalized partial differential equations in conservation form

$$\frac{\partial}{\partial \xi_i} \left[ \rho w_k \mathbf{q} - \Gamma_q \left( \frac{\partial \mathbf{q}}{\partial \xi_i} \frac{\partial \xi_i}{\partial x_k} \right) \right] \frac{\partial \xi_j}{\partial \xi_k} = S_q \quad (16)$$

where  $\mathbf{q}=\{1, w_1, w_2, w_3, k, \varepsilon\}^T$ , in which the bracket denotes a vector matrix and  $T$  is the transposition of the matrix.  $i, j, k=1, 2, 3$  denote the three coordinate directions.  $\Gamma_q$  and  $S_q$  represent the effective diffusion coefficient and the source term,

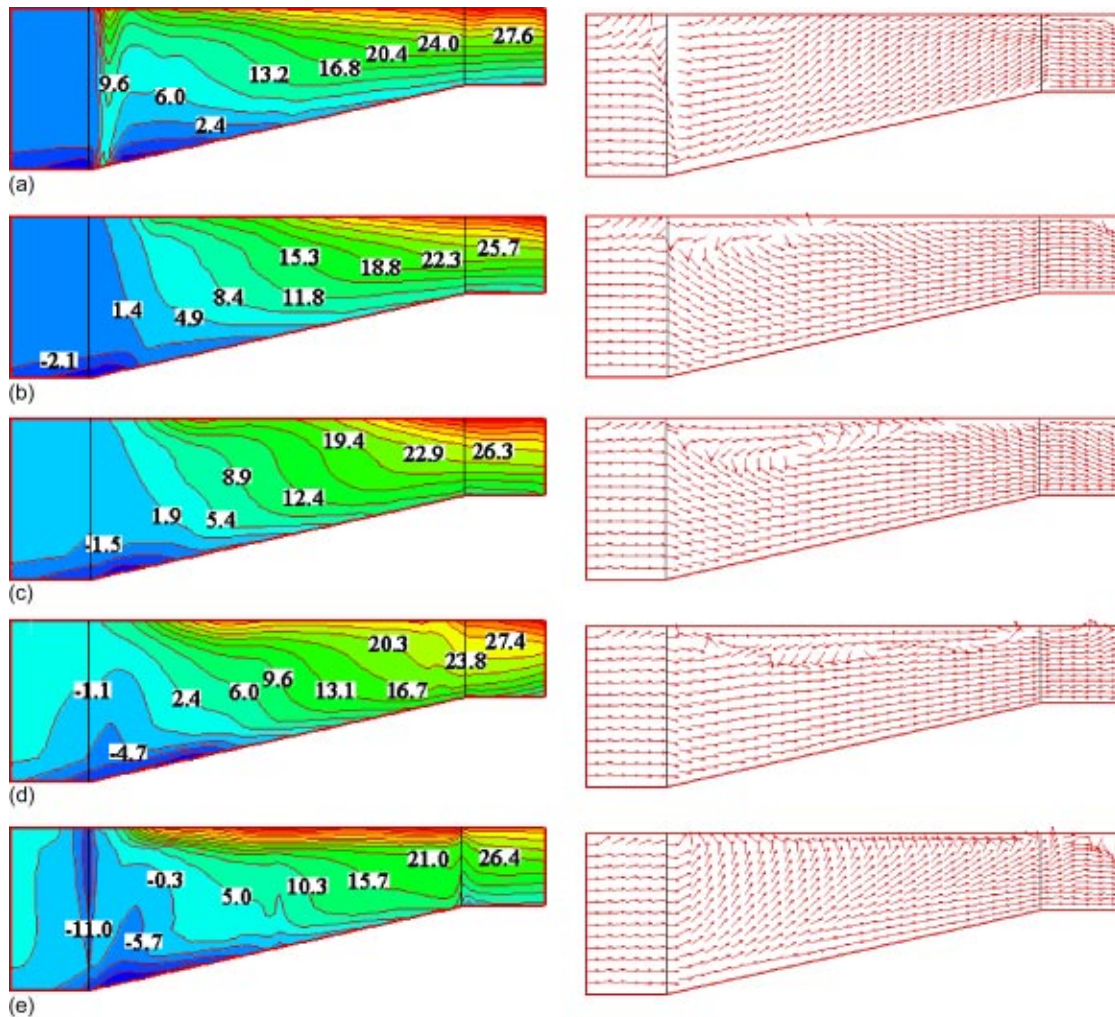
respectively.

Above steady flow governing equations are numerically calculated by the finite difference method. A fully staggered arrangement of dependent variables, in which the velocity components are taken at the centers of cell surfaces in the same directions of velocity components, while scalar variables are taken at the cell center, is adopted in discretization of these equations over all the individuals of computational cells. The diffusion and source terms are discretized by the second-order central difference scheme, and the convection term is approximated by the hybrid scheme with second-order accuracy [18]. The algebraic equations resulted by discretization of flow governing equations are solved by the widely used SIMPLEC algorithm.

### 3 Numerical Results and Discussions

The described approach was applied to the hydraulic design of a high specific speed pump impeller. The working fluid was taken to be the mixture of air and water. The gas volume fraction at the design condition was given to be 20%. Basic working parameters of the pump stage were given to be that the total volume flow rate  $Q=40 \text{ m}^3/\text{s}$ , the pressure increase  $\Delta P=0.2 \text{ MPa}$  and the rotational frequency  $\omega=25 \text{ s}^{-1}$ . As for the geometry parameters, the hub diameter at the inlet of impeller was given to be  $d_{h1}=0.8d$ , and the hub diameter at the outlet was given to be  $d_{h2}=0.9d$ . The blade number was selected to be  $N_b=4$  in order to reduce the total pressure load of a single blade. The blade geometry was calculated for a specified velocity torque distribution along streamlines on the given meridional geometry by iterative calculation of the mean  $S_{2m}$  surface and  $S_1$  surfaces. The convergence criterion for the inverse calculation was given to be that the relative change of meridional streamlines is less than  $5.0 \times 10^{-4}$  and the relative error of blade geometry iteration on the  $S_1$  surfaces is less than  $1.0 \times 10^{-3}$ . Since the pressure gradient has a great influence on the flow separation of gas-liquid two-phase flow, which may give rise to the phenomenon of gas blockage in blade passage, the pressure distribution was carefully controlled by adjusting the design specification of velocity torque distribution according to the result of flow analysis.

Figure 3 shows the computation domain and the body-fitted grid arrangement employed in the flow analysis. For the computational domain, a uniform velocity distribution was imposed at the inlet. The turbulence kinetic energy was given to be that  $k_{in}=0.03w_{in}$ , where  $w_{in}$  denotes the velocity at the inlet, and the turbulence dissipation rate was given to be  $\varepsilon_{in}=C_\mu k_{in}^{3/2}/l_{in}$  in which  $l_{in}=0.015d$  denotes the turbulent scale. At the outlet the normal gradients of velocity components,  $k$  and  $\varepsilon$  were given to be zero, respectively. At two pairs of circumferential boundaries connected to blade surfaces, the periodic boundary condition was imposed. At wall boundaries (the pressure and suction blade surfaces, the tip and hub walls), the nonslip condition of viscous fluid was imposed by applying the logarithmic wall function in the near region of walls [19]. In this way, the need to employ fine computational cells within wall boundary layers, which is associated with computing cost, was avoided. For the pressure a reference pressure was specified at the origin of coordinates (one corner node) on the inlet boundary and the Neumann condition was applied to all boundaries. The flow analyses were performed with the body-fitted grid shown in Fig. 3, and the convergence criterion for the iterative calculation of velocity and pressure fields was given to be that the relative changes of velocity and pressure are less than  $1.0 \times 10^{-3}$  and  $0.5 \times 10^{-4}$ , respectively. Regarding the resolution of computational grids, the effect of cell size was investigated by adjusting the number of cell nodes. It was shown that the computation result gets into convergence as computational cells increase. When the number of cell nodes is increased to  $203 \times 41 \times 15$ , the influence of cell size becomes very weak and the computation accuracy is acceptable. Thus, the computational



**Fig. 4 Distributions of pressure contour (left) and velocity vector (right) in sections parallel to the blade surface between two adjacent blades: (a) in section close to the pressure surface ( $\xi_2=5\%$ ), (b) in section at  $\xi_2=25\%$  (c) in section at the middle of blade passage ( $\xi_2=50\%$ ), (d) in section at  $\xi_2=75\%$ , and (e) in section close to the suction surface ( $\xi_2=95\%$ )**

grid shown in Fig. 3 whose node numbers are  $203 \times 41 \times 15$  in three body-fitted directions of  $\xi_1$ ,  $\xi_2$ , and  $\xi_3$ , respectively, was adopted hereafter.

Figure 4 shows pressure and velocity distributions in sections parallel to the blade surface in the flow passage between two adjacent blades under the design condition. Figures 4(a)–4(e) are pressure contours (left) and velocity vectors (right) in sections where  $\xi_2$  equals 5% (close to the pressure surface where  $\xi_2=0$ ), 25%, 50% (the middle of blade passage), 75%, and 95% (close to the suction surface where  $\xi_2=100\%$ ), respectively. The result demonstrates that the pressure increases overall in both directions from the hub to the tip and from the blade leading edge to the trailing edge. The pressure gradient in the radial direction is greater than that in the axial direction, especially in the area near to the trailing edge. It may be due to the effect of centrifugal force that plays a dominant role in this type of impeller. Thus, a narrow meridional flow passage in radial direction was adopted to suppress the radial pressure difference. At the inlet close to the hub wall a local low-pressure region is formed on the suction side. Under the effect of high pressure gradient small gas bubbles dispersed in water are easily to gather in the local low-pressure area and thus the phenomenon of gas blockage may be caused. For this reason the pressure load of impeller blade was concentrated to the

rear part near the hub wall. In order to obtain a smooth pressure distribution the impeller blade was back-loaded at the hub side compared to the tip side by defining the dimensionless distribution of velocity torque as shown in Fig. 2. According to the velocity vector distributions, we know that a tip vortex sheet is formed behind the tip clearance near to the casing wall. To reduce the tip leakage and the tip vortex loss, the tip clearance was given small as possible, considering the manufacturing requirement. Figure 4(a) shows also that a small flow incidence takes place at the inlet on the pressure side, which may be due to the influence of blade thickness. So, the pressure rises to some extent along the blade leading edge for the effect of flow attacking.

Figure 5 shows pressure and velocity distributions in circumferential sections from the hub to the tip, in which (a), (b), and (c) are pressure contours (left) and velocity vectors (right) in sections, where  $\xi_3$  equals 7% (close to the hub wall where  $\xi_3=0$ ), 50% (the middle span), and 93% (close to the tip wall where  $\xi_3=100\%$ ), respectively. The result demonstrates that in the main flow area the pressure increases smoothly from the inlet to the outlet and the pressure gradient in the crosswise direction of streamlines is relatively small except in a small area at the inlet near to the suction side close to the hub wall. In consideration of the problem of gas-liquid two-phase flow blockage, the blade loading was ad-

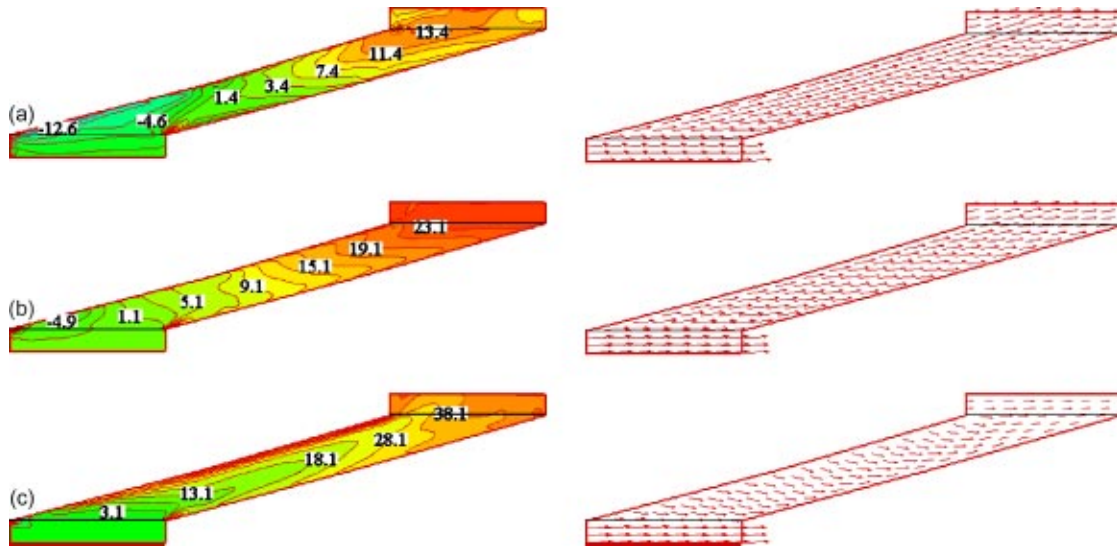


Fig. 5 Distributions of pressure contour (left) and velocity vector (right) in circumferential sections: (a) In section close to the hub wall ( $\xi_3=7\%$ ), (b) In section at the middle span ( $\xi_3=50\%$ ), and (c) In section close to the tip wall ( $\xi_3=93\%$ )

justed as uniformly as possible by modifying the design specification of  $V_{\theta r}$  distribution so as to suppress the pressure gradient in the streamline direction and the pressure difference in the cross-wise direction. Figure 5(c) shows that the pressure in a small area behind the tip clearance varies sharply in the circumferential direction for the influence of tip vortex sheet. However, the pressure area is so small that its influence on the gas blockage may be very little. Above results demonstrate that the pressure in the main area of blade passage varies smoothly and the impeller is expected to work well for gas-liquid two phase flow.

## 4 Experimental Validation

**4.1 Experimental Apparatus and Measuring Methods.** To verify the validity of design computation with the combined approach, hydraulic performance of the designed impeller was investigated experimentally. Figure 6 shows the schematic diagram of gas-liquid two-phase flow pump performance test apparatus applied. The system consists of a water supply section ((1)–(4)), an air intake section ((5)–(8)), a pump section ((9)–(11)), and an exhaust section of two-phase fluid media ((12)–(13)). Experiments were performed with the mixture of air and water. The water supply section and the air intake section are connected to the

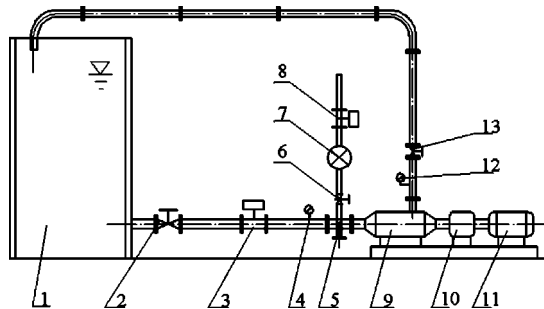


Fig. 6 Schematic diagram of gas-liquid two-phase flow pump performance test apparatus: (1) water tank, (2) regulating valve, (3) turbine flowmeter, (4) pressure gauge, (5) air bubble dispersion device, (6) regulating valve, (7) air compressor, (8) float flowmeter, (9) multiphase flow pump, (10) composite torque detector, (11) motor, (12) pressure gage, and (13) regulating valve

pump section via an air bubble dispersion device in which small air bubbles are generated with a porous device and the bubbles are fully dispersed into the water. The gas volume fraction of two-phase fluid media is controlled by adjusting the air flow rate. The discharge of the pump is directed to an open water tank so that the air contained in the two-phase fluid mixture separates and then exhausts naturally, while the water only flows into the water tank. The volume flow rates of air and water are measured by a float flowmeter with accuracy of  $\pm 0.5\%$  and a turbine flowmeter with accuracy of  $\pm 0.5\%$ , respectively. The suction pressure and the difference of the suction and the discharge pressures are measured by pressure gages with accuracy of  $\pm 0.25\%$ . The torque driving the pump and the rotational frequency of the pump are measured by a composite torque detector, and accuracies of torque and rotational frequency measurement are  $\pm 0.1\%$  similarly. Through uncertainty analysis of the above system the relative error of pump efficiency measurement is estimated to be within  $\pm 0.91\%$ , including systematic and random errors.

**4.2 Performance of Designed Pump.** With regard to the performance of designed pump stage, its total working head and hydraulic efficiency are evaluated experimentally under different working conditions. For the present gas-liquid two-phase flow pump, the total differential head is defined in the following way according to the mass fraction of gas and liquid phases by assuming that the velocity difference between gas and liquid media is small enough [20]

$$H = \frac{P_d - P_s}{\rho_l g} + \frac{V_d^2 - V_s^2}{2g} + h_{ds} + \frac{1}{g} \int_{P_s}^{P_d} \frac{Q_g dp}{Q_g \rho_g + Q_l \rho_l} \quad (17)$$

where  $P_s$  and  $P_d$  denote the mean suction pressure measured at the entrance and the mean discharge pressure measured at the exit of pump stage, respectively.  $V_s$  and  $V_d$  are mean velocities at corresponding positions, which are estimated according to the total volume flow rate.  $h_{ds}$  denotes the geometry altitude from the entrance to the exit. Then, a differential head coefficient  $\psi$  is defined as follows based on the above:

$$\psi = gH/u_2^2 \quad (18)$$

in which  $u_2$  denotes the circumferential velocity at the tip of im-

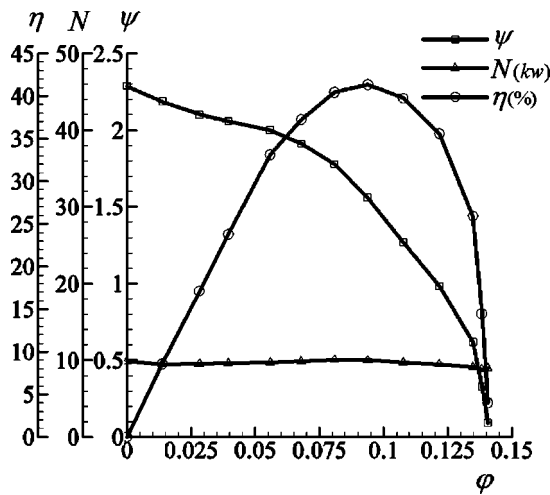


Fig. 7 Hydraulic performance curves in pumping single-phase flow of water ( $\varphi_g=0$ )

peller in the outlet.

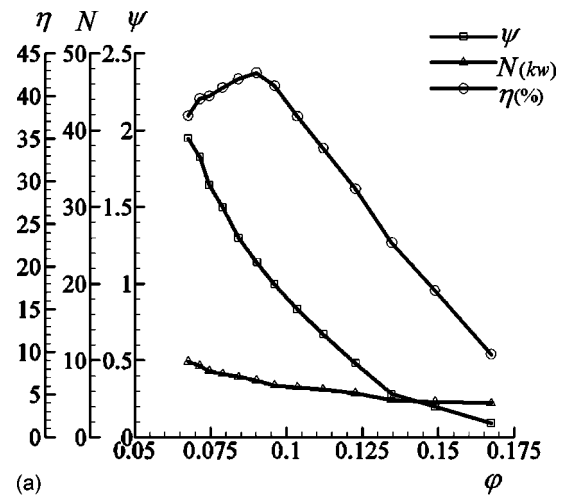
Similarly, concerning the through flow property a total volume flow rate coefficient is defined as follows:

$$\varphi = V_{m2}/u_2 \quad (19)$$

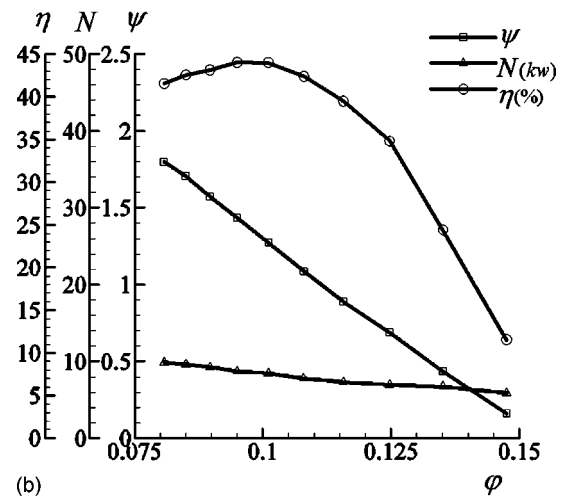
where  $V_{m2}$  denotes the mean meridional velocity at the outlet of pump impeller. We know that the total volume flow rate is composed of gas and liquid phase fluid media. So, the total flow rate coefficient may be divided into two components of the gas-phase (air) and the liquid-phase (water), and it is written to be  $\varphi = \varphi_g + \varphi_l$ . As stated previously the volume flow rate of gas phase is a dependent variable of working pressure and the flow rate coefficient of gas phase varies through pump. For the convenience the gas volume flow rate coefficient and the gas volume fraction under the suction pressure are taken as representative ones.

First, the performance of designed impeller in pumping single phase fluid of pure water ( $\varphi_g=0$ ) was investigated. Figure 7 shows hydraulic performance curves for the single-phase flow of water, where symbols  $\square$ ,  $\triangle$ , and  $\circ$  denote the differential head coefficient  $\psi$ , the shaft power  $N$ , and the hydraulic efficiency  $\eta$  varying with the flow rate coefficient  $\varphi$ , respectively. The figure is, on the whole, similar to the performance chart of a single-phase axial flow water pump. The differential head coefficient varies monotonically with the flow rate coefficient, and the designed pump works satisfactorily in the case of small flow rate also. Under the optimum working condition, the optimum hydraulic efficiency is about 41.3% when  $\varphi=0.094$  and  $\psi=1.56$ . As the helical axial pump designed for gas-liquid two-phase flow consists of a rotational impeller with long narrow flow passage and a stationary diffuser with strong expansion flow passage, the hydraulic loss is relatively large. So, the optimum hydraulic efficiency of a designed pump in pumping pure water flow is relatively low compared to conventional single-phase axial water pumps.

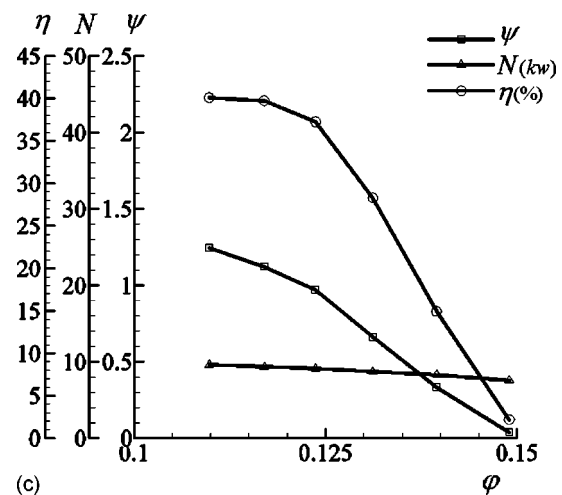
Second, the performance of designed pump in pumping two-phase fluid mixture was investigated by changing volume flow rates of liquid phase and gas phase fluids, respectively. Figure 8 presents some examples of performance curves of the designed pump under a certain flow rate coefficient of liquid-phase (water), where 8(a)–8(c) show variations of  $\psi$ ,  $N$ , and  $\eta$  with the total flow rate coefficient  $\varphi$  when the flow rate coefficient of liquid-phase  $\varphi_l$  equals 0.068, 0.081, and 0.101, respectively. According to the results we know that the differential head coefficient decreases quickly with the increase of gas volume flow rate when the flow rate of liquid-phase is relatively small (Fig. 8(a)). However, when the liquid flow rate is relatively large (Fig. 8(c)), the differential head coefficient decreases slowly with the increase of gas volume



(a)



(b)



(c)

Fig. 8 Hydraulic performance in pumping gas-liquid two-phase flow under a certain liquid flow rate: (a)  $\varphi_l=0.068$ , (b)  $\varphi_l=0.081$ , and (c)  $\varphi_l=0.101$

flow rate. When  $\varphi_l=0.081$ , the differential head coefficient decreases nearly linearly with the increase of gas volume flow rate, and the pump works at a high hydraulic efficiency level in a wide flow rate range. Under a given liquid flow rate, the shaft power decreases with the increase of gas flow rate, which may be due to the variation of the average density of multiphase fluid mixture.

**Table 1** Variation of differential head coefficient  $\psi$  with  $\varphi_l$

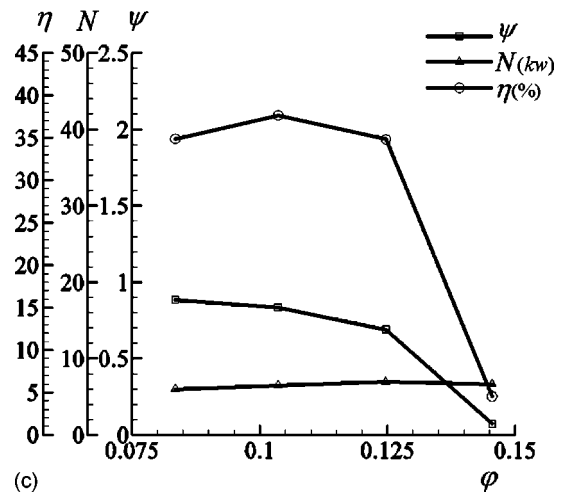
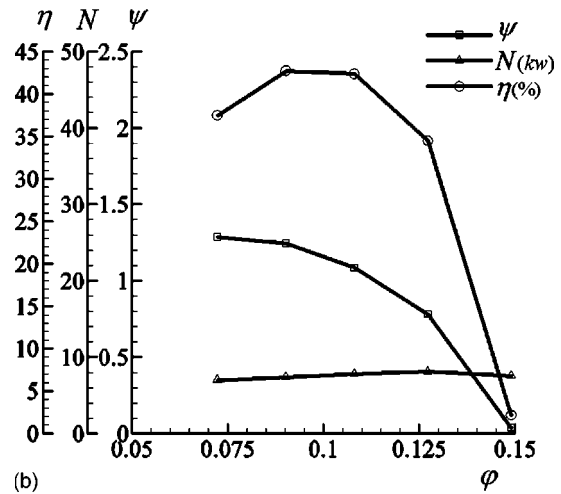
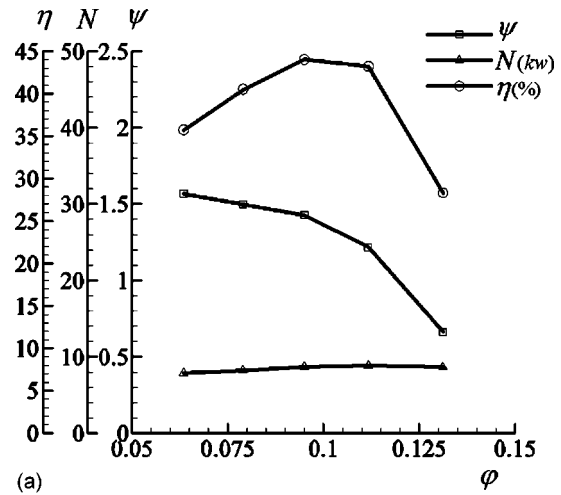
	$\varphi_l=0.054$	$\varphi_l=0.068$	$\varphi_l=0.081$	$\varphi_l=0.098$	$\varphi_l=0.101$
$\varphi=0.1$	0.60	0.95	1.31	1.43	1.40
$\varphi=0.125$	0.19	0.47	0.69	0.89	0.91

The optimum working condition may be found to be that  $\varphi_l=0.081$  and  $\varphi=0.096$ . Under this condition, the gas volume fraction is about 15.6%. The optimum hydraulic efficiency is about 44.0%, which is higher than that in pumping the single-phase fluid of water. The reason may be explained that the pump impeller was designed for the gas-liquid two-phase fluid mixture whose gas volume fraction is specified to be 20%.

Figure 8 demonstrates that the designed pump works normally in a wide range of gas volume fraction. As shown in the figure the gas volume fraction is about 33% when  $\varphi_l=0.101$  and  $\varphi=0.15$  and extends to 46% when  $\varphi_l=0.081$  and  $\varphi=0.15$ . It reaches to 61% when  $\varphi_l=0.068$  and  $\varphi=0.175$  although the differential head coefficient and the hydraulic efficiency decrease greatly. Table 1 shows experimental results of the differential head coefficient varying with the liquid flow rate coefficient when the total flow rate coefficient equals 0.1 and 0.125, respectively. From Table 1 we know that the differential head coefficient increases with the increase of liquid flow rate coefficient when the total flow rate coefficient is kept to a certain value. However, under a certain liquid flow rate coefficient, the differential head coefficient decreases with the increase of total volume flow rate coefficient. When  $\varphi_l=0.054$  and  $\varphi=0.125$  the gas volume fraction is about 56.8% and the head coefficient decreases to 0.19 as shown in the table.

Table 2 shows experimental results of the differential head coefficient varying with the gas volume fraction when the total flow rate coefficient is given to be 0.1 and 0.125. The result demonstrates that the differential head coefficient decreases slowly with the increase of gas volume fraction under a certain total flow rate coefficient. Under a given gas volume fraction the differential head coefficient decreases quickly with the increase of total flow rate. Experiment results reveals that the designed pump stage works normally in a wide flow rate range until the gas volume fraction increases to over 50%. When the gas volume fraction is greater than 50.0%, the differential head coefficient and the hydraulic efficiency decrease greatly. The performance of multiphase pump is affected obviously by the gas volume fraction due to the change of mean density of multiphase fluid mixture.

Figure 9 presents some examples of performance curves of the designed pump under a certain gas volume fraction, where 9(a)–9(c) show variations of  $\psi$ ,  $N$ , and  $\eta$  with the total flow rate coefficient  $\varphi$  when the gas volume fraction GVF equals 15.0%, 25.0%, and 35.0%, respectively. According to the results we know that the optimum working condition changes slightly under different gas volume fractions. The optimum hydraulic efficiency keeps a high level when the gas volume fraction is less than 25%, but decreases obviously when the gas volume fraction increases to 35%. The above results demonstrate that the designed pump works satisfactorily in a wide range of gas volume fraction and flow rate. Its optimum hydraulic efficiency reaches to the maximum of 44.0% when the gas volume fraction is about 15.6% and the total volume fraction equals 0.096. Compared to the hydraulic efficiency of similar pumps [21,22], the maximum hydraulic effi-



**Fig. 9** Hydraulic performance in pumping gas-liquid two-phase flow under a certain gas volume fraction: (a) GVF = 15.0%, (b) GVF = 25.0%, and (c) GVF = 35.0%

**Table 2** Variation of differential head coefficient  $\psi$  with GVF (%) when  $\varphi$  equals 0.1 and 0.125

	GVF=0.	GVF=5.0	GVF=15.0	GVF=25.0	GVF=35.0	GVF=45.0	GVF=50.0	GVF=55.0
$\varphi=0.1$	1.4	1.44	1.4	1.2	0.88	0.56	0.41	0.28
$\varphi=0.125$	0.81	0.91	0.89	0.82	0.69	0.50	0.35	0.22

ciency of the present pump is proved to be higher prominently. The validity of design computation has been proved by experimental results, and the reliability of present approach is demonstrated by the good performance of designed impeller.

## 5 Conclusions

A combined approach of inverse method and direct flow analysis has been presented for the hydrodynamic design of gas-liquid two-phase flow rotodynamic pump impeller. By treating the two-phase mixture as a pseudo-single-phase homogeneous fluid media under the design condition, the geometry of impeller blades is designed for a specified velocity torque distribution and a favorable flow pattern is worked out by further modifying the design specification according to the direct turbulent flow analysis.

The design computation of helical axial impeller for multiphase flow pumping shows that the centrifugal force plays a dominant important role in this type of impeller, and a local low-pressure region is formed at the inlet close to the intersection of the hub wall and the suction surface where the phenomenon of gas blockage is easily to be caused. To obtain a smooth pressure distribution the impeller blade was back-loaded at the hub side compared to the tip side.

Experimental results demonstrate that the designed pump has a maximum hydraulic efficiency of 44.0% when the gas volume fraction of two-phase fluid mixture is about 15.6%, which is higher than the optimum hydraulic efficiency in pumping the single-phase flow of water. The pump works normally in a wide flow rate range until the gas volume fraction increases to over 50%.

## Nomenclature

$d$	= outer diameter of impeller
$f$	= dimensionless $V_{\theta r}$ distribution function
$g$	= gravity
GVF	= gas volume fraction
$H$	= differential head
$k$	= turbulence energy
$m$	= meridional streamline coordinate
$N$	= shaft power
$N_b$	= number of blades
$p$	= local pressure
$Q$	= total volume flow rate of two-phase flow
$Q_g$	= volume flow rate of gas phase
$Q_l$	= volume flow rate of liquid phase
$r$	= radial coordinate
$V$	= mean absolute velocity
$w$	= relative velocity
$z$	= axial coordinate
$\delta_{ij}$	= Kroneker delta function
$\varepsilon$	= turbulence dissipation rate
$\eta$	= hydraulic efficiency
$\varphi$	= total flow rate coefficient
$\varphi_g$	= flow rate coefficient of gas phase
$\varphi_l$	= flow rate coefficient of liquid phase
$\mu$	= mean viscosity of two-phase medium
$\mu_g$	= viscosity of gas phase
$\mu_l$	= viscosity of liquid phase
$\theta$	= circumferential coordinate
$\rho$	= mean density of two-phase medium
$\rho_g$	= density of gas phase

$\rho_l$	= density of liquid phase
$\omega$	= rotational frequency of impeller
$\xi_1$	= curvilinear coordinate from the inlet to the outlet
$\xi_2$	= curvilinear coordinate from the pressure to the suction surface
$\xi_3$	= curvilinear coordinate from the hub to the tip
$\psi$	= differentiahead coefficient

## References

- [1] Porto, D., and Larson, L. A., 1996, "Multiphase Pump Field Trials Demonstrate Practical Application for the Technology," *Proc. Society of Petroleum Engineers (SPE) Annual Technical Meeting*, Houston, Oct. 6–9, Paper No. 36590.
- [2] He, L., and Sato, K., 2001, "Numerical Solution of Incompressible Unsteady Flows in Turbomachinery," *ASME J. Fluids Eng.*, **123**(3), pp. 680–685.
- [3] Muggli, F.-A., and Holbein, P., 2002, "CFD Calculation of a Mixed Flow Pump Characteristic From Shutoff to Maximum Flow," *ASME J. Fluids Eng.*, **124**(3), pp. 798–802.
- [4] Lane, G. L., Schwarza, M. P., and Evansb, G. M., 2002, "Predicting Gas-Liquid Flow in a Mechanically Stirred Tank," *Appl. Math. Model.*, **26**(2), pp. 223–235.
- [5] Gregor, C., Stojan, P., and Iztok, T., 2000, "Upgrade of the VOF Method for the Simulation of the Dispersed Flow," *Proc. ASME FEDSM'00, FED-251*, ASME, New York, ASME Paper No. FEDSM2000-11253.
- [6] Zhao, X. L., Sun, C. L., and Wu, C. H., 1984, "A Simple Method for Solving Three-dimensional Inverse Problems of Turbomachine Flow and Annular Constraint Condition," ASME Paper No. 84-GT-198.
- [7] Wu, C. H., 1952, "A General Theory of Three-Dimensional Flow in Subsonic Turbomachines of Radial-, Axial-, and Mixed Flow Types," NACA TN-D 2604.
- [8] Jenkins, R. M., and Moore, D. A., 1993, "An Inverse Calculation Technique for Quasi-Three-Dimensional Turbomachinery Cascades," *Appl. Math. Comput.*, **57**(2), pp. 197–204.
- [9] Peng, G., Fujikwa, S., and Cao, S., 1998, "An Advanced Quasi-Three-Dimensional Inverse Computation Model for Axial Flow Pump Impeller Design," *Proc. XIX IAHR Symposium- Hydraulic Machinery and Cavitation*, H. Brekke et al., eds., World Scientific, Singapore, pp. 722–733.
- [10] Tan, C. S., Hawthorne, W. R., McCune, J. E., and Wang, C., 1984, "Theory of Blade Design for Large Deflection: Part II- Annular Cascades," *ASME J. Eng. Gas Turbines Power*, **106**(2), pp. 354–365.
- [11] Peng, G., Cao, S., Ishizuka, M., and Hayama, S., 2001, "Fully Three-Dimensional Inverse Computation of Hydraulic Impeller Using Finite Element Method," *Comput. Fluid Dyn. J.*, **10**(2), pp. 247–254.
- [12] Goto, A., Nohmi, M., Sakurai, T., and Sogawa, Y., 2002, "Hydrodynamic Design System of for Pumps Based on 3-D CAD, CFD, and Inverse Design Method," *ASME J. Fluids Eng.*, **124**(2), pp. 329–335.
- [13] Beattie, D. R. H., and Whally, P. B., 1982, "A Simple Two-Phase Frictional Pressure Drop Calculation Method," *Int. J. Multiphase Flow*, **8**(2), pp. 83–87.
- [14] Peng, G., Cao, S., Ishizuka, M., and Hayama, S., 2002, "Design Optimization of Axial Flow Hydraulic Turbine Runner Part I: An Improved Q3D Inverse Method," *Int. J. Numer. Methods Fluids*, **39**(6), pp. 517–531.
- [15] Zangeneh, M., 1991, "A Compressible Three Dimensional Blade Design Method for Radial and Mixed Flow Turbomachinery Blades," *Int. J. Numer. Methods Fluids*, **13**(7), pp. 599–624.
- [16] Peng, G., Cao, S., Ishizuka, M., and Hayama, S., 2002, "Design Optimization of Axial Flow Hydraulic Turbine Runner Part II: Multi-object Constrained Optimization Method," *Int. J. Numer. Methods Fluids*, **39**(6), pp. 533–548.
- [17] Ferziger, J. H., and Milovan, P., 1999, *Computational Methods for Fluid Dynamics*, 2nd Edition, Springer, New York, pp. 277–286.
- [18] Cao, S., et al., 1999, "Three-Dimensional Turbulent Flow in a Centrifugal Pump Impeller Under Design and Off-Design Operating Conditions," *Proc. 3rd ASME/JSME Joint Fluids Engineering Conference*, FED- 248, ASME, New York, ASME Paper No. FEDSM99-6872.
- [19] Schlichting, H., 2000, *Boundary-Layer Theory*, 8th. Edition, Springer-Verlag, pp. 417–442.
- [20] Furuya, O., 1985, "An Analytical Model for Prediction of Two-Phase (Non-condensable) Flow Pump Performance," *ASME J. Fluids Eng.*, **107**(1), pp. 139–147.
- [21] Hellmann, D. H., 1995, "Pumps for Multiphase Boosting," *Proc. 2nd Int. Conference on Pumps and Fans*, Beijing, Vol. 1, pp. 43–46.
- [22] Salis, J., Corder, M., and Birnov, M., 1998, "Multiphase Pumping Comes of Age," *World Pumps*, **1998**(34), pp. 53–54.



# Improvements in Fixed-Valve Micropump Performance Through Shape Optimization of Valves

Adrian R. Gamboa  
Christopher J. Morris  
Fred K. Forster<sup>1</sup>  
e-mail: forster@u.washington.edu

Department of Mechanical Engineering,  
Campus Box 352600,  
University of Washington, Seattle, Washington  
98195-2600

*The fixed-geometry valve micropump is a seemingly simple device in which the interaction between mechanical, electrical, and fluidic components produces a maximum output near resonance. This type of pump offers advantages such as scalability, durability, and ease of fabrication in a variety of materials. Our past work focused on the development of a linear dynamic model for pump design based on maximizing resonance, while little has been done to improve valve shape. Here we present a method for optimizing valve shape using two-dimensional computational fluid dynamics in conjunction with an optimization procedure. A Tesla-type valve was optimized using a set of six independent, non-dimensional geometric design variables. The result was a 25% higher ratio of reverse to forward flow resistance (diodicity) averaged over the Reynolds number range  $0 < Re \leq 2000$  compared to calculated values for an empirically designed, commonly used Tesla-type valve shape. The optimized shape was realized with no increase in forward flow resistance. A linear dynamic model, modified to include a number of effects that limit pump performance such as cavitation, was used to design pumps based on the new valve. Prototype plastic pumps were fabricated and tested. Steady-flow tests verified the predicted improvement in diodicity. More importantly, the modest increase in diodicity resulted in measured block-load pressure and no-load flow three times higher compared to an identical pump with non-optimized valves. The large performance increase observed demonstrated the importance of valve shape optimization in the overall design process for fixed-valve micropumps. [DOI: 10.1115/1.1891151]*

## 1 Introduction

A variety of micropumps exist including those based on the combination of a deformable membrane, a piezoelectric bimorph actuator, and fixed geometry valves, i.e., "No Moving Parts Valves" (NMPV). Such valves develop a different pressure drop in the forward and reverse flow directions due to shape rather than mechanical moving parts. Orienting inlet and outlet valves in the preferential flow direction enables pumps based on these valves to generate net flow. Meso- and micro-scale pumps utilizing a variety of fix-valve configurations have been reported [1–3]. Some positive attributes of fixed-valve micropumps are simplicity of fabrication, versatility in pumping particle-laden fluids [4,5], and flexibility in designing for resonance, since the frequency of operation is not limited by mechanical valve dynamics.

The three primary steps of the design process investigated in this study with the goal of increasing the performance of NMPV micropumps are 1) optimizing valve shape, 2) predicting pump resonant behavior with a linear dynamic model, and 3) utilizing a system optimization technique based on the linear model to determine the best values for all geometric parameters, including valve size. The first step is entirely new and described in detail herein. The second step is accomplished by modeling the valves as straight channels of rectangular cross section, in which the fluid behavior is governed by the unsteady Navier-Stokes equations [6]. Step three, a systematic investigation of multiple design cases [7], was enhanced as part of this study by considering factors limiting performance, including available supply voltage, piezoelectric depolarization, and cavitation of the working fluid. In this study new techniques were used to fabricate plastic pumps, rather than

silicon-based devices reported in the past, which was part of an overall effort to design small scale phase-change cooling systems for electronics. The results presented consist of work previously reported in a proceedings paper [8] with comparisons of computational and experimental results.

To optimize valve shape, diodicity  $Di$  was used as the basic measure of valve performance. This parameter is the ratio of the pressure drop in the reverse direction to that in the forward direction at a given steady-state volume flow rate,

$$Di = \frac{\Delta p_r}{\Delta p_f} \quad (1)$$

The use of this steady flow measure of valve performance to improve the design of harmonically driven micropumps is a key hypothesis of this study. It is partially justified by previous studies of pump resonance based on the linear dynamic modeling with straight rectangular channels in the place of valves. Based on such modeling and experimental verification, maximum pump resonance typically occurs near the corner frequency of the valve fluid impedance curve [9], i.e., near a frequency, around which inertial effects are not dominant. In addition, the complexity of optimization based on transient analysis is so high, quasi-steady optimization was investigated to determine its value. Furthermore, even though fluid inertia has a first-order effect on pump resonance, because its effect is typically greater than that due to the mass of the pump membrane [6], the directional flow behavior of the valves is assumed quasi-steady, similar to that of an electrical diode for which inductance is neglected.

In this paper shape optimization of Tesla-type valves first described by Tesla [10] and first utilized in a micropump by Forster et al. [3] is presented. The basic procedure used is applicable to any parametrically described valve shape, such as the simple diffuser [2,11], nozzle-diffuser<sup>12</sup>, filleted diffuser<sup>13</sup>, and tesser valve<sup>14</sup>.

<sup>1</sup>Corresponding author

Contributed by the Fluids Engineering Division for publication in the JOURNAL OF FLUIDS ENGINEERING. Manuscript received by the Fluids Engineering Division November 3, 2002. Revised manuscript received December 5, 2004. Review conducted by K. Breuer.

## 2 Methods

The methods utilized in this study are presented in four parts. First, valve shape optimization using commercial computational fluid dynamic (CFD) software is described. Valve sizing is then described based on a linear model of pump resonance. Plastic pump fabrication methods used to manufacture prototypes are then described. Lastly, testing methods are described that were used to examine how valve shape affected pump performance.

**2.1 Valve Fluid Dynamics.** The FLOTRAN component of ANSYS version 6.1 (ANSYS, Inc., Canonsburg, PA) was utilized to calculate velocity and pressure throughout the Tesla-type valve. Optimization of valve shape to maximize diodicity was accomplished through the use of a parametric description of the Tesla-type valve based on six geometric design variables. Optimization was performed to determine the best set of these design variables with the ANSYS Subproblem Approximation method that utilized the results of the flow field calculations for each set of design variables considered.

**2.2 Flow Field Calculations.** Solutions of the Navier–Stokes equations were confined to two-dimensional, incompressible, and steady-state laminar flow. By solving these equations in non-dimensional form, a universal solution was obtained for any size valve of a particular shape that depended only on Reynolds number. The dimensionless quantities used were

$$\tilde{\mathbf{u}} \equiv \frac{\mathbf{u}}{2U}, \quad \tilde{p} \equiv \frac{p}{\rho(2U)^2}, \quad \tilde{\mathbf{r}} \equiv \frac{\mathbf{r}}{L}, \quad (2)$$

where  $U$  is the characteristic velocity, and  $L$  is the characteristic length. For the Tesla-type valve  $U$  was chosen as the mean flow velocity in the inlet channel and  $L$  was the channel width  $w_v$ . The dimensionless form of the incompressible steady-state Navier–Stokes equations is then

$$\tilde{\mathbf{u}} \cdot \tilde{\nabla} \tilde{\mathbf{u}} = -\tilde{\nabla} \tilde{p} + \frac{1}{\text{Re}} \tilde{\nabla}^2 \tilde{\mathbf{u}}, \quad \text{Re} = \frac{2\rho UL}{\mu} = \frac{\rho U D_h}{\mu}, \quad (3)$$

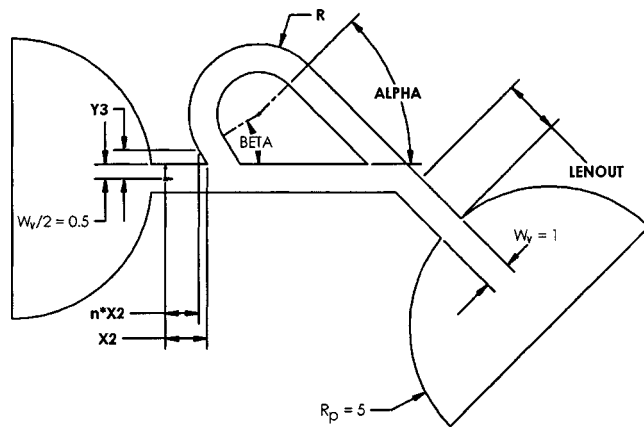
where the dimensionless operator  $\tilde{\nabla} \equiv L\nabla$  and  $D_h = 2w_v$  is the hydraulic diameter. To simplify the assignment of  $\text{Re}$  in the non-dimensional computations, for which valve width is unity, i.e.,  $D_h = 2$ , velocity and density were chosen such that  $U = 1/2$  and  $\rho = 1$ . With these assignments, the fluid dynamic viscosity in the CFD model was assigned the value

$$\mu_{\text{CFD}} = 1/\text{Re}. \quad (4)$$

The computational grid was designed to adapt to changes in geometry and maintain sufficient grid densities in areas of large velocity and pressure gradients. This was done by carefully biasing element size. To speed solution time unnecessary elements were reduced by using coarse grids in appropriate areas and reducing elements in the streamwise direction along long channel lengths. Rectangular elements were used, with 16 elements across each valve channel resulting in 7000 to 10 000 total elements. Grid independence was checked by doubling the number of elements and determining that the solution changed less than 4%.

Inlet and outlet boundary conditions were applied to the straight walls of plenums, which were used to model actual plenums and pump chambers (see Fig. 1). The inlet condition was uniform velocity, and the outlet condition was zero pressure. Finally, the no-slip velocity condition was applied to valve walls and the curved walls of the plenums.

Solution options were chosen based on accuracy, stability, and execution time. The velocity and pressure were calculated using the semi-direct solvers Conjugate Residual (CR) and the Pre-Conditioned Conjugate Residual (PCCR) methods, respectively. Solver relaxation was fine-tuned to decrease solution time while maintaining solution accuracy. Coupling between the momentum and pressure equations was handled by an enhanced Semi-Implicit Method for Pressure Linked Equations (SIMPLE) algorithm, the



**Fig. 1 Design variables for the Tesla-type valve:** 1) the length of the inlet segment in forward flow  $X_2$ , 2) scale factor  $n$  yielding the coordinate  $nX_2$ , and 3) coordinate  $Y_3$  that defined the outer tangent location of the return section of the loop segment, 4) loop outer radius  $R$ , 5) outlet segment length  $\text{LENOUT}$ , and (6) outlet segment angle  $\alpha$ . The origin of coordinates is on the centerline of the inlet channel, one-half channel width from its left end.

SIMPLEN method. The advection scheme for the momentum equation used the second-order accurate Streamline Upwind/Petrov-Galerkin (SUPG) method while the pressure equation used the first-order accurate Monotone Streamline Upwind (MSU) method.

Convergence was controlled with a convergence monitor for each degree of freedom (DOF). The convergence monitor was based on a calculation of the sum of changes in DOF between the current iteration and previous iteration divided by the sum of the current DOF. The convergence monitors were relaxed by one order of magnitude from default values to  $10^{-1}$  for velocity DOFs and to  $10^{-7}$  for pressure.

Flow field calculations were performed on a cluster of ten IBM RS/6000 computers running the AIX operating system. Thirteen values of Reynolds number over the range  $0 < \text{Re} \leq 2000$  were considered, and at each value calculations were performed in both the forward and reverse flow direction for each valve shape considered.

**2.3 Shape Optimization.** To optimize valve shape based on solutions for the flow field, valve geometry was described with six independent non-dimensional design variables as shown in Fig. 1. Since the non-dimensionalization was based on valve channel width, that parameter was unity and therefore not one of the design variables. Special attention was paid to the loop return region, which consisted of a straight channel segment oriented at the angle  $\beta$ . This angle was not one of the design variables but was based on the coordinates  $nX_2$  and  $Y_3$ . Describing the flow loop in this manner avoided interference with the plenum and yielded a wider range of  $\beta$  than was possible with the parametric model previously investigated<sup>15</sup>. For comparison a second valve was modeled based on an empirically designed, commonly used valve reported previously [6], and referred to as a Tesla-type I valve in that study and here simply referred to as the reference valve. It differed slightly from the Tesla-type I valve, for which the constant radius flow loop intersects the main channel at a right angle. The reference valve flow loop return segments intersected the main channel at approximately nine degrees from perpendicular.

To maximize valve diodicity an object function to be maximized was based on the integral over Reynolds number of the product  $\text{Di}$  and a weighting function,

$$\int_{\text{Re}_{\min}}^{\text{Re}_{\max}} \frac{Di}{(\Delta\tilde{p}_r)^m} d\text{Re}, \quad (5)$$

where in this study  $\text{Re}_{\min}=0$ ,  $\text{Re}_{\max}=2000$ , and  $m=1$ . The weighting function chosen was used to control valve resistance while maximizing diodicity. The values of  $\Delta\tilde{p}_r$  and  $\Delta\tilde{p}_r$  in Eq. (5) were determined from the calculated pressure at the midpoint of the centerline of each plenum shown in Fig. 1. This location was not critical because pressure was relatively uniform over much of each plenum.

**2.4 Valve Sizing.** Valve size was determined by examining multiple pump designs with a previously reported linear model of pump resonance [6], which was in the form of code written in MATLAB (version 6.5, The Mathworks, Inc, Natick, MA). Starting with a particular pump chamber diameter, optimization of other pump parameters was mainly directed toward determining the best combination of actuator geometry (cover plate thickness and piezoelectric element radius and thickness) and valve size. This approach was based on the fact that pump resonance is primarily determined by driving element stiffness and inertance of the fluid in the valves.

For this study the existing linear model was extended to include important voltage-limiting effects. First, cavitation often limits maximum pump performance. In addition, the voltage applied to the piezoelectric element must not cause the electrical field across it to exceed the depolarization level  $E_{\text{depol}}$ . Lastly,  $V_{s,\text{max}}$  is the maximum (zero-to-peak) voltage amplitude generated by the supply amplifier. Based on static cavitation pressure  $P_{\text{cav}}$  in the pump chamber, the maximum possible (or cutoff) voltage  $V_{s,c}$  that can be applied is

$$V_{s,c} = \min \left[ \frac{P_{cm} - P_{\text{cav}}}{P_c}, E_{\text{depol}} t_p, V_{s,\text{max}} \right], \quad (6)$$

where  $P_c$  is the harmonic amplitude of the pump chamber pressure per volt about the time-averaged mean chamber pressure  $P_{cm}$  and  $t_p$  is the piezoelectric element thickness. Since  $P_c$  is a function of frequency, so is  $V_{s,c}$ . It follows that the outlet valve volume flow rate harmonic amplitude, like any other model output variable, also has a frequency-dependent cutoff value

$$Q_{0,c} = V_{s,c} Q_0, \quad (7)$$

where  $Q_0$  is harmonic amplitude of the outlet valve volume flow rate per volt.

The effect of reduced static pressure in the valves due to fluid velocity was also taken into account by replacing the voltage limit due to static cavitation in Eq. (6) with the solution for  $V_s$  in the relation

$$V_s P_c = P_{cm} - \frac{1}{2} \rho (Q_0 V_s / A_v)^2 - P_{\text{cav}}, \quad (8)$$

where  $A_v$  is the cross-sectional area of the valve channels, and where it is assumed the inlet and outlet valves are identical. The result is given by

$$V_{s,c} = \min \left[ \dots \frac{A_v^2 P_c}{\rho Q_0^2} \left( \sqrt{1 + \frac{2\rho Q_0^2}{A_v^2 P_c^2} (P_{cm} - P_{\text{cav}}) - 1} \right), E_{\text{depol}} t_p, V_{s,\text{max}} \right]. \quad (9)$$

For purpose of calculation, Eq. (9) may be an inappropriate form when the dynamic pressure effect approaches zero, which is equivalent to  $\rho$  approaching zero. Taking the limit of this expression as  $\rho \rightarrow 0$  and using a binomial expansion for the radical, Eq. (9) reduces to Eq. (6) to order  $\rho^2$ . Thus the two expressions can be combined based on the value of

**Table 1 Geometric parameters for fabricated pumps. Additional parameters common to all pumps are described in the text.**

Pump ID	Tesla valve type	Valve width $w_v$ ( $\mu\text{m}$ )	Valve aspect ratio $d_v/w_v$	Normalized valve length $L_v/w_v$	Memb. thick. ( $\mu\text{m}$ )
p28	opt	135	2.78	15.5	460
p29	opt	500	2.42	15.5	460
p30	ref	300	2.50	16.7	270
p31	opt	300	2.50	15.5	270

$$\epsilon = \frac{\rho Q_0^2}{A_v^2 P_c} \frac{P_{cm} - P_{\text{cav}}}{P_c}, \quad (10)$$

or

$$V_{s,c} = \begin{cases} \text{Eq. (6)} & \text{if } \epsilon < \epsilon_0 \\ \text{Eq. (9)} & \text{otherwise,} \end{cases} \quad (11)$$

where  $\epsilon_0$  is the smallest number that can be differentiated from unity. Using MATLAB on a Pentium III PC  $\epsilon_0 \approx 2 \times 10^{-16}$ .

With the above performance-limiting effects considered, the linear system model was used to investigate a wide range of membrane thicknesses and valve sizes. As in [6], the electro-mechanical parameters of the piezoelectrically driven membrane were calculated with finite element analysis, and these values were utilized for the linear system model. A three-dimensional model was used to capture the effects of the non-axisymmetric piezoelectric actuator used (see the next section). The valve equivalent lengths, or the straight channel lengths used to represent the valves, were calculated based on an average path between the forward and reverse directions through the valve, as in [6]. Based on the results of the linear model, several pumps were fabricated.

**2.5 Pump Fabrication.** Pumps with 10-mm-diam chambers were fabricated by conventional machining techniques using 125  $\mu\text{m}$  and larger end mills (Kemmer Präzision) and a miniature milling machine (Model 5410, Sherline Products Inc., Vista, CA) modified for computer numerical control (CNC) (Model 999-6100-005, MicroKinetics Corp., Kennesaw, GA). This allowed rapid progression from CAD design to prototype compared to silicon-based micro-fabrication.

Pump chamber and valves were machined in acrylic to equal depths. Polycarbonate membranes were bonded to the housings using a cyanoacrylate adhesive (Loctite 420 Superbond). Piezoelectric wafers 9 mm in diameter and 127  $\mu\text{m}$  thick (PZT-5A, Piezosystems, Cambridge, MA) were bonded to the membranes using the same adhesive. Electrical connections were made to a 1.5-mm-wide "tab" on the piezoelectric driver that extended 2.5 mm beyond the pump chamber. A small pocket was cut through the membrane and into the pump housing below this tab to allow for electrical lead clearance. The pump inlets and outlets were made by gluing 2.08 mm inside diameter stainless steel tubes with a rapid-cure epoxy. Table 1 gives the different geometric parameters for the four pumps constructed and tested in this study. Note that pumps 30 and 31 only differ with respect to valve type.

**2.6 Pump Experiments.** For comparison with CFD results, diodicity versus Reynolds number for pumps 30 and 31 were measured. For each value of  $\text{Re}$ , a syringe pump (Model 200, KD Scientific, Boston, MA) delivered steady flow, and pressure drop was measured with a water column for pressures below 5 kPa, and a pressure transducer (EPI-127, Entran Sensors & Electronics, Fairfield, NJ) for pressures above that value. The resulting pressure drop was divided by two to arrive at  $\Delta p$  across a single valve, assuming each valve experienced the same entry and exit effects

**Table 2 Optimized and reference Tesla-type valve parameters. Linear dimensions are normalized by channel width.**

Valve	$X_2$	$n$	$Y_3$	LENOUT	$R$	$\alpha$	$\beta$	Average Di
Optimized	1.60	0.797	0.608	2.94	2.35	41.9°	71.7°	1.50
Reference	1.50	0.990	0.600	2.00	2.50	45.0°	8.53°	1.21

and negligible pressure drop through the pump chamber. Finally, Di was calculated from measured values for  $\Delta p_r$  and  $\Delta p_f$  according to Eq. (1).

Linear model predictions of membrane velocity resonance were compared to experimental data by measuring the resonance behavior of each pump. First isopropanol alcohol was used for priming. Then each pump was filled by flushing with 10 ml of de-ionized water that had been degassed by boiling for 10 min and cooled to room temperature. Tubes used for filling were disconnected so that menisci of water were visible at the ends of the stainless steel inlet/outlet tubes. The membrane centerline velocity was measured using a laser vibrometer (Model OVF 302, Polytec, Waldbronn Germany), while a signal generator (Model 19, Wavetek, United Kingdom) applied a harmonic input voltage to the pump actuator through an amplifier (EPA-102, Piezosystems Inc., Cambridge, MA).

Finally, to compare pump performance, measurements were made for each pump at two outlet static pressure loads: blocked-flow, i.e., the pressure at which net flow ceased, and no-load flow, both with the inlet held at atmospheric pressure. For blocked-flow the pressure was measured with the pressure transducer, which was connected to the pump outlet with a 5-cm-long piece of tubing having a compliance of approximately  $0.0015 \text{ mm}^3/\text{Pa}$ . Flow rate at zero pressure was measured by inserting the pump inlet tube into a petri dish filled with degassed water, and allowing the outlet tube to discharge to another petri dish on an electronic scale (1205 MP, Sartorius, Westbury, NY) at the same hydrostatic pressure. The time for a change in mass of at least 250 mg to occur was recorded, and the flow rate was calculated using the density of water (taken as  $1000 \text{ kg/m}^3$ ). Performance measurements for a particular supply voltage were made at the highest frequency attained, which corresponded to the frequency at which either cavitation or resonance occurred. The ambient temperature for all tests was  $26 \pm 1 \text{ }^\circ\text{C}$ .

### 3 Results and Discussion

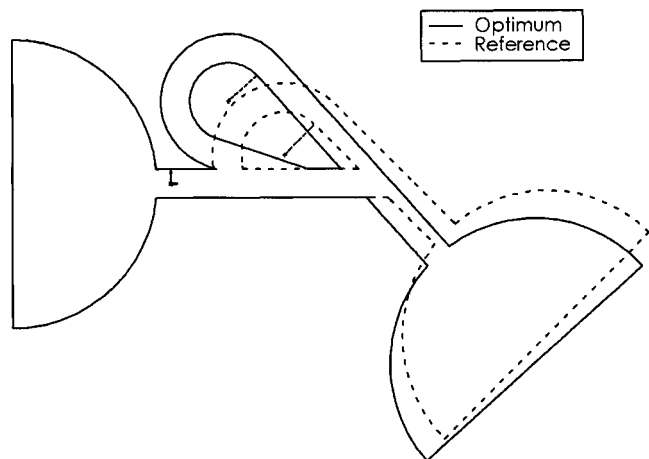
**3.1 Valve Shape Optimization.** The optimization calculations required consideration of up to 40 different sets of design variables. Approximately 1000 separate flow field calculations were performed, each taking from 3000 to 8000 cpu-seconds depending on valve shape. The resulting optimized design variables along with the reference valve geometry are shown in Table 2, and the corresponding shapes in graphic form are shown in Fig. 2. The return angle  $\beta$  (determined by the design variables  $X_2$ ,  $Y_3$ , and  $n$ ) was found to be substantially larger for the optimized valve. Vector plots of the velocity in the loop return region of these valves shown in Figs. 3 and 4 reveal that by increasing  $\beta$ , flow in the loop section is directed to oppose flow in the main channel. This suggests that the losses generated by introducing the fluid with a velocity component opposite to the pressure gradient in the main channel may be important for maximizing diodicity. While this may seem obvious, it should be noted that if this observation is correct, other details of the loop geometry need to be such that significant flow occurs in the loop during the reverse flow period. More work is necessary to understand this more fully, as the optimized Tesla-type valve appears to be a subtle balance of channel lengths and orientations.

Figure 5 shows the CFD results for  $\Delta p_r$  and  $\Delta p_f$  dimensionalized for the size of the valves used in pumps p30 and p31 in accordance with Eq. (2) and properties of water at  $25 \text{ }^\circ\text{C}$ . The

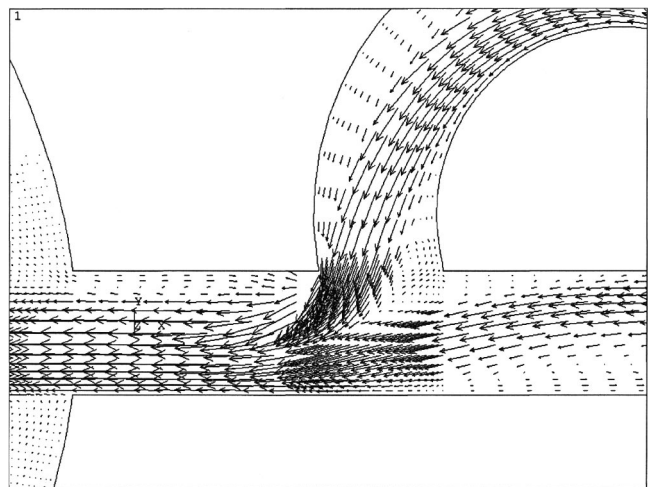
optimized valve was found to have a significant increase in  $\Delta p_r$  with little difference in  $\Delta p_f$  compared to the reference valve. For the optimized valve  $\Delta p_r$  was over 30% higher for  $1000 < \text{Re} < 2000$ , while  $\Delta p_f$  was consistently within 1–2% of the reference valve values. This behavior may be the result of the weighting function used in the object function Eq. (5), incorporated to minimize losses in the forward direction. Thus, the weighting function chosen was successful in controlling a specific fluid dynamic characteristic while diodicity was optimized.

The experimental results for forward and reverse steady flow pressure drop are shown in Fig. 6 for devices p30 and p31. The qualitative agreement with the calculated values shown in Fig. 5 is good. And, as was seen with the CFD calculations, the optimized valves showed a significant increase in  $\Delta p_r$  with little difference in  $\Delta p_f$  compared to the reference valve.

The graph of diodicity versus Reynolds number for the optimized and reference valves is shown in Fig. 7. Calculated diodic-



**Fig. 2 Optimized and reference Tesla-type valve**



**Fig. 3 Vector plot of the velocity in the flow loop return region of the reference valve**

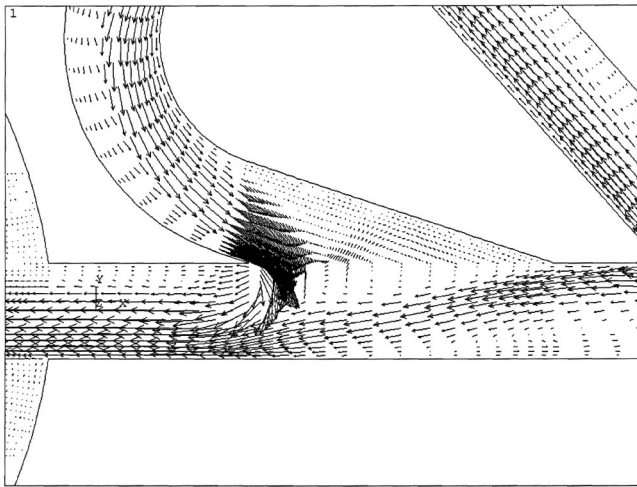


Fig. 4 Vector plot of the velocity in the flow loop return region of the optimized valve

ity increased by a maximum of 37% at  $Re=2000$  and by an average of 25% over the range  $0 < Re < 2000$ , and similar results are apparent from the experimental data. However, while the degree of improvement is quite similar for both calculated and measured results, there are distinct differences in the shape of the curves. The measured values for the optimized valve are significantly higher than those calculated for  $Re < 500$ , and a similar behavior may exist for the reference valve. In addition, the measured diodicity for the reference valve does not monotonically increase, a behavior seen in all three of the other curves.

The primary reason for differences between calculated and measured diodicity is most likely related to the limitations of the two-dimensional (2-D) modeling. A physical argument for the 2-D calculations predicting higher diodicity than measured is that loss mechanisms in the Tesla-type valve may be primarily due to out-of-plane vorticity, which may be overestimated in the 2-D model. However, this cannot explain the behavior at lower Reynolds number. Additional three-dimensional (3-D) modeling is necessary to understand these differences more fully. Nevertheless, the results shown in Fig. 7 demonstrate the ability of 2-D modeling to improve valve performance.

It should be noted that in this study the Reynolds number range was  $0 < Re < 2000$ . However, depending on pump chamber size

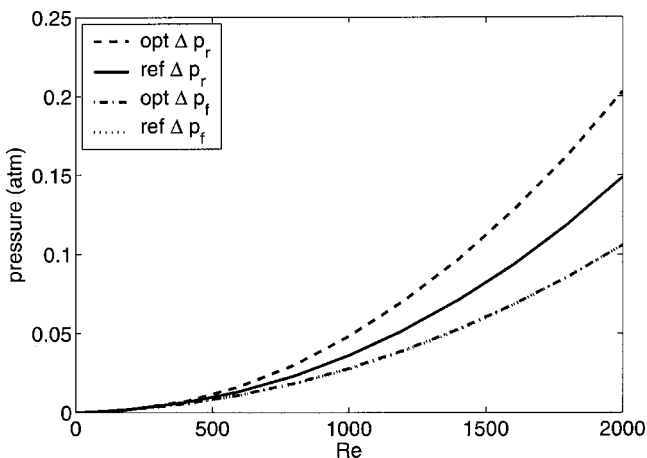


Fig. 5 Calculated reverse and forward pressure drop for the optimized (opt) and reference (ref) Tesla-type valves, based on 2-D CFD results for  $w_v=300 \mu m$  and water at  $25^\circ C$ . Note the curves for forward flow are nearly identical.

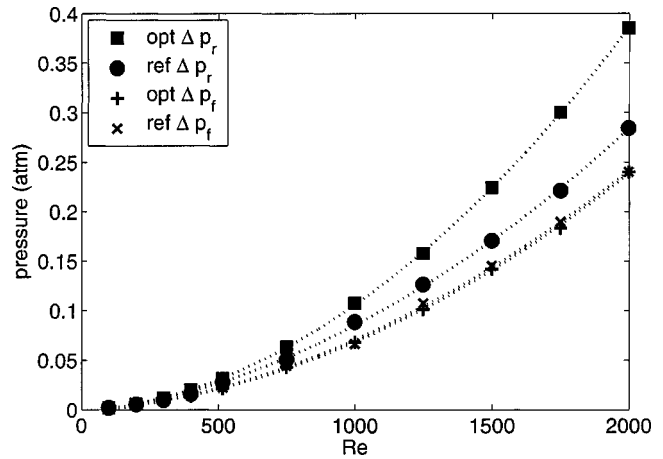


Fig. 6 Measured reverse and forward pressure drop for the optimized (opt) and reference (ref) Tesla-type valves, for devices p30 and p31 and water at  $25^\circ C$ . The dotted curves are second-order polynomials fit to the data for use in estimating diodicity versus Reynolds number

and expected flow rates, the range of  $Re$  considered for shape optimization could be matched to actual values through an iterative process. This may be a fruitful approach since the shape optimization process could yield different results depending on the range considered.

**3.2 Valve Sizing.** The linear pump model based on reduced-order parameters allowed for the consideration of multiple design cases and revealed many interesting results about valve size in terms of the amplitude of various harmonic output parameters per unit input voltage and at maximum possible input voltage. Figure 8 shows the membrane velocity amplitude per unit input voltage versus valve width and membrane thickness for a 10-mm-diam polycarbonate membrane, with a 2.5 valve depth-to-width aspect ratio, a chamber depth equal to the valve depth, and a length-to-width ratio of 16, a value between that of the optimized and reference valve (see Table 1). The results in Fig. 8 ignore the voltage limitation effects. Larger membrane thickness yields larger membrane velocities for a given valve size. This is consistent with past findings on the importance of stiff membranes [10]. In addition, larger valve size for a given membrane thickness also yields higher membrane velocity due to lower valve resistance. All other

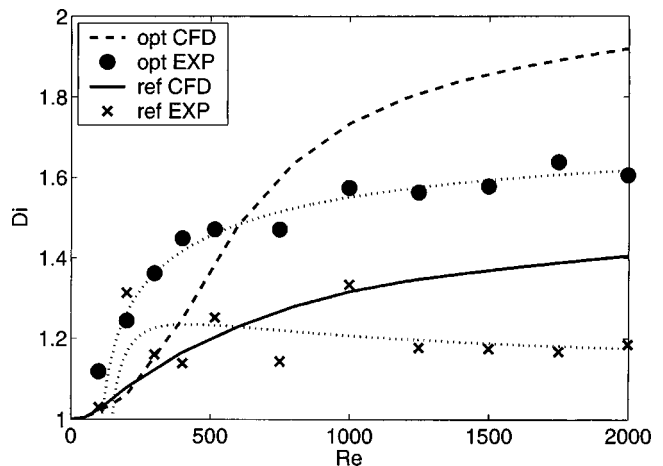
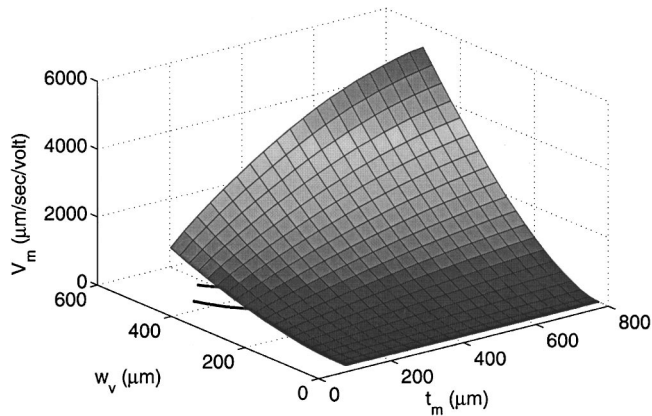


Fig. 7 Comparisons of calculated (CFD) and measured (EXP)  $Di$  versus  $Re$  for the optimized (opt) and reference (ref) Tesla-type valves. The dotted curves are calculated diodicity based on the polynomials fit to the data shown in Fig. 6.

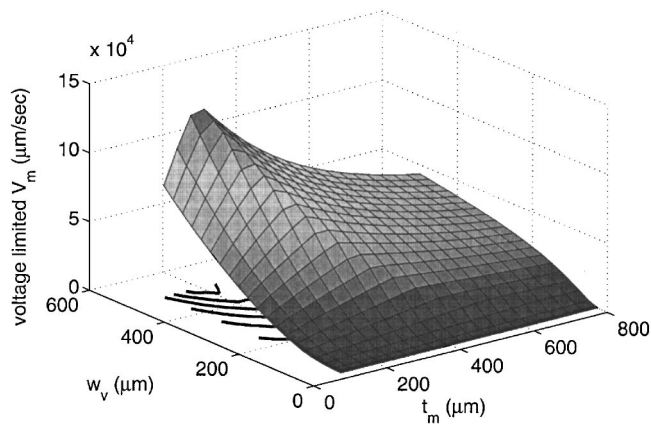


**Fig. 8** Membrane velocity harmonic amplitude  $V_m$  versus valve width  $w_v$  and polycarbonate membrane thickness  $t_m$  for a 10-mm-diam pump with a 2.5 valve depth-to-width aspect ratio, a chamber depth equal to the valve depth, and a valve length-to-width ratio of 16. The piezoelectric element size was held constant at 9 mm in diameter and 127  $\mu\text{m}$  thick. Each point on the surface corresponds, in general, to a different driving frequency.

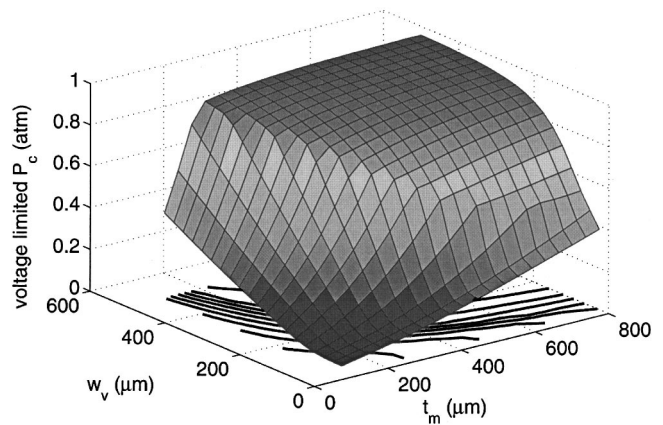
model output parameters followed these two trends of higher values with thicker membranes and larger valves when considered on a per unit voltage basis.

Significantly different design surfaces resulted when the voltage was limited according to Eq. (11). This is seen in Fig. 9, which shows membrane velocity harmonic amplitude corresponding to the maximum input voltage possible, which in general is different at each design point. Figure 10 shows the corresponding chamber pressure harmonic amplitude, which exhibits a large “shelf” across much of the design space at a value of approximately 1 atm. This indicates that pumps built within that region are predicted to have cavitation as the limiting factor and that the response surfaces for all output parameters in that region will be affected. In the case of membrane velocity the peak value occurred at the edge of the “shelf” where valve size was large and membrane thickness was low, whereas without voltage limitations considered it occurred at large valve size and large membrane thickness.

Figure 11 shows the voltage-limited harmonic amplitude of valve Reynolds number as a function of valve width and mem-



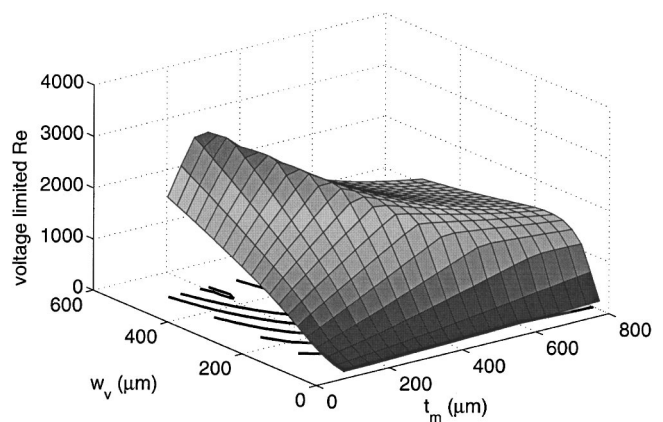
**Fig. 9** Voltage-limited membrane velocity harmonic amplitude versus valve width and polycarbonate membrane thickness for the same combination of parameters as in Fig. 8. The voltage limits account for a 180 V supply maximum, a depoling electric field of  $5 \times 10^5$  V/m, and a cavitation pressure equal to vapor pressure at 25 °C.



**Fig. 10** Voltage-limited chamber pressure harmonic amplitude versus valve width and polycarbonate membrane thickness for the same combination of parameters as in Fig. 8. The voltage limits were accounted for in the same way as in Fig. 9.

brane thickness. This parameter was derived from the voltage-limited valve flow rate harmonic amplitude according to the expression  $Re = \rho Q_0 D_h / A_v \mu$ . It should be an important parameter on which to optimize net pump performance in terms of net flow and net pressure, given that the results from CFD calculations and experiment show higher diodicity with increasing Reynolds number as shown in Fig. 7. The maximum value of Reynolds number harmonic amplitude shown in Fig. 11 occurs in the region of larger valve size and smaller membrane thickness. It is reasonable to expect the maximum value in this region, because the lower flow restriction of larger valves allows the volume flow rate induced by the membrane motion to be translated into valve flow rather than compression of compliance elements, such as gas in the working fluid, and the lower flow resistance results in less system damping and consequently higher resonant amplitudes. However, eventually the valves become so large that the resonant amplitude of membrane motion and the ensuing valve flow rate falls due, in part, to the lower inertance of larger valves that plays an important role in system resonance. Additionally, Reynolds number is inversely proportional to valve size for the same flow rate. Thus, sizing valves for maximum Reynolds number alone should lead to good net flow rate performance but only at low net pressure head.

The above-described situation is reversed for stiffer membrane



**Fig. 11** Voltage-limited valve Re harmonic amplitude versus valve width and polycarbonate membrane thickness for the same combination of parameters as in Fig. 8. The voltage limits were accounted for in the same way as in Fig. 9. The maximum is near  $[t_m, w_v] = [400, 200]$   $\mu\text{m}$ .

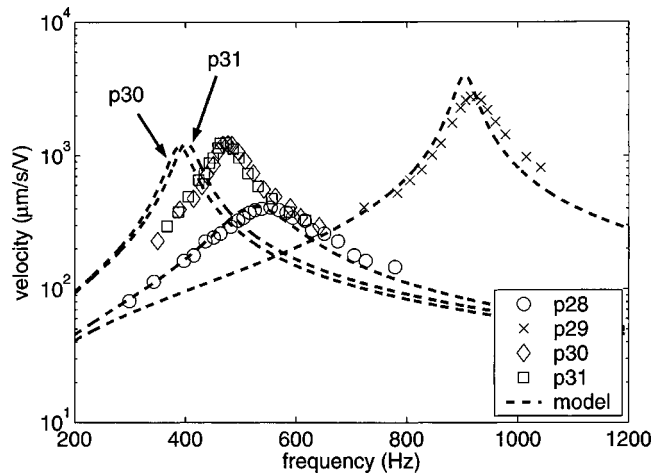


**Fig. 12** A 10 mm pump chamber with 300- $\mu\text{m}$ -wide optimized Tesla valves from Table 2. The pump body is acrylic, and a PZT-5A actuator is bonded to a 270- $\mu\text{m}$ -thick polycarbonate membrane. The electronic computer chip indicates its intended application.

and smaller valve size, which are expected to generate a lower net flow but higher net pressure at the same cavitation-limited chamber pressure amplitude. From Fig. 11 it is seen that the maximum Reynolds number for any valve size occurs along a ridge that runs from large valve size and small membrane thickness to small valve size and large membrane thickness, which corresponds to the boundary of the cavitation region shown in Fig. 10. Thus, from the results of the linear system model, it is expected that the nonlinear effect of valve diodicity for combinations of valve size and membrane stiffness that lie along the ridge will result in pump performance in terms of high no load flow, high block load pressure or optimal combinations of these two extremes. In other words, utilizing the ridge may allow customizing net pressure versus net flow performance for particular applications. Because of the potential for optimal pumps in this sense, pumps were built with different membrane thickness and valve size to investigate combinations of valve size and membrane thickness between the opposite corners of the design space.

**3.3 Pump Resonance and Performance.** The four pumps in this study were chosen to have a variety of parameter combinations. Figure 12 shows the pump identified as p31. This pump, as well as each pump from Table 1, was tested at both low voltage for resonant behavior and at high voltage for pump performance. The measured resonant behavior at low voltage is shown in Fig. 13 where it can be seen that good agreement was obtained for the model predictions of membrane velocity for each of the design parameter combinations. The disagreement in predicted frequency for devices p30 and p31 was well within reason considering that model predictions were made entirely based on first principles [6]. It is also seen that pumps p30 and p31 had very similar linear behavior when viewed as pairs of model predictions or measured results. This was apparently the result of the fact that their different shapes caused only a small difference in average path length-to-width ratio, 15.5 for the optimized valve and 16.7 for the reference valve.

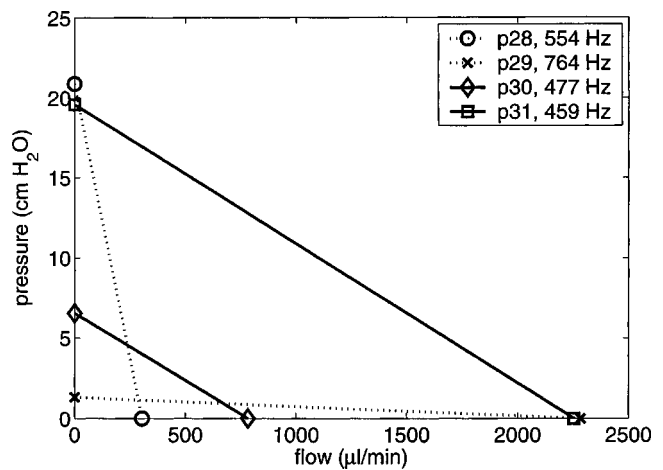
The measured high-voltage pump behavior is shown in terms of pump performance Fig. 14. Conclusions may be drawn about the three pumps with the same valve shape but with different valve



**Fig. 13** Measured membrane centerline velocity-per-volt (symbols) compared with model predictions (---) for all pumps in Table 1. Actuation voltage for the measurements was approximately 3 V peak-to-peak.

sizes and membrane thicknesses. The behavior of pump p28 relative to pump p29 indicates that the former did better in net pressure but poorer in net flow, consistent with the argument presented in the previous section. It was somewhat surprising that p31 produced a performance curve that equaled the block load pressure of p28 while producing significantly better no load flow. This may be an indication that pumps corresponding to the ridge of the Re surface in Fig. 11 represent good designs, but the trade-off between pressure and flow performance is not completely understood. Future work should aim to accurately quantify the predictions of net flow and pressure from the linear model, so that a pump may be more accurately designed for desired performance in terms of both pressure and flow.

Most notable of the results shown in Fig. 14 is the comparison between pumps p30 and p31. Pump p31 was nearly identical to p30 in terms of the linear model parameters characterizing it as demonstrated in Fig. 13. Yet pump p31 with shape optimized valves is seen to have nearly three times the performance of pump p30 at approximately the same driving level in terms of both pressure and flow developed. This result is qualitatively consistent



**Fig. 14** Measured pressure-flow pump performance curves for the pumps shown in Table 1 at approximately 120 V peak-to-peak and the highest frequency at which each pump successfully operated. Lines are drawn between points for clarity. The performance enhancement between p30 and p31, made possible by valve shape optimization, is clearly shown.

with even the simplest models relating net flow to diodicity, which show that for values of diodicity less than two, small improvements in diodicity lead to relatively large improvements in net flow rate ([3], Fig. 1). The fact that the improvement was so large could be due to effects caused by unsteady flow that were not included in the quasi-steady valve flow calculations. Nevertheless, the measured improvement validates the approach used in this study to determine *how* to achieve higher diodicity for improved pump performance.

#### 4 Conclusions

A design process for optimizing fixed-geometry valve shape and size was accomplished. Optimization of valve shape using CFD that incorporated automatic search methods was demonstrated on a Tesla-type valve with a significant increase in calculated diodicity compared to a commonly used reference valve over the range Reynolds number  $0 < Re \leq 2000$ . The calculated results compared favorably with experiment. A linear system model was used to determine valve size and membrane thickness for best pump performance. Pump fabrication techniques utilizing CNC machining of acrylic plastic were introduced as a rapid micropump prototyping technique. Measurements made on the fabricated pumps showed that net pressure and flow for a pump with optimized valve shape was nearly three times larger than that for an identical pump but with valves of non-optimized shape.

This study also demonstrated the value of the linear model used in that it was originally developed for silicon/Pyrex fabrication, but was used successfully in this study for designs in acrylic/polycarbonate, which have significantly different material properties. And the basic simplicity of fabrication for NMPV pumps was demonstrated by the ease with which we were able to fabricate pumps using new materials.

#### Acknowledgments

This work was supported in part by a subcontract from NASA Goddard Space Flight Center contract NASS-03059 awarded to MicroEnergy Technologies Inc., Washington Technology Center Research Technology Development Agreement WTC FTI 03-10, a fellowship from the University of Washington Graduate Opportunities & Minority Achievement Program, and a grant from the Hispanic Scholarship Fund.

#### Nomenclature

$A_v$	= valve cross-sectional area (m <sup>2</sup> )
$D_h$	= valve hydraulic diameter $2(w_v d_v)/(w_v + d_v)$ (m)
$Di$	= steady-state valve diodicity $\Delta p_r/\Delta p_f$
$d_v$	= valve depth (m)
$E_{\text{depol}}$	= piezoelectric depolarization limit $[5 \times 10^5 \text{ V/m}]$
$L_v$	= valve length (m)
LENOUT	= valve outlet segment length (m)
$n$	= $nX_2$ is a coordinate location for the valve loop straight segment (see Fig. 1)
$p$	= pressure (Pa)
$P_c$	= amplitude of harmonic chamber pressure about $P_{cm}$ (Pa)
$P_{cm}$	= temporal mean (dc) chamber pressure (Pa)
$Q_0$	= amplitude of harmonic volume flow rate through outlet valve (m <sup>3</sup> /s)
$\mathbf{r}$	= position vector (m)
$R$	= valve loop segment outer radius (m)

$R_p$	= plenum radius (m)
$Re$	= valve Reynolds number $\rho U D_h/\mu$
$t_m$	= cover plate (membrane) thickness (m)
$t_p$	= piezoelectric element thickness (m)
$u$	= velocity (m/s)
$U$	= valve characteristic velocity (m/s)
$V_m$	= amplitude of harmonic velocity of membrane centerline velocity (m/s)
$V_s$	= supply voltage (V)
$w_v$	= valve width (m)
$X_2$	= valve inlet segment length (m)
$Y_3$	= a coordinate location for the valve loop straight segment (see Fig. 1) (m)
$\alpha$	= valve outlet segment angle
$\beta$	= valve loop return segment angle
$\mu$	= absolute viscosity (Pa s)
$\mu_{\text{CFD}}$	= CFD model viscosity (Pa s)
$\rho$	= density (kg/m <sup>3</sup> )
$(\bar{\quad})$	= non-dimensional quantity
$(\quad)_f$	= forward direction
$(\quad)_r$	= reverse direction

#### References

- [1] Stemme, E., and Stemme, G., 1993, "A valveless diffuser/nozzle-based fluid pump," *Sens. Actuators, A*, **39**, pp. 159–167.
- [2] Gerlach, T., and Wurmus, H., 1995, "Working principle and performance of the dynamic micropump," *Sens. Actuators, A*, **50**, pp. 135–140.
- [3] Forster, F., Bardell, R., Afromowitz, M., and Sharma, N., 1995, "Design, fabrication and testing of fixed-valve micropumps," in *Proceedings of the ASME Fluids Engineering Division 1995*, San Francisco, D. C. Wiggert et al. (Eds.), ASME, Vol. FED-234, pp. 39–44.
- [4] Jang, L.-S., Morris, C. J., Sharma, N. R., Bardell, R. L., and Forster, F. K., 1999, "Transport of particle-laden fluids through fixed-valve micropumps," in *Micro-Electro-Mechanical Systems (MEMS)*, 1999 ASME International Mechanical Engineering Congress and Exposition, A. P. Lee et al. (Eds.), Vol. MEMS-1, pp. 503–509.
- [5] Jang, L.-S., Sharma, N. R., and Forster, F. K., 2000, "The effect of particles on the performance of fixed-valve micropumps," in *Micro Total Analysis Systems 2000*, A. van den Berg, W. Olthuis, and P. Bergveld (Eds.), pp. 283–286.
- [6] Morris, C. J., and Forster, F. K., 2003, "Low-order modeling of resonance for fixed-valve micropumps based on first principles," *J. Microelectromech. Syst.*, **12**(3), pp. 325–334.
- [7] Williams, B. E., and Forster, F. K., 2001, "Micropump design for optimum pressure/flow characteristics," in *Micro-Electro-Mechanical Systems (MEMS)*, ASME International Mechanical Engineering Congress and Exposition, A. P. Lee (Ed.), ASME, Vol. MEMS-3, pp. 647–655.
- [8] Gamboa, A. R., Morris, C. J., and Forster, F. K., 2003, "Optimized fixed-geometry valves for laminar flow micropumps," in *Proceedings of the ASME Fluids Engineering Division 2003* (Washington, DC), Vol. FED-259, pp. 525–534.
- [9] Morris, C. J., and Forster, F. K., 2004, "Oscillatory flow in microchannels: Comparison of exact and approximate impedance models with experiment," *Exp. Fluids*, **36**(6), pp. 928–937.
- [10] Tesla, N., 1920, "Valvular Conduit," U.S. Patent No. 1,329,559.
- [11] Groisman, A., and Quake, S. R., 2004, "A Microfluidic Rectifier: Anisotropic Flow Resistance at Low Reynolds Numbers," *Phys. Rev. Lett.*, **92**(9), pp. 094501.
- [12] Olsson, A., Enoksson, P., Stemme, G., and Stemme, E., 1995, "A Valve-less Planar Pump in Silicon," in *Transducers '95* (Stockholm), Vol. 2, pp. 291–294.
- [13] Olsson, A., Stemme, G., and Stemme, E., 1999, "Numerical Simulations of Flat-Walled Diffuser Elements for Valveless Micropumps," in *Proceedings of the Microsystems Modeling Conference*, pp. 585–588.
- [14] Forster, F. K., and Williams, B. E., 2002, "Parametric design of fixed-geometry microvalves—the Tesser valve," in *Proceedings of the ASME Fluids Engineering Division*, International Mechanical Engineering Congress and Exposition, A. Ogut (Ed.), ASME, Vol. FED-258, pp. 431–437.
- [15] Bardell, R., Sharma, R., Forster, F. K., Afromowitz, M. A., and Penney, R., 1997, "Designing high-performance micro-pumps based on no-moving-parts valves," in *Micro-Electro-Mechanical Systems (MEMS)*, ASME International Mechanical Engineering Congress and Exposition (Dallas), L. Lin, K. E. Goodson et al. (Eds.), ASME, Vol. DSC-234/HTD-354, pp. 47–53.



Mei Feng<sup>1</sup>  
Jaime Gonzalez  
James A. Olson

Pulp and Paper Centre and Department of  
Mechanical Engineering, The University of British  
Columbia, 2385 East Mall, Vancouver BC,  
Canada, V6T 1Z4

**Carl Ollivier-Gooch**  
Department of Mechanical Engineering,  
The University of British Columbia,  
2324 Main Mall, Vancouver BC,  
Canada, V6T 1C4

**Robert W. Gooding**  
Advanced Fiber Technologies (AFT) Inc.,  
Montreal QC, Canada, H4A 1G2

# Numerical Simulation and Experimental Measurement of Pressure Pulses Produced by a Pulp Screen Foil Rotor

*Pressure screening is an efficient means of removing various contaminants that degrade the appearance and strength of paper. A critical component of a screen is the rotor, which induces a tangential velocity to the suspension and produces pressure pulses to keep the screen apertures clear. To understand the effect of key design and operating variables for a NACA foil rotor, a computational fluid dynamic (CFD) simulation was developed using FLUENT, and the results were compared to experimental measurements. Comparing the pressure pulses obtained through CFD to experimental measurements over a wide range of foil tip speeds, clearances, angles of attack, and foil cambers, general trends of the pressure pulses were similar, but the overall computed values were 40% smaller than the measured values. The pressure pulse peak was found to increase linearly with the square of tip speed for all the angles of attack studied. The maximum magnitudes of negative pressure pulse occurred for the NACA 0012 and 4312 foils at a 5 deg angle of attack and for the NACA 8312 foil at 0 deg. The stall angle of attack was found to be ~5 deg for NACA 8312, ~10 deg for NACA 4312, and ~15 deg for NACA 0012. The positive pressure peak near the leading edge of the foil was eliminated for foils operating at a positive angle of attack. The magnitude of the negative pressure coefficient peak increased as clearance decreased. Increased camber increases both the magnitude and width of the negative pressure pulse. [DOI: 10.1115/1.1881672]*

## Introduction

Pulp screens are used in virtually all pulp and paper operations worldwide. Pressure screening is the most industrially effective means of removing oversized contaminants that can degrade the appearance and strength of paper. Pressure screens are increasingly used to fractionate fibers by length so that the long or short fiber streams can be processed separately or used in high-value paper grades. For these reasons, pressure screens are assuming a special importance in the production of mechanical and recycled pulps, as well as for the manufacture of high-quality mechanical printing papers.

Pulp screens divide a contaminated feed flow into an accept stream of clean pulp and a reject stream laden with contaminants. During screening, the pulp and contaminants typically enter the screening zone tangentially. The pulp suspension flows between a rotor and the inlet side of a cylindrical screen. The fibers flow through the apertures in the screen cylinder and exit through the accept port. The oversized particles and a fraction of the long fibers are retained by the screen cylinder and travel down the annulus, leaving the screen through the reject port. To prevent the apertures from becoming plugged by the fibers, foils are passed over the feed side of the screen surface to create negative pressure pulses that backflush the apertures. The screen rotor comprises the foils, or some other pulse-inducing hydrodynamic elements, and the support structure.

The rotor plays a critical role in screen operation. Despite various differences in rotor design, all rotors serve two main functions. One function is to accelerate the pulp suspension on the

feed side of the screen to a high tangential velocity. This induces turbulence at the surface of the screen plate, which mixes the suspension and keeps the pulp fluidized. The second, and more important, function is to create a negative pressure pulse that backflushes the screen apertures, clearing any fiber accumulations and preventing plugging of the apertures.

The principal measures of screen performance are (i) contaminant removal efficiency, defined as the mass percentage of contaminants leaving the screen through the reject port relative to that entering the screen; (ii) capacity, the maximum mass flow rate of pulp in the accept stream; (iii) power consumption, the power consumed by the rotor normalized by the accept mass flow rate of fibers; and (iv) reject rate, the mass flow of fibers rejected with the contaminants. Achieving high capacity and high efficiency with reduced power consumption at a low reject rate is the goal of an optimal screen design.

Although rotor design is critical in determining pulp screen performance, the mechanism of pressure pulse generation and the factors that affect the magnitude and shape of the pressure pulse are not well understood. To better understand the critical rotor design factors affecting screen performance, computational fluid dynamics (CFD) was used to analyze the complex flow created by the rotor. In particular, this study considered how the key design and operating variables (i.e., rotational speed, clearance, angle of attack and camber of a NACA foil rotor) influence the pressure pulse at the screen plate surface. The numerical results were also compared to experimental measurements. This information provides a basic physical understanding of rotor performance and provides an experimentally validated computational tool for optimal rotor design.

## Literature Review

The pressure pulse generated by a foil rotor has been the subject of little published research. However, a few studies have given quantitative information about the effect of rotor design

<sup>1</sup>Now with Temec Engineering Group Ltd. Suite 375, 6450 Roberts St., Burnaby, BC, Canada, V5G 4E1

Contributed by the Fluids Engineering Division for publication in the JOURNAL OF FLUIDS ENGINEERING. Manuscript received by the Fluids Engineering Division August 11, 2003; revised manuscript received October 29, 2004. Review conducted by H. Johari.

parameters. The literature review given here represents the development of experimental and computational studies on rotor design in the pulp and paper industry.

Some experimental studies have been conducted to explain how screening performance is affected by the pressure pulse generated by the rotor. According to Niinimäki and Dahl [1], pressure pulses influence screening in two ways. First, the suction pressure pulses keep the screen apertures unplugged by disrupting the fiber mat and lifting the lodged particles away from apertures into the turbulent zone above the screen plate. Also, the suction pulses move a considerable amount of water and fines from the accept chamber back into the screen basket, and thus dilute pulp on the inner surface of the screen basket. According to Cox and Fredriksson [2], dewatering or thickening occurs during the phase of positive flow through the screen plate. This loss of water is compensated by filtrate recovered from the accept side of the screen basket by a long suction pulse. The amount of filtrate recovered can be controlled by the intensity and duration of the suction pulse.

Further experimental studies have been done on the factors that influence the shape and magnitude of the rotor pressure pulse and the effect of these pulse parameters on screen performance. Levis [3] studied the pressure pulse created by a foil-type rotor for screening of secondary fibers. He stated that the magnitude and shape of the pressure pulse were dependent on the foil shape, tip speed, and clearance between the foil and the screen cylinder. Levis suggested that as rotor speed was increased, the magnitude of the pressure pulse increased. Furthermore, he hypothesized that higher pulse magnitudes decreased the contaminant removal efficiency but increased the maximum capacity of the screen. He showed that a critical tip speed existed after which no further increase in capacity was achieved by increasing the rotor speed. Repo and Sundholm [4] investigated the effect of rotor speed on separation of coarse fibers in a pressure screen. Their experimental results indicated that decreasing rotor speed reduced the mass reject rate and improved separation efficiency compared to a higher speed. Gooding [5] measured the pressure pulse in an industrial Hooper PSV 2100 pulp screen. His results showed that increasing rotor speed strongly increased pulse strength. Although increased rotor speed shortened the duration of the pulse, the shape of the pulse was relatively unchanged. Increasing the speed of the rotor can consume significantly more power. Levis [3] found that the consumed power increased with rotor tip speed to the power of 2.5. Niinimäki [6] presented the power consumption measured at different rotor speeds and pulp consistencies. He showed that power consumption increased as rotating speed increased and consistency had only a small effect on power consumption.

Typical experimental studies on the effects of clearance and foil angle of attack were reported by Yu and DeFoe [7] and Niinimäki [6]. Yu and DeFoe [7] studied the pressure pulse signatures for a foil rotor and contoured drum rotor. The results of Yu and DeFoe showed a significant decrease in pulse magnitude for foil-type rotors when clearance increased. Niinimäki [6] reported the effects of clearance between the foil and screen surface on screen performance. As the clearance was reduced, the magnitude of the pulse increased, so screening efficiency decreased and capacity increased. He found that changes in foil angle of attack had a significant effect on screen performance. Furthermore, he showed that a greater angle of attack reduced the screening efficiency markedly with a corresponding increase in screen capacity. In addition, Niinimäki suggested that screen performance can be optimized by adjusting the foil angle of attack, especially if screening at higher consistencies.

The interaction between the fibers makes the flow behavior of pulp suspensions quite different from water. It was shown experimentally by Gonzalez [8] and Wikström [9] that the magnitude of pressure pulses decrease as the consistency increases.

A significant number of CFD studies examined the flow around a two-dimensional (2D) foil. Although there are still challenges

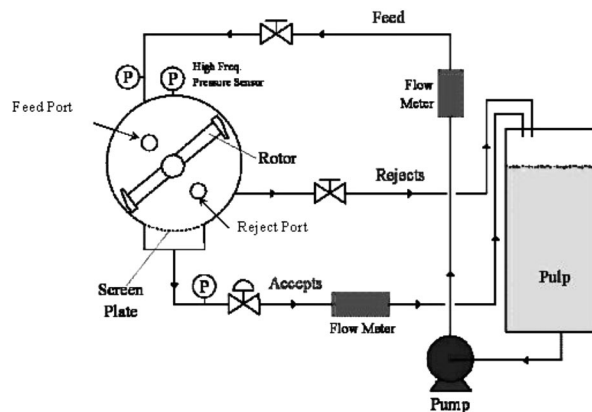


Fig. 1 Schematic diagram of cross-sectional screen

for CFD prediction of turbulent shear and separation, computations can generally predict surface pressures, velocity profiles, skin friction, lift, and drag with reasonably good accuracy at angles of attack below stall. Standard CFD methods provide reasonable prediction of flow variations with Reynolds numbers below stall, but predictions of when stall occurs are inconsistent and the skin friction predictions are often too high. Even with these limitations, CFD is a powerful technique for industrial equipment design and optimization.

Despite a rapid and substantial increase in the use of computer simulation in the pulp and paper industry in recent years, little CFD research has been done to study the pressure pulse generated by foil-type rotors. One useful study in this area was made by Karvinen and Halonen [10] who assessed rotor pressure pulsations using experimental and computational techniques. They found that the backflushing action of the pressure pulse was created by the acceleration of the flow through the gap between the moving rotor tip and stationary screen plate. This acceleration caused the local pressure on the feed side of the screen plate to decrease to the point that the flow through the aperture reversed. The flow then passed from the accept side of the screen plate to the feed side and released any plugged fibers. They used numerical methods to calculate the turbulent velocity field in a clearance between the rotating foil and screen basket and to simulate the pressure pulse generated in a screen. Their results showed that the foil shape greatly affected the form of pressure pulse. In addition, they found that the peak-to-peak pressure difference (maximum pressure minus minimum pressure) increased rapidly with increased rotational speed.

Marko and LaRiviere [11] used CFD software to model a 2D slice of an industrial pressure screen. Their results showed that the pressure pulse signatures had a reasonable correlation between the measurements and numerical predictions. It was found that mesh shape and density were very important to provide a good correlation with experimental results. Wikström [9] investigated the hydrodynamics inside a pulp screen using commercial CFD simulation software. Although the general flow behavior was captured well, pressure pulse data showed a deviation in absolute values when comparing simulations and experiments for water. CFD model overestimated the magnitude of pressure pulses, and simulation showed a delay in pressure drop at the beginning of the pulse.

None of the CFD studies on pressure-pulse generation included the detailed information required to evaluate the quality of the CFD analysis. Moreover, while several studies have compared foil shapes, none has examined a generic foil shape and considered how parameters affect flow patterns and the pressure pulse.

This work focuses on examining the pressure produced on the surface of a screen cylinder. We do not include the details of the cylinder because the geometry of the cylinder varies significantly

between manufacturers and applications. We consider a simple smooth surface to represent the cylinder. In addition, we assume that no flow is going through the cylinder for two reasons: (i) we consider the flow through the cylinder to be small with respect to the tangential velocity and (ii) we are specifically interested in the pressure that can be generated at the point where the cylinder is plugged with pulp fibers and there is no longer any fluid flow through the cylinder.

## Experimental Apparatus

The pressure pulses induced by foil rotors were measured for a wide range of design and operating variables. These measurements were of interest in their own right, but also served as a basis to validate the subsequent CFD solutions.

A laboratory cross sectional screen (CSS) was designed to simulate a slice of an industrial PSV 2100 pressure screen, as has been done in several experimental studies (e.g., [8,12–14]). Figure 1 shows a schematic of the flow loop and the principal components of this apparatus. The CSS test section has a diameter of 30 cm and depth of 5 cm. A 6 cm wide removable screen cylinder coupon is located in the bottom wall, with the remaining circumference a solid wall. The flow loop consists of a 150 l reservoir tank, a mixer, pump, two flow meters, two pressure transducers, valves, and PVC piping. A flow meter and pressure sensor are installed in both the feed and reject lines to monitor flow rate and pressure. The test fluid (in this study water) flows through a 25 mm diameter round pipe and flow meter and then enters the CSS through the feed port at the upper part of the CSS. Some of the suspension flows out through the openings of the slot coupon (i.e., the accept flow). The accept flow is approximately zero for this study. The rest (i.e., the reject flow) leaves the test section through the reject port and flows back to the reservoir tank.

A high-speed data acquisition system was used to record the form of the pressure pulsations. In particular, a high-frequency, 4 mm diameter pressure transducer was installed flush with the inside (feed) surface on the top wall of the CSS. This top wall represents the screen cylinder in an industrial pressure screen.

The pressure sensor was a strain-gage-based transducer with a specified accuracy of less than  $\pm 0.5\%$ . The pressure transducer was calibrated with a standardized static pressure calibrator to ensure the measurement bias is less than 0.5% of the maximum pressure. The measured pressure was fluctuating due to the turbulent motion of the fluid. The standard deviation is 3 kPa, which corresponds to a pressure coefficient fluctuation of 0.074 at the lowest rotor velocity of 9 m/s. To more accurately estimate the mean pressure profile, 120 pulses were averaged to provide a 95% confidence interval in the measured  $C_p$  of  $\pm 0.006$ .

An optical encoder, with a resolution of 2048 signals per revolution, was installed on the shaft of the rotor to precisely measure the position of the rotor. The rotary position sensor locates the position of the rotor to within an arc length of 0.5 mm. The resulting foil position is then  $\pm 0.25$  mm or in terms of chord length is  $\pm 0.625\%$  of chord for the 40 mm long foils used in this study. The position sensor is continuously recorded by the data acquisition system to provide a highly accurate rotational speed and foil tip speed. Tip speed is estimated to have an accuracy greater than  $\pm 0.1\%$ .

The CSS has been designed to measure the effect of some key operating and rotor design variables on screen performance and pulse generation. Figure 2 shows a schematic of the foil and defines the angle of attack and clearance. The rotor is driven by a 7.5 kW electric motor, controlled by a variable frequency drive. The gap between the outer wall and the foil was set using machine calipers and is extremely accurate. The estimate of the error is less than 0.05 mm. The accuracy of the measured angle of attack is estimated to be approximately  $\pm 0.1$  deg. Angle was also set using machined calipers.

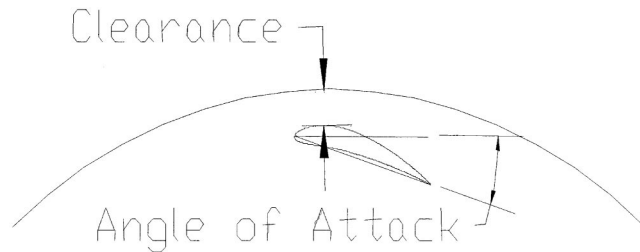


Fig. 2 Schematic of foil showing angle of attack and clearance

## CFD Model

CFD evaluations were conducted to extend and support the experimental measurements and to provide a more complete understanding of how some key rotor parameters affect the flow structures around the foil and the resulting pressure pulse profile. Numerical results were used to establish the relationship between the pressure pulse shape and rotor design and operating variables (e.g., rotating speed, angle of attack, foil clearance, and camber).

**Numerical Method.** The commercial code FLUENT 5.4 (Fluent Inc. [15]) was used for the numerical solution of the Navier-Stokes equations. The numerical method is based on a finite volume formulation applicable to structured grids. All variables, including velocity components and pressure, are averages applied to a control volume. A second-order spatial interpolation method was employed to obtain the velocity components and pressure on the control volume faces from those at the control volume centers. The control volume face values of the dependent variables are used to evaluate the convective fluxes.

Fluent's segregated steady-state solver was used for the numerical simulations. The numerical method is based on a multiblock, finite-volume formulation to solve the discretized Navier-Stokes equations in conjunction with the turbulence model. The SIMPLEC algorithm is used to couple pressure and velocity. A second-order upwind scheme was used for the space discretization of the convection terms in momentum and turbulence equations in all simulations. Also, a second-order accurate scheme was used to interpolate the pressure value on the control volume faces from those at the control volume centers in the momentum equations. The diffusion terms are approximated by a second-order accurate central-difference scheme. The stopping criteria for all calculations were when all residuals were below  $10^{-5}$ .

The standard  $k-\epsilon$  turbulence model is used for all calculations. Transport equations for  $k$ , the kinetic energy of turbulence, and  $\epsilon$ , the rate of dissipation, are solved together with the continuity and momentum equations.

**Mesh Generation.** Gambit, the meshing tool packaged with FLUENT CFD software, was used to generate a 2D multiblock mesh based on the surface information obtained from models of the experimental CSS apparatus. Figure 3 shows a structured multiblock grid typical of those used in this study. A C-mesh is used around the foil to provide good resolution around the leading edge of the foil, in the wake, and in the boundary layer. Because a logarithmic wall law is used to compute the skin friction coefficient, the first grid cell near the airfoil should be in the logarithmic region, i.e., the dimensionless distance to wall ( $y^+ = U_\tau y / \nu$ , where  $U_\tau$  is the friction velocity,  $y$  is the physical distance of the first centroid from the wall, and  $\nu$  is the kinematic viscosity) for the first cell center should be between 30 and 60. Near-wall mesh spacing was checked as a postprocessing step to ensure that this requirement was met. An  $H$  mesh is used up- and downstream of the foil to provide good mesh quality elsewhere.

**Boundary Conditions for Fluid Flow.** A rotating reference frame was used so that the flow was modeled in a coordinate system moving at the same speed as the rotating foil. In this case,

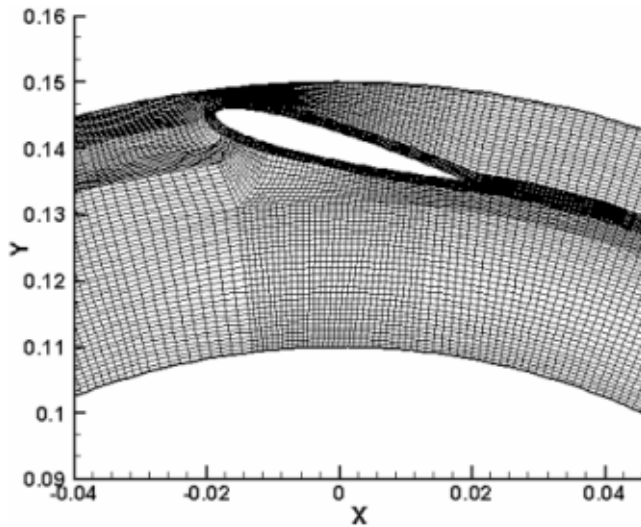


Fig. 3 Representative computational mesh

the flow was steady relative to the rotating frame. For the wall boundary conditions, the relative angular velocity was set to zero for the foil and inner wall, which moves at the speed of the rotating frame and, hence, are stationary in the rotating frame. The outer wall is stationary in the nonrotating frame of reference, therefore the velocity was set to zero in the absolute reference frame. If the wall velocities are specified in this manner, then only the rotating speed of the reference frame needs to be changed when there is a change in rotating speed of the foil.

The simplification of a rotating inner wall allows us to efficiently model the area of interest near the foil. The inner wall is not a physical wall but is a boundary that represents the portion of the fluid that rotates as a solid body with the rotor. We chose this boundary condition so that the fluid is rotating with the same rotational velocity as the rotor far from the cylinder (outer wall). This simplification allows us to only model the area of interest, around the foil near the wall.

Due to symmetry of the flow domain, calculations were performed for a sector of 180 deg (Fig. 4) and periodic boundary conditions were imposed in the circumferential directions at the two ends of the sector. The flow entering the computational model through one periodic plane was set identical to the flow exiting the domain through the opposite periodic plane.

**Model Validation.** The pressure pulsations are affected by the turbulence model used, especially for separated flows. Therefore, it is worth considering the errors in the  $k-\epsilon$  model for CFD study of pressure pulsation. Model validation was conducted by calcu-

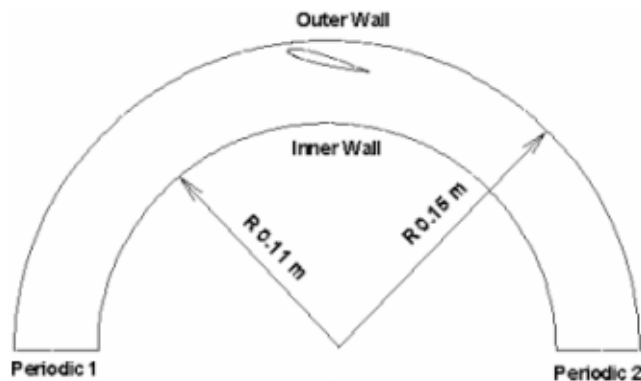


Fig. 4 Calculation domain and boundary conditions

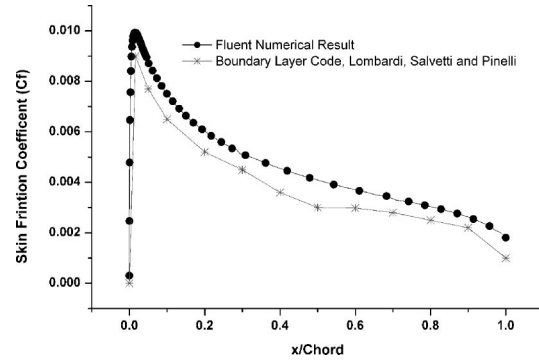


Fig. 5 Computed skin friction coefficient distributions over an NACA 0012 airfoil

lating the skin friction on a NACA 0012 (zero camber) airfoil in a straight channel at zero angle of attack for Reynolds number ( $Re$ , defined as  $Re = \rho Uc / \mu$ , where  $\rho$  is the density,  $U$  is the inlet velocity,  $c$  is the chord of the foil, and  $\mu$  is the dynamic viscosity) of  $3 \times 10^6$ . In Fig. 5, the local friction drag coefficient ( $C_f$ ) distribution obtained by the  $k-\epsilon$  model shows reasonable agreement (i.e., within 10%) with the numerical results calculated using a boundary layer code by Lombardi et al. [16]. The airfoil skin friction coefficient rapidly increases from a value of zero at the stagnation point to a peak value shortly downstream of the leading edge. This rapid increase is due to the rapidly increasing velocity as the flow external to the boundary layer rapidly expands around the leading edge. Beyond the peak,  $C_f$  monotonically decreases in the same qualitative manner as for a flat plate. The results for friction drag from the boundary layer code of Lombardi et al. [16] had been validated with experiment and were considered the baseline for accuracy. Based on this validation case of an airfoil, we have reasonable confidence in the predicted drag coefficient for attached flows.

For the configuration of interest in this study of a foil moving near a curved wall, a mesh refinement study has been conducted for the extreme cases of our test matrix. The pressure and velocity were shown to be independent of the number of cells used above the number used in this study.

## Results and Discussion

The pulse form for a range of rotor variables was examined using the aforementioned experimental measurements and CFD estimates. The technical characteristics and range of variables tested in the present experimental and numerical study and in industry applications are listed in Table 1.

The foil shape is defined by the NACA four-digit designation. The first digit defines the percent camber of the foil, the second digit defines the location of the camber in tenths of chord from the leading edge, and the last two digits define the thickness of the foil as a percent of chord (e.g., [17]).

The comparison of CFD predictions with the corresponding experimental measurements is valuable for the assessment of CFD simulations. It was found that although features and general trends of the pressure pulses were similar, the overall computed values of pressure pulse were 40–50% smaller than the measured values. The reason for the discrepancies might be that the 2D physical model used in the CFD study did not account the complex three-dimensional (3D) flow features in the experimental CSS. The presence of the side walls at the front and back of the CSS slows the rotational velocity of the fluid relative to the foil. The increased relative velocity would account for the higher experimentally measured pressure pulses than that calculated. In industrial pressure screens, there are no front and back walls to slow the fluid, and we would expect better correlation.

**Table 1 Technical characteristics and variables in present numerical and experimental study and in industry applications**

Characteristics and parameters	Present numerical and experimental study	Industry applications
Fluid	Water (20 °C)	Pulp suspension (60–90 °C)
Screen cylinder diameter	0.3 m	0.3–1 m
Foils	NACA 0012, 4312, and 8312, all with a chord length of 40 mm	Hooper etc., chord length from 30–80 mm
Rotor rotating speed	600, 800, 1000, 1200 and 1400 rpm	500–1000 rpm
Clearance between the foil and screen plate	2, 3, 4, and 5 mm	2–10 mm
Foil angle of attack	0, 5, 10, 15, and 20 deg	N/A

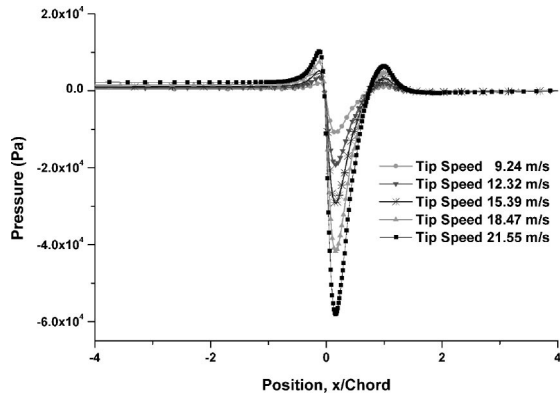
**Tip Speed.** Pressure pulses at the outer wall were calculated using CFD at five different rotational speeds for 0 deg angle of attack. The negative suction pressure peaks varied between 10 kPa at 600 rpm (tip speed=9.24 m/s) and 60 kPa at 1400 rpm (tip speed=21.55 m/s) for a NACA 0012 (zero camber) airfoil, as shown in Fig. 6. The magnitudes of both positive and negative pressure pulses increased with increased rotating speed for all the angles of attack studied. Pressure coefficient ( $C_p$ , defined as  $p/\frac{1}{2}\rho U_{tip}^2$ , where  $P$  is the pressure,  $\rho$  is the density, and  $U_{tip}$  is rotor tip speed) was obtained by normalizing the pressure with the dynamic pressure associated with the foil tip speed and fluid density. All the pressure curves in Fig. 6 collapsed into a single  $C_p$  curve, as shown in Fig. 7.

A comparison of the CFD and experimental results for the case of 0 deg angle of attack can be obtained by comparing the results of Figs. 7 and 8. The forms of the pressure pulses at the outer wall are similar, but CFD under predicts the  $C_p$  magnitude of the negative pulse by about 40%. Likewise, the agreement of the nondimensional pressure pulse form for a 20 deg angle of attack be-

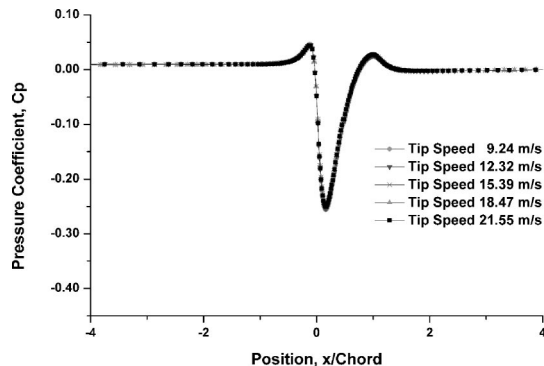
tween the CFD calculation (Fig. 9) and measurements (Fig. 10) is good—but CFD estimates under predict the  $C_p$  magnitude of the suction pulse by 50%. The collapsed  $C_p$  curves in Figs. 7 and 9 indicate that magnitudes of positive and negative suction pressure pulse peak are proportional to the square of the tip velocity of the foil.

**Angle of Attack.** The variation of pressure distribution and flow pattern with angle of attack for a NACA 0012 foil are shown in Fig. 11. For a low angle of attack (<10 deg) the flow passes smoothly over the foil and is attached over most of the surface. However, as the angle of attack increases beyond 10 deg, the flow tends to separate from the top surface of the foil, creating a vortex that extends beyond the trailing edge of the foil, as shown by the streamlines in the figure. One consequence of the separated flow at high angles of attack is a large increase in pressure drag on the foil. Under these conditions, the increase in drag will increase the amount of power required to operate the rotor.

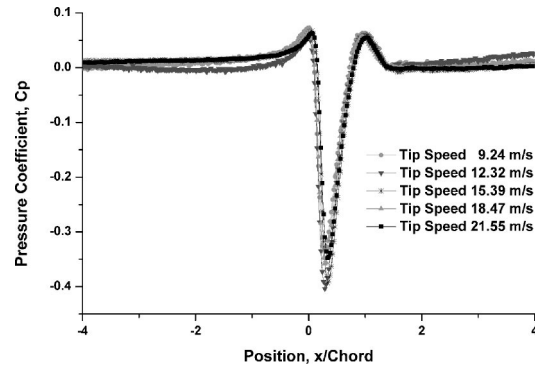
Figure 12 shows the calculated pressure pulse profiles on the screen cylinder surface for the NACA 0012 foil with five different angles of attack (0, 5, 10, 15, and 20 deg) at a constant clearance.



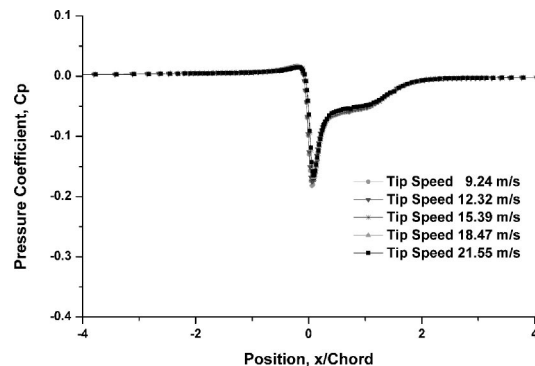
**Fig. 6 Numerical estimates of effect of rotating speed on pressure pulse (0 deg angle of attack constant gap)**



**Fig. 7 Numerical pressure coefficient versus position, x/Chord, (0 deg angle of attack constant gap)**



**Fig. 8 Experimental pressure coefficient versus position, x/Chord (0 deg angle of attack)**



**Fig. 9 Numerical pressure coefficient versus position, x/Chord (20 deg angle of attack)**

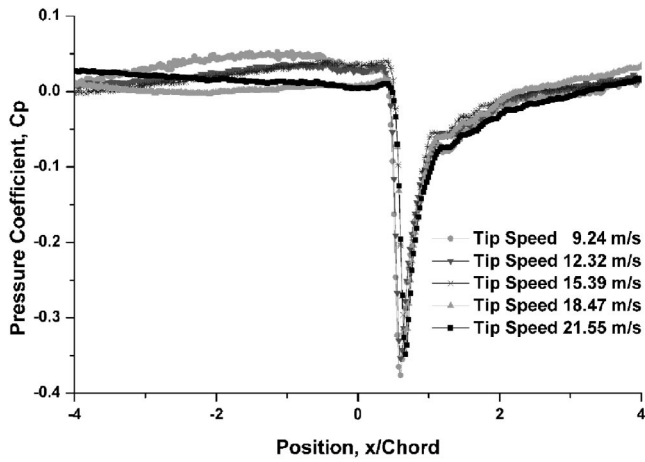


Fig. 10 Experimental pressure coefficient versus position,  $x/\text{Chord}$  (20 deg angle of attack)

The corresponding experimental results for the effect of angle of attack are shown in Fig. 13. There is a very good correspondence between the experimental measurements and numerical predictions for the form of the pulses and effect of changes in angle of attack. Both numerical results (Fig. 12) and experimental results (Fig. 13) show that a 5 deg angle of attack has the highest magnitude of negative suction pressure pulse. Both experimentally and computationally, the value of negative suction pulse peak for a 0 deg angle of attack falls between the values for a 15 and 20 deg angle of attack. As the angle of attack increases beyond 5 deg, the  $C_p$  magnitude of the negative suction pulse decreases

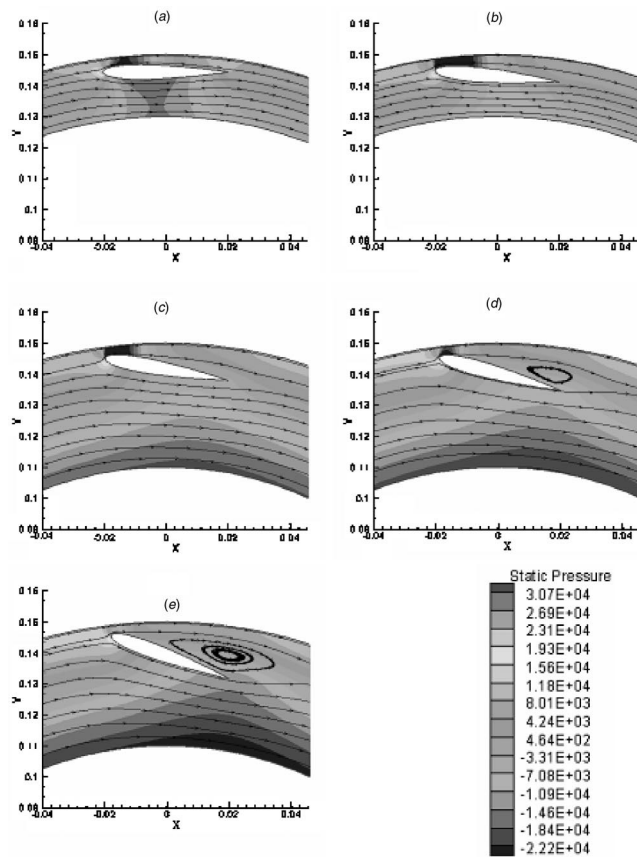


Fig. 11 Pressure contour and particle path lines. degree of attack (a)=0, (b)=5, (c)=10, (d)=15, and (e)=20

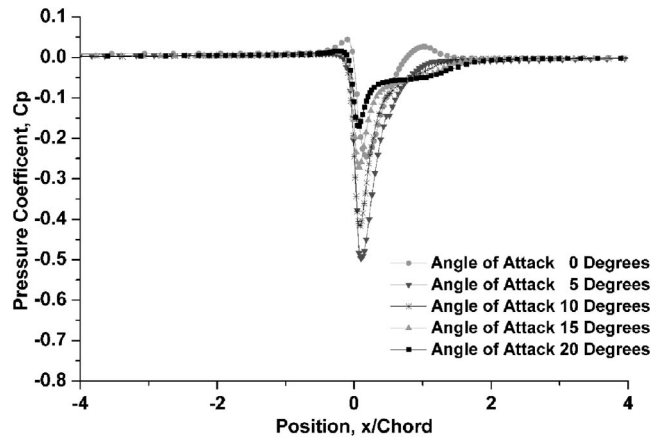


Fig. 12 Numerical pressure coefficient versus position,  $x/\text{Chord}$  for five different angles of attack

with increased angle of attack.

When the foil is at a nonzero angle of attack, greater than or equal to 5 deg, the positive pressure pulse at the leading and trailing edges of the foil are  $\sim 0$ . The positive pressure pulse is reduced for positive angles of attack because the stagnation point at the leading edge of the foil is located on the surface of the foil opposite to the screen cylinder and the foil effectively blocks the high-pressure region around the stagnation point from the cylinder. The resulting pressure pulse is flat with a sharp negative peak only in the vicinity of the foil. Reduction of the positive pressure pulse while maintaining a high negative pulse may significantly increase contaminant and fractionation efficiency of the screen by avoiding any tendency for the rotor to force contaminants through the apertures, while at the same time providing the strong back-flushing pulse that ensures good screen capacity.

Figures 12 (CFD) and 13 (experimental) both show a pressure plateau after the negative pressure peak for angles of attack  $> 15$  deg. This plateau would appear to be a result of flow separation from the upper surface of the foil. It is not clear that this aspect of the pulse form offers any particular benefit in the operation of the pulp screen rotor. What the above data do show is that the foil angle of attack has a strong effect on the shape and  $C_p$  magnitude of the pressure pulse and must be optimized for specific applications, especially if higher consistency screening is the desired purpose.

**Foil Clearance.** The clearance between the foil and screen cylinder may be adjusted in industrial screening applications to en-

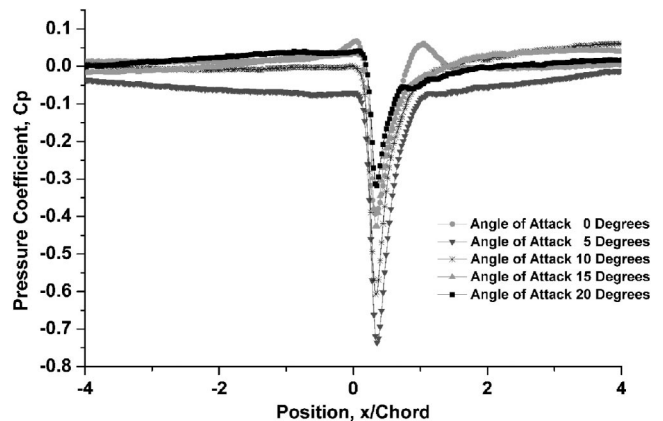


Fig. 13 Experimental pressure coefficient versus position,  $x/\text{Chord}$  for five different angles of attack

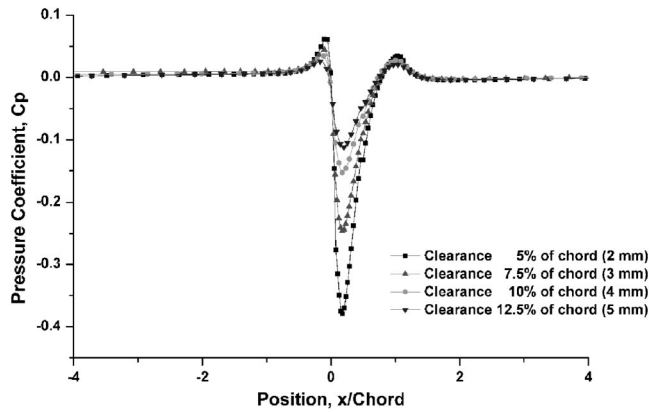


Fig. 14 Numerical pressure coefficient versus position,  $x/\text{Chord}$  for four different clearances (0 deg angle of attack)

hance the pressure pulsation. Pressure pulses for three different angles of attack (0, 5, and 20 deg) with a range of clearances 2–5 mm (5%, 7.5%, 10%, and 12.5% of chord) are shown in Figs. 14–16. Although increasing the clearance decreases the  $C_p$  magnitude of both the positive and negative pressure pulse peaks, it appears to have a stronger effect on the suction pressure peak. The tip speed is held constant at 18.47 m/s.

Figure 17 shows the  $C_p$  magnitude of the computed negative suction pressure peaks as a function of clearance for the range of angles of attack along with experimental results for the zero angle of attack. The experimental and computed peaks demonstrate the same trend: reducing the clearance increases the  $C_p$  magnitude of the negative pressure pulse. We also see that the foil at 5 deg angle of attack, which creates the greatest  $C_p$  magnitude of negative peak, is the most sensitive to variations in clearance.

Decreasing the clearance increases the  $C_p$  magnitude of the pressure pulse and the rotor's ability to clear plugged apertures. A smaller clearance also increases the probability of large contaminants becoming wedged between the cylinder and the rotor and potentially damaging the cylinder. For this reason, foil clearances are seldom below 2 mm.

**Foil Camber.** Classical aerodynamics theory predicts that a cambered airfoil will produce more lift than a noncambered airfoil at a given angle of attack. The same mechanism will result in a higher magnitude of negative pressure pulse on the screen cylinder. The degree of camber is the maximum distance between the mean camber line and the chord line in percent of chord. To determine the effect of foil camber on the  $C_p$  magnitude and shape

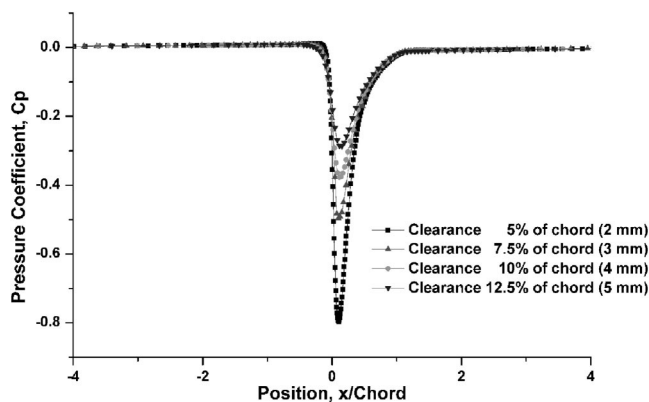


Fig. 15 Numerical pressure coefficient versus position,  $x/\text{Chord}$  for four different clearances (5 deg angle of attack)

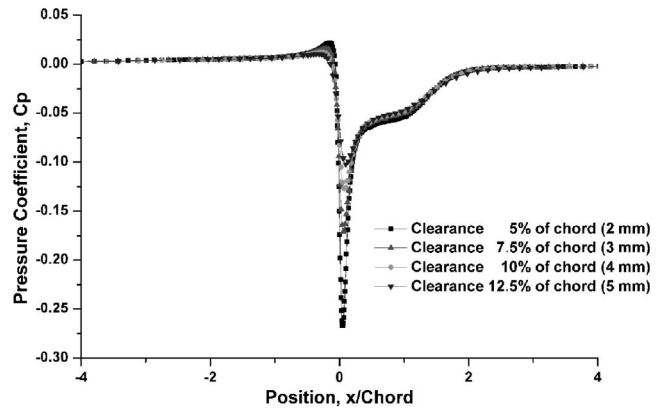


Fig. 16 Numerical pressure coefficient versus position,  $x/\text{Chord}$  for four different clearances (20 deg angle of attack)

of the rotor pressure pulse, numerical and experimental studies were conducted with NACA 0012 (no camber), NACA 4312 (4% camber), and NACA 8312 (8% camber) foils.

Figure 18 shows the numerically determined pressure pulses for the three airfoils with 0%, 4%, and 8% camber at 0 deg angle of attack. The increased camber increases both the  $C_p$  magnitude and width of the negative pressure pulse. Figure 19 shows the experimentally determined pressure pulses for the same three airfoils as Fig. 18 (0%, 4%, and 8% camber). The experimentally measured pressure pulses show the same increase in  $C_p$  magnitude and width as shown in the numerical results.

Figures 20 and 21 show the flow streamlines and pressure distribution for the NACA 4312 (4% camber) and NACA 8312 (8% camber) at five angles of attack equal to 0, 5, 10, 15, and 20 deg. The filled pressure contours show that the stagnation point progressively moves downstream of the leading edge over the bottom surface of the airfoil as the angle of attack is increased. This results in a decrease of the positive pressure pulse at the screen cylinder surface near the leading edge of the foil.

As foil camber is increased, the adverse pressure gradient on the foil surface facing the screen cylinder increases, and the flow separates at lower angles of attack. The stall angle of attack is  $\sim 5$  deg for NACA 8312,  $\sim 10$  deg for NACA 4312, and  $\sim 15$  deg for NACA 0012. More precise determination of the stall angle would require computation at intermediate angles of attack. The stalling phenomenon shown in Figs. 20 and 21 is termed “trailing-edge stall.” We see a progressive and gradual movement of separation from the trailing edge toward the leading edge as the angle

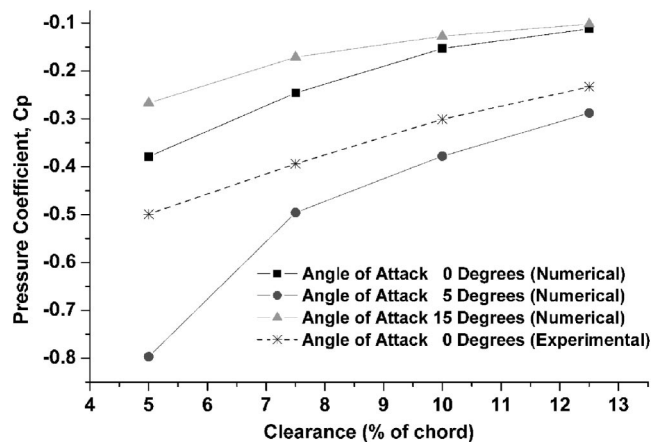


Fig. 17 Numerical and experimental suction pressure coefficient peak versus clearance for three different angles of attack

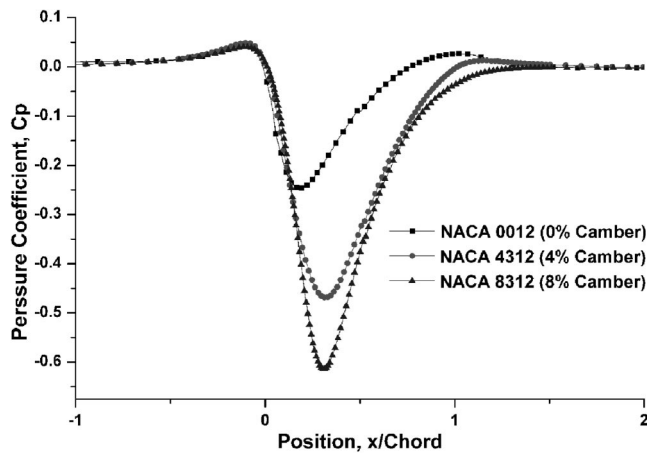


Fig. 18 Numerical pressure coefficient versus position ( $x/$ Chord) for 0 deg angle of attack

of attack is increased. The larger low-pressure region for cambered foils in the gap between the rotating foil and screen cylinder means that the width (or duration) of the negative pressure pulse is larger for cambered foils than for noncambered foils.

Figures 22 and 23 show the numerical and experimental pressure pulse profiles on the screen cylinder wall for a NACA 4312 foil with five different angles of attack (0, 5, 10, 15, and 20 deg). These figures show that 5 deg angle of attack has the highest negative suction pressure pulse and, thus, is expected to give the highest capacity. As the angle of attack increases beyond 5 deg, the  $C_p$  magnitude of the negative suction pulse decreases. The positive pressure peak near the leading edge of the foil is completely eliminated for foils operating at a positive angle of attack.

Figure 24 shows the computed pressure pulses at the screen cylinder for the NACA 8312 foil. This figure indicates that the  $C_p$  magnitude of the negative suction pulse decreases as the angle of attack increases due to the onset of separation. Thus for a NACA 8312 foil the maximum magnitude of pressure pulse occurs at 0 deg angle of attack.

Figure 25 shows the minimum pressure coefficients of the pressure pulses for the three cambers over all angles of attack for both the experimental and numerical results. The numerical and experimental  $C_p$  magnitudes of pressure pulse peak have the same trends. The  $C_p$  magnitudes of negative pressure peak obtained by experimental measurements are larger than the ones obtained by CFD calculations. There are substantial deviations of negative pulse peak for the NACA 4312 at 15 and 20 deg angle of attack

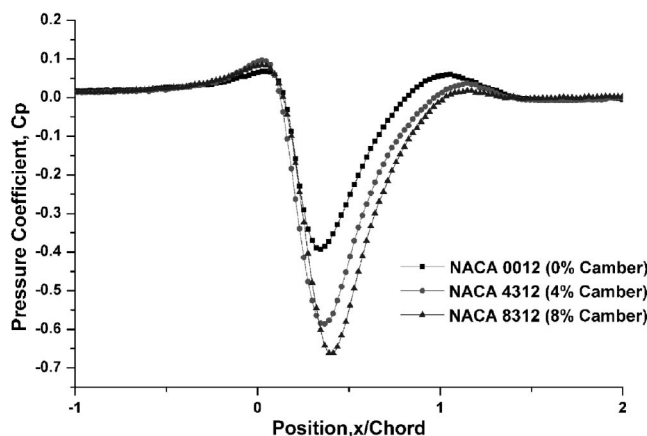


Fig. 19 Experimental pressure coefficient versus position ( $x/$ Chord) for 0 deg angle of attack

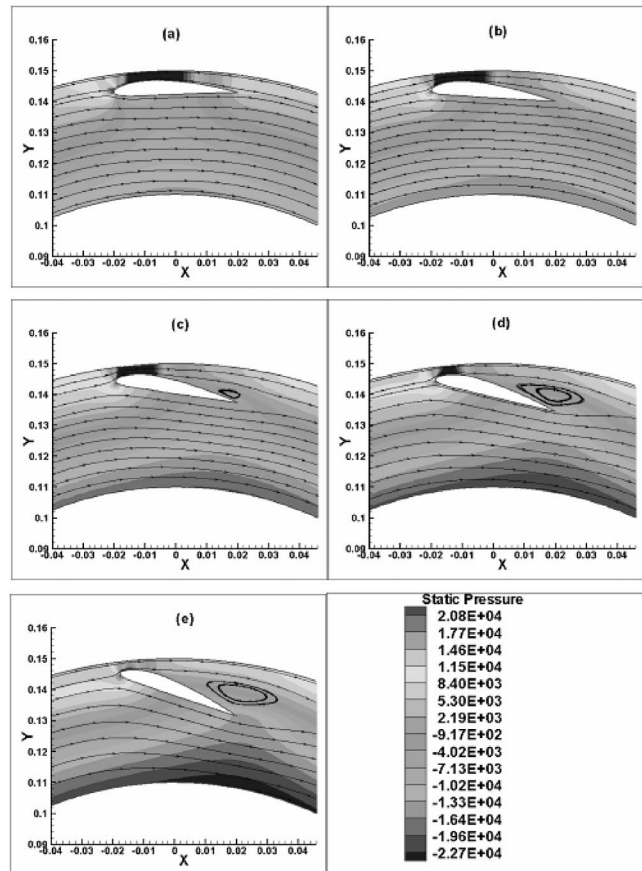


Fig. 20 Pressure contour and particle path lines for NACA 4312: degree of angle of attack (a)=0, (b)=5, (c)=10, (d)=15, and (e)=20

between CFD calculations and the experimental data. The reason for the discrepancy between the experimental and numerical pressure peaks for these two points is unknown.

For the three foils and five different angles of attack that were studied, the NACA 4312 (4% camber) at 5 deg angle of attack provided the highest magnitude of negative suction pulse peak. As angle of attack increased beyond 5 deg, the  $C_p$  magnitude of the negative suction pulse decreased with increased angle of attack because of flow separation. The largest negative peak for the NACA 8312 foil occurred at 0 deg angle of attack. This is because flow separation occurred at less than 5 deg angle of attack.

The ideal pulse form has not been established in the published literature. Intuitively, the negative pressure pulse magnitude and width would be the key parameters. Figure 26 shows that the negative pressure pulse width, defined as the width at half the negative pressure pulse, decreased as angle of attack increased for NACA 0012, 4312, and 8312 foils. The pulse widths for cambered foils were wider than that for noncambered foil.

The “normalized pulse strength” is proposed here as an alternate, and perhaps more effective, means of characterizing the effectiveness of a foil pulse. The normalized pulse strength is defined as the pulse width normalized by chord length multiplied by minimum pressure coefficient. Figure 27 shows that the normalized pulse strength for NACA 4312 at 5 deg and NACA 8312 at 0 deg had the highest value with almost the same magnitude.

## Discussion

The shape and magnitude of the rotor-induced pressure pulses are widely believed to have a fundamental effect on screen capacity, efficiency, and other key operating parameters. A positive



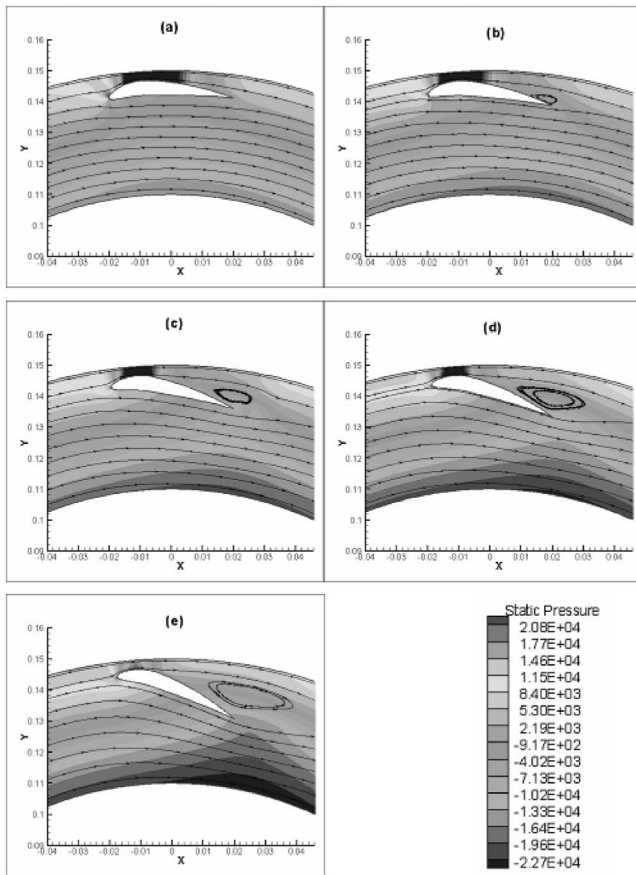


Fig. 21 Pressure contour and particle path lines for NACA 8312: degree of angle of attack (a)=0, (b)=5, (c)=10, (d)=15, and (e)=20

pressure pulse component is hypothesized to decrease the contaminant removal efficiency of the screen. This is because the high positive pressure pulse (found at the leading and trailing edge of the foil at 0 deg angle of attack) might force contaminants through narrow apertures. This might be especially true for flexible fibers

and deformable contaminant particles (such as “stickies”), which are adhesives found in recycled pulp. In this regard, the small or nonexistent positive pressure pulses generated by foils at nonzero angle of attack would be ideal for removing deformable contaminants.

The maximum achievable capacity is thought to be strongly correlated with the magnitude of the negative pressure pulse. The negative pulse reverses the flow through the apertures, backflushing the apertures and clearing particles lodged near the slot inlet and lifting them into the turbulent zone. As the peak strength increases, the suction pulse is more effective at clearing the screening apertures. Increasing the rotation speed will increase the pulse strength and the frequency of pulses. This correlation would be expected to exist only over a limited range, however, since too high a backflushing flow would reduce the net volumetric flow through the screen cylinder without producing any benefit.

Using a foil that produces a strong negative pressure peak provides the opportunity to reduce the total energy consumed by the rotor by providing a sufficient negative pulse at a low rotational speed. Ideally, the rotor speed would be set just high enough to meet the required capacity and runnability but no higher to minimize energy usage. Optimization of the rotational speed, clearance, angle of attack, and foil camber makes it possible to achieve increased efficiency at a reduced power consumption for each pulp type.

As discussed previously, the ability of the foil to remove pulp accumulation may be due to a combination of pulse height and width. For this reason, a “normalized pulse strength” term was defined as a combination of both width and magnitude of the pulse. The “performance” of the screen is indeed a composite of several indices, including capacity, efficiency, power, etc. Likewise the rotor produces several actions, including the backflushing duration, backflushing strength, pulp fluidization, rotational acceleration, etc. The interrelationships are typically nonlinear, and a single parameter is very unlikely to capture all of what is sought in “rotor performance.” However there may be composite parameters, such as normalized pulse strength, which more completely reflect the rotor action and facilitate rotor optimization. This will facilitate the conduct of more fundamental studies that seek to understand and optimize the form of the pressure pulse as a function of variables related to the shape and positioning of the rotor foil.

One should, of course, be cautious not to overstate the imme-

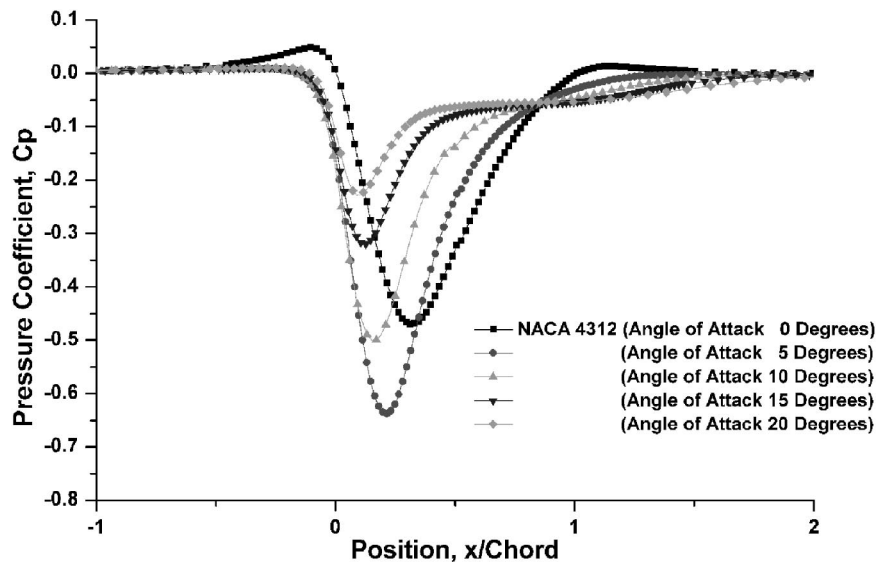


Fig. 22 Numerical pressure coefficient versus position (x/Chord), NACA4312 (five angles of attack)

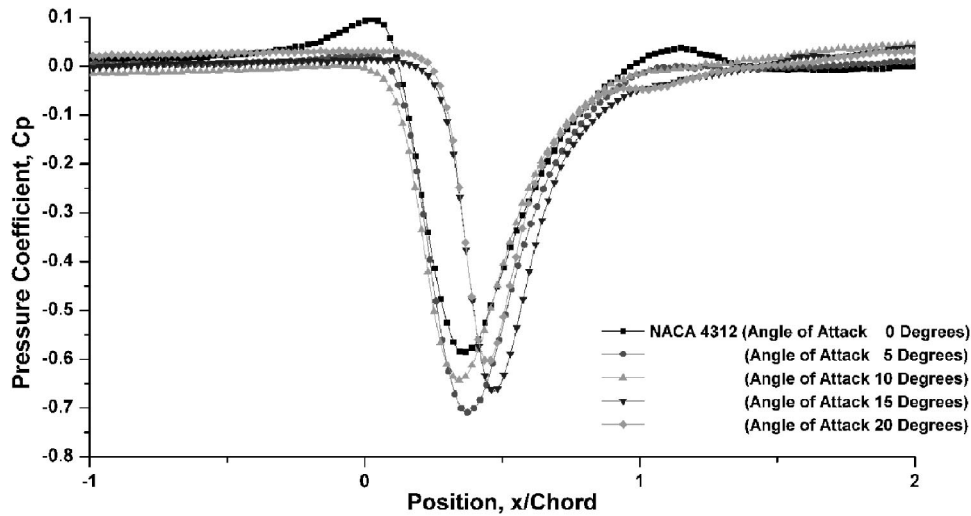


Fig. 23 Experimental pressure coefficient versus position ( $x/\text{Chord}$ ), NACA4312 (five angles of attack)

diate industrial impact of this study. The tests and simulation work shown above was made for water flows, not pulp. There are substantial differences in the character and behavior of these fluids. Likewise the lack of a clear model for what constitutes an “ideal” rotor pulse limits the immediate impact of this work. That said, this detailed study does point toward some clear opportunities for improvements in rotor design and for a better appreciation of the sensitivity of the pressure pulses to common rotor variables.

### Conclusions

Using both numerical and experimental approaches, the key design and operating variables affecting the pressure pulse on the surface of a pressure screen cylinder were investigated. Although the general pressure pulse signatures were captured well by the CFD model over a wide range of foil tip speed, clearance, angle of attack, and foil camber, comparison with experimental pressure pulse measurements showed deviations in  $C_p$  values by up to 50%.

Tip speed, angle of attack, clearance, and camber were all found to significantly affect the pressure pulse generated by the foil. In particular, it was shown that:

1. The magnitude of the pressure pulse peak increased linearly with the square of rotor tip speed for all angles of attack studied.
2. The maximum magnitude of negative pressure pulse occurred for the NACA 0012 and 4312 foils at 5 deg angle of attack and NACA 8312 at 0 deg. The positive pressure peak

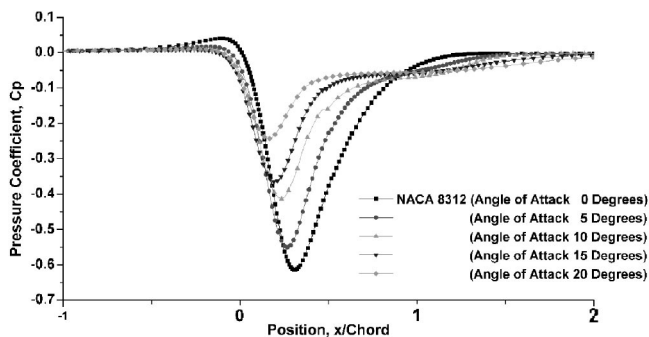


Fig. 24 Numerical pressure coefficient versus position ( $x/\text{Chord}$ ), NACA8312 (five angles of attack)

near the leading edge of the foil was completely eliminated for foils operating at greater or equal to 5 deg angle of attack.

3. The  $C_p$  magnitude of the negative pressure peak increased as clearance decreased.
4. The stall angle of attack was  $\sim 5$  deg for NACA 8312,  $\sim 10$  deg for NACA 4312, and  $\sim 15$  deg for NACA 0012. As the foil camber was increased, the flow separated at lower angles of attack because of the higher adverse pressure gradient on the foil surface near the screen cylinder.
5. The  $C_p$  magnitude and the width of the negative suction pulse increased with increased camber.

Most importantly, we have shown that CFD is an important tool for the optimal design and operation of rotors in industrial pressure screens.

### Acknowledgments

The financial and technical support of Advanced Fiber Technologies (AFT), the Pulp and Paper Research Institute of Canada

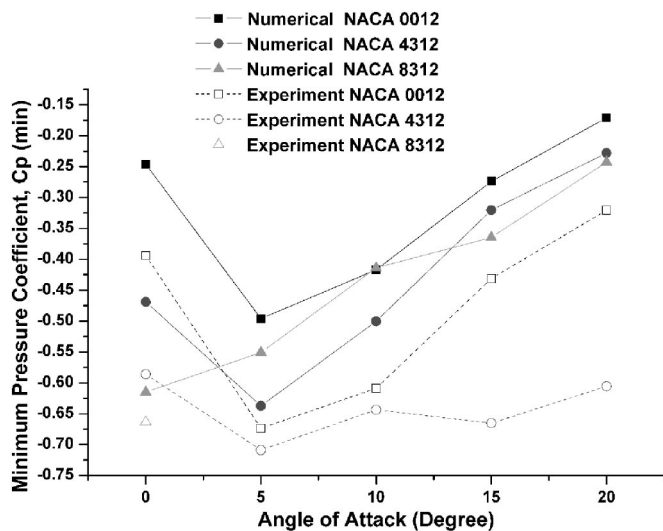


Fig. 25 Numerical and experimental minimum pressure coefficient versus angle of attack (deg)

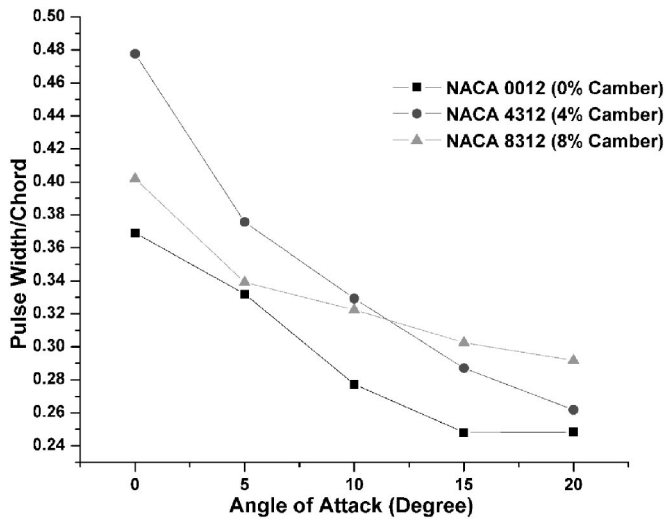


Fig. 26 Numerical pressure pulse width versus angle of attack

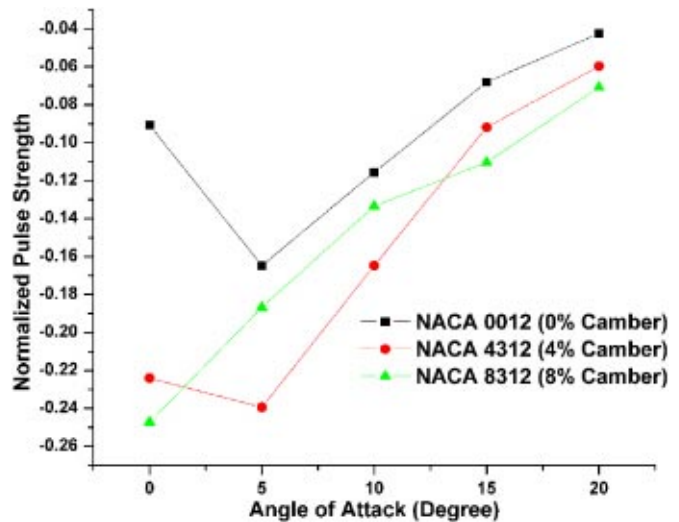


Fig. 27 Numerical normalized pressure pulse strength versus angle of attack

(Paprican), the Natural Sciences and Engineering Research Council of Canada (NSERC), and the UBC Advanced Papermaking Initiative (API) is gratefully acknowledged.

## References

- Niinimäki, J., and Dahl, O., 1998, "A Comparison of Pressure Screen Baskets With Different Slot Widths and Profile Heights. Selection of the Right Surface for a Groundwood Application," *Pap. Puu*, **80**(8), pp. 31–45.
- Cox, M., Fredriksson, B., and Koikkalainen, J., 2000, "Mill Experience With High-Consistency, Screening Technology for Recycled Fibre," *Pap. Technol. (Bury, U.K.)*, **41**(9), pp. 31–36.
- Levis, S. H., 1991, "Screening of Secondary Fibers," *Prog. Pap. Recyc.*, **5**(1), pp. 31–45.
- Repo, K., and Sundholm, J., 1996, "The Effect of Rotor Speed on the Separation of Coarse Fibres in Pressure Screening With Narrow Slots," *Pulp Pap. Can.*, **97**(7), pp. T253–T257.
- Gooding, R. W., 1996, "Flow Resistance of Screen Plate Apertures," Ph.D. thesis, The University of British Columbia.
- Niinimäki, J., 1999, "Phenomena Affecting the Efficiency of a Pressure Screen," *Tappi Pulping Conf.*, pp. 957–966.
- Yu, C. J., and DeFoe, R. J., 1994, "Fundamental Study of Screening Hydraulics Part 3: Model for Calculating Effective Open Area," *Tappi J.*, **77**(9), pp. 125–131.
- Gonzalez, J. A., 2002, "Characterization of Design Parameters for a Free Foil Rotor in a Pressure Screen," M.A.Sc. thesis, The University of British Columbia.
- Wikström, T., 2002, "Transition Modelling of Pulp Suspensions Applied to a Pressure Screen," *J. Pulp Pap. Sci.*, **28**(11), pp. 374–378.
- Karvinen, R., and Halonen, L., 1984, "The Effect of Various Factors on Pressure Pulsation of a Screen," *Pap. Puu*, **66**(2), pp. 80–83.
- Marko, J. J., and LaRivière, C. J., 1999, "The Use of Computational Fluid Dynamics (CFD) in Pressure Screen Design," *Tappi Papermakers Conf.*, pp. 1477–1482.
- Pinon, V., Gooding, R. W., and Olson, J. A., 2003, "Measurements of Pressure Pulses From a Solid Core Screen Rotor," *Tappi J.*, **2**(10), pp. 9–12.
- Olson, J. A., and Wherrett, G. W., 1998, "A Model of Fibre Fractionation by Slotted Screen Apertures," *J. Pulp Pap. Sci.*, **24**(12), pp. 398–403.
- Kumar, A., 1991, "Passage of Fibres Through Screen Apertures," Ph.D. thesis, The University of British Columbia.
- Fluent Inc., 1998, *Fluent Users Guide*, Fluent Inc.
- Lombardi, G., Salvetti, M. V., and Pinelli, d., 2000, "Numerical Evaluation of Airfoil Friction Drag," *J. Aircr.*, **37**(2), pp. 354–356.
- Abbott, I. H., and Von Doenhoff, A. E., 1949, *Theory of Wing Sections*, McGraw-Hill, New York.

# Vortex Breakdown in a Differentially Rotating Cylindrical Container

**Teruaki Koide\***

Associate Professor  
Department of Mechanical Engineering, Tokyo  
Metropolitan College of Technology,  
1-10-40 Higashi-Ohi, Shinagawa-ku, Tokyo  
140-0011, Japan

**Hide S. Koyama**

Professor  
Department of Mechanical Engineering, Tokyo  
Denki University,  
2-2 Kanda-Nishikicho, Chiyoda-ku, Tokyo  
101-8457, Japan

*Numerical studies are reported on the vortex breakdown in a differentially-rotating cylindrical container in which the top endwall rotates at a high angular velocity  $\Omega_t$  and the cylinder and bottom endwall rotate at a low angular velocity  $\Omega_{sb}$ . Critical boundaries and the location and size of the vortex breakdown bubble are quite different from the case when the top endwall rotates and the cylinder and the bottom endwall are stationary. As  $|\Omega_{sb}/\Omega_t|$  is increased, the breakdown bubble moves toward downstream for  $\Omega_{sb}/\Omega_t < 0$ , whereas the bubble moves toward upstream for  $\Omega_{sb}/\Omega_t > 0$ . The Brown and Lopez criterion is extended to a differentially-rotating container. [DOI: 10.1115/1.1852482]*

**Keywords:** Vortex Breakdown, Numerical Simulation, Coriolis Force, Swirling Flow

## 1 Introduction

Characteristics of flows and associated transport phenomena of a viscous fluid in a rotating vessel have been extensively studied. General features of rotating flows provide a fertile ground for basic fluid dynamics research. Also, a proper understanding of the flow process is vital to the design and operation of modern high-performance rotating machinery.

One canonical configuration is the flow of an incompressible fluid which fills a closed cylindrical container. Flow in the cylindrical container is characterized by three rotational Reynolds numbers  $Re = \Omega_t R^2/\nu$ ,  $\Omega_s R^2/\nu$ , and  $\Omega_b R^2/\nu$ , and the cylinder aspect ratio  $H/R$ , where  $\Omega_t$ ,  $\Omega_s$ , and  $\Omega_b$  denote the angular velocities of the top endwall, cylinder sidewall, and bottom endwall, respectively;  $R$  and  $H$  are the cylinder inner radius and height, respectively; and  $\nu$  is the kinematic viscosity of the working fluid.

Vogel [1] observed experimentally the vortex breakdown in an enclosed cylindrical container with a rotating endwall ( $\Omega_t \neq 0$ ,  $\Omega_b = 0$ , and  $\Omega_s = 0$ ), and showed a critical boundary curve, in the plane of  $Re = R^2 \Omega_t/\nu$  and  $H/R$ , which indicates the boundary of appearance and disappearance of the vortex breakdown. The vortex breakdown is the term used to describe a flow phenomenon in which the sudden appearance of a weak meridional recirculation is observed on the axis of the cylinder. Escudier [2] extended Vogel's study and showed the behavior of the flow in  $(Re-H/R)$ -plane, in systematically organized flow visualization studies, which disclosed the existence of single, double, and triple breakdown bubbles in an extensive range. Many other researchers followed Escudier, e.g., Lugt and Hasussling [3], Lugt and Aboud [4], Daube and Sorensen [5], Lopez [6], Brown and Lopez [7], Tsitverblit [8], Sotiropoulos and Ventikos [9], and Fujimura et al. [10].

The influence of weak co- and counter-rotation of the bottom endwall on the vortex breakdown in a closed cylindrical container ( $|\Omega_b/\Omega_t| \ll 1$  and  $\Omega_s = 0$ ) was studied experimentally by Roesner [11] and Bar-Yoseph et al. [12]. It was shown that weak corotation of the bottom endwall promoted vortex breakdown in a flow with out meridional recirculation. Weak counter-rotation suppressed an existing vortex breakdown bubble and changed the meridional flow to a single vortex breakdown.

Valentine and Jahnke [13] examined numerically the flow field

in which the top and bottom endwalls corotate at a same angular velocity while the sidewall is at rest ( $\Omega_t/\Omega_b = 1$  and  $\Omega_s = 0$ ). It was demonstrated that the stagnation points were visible on the axis between the midplane of symmetry and the rotating endwalls for appropriate values of the rotational Reynolds number and the cylinder aspect ratio. As the Reynolds number increased beyond the critical value, a toroidal (or ring) vortex surrounding a columnar vortex core in the meridional-plane was discernible.

Gelfgat et al. [14] studied numerically a steady and oscillatory instability of swirling flow in a cylindrical container with independently rotating top and bottom endwalls ( $-1 < \Omega_b/\Omega_t < 1$  and  $\Omega_s = 0$ ). For the steady states, they present that weak counter-rotation of the bottom endwall ( $-1 \ll \Omega_b/\Omega_t < 0$ ) may suppress the vortex breakdown. Stronger counter-rotation induces a stable steady vortex breakdown at relatively large Reynolds numbers for which a vortex breakdown does not appear in the case of the stationary bottom endwall. Weak corotation ( $\Omega_b/\Omega_t \ll 1$ ) promotes the vortex breakdown at lower Reynolds numbers than in the cylinder with stationary endwall. Stronger corotation of the bottom endwall leads to the detachment of the recirculation zone from the axis and formation of an additional vortex ring.

Watson and Neitzel [15] carried out numerical studies on the swirl flow in a corotating container in which the cylinder sidewall and the top endwall as a unit rotate in the same direction with respect to the rotating bottom endwall ( $\Omega_{ts}/\Omega_b \ll 1$ ). They used as parameter, the relative rotational Reynolds number  $Re_\Delta$  based on the angular velocity difference  $\Omega_b - \Omega_{ts}$ , and the angular velocity ratio  $\Omega_{ts}/\Omega_b$ . With increasing the angular velocity ratio at a constant  $Re_\Delta = (\Omega_b - \Omega_{ts})R^2/\nu$ , the recirculation zone was found to locate upstream, and with further increase of the angular velocity ratio, it finally disappeared. An inviscid breakdown criterion proposed by Brown and Lopez [7] was examined using the numerical solutions. According to the Brown and Lopez' criterion, for the occurrence of vortex breakdown, the helix angle of the velocity vector must be greater than that of the vorticity vector on a stream surface in the upstream of the recirculation zone. Watson and Neitzel concluded that the criterion of Brown and Lopez is satisfied only within the breakdown bubble itself.

Fujimura et al. [16] investigated experimentally the vortex breakdown phenomena in a differentially rotating cylindrical container in which the top endwall rotates at a relatively high angular velocity  $\Omega_t$ , and the bottom endwall and the sidewall rotate at a low angular velocity  $\Omega_{sb}$ . For a fixed cylinder aspect ratio, and for a given relative rotational Reynolds number  $Re_\Delta = (\Omega_t - \Omega_{sb})R^2/\nu$  based on the angular velocity difference  $\Omega_t - \Omega_{sb}$ , the flow behavior is examined as  $|\Omega_{sb}/\Omega_t|$  increases. For a corotation

\*email: koide@tokyo-tmct.ac.jp

Contributed by the Fluids Engineering Division for publication on the JOURNAL OF FLUIDS ENGINEERING. Manuscript received by the Fluids Engineering Division August 21, 2003; revised manuscript received October 6, 2004. Review Conducted by: J. Marshall.

case ( $\Omega_{sb}/\Omega_t > 0$ ), the breakdown bubble is located closer to the bottom endwall disk. However, for a counter-rotation case ( $\Omega_{sb}/\Omega_t < 0$ ), the bubble is seen closer to the top endwall disk. For sufficiently large values of  $\Omega_{sb}$ , the bubble ceases to exist for both corotation and counter-rotation cases.

The main objective of the present study is to report the numerical simulations on vortex breakdown in a differentially rotating cylindrical container. In the present situation, the top endwall disk rotates at a relatively high angular velocity  $\Omega_t$ , while the cylinder sidewall and bottom endwall rotate in unison at a low angular velocity  $\Omega_{sb}$ . The present numerical results are compared with the experimental results. Of interest are the cases when the overall Reynolds number based on the angular velocity difference  $\Omega_t - \Omega_{sb}$  is large, but the magnitude of the angular velocity ratio is small  $|\Omega_{sb}/\Omega_t| \ll 1$ . Both cases of a corotation ( $\Omega_{sb}/\Omega_t > 0$ ) and a counter-rotation ( $\Omega_{sb}/\Omega_t < 0$ ) are considered. Numerical studies on an only corotation case have been carried out by Watson and Neitzel [15]. It is found that the global flow features undergo substantial changes by introducing small differential rotations of the top endwall and cylinder sidewall.

It is noted that, although the previous studies on vortex breakdown have dealt with the various geometries, the numerical results simulated by Watson and Neitzel [15], and experimental observations carried out by one of the authors [16] are the only reports in the literature on vortex breakdown in a differentially rotating cylindrical container, in other words  $\Omega_t \neq 0$  and  $\Omega_b = \Omega_s \neq 0$ . This paper aims to portray the prominent flow characteristics in a differentially rotating container, which exhibits qualitative differences from the cases of  $\Omega_t \neq 0$  and  $\Omega_b = \Omega_s = 0$ .

Several plausible arguments for the physical mechanism of vortex breakdown have been put forth, including boundary-layer separation, hydrodynamic instability, hydraulic jump, and wave propagation. Of particular interest is the proposal by Brown and Lopez [7], which was based on the production of a negative azimuthal component of vorticity. Jahnke and Valentine [17], as well as Watson and Neitzel [15], for similar flow geometries, attempted to apply and extend the criterion of Brown and Lopez. In the present paper, assuming a steady, inviscid, axisymmetric swirling flow in a rotating system which rotates at same angular velocity of the bottom and cylinder sidewall, we extend the criterion of Brown and Lopez in a differentially rotating container to make clear the influence of the bottom and cylinder sidewall rotation on the appearance of vortex breakdown.

## 2 Numerical Methods

Rotating cylindrical coordinates are adopted to make clear the effects of the rotation of the cylinder sidewall and bottom endwall, in other words the Coriolis force, on the swirl flow in a closed differentially rotating cylindrical container in which the top endwall rotates at a relatively high angular velocity  $\Omega_t$ , and the side wall and bottom endwall rotate at a low angular velocity  $\Omega_{sb}$ . For a fixed cylinder aspect ratio, and for a given relative rotational Reynolds number based on the angular velocity difference  $\Omega_t - \Omega_{sb}$ , the flow behavior is examined with increasing  $|\Omega_{sb}/\Omega_t|$ . For stationary cases ( $\Omega_{sb} = 0$ ), one of the authors stated from the flow visualization observations and the three-component velocity measurements that, as ascertained explicitly in the original experiments of Escudier [2], the global flow patterns were found to be highly axisymmetric for the governing parameter ranges of  $Re < 2.60 \times 10^3$  and  $H/R < 3.3$  [10]. Through the experimental visualization, Spohn et al. [18] showed that the asymmetry appears at the downstream end of the steady breakdown bubbles. For corotation and counter-rotation cases ( $\Omega_{sb}/\Omega_t > 0$  and  $\Omega_{sb}/\Omega_t < 0$ ), the flow visualization results [16] were consistent with the basic assumption of axisymmetry in the present parameter ranges. From the results, a rotational azimuthal symmetry was assumed in the present numerical calculation ranges. However, in the recent numerical studies (e.g., Sotiropoulos and Ventikos [9], Sotiropoulos et al. [19], and Serre and Bontoux [20,21]), the unsteady,

three-dimensional Navier-Stokes equations were numerically solved, and the asymmetrical features of the flow were revealed. Therefore, the present calculations are incomplete to clarify the nonaxisymmetric nature of the flow, but relevant to predict correctly of the onset of vortex breakdown, and reproduce the size and location of the breakdown bubbles.

Dimensional quantities of the length ( $r^*, z^*$ ), the time  $t^*$ , the velocity components ( $u^*, v^*, w^*$ ) corresponded to the cylindrical coordinates ( $r^*, \theta^*, z^*$ ), and the pressure ( $p^* - p_e^*$ ) which is the pressure deviation from its equilibrium value  $p_e^*$  is scaled by using the radius of the cylinder  $R$  and  $(\Omega_t - \Omega_{sb})$  as follows:

$$(r, z) = (r^*, z^*)/R, \quad t = t^*(\Omega_t - \Omega_{sb}),$$

$$(u, v, w) = (u^*, v^*, w^*)/R(\Omega_t - \Omega_{sb}),$$

$$p = (p^* - p_e^*)/\rho(\Omega_t - \Omega_{sb})^2 R^2.$$

Using the above nondimensional quantities, we have the momentum equations in the radial, azimuthal, and axial directions, and the continuity equation as follows:

$$\frac{Du}{Dt} = \frac{v^2}{r} - \frac{\partial p}{\partial r} + \frac{v}{Ro} + \frac{1}{Re_\Delta} \left( \Delta u - \frac{u}{r^2} \right), \quad (1)$$

$$\frac{Dv}{Dt} = -\frac{uv}{r} - \frac{u}{Ro} + \frac{1}{Re_\Delta} \left( \Delta v - \frac{v}{r^2} \right), \quad (2)$$

$$\frac{Dw}{Dt} = -\frac{\partial p}{\partial z} + \frac{1}{Re_\Delta} \Delta w, \quad (3)$$

where

$$\frac{D}{Dt} \equiv \frac{\partial}{\partial t} + u \frac{\partial}{\partial r} + w \frac{\partial}{\partial z}, \quad \Delta \equiv \frac{\partial^2}{\partial r^2} + \frac{1}{r} \frac{\partial}{\partial r} + \frac{\partial^2}{\partial z^2},$$

and

$$\frac{1}{r} \frac{\partial(ru)}{\partial r} + \frac{\partial w}{\partial z} = 0. \quad (4)$$

In the above,  $Re_\Delta = R^2(\Omega_t - \Omega_{sb})/v$  is the relative rotational Reynolds number and  $Ro = (\Omega_t - \Omega_{sb})/2\Omega_{sb}$  is the Rossby number, which are based on the angular velocity difference ( $\Omega_t - \Omega_{sb}$ ). To compare with some experimental results, the rotational Reynolds number  $Re = R^2\Omega_t/v$  based on the angular velocity  $\Omega_t$  of the top endwall, and the Ekman number  $Ek = v/2\Omega_{sb}R^2 (= Ro/Re_\Delta)$  will also be useful.

The boundary conditions were nonslip on the solid walls and symmetry at the axis

$$z=0, \quad 0 < r < 1,$$

$$\frac{\partial p}{\partial z} = \frac{1}{Re_\Delta} \frac{\partial^2 w}{\partial z^2}, \quad u=0, \quad v=0, \quad w=0,$$

$$z=H/R, \quad 0 < r < 1,$$

$$\frac{\partial p}{\partial z} = \frac{1}{Re_\Delta} \frac{\partial^2 w}{\partial z^2}, \quad u=0, \quad v=r, \quad w=0,$$

$$r=1, \quad 0 \leq z \leq H/R,$$

$$\frac{\partial p}{\partial r} = \frac{1}{Re_\Delta} \frac{\partial^2 u}{\partial r^2}, \quad u=0, \quad v=0, \quad w=0,$$

$$r=0, \quad 0 \leq z \leq H/R,$$

$$\frac{\partial p}{\partial r} = 0, \quad u=0, \quad v=0, \quad \frac{\partial w}{\partial r} = 0. \quad (5)$$

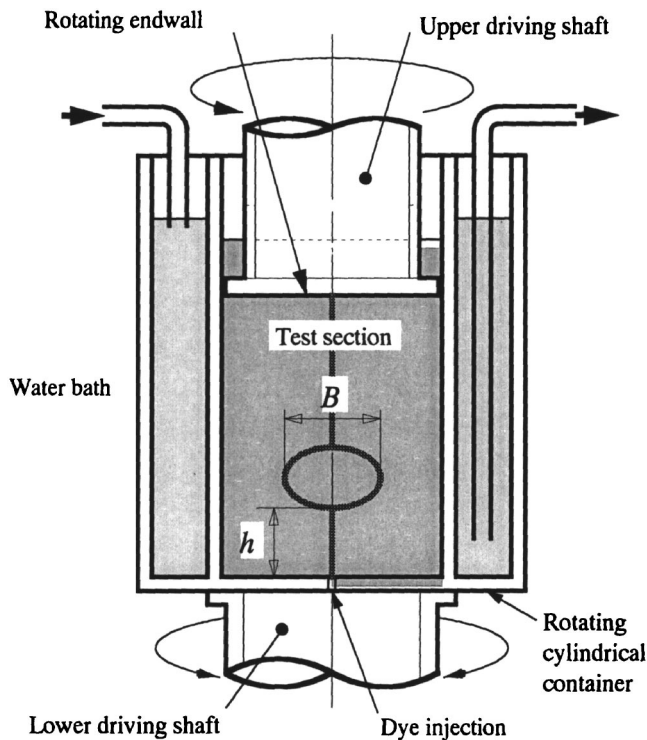


Fig. 1 Experimental apparatus

As the initial condition, the fluid was stationary at  $t=0$ , and then the top endwall rotated impulsively at the constant angular velocity for  $t>0$ . The time-dependent calculation was done until the steady state is reached. The steady state was confirmed when the average of maximum variation of the velocity components over 100 iterations of time step was less than  $1.0 \times 10^{-3}$ . Numerical solutions were obtained by the finite difference method. For the advection terms, one of the upwind third-order schemes developed by Kawamura and Kuwahara [22] was applied. Accuracy at the boundary corresponded to second order. For the method of coupling momentum and continuity equation, the SIMPLE scheme was employed. Time integration is carried out by the second-order Crank-Nicolson scheme. We utilized stretched grids which were fine near the solid walls and central axis. Typical grid points were 100 (in radial direction)  $\times$  200 (in axial direction) for  $H/R=2.0$  and  $Re_{\Delta}=2060$ . As for this grid size, the increments were 0.004–0.015 in radial and axial direction and the time interval was 0.001. In each time step, iterative calculations were stopped when the

value of the left side of the continuity equation, Eq. (4), was converged less than  $1.0 \times 10^{-3}$ . The calculation run was also done for  $H/R=2.0$  and  $Re_{\Delta}=2060$  on the grid size of  $300 \times 500$  which was the finest resolution. Between the results on the grid size of  $100 \times 200$  and  $300 \times 500$ , no significant difference was found.

### 3 Experimental Methods

One of the present authors carried out experimental studies on the vortex breakdown in a differentially rotating cylindrical container in which the top endwall rotated at a high angular velocity and the cylinder and bottom endwall rotated at a low angular velocity. Since some of the experimental results were compared with the present numerical results, we explain briefly the experimental apparatus and procedure in the following. The details are available in the literature [16].

Figure 1 shows the experimental apparatus consisting of a container made of a pyrex glass cylinder, a top endwall, a bottom endwall, two driving shafts and a transparent outer water bath. The top endwall, and the cylinder sidewall and bottom endwall were mounted to the upper and lower driving shaft, respectively, which were driven by ac servomotors, thus the corotation or the counter-rotation of the cylindrical container and the top endwall were attained at different angular velocities, independently. The working fluid was a glycerine-water mixture of 80 wt %, and was kept at a fixed temperature  $25.0 \pm 0.1^{\circ}\text{C}$  by a cylindrical outer water bath controlled thermostatically. Viscosity of the working fluid was measured after each experimental run. It is notable that the dependence of the kinematic viscosity on temperature is appreciable. The overall uncertainty in the Reynolds number is less than  $\pm 1\%$ . A limited quantity of dye was injected into the container through a 1 mm diameter hole at the center of the bottom endwall. Dye streaklines in the meridional plane were illuminated by a sheet of light. The streaklines were photographed by a high-resolution charge-coupled device camera.

### 4 Results

**4.1 Meridional Flow.** Figure 2 shows the contour plots of stream function together with the photographs of meridional-plane streaklines for  $H/R=2.0$  and  $Re_{\Delta}=2060$  with varying  $Ek$ . It is evident that the numerical solutions are substantially consistent with flow visualization results in terms of the locations and the shape of the vortex breakdown bubbles. The views of the streaklines are distorted in radial direction, due to the lens effect of the cylindrical sidewalls. This effect was compensated in the measurements of the maximum outer diameter of the breakdown bubble. Figures 2(a)–2(c), 2(d), and 2(e)–2(h) correspond to the counter-rotation, stationary, and corotation case, respectively. For the stationary case, as shown in Fig. 2(d), two breakdown bubbles are seen. For the counter-rotation case, as  $Ek$  decreases, the break-

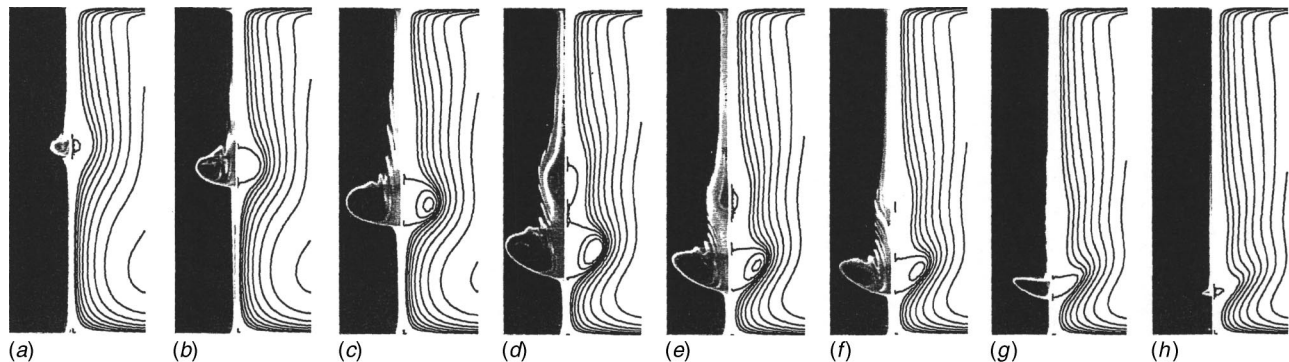


Fig. 2 Numerical and experimental results on the vortex breakdown in a differentially rotating container for  $H/R=2.0$  and  $Re_{\Delta}=2060$  with varying  $Ek$ . (a)–(c) counter-rotation case; (d) stationary case; (e)–(h) corotation case. (a)  $|Ek|=0.0104$ ; (b) 0.0113; (c) 0.0146; (d)  $Ek=\infty$ ; (e) 0.0217; (f) 0.0146; (g) 0.0880; and (h) 0.007

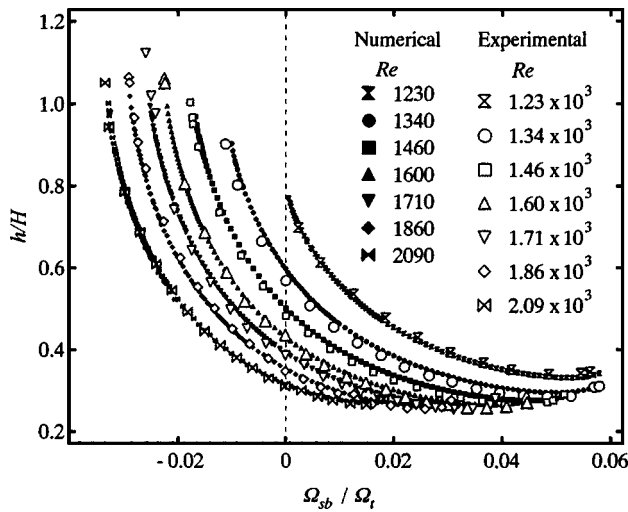


Fig. 3 Locations of upstream stagnation point of the breakdown bubble  $h/H$  for  $H/R=1.75$  at various fixed  $Re$  (experimental uncertainty in  $h/H$ : less than  $\pm 0.5\%$ ; in  $Re$ : less than  $\pm 1\%$ )

down bubble shifts toward downstream (closer to the top endwall), and reduces in size. For the corotation case, as  $Ek$  decreases, the breakdown bubble shifts toward upstream (closer to the bottom endwall), and gradually becomes small in size, then almost disappears, as shown in Fig. 2(h). Numerical solutions are in close agreement with the experimental results.

**4.2 Location of the Stagnation Point and Radius of the Breakdown Bubble.** Based upon the numerical solutions for  $H/R=1.75$  and various  $Re$ , we estimated the axial height  $h$  of the upstream stagnation point of breakdown bubble from the bottom endwall. Figure 3 shows the diagram of  $h/H$  versus the angular velocity ratio  $\Omega_{sb}/\Omega_t$ . For experimental convenience, the angular velocity of the top endwall  $\Omega_t$  was fixed at a constant, while the angular velocity of the container  $|\Omega_{sb}|$  was increased gradually in the corotation or counter-rotation direction with respect to the rotation direction of the top endwall. The numerical results are in good agreement with the experimental results, as shown in Fig. 3. For the counter-rotation case ( $\Omega_{sb}/\Omega_t < 0$ ), as  $\Omega_{sb}/\Omega_t$  decreases,  $h/H$  increases, i.e., the breakdown bubble shifts downstream rapidly until the bubble disappears at a certain minimum  $\Omega_{sb}/\Omega_t$ . For larger  $Re$ , the breakdown bubble disappears at a smaller  $\Omega_{sb}/\Omega_t$ . For the corotation case ( $\Omega_{sb}/\Omega_t > 0$ ), as  $\Omega_{sb}/\Omega_t$  increases,  $h/H$  decreases asymptotically until the bubble disappears at a certain maximum  $\Omega_{sb}/\Omega_t$ . When  $\Omega_{sb}/\Omega_t$  is slightly smaller than the maximum value, the location of the bubble shifts slightly toward the top endwall. With increasing  $Re$ , the bubble disappears at a smaller value of maximum  $\Omega_{sb}/\Omega_t$ .

The maximum outer diameter  $B$  of the breakdown bubble was estimated, and the values of  $B/2R$  for  $Re$  and  $\Omega_{sb}/\Omega_t$  were compared with the experimental results, as shown in Fig. 4. As described in the previous section, lens effect of the cylindrical side-walls in the experiment was compensated geometrically and calibrated. For each fixed  $Re$ ,  $B/2R$  grows from the smallest  $\Omega_{sb}/\Omega_t$ , and attains the maximum outer diameter at a certain  $\Omega_{sb}/\Omega_t$ , then diminishes with increasing of  $\Omega_{sb}/\Omega_t$  and finally disappears. As  $Re$  increases, the maximum  $B/2R$  becomes larger.

For fixed  $Re_\Delta=2060$  and  $H/R=2.0$ , with varying  $Ek$ , we have estimated  $h/H$  from the numerical solutions, as shown in Fig. 5. For the counter-rotation case, as  $|Ek|$  decreases,  $h/H$  increases, whereas, for the corotation case,  $h/H$  decreases as  $Ek$  decreases. For the corotation case, the stagnation point disappeared for smaller  $|Ek|$  than that for the counter-rotation case.

For corotation cases ( $\Omega_{sb}/\Omega_t > 0$ ), numerical simulations were performed by Watson and Neitzel [15] for fixed values of  $Re_\Delta$  and

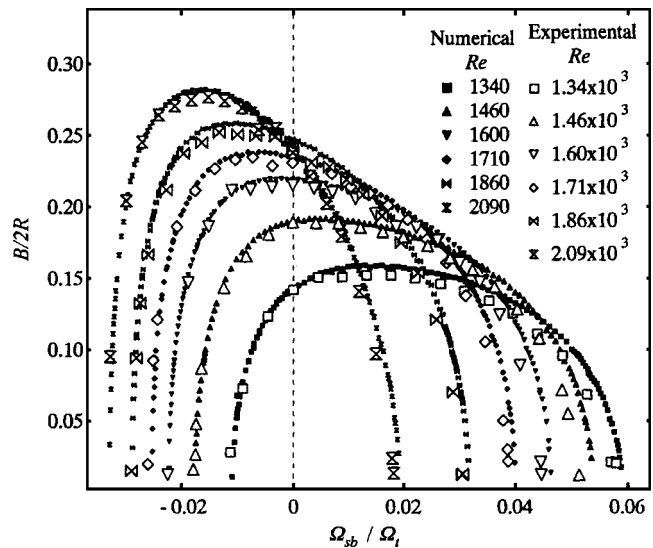


Fig. 4 Maximum outer diameters of the breakdown bubble  $B/2R$  for  $H/R=1.75$  at various fixed  $Re$  (experimental uncertainty in  $B/2R$ : less than  $\pm 0.5\%$ ; in  $Re$ : less than  $\pm 1\%$ )

$H/R$ , and with  $\Omega_{sb}/\Omega_t$  varying. The results illustrated the variations in the radius of the breakdown bubble for ( $H/R=1.50$  and  $2.00$ ,  $Re_\Delta=1500$ ), and for ( $H/R=1.75$ ,  $Re_\Delta=1748$ ). Also, the locations of the upstream side stagnation point for ( $H/R=1.75$ ,  $Re_\Delta=1748$ ) were computed. These numerical results, the present numerical results and the experimental observations [16] are in reasonable qualitative agreement.

**4.3 Critical Boundary Curves.** Ranges of the vortex breakdown occurrence in the ( $Re_\Delta$ - $H/R$ )-plane, based on the numerical data, for the stationary case ( $\Omega_{sb}=0$ ), and the corotation and counter-rotation cases ( $\Omega_{sb}/\Omega_t > 0$  and  $\Omega_{sb}/\Omega_t < 0$ ) at  $|Ek|=0.0113$  are shown in Fig. 6. We confirmed the present numerical results and the experimental results [16] of the critical boundary curves for  $\Omega_{sb}=0$  were in close agreement with the Escudier [2] and Roesner's [11] experiments (not shown in this figure). For  $|Ek|=0.0113$ , the present numerical and experimental results

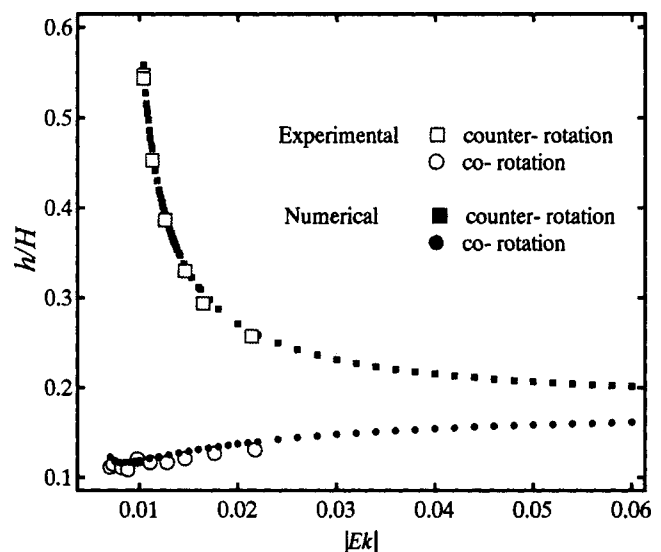


Fig. 5 Locations of upstream stagnation point of the breakdown bubble  $h/H$  for  $H/R=2.0$  and  $Re_\Delta=2060$  (Experimental uncertainty in  $h/H$ : less than  $\pm 0.5\%$ ; in  $Re_\Delta$ : less than  $\pm 1\%$ )

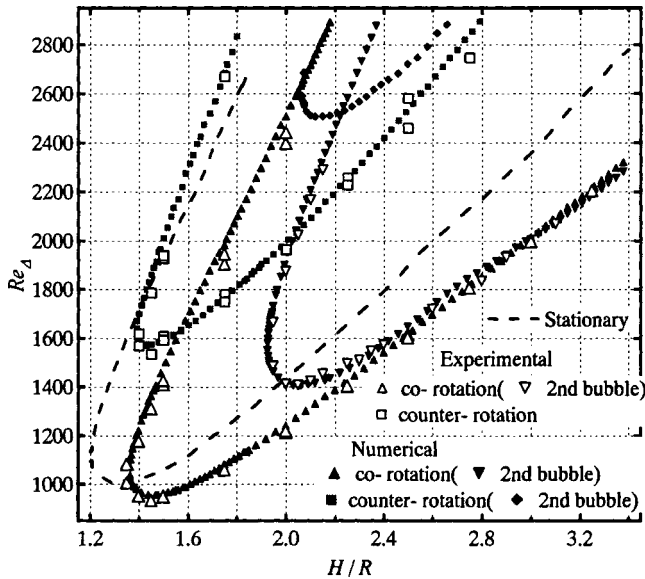


Fig. 6 Critical boundaries for the vortex breakdown in a differentially rotating container for  $|Ek|=0.0113$  (experimental uncertainty in  $H/R$ : less than  $\pm 0.5\%$ ; in  $Re_\Delta$ : less than  $\pm 1\%$ )

showed favorable agreement. For the numerical calculation, we divided  $Re_\Delta$ - $H/R$  regions for setting grid point sizes with suitable increments. Minimum radial grid points were 70 for  $Re \leq 2000$  and maximum points were 110 for  $Re \leq 3000$ . Figure 6 indicates that, for the corotation case, the upper and lower critical  $Re_\Delta$  become smaller in comparison with the stationary case, and that, for the counter-rotation case, while the lower critical  $Re_\Delta$  becomes larger, the upper critical  $Re_\Delta$  does not show remarkable difference in comparison with the boundary curve for the stationary case. Also, the critical boundary curves for the second bubble were shown. The critical  $Re_\Delta$  dividing steady and unsteady states were not clarified in the present study.

## 5 Discussion

The effects of the simultaneous rotation of the cylinder sidewall and bottom endwall, rotating at a low angular velocity  $\Omega_{sb}$ , when

the top endwall rotates at a relatively high angular velocity  $\Omega_t$ , are remarkable, even for a considerably small angular velocity ratio  $|\Omega_{sb}/\Omega_t| \ll 1$ . When the relative rotational Reynolds number  $Re_\Delta$  is fixed, which is based on the angular velocity difference  $\Omega_t - \Omega_{sb}$ , the relative magnitudes of swirls produced by the top endwall rotation can be considered as almost the same, regardless of the stationary, corotation, and counter-rotation cases ( $\Omega_{sb} = 0$ ,  $\Omega_{sb}/\Omega_t > 0$ , and  $\Omega_{sb}/\Omega_t < 0$ ). The nonzero  $\Omega_{sb}$  seems to influence and complicate the development of the Stewartson layer on the container sidewall, the Ekman layer on the container bottom endwall, and the vortex core flow near the axis of the cylinder.

The objective of the present paper is to clarify the effects of the simultaneous rotation of the cylinder sidewall and bottom endwall on the vortex breakdown with holding  $Re_\Delta$  constant. Under the corresponding geometry, for the corotation case, Watson and Neitzel [15] state that with increasing  $\Omega_{sb}/\Omega_t$ , the swirling flow approaches a state of the rigid-body rotation, and the breakdown bubbles reduce in size and move upstream, because  $Re = R^2\Omega_t/\nu$  must increase to hold  $Re_\Delta$  constant. We consider both cases of a corotation ( $\Omega_{sb}/\Omega_t > 0$ ) and a counter-rotation ( $\Omega_{sb}/\Omega_t < 0$ ), and make clear the influences of the Coriolis force quantitatively by introducing the rotating reference frame, which leads to the clarification for the effect of small differential rotations of the top endwall and cylinder sidewall.

In this section, we show the distributions of the angular momentum and the individual terms in the momentum equation along the streamlines for the stationary, corotation, and counter-rotation case. We try to derive a criterion according the criterion of Brown and Lopez [7] in a rotating reference frame to make clear the influence of a differentially rotating container on the appearance of vortex breakdown.

**5.1 Angular Momentum Along a Streamline.** For fixed  $H/R = 2.0$  and  $Re_\Delta = 2060$ , contour plots of meridional-plane streamlines of stream function  $\Psi = 0.0001$  and distributions of the angular momentum  $rv$  along the streamlines for the stationary, corotation, and counter-rotation case ( $\Omega_{sb} = 0$ ,  $\Omega_{sb}/\Omega_t > 0$ , and  $\Omega_{sb}/\Omega_t < 0$ ) are shown in Fig. 7. Relatively small and large differences between the contour streamlines can be observed in the Ekman layers on the cylinder bottom endwall and in the vortex core flows near the axis of the cylinder, respectively [see Fig. 7(a)]. The development of the Ekman layer seems to be suppressed slightly by the corotation and promoted slightly by the

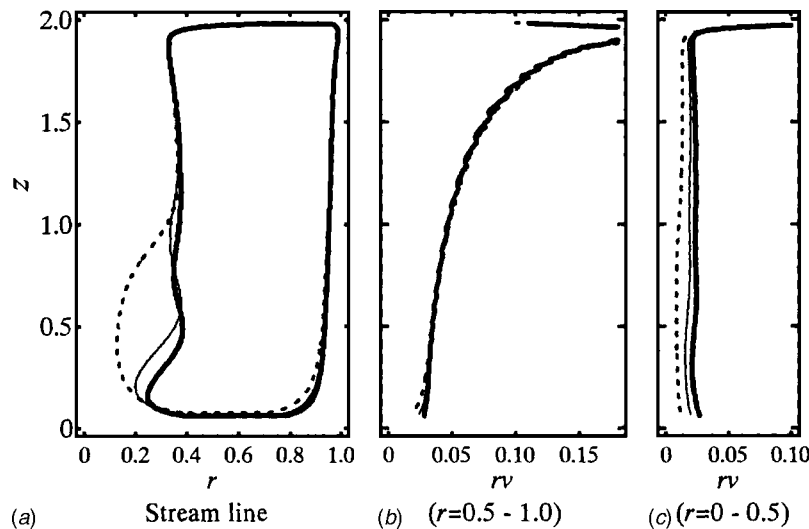
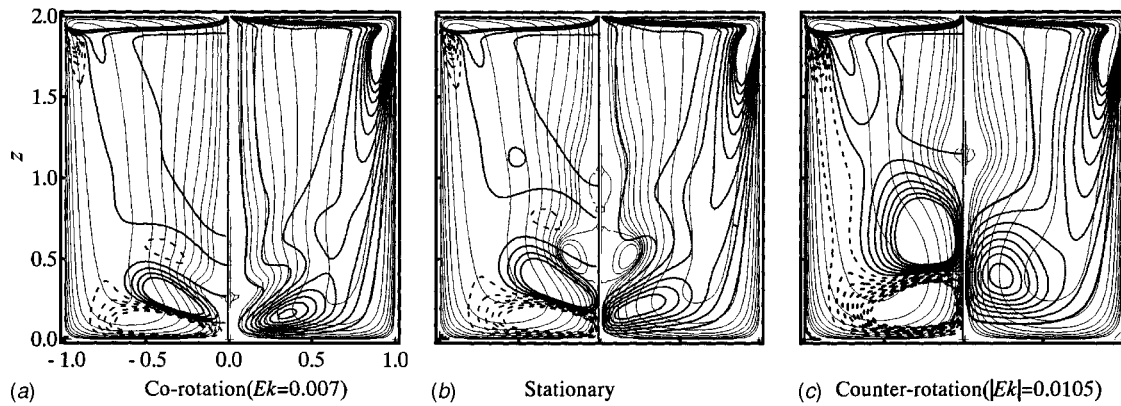


Fig. 7 Streamlines of  $\Psi = 0.0001$  and distributions of angular momentum  $rv$  along the streamlines in a differentially rotating container for  $H/R = 2.0$  and  $Re_\Delta = 2060$ . —: stationary case ( $Ek = \infty$ ); - - -: corotation case ( $Ek = 0.011$ ); ···: counter-rotation case ( $|Ek| = 0.011$ )





**Fig. 8 Contour plots of  $-uv/r$  (—; positive; ···; negative, left) and  $v^2/r$  (right) overlapping the streamlines (—) for  $H/R=2.0$  and  $Re_{\Delta}=2060$**

counter-rotation, which is also observed from the crowdedness of the streamlines in the Ekman layer (see Fig. 8). As shown in Figs. 7(b) and 7(c), in the Ekman layers,  $rv$  along the streamline increases for the corotation case ( $\Omega_{sb}/\Omega_t > 0$ ) and decreases for the counter-rotation ( $\Omega_{sb}/\Omega_t < 0$ ) as compared with the stationary case ( $\Omega_{sb} = 0$ ). The  $rv$  is almost conserved along the streamline in the vortex core flow around the axis of the cylinder for the stationary, corotation, and counter-rotation cases. However, there are no differences between the streamlines and the distributions of  $rv$  in the Stewartson layers.

In the momentum equations, Eqs. (1) and (2), the centrifugal force  $v^2/r$  and the Coriolis force  $-uv/r$  may be interpreted as main source terms and the Coriolis forces  $v/Ro$  and  $-u/Ro$  may be interpreted as additional source terms due to the rotation of the cylinder sidewall and bottom endwall for the radial velocity  $u$  and the azimuthal velocity  $v$ , respectively. The signs of  $v/Ro$  and  $-u/Ro$  are same as  $v^2/r$  and  $-uv/r$ , respectively, for the corotation case, and reverse for the counter-rotation case. In the Stewartson and Ekman layers, and in the converging vortex core flow near the center of the bottom endwall ( $v > 0$  and  $u < 0$ ),  $v/Ro$  and  $-u/Ro$ , respectively, act in the radial outward (inward) direction as to decrease (increase) the negative radial velocity  $u$  and act in the positive (negative) azimuthal direction as to increase (decrease) the azimuthal velocity  $v$  for the corotation (counter-rotation) case [ $\Omega_{sb}/\Omega_t > 0$  ( $\Omega_{sb}/\Omega_t < 0$ )]. In the diverging vortex core flow ( $v > 0$  and  $u > 0$ ) near the axis of the cylinder,  $v/Ro$  and  $-u/Ro$  act in the radial outward (inward) direction and in the negative (positive) azimuthal direction, respectively, for the corotation (counter-rotation) case. The  $|u|$  in the Ekman layer and converging vortex core flow is larger than that in the diverging vortex core flow. Consequently, the corotation seems to retard the decrease of the swirl, and the counter-rotation appears to facilitate the decrease of the swirl, especially, in the Ekman layer. And, in the diverging vortex core flow, the corotation (counter-rotation) seems to extend (narrow) the diverging angle.

**5.2 Evaluation of the Terms in Radial and Azimuthal Equation.** According to the criterion for the appearance of vortex breakdown bubble in a closed cylindrical container with one rotating endwall disk ( $\Omega_t \neq 0$  and  $\Omega_b = \Omega_s = 0$ ), Gelfgat et al. [23] have shown that the convective transport of the azimuthal velocity  $v$  results in a nonmonotone axial distribution of the centrifugal force  $v^2/r$ , which is the main reason for the change of signs of the azimuthal vorticity  $\eta$  and  $\partial(v^2/r)/\partial z$ . On the concave part of a streamline near the axis of the cylinder, which corresponds to a location of incipient vortex breakdown, the radial velocity  $u$  changes its sign from positive to negative. This results in the change of sign of the Coriolis force  $-uv/r$  because  $v$  is always positive. The negative Coriolis force increases  $v$  such that one can see weak local maxima and minima in the axial distribution of

$v^2/r$ . This local decrease and increase of  $v^2/r$  lead to the appearance of additional motion which results in a recirculation. From the detailed numerical solutions, Gelfgat et al. considered to add the change of sign of  $\partial(v^2/r)/\partial z$  as another necessary condition to the generation of negative  $\eta$  for the appearance of the vortex breakdown bubble proposed by Brown and Lopez [7].

For fixed  $H/R=2.0$  and  $Re_{\Delta}=2060$ , for the stationary, corotation and counter-rotation cases, the contour plots of the centrifugal force  $v^2/r$ , on the right half of the figure, and the Coriolis force  $-uv/r$ , on the left half of the figure, which are overlapped with the streamlines in the meridional plane, are shown in Fig. 8. The individual terms of convective, centrifugal  $v^2/r$ , pressure gradient, Coriolis  $v/Ro$ , and viscous in the momentum equation in the radial direction Eq. (1), and convective  $-uv/r$ , Coriolis  $-u/Ro$ , and viscous in the azimuthal direction Eq. (2), estimated along the streamline of stream function  $\Psi=0.00001$  by using the present numerical solutions are shown in Figs. 9 and 10, respectively. The Ekman numbers  $Ek=0.007$  and  $-0.0105$  are selected, respectively, as a near critical state before breakdown bubble disappears for the corotation and counter-rotation cases. Figures 8(b), 9(b), and 10(b) correspond to Fig. 2(d) which is the stationary case with two breakdown bubbles.

As Gelfgat et al. [23] pointed out, the negative and positive regions of the Coriolis force  $-uv/r$  are observed between the bottom endwall and the upstream stagnation point of the first breakdown bubble, and local maximum of the centrifugal force  $v^2/r$  is observed near the extreme of a streamline as shown in Fig. 8(b), for the stationary case ( $Ro=\infty$ ). The azimuthal velocity  $v$  is always positive, and the radial velocity  $u$  changes its sign from negative to positive on a convex streamline near the axis of the cylinder and from positive to negative on a concave streamline. The distributions of the individual terms in Eqs. (1) and (2), except the Coriolis terms  $v/Ro$  and  $-u/Ro$ , as well as the negative and positive regions of  $-uv/r$  and a large hill of  $v^2/r$  are compressed toward the bottom endwall for the corotation case [see Figs. 8(a), 9(a), and 10(a)], and extended for the counter-rotation case [see Figs. 8(c), 9(c), and 10(c)] as compared with the stationary case [see Figs. 8(b), 9(b), and 10(b)]. These distributions correspond to the movement of the breakdown bubble which shifts toward upstream, i.e., toward the bottom endwall for the corotation case, and toward downstream, i.e., the top endwall for the counter-rotation case. As shown in Figs. 9(a) and 9(c), the Coriolis force  $v/Ro$  acts in the radial outward direction for the corotation case ( $v > 0$  and  $Ro > 0$ ) and in the radial inward direction for the counter-rotation case ( $v > 0$  and  $Ro < 0$ ). The centrifugal force  $v^2/r$  acts always in the radial outward direction, and is nearly constant along the streamline near the axis of the cylinder. The Coriolis force  $-u/Ro$  acts in the positive (negative) azimuthal direction in the converging flow ( $u < 0$ ), and acts in the

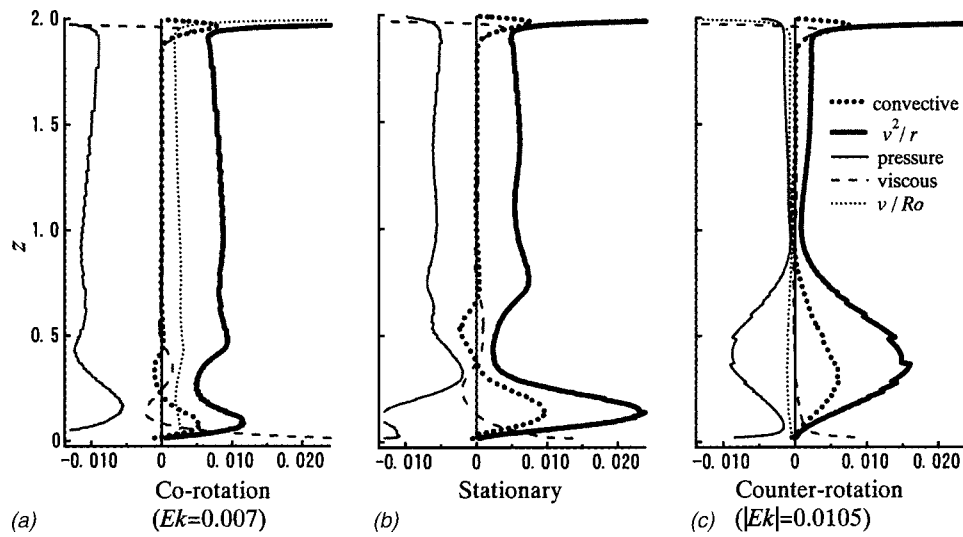


Fig. 9 Evaluations of terms in the radial direction Eq. (1), along the streamlines of ( $\Psi=0.00001$ ) for  $H/R=2.0$  and  $Re_{\Delta}=2060$

negative (positive) direction in the diverging flow ( $u>0$ ) for the corotation (counter-rotation) case, respectively, as shown in Figs. 10(a) and 10(c). It seems that the influences of  $v/Ro$  and  $-u/Ro$  cannot be ignored as compared with  $v^2/r$  and  $-uv/r$ , respectively, near the stagnation points.

Taking the curl of the momentum equation, the components of which are Eqs. (1), (2), and (3), the nondimensional vorticity transport equation in the cylindrical coordinates, rotating at  $\Omega_{sb}$  is derived. The components are

$$\frac{D\xi}{Dt} = \frac{\partial}{\partial z} \left( \frac{uv}{r} + \frac{u}{Ro} \right) + \frac{1}{Re_{\Delta}} \left( \Delta\xi - \frac{\xi}{r^2} \right), \quad (6)$$

$$\frac{D\eta}{Dt} = \frac{\partial}{\partial z} \left( \frac{v^2}{r} + \frac{v}{Ro} \right) + \frac{1}{Re_{\Delta}} \left( \Delta\eta - \frac{\eta}{r^2} \right), \quad (7)$$

$$\frac{D\zeta}{Dt} = -\frac{1}{r} \frac{\partial}{\partial r} \left( \frac{uv}{r} + \frac{u}{Ro} \right) + \frac{1}{Re_{\Delta}} \Delta\zeta, \quad (8)$$

where  $\xi = -\partial v / \partial z$ ,  $\eta = \partial u / \partial z - \partial w / \partial r$ , and  $\zeta = (1/r)(\partial(rv) / \partial r)$  are the radial, azimuthal, and axial components of the vorticity, respectively. It is clear from Eqs. (6), (7), and (8) that the axial derivatives of the negative Coriolis force  $uv/r$  and centrifugal force  $v^2/r$  and the radial derivative of the Coriolis force  $-uv/r$  may be interpreted as main source terms (see Gelfgat et al. [14]) and the axial derivatives of the negative Coriolis force  $u/Ro$  and centrifugal force  $v/Ro$  and the radial derivative of the Coriolis force  $-u/Ro$  may be interpreted as additional source terms due to the rotation of the cylinder sidewall and bottom endwall for  $\xi$ ,  $\eta$ , and  $\zeta$ , respectively, in other words  $\xi$ ,  $\eta$ , and  $\zeta$  will be changed along the streamline due to the axial derivatives of  $(uv/r + u/Ro)$  and  $(v^2/r + v/Ro)$ , and the radial derivatives of  $-(uv/r + u/Ro)$ , respectively. Consequently, the axial distributions of  $u/Ro$  and  $v/Ro$  seem to amplitude (attenuate) the non-monotone axial distributions of the azimuthal velocity  $v$  and radial velocity  $u$  on the convex and concave streamline near the axis of the cylinder for the corotation (counter-rotation) case [ $Ro>0$ ]

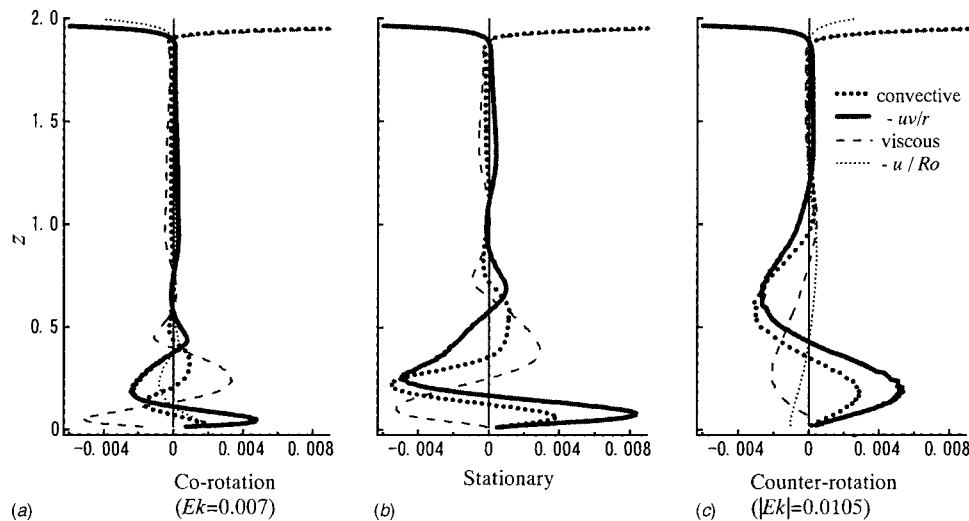


Fig. 10 Evaluations of terms in the azimuthal direction Eq. (2), along the streamline of ( $\Psi=0.00001$ ) for  $H/R=2.0$  and  $Re_{\Delta}=2060$

( $Ro < 0$ )]. In the Ekman layer and converging vortex core flow ( $u < 0$  and  $v > 0$ ) near the center of the bottom endwall, the magnitude of the swirl, i.e.,  $\zeta$  will be increased along the streamline due to the radial derivation of  $-u/Ro$  for the co-rotation case ( $Ro > 0$ ) and decreased for the counter-rotation case ( $Ro < 0$ ). Whereas, in the diverging vortex core flow ( $u > 0$  and  $v > 0$ ), the magnitude of the swirl will be decreased for the corotation case and increased for the counter-rotation case, but smaller than that in the Ekman layer and converging vortex core flow.

**5.3 Brown and Lopez Criterion Described in Rotating Cylindrical Coordinates.** For the enclosed swirl flow in which one endwall rotates and another endwall and cylinder sidewall are stationary, Brown and Lopez [7] assumed an axisymmetric steady, inviscid central core flow, and the conservation of the angular momentum  $rv$  and the total head  $p + (u^2 + v^2 + w^2)/2$  on the stream surfaces. Brown and Lopez derived a criterion for the occurrence of vortex breakdown in which the helix angle of the velocity vector must be greater than that of the vorticity vector on a diverging stream surface in the upstream of the recirculation zone.

Watson and Neitzel [15] simulated the flows in a closed container under the same geometry and boundary conditions of the present study as a modified Escudier problem, and using the numerical results, tested the validity of the Brown and Lopez criterion as a predictive tool for the occurrence of vortex breakdown. However, they seemed to take no interest in estimating the effect of the container-rotation on the occurrence of vortex breakdown. In the present study, to make clear the influence of the container-rotation on the appearance of vortex breakdown, we derive a modified criterion of Brown and Lopez in a rotating reference frame.

We applied the methodology proposed by Brown and Lopez for the criterion of vortex breakdown occurrence to a differentially rotating cylindrical container under present discussion. It is made clear in the previous discussion that the Coriolis force  $v/Ro$  cannot be ignored compared with the viscous force in the central vortex core flow. Assuming an axisymmetric steady, inviscid, central core flow in a rotating coordinate system which rotates at the same angular velocity of the bottom endwall and cylinder sidewall, the momentum equation in the radial direction can be expressed as

$$u \frac{\partial u}{\partial r} + w \frac{\partial u}{\partial z} = \frac{v^2}{r} - \frac{\partial p}{\partial r} + \frac{v}{Ro}. \quad (9)$$

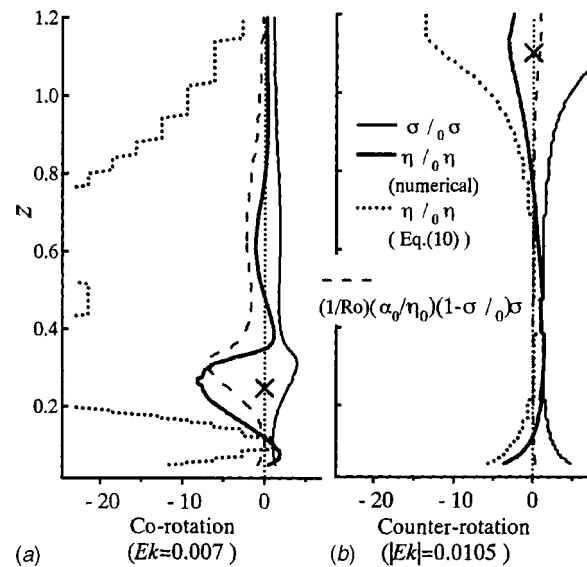
In the above, as we mentioned previously, the positive and negative sign of the Rossby number  $Ro$  correspond to the corotation and counter-rotation case, respectively. According to the procedure of Brown and Lopez, the azimuthal vorticity  $\eta$  on a stream surface in the central core flow is obtained from Eq. (9) as follows:

$$\frac{\eta}{\eta_0} = \frac{\sigma_0}{\sigma} \left( \frac{\alpha_0}{\beta_0} \right) - \frac{\sigma}{\sigma_0} \left( \frac{\alpha_0}{\beta_0} - 1 \right) + \frac{1}{Ro} \frac{\alpha_0}{\eta_0} \left( 1 - \frac{\sigma}{\sigma_0} \right), \quad (10)$$

where  $\sigma$ ,  $\alpha = v/w$ , and  $\beta = \eta/\zeta$  are the radius of a stream surface, the tangents of the helix angle for the velocity and the vorticity, respectively, and subscript 0 indicating the quantities at the reference point at which  $\sigma$  is a minimum radius. Taking  $d(\eta/\eta_0)/d(\sigma/\sigma_0)$ , we have a necessary condition for which  $\eta/\eta_0$  becomes negative as follows:

$$\left( \frac{\alpha_0}{\beta_0} \right) \left\{ \left( \frac{\sigma_0}{\sigma} \right)^2 + 1 \right\} - 1 + \frac{1}{Ro} \frac{\alpha_0}{\eta_0} > 0. \quad (11)$$

It is seen from Eq. (10) that, for  $\eta_0$  positive, as  $\sigma/\sigma_0$  increases from unity,  $\eta/\eta_0$  can become negative on a diverging stream surface if Eq. (11) is satisfied. If  $\eta_0$ ,  $\sigma_0$ ,  $\alpha_0$ , and  $\beta_0$  are fixed, since  $(\alpha_0/\eta_0)(1 - \sigma/\sigma_0)$  is negative,  $\eta/\eta_0$  becomes negative at a smaller  $\sigma/\sigma_0$  for a corotation case ( $Ro > 0$ ), in other words  $\Omega_{sb}/\Omega_t > 0$ ), and at a larger  $\sigma/\sigma_0$  for a counter-rotation case



**Fig. 11 Distributions of  $\sigma/\sigma_0$ ,  $\eta/\eta_0$  [estimated from Eq. (10) and the numerical solutions] and  $(1/Ro)(\alpha_0/\eta_0)(1 - \sigma/\sigma_0)$  in Eq. (10) along the streamlines ( $\Psi=0.00001$ ) for  $H/R=2.0$  and  $Re_\Delta=2060$**

( $Ro < 0$ , in other words  $\Omega_{sb}/\Omega_t < 0$ ), as compared with a stationary case ( $Ro = \infty$ ). As  $|Ro|$  decreases,  $\sigma/\sigma_0$  at  $\eta/\eta_0 = 0$  decreases (increases) for the corotation (counter-rotation) case. The decrease (increase) of  $\sigma/\sigma_0$  at  $\eta/\eta_0 = 0$  indicates that the appearance point of vortex breakdown is located closer to the bottom (top) endwall. These analytical explanations are in broad qualitative agreement with the experimental results.

Figure 11 shows the distributions of  $\eta/\eta_0$  estimated from the numerical solutions and Eq. (10) along the stream surfaces of  $\Psi=0.00001$  for the corotation and counter-rotation case. The  $Ek=0.007$  and  $|Ek|=0.0105$  are selected as a somewhat large value of critical  $|Ek|$  for the corotation and counter-rotation case, respectively. Locations of the upstream stagnation point of the vortex breakdown (shown by symbol  $\times$ ) are  $z=0.25$  and  $1.10$ , respectively, for the corotation and counter-rotation case. The  $\eta/\eta_0$  is positive at the throat at which  $\sigma$  is minimum and, as  $\sigma/\sigma_0$  increases,  $\eta/\eta_0$  decreases rapidly toward the stagnation point for both cases. Locations of  $\eta/\eta_0 = 0$  from the numerical calculations and Eq. (10) are mostly in agreement. The Coriolis term  $(1/Ro)(\alpha_0/\eta_0)(1 - \sigma/\sigma_0)$  in Eq. (10), shown by the dashed line in Fig. 11, is relatively small, but increases toward the stagnation point of breakdown bubble. For each case of corotation and counter-rotation, the left side of Eq. (11), not shown in Fig. 11, is satisfied in the entire core region except near and inside the breakdown bubble, and also satisfied at smaller  $|Ek|$  at which the vortex breakdown can not be seen.

## 6 Concluding Remarks

Numerical studies were carried out on the vortex breakdown in a differentially rotating container. The effects of the differential rotations of the container walls on the vortex breakdown were notable. The problem for the vortex breakdown with one endwall rotating in a cylindrical container was also simulated and considered.

For a fixed relative Reynolds number  $Re_\Delta$ , for a corotation case, as the Ekman number  $Ek$  decreases, the vortex breakdown bubble moves toward upstream, whereas, for a counter-rotation case, the vortex breakdown bubble moves toward downstream. For each case, the vortex breakdown disappears at a certain value of  $Ek$ .

Critical boundaries in the  $(Re_{\Delta}-H/R)$ -plane, distributions of the location of upstream stagnation point and maximum outer diameter of the breakdown bubble were obtained for the stationary, corotation, and counter-rotation cases. These numerical results were in excellent agreement with the experimental results.

Discussing the contour plots of stream function  $-uv/r$ ,  $v^2/r$  and the distributions of the individual terms in the radial and azimuthal direction equations along a convex-concave streamline, it has been shown that axial nonmonotone distributions of the Coriolis forces  $v/Ro$  and  $-u/Ro$ , accelerate the occurrence of vortex breakdown for the corotation case and decelerate the occurrence for the counter-rotation case.

Using the equation of motion in the rotating frame, the original methodology of Brown and Lopez for the occurrence of vortex breakdown is extended to a differentially rotating cylindrical container. A criterion for the occurrence of breakdown is derived which includes the Coriolis term. Analytical explanations of the criterion clarify the influence of the simultaneous rotation of the sidewall and bottom endwall on the vortex breakdown.

### Acknowledgments

The authors express their thanks to Dr. Nobukazu Tanaka, Central Research Institute of Electric Power of Industry, for his advice in the development of the present numerical code. Thanks also go to their laboratory colleagues, Mr. Kazuyuki Fujimura and Mr. Kouichi Kawasaki for their assistance in the experimental work. Appreciation is extended to the referees for explicit and useful comments. Their suggestions led to improvements in the revised version.

### References

[1] Vogel, H. U., 1968, "Experimentelle Ergebnisse ueber die Laminare Stroemung in einen zylindrischen Gehaeuse mit darin rotierender Scheibe," Max-Planck-Institut fuer Stroemungsforschung, Goertingen, Bericht 6.

[2] Escudier, M. P., 1984, "Observations of the Flow Produced in a Cylindrical Container by a Rotating Endwall," *Exp. Fluids*, **2**, pp. 189–196.

[3] Lugt, H. J., and Hasusling, H. J., 1982, "Axisymmetric Vortex Breakdown in Rotating Fluid Within a Container," *Trans. ASME, J. Appl. Mech.*, **49**, pp. 921–923.

[4] Lugt, H. J., and Abboud, M., 1987, "Axisymmetric Vortex Breakdown With and Without Temperature Effects in a Container With a Rotating Lid," *J. Fluid Mech.*, **179**, pp. 179–200.

[5] Duabe, O., and Sorensen, J. N., 1989, "Simulation Numerique de l'Ecoulement Periodique Axisymetrique Dans une Cavite Cylindrique," *Acad. Sci., Paris, C. R.*, **308**, pp. 463–469.

[6] Lopez, J. M., 1990, "Axisymmetric Vortex Breakdown. Part 1. Confined Swirling Flow," *J. Fluid Mech.*, **221**, pp. 533–552.

[7] Brown, G. L., and Lopez, J. M., 1990, "Axisymmetric Vortex Breakdown. Part 2. Physical Mechanisms," *J. Fluid Mech.*, **221**, pp. 553–576.

[8] Tsitverbilt, N., 1993, "Vortex Breakdown in a Cylindrical Container in the Light Continuation of a Steady Solution," *Fluid Dyn. Res.*, **11**, pp. 19–35.

[9] Sotiropoulos, F., and Ventikos, Y., 2001, "The Three-Dimensional Structure of Confined Swirling Flows With Breakdown," *J. Fluid Mech.*, **426**, pp. 155–175.

[10] Fujimura, K., Yoshizawa, H., Iwatsu, R., Koyama, H. S., and Hyun, J. M., 2001, "Velocity Measurements of Vortex Breakdown in an Enclosed Cylinder," *ASME J. Fluids Eng.*, **123**, pp. 604–611.

[11] Roesner, K. G., 1989, "Recirculation Zones in a Cylinder With Rotating Lid," *Topological Fluid Mechanics, Proceedings of the IUTAM Symposium*, edited by A. Tsinober and H. K. Moffat, Cambridge University Press, CA, pp. 699–708.

[12] Bar-Yoseph, P. Z., Solan, A., and Roesner, K. G., 1990, "Recirculation Zones in a Cylinder With Rotating Lid," *Z. Angew. Math. Mech.*, **70**, pp. 442–444.

[13] Valentine, D. T., and Jahnke, C. C., 1994, "Flows Induced in a Cylinder With Both Endwalls Rotating," *Phys. Fluids*, **6**, pp. 2702–2710.

[14] Gelfgat, A. Yu., Bar-Yoseph, P. Z., and Solan, A., 1996, "Steady States and Oscillatory Instability of Swirling Flow in a Cylinder With Rotating Top and Bottom," *Phys. Fluids*, **8**, pp. 2614–2625.

[15] Watson, J. P., and Neitzel, G. P., 1996, "Numerical Evaluation of a Vortex-Breakdown Criterion," *Phys. Fluids*, **8**, pp. 3063–3071.

[16] Fujimura, K., Koyama, H. S., and Hyun, J. M., 2004, "An Experimental Study on Vortex Breakdown in a Differentially Rotating Cylindrical Container," *Exp. Fluids*, **36**, pp. 339–407.

[17] Jahnke, C. C., and Valentine, D. T., 1998, "Recirculation Zones in a Cylindrical Container," *ASME Trans. J. Fluids Eng.*, **120**, pp. 680–684.

[18] Spohn, A., Mory, M., and Hopfinger, E. J., 1998, "Experiments on Vortex Breakdown in a Confined Flow Generated by a Rotating Disk," *J. Fluid Mech.*, **370**, pp. 73–99.

[19] Sotiropoulos, F., Ventikos, Y., and Lackey, T. C., 2001, "Chaotic Advection in Three-Dimensional Stationary Vortex-Breakdown Bubbles," *J. Fluid Mech.*, **444**, pp. 257–297.

[20] Serre, E., and Bontoux, P., 2001, "Three-Dimensional Swirling Flow With a Precessing Vortex Breakdown in a Rotor-Stator Cylinder," *Phys. Fluids*, **13**, pp. 3500–3503.

[21] Serre, E., and Bontoux, P., 2002, "Vortex Breakdown in a Three-Dimensional Swirling Flow," *J. Fluid Mech.*, **459**, pp. 347–370.

[22] Kawamura, T., and Kuwahara, K., 1984, "Computation of High Reynolds Number Flow Around a Circular Cylinder With Surface Roughness," *AIAA Paper*, 840340.

[23] Gelfgat, A. Yu., Bar-yoseph, P. Z., and Solan, A., 1996, "Stability of Confined Swirling Flow With and Without Vortex Breakdown," *J. Fluid Mech.*, **311**, pp. 1–36.

# A New Class of Synthetic Jet Actuators—Part I: Design, Fabrication and Bench Top Characterization

J. L. Gilarranz<sup>‡</sup>

L. W. Traub<sup>†</sup>

O. K. Rediniotis<sup>\*</sup>

Department of Aerospace Engineering, Texas  
A&M University,  
College Station, Texas 77843-3141

*Although the potential of synthetic jets as flow separation control actuators has been demonstrated in the existing literature, there is a large gap between the synthetic jet actuators (SJA) used in laboratory demonstrations and the SJAs needed in realistic, full-scale applications, in terms of compactness, weight, efficiency, control authority and power density. In most cases, the SJAs used in demonstrations are either too large or too weak for realistic applications. In this work, we present the development of a new class of high-power synthetic jet actuators for realistic flow control applications. The operating principle of the actuator is the same as that of crankshaft driven piston engines, which makes a significant part of the technology necessary for the actuator development available off-the-shelf. The design of the actuator is modular and scalable. Several “building block” units can be stacked in series to create the actuator of the desired size. Moreover, active exit slot reconfiguration, in the form of variable exit slot width, decouples the actuator frequency from the actuator jet momentum coefficient and allows the user to set the two independently (within limits). Part I of this paper presents the design, fabrication and bench top characterization of the actuator. Several versions of the actuator were designed, built and tested, leading up to the development of a six-piston compact actuator that has a maximum power consumption of 1200 W (1.6 hp) and can produce (for the tested conditions) peak exit velocities as high as 124 m/s. In Part II, the actuator was housed in the interior of a NACA0015 profiled wing with a chord of 0.375 m (14.75 inches). The assembly’s performance in controlling flow separation was studied in the wind tunnel. [DOI: 10.1115/1.1839931]*

## Introduction

Current research in the area of synthetic jet actuation includes investigation of the performance of this technology for modifying the lift, drag and flight control characteristics of unconventional airfoils as well as flow separation over bluff bodies [1–7]. This technology could lead to elimination, reduction or manipulation of steady and unsteady flow separation over a wing/blade, via active flow control and in a “hingeless” manner (no conventional moving control surfaces). An application of this technology may be active modification of the pressure distribution over an aerodynamic surface, leading to “dynamic virtual shaping” [8,9]. Jet vectoring is also another area of flow control that can benefit from the application of synthetic jet actuators [10–12]. This area is of great importance in the development of jet engine exhaust systems as well as in the area of control surface augmentation. Flow manipulation via synthetic jets could open new horizons in vehicle control and presents an exciting alternative over conventional control surfaces. Hingeless flow control could allow the optimization of the aerodynamics without disrupting the physical outside geometry of the vehicle and, therefore, to a large extent, its radar signature.

In most efforts in the existing literature, the synthetic jet actuators (SJA) are either powered piezoelectrically [13,14] or are powered from external hardware. For example, in the work of Greenblatt and Wygnanski [6], as well as in Seifert and Pack [5], the

mechanism used to generate the pressure fluctuations necessary for the oscillatory blowing was a pneumatic mechanism, with most of the hardware residing outside the test section. Similarly, McCormick [15], presented an electromagnetic based method to produce the synthetic jet, in which most of the hardware was also outside of the test section. Several modeling techniques have been proposed in order to simulate the behavior of synthetic jet actuators and theoretically characterize the flowfields that they produce [15–18]. Due to the complexity of the flowfield generated by the synthetic jet actuators, most of the models have had to be “calibrated” in order to match the theoretical predictions with the experimental measurements.

For many air and water vehicle applications, the SJA will need to be compact in order to be housed inside the control surface of the body whose aerodynamic–hydrodynamic characteristics it is trying to modify. Piezoceramic-based synthetic jet actuators offer a promising alternative since they can be small enough to be housed inside the control surface. Limitations of piezoceramics-based SJAs include performance deterioration when operating at frequencies away from the actuator resonance frequencies and limited maximum deflection amplitudes. This work addresses the continuing need for compact, high-power synthetic jet actuators that can meet the size, weight, efficiency and power density requirements of realistic, full-scale flow control applications. As such, we present the development of a new class of high power synthetic jet actuators. The structure of this article is as follows: First we discuss the principle of operation of the actuator along with design considerations. Then, the fabrication and characterization of a single actuator “building block” is presented. Subsequently, the development and characterization of a multi-piston actuator, consisting of multiple actuator “building blocks” is pre-

<sup>‡</sup>Graduate Research Assistant, Student Member AIAA.

<sup>†</sup>Research Scientist, Member AIAA.

<sup>\*</sup>Associate Professor, Associate Fellow AIAA.

Contributed by the Fluids Engineering Division for publication in the JOURNAL OF FLUIDS ENGINEERING. Manuscript received by the Fluids Engineering Division August 12, 2003; revised manuscript received February 25, 2004. Associate Editor: William W. Copenhaver.

sented. In Part II, the effectiveness of the actuator is demonstrated in wind-tunnel flow separation control experiments over a two-dimensional wing.

### Actuator Design

As mentioned, piezoceramics-based SJAs exhibit performance limitations in full-scale flow control applications. To understand these limitations, let us consider the application of SJAs to flow separation control over an airfoil/blade. It is acknowledged in the literature that for such applications, the optimal nondimensional actuation frequency,  $F^+$ , is on the order of 1 [5].  $F^+$  is defined as:

$$F^+ = f \frac{x_{te}}{U_\infty} \quad (1)$$

Moreover, the literature indicates that jet momentum coefficients ( $C_\mu$ ) of at least 0.002, are necessary before any substantial effects on the flow can be observed. The jet momentum coefficient,  $C_\mu$ , has been defined in many ways in the available literature. In this paper we define it as:

$$C_\mu = \frac{h(\rho u_{\max}^2)_{\text{jet}}}{c(\rho U^2)_\infty} \quad (2)$$

This definition of  $C_\mu$  can also be found in the work of McCormick [15].  $C_\mu$  may also be defined using the RMS value of the slot exit velocity [5] or even the average value of the velocity at the jet exit [19,20].

For practical separation control applications, in either fixed or rotary wing configurations, a typical freestream would be on the order of  $M=0.5$ .  $x_{te}$  would be on the order of the wing/blade chord or flap which we take it to be on the order of 0.6 m to illustrate the application perspectives with a practical example. For typical realistic rotorcraft blade geometry, the entire SJA assembly would have to be accommodated within the internal volume upstream of the spar. Therefore, per unit span, the size of the SJA assembly would be on the order of the cross section of that internal volume. For a typical blade geometry, this dimension was estimated to be at most on the order of 0.07 m. For these numbers, using Eq. (1) we get that the optimal excitation frequency is around 300 Hz. Using Eq. (2) and incompressible continuity, while assuming sinusoidal motion of the pistons with two jet exit width values, 1 and 6 mm (representing the low and high end of a typical width size spectrum), we get:

For  $h=0.001$  m:  $u_{\max}=186$  m/s, SJA piston oscillation amplitude=1.5 mm

For  $h=0.006$  m:  $u_{\max}=76$  m/s, SJA piston oscillation amplitude=3.6 mm.

Therefore, expected peak-to-peak strokes of the SJA piston would be on the order of 3 mm at a frequency around 300 Hz. These results are not optimal for piezoelectric actuation. The required amplitudes are significantly larger than what piezoceramics are typically capable of and the required frequencies are lower than those at which piezoceramics have competitive power densities. In contrast, these numbers are suitable for reciprocating motor actuation. Compact electric motors exist, off-the-shelf, with optimal performance at around 18 000 rpm (or 300 Hz), measuring 25 mm in diameter and 37 mm in length, weighing 70 grams (2.5 ounces) and with very competitive power densities (400 Watts per 70 grams, or 5.7 W/gm).

In this study, the proposed principle of the SJA driving mechanism is well developed, having been extensively utilized in a variety of engines, see Fig. 1. The driving mechanism consists of a DC motor driving a crankshaft, which in turn drives the piston through the connecting rod. This design offers the following benefits:

- It can achieve piston oscillation amplitudes at least an order of magnitude higher than piezoelectric actuators;
- it eliminates the dependence of oscillation amplitude on the oscillation frequency, which limits piezoceramic mechanisms;

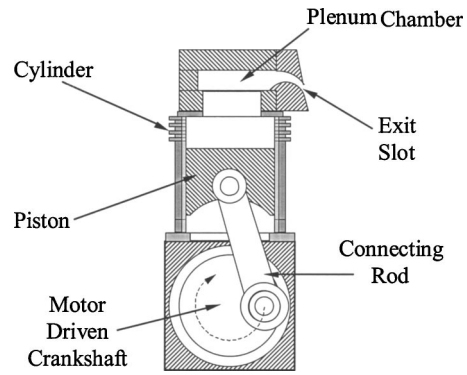


Fig. 1 Principle of SJA driving mechanism

- with available state-of-the-art, high power-density electric motors it can match and exceed the power densities of piezoceramic mechanisms;
- it requires significantly smaller driving voltages.

One apparent drawback of the proposed design is the fact that the frequency of actuation (and thus  $F^+$ ) and the achieved jet momentum coefficient,  $C_\mu$ , cannot be independently controlled, since, for a fixed exit slot geometry and fixed piston oscillation amplitudes, the maximum jet exit velocity is determined by the actuation frequency. However, as will be discussed later, this limitation can be eliminated relatively easily via a variable-width exit slot.

### Fabrication and Testing of a Single Piston SJA

A single piston SJA was first fabricated for testing, as shown in Fig. 2 in two different views. It was fabricated using spare parts from an O.S. Engines F.S.52S four stroke model engine. For our case, the cylinder head is removed from the engine and the piston cylinder is attached to a plenum chamber as shown in the figure. The chamber is closed on all sides except for a slot machined on one of its walls. The chamber's internal dimensions (depth×width×length) were 10.1 mm×25.4 mm×63.5 mm (0.4"×1.0"×2.5"), and it could be configured with one of two possible slots, one measuring (length×width) 76.2 mm×0.8 mm (3.0"×0.032") and the other 76.2 mm×1.6 mm (3.0"×0.064"). These two different exit slot widths were tested (with the same chamber internal volume) to help assess the effects of slot dimensions on flow compressibility. The engine piston has a diameter of 23.0 mm (0.906"), a maximum peak-to-peak oscillation amplitude of 20.6 mm (0.811") and a total displacement volume of 8.56 cc (0.52 inches<sup>3</sup>). This SJA prototype was driven by a small electric motor, with a maximum rated power of 325 W.

In order to characterize the flowfield generated by the synthetic jet actuator, it was installed on a dedicated test bench. The test bench consisted of a 0.6 m×0.9 m optical table (similar to the ones used for aligning laser optic elements) on which the actuator was mounted using a mounting plate. A three component traversing system was used to provide accurate placement of the measurement probes. The traversing system was based on a Unidex 12 controller, which was connected to a data acquisition computer via a serial port. The positioning accuracy of this system is within 0.01 mm. The operating frequency of the actuator was measured using a Bently Nevada 3300 type proximity probe system connected to a frequency digital display. The proximity probe was placed in such a way that it sensed a coupling that was designed for this purpose and that was attached to the shaft of the electrical motor (Fig. 2). The coupling had a notch machined into its surface, which caused a change in the output voltage of the probe every time the notch passed in front of the proximity probe. This periodic change in voltage was measured by a Fluke multimeter with a frequency measurement capability. This system was able to

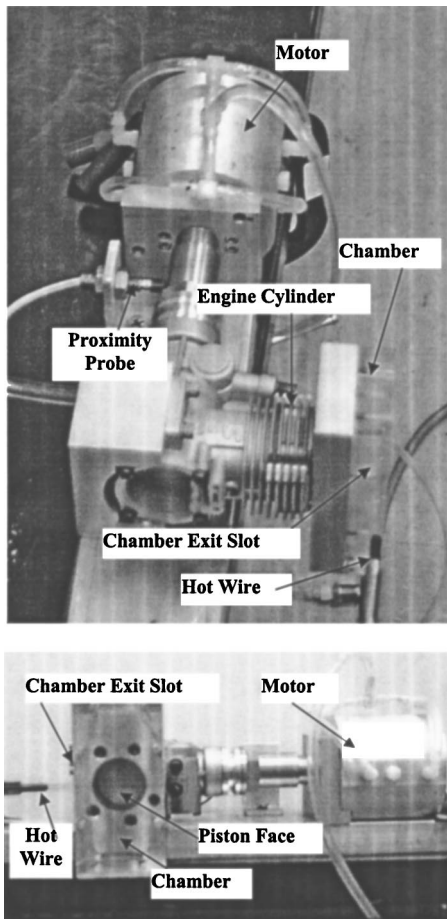
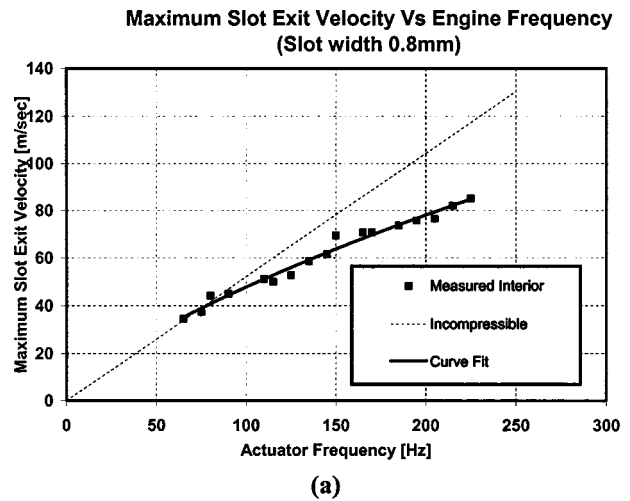


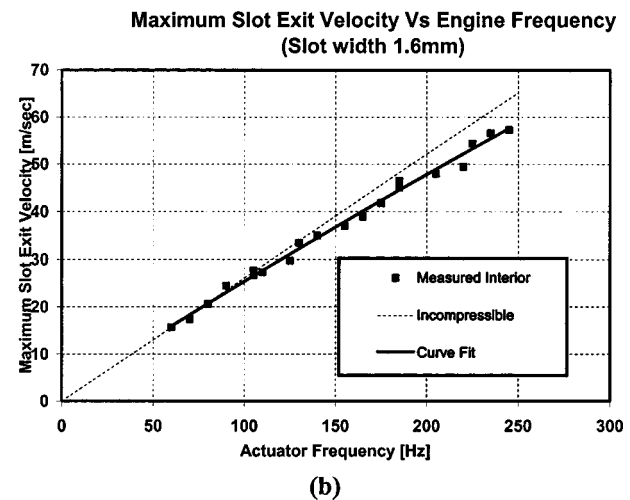
Fig. 2 Two views of the single piston SJA

measure the frequency with an accuracy of 0.1 Hz and a standard deviation of 0.03 Hz. A Hewlett Packard 6269B DC power supply was used to provide the required electrical power to the actuator. Cooling air was provided to the electrical motor used to drive the actuators to extend the time period for which the actuators could be operated continuously at high frequency. Hot-wire anemometry was employed for the single-piston actuator characterization. Flow velocity data was obtained at the slot exit for a range of oscillation frequencies, via a single wire TSI 1201 hot-wire probe interfaced with an A. A. Lab Systems Anemometer. The system was operated in the constant temperature mode. The hot-wire data was acquired by a P.C. equipped with a 16 bit A/D board. The hot-wire calibration was performed using a TSI 1125 probe calibrator while monitoring the chamber pressure with an Edwards Barocell pressure transducer. For the pressure range of interest the accuracy of the Barocell was within  $\pm 6.5$  Pa (0.05 Torr). The combination of these systems (anemometer, calibrator, data-acquisition board) yielded a velocity measurement accuracy of 0.9 m/s, with a standard deviation of 0.65 m/s.

Figure 3 presents the maximum velocity magnitude, inside the exit slot in the middle of its width, for the two different slot widths, 0.8 and 1.6 mm. In each plot, the theoretically calculated incompressible velocity maximum (from the incompressible continuity equation) is also given. Assuming no leaks between the piston and the cylinder, the difference between the theoretical and measured curves, gives us an idea of the compressibility effects. Several observations can be made. First, for this displacement volume and these slot widths, exit velocities as high as 85 m/s can be achieved. Deviations from the ideal case (incompressible) are more pronounced for the narrow slot (0.8 mm) and for higher oscillation frequencies. The reduction in velocity may be attrib-



(a)



(b)

Fig. 3 Theoretical and measured maximum velocity at the exit slot for two slot widths: (a) Slot width=0.80 mm and (b) slot width=1.60 mm

uted to compressibility effects as well as greater losses through the slot orifice for the 0.8 mm configuration. For low frequencies the compressibility effects are lessened. For the narrow slot, the curves start diverging from each other sooner (at around 80 Hz) than for the wider slot (at around 110 Hz). Note that at the high frequency end (around 250 Hz), the measured velocities only differ by 50% (60 and 90 m/s, for the wide and narrow slots, respectively), while their incompressible theoretical values differ by 100% (65 and 130 m/s, for the wide and narrow slots, respectively). Figure 4 presents the variation of the maximum exit velocity over the slot length. Little variation can be seen, with significant magnitude drop only very close to the slot end.

### Multipiston Actuator

A schematic of the multipiston actuator is shown in Fig. 5. It is composed of 6 pistons (acting as reciprocating compressors) mounted on a crankshaft, which is driven by two DC motors (Astro-Flight Cobalt 341). Each piston had a diameter of 27.7 mm (1.09") with a peak-to-peak piston stroke of 22.0 mm (0.866"), which produced a displacement volume of 13.25 cc (0.809 cubic inches). Each electric motor measured 67.564 mm (2.66") in length and 37.3 mm (1.47") in diameter, had a maximum power of 1000 W and weighed 340 grams (12 oz), giving 2.94 W/gm. For compactness reasons, the motors were arranged in parallel to the crankshaft in order to avoid increasing the span of the device.

### Slot Spanwise Velocity Distribution

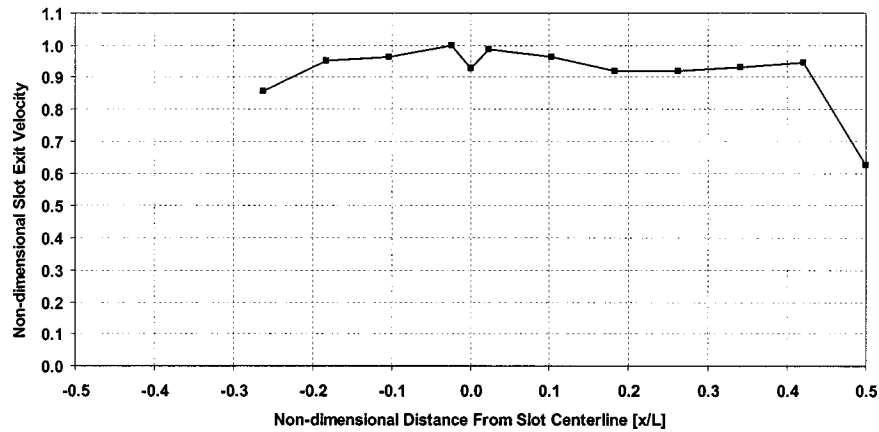


Fig. 4 Variation of measured maximum velocity over the length of the exit slot

Figure 6 shows a schematic of two different versions of the plenum cross section, illustrating the exit slot geometry and slot-width variation technique. In the version illustrated in Fig. 6(a) the cross section of the internal plenum volume measured  $6.4 \times 25.4 \text{ mm}^2$  ( $0.25 \times 1.00 \text{ inches}^2$ ). The exit slot was curved in order to take advantage of the “Coanda” effect in generating an exit jet that is tangential to the wing surface, as discussed later. In order to study exit-slot-width effects as well as be able to vary the exit velocity independently of the actuator frequency, we also developed a second plenum with a continuously variable exit slot width. This is shown in Fig. 6(b). A cam has been used to control the width of the exit slot of the actuator. This cam stretches over the entire length–span of the plenum housing–exit slot. Again, the design forces the airflow to turn with the ambient flow creating a surface tangential synthetic jet. The cam can be rotated to continuously vary the slot width from 0 to 1.2 mm. The cam is represented in black and the plenum housing in gray. The use of a stepper motor allows the cam to be rotated to a desired position. The range of exit slot width variation was decided upon, based on the following considerations. The maximum achievable wind tunnel speed (see Part II) was 50 m/s. This, along with the given wing dimensions (chord length of 0.375 m) and an  $F^+$  of 1, yielded a maximum required frequency of about 150 Hz. The frequency of the SJA could be varied from 0 to 200 Hz. For the given piston stroke and displacement volume, the exit slot maximum velocity could be expressed as a function of frequency and exit slot width. From the above, Fig. 7 was generated, presenting the variation of the jet momentum coefficient  $C_{\mu}$  and its dependence on frequency

and slot width for a given freestream velocity of 50 m/s. It should be noted here that Fig. 7 does not account for compressibility effects. This, along with the fact that the smaller the slot width the stronger the compressibility effects, and keeping in mind that we must have a  $C_{\mu}$  of at least 0.002 [10] for an optimal frequency of 150 Hz, led us to choose a slot width of 2 mm (0.12”) for the fixed-slot-width configuration. As seen later and as it was intended in the design, the fixed-slot-width configuration did not generate any noticeable compressibility effects. In order to be able to study the effects of compressibility within the SJA, the variable-slot-width configuration was designed to achieve a range of smaller slot widths.

Figure 8 shows pictures of the multi-piston SJA illustrating details on cylinder arrangement, motor mounting, slot geometry (for the fixed-slot-width configuration) and cylinder phasing. It should be noted that the cylinders had to be properly phased in order to reduce array vibration. Referring to the middle picture of Fig. 8 and numbering the cylinders from 1 to 6, starting from the left, the phasing is as follows: Cylinders 1 and 6 at 240 degrees, cylinders 2 and 5 at 120 degrees and cylinders 3 and 4 at 0 degrees. It was found that the reduction in vibration severity from the unphased to the phased SJA operation was dramatic. In turn, this phasing required the compartmentalization of the plenum, as it is obvious that if the plenum was not divided into six individual compartments, each one corresponding to one of the six cylinders, the engine phasing would result in near zero net volume change during an operation cycle and thus little synthetic jet effect. More

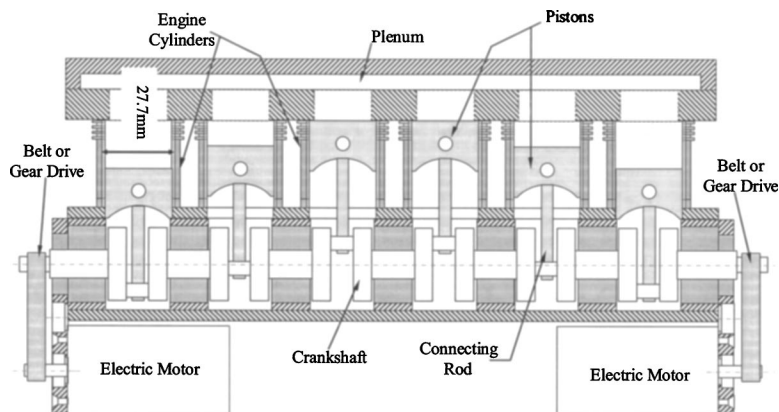


Fig. 5 Schematic of multi-piston SJA



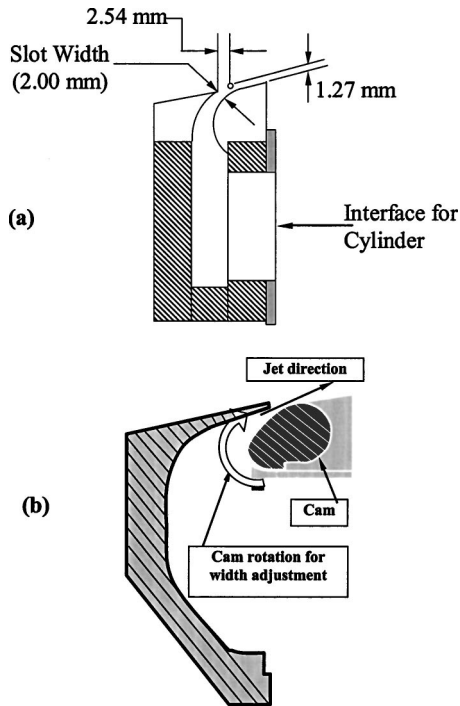


Fig. 6 Plenum cross section showing exit slot geometry: (a) Fixed slot geometry and (b) variable slot geometry

details concerning the development and design of the actuators may be found in the work by Gilarranz [21] and by Gilarranz et al. [22].

### Characterization of the Multi-Piston Actuator

The SJA array was first tested in a stand-alone configuration in order to document the maximum exit velocity as a function of frequency and spanwise location as well as investigate the effects of cylinder phasing and plenum compartmentalization to the flow. For these tests, the experimental setup, previously described, was used. For these tests, velocity measurements were acquired via two different means in order to establish confidence in the measurements: The hot-wire instrumentation described earlier and a fast-response stagnation pressure probe (Fig. 9). This pressure probe used a 50 mm long stainless-steel hypodermic tube with an

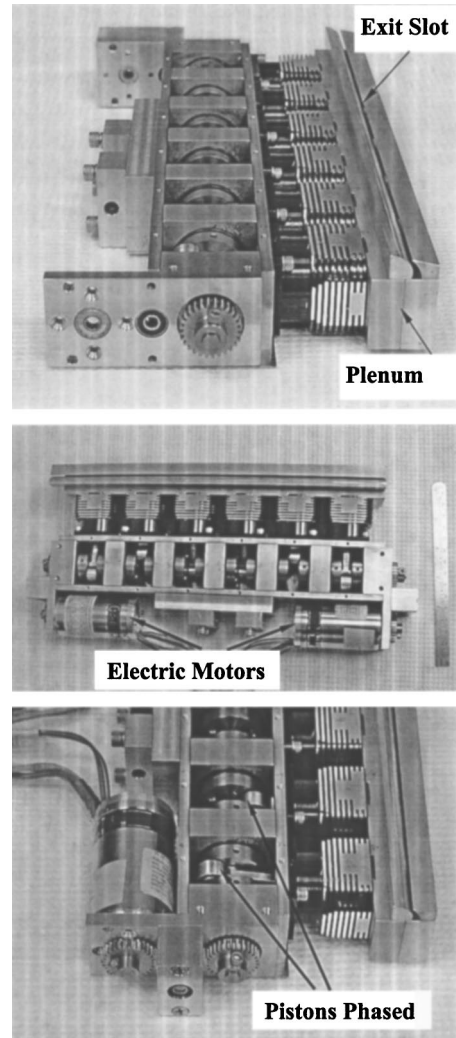


Fig. 8 Pictures of multipiston actuator, showing motor mounting, cylinder phasing and exit slot geometry

inner diameter of 0.25 mm. The end of this tube was interfaced with a fast-response, differential pressure transducer, an Endevco Model 8507C-2 with a pressure range of  $\pm 13.6$  kPa and a full-

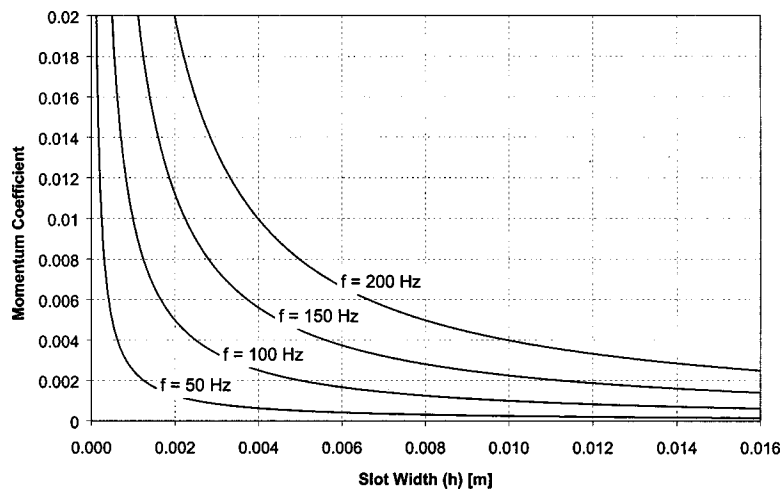


Fig. 7 Dependence of  $C_{\mu}$  on frequency and slot width for  $U_{\infty} = 50$  m/s, incompressible assumption

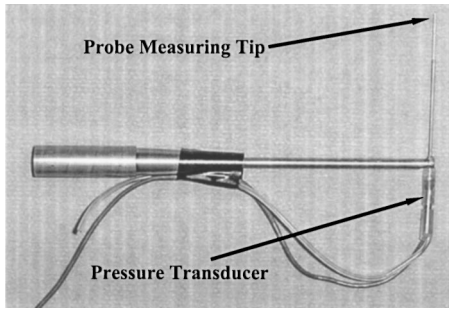


Fig. 9 Fast-response stagnation probe

scale voltage output of 300 mV. The transducer was calibrated against the Barocell pressure transducer, over the pressure range encountered in the measurement, i.e., from 0 to 7.5 kPa. An Entran voltage amplifier (model IMV-15/10/100A-WW) with a gain of 100 was used to amplify the pressure transducer output signal, which was subsequently sampled by a P.C. equipped with a 16-bit A/D board. The combination of the above components and procedures resulted in the capability of measuring pressure with a resolution of 1 Pa and an accuracy of 6.5 Pa.

The stagnation pressure probe was also dynamically calibrated to assess the effect of the 50 mm long pressure tubing. Details of the calibration can be found in the work of Johansen [23]. Figure 10 presents the probe's frequency response (magnitude and phase). For frequencies up to 400 Hz, the probe's behavior is

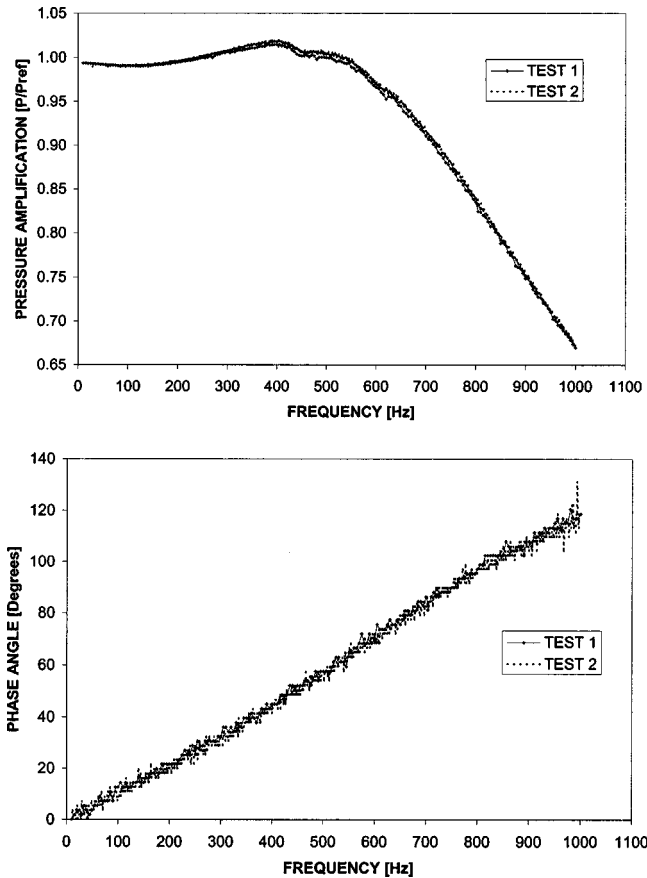


Fig. 10 Frequency response of fast-response stagnation probe

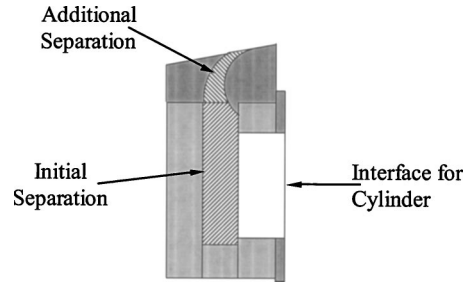


Fig. 11 Schematic of plenum separation walls

similar to a system with a critically damped dynamic response, as seen in Fig. 10. Note that for frequencies of up to 400 Hz the amplification by the pneumatic system (which consists of the pressure transmitting tubing and pressure transducer cavity), of the measured pressure is within 1.5% percent of the actual value. The phase lag up to 400 Hz is however non-negligible (up to 40 deg). Since, in these tests our interest was to study the maximum velocity at the actuator exit and the tests were ensemble averaged, this phase lag is of no consequence. Thus, no correction was employed.

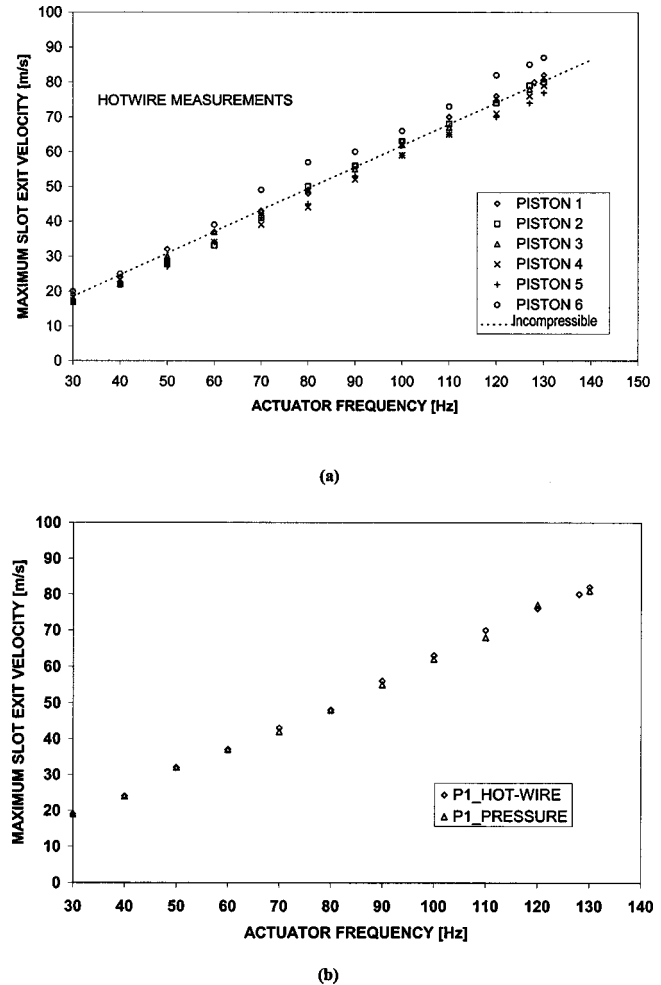


Fig. 12 Maximum exit velocity as a function of actuator frequency: (a) Comparison of hot-wire measurements and predictions using the continuity equation for incompressible flow, for all six pistons. (b) Comparison of hot-wire and fast-response stagnation probe measurements for piston #1.

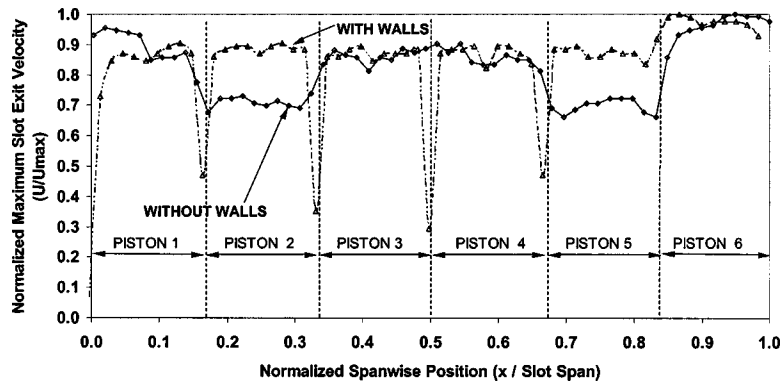


Fig. 13 Effects of the extended plenum separation walls on the spanwise distribution of the maximum jet exit velocity, for an actuator frequency of 120 Hz

Initially, due to the difficulty of fabricating separating walls that extended into the exit slot only the plenum section was compartmentalized, as shown in Fig. 11. However, the velocity distribution in the spanwise direction with this configuration showed that there were still strong interactions between the jets generated by adjacent piston due to their different phasing leading to reduced maximum exit jet velocity. This required the separating walls to be extended into the exit slot, as shown in Fig. 11. Subsequent tests performed on the actuator after these modifications were made, showed that the extension of the walls practically eliminated the adverse effects of the piston interactions on the maximum exit velocity.

For the fixed-slot-width configuration, the bench tests involved two studies. The first set of tests consisted of the measurement of the instantaneous slot exit velocity, for each of the six piston/plenum compartments, at a fixed position, for a range of actuator frequencies. Each of the six measurement locations was centered over a piston. The actuator frequency was varied between 30 and 130 Hz, in 10 Hz increments. The second set of tests consisted of measuring the slot exit velocity of the actuator as a function of spanwise location (by traversing the measuring probe) at a fixed actuator frequency.

Figure 12 presents the maximum velocity magnitude, measured at the exit of each one of the piston exit slots in the middle of its width, as a function of actuator frequency. Figure 12(a) shows a comparison between the hotwire measurements and the theoretical value calculated using the incompressible continuity equation. As it may be seen in the figure, the measured values and the theoretical predictions agree quite well, despite the fact that compressibility effects were not accounted for. This is due to the fact that

the exit slot was designed to be wide enough to minimize compressibility effects inside the piston chambers. Also of interest is the fact that velocities up to 85 m/s were obtained for an actuator frequency of 130 Hz. The differences between the curves corresponding to measurements made for each one of the pistons may be due to several factors. Although care was taken during the machining of the curved surfaces of the exit slots and during the assembly of the actuator components, small differences in the slot width for different pistons or uneven wear between the piston rings and the cylinder lining may account for part of the difference in the exit velocities measured at different pistons. Also, considering that the slot has a width of 2 mm, any misalignment of the probe could affect the measurements. Figure 12(b) shows a comparison between the measurements of the maximum exit velocity acquired with hot-wire anemometry and with the fast-response stagnation probe. Individual plots were generated for each one of the pistons, however, to avoid redundancy, we only include here the one corresponding to piston #1. As may be seen, agreement between the two measurements is very good.

Figure 13 shows the spanwise distribution of the maximum exit velocity for an actuator frequency of 120 Hz. The figure shows the data corresponding to measurements performed before and after the extension of the separating walls into the exit slot. As seen in the figure, for the case of the measurements performed before the extension of the separating walls, the minimum exit velocity was achieved for pistons 2 and 5. This is because both of the neighboring pistons are out of phase. On the other hand, pistons 1 and 6 present the highest exit velocity, as they each only have one neighboring piston that is out of phase. Finally pistons 3 and 4 present an intermediate value as these pistons have one out of

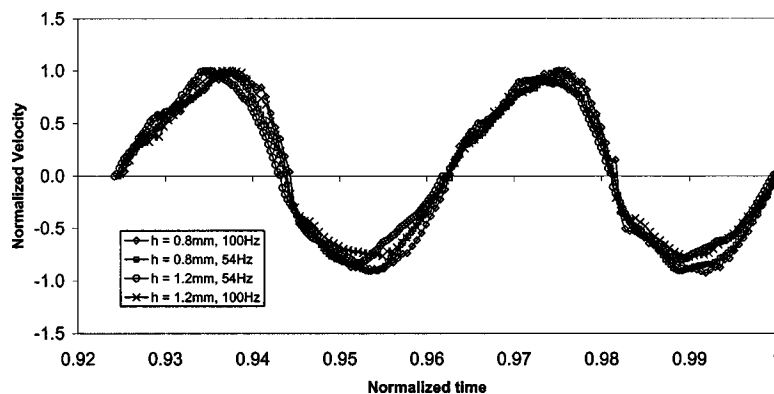


Fig. 14 Effect of SJA frequency and slot width on normalized SJA exit velocity

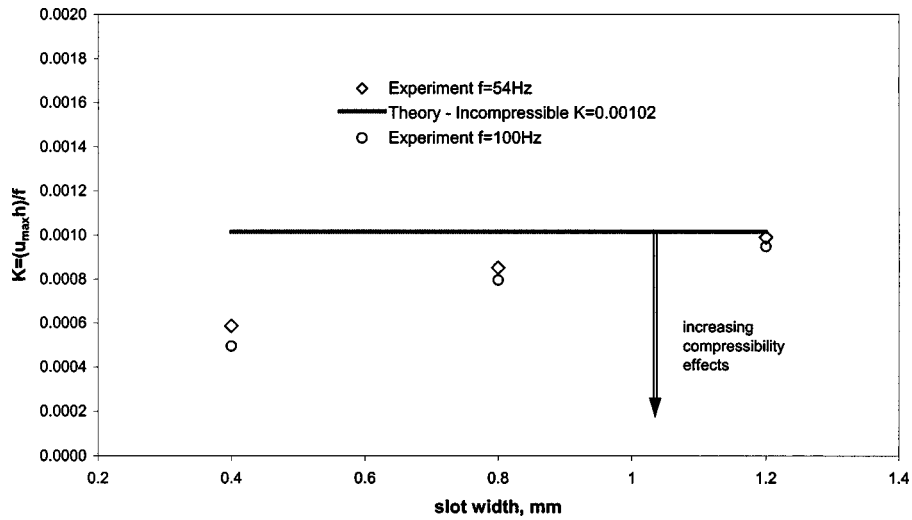
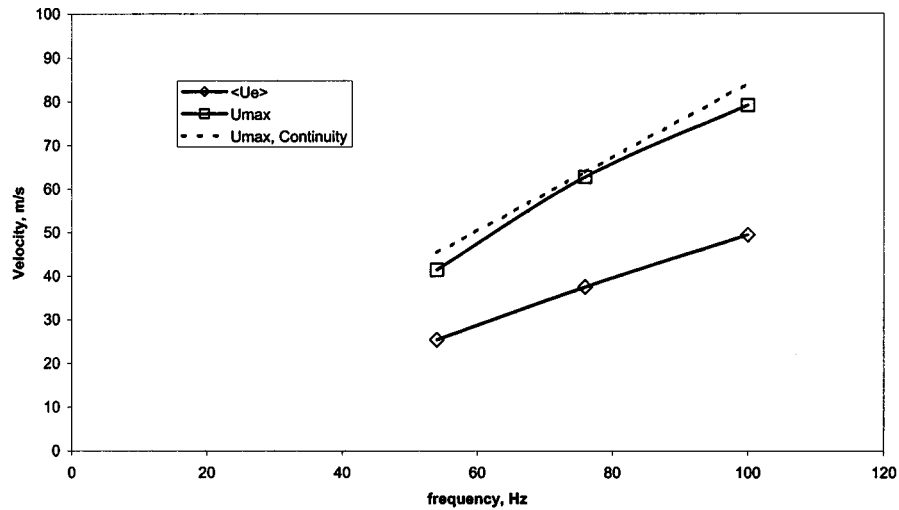
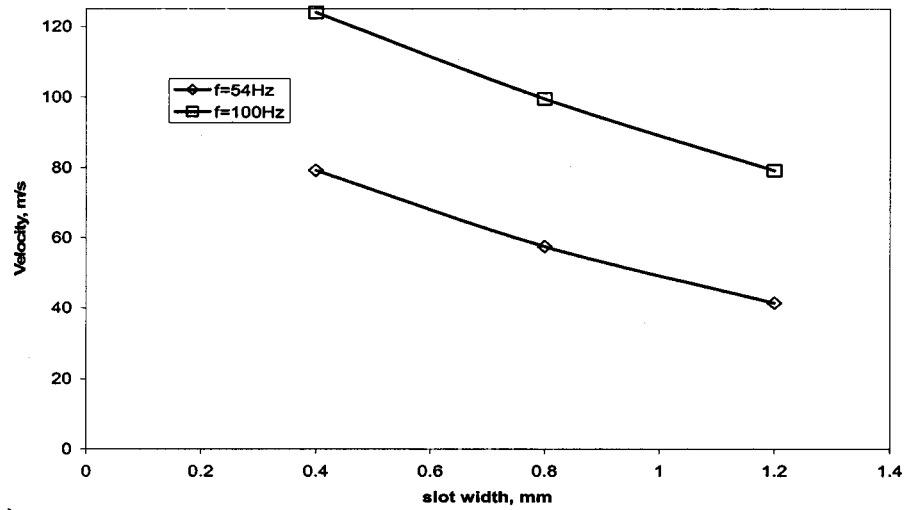


Fig. 15 Effect of compressibility on the jet exit parameter K



(a)



(b)

Fig. 16 Effect of frequency and slot width on SJA exit velocity: (a) Velocity dependence on frequency, slot width=1.2 mm, (b) maximum SJA exit velocity as a function of slot width

phase piston on one side and one in-phase piston on the other side. As seen in the figure, this strong interaction between the out-of-phase pistons was greatly reduced after the installation of the separating walls within the slot. However, for this new configuration the wake of the separating walls is now evident.

The performance of the variable-slot-width SJA actuator was subsequently studied. Figure 14 shows normalized time and velocity for four data sets. The velocities have been derectified to show the correct sign. As may be seen, the exit velocities are nearly sinusoidal, with little effect due to frequency or slot exit width variation. Figure 15 investigates effects of compressibility. The parameter  $K$  (determined from the continuity equation) should be a constant for a given piston diameter and stroke combination if the flow behaves as incompressible. As may be seen, for a 1.2 mm slot width, the flow is nearly incompressible. Reducing the slot width induces significant compressibility effects. Higher SJA frequency is also seen to increase compressibility effects, but to a far lesser extent than slot exit width. Finally, the SJA performance, quantified in terms of exit velocity, is presented in Figs. 16(a) and 16(b). For a 1.2 mm slot exit, as seen in Fig. 16(a), the exit velocity is seen to vary almost linearly with actuator frequency (at least for this range of frequencies), reflecting the marginal effect of compressibility for this geometry. Figure 16(b) shows the maximum velocity measured at the slot exit for slot widths of 0.4, 0.8, and 1.2 mm. Although the sparse nature of the data mitigates establishment of characteristic trends, the form of the data suggests a linear dependence of velocity on frequency in this range. As continuity considerations may infer, reducing the slot exit width increases jet exit velocity. However, compressibility effects lessen the relative increase in velocity. Nonetheless, for a 0.4 mm slot exit, an exit velocity of 124 m/s was recorded at a frequency of 100 Hz.

## Conclusions

In this work, we presented the development and characterization of a compact, high-power synthetic jet actuator for flow separation control applications. The principle driving mechanism of the new actuator is well developed and has been extensively utilized in a variety of engines. The driving mechanism consists of a DC motor driving a crankshaft, which in turn drives a series of pistons through connecting rods. This design offers significant benefits over piezoceramic driving mechanisms including piston oscillation amplitudes at least an order of magnitude higher, elimination of the dependence of oscillation amplitude on the oscillation frequency, compactness and high available power, and significantly smaller driving voltage requirements. The developed actuators are compact enough to fit in the interior of a 0.375 m chord, NACA 0015 profiled wing (see Part II), have maximum power of 1200 W and could produce exit velocities as high as 124 m/s.

For the fixed-exit-slot-geometry version of the actuator the frequency of actuation (and thus  $F^+$ ) and the achieved jet momentum coefficient cannot be independently controlled since for a fixed exit slot geometry and fixed piston oscillation amplitudes, the jet exit velocity is determined by the actuation frequency. This limitation was resolved in the actuator version with active exit slot reconfiguration, in the form of variable exit slot width. Exit slot width variation allows decoupling of the actuator frequency from the actuator jet momentum coefficient.

For the case of the single piston actuator, hot-wire measurements at the exit of the SJA plenum showed the existence of compressibility effects. These effects are greater as the actuator frequency increases, the exit slot width decreases, or the combined plenum-cylinder internal volume increases. In the multipiston actuator the need to properly phase the motion of the pistons in order to eliminate vibration lead to the need to compartmentalize the plenum. Extension of the compartment separators into the exit slot eliminated cross-talk between adjacent, out of phase pistons. Study of the variable-slot-width version of the actuator

showed that (for frequencies up to 100 Hz) compressibility effects are negligible for slot widths larger than 1.2 mm. For smaller slot widths, significant compressibility effects are introduced. Decreasing the slot width has a significantly more pronounced effect on compressibility than proportionally increasing the actuation frequency.

## Acknowledgments

This work was sponsored by the Air Force Office of Scientific Research, under Contract No. F49620-01-1-0012. The authors would like to thank Dr. Thomas Beutner, the technical monitor for the project, for his support. The authors would also like to thank Mr. Rick Allen for his valuable help with the actuator fabrication and Mr. José Gilarranz, Sr. for his help and advice during the assembly and testing of the actuator. The authors would also like to thank the reviewers for their helpful comments and suggestions.

## Nomenclature

$c$	= chord length, [m]
$C_\mu$	= jet momentum coefficient
$h$	= width of exit slot, [m]
$F^+$	= nondimensional actuator frequency
$f$	= frequency of actuation, [Hz]
$K$	= compressibility parameter
$L$	= slot length, [m]
$M$	= Mach number
$P$	= pressure, [Pa]
$U_\infty$	= freestream velocity, [m/s]
$u$	= velocity at the slot exit, [m/s]
$u_{\max}$	= maximum jet exit velocity, [m/s]
$\langle u_e \rangle$	= RMS value of the slot exit velocity magnitude, [m/s]
$\rho$	= density of gas, [kg/m <sup>3</sup> ]
$x_{te}$	= distance from the actuator exit slot to the wing trailing edge, [m]

## References

- [1] Amitay, M., Smith, B. L., and Glezer, A., 1998, "Aerodynamic Flow Control Using Synthetic Jet Technology," AIAA Paper No. 98-0208.
- [2] Smith, D., Amitay, M., Kibens, V., Parekh, D., and Glezer, A., 1998, "Modifications of Lifting Body Aerodynamics Using Synthetic Jet Actuators," AIAA Paper No. 98-0209.
- [3] Seifert, A., Bachat, T., Koss, D., Shepshelovich, M., and Wagnanski, I., 1993, "Oscillatory Blowing: A Tool to Delay Boundary-Layer Separation," AIAA J., **31**, No. 11, pp. 2052–2060.
- [4] Seifert, A., and Pack, L., 1998, "Oscillatory Excitation of Separation at High Reynolds Number," AIAA Paper No. 98-0214.
- [5] Seifert, A., and Pack, L., 1999, "Oscillatory Excitation of Unsteady Compressible Flows Over Airfoils at Flight Reynolds Number," AIAA Paper No. 99-0925.
- [6] Greenblatt, D., and Wagnanski, I., 1998, "Dynamic Stall Control by Oscillatory Forcing," AIAA Paper No. 98-0676.
- [7] Greenblatt, D., Darabi, A., Nishri, B., and Wagnanski, I., 1998, "Separation Control by Periodic Addition of Momentum With Particular Emphasis on Dynamic Stall," Proceedings Heli Japan 98, Paper T3-4, American Helicopter Society.
- [8] Honohan, A. M., Amitay, M., and Glezer, A., 2000, "Aerodynamic Control Using Synthetic Jets," AIAA Paper No. 2000-2401.
- [9] Parekh, D. E., and Glezer, A., 2000, "AVIA: Adaptive Virtual Aerosurface," AIAA Paper No. 2000-2474.
- [10] Smith, B. L., and Glezer, A., 1997, "Vectoring and Small-Scale Motions Effected in Free Shear Flows Using Synthetic Jet Actuators," AIAA Paper No. 97-0213.
- [11] Smith, B. L., Trautman, M. A., and Glezer, A., 1999, "Controlled Interactions of Adjacent Synthetic Jets," AIAA Paper No. 99-0669.
- [12] Pack, L., and Seifert, A., 1999, "Periodic Excitation for Jet Vectoring and Enhanced Spreading," AIAA Paper No. 99-0672.
- [13] Rathnasingham, R., and Breuer, K., 1997, "Coupled Fluid-Structural Characteristics of Actuators for Flow Control," AIAA J., **35**, pp. 832–837.
- [14] Seifert, A., Eliahu, S., Greenblatt, D., and Wagnanski, I., 1998, "On the Use of Piezoelectric Actuators for Airfoil Separation Control," AIAA J., **36**, pp. 1535–1537.
- [15] McCormick, D., 2000, "Boundary Layer Separation Control With Directed Synthetic Jets," AIAA Paper No. 2000-0519.
- [16] Rizzetta, D., Visbal, M., and Stanek, M., 1999, "Numerical Investigations of Synthetic-Jet Flow Fields," AIAA J., **37**, pp. 919–927.

- [17] Rao, P., Gilarranz, J. L., Ko, J., Strganac, T., and Rediniotis, O. K., 2000, "Flow Separation Control Via Synthetic Jet Actuation," AIAA Paper 2000-0407.
- [18] Müller, M., Bernal, L., Moran, R., Washabaugh, P., Parviz, B., and Najafi, K., 2000, "Micromachined Acoustic Resonators for Microjet Propulsion," AIAA Paper 2000-0547.
- [19] Amitay, M., Honohan, A., Trautman, M., and Glezer, A., 1997, "Modification of the Aerodynamic Characteristics of Bluff Bodies Using Fluidic Actuators," AIAA Paper No. 97-2004.
- [20] Seifert, A., Darabi, A., and Wagnanski, I., 1996, "Delay of Airfoil Stall by Periodic Excitation," AIAA J., **33**, No. 4.
- [21] Gilarranz, J. L., 2001, "Development of High-Power, Compact Synthetic Jet Actuators for Flow Separation Control," Ph.D. Dissertation, Texas A&M University, Texas.
- [22] Gilarranz, J. L., Traub, L. W., and Rediniotis, O. K., 2002, "Characterization of a Compact, High-Power Synthetic Jet Actuator for Flow Separation Control," AIAA Paper No. 2002-0127.
- [23] Johansen, E. S., 2002, "Development of a Fast-Response Multi-Hole Probe for Unsteady and Turbulent Flowfields," Ph.D. Dissertation, Texas A&M University, College Station, Texas.

# A New Class of Synthetic Jet Actuators—Part II: Application to Flow Separation Control

**J. L. Gilarranz**

Graduate Research Assistant,  
Student Member AIAA

**L. W. Traub**

Research Scientist, Member AIAA

**O. K. Rediniotis**

Associate Professor, Associate Fellow AIAA

Department of Aerospace Engineering,  
Texas A&M University  
College Station, Texas 77843-3141, USA

*In this work we present the application of the new synthetic jet actuator (SJA) to flow separation control over a NACA 0015 wing. The actuator is compact enough to fit in the interior of the wing that has a chord of 0.375 m. The wing was tested in the Texas A&M University Aerospace Engineering 3 ft×4 ft wind tunnel. An experimental investigation into the effects of the synthetic jet actuator on the performance of the wing is described. Emphasis is placed on the capabilities of the actuator to control the separation of the flow over the wing at high angles of attack. The results include force balance measurements, on surface and off surface flow visualization, surface pressure measurements, and wake surveys. All of the reported tests were performed at a free-stream velocity of 35 m/s, corresponding to a Reynolds number of  $8.96 \times 10^5$ . The angle of attack was varied from  $-2.0$  deg to  $29.0$  deg. For the results presented, at angles of attack lower than 10 deg, the actuator has minimal effects. At higher angles of attack, the SJA delays the onset of stall. The use of the actuator causes an 80% increase in the maximum lift coefficient, while the angle at which stall occurs is increased from 12 to 18 deg. The drag on the wing is decreased as a consequence of SJA actuation. For angles of attack larger than 18 deg, where the wing experiences massive separation, the SJA still provides a moderate amount of lift augmentation compared to the unforced case. At angles of attack larger than  $25^\circ$ , a larger frequency of actuation is required to produce significant effects.*

[DOI: 10.1115/1.1882393]

## Introduction

For the case of flows over solid surfaces, the separation of the boundary layer is associated with large energy losses, and in many applications adversely affects the aerodynamic loads in the form of lift loss and drag increase. Therefore, there is a strong incentive to delay, eliminate, or manipulate the occurrence of flow separation. For example, if the separation of the boundary layer formed over a bluff body is delayed, the pressure drag is greatly reduced; also, separation delay will permit the operation of an airfoil/wing at higher angles of attack. In turbomachinery flows, for example, the delay or elimination of separation can increase the pressure recovery in a diffuser.

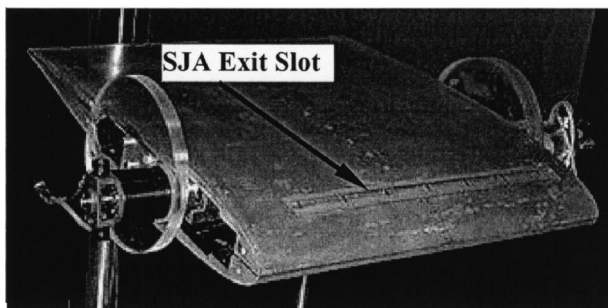
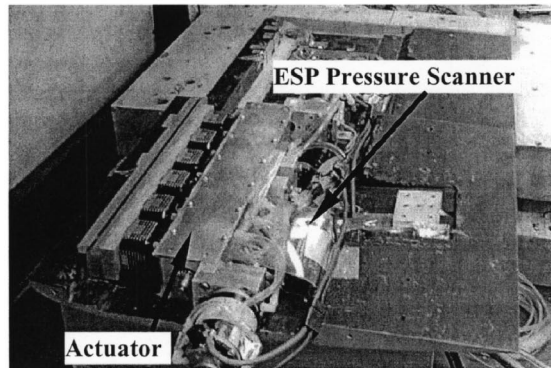
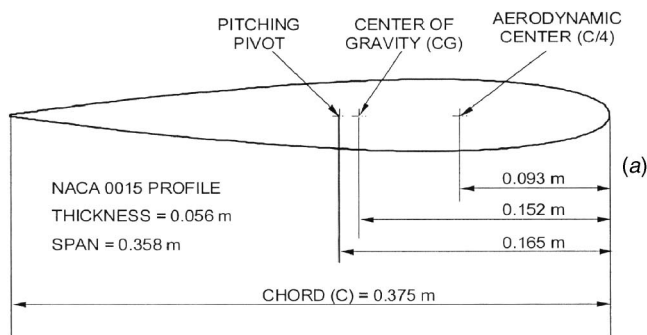
Many researchers have developed and tested methods of separation control in a variety of applications. Chang [1] presents an extensive review of flow separation techniques prior to 1976. Gad-el-Hak and Bushnell [2] provide a comprehensive review on the research in the area of separation control prior to 1991. Typically, the separation control techniques are grouped in two categories: passive and active. Most of the techniques developed for passive separation control may be found in the review by Gad-el-Hak and Bushnell [2]. However, our interest focuses on dynamic separation control techniques. The use of moving boundaries, which utilize the no-slip condition at the surface in order to energize the fluid close to the wall, has been explored in the past. For example, rotating cylinders have been used to delay separation at the leading and trailing edges of airfoils and control surfaces as well as at flap junctures (Johnson et al. [3], Mokhtarian and Modi [4], Modi et al. [5], and Alvarez-Calderon [6]). The momentum of the boundary layer may also be enhanced by means of injection of a fluid into the near wall vicinity. This fluid may be injected parallel to the surface (tangential blowing) in order to directly increase the momentum of the boundary layer or may be injected

perpendicular to the wall (normal blowing) in order to increase the mixing rate in the shear layer. There is a great amount of literature that is readily available in the area of steady blowing. Gad-el-Hak [7] provides an extensive review of this area. The use of tangential jet blowing over highly curved surfaces (utilizing the “Coanda” effect) has proved to be a very effective way of augmenting aerodynamic forces without the need of moving surfaces. This type of flow control is often referred to as circulation control. Englar [8] presents and discusses a large variety of proven uses of the circulation control concept for boundary layer control as well as for augmentation/modification of the aerodynamic characteristics of aircraft and fluid handling machinery.

The use of pulsed jets emanating from the surface has been shown to have benefits as separation control devices (McManus et al. [9] and McManus and Magil [10]). These pulsed jets have the ability to produce a large amount of vorticity and to enhance the momentum transport within the boundary layer, thus achieving fairly good stall suppression. Other active methods of controlling boundary layer separation and reattachment include acoustic excitations (Huang et al. [11], Hsiao et al. [12]) and periodic forcing of the velocity field by means of an oscillating flap or wire (Koga et al. [13] and Bar-Sever [14]), etc. The publications by Lachman [15] and Chang [1] and the reviews by Gad-el-Hak [16] and Gad-el-Hak and Bushnell [2] provide extensive information and further references on this topic.

In the recent years the development of the so-called “synthetic jet” or “zero net mass flux” devices and their potential for flow control; especially separation control, mixing enhancement and fluidic thrust vectoring has received a great amount of attention from the fluid dynamics community. The existing literature presents promising applications of the synthetic jet technology to flow separation under both laboratory and real flight conditions (Greenblatt and Wygnanski [17], Greenblatt et al. [18], Seifert and Pack [19], Pack and Seifert [20], and Seifert and Pack [21]). A large quantity of numerical computations and simulations have been produced in the area of flow separation control over lifting surfaces via synthetic jet actuators (Donovan et al. [22], Hassan

Contributed by the Fluids Engineering Division for publication in the JOURNAL OF FLUIDS ENGINEERING. Manuscript received by the Fluids Engineering Division August 21, 2003; revised manuscript received, July 28, 2004. Review conducted by W. Copenhagen.



**Fig. 1** Wind tunnel model: (a) Geometric details. (b) Internal assembly details of the wing showing the ESP pressure scanner and the synthetic jet actuator. (c) Assembled wing showing the SJA exit slot location.

and Munts [23], He and Kral [24], and He et al. [25]). Another application of synthetic jet technology is the control of the aerodynamic performance of lifting surfaces through fluidic modifications of their apparent aerodynamic shape (Amitay et al. [26], Honohan et al. [27], and Parekh and Glezer [28]). Jet vectoring has also become an area of flow control that can receive benefits from the application of synthetic jet actuators (Smith and Glezer [29], Smith et al. [30], and Pack and Seifert [31]). This is of importance in the development of jet engine exhaust systems as well as in the area of control surface performance augmentation.

The application of synthetic jets to flow separation control is based on their ability to energize the boundary layer. The synthetic jet actuator (SJA) that will be discussed in this work adds momentum to the boundary layer in several ways. During the suction part of the cycle, it draws the low momentum fluid in the boundary layer inside the cavity, thereby bringing the higher momentum fluid at the boundary layer edge nearer to the surface. During the blowing part of the cycle, it adds the same fluid with higher momentum to the flow, almost tangentially to the surface. The average “effective” momentum added over the entire cycle replenishes part of the momentum deficit in the boundary layer. The actuator not only produces momentum itself, but also enhances the ability of the boundary layer to overcome adverse pressure

**Table 1** Chordwise location of the pressure taps

Tap number	Chordwise location ( $x/c$ )	
	Top	Bottom
1	0.000	0.003
2	0.003	0.014
3	0.012	0.027
4	0.027	0.051
5	0.054	0.083
6	0.085	0.136
7	0.156	0.197
8	0.200	0.254
9	0.251	0.325
10	0.315	0.386
11	0.386	0.488
12	0.464	0.580
13	0.546	0.661
14	0.631	0.780
15	0.715	0.888
16	0.824	...
17	0.942	...

(b)

gradients downstream. This is achieved through mixing of the low momentum fluid near the surface with the high momentum external flow. The effectiveness of this mixing process relates to the high receptivity of the shear layer emanating from the point of separation. Proper excitation of the shear layer promotes the development of its natural instability causing resonance, which leads to the formation of large vortical structures. These flow structures in turn promote boundary layer mixing and hence momentum exchange between the outer and inner parts of the boundary layer.

In this part of our work, the effectiveness of the actuator, characterized in Part I, is demonstrated in wind-tunnel flow separation control experiments over a two-dimensional airfoil.

(c)

### Experimental Setup and Procedures

**Wing Model.** In order to test the separation control capabilities and performance of the actuator, it was placed inside a NACA 0015 profiled wing with a chord of 0.375 m and a span of 0.358 m. Testing was conducted in the 3 ft×4 ft wind tunnel at the Department of Aerospace Engineering of Texas A&M University. Figure 1(a) shows the geometric details of the wing model. The wing was fabricated out of Freeman Industries REPRO 95 aluminum filled epoxy. In order to provide easy access to the actuator and other instrumentation that was to be installed inside the wing, as well as to facilitate the fabrication process of the wing, it was fabricated in two halves (top and bottom) with a chamber to house the actuator and auxiliary instrumentation. The bottom half of the wing with the actuator and an ESP pressure scanner installed on it, is shown in Fig. 1(b). The exit slot of the actuator was placed at 12% of the chord (measured from the leading edge), on the top half of the wing (Fig. 1(c)). This location was selected to provide sufficient volume to accommodate the SJA in the wing. As discussed in Part I, the exit slot was machined so that the jet exits tangentially to the surface of the wing. The slot has a width of 2 mm and a length (spanwise) of 44.7 mm.

The wing was equipped with 32 pressure taps distributed on the upper and lower surfaces. Table 1 shows the nondimensional chordwise locations of the pressure taps measured from the leading edge of the wing. The pressure taps were located close to the center of the wing span and were slightly offset with respect to each other in the spanwise direction in order to reduce interference. The pressure ports were connected, via Tygon tubing, to a 32-channel ESP electronic pressure scanner with a pressure range of  $\pm 5.0$  kPa. Repeated measurements indicated a standard deviation of 3.2 Pa. The pressure scanner was also installed inside the wing, as shown in Fig. 1(b).

In order to enforce a two-dimensional flow field over the wing (i.e., to eliminate the three-dimensional effects due to its finite span) the wing was placed between two Plexiglas end plates (Fig.



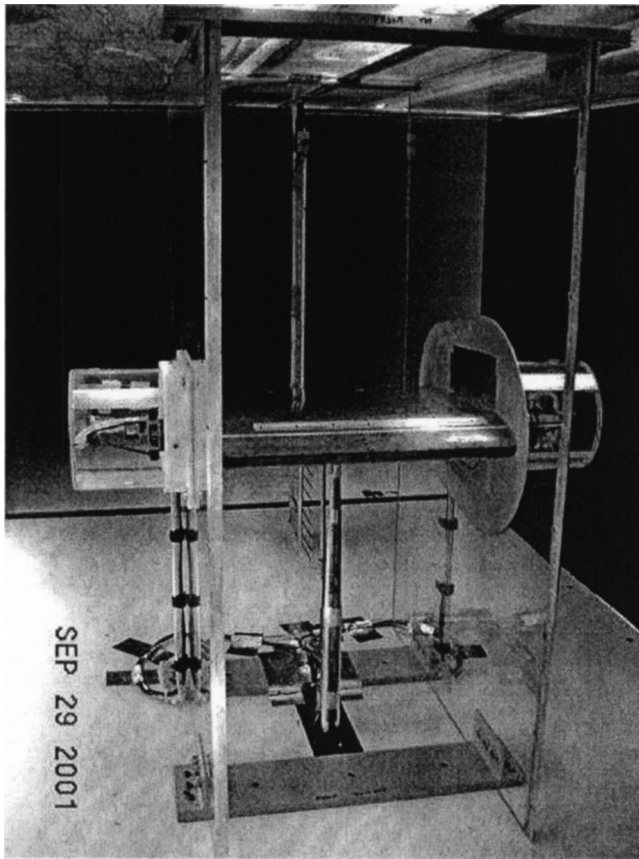


Fig. 2 Final configuration of the wind-tunnel experimental setup

2). The end plates were not physically attached to the wing; hence they did not transfer any forces to the wing. There was a small clearance between each plate and the wing (0.8 mm) [32]. This was necessary to ensure that no contamination of the wing aerodynamic forces was introduced by the end plates. The fact that the motors extended from the sides of the wing required that the motors be shielded from the free-stream in the wind tunnel, such that they did not contaminate the aerodynamic force measurements. This was achieved by installing hollow cylinders attached to the Plexiglas end plates, as shown in Fig. 2, which shows the final configuration of the wind-tunnel experimental setup.

**Wind Tunnel Facility.** The aerodynamic tests were performed in the Texas A&M University's 3 ft×4 ft continuous wind tunnel at a free-stream velocity of 35 m/s, with a resulting Reynolds number, based on the wing chord, of  $Re=8.96 \times 10^5$ . The wind tunnel has a turbulence intensity of 0.3% at a freestream velocity of 35 m/s. The free-stream velocity was determined using a wall mounted Pitot tube, manufactured by United Sensors, with a tip diameter of 3.175 mm. Differential pressure was measured using an Omega PX139 series pressure transducer with a range of  $\pm 2.0$  kPa, which can resolve pressures down to 1 Pa. Repeated tests using this transducer to calculate velocity indicated a standard deviation of 0.22 m/s. The output of a thermocouple, installed in the test section, was measured by an Omega I-Series temperature and process monitor with a voltage measurement resolution of  $1 \mu V$ . This monitor was interfaced with the wind tunnel data acquisition code via an Ethernet connection. The uncertainty for the temperature measurement was estimated to be  $\pm 1$  K. The uncertainty in the measurement of the free-stream velocity was 0.46 m/s.

**Force Balance.** A three component Aerolab pyramidal bal-

ance was used for force and moment measurements. The balance measures two forces (lift and drag) as well as pitching moment. These components are measured directly by three strain gauge load cells. The accuracy of the balance was estimated at 0.5% of full scale for lift, drag, and pitching moment. Through repeated data runs, repeatability of the balance for lift, drag, and pitching moment was estimated to be  $\Delta C_L=0.001$ ,  $\Delta C_D=0.001$ , and  $\Delta C_m=0.0008$ .

The model pitch (angle of attack) was adjusted using a stepper motor, which was connected to a worm-gear mechanism. A high-resolution optical encoder was connected to the mechanism and its output was fed into the data acquisition setup via a digital read out display with a RS232 output. Model angle of attack could be set and measured with an accuracy of 0.05 deg. Force balance data as well as wind tunnel dynamic pressure and temperature were acquired using a PC equipped with a 16 bit A/D board.

The force balance measurement part of the tests consisted of pitching the model through an angle of attack range from  $-2$  to 29 deg. Data was typically recorded at 2 deg intervals. In the vicinity of the maximum lift coefficient, smaller increments were used where necessary. Pitching moment was taken about the quarter chord. Data was taken both with and without SJA actuation. The data taken with the actuator off provided a baseline for comparison. For the actuated case (SJA on), data was taken with the actuator operating at frequencies of 60, 80, 100, 120 and 130 Hz. In this study, solid and wake blockage were corrected for using the method presented in Rae and Pope [32].

**Flow Visualization.** Both on- and off-surface flow visualization techniques were used. The on-surface visualization was accomplished using titanium dioxide suspended in a mixture of kerosene, linseed oil and oleic acid. In addition to this method, tufts were also placed on the upper surface of the wing in order to provide a second means of surface flow visualization. For off-surface flow visualization, smoke was injected upstream of the wing. All of the tests were run at a free-stream velocity of 35 m/s, at angles of attack of 8, 12, 16, 18, and 20 deg. All of the flow visualization tests were performed with and without operation of the synthetic jet actuator. For the case in which the actuator was not operated, the exit slot of the actuator was covered so that the titanium dioxide mixture did not enter the actuator plenum. For the case in which the actuator was used, it was operated at a frequency of 120 Hz. Video footage and digital still images were recorded during these tests and analyzed subsequently to determine the characteristics of the flowfield for the above-mentioned conditions.

**Surface Pressure Measurements.** Surface pressures were measured for an angle of attack range from  $-2$  to 29 deg. The tests were run at a free-stream velocity of 35 m/s. Data was taken both with and without actuation. For the actuated case, data was taken with the actuator operating at frequencies of 60, 80, 100, 120, and 130 Hz. The surface pressures were evaluated using a 32-channel ESP pressure sensor with a range of  $\pm 5.0$  KPa. Calibration of the ESP was checked by sequentially comparing a reference pressure imposed on each channel against the value measured by an Edwards Barocell pressure transducer (which has an accuracy of  $\pm 6.5$  Pa). Agreement between the Barocell and the ESP was generally within 1%. Prior to each test the ESP was zeroed to reduce drift. After completing each test the ESP was zeroed to ascertain if the zeros had drifted significantly during the test. The pressures measured by the ESP were digitized using a 12 bit A/D board. With this configuration, the uncertainty in the pressure coefficient measurements was calculated to be 0.03. Each time data was taken; the pressures at each location were sampled 200 times and averaged. After the conditions of the experiment changed (i.e., a change in  $\alpha$  or a change in the actuator frequency), data measurement was delayed for 5 s to allow the pressures to stabilize.

**Wake Surveys.** In order to better evaluate the performance of

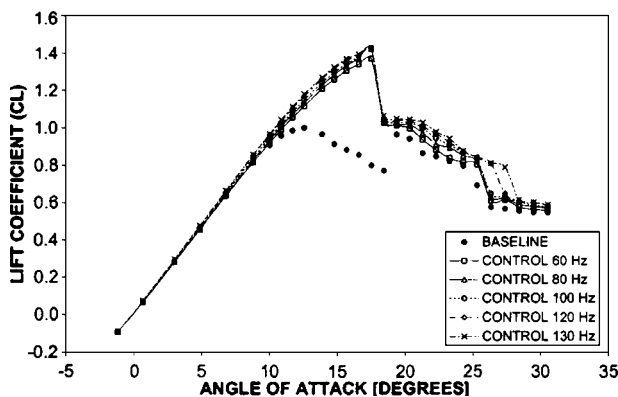
**Table 2 Summary of SJA performance parameters**

$f$ , Hz	$C_\mu$	$u_{max}$ , m/s	$F^+$	$u_{max}/U_\infty$
60	0.0051	36	0.57	1.03
80	0.0093	48	0.75	1.37
100	0.0147	61	0.94	1.74
120	0.0123	75	1.13	2.14
130	0.0254	81	1.23	2.31

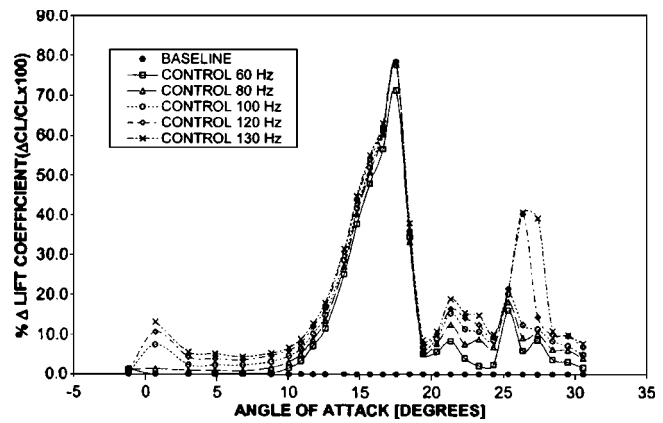
the actuator as a flow separation control device, wake surveys were performed downstream of the wing by traversing a Pitot rake placed at a distance of  $x/C=1.2$  behind the trailing edge (measured when the wing is at an angle of attack of 0 deg). The rake was fabricated with 32, 1.5 mm diameter (O.D.) tubes, spaced 25.4 mm apart, which were connected to a 32-channel ESP pressure scanner. Gilarranz [33] provides details of the wake rake construction and installation within the wind tunnel. Due to the fact that the separation between the tubes was rather large, a good resolution of the wake profile was obtained by traversing the rake vertically to nine positions for each operating condition. This yielded a vertical spatial resolution of 2.54 mm between the data points. For each location, the pressures were sampled 200 times and averaged. Data was taken both with and without actuation. For the actuated case, data was taken with the actuator operating at frequencies of 60, 80, 100, 120, and 130 Hz.

**Results and Discussion**

**Force Balance Measurements.** Figures 3 through 6 present the effect of SJA operation on the aerodynamic performance of the wing. Table 2 presents a summary of SJA performance parameters. As seen in Fig. 3, at angles of attack below 10 deg, an increase in the actuator frequency causes a slight increase in the lift curve slope. It was found that, for actuator frequencies between 60 and 130 Hz, the increase in the lift curve slope scales linearly with actuator frequency. The use of the SJA causes a dramatic increase in the value of  $CL_{max}$  (Fig. 3). This is also shown in Fig. 4, which presents the increase in lift coefficient ( $\Delta CL$ ) vs angle of attack as a percentage of the lift without SJA actuation. The operation of the SJA (at any frequency) extends the range of angles of attack for which the wing may be operated without stalling. The angle of attack for which stall occurs was increased from 12 deg for a basic wing to 18 deg for the case of SJA actuation. As shown in Fig. 3, in the range of frequencies that were tested, the frequency of actuation does not seem to have a significant effect on the magnitude of  $CL_{max}$ , in fact, the data



**Fig. 3 Effect of the synthetic jet actuator on the aerodynamic performance of the test wing. Lift coefficient (CL) vs angle of attack ( $\alpha$ ).**



**Fig. 4 Effect of the synthetic jet actuator on the aerodynamic performance of the test wing. Percentage change in the lift coefficient ( $\Delta CL$ ) vs angle of attack ( $\alpha$ ).**

suggests a frequency or momentum saturation. For these tests  $CL_{max}$  had a low value due to the fact that the Reynolds number of the tests is relatively low (Traub [34]).

Figure 3 also shows that the basic wing has a docile stall, which is typical of an aft stall (also referred to as trailing edge stall). This type of stall mechanism is typical for thick airfoils (with thick leading edges) and is characterized by the gradual upstream movement of the separated flow region from the trailing edge, as the angle of attack increases. With SJA actuation, the stall mechanism is more analogous to so-called leading edge short bubble stall. This mechanism is characterized by the formation of a short bubble near the leading edge. The size of the bubble generally does not vary much with incidence (it may shorten slightly) until it bursts, with the consequent massive separation, indicating stall. As seen in the figure, the lift curve presents a sharp peak close to  $CL_{max}$ , and decreases rapidly above the stall angle. This behavior is very similar to that corresponding to the leading edge stall mechanism.

For  $\alpha > 18$  deg, once massive stall has occurred on both airfoil configurations (basic and actuated), the operation of the synthetic jet still provides a small amount of lift augmentation, however, the effects of the actuator are relatively small. It may be seen that for angles of attack larger than 25 deg, a high frequency of actuation is required to produce any noticeable effects, i.e. only actuation at frequencies above 100 Hz seem to produce any appreciable lift augmentation. For angles of attack higher than 25 deg, SJA actuation still provides lift augmentation as high as 40% (Fig. 4).

Figure 5 shows that the use of the SJA reduces drag at high  $C_L$ . This was further verified by an inspection of the wake surveys that will be discussed later. For lift coefficients below 1.0 ( $\alpha < 10$  deg), the use of the SJA does not seem to have any significant effect over the drag coefficient (Fig. 5, lower branch). The decrease in drag at angles of attack between 10 and 18 deg ( $C_L$  between 1.0 and 1.4, respectively) is due to the suppression of the separated region over the wing, with its resulting reduction of pressure drag.

Figure 6 shows the effect of the synthetic jet actuators on the pitching moment of the airfoil. The slight slope of the pitching moment curve is due to the fact that the pitching moment coefficient was calculated about the quarter chord position measured from the leading edge ( $x = 1/4 C$ ), which is the theoretical position of the aerodynamic center for NACA symmetrical profiles. However, our calculations showed that the location of the aerodynamic center for the wing is at 30% of the chord (Gilarranz [33]). It is suspected that this difference is caused by the relatively large thickness of the trailing edge of the airfoil. Summers and Page [35] showed experimentally that as the trailing edge thickness of their test wing was increased, more lift was carried over the rear portion of the airfoil section, with an increase in the slope of the

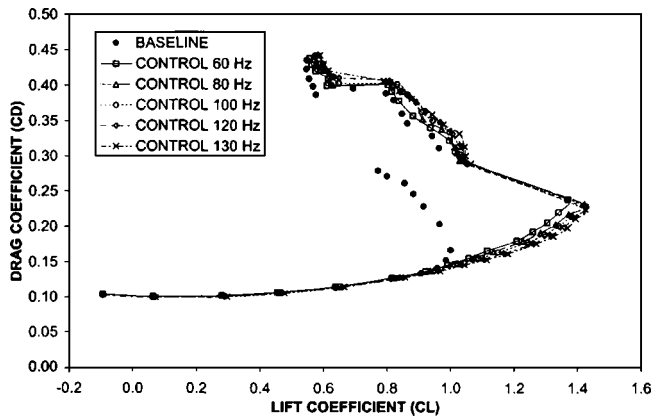


Fig. 5 Effect of synthetic jet actuator on the aerodynamic performance of the test wing. Drag coefficient ( $C_D$ ) vs lift coefficient ( $C_L$ ).

pitching moment curves. This would explain a rearward shift in the aerodynamic center of the wing. Furthermore, asymmetry in the construction of the wing halves may also be a contributing factor to this shift. Returning to Fig. 6, it may be seen that stall is characterized by a strong nose-down pitching moment. The effects of the SJA are to delay stall, hence the occurrence of the strong nose-down pitching moment is delayed for the actuated case. Note that for lift coefficients lower than 1.0 (i.e., before the basic wing stalls), higher actuation frequencies result in a larger nose-down pitching moment. This is due to the fact that wing loading moves farther aft [33]. At lift coefficients between 1.0 and 1.2 the frequency of actuation does not seem to have any effect over the pitching moment, however, as the lift coefficient increases beyond this value, the higher frequencies of actuation delay the occurrence of stall to higher lift coefficient values.

**Flow Visualization.** Figure 7 shows smoke flow visualization without (top) and with (bottom) actuation for an angle of attack of 25 deg and a free-stream (right to left) velocity of 35 m/s. Without actuation the flow separates close to the leading edge and the wing is in the post-stall region. With actuation, the flow appears to remain attached over the wing chord.

Figure 8 shows the limiting streamlines downstream of the SJA exit slot. The image was taken with the actuator operating at a frequency of 120 Hz with no free stream imposed on the wing, i.e., quiescent conditions. Note that for this case, there are five distinct flow regions clearly visible in the pictures. Notice that the

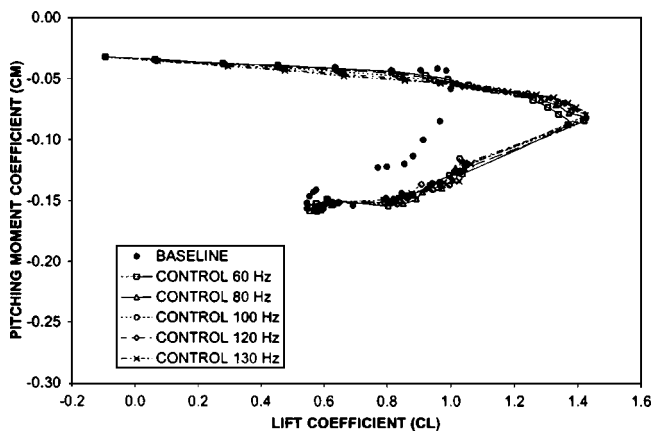
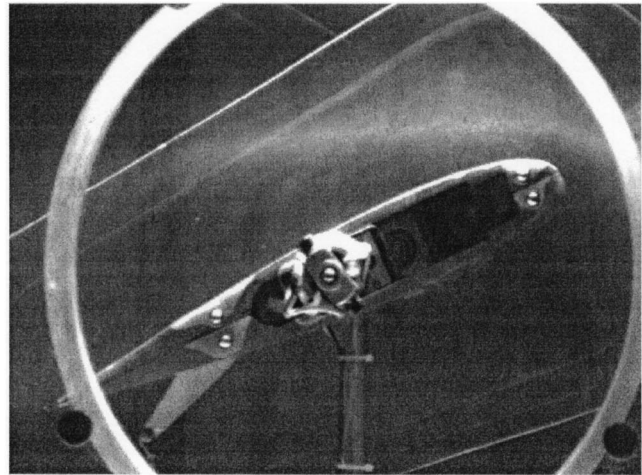
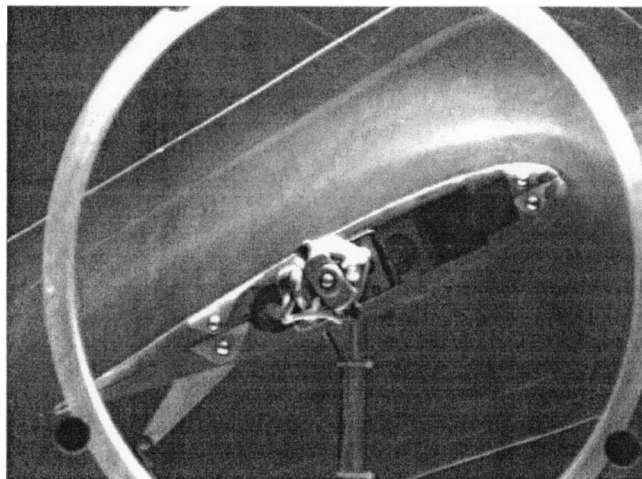


Fig. 6 Effect of synthetic jet actuator on the aerodynamic performance of the test wing. Pitching moment coefficient ( $C_M$ ) vs lift coefficient ( $C_L$ ).



(a)



(b)

Fig. 7 Flow visualization over the wing at  $\alpha=25$  deg and a free-stream velocity of 35 m/s: (a) without SJA actuation and (b) with SJA actuation at 120 Hz

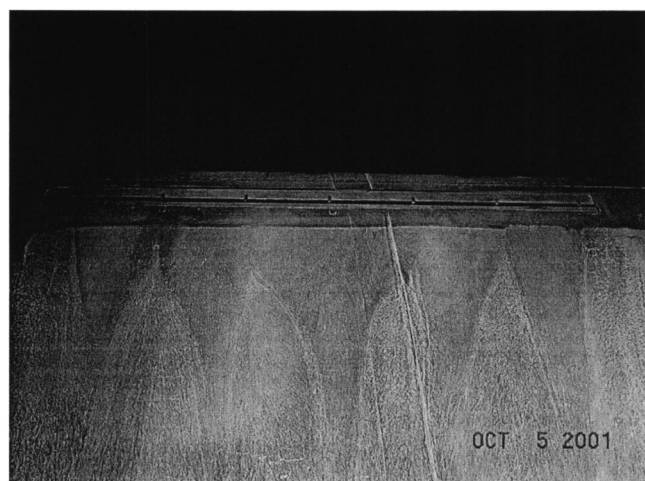
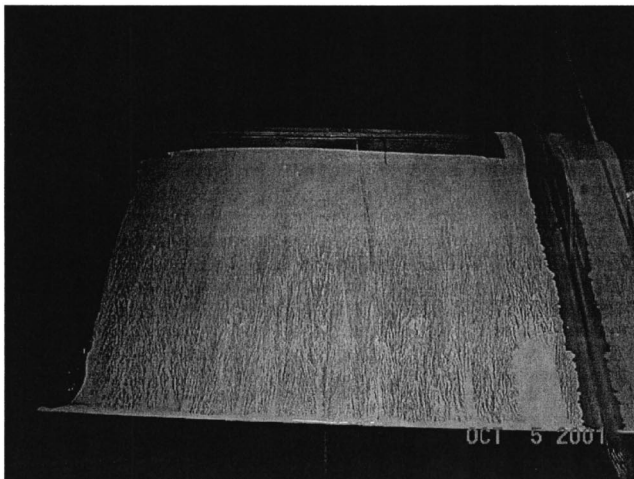


Fig. 8 Oil surface flow visualization of the test wing. Synthetic jet actuator operating at a frequency of 120 Hz. Wind tunnel off ( $U_\infty=0$  m/s).



(a)

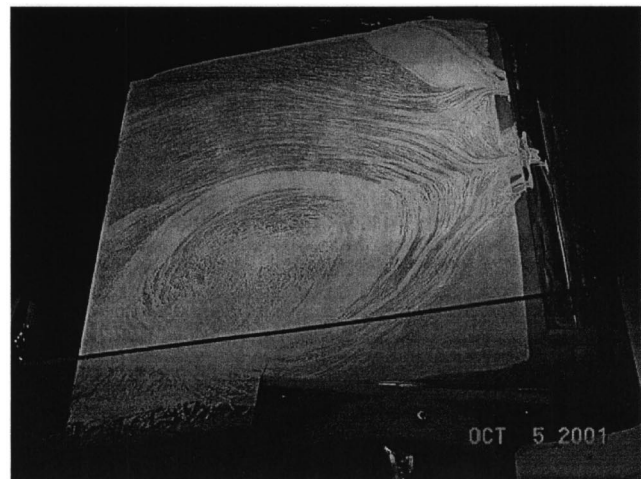


(b)

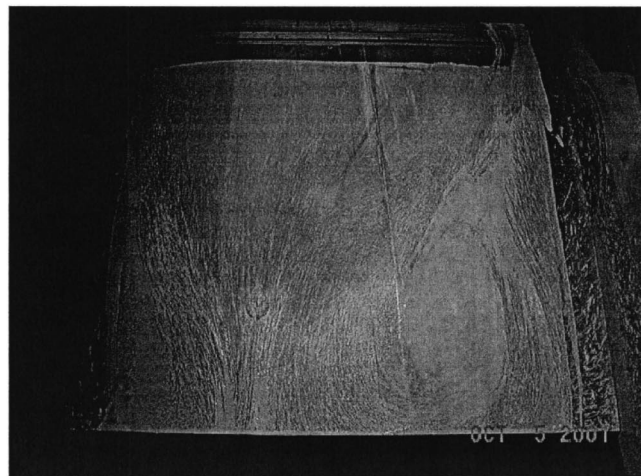
**Fig. 9** Oil surface flow visualization of the test wing at  $\alpha=12$  deg,  $U_\infty=35$  m/s. (a) corresponds to no control, and (b) corresponds to control at 120 Hz.

center region encompasses the exit of the two center slots, which are in phase. The other four regions correspond to the exit of each one of the other four pistons, which are out of phase with the pistons located on either side. The curvature of the surface streamlines suggests the possible presence of streamwise vortices, at the edge of each individual jet, which may be produced as a result of the strong shear caused by the difference in the phasing of the pistons. No evidence of such structures was encountered in the rest of the tests performed on the wing in the presence of free stream.

Figures 9–11 show images of the limiting surface streamlines for the tests performed at a free-stream velocity of 35 m/s. These images include pictures of the limiting streamlines with and without actuation at 120 Hz, for angles of attack of 12, 16, and 20 deg. At  $\alpha=12$  deg (Fig. 9), for the case of the flow without actuation, image (a) shows clear evidence of the presence of trailing edge separation, with two very distinct counter-rotating open recirculation regions close to the trailing edge of the wing. For the actuated case, image (b) shows that the synthetic jet actuators have completely reattached the flow, eliminating the trailing edge separation. Figure 10 shows the limiting streamlines for the wing at  $\alpha=16$  deg. For this case, image (a) shows almost complete upper surface separation, i.e., the extent of the separated region almost reaches as far upstream as 20% of the chord (measured from the leading edge). Note that there are two recirculating regions: a large one close to the center of the wing and a smaller one close to the top edge of image (a) (the left side of the wing when seen



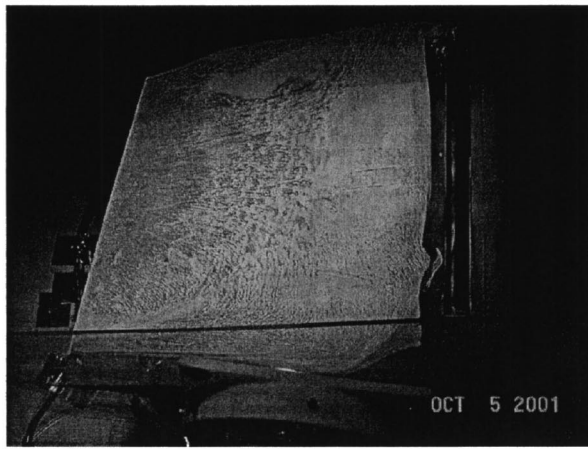
(a)



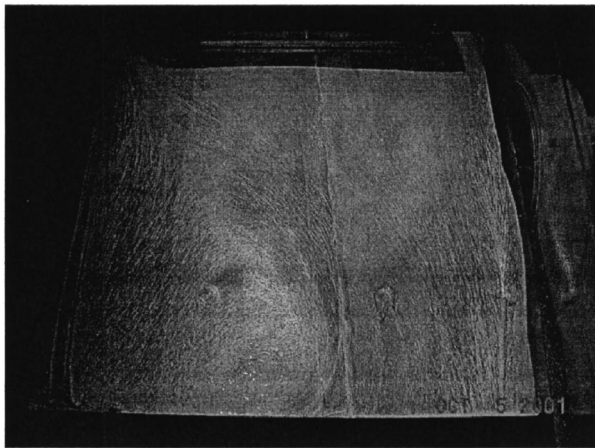
(b)

**Fig. 10** Oil surface flow visualization of the test wing at  $\alpha=16$  deg,  $U_\infty=35$  m/s. (a) corresponds to no control ( $U_\infty$  from right), and (b) corresponds to control at 120 Hz ( $U_\infty$  from the top).

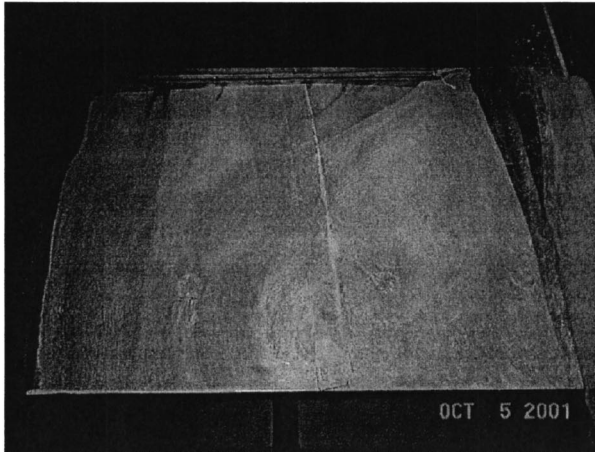
from behind). For the actuated case, image (b) shows that the synthetic jet actuator has kept most of the flow attached over the center span of the wing, however, there is still a sizable recirculation region on the right-hand side of image (b), and a smaller one on the left-hand side of image (b). The presence of these separated regions may be due to the fact that the SJA does not cover the entire span of the wing; hence it has no control authority over regions that are close to the side plates. At  $\alpha=20$  deg (Fig. 11) for the case of no control, it may be seen that the flow is now completely separated and that the velocity of the flow close to the surface has a strong upstream component (physically observed during the experiment). This is shown by the large oil deposits close to the actuator exit. The controlled case showed that for this angle of attack, the synthetic jet actuator was able to keep the flow attached over the whole chord line for half of the wing. It is of particular interest to mention that if the actuators were turned on after the free stream had reached its value of 35 m/s, the flow separated over the left half of the wing (Fig. 11(b)). However, if the actuator was turned on before the wind tunnel, then the flow separated on the right half of the wing (Fig. 11(c)). The presence of these separated regions are due to the fact that the SJA exit slot does not cover the entire span of the wing, but there is a small distance between the slot edges and the wing end plates. The alternating of the separation region between the right and left halves of the wing indicates the presence of an instability, which is sensitive to the initial conditions (actuator on first or tunnel on first). The instability's nature is as yet unknown.



(a)



(b)



(c)

**Fig. 11 Oil surface flow visualization of the test wing at  $\alpha=20$  deg,  $U_\infty=35$  m/s. (a) corresponds to no control ( $U_\infty$  from right), while (b) and (c) correspond to control at 120 Hz ( $U_\infty$  from the top).**

**Surface Pressure Measurements.** Figure 12 shows surface pressure measurements on the wing at a free-stream velocity of 35 m/s and several angles of attack. The pressure taps on the upper and lower surfaces were placed close to the midspan of the wing. Therefore, the pressure measured by some of the pressure taps on the bottom surface of the wing were affected by the wake of the sting that supported the wing. The area of the flow field that was affected by the wake of the sting is clearly marked in the figures. Figure 12(a) shows the pressure distribution for an angle of attack

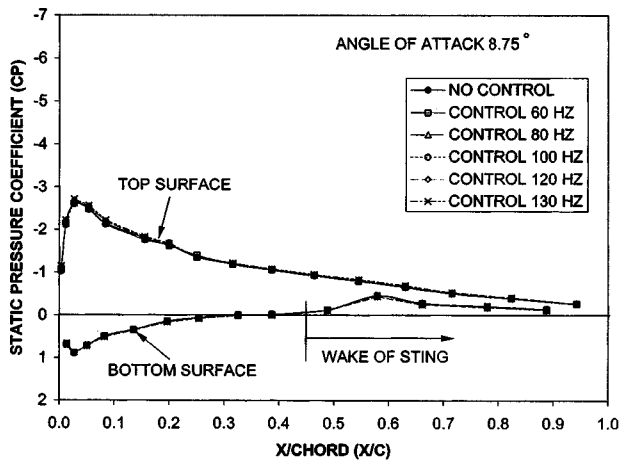
of  $8.75^\circ$ . Note that for this angle (as well as for all angles of attack for which the flow is attached) SJA actuation, irrespective of actuation frequency, does not appear to have any *significant* effect on the pressure distribution over the wing. The effect of the sting on the pressure distribution over the aft part of the lower wing surface is evident.

For the case of  $\alpha=12.6$  deg (Fig. 12(b)), comparing the pressure distribution of the basic wing and the one generated with actuation of the SJA, it is evident that the synthetic jet has a global effect over the pressure distribution on the suction surface of the wing. For the basic wing (no actuation) trailing edge separation is now visible and extends from about 60% of the chord to the trailing edge. Increasing the actuation frequency only has an effect on the front 20% of the upper wing surface. Higher frequency causes higher suction. The pressure distribution on the lower surface of the wing is only marginally affected by SJA actuation.

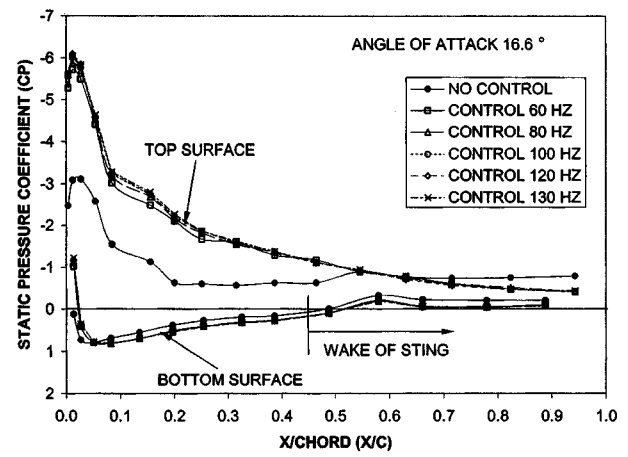
An increase of the angle of attack produced a further increase of the suction peak for the actuated case. The pressure also increased on the windward (pressure) side of the wing with SJA actuation compared to the basic wing. Upper surface suction decreased significantly over most of the basic wing due to large trailing edge flow separation extending over approximately 80% of the chord (see Figs. 12(c) and 12(d)). The suction peak for the actuated cases reaches a maximum at an angle of attack of  $17.6$  deg (Fig. 12(e)). In this range of angles of attack (approximately between 12 deg and 18 deg), the frequency of actuation has a small effect on the pressure distribution over the wing. This is of practical importance, since for the case of the dc motor-driven SJA, the power input to the actuator increases for an increase in actuator frequency and jet momentum coefficient, hence using a lower actuation frequency (without compromising the beneficial effects of the actuation on the pressure distribution) would require less power.

Figure 12(f) shows the pressure distribution for  $\alpha=18.6$  deg. It is interesting to note that within just 1 deg, the suction peak (for the actuated cases) has decreased drastically and 70% of the airfoil suction is lost. This indicates a violent stall, and although there is no doubt that for this case the separation mechanism is a trailing edge stall, its characteristics are more similar to the case of short bubble leading edge stall. A further increase of the angle of attack to  $19.4$  deg (Fig. 12(g)) continues to reduce the suction peak for the actuated case with concomitant massive separation over the top half of the wing. On the other hand, the suction peak of the basic wing has increased, and the pressure on the bottom surface of the wing no longer seems affected by the SJA. For the case of  $25.4$  deg (Fig. 12(h)), the basic wing is totally stalled (there is no suction peak and the pressure distribution has the flat appearance associated with separation), while for the actuated case the suction peak near the leading edge is still maintained. As the angle of attack increases, only actuation at higher frequencies is able to sustain a suction peak on the upper surface of the wing. For example, at  $\alpha=26.4$  deg (Fig. 12(i)) only the curves for 120 and 130 Hz produce a suction peak over the upper surface of the wing, while at  $27.3$  deg (Fig. 12(j)), only the peak at 130 Hz is visible. Finally, at  $28.4^\circ$  (Fig. 12(k)) the SJA loses all control authority (for the actuation frequencies and amplitudes tested here) and the wing is stalled for both actuated and nonactuated cases.

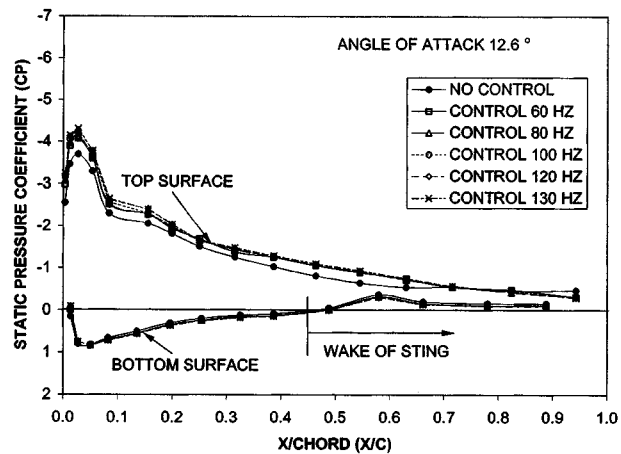
**Wake Surveys.** Figure 13 shows the results from the wake surveys of the flow field at a location of  $x/C=1.2$  downstream of the wing trailing edge (measured with the wing at  $\alpha=0$  deg). For these plots, the free-stream velocity was 35 m/s. Figure 13(a) shows the wake of the airfoil for an angle of attack of 0 deg. For this case the wake is very narrow and the effects of the SJA are very small. At  $\alpha=8$  deg (Fig. 13(b)), the wake becomes wider and the peak velocity deficit is higher, representing the manifestation of profile drag. The effects of the SJA are now noticeable, and although the flow for the basic wing is completely attached, the SJA narrowed the wake and reduced the velocity deficit, suggest-



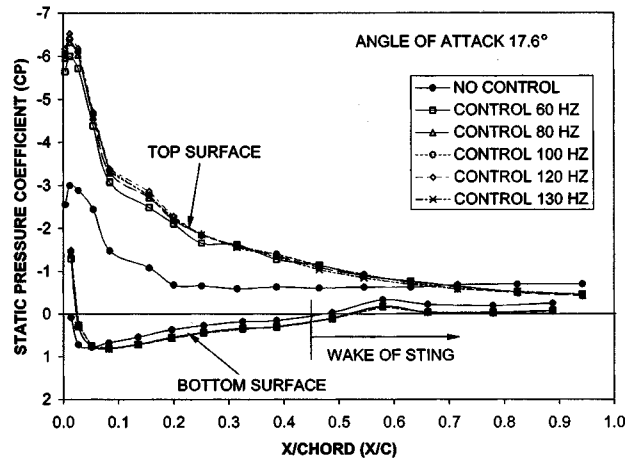
(a)



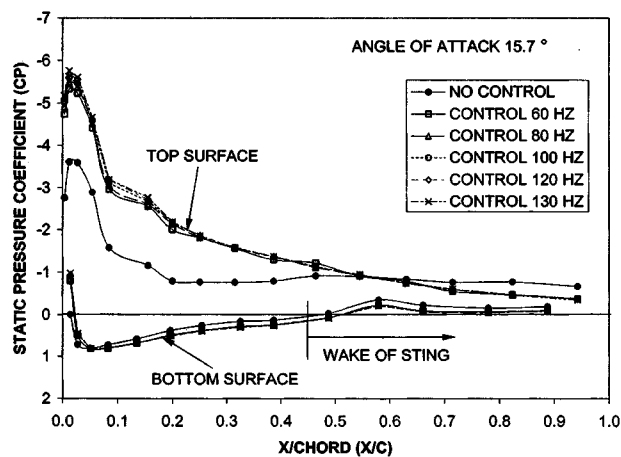
(d)



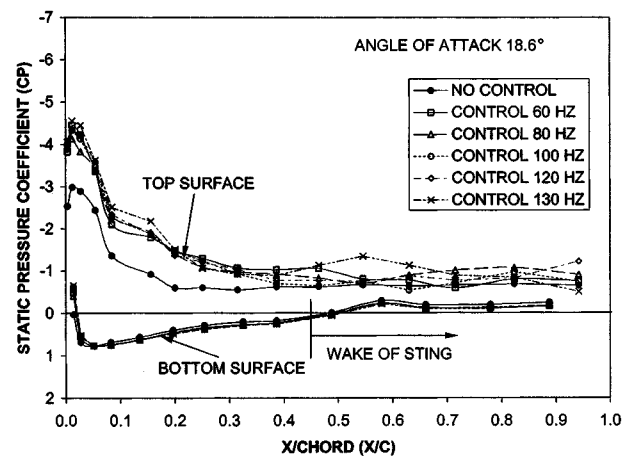
(b)



(e)



(c)



(f)

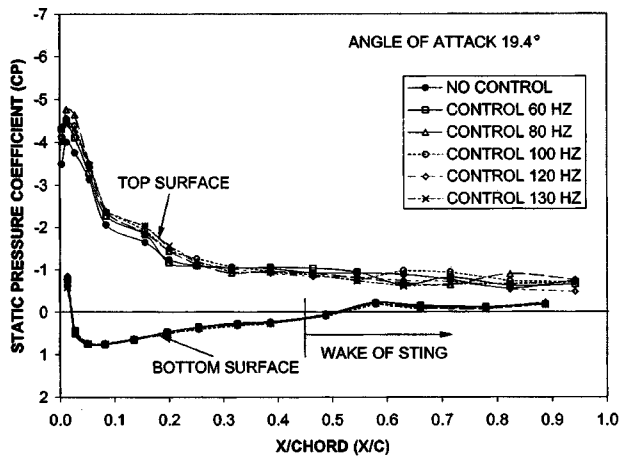
Fig. 12 Effects of synthetic jet actuation on the wing surface pressure distribution at  $U_\infty = 35$  m/s and for the following angles of attack: (a) 8.75 deg, (b) 12.6 deg, (c) 15.7 deg, (d) 16.6 deg, (e) 17.6 deg, (f) 18.6 deg, (g) 19.4 deg, (h) 25.4 deg, (i) 26.4 deg, (j)  $\alpha = 27.3$  deg, (k) 28.4 deg

ing a reduction in profile drag. For the range of angles of attack between 12 and 18 (Figs. 13(c)–13(e)) the flow for the basic wing shows signs of separation as the wake becomes wider with increasing  $\alpha$  and the magnitude of the velocity deficit increases. For the actuated case, the trend seems to be that higher frequencies of actuation produce narrower wakes and a smaller velocity deficit. For an angle of attack of 20 deg, the wake widens dramatically

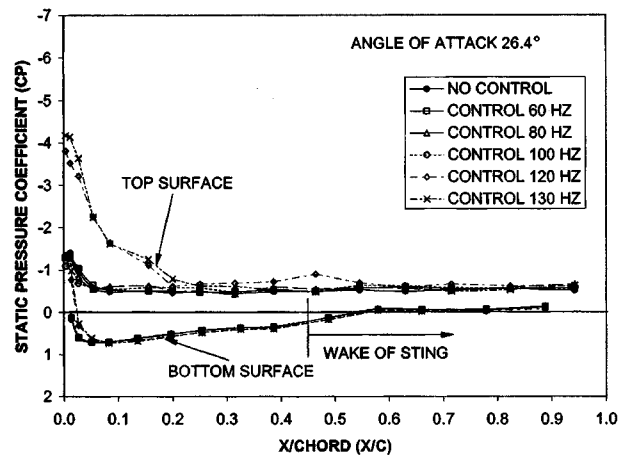
due to massive separation, and the actuator seems to have no control authority over the characteristics of the wake.

## Conclusions

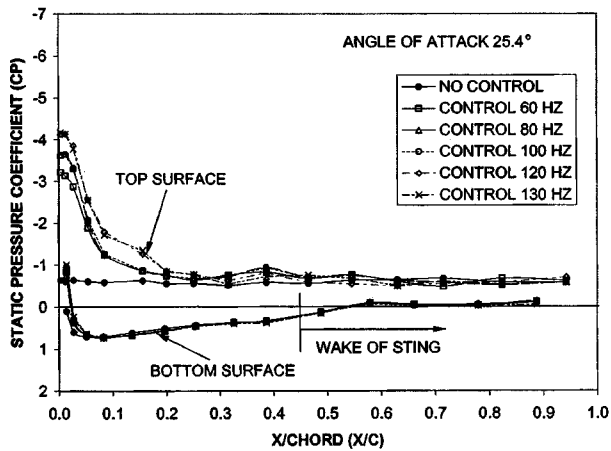
The synthetic jet actuator developed and characterized in Part I was applied toward flow separation control over a NACA0015



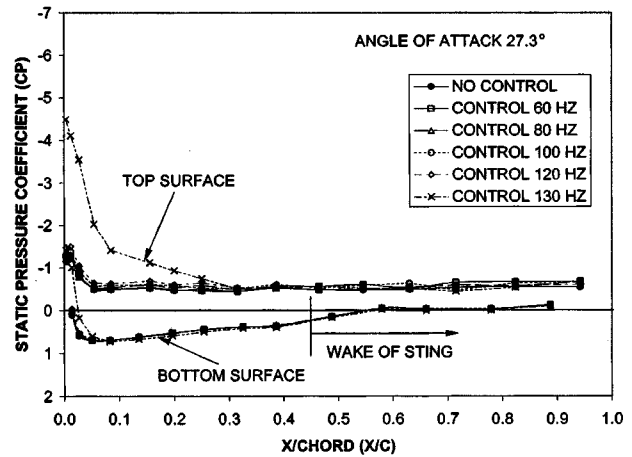
(g)



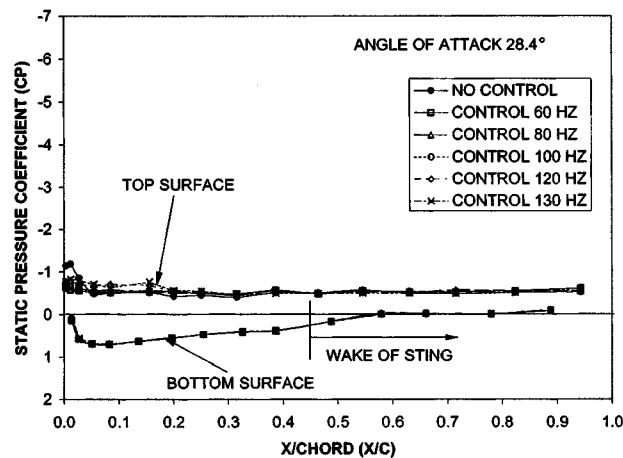
(i)



(h)



(j)



(k)

Fig. 12 (continued)

profiled wing. The actuator was housed inside the wing and was tested in a wind tunnel. An experimental investigation into the effects of a synthetic jet actuator on the performance of the wing was undertaken. Emphasis was placed on the capabilities of the actuator to control the separation of the flow over the wing at high angles of attack. The investigation included the use of force balance measurements, on-surface oil flow visualization, off-surface smoke flow visualization, surface pressure measurements, and wake surveys. The tests were performed at a free-stream velocity

of 35 m/s, corresponding to a chord Reynolds number of  $8.96 \times 10^5$ . The angle of attack was varied from  $-2.0$  to  $29$  deg.

For  $\alpha < 10$  deg, the lift curve slope shows a weak dependency on frequency, with a small increase in slope with  $f$ . For this range of  $\alpha$ , static pressure distribution measurements showed that the SJA only affected the flow over the first 25% of the chord. At higher angles of attack, the SJA extends the range of  $\alpha$  for which the wing may be operated without stalling. The use of the actuator

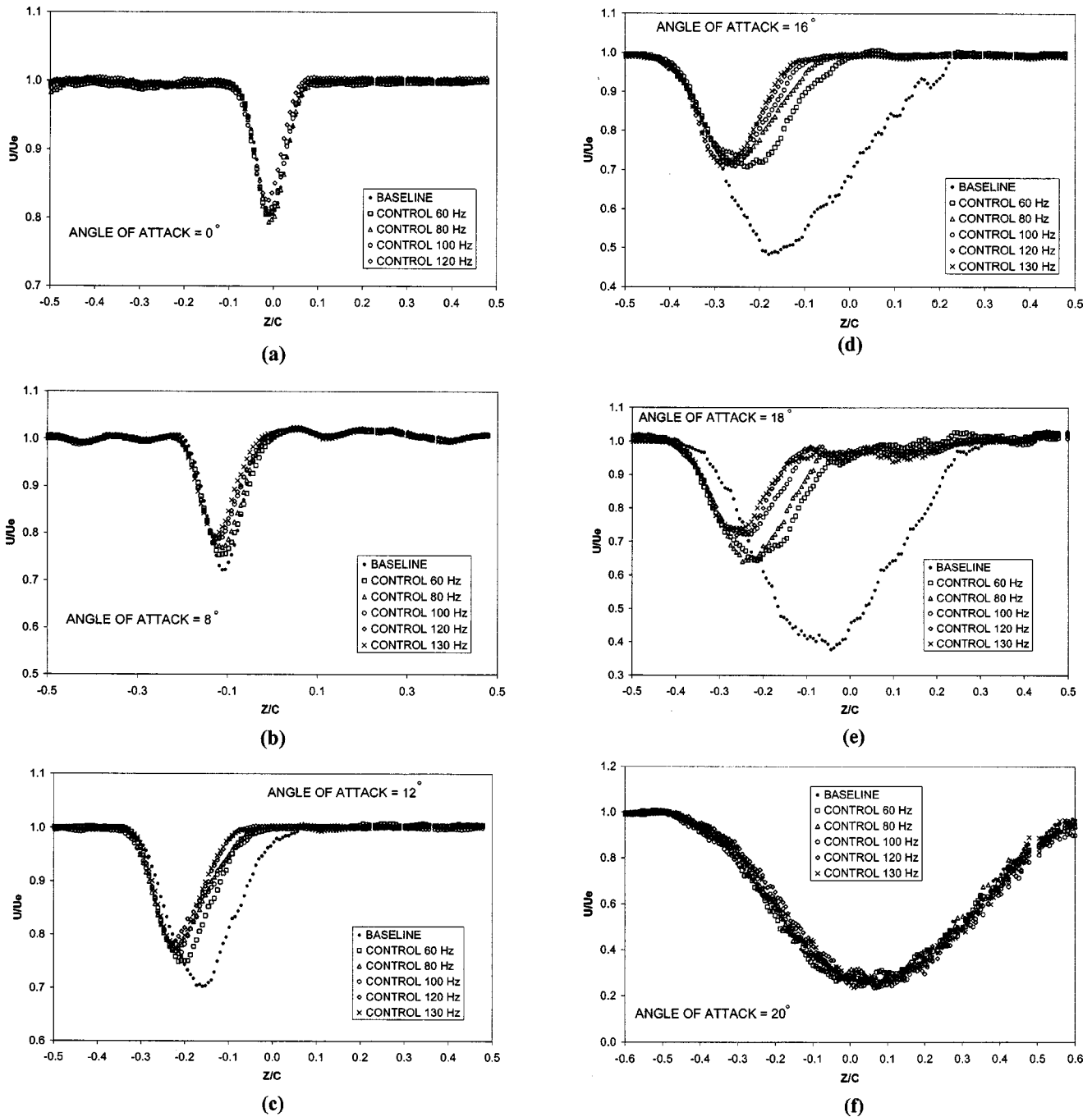


Fig. 13 Wake surveys at a free stream of  $U_\infty = 35$  m/s and at the following angles of attack: (a) 0.0 deg, (b) 8.0 deg, (c) 12.0 deg, (d) 16.0 deg, (e) 18.0 deg, and (f) 20.0 deg

causes an 80% increase in the value of  $CL_{max}$ , and the angle at which stall occurs is increased from 12 to 18 deg. In this range of  $\alpha$ , the effects of the SJA are global, i.e., the actuator affects the flow over the whole wing, including the flow over the pressure surface. The actuation frequency has a small effect over the pressure distribution in this range of  $\alpha$ . For  $\alpha > 18$  deg (massive stall), the operation of the SJA still provides a small amount of lift augmentation. For  $\alpha > 25$  deg, a large actuation frequency is required to produce any noticeable effects. For this range of  $\alpha$ , it was shown that the effect of the actuator once again became localized, affecting only the first 25% of the chord.

The operation of the SJA augments the available lift by delaying the occurrence of separation, with its associated losses. The drag on the wing is decreased as a consequence of SJA actuation;

this was verified with the force balance measurements and by an analysis of the wake surveys. The basic wing showed a very docile stall typical of thick airfoils with trailing edge separation, however, with actuation, the stall was violent and abrupt.

#### Acknowledgments

This work was sponsored by the Air Force Office of Scientific Research, under Contract No. F49620-01-1-0012. The authors would like to thank Dr. Thomas Beutner, the technical monitor for the project, for his support. The authors would also like to thank Mr. Rick Allen for his valuable help with the actuator fabrication and Mr. José Gilarranz, Sr. for his help and advice during the



assembly and testing of the actuator. The authors would like to thank the reviewers for their helpful comments and suggestions.

## Nomenclature

- $c$  = chord length [m]  
 $C_\mu$  = jet momentum coefficient  
 $CL$  = lift coefficient  
 $CD$  = drag coefficient  
 $CP$  = pressure coefficient  
 $CM$  = pitching moment coefficient  
 $F^+$  = nondimensional actuator frequency  
 $f$  = frequency of actuation [Hz]  
 $L$  = slot length [m]  
 $M$  = Mach number  
 $U_\infty$  = freestream velocity [m/s]  
 $u_{\max}$  = maximum jet exit velocity [m/s]  
 $\langle u_e \rangle$  = RMS value of the slot exit velocity [m/s]  
 $sw$  = slot width [mm]  
 $X$  = chordwise co-ordinate [m]  
 $\alpha$  = angle of attack [ $^\circ$ ]

## References

- [1] Chang, P. K., 1976, *Control of Flow Separation*, Hemisphere Publishing, Washington, DC, pp. 1–84, 154–412.
- [2] Gad-el-Hak, M., and Bushnell, D., 1991, "Separation Control: Review," *ASME J. Fluids Eng.*, **113**, pp. 5–30.
- [3] Johnson, W. S., Tennant, J. S., and Stamps, R. E., 1975, "Leading-Edge Rotating Cylinder for Boundary Layer Control on Lifting Surfaces," *AIAA Journal Hydraulics*, **9**, pp. 76–78.
- [4] Mokhtarian, F., and Modi, V. J., 1988, "Fluid Dynamics of Airfoils With Moving Surface Boundary-Layer Control," *J. Aircr.*, **25**, pp. 163–169.
- [5] Modi, V. J., Mokhtarian, F., Fernando, M., and Yokomizo, T., 1989, "Moving Surface Boundary Layer Control as Applied to 2-D Airfoils," *AIAA Paper No. 89-0296*.
- [6] Alvarez-Calderon, A., 1964, "Rotating Cylinder Flaps of V/STOL Aircraft," *Aircraft Engineering*, **36**, pp. 304–309.
- [7] Gad-el-Hak, M., 2000, *Flow Control: Passive, Active, and Reactive Flow Management*, Cambridge University Press, New York, pp. 150–188.
- [8] Englar, R. J., 2000, "Circulation Control Pneumatic Aerodynamics: Blown Force and Moment Augmentation and Modification; Past, Present and Future," *AIAA Paper No. 2000-2541*.
- [9] McManus, K., Ducharme, A., Goldey, C., and Magil, J., 1996, "Pulsed Jet Actuators for Suppressing Flow Separation," *AIAA Paper No. 96-0442*.
- [10] McManus, K., and Magil, J., 1997, "Airfoil Performance Enhancement Using Pulsed Jet Separation Control," *AIAA Paper No. 97-1971*.
- [11] Huang, L. S., Maestrello, L., and Briant, T. D., 1987, "Separation Control Over an Airfoil at High Angles of Attack by Sound Emanating From the Surface," *AIAA Paper No. 87-1261*.
- [12] Hsiao, F. B., Liu, C. F., and Shyu, J. Y., 1990, "Control of Wall Separated Flow by Internal Acoustic Excitation," *AIAA J.*, **28**, pp. 1440–1446.
- [13] Koga, D. J., Reisenhel, P., and Nagib, H. M., 1984, "Control of Separated Flowfields Using Forced Unsteadiness," *Fluids and Heat Transfer Report No. R-84-1*, Illinois Institute of Technology, Chicago, IL.
- [14] Bar-Sever, A., 1989, "Separation Control on an Airfoil by Periodic Forcing," *AIAA J.*, **27**, pp. 820–821.
- [15] Lachman, G. V., 1961, *Boundary Layer and Flow Control*, Pergamon Press, Oxford, Great Britain, Vols. 1 and 2.
- [16] Gad-el-Hak, M., 1990, "Control of Low-Speed Airfoil Aerodynamics," *AIAA J.*, **28**, pp. 1537–1552.
- [17] Greenblatt, D., and Wygnanski, I., 1998, "Dynamic Stall Control by Oscillatory Forcing," *AIAA Paper No. 98-0676*.
- [18] Greenblatt, D., Darabi, A., Nishri, B., and Wygnanski, I., 1998, "Separation Control By Periodic Addition of Momentum With Particular Emphasis on Dynamic Stall," *Proceedings Heli Japan 98*, Paper T3-4, American Helicopter Society.
- [19] Seifert, A., and Pack, L., 1999b, "Oscillatory Excitation of Unsteady Compressible Flows Over Airfoils at Flight Reynolds Number," *AIAA Paper No. 99-0925*.
- [20] Pack, L., and Seifert, A., 2000, "Dynamics of Active Separation Control at High Reynolds Numbers," *AIAA Paper No. 2000-0409*.
- [21] Seifert, A., and Pack, L., 2000, "Separation Control at Flight Reynolds Numbers: Lessons Learned and Future Directions," *AIAA Paper No. 2000-2542*.
- [22] Donovan, J. F., Kral, L. D., and Cary, A. W., 1998, "Active Flow Control Applied to an Airfoil," *AIAA Paper No. 98-0210*.
- [23] Hassan, A., and Munts, E. A., 2000, "Transverse and Near-Tangential Synthetic Jets for Aerodynamic Flow Control," *AIAA Paper No. 2000-4334*.
- [24] He, Y., and Kral, L., 2000, "Post-Stall Control on an Airfoil Using Localized Jet Actuators," *AIAA Paper No. 2000-0408*.
- [25] He, Y., Cary, A. W., and Peters, D. A., 2001, "Parametric and Dynamic Modeling for Synthetic Jet Control of a Post-Stall Airfoil," *AIAA Paper No. 2001-0733*.
- [26] Amitay, M., Smith, B. L., and Glezer, A., 1998, "Aerodynamic Flow Control Using Synthetic Jet Technology," *AIAA Paper No. 98-0208*.
- [27] Honohan, A. M., Amitay, M., and Glezer, A., 2000, "Aerodynamic Control Using Synthetic Jets," *AIAA Paper No. 2000-2401*.
- [28] Parekh, D. E., and Glezer, A., 2000, "AVIA: Adaptive Virtual Aerosurface," *AIAA Paper No. 2000-2474*.
- [29] Smith, B. L., and Glezer, A., 1997, "Vectoring and Small-Scale Motions Effected in Free Shear Flows Using Synthetic Jet Actuators," *AIAA Paper No. 97-0213*.
- [30] Smith, B. L., Trautman, M. A., and Glezer, A., 1999, "Controlled Interactions of Adjacent Synthetic Jets," *AIAA Paper No. 99-0669*.
- [31] Pack, L., and Seifert, A., 1999, "Periodic Excitation for Jet Vectoring and Enhanced Spreading," *AIAA Paper No. 99-0672*.
- [32] Rae, W., and Pope, A., 1984, *Low Speed Wind Tunnel Testing*, Wiley, New York, pp. 199–208, 362–424.
- [33] Gilarranz, J. L., 2001, "Development of High-Power, Compact Synthetic Jet Actuators for Flow Separation Control," Ph.D. dissertation, Texas A&M University, Texas.
- [34] Traub, L. W., 1992, "A Subsonic Wind-Tunnel Investigation of the Effect of Sharp Edged Sheared Tips on a Moderate Aspect Ratio Flat Plate Wing," M.S. thesis, University of the Witwatersrand, Johannesburg, South Africa.
- [35] Summers, J. L., and Page, W. A., 1950, "Lift and Moment Characteristics at Subsonic Mach Numbers of Four 10-Percent-Thick Airfoil Sections of Varying Trailing-Edge Thickness," *NACA R. M. A50J09*, NACA, Washington D.C.

# Development of an Experimental Correlation for a Pressure Loss at a Side Orifice

Ho-Yun Nam<sup>1</sup>

e-mail: hynam@kaeri.re.kr

Jong-Man Kim

Kyung-Won Seo

Seok-Ki Choi

Korea Atomic Energy Research Institute, Fluid System Engineering Division, 150 Deokjin-dong, Yuseong-gu, Daejeon, 305-353, Korea

*An experimental study has been carried out to measure the pressure loss at the side orifice of a liquid metal reactor fuel assembly. The characteristics of the pressure loss at the side orifice are investigated using the experimental data measured from 17 different types of side orifices that have different geometric shapes, dimensions, and arrangements of nozzles, and a correlation that covers the whole flow range by one equation is developed. The error range of the correlation is within  $\pm 10\%$ , and most of the errors occurred in a region where the Reynolds number is small. The range of Reynolds numbers based on the hydraulic diameter of the orifice is 2000–350,000. It is found that the geometric factor is the most important parameter for the pressure loss when the Reynolds number is  $>30,000$ . As the Reynolds number becomes smaller, its effect becomes larger, and when the Reynolds number is small, it is the most important parameter for the pressure loss at the side orifices. The measured data shows a trend that the pressure loss coefficient increases as the number of orifices increases, and the effect of the longitudinal arrangement is small. [DOI: 10.1115/1.1881694]*

## 1 Introduction

The fuel assemblies of a liquid metal reactor are contained in a hexagonal-shaped duct to control the flow rate of the coolant in a normal operation and to prevent the propagation of the sodium vapor in an abnormal accident. The flow rate of the coolant is controlled by the side orifice, which consists of several nozzles in the lower part of the fuel assembly. The pressure loss at the side orifice is affected by several parameters, such as the geometric dimension, shape, and the number of nozzles and their arrangement. The pressure loss in a fuel assembly is also an important parameter for reactor safety to control the flow redistribution in the transient state and natural circulation. Thus, the pressure loss at the side orifice should be clearly understood for the whole flow range during the operation of a liquid metal reactor. However, the experimental correlations for the pressure loss in a side orifice reported in the literature to date are limited, and the existing correlations show considerable differences from the newly measured data.

When the lateral flow enters into the tube through the side orifice, the pressure loss is much larger than that with a straight entrance and sudden expansion. On the basis of the visual observation [1], the jet (which enters through an orifice into the tube) flows to the opposite wall, spreads in all directions, and forms two rotating streams. In the Idelchik handbook [2], the pressure loss at a side orifice can be obtained from a diagram using relative area and relative distance from the orifice to the downstream pipe. The pressure loss coefficient for the side orifice given in this handbook is limited to the rectangular-shaped orifice in a pipe wall having one or two nozzles, and the range of the Reynolds number based on the hydraulic diameter of the nozzle is above 10,000. The number of nozzles in the fuel assembly of a liquid metal reactor is usually six to nine, and the typical ratio of the area of the nozzle and that of the downstream pipe is about 0.15. Thus, the pressure loss coefficient given in this handbook is not sufficient for the design of the orifice in the fuel assembly of a liquid metal reactor.

The objective of the present study is to investigate the pressure loss at the side orifice and to develop a pressure loss coefficient correlation for a whole flow range. We have carried out two types of experiments to measure the pressure loss coefficient at the side orifice. The first experiment is performed to measure the pressure loss in several shapes of orifices at a lower flow-rate range. There are one to six nozzles in a side orifice, and the shapes of the nozzles are circular, rounded rectangular, and rectangular. In the case when the number of nozzles is six, two types of arrangements (rectangular and staggered rectangular) are considered. The experiments are conducted for 16 different geometric shapes. The second experiment is conducted for a full-scale fuel assembly using water as a working fluid. In this experiment the side orifice consists of nine nozzles, whose shapes are sharp edged and rounded rectangular. The nozzles are arranged in such a way that there are three in the transverse direction and three in the longitudinal direction in a staggered arrangement. A correlation for the pressure loss coefficient, which covers the whole flow range, is developed using the data produced from the experiments. The flow range considered in the present study is higher than that of the practical reactor operation.

## 2 Experiment

**2.1 Test Section of Experiment 1.** The test section used in experiment 1 is shown in Fig. 1. The water flows into the large tank and passes through the side orifice which consists of several nozzles installed at the side wall of the 80 mm dia pipe. The inlet nozzle edges are sharp, and the shapes of other nozzles are circular, rounded rectangular, and rectangular. A side orifice consists of one to six nozzles at the side wall of the pipe. When the number of nozzles is  $<6$ , the nozzles are installed with an equal angle in the circumferential direction. When the number of nozzles is 6, three orifices are installed equally in the circumferential direction with two lines in the longitudinal direction. In this case, two types of arrangements, regular and staggered, are considered. Thus, the experimental data is produced for a total of 16 different cases. Table 1 shows the dimensions and arrangements of the orifices considered in the present study. The flow rate is measured by two magnetic flow meters, and the pressure drop is measured by a combination of two OMEGA differential pressure meters according to the flow rate. The range of Reynolds numbers based on the

<sup>1</sup>Corresponding author.

Contributed by the Fluids Engineering Division for publication in the JOURNAL OF FLUIDS ENGINEERING. Manuscript received by the Fluids Engineering Division March 25, 2004; revised manuscript received, October 27, 2004. Review conducted by J. Lee.

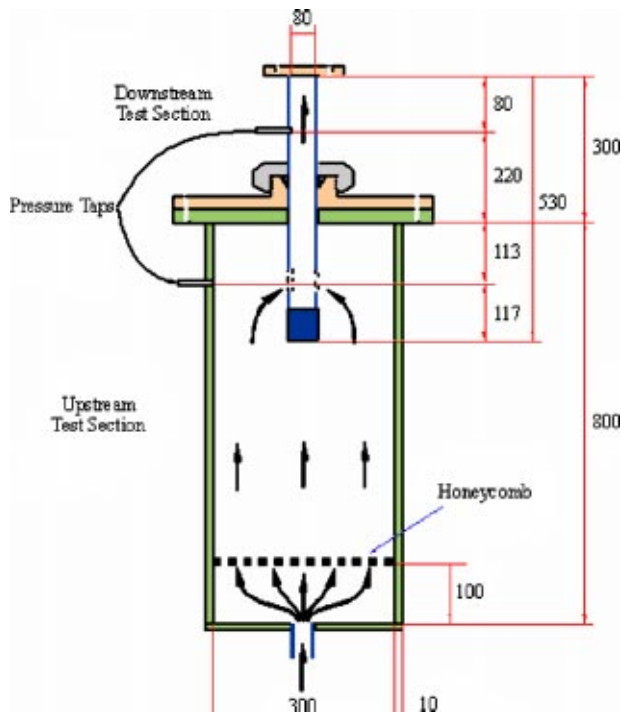


Fig. 1 Schematic diagram of the test section for experiment 1

hydraulic diameter of the orifice for this experiment is 2,000–50,000 and a total of 529 experimental data is produced. The temperature of the water is about 20 °C.

**2.2 Test Section of Experiment 2.** The test section of experiment-2 is shown in Fig. 2. In this experiment a full size fuel assembly based on the conceptual design of KALIMER (Korea Advanced Liquid Metal Reactor) is considered. The side orifice with 9 rounded rectangular shaped nozzles is installed in a staggered way such that 3 nozzles are in the transverse direction with 3 lines in the longitudinal direction, as shown in Fig. 2. The dimensions and shapes of the orifice are shown in the last line of Table 1. In this experiment the flow rate is measured by a combi-

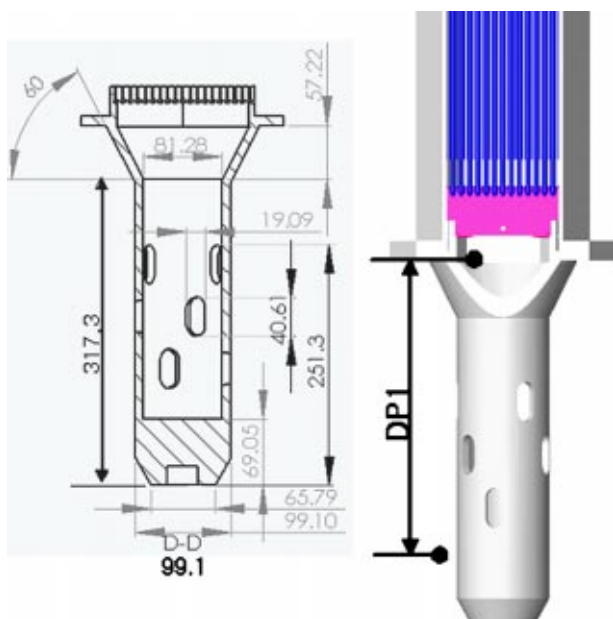


Fig. 2 Schematic diagram of the test section for experiment 2

nation of 3 turbine flow meters installed parallel to each other according to the amount of the flow rate. The pressure loss was measured by two OMEGA differential pressure meters. The experimental range of the Reynolds number based on the hydraulic diameter of the orifice is 10,000–350,000 and 134 experimental data are produced from this experiment.

**2.3 Measurement Method of the Pressure Drop.** The pressure loss at the side orifice is measured between the two locations, a location where the flow is injected into the orifice and a location at a fixed distance from the end of the orifice, to install the differential pressure meters easily. Thus, the pressure drop measured in this way includes the pressure drop from the end of the orifice to the fixed distance from the orifice outlet in the downstream direction. The measured pressure drop includes the pressure drop in the pipe in the experiment-1 and the pressure drop in the pipe and diffuser in the experiment-2. The pressure drop at the side orifice  $\delta P_{or}$  can be obtained by subtracting the pressure drop in the downstream direction from the orifice outlet  $\delta P_d$  from the total pressure drop  $\delta P_m$  by the following equation:

$$\delta P_{or} = \delta P_m - \delta P_d \quad (1)$$

The friction factor for a flow in a circular pipe in the downstream direction is calculated by  $f=64/Re$  when the Reynolds number is smaller than 2000 and by  $f=0.3164/Re^{1/4}$  when the Reynolds number is greater than 3500 and by  $f=6.1 \times 10^{-6}(Re - 2000) + 0.032$  in between those numbers. In the experiment-2 there exists a diffuser with a 60° angle and an area ratio of 2.4 in the lower part of the test section. The pressure loss coefficient for the diffuser is set as 0.37 regardless of the Reynolds number since the Reynolds number is high enough to use this value in experiment-2. The pressure loss coefficient for the side orifice can be expressed as follows:

$$f_{or} = \frac{2\delta P_{or}}{\rho V_o^2} \quad (2)$$

where  $\rho$  is the density of the water and the  $V_o$  is the velocity at the nozzle.

**2.4 Experimental Error.** The experimental data was obtained by averaging 100 data per one case using the HP3852 measuring device with an integral voltmeter. The  $t$ -value is 1.99 to have a 95% confidence. We can neglect the error by a density difference since the temperature difference is maintained to within  $\pm 0.5^\circ\text{C}$ . Most of the errors for the pressure drop originated from the measurement of the flow rate and the differential pressure. The flow rate was measured by the magnetic flow meter in experiment-1 and by the turbine flow meters in experiment-2. The accuracy of the magnetic flow meter is 0.5% of a span and the error of the turbine flow meter is 0.5% of a reading or 0.25% of a span. Thus, the maximum error of a flow rate is 2.5% for experiment-1 in the lower flow rate region and the maximum value of the standard deviation of the measured flow rate is 0.2%. The errors of measuring the flow rate except that from the measuring device itself are the error from the standard deviation of the data, the error from the calibration and that from measuring the geometry of the experimental apparatus. The maximum total error is less than 0.6%. Thus, the measuring error for the flow rate is  $0.8 \pm 2.7\%$ . The differential pressure is measured by the OMEGA PX750 series differential pressure meter. The accuracy of this differential meter was 0.2% of a span. Several differential pressure meters are used according to the magnitude of the differential pressure, and the maximum error occurred at a lower differential pressure range and its maximum value was around 8%. The pressure loss at the downstream region  $\delta P_d$  is less than 1/10 of the measured pressure loss  $\delta P_m$ . If we consider that the error for the calculation of the friction factor is 10%, the error of the pressure loss at the downstream region  $\delta P_d$  is less than 1%. Thus, the maximum error for measuring the differential pressure is around

**Table 1 Dimensions and arrangements for the orifices**

Number of nozzle		1	2	3	4	6 regular	6 staggered	9 staggered
Number of row								
Shape (mm)		1	1	1	1	2	2	3
	Circle	diameter	30	30	30	30	30	-
		pitch	-	-	-	54	54	-
		end gap	32	32	32	5	5	-
Rounded rectangular	wide	20	20	20	20	20	20	19.1
	height	40	40	40	40	40	40	40.6
	pitch	-	-	-	-	54	54	54.5
Rectangular	end gap	27	27	27	27	0.	0.	23
	wide	20	18	18	18	-	-	-
	height	40	40	40	40	-	-	-
	pitch	-	-	-	-	-	-	-
	end gap	27	27	27	27	-	-	-

8.1%. If we apply the error propagation for the calculation of Eq. (2), the maximum error of the measurement of the pressure drop coefficient is less than 9% in the low flow rate range. If we consider the 4.5% error as having a 95% confidence in the curve fitting, the maximum error is around 10%.

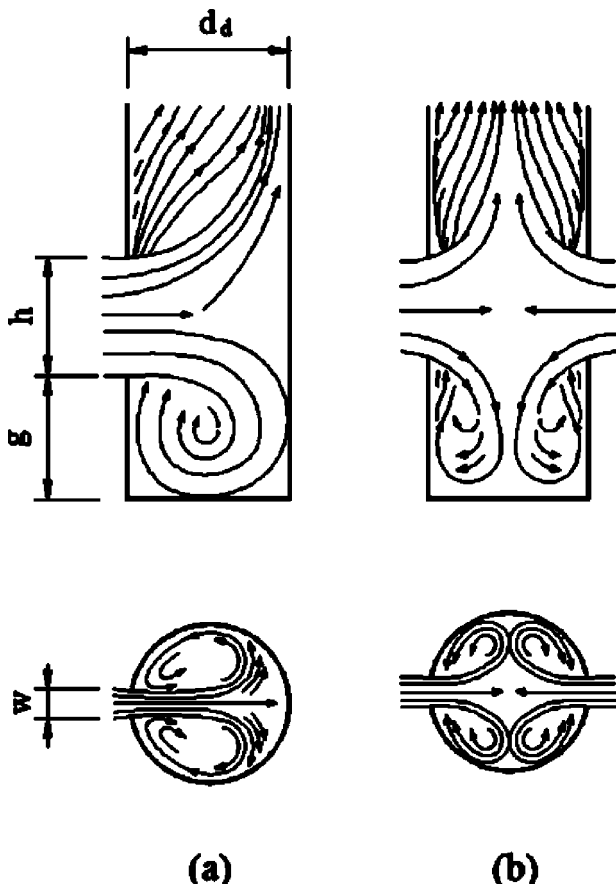
### 3 Experimental Results and Discussion

**3.1 Pressure Drop in the Side Orifice.** The pressure loss in the side orifice of a liquid metal reactor fuel assembly where the flow passes through the side orifice turns in a 90 degree direction and flows in a singular downstream direction is larger than the pressure loss in the orifice installed in the straight pipe or that in the abrupt expansion pipe. Figure 3 shows the expected flow paths in the orifice having one or two nozzles. The jet type flow which

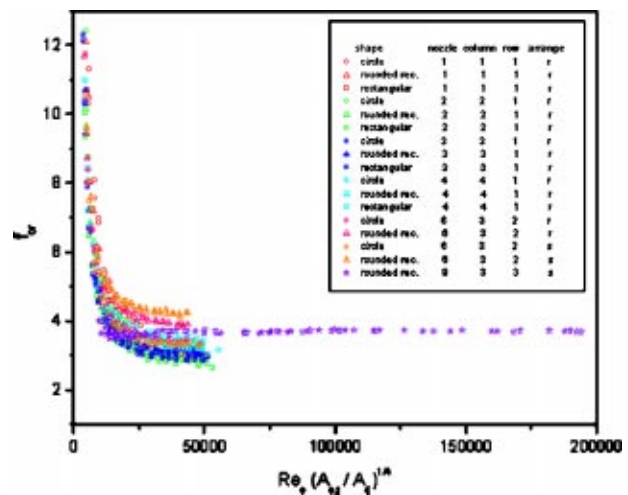
passes through this nozzle flows in all directions and turns 180 deg at the opposite side wall and forms two recirculating-type flows on the incoming side wall. Thus, the ratio of the diameter of the downstream pipe and the hydraulic diameter of the nozzle as well as the distance between the nozzle inlet and the opposite side wall are important parameters for analyzing the pressure loss in this type of orifice. When the number of nozzles is 1 and the ratio of the area of the orifice and the area of the downstream pipe is  $<0.8$ , the pressure loss coefficient increases with the increase of the area ratio. It also increases with a decrease of the ratio between the width of the nozzle and the diameter of the downstream pipe. Idelchik [2] found that the pressure loss at the side orifice with two nozzles in an opposite direction is higher than that with one nozzle and explained that this phenomenon is due to an increase of the area ratio.

There are many parameters that influence the pressure loss in the side orifice, and the following parameters should be considered in developing the experimental correlation: (i) the pressure loss in the orifice itself, (ii) the ratio between the dimensions of the orifice and that of the downstream pipe, (iii) the effect of the arrangement of the orifice in the transverse direction, and (iv) the effect of the arrangement of the orifice in the longitudinal direction.

According to the experimental data as shown in Fig. 4, when the Reynolds number is high, the effect of the Reynolds number on the pressure loss in the side orifice is small and the pressure loss coefficient depends greatly on the geometric factor  $F_g$ . But in the low Reynolds number region, the pressure loss coefficient



**Fig. 3** Types of flow paths at the side orifice according to the number of nozzles: (a) one nozzle and (b) two nozzles



**Fig. 4** The pressure loss coefficient according to the nondimensional parameter for several types of orifices

rapidly increases with the decrease of the Reynolds number. Thus, the pressure loss coefficient of the side orifice can be written as follows:

$$f_{or} = (1.0 + F_{Re})F_g \quad (3)$$

In the above equation,  $F_{Re}$  represents the effect of the Reynolds number on the pressure loss coefficient, which should be converged to zero when the Reynolds number is high and, thus, should increase with the decrease of the Reynolds number. The geometric factor in Eq. (3) can be written as follows for the present experiment:

$$F_g = F_d * F_o + F_c + F_r \quad (4)$$

where  $F_o$  is the pressure loss coefficient in the orifice itself and  $F_d$  represents the mutual effect between the orifice and the downstream pipe.  $F_c$  and  $F_r$  represent the effects of the arrangements in the transverse and longitudinal directions, respectively.

**3.2 Pressure Loss Parameters.** The pressure loss coefficient for one nozzle in the straight pipe can be generally written as follows:

$$F_o = \frac{\Delta p}{\frac{1}{2}\rho V_o^2} = \xi' \left(1 - \frac{A_o}{A_1}\right) + \left(1 - \frac{A_o}{A_2}\right)^2 + \tau \left(1 - \frac{A_o}{A_1}\right)^{0.5} \left(1 - \frac{A_o}{A_2}\right) + \xi_{fr} \quad (5)$$

where  $\rho$  is the density of the fluid and  $V_o$  is the fluid velocity in the nozzle. In the Eq. (5) the subscripts 1,  $o$ , and 2 represent the inlet condition, nozzle, and outlet condition, respectively;  $A$  represents the area; and  $\xi'$  is a coefficient that depends on the shape of the nozzle inlet edge and varies from 0.5 to 1.  $\xi_{fr}$  is the pressure loss coefficient due to friction in the nozzle and can be neglected when the ratio between the thickness and diameter of the nozzle is small.  $\tau$  is the geometric parameter that affects the flow when the fluid passes through the orifice, and it can be written as follows when the ratio between the thickness  $t_o$  and the hydraulic diameter  $d_h$  of the nozzle is  $<0.4$  [2]:

$$\tau = 1.4 - 0.8 \frac{t_o}{d_h} \quad (6)$$

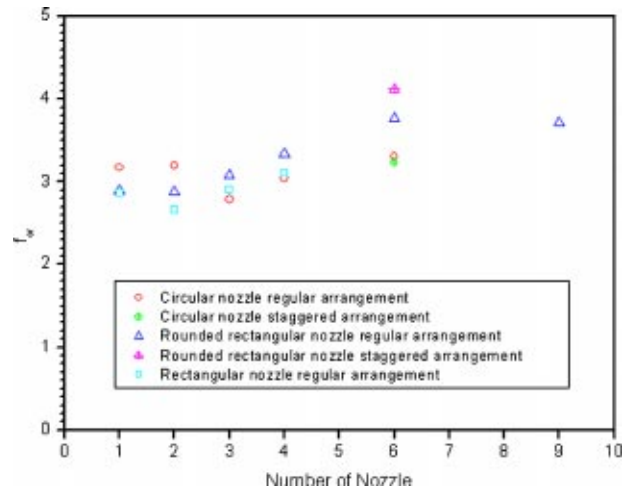
Equation (5) can be written as follows when the upstream inlet area is large ( $A_1 = \infty$ ) and we neglect the pressure loss due to friction ( $\xi_{fr}$ ) in the orifice

$$F_o = \xi' + \left(1 - \frac{A_o}{A_2}\right)^2 + \tau \left(1 - \frac{A_o}{A_2}\right) \quad (7)$$

According to Idelchik [2], the pressure loss coefficient increases with an increase of the area ratio between the orifice and the downstream pipe. If we consider the graph given in Idelchik and the experimental data, then this effect is approximately proportional to  $(A_o/A_d)^{1/3}$ . If we use  $d_h^2$  instead of  $A_o$  for a better correlation with our data, then the pressure loss coefficient is proportional to  $(d_h^2/A_d)^{1/3}$ . Then, the first term of Eq. (4) can be written as follows:

$$F_d F_o = \left[ \xi' + \left(1 - \frac{A_o}{A_2}\right)^2 + \tau \left(1 - \frac{A_o}{A_2}\right) \right] \left( \frac{d_h^2}{A_d} \right)^{1/3} \quad (8)$$

Through a comparison of the above equation with the experimental data, the value of  $\xi'$  is set at  $\xi' = 0.6$  for the circular orifice, and  $\xi' = 1.0$  for the rectangular and rounded rectangular nozzles. The value of  $A_o/A_2$  is a form loss factor, which is a very important factor. When the number of nozzles is 1, the jet type flow from the nozzle reaches the opposite wall directly. In this case, if we consider that the outlet condition of nozzle is the same as the downstream condition, we can use  $A_2 = A_d$ . When the number of the nozzles is  $>1$ , the jet-type flow reaches the center of the pipe because of a collision with the other jet flow. In this case we set



**Fig. 5 Experimental data of the average pressure loss coefficient for the different orifices when the Reynolds number is  $\sim 30,000$**

$$A_2 = \frac{1}{2}A_d$$

Figure 5 shows the pressure loss coefficient averaged for all the types of side orifices considered in the present study when the Reynolds number is  $\sim 30,000$ , where the geometric shape is a more important factor for the pressure loss than the Reynolds number. In this figure, the  $x$  coordinate is the number of orifices, and we can observe that the pressure loss coefficient increases with an increase in the number of the orifices. The diagram of 4-22 in Idelchik [2] shows the pressure loss coefficient when the flow passes through the circular screen for the two cases of the transverse and longitudinal arrangements. The pressure loss coefficient is expressed in terms of the velocity ratio between the main flow and the screen flow. If the velocity ratio is increased, then the pressure loss coefficient decreases a little and has its minimum value when the ratio is 0.5. The pressure loss coefficient is zero when the ratio is 1 and increases linearly if this ratio is further increased. However, it is difficult to use this behavior for developing the experimental correlation. According to the analysis of the experimental data, we could express the effect of the transverse arrangement for  $A_o/A_d$  as  $<0.2$  as follows:

$$F_c = 2.5(N_c - 1) \frac{A_o}{A_d} \quad (9)$$

It is difficult to describe the effect of the longitudinal arrangement in the downstream flow direction due to the lack of experimental data. We describe it here by using a some of the experimental data we have produced. In our experiment it was observed that a more-than-two longitudinal arrangement results in a larger pressure loss coefficient than a single longitudinal arrangement, however, the difference between the two and three longitudinal arrangements was small. The effect of the arrangement is unclear in our experiment. For a rounded-rectangular orifice the staggered arrangement results in a larger pressure loss coefficient than the regular arrangement; however, for a circular orifice, the staggered arrangement results in a smaller pressure loss coefficient than the regular arrangement. Thus, the effect of the longitudinal arrangement can be expressed in terms of the number of longitudinal arrangements  $N_r$ , the ratio of the number between the transverse and longitudinal arrangement ( $N_c/N_r$ ), the ratio of the pitch and the hydraulic diameter of the orifice ( $p_s/d_h$ ), and the ratio between the height and width of the orifice ( $h/w$ ). If the ratio between the height and width of the nozzle is high, then the form loss factor can be increased as in the case of the expansion pipe, and if the length of the orifice is increased, then the pressure loss coefficient can be increased due to the effect of the nozzle in the opposite

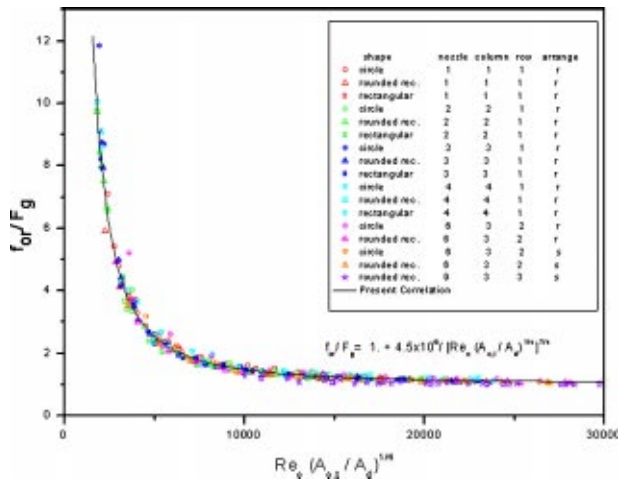


Fig. 6 Effect of the Reynolds number on the pressure loss coefficient of the side orifices

side wall. From the analysis of the experimental data, we could express the effect of the longitudinal arrangement as follows:

$$F_r = 0.14(N_r - 1)^{1/4} \frac{N_c h p_s}{N_r w d_h} \quad (10)$$

**3.3 Experimental Correlation and Validation.** If we insert Eqs. (8)–(10) into Eq. (4), the geometric factor  $F_g$  of the orifice can be written as follows:

$$F_g = \left[ \xi' + \left(1 - \frac{A_o}{A_2}\right)^2 + \tau \left(1 - \frac{A_o}{A_2}\right) \right] \left( \frac{d_h^2}{A_d} \right)^{1/3} + 2.5(N_c - 1)^{2/3} \frac{A_o}{A_d} + 0.14(N_r - 1)^{1/4} \frac{N_c h p_s}{N_r w d_h} \quad (11)$$

If we divide the pressure loss coefficient obtained from the experiment data shown in Fig. 4 by the geometric factor given by Eq. (11) and plot it in terms of  $Re(A_{o,t}/A_d)^{1/4}$ , we can obtain Fig. 6. In this figure,  $A_{o,t}$  is the total area of the nozzles. If we curve-fit the data in Fig. 6, we obtain the following equation for the effect of the Reynolds number ( $F_{Re}$ ) in Eq. (3):

$$F_{Re} = \frac{4.5 \times 10^6}{\left[ Re \left( \frac{A_{o,t}}{A_d} \right)^{1/4} \right]^{7/4}} \quad (12)$$

If we insert Eq. (12) into Eq. (3), we can obtain the pressure loss coefficient correlation for the side orifice as follows:

$$f_{or} = F_g \left\{ 1 + \frac{4.5 \times 10^6}{\left[ Re \left( \frac{A_{o,t}}{A_d} \right)^{1/4} \right]^{7/4}} \right\} \quad (13)$$

where  $F_g$  is given by Eq. (11). Figure 7 shows the comparison of the pressure drop obtained from the experiment and that calculated by Eq. (13).

## 4 Conclusions

An experimental study has been carried out to measure the pressure loss at the side orifice of a liquid metal reactor fuel assembly. The pressure loss at the side orifice is investigated using the experimental data measured from 17 different types of side orifices, which have different geometric shapes, dimensions, and arrangements. A simple correlation, which covers the whole flow range by one equation, is developed for the pressure loss at the side orifices. The range of Reynolds numbers based on the hy-

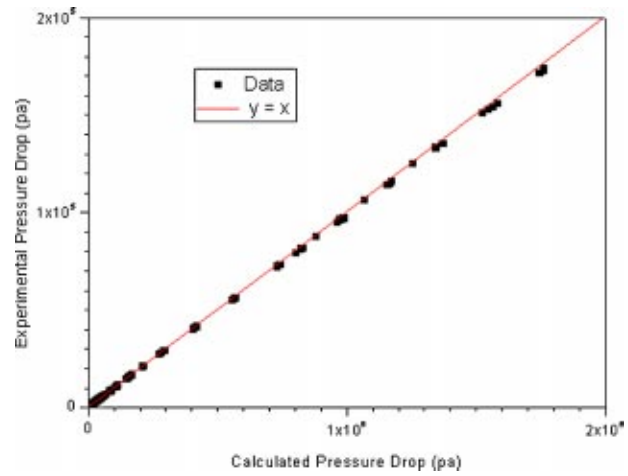


Fig. 7 Comparison of the experimental data and the correlation for the pressure loss in the orifice

draulic diameter of the orifice is 2000–350,000. The error range of the correlation for the pressure loss at the side wall orifice developed in the present study is within  $\pm 10\%$  to obtain a 95% reliability according to the ASME error analysis. Most of the errors occurred in a region where the Reynolds number is small.

## Acknowledgments

This study has been carried out under the nuclear research and development program by Ministry of Science and Technology of Korea.

## Nomenclature

- $A$  = area
- $d$  = diameter of orifice
- $d_h$  = hydraulic diameter of orifice
- $F$  = factor
- $f$  = pressure loss coefficient
- $g$  = end gap
- $h$  = height of orifice
- $N$  = number of orifice
- $\Delta p$  = pressure drop
- $p_s$  = pitch of orifice
- $Re$  = Reynolds number
- $t_o$  = thickness of orifice
- $V$  = flow velocity
- $w$  = width of orifice

## Greek

- $\rho$  = density
- $\tau$  = geometric parameter of orifice

## Subscript

- $c$  = pertaining to column
- $d$  = pertaining to downstream
- $g$  = pertaining to geometric factor
- $o$  = pertaining to single orifice
- $or$  = pertaining to side orifice
- $r$  = pertaining to row
- 1 = pertaining to inlet condition
- 2 = pertaining to outlet condition

## References

- [1] Khanzhonkov V. I., and Davydonko, N. I., 1959, "Resistance of Side Orifices of the Thermal Section of a Pipeline," *Prom. Arodin.* No. 15, pp. 38–46, Oborongiz, Moscow.
- [2] I. E. Idelchik, 1987, *Handbook of Hydraulic Resistance*, Second Edition, Hemisphere, Washington.

## New Mixing-Length Approach for the Mean Velocity Profile of Turbulent Boundary Layers

M. H. Buschmann

Institut für Strömungsmechanik, Technische Universität  
Dresden, 01060 Dresden, Germany  
e-mail: hanno@ism.mw.tu-dresden.de

M. Gad-el-Hak

Department of Mechanical Engineering, Virginia  
Commonwealth University, Richmond, VA 23284, USA  
e-mail: gadelhak@vcu.edu

### Introduction

There has been considerable controversy during the past few years concerning the validity of the universal logarithmic law that describes the mean velocity profile in the overlap region of a turbulent wall-bounded flow [1,2]. The present authors recently advanced a generalized logarithmic law to describe such overlap region [3,4]. This law was derived based on a consequent extension of the classical two-layer approach to higher-order terms involving the Kármán number  $\delta^+$  and the dimensionless wall normal coordinate  $y^+$ . As compared to either the simple log law or the power law, the Reynolds-number-dependent generalized law provides a superior fit to existing high-fidelity data.

Written in terms of inner variables, the generalized log law reads

$$u^+ = \sum_{j=0}^{\infty} \varepsilon^j \left[ \frac{1}{\kappa_j} \ln(y^+ + D_j) + A_j \exp(-B_j \eta) \right] \quad (1)$$

where  $u^+ = u/u_\tau$ ,  $y^+ = y u_\tau / \nu$ ,  $\eta = y / \delta$ ,  $u_\tau = (\tau_w / \rho)^{1/2}$ ,  $u$  is the mean streamwise velocity,  $y$  is the coordinate normal to the wall,  $\nu$  and  $\rho$  are, respectively, the kinematic viscosity and density of the fluid,  $u_\tau$  is the friction velocity,  $\tau_w$  is the wall shear stress, and  $\delta$  is the boundary layer thickness. The parameter  $\varepsilon$  is the reciprocal of the Kármán number,  $\delta^+ = \delta u_\tau / \nu$ , which is the ratio of the outer to inner length scale. The parameters  $\kappa_j$ ,  $D_j$ ,  $A_j$ , and  $B_j$  are, in general, Reynolds-number dependent and have to be obtained from experiments. Following Lindgren et al. [5], we assume that all the additive constants in the argument of the logarithm,  $D_j$  in (1), are a single, Reynolds-number-independent constant  $D$ . Equation (1) can then be rearranged to read

$$u^+ = \left( \frac{1}{\kappa_0} + \frac{1}{\delta^+ \kappa_1} + \frac{1}{\delta^{+2} \kappa_2} + \dots \right) \ln(y^+ + D) + A_0 \exp(-B_0 \eta) + \frac{A_1}{\delta^+} \exp(-B_1 \eta) + \frac{A_2}{\delta^{+2}} \exp(-B_2 \eta) + \dots \quad (2)$$

For the inner layer,  $\eta \rightarrow 0$  and all the exponential terms become of order one. Equation (2) can then be rewritten as

$$u^+ = \frac{1}{\kappa} \ln(y^+ + D) + A \quad (3)$$

where

$$\frac{1}{\kappa} = \sum_{i=0}^{\infty} \frac{1}{\delta^{+i} \kappa_i} \quad \text{and} \quad A = \sum_{i=0}^{\infty} \frac{1}{\delta^{+i}} A_i$$

The additive constant  $D$  changes the linear velocity distribution in a semi-log plot of the overlap region to a concave shape. For  $\delta^+ \rightarrow \infty$ , the leading term of the generalized logarithmic law in the inner layer reads

$$u^+ = \frac{1}{\kappa_0} \ln(y^+ + D) + A_0 \quad (4)$$

which is identical with the logarithmic mean velocity profile derived from first principles by Oberlack [6], who used Lie-Group analysis. That law was subsequently validated by Lindgren et al. [5], who used the experimental database of Österlund [7].

Although the parameters of the simple logarithmic law,  $\kappa_0$  and  $A_0$ , are usually termed *Kármán constant* and *additive constant* and understood to be Reynolds-number independent, the generalized logarithmic law in the inner-layer limit (3) shows a clear Reynolds number dependence of these parameters. The dependence of fully developed turbulent boundary layer and channel flow on the Reynolds number is real, as illustrated by the following three physical arguments, previously detailed in Ref. [8]. First, the Reynolds stress gradient and not the Reynolds stress itself appears in the streamwise momentum equation. To balance the inevitable pressure gradient in channel and pipe flows, viscous forces must be important—at least in these types of flows—in a region that has traditionally been claimed to be inertial [9]. Second, in a truly inviscid region, a complete turbulence energy cascade that includes a dissipation range cannot take place [10]. However, from experiments such a region is not known to exist within turbulent boundary layer, pipe, or channel flows. Third, from experiments it is known that viscous structures reside in the so-called inertial sublayer [11]. That consequently leads to the conclusion that turbulence quantities expressed in wall units must depend on Reynolds number, however weakly.

If we grant that (3)—and at sufficiently high Reynolds numbers (4)—describes the streamwise mean velocity profile in the overlap region of the canonical wall-bounded flow, the question is then, how to extend that description all the way to the wall, i.e. to the buffer layer and viscous sublayer? The resulting velocity profile is of significant practical importance. For example, such profile can

Contributed by the Fluids Engineering Division for publication in the JOURNAL OF FLUIDS ENGINEERING. Manuscript received by the Fluids Engineering Division June 11, 2004; revised manuscript received, January 17, 2005. Review conducted by T. Gatski.

be used for the appropriate construction of CFD codes and for proper calibration of certain near-wall probes such as Preston tubes. In this technical brief, a mixing-length approach is used to extend the generalized log law to the wall.

### Mixing-Length Approach

Like the standard (universal) log law, the generalized log law in the near-wall region (3) does not reach all the way down to the wall. Algebraic turbulence models (e.g., mixing-length and eddy-viscosity approaches) represent the simplest form of turbulence modeling and are traditionally used to close the gap between the wall and the onset of the log law. A detailed review of such models is given by Granville [12]. None of the known approaches thus far takes into consideration the additive constant inside the logarithm,  $D$ , because they are all designed to reproduce the standard log law in the overlap region. As a matter of fact, the additive constant perceptibly changes the profile right above the buffer layer, precisely the region that is described by an algebraic turbulence model. Therefore,  $D$  has to be included in such an approach. Moreover, none of the previous mixing-length or eddy-viscosity approaches takes into account the Reynolds-number dependency of the parameters of the mean velocity profiles. This is an important physical feature of the flow, however, and will be considered herein.

The concept of mixing length was originally introduced by Prandtl [13]. Based on an analogy with the kinetic theory of gases, Prandtl concluded that there must be a mixing length for *fluid parcels* that should be analogous to the molecular mean-free path, but much larger. Thus, the Reynolds stress is written in terms of the mean velocity gradient

$$-\overline{\rho u'v'} = \rho l^2 \left( \frac{\partial u}{\partial y} \right)^2 \quad (5)$$

where  $l$  is the mixing length, and  $u'$  and  $v'$  are the velocity fluctuations in, respectively, the streamwise and normal direction. The total stress consists of a viscous and a turbulent part,

$$\tau^+ = \frac{\partial u^+}{\partial y^+} + l^{+2} \left( \frac{\partial u^+}{\partial y^+} \right)^2 \quad (6)$$

where  $\tau^+ = \tau/\tau_w$ , and  $l^+ = lu_\tau/\nu$ . Solving the above quadratic equation, leads to the mean velocity gradient

$$\frac{\partial u^+}{\partial y^+} = \frac{2\tau^+}{1 + (1 + 4\tau^{+2})^{1/2}} \quad (7)$$

Finally, the mean velocity profile in the inner layer results from integrating (7) and recognizing that in this layer  $\tau^+ \approx 1$ , see, for example, Ref. [12]. Thus,

$$u^+ \approx \int_0^{y^+} \frac{2dy^+}{1 + (1 + 4l^{+2})^{1/2}} \quad (8)$$

This integral can readily be performed numerically once an expression for the mixing length is assumed. In the log region,  $l = \kappa y$ , and in the viscous sublayer and buffer layer, van Driest [14] proposed a damping function to slow down the growth of the turbulent stress in the vicinity of the wall. He assumed

$$l^+ = \kappa y^+ \left[ 1 - \exp\left(-\frac{y^+}{\lambda}\right) \right] \quad (9)$$

where  $\lambda$  is the damping factor, which is related to the additive constant in the log law. In fact, the van Driest's approach, applied to the universal log law, leads to an overcorrection of the turbulence stress behavior near the wall,

$$-\overline{u'v'} = \frac{\kappa^2 y^{+4}}{\lambda^2} + O(y^{+5}) \quad (10)$$

Subsequent improvements in the damping function by Chapman and Kuhn [15] and Granville [12] resulted in the correct near-wall behavior of the Reynolds stress, i.e.,  $-\overline{u'v'} \sim y^{+3}$ .

In the present paper, we similarly modify the van Driest's damping function to achieve the correct asymptotic behavior of the Reynolds stress near the wall, as well as to adapt to the generalized log law farther away from the wall. Thus,

$$l^+ = \kappa(y^+ - D) \left[ 1 - \exp\left(-\frac{y^+}{\lambda}\right) \right]^{3/2} \quad (11)$$

At sufficiently large  $y^+$ , the exponential term diminishes and the generalized log law (3) is recovered. Using a Taylor series expansion around  $y=0$ , the Reynolds stress in this formulation is readily computed as

$$-\overline{u'v'} = \frac{D^2 \kappa^2 y^{+3}}{\lambda^3} + O(y^{+4}) \quad (12)$$

which preserves the correct near-wall behavior of the Reynolds stress [16].

### Determination of the Parameters

The Kármán-number-dependent parameters in (3) have to be determined from high-quality experimental data that cover a wide Reynolds number range. Such a data set is provided by Österlund [7]. Using the Levenberg–Marquardt algorithm [17], a nonlinear fit of each velocity profile in this data set was carried out. The

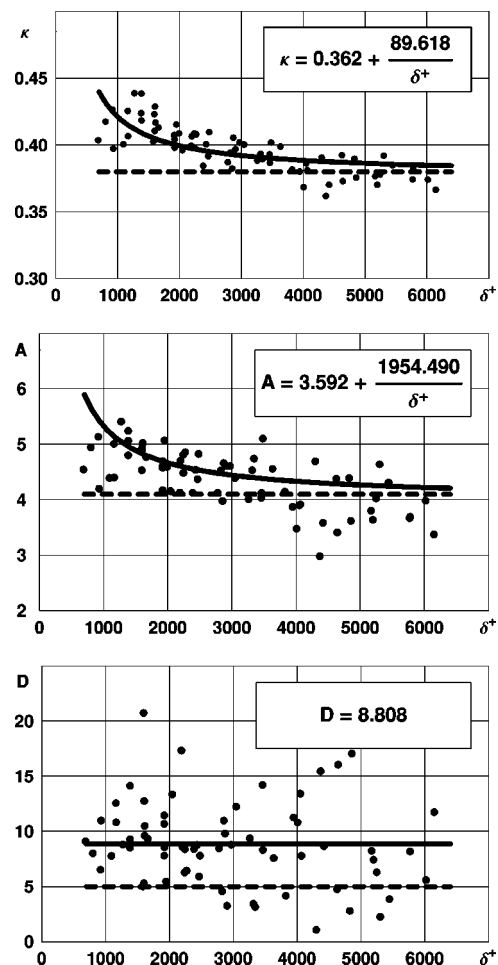


Fig. 1 Parameters of the velocity profile (3). Solid lines represent formulas in the small boxes. Dashed lines show parameters for simple log law according to [7],  $\kappa=0.38$  and  $A=4.1$ , and according to [5],  $D=5.0$ .



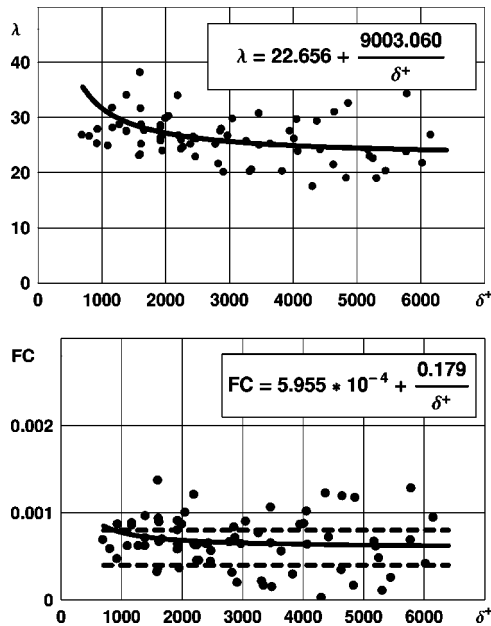


Fig. 2 Damping factor of the proposed mixing-length expression and first coefficient of the Taylor series expansion of Reynolds shear stress in the vicinity of the wall. Solid lines represent formulas in the small boxes. Dashed lines show the range of first coefficient values according to [18],  $FC=4 \times 10^{-4}-8 \times 10^{-4}$ .

outcomes of this procedure are the parameters  $\kappa$  and  $D$  appearing in the velocity profile (3) and the damping factor  $\lambda$  from the mixing-length expression (11). The parameter  $A$  is obtained by equating (3) and the integral of (7)

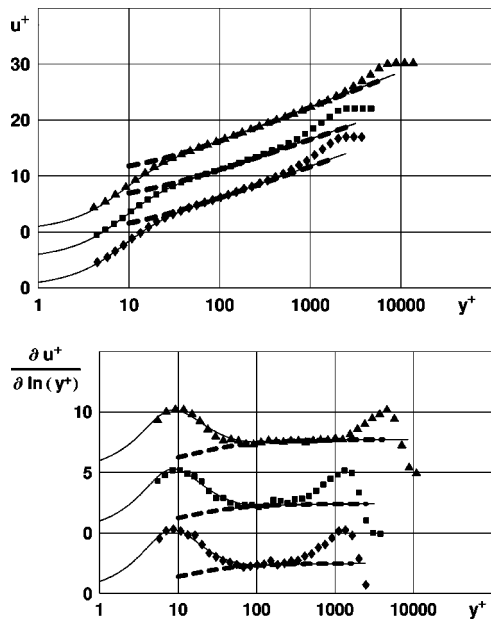


Fig. 3 Mean velocity and velocity gradient profiles for different Kármán numbers. Solid lines result from the proposed mixing-length theory and numerically integrating Eq. (8). Dashed lines are according to Eq. (3), without mixing-length approach. Data from Ref. [7],  $\diamond \delta^+=1,092$  ( $Re_\theta=4,312$ );  $\blacksquare \delta^+=1,661$  ( $Re_\theta=6,930$ ); and  $\blacktriangle \delta^+=6,147$  ( $Re_\theta=27,320$ ).

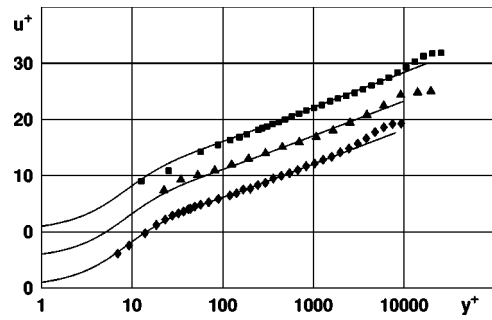


Fig. 4 Comparison of experimental mean velocity profiles and the new mixing-length theory. Data from Ref. [19],  $\geq \delta^+=7,274$  ( $Re_\theta=20,920$ );  $\blacksquare \delta^+=19,926$  ( $Re_\theta=57,720$ ). Data from Ref. [20],  $\blacklozenge \delta^+=10,022$  ( $Re_\theta=30,850$ ).

$$A = \int_0^{y_B^+} \frac{\partial u^+}{\partial y^+} dy^+ - \frac{1}{\kappa} \ln(y_B^+ + D) \quad (13)$$

where  $y_B^+$  is sufficiently large to be within the region where (3) is valid [12]. The resulting parameters are compiled in Figs. 1 and 2.

Both  $\kappa$  and  $A$  show a Kármán-number-dependent behavior and asymptote to values very close to the values proposed by Österlund [7] for  $Re_\theta > 2000$ ,  $\kappa=0.38$ , and  $A=4.1$ . The reverse trends for data below  $\delta^+ \approx 1,200$  are clear indication of the customary low-Reynolds-number effects, not to be confused with the moderate-to-high Reynolds number effects considered herein [4]. The parameter  $D$  has an average value of 8.2, which is comparable to the value  $D=5$  reported by Lindgren et al. [5]. The larger scatter in the values of  $D$  as compared to those for  $\kappa$  and  $A$  is caused by the diminutiveness of the region where  $D$  has an influence. This region is typically represented by only a few experimental data points. In the nonlinear fit we conducted, those points are much “weaker” than the many data points from the entire logarithmic region. Therefore, the parameter  $D$  is somewhat overwhelmed by the other two parameters, and the uncertainty in its value approaches  $\pm 20\%$ . Had there been denser data taken closer to the wall, the scatter in  $D$  would have been moderated.

Figure 2 shows, as expected, that the damping factor  $\lambda$  also has a clear Reynolds-number dependence. The first coefficient,  $FC = D^2 \kappa^2 / \lambda^3$ , of the Taylor series expansion of the Reynolds shear stress expressed in (12) is also shown in Fig. 2, and is almost constant throughout the entire Kármán number range analyzed herein. It has an average value of about  $6.5 \times 10^{-4}$ , which is well within the range of  $4 \times 10^{-4} - 8 \times 10^{-4}$  given for this coefficient by Gersten and Herwig [18]. The three parameters  $\kappa$ ,  $A$ , and  $\lambda$  can be reasonably well represented as functions of the reciprocal of the Kármán number, as depicted in the boxed formulas in Figs. 1 and 2.

Using the present approach, three calculated mean velocity profiles and their gradients are compared in Fig. 3 to the experimental data of Österlund [7]. The profiles are staggered vertically for clarity. Over the broad range of Reynolds numbers tested, the agreement between the experiment and the present theory is excellent throughout the entire inner layer of the boundary layer. The slight concave shape of the profiles in the usual log region results from the additive parameter  $D$  inside the argument of the logarithm. Consequently, this parameter also leads to a slight under-shoot in the slope of the profile.

Figure 4 shows a comparison of our mixing-length theory with data from two other experiments, Nockemann et al. [19] and De-Graaff [20]. The necessary parameters were calculated using the functions  $\kappa(\delta^+)$  and  $A(\delta^+)$  and the constant  $D$ , as depicted in Fig. 1. The agreement between the experimental data and the calculated mean velocity profiles is very good. Note that the depicted experimental profiles were not used to determine those three pa-

rameters, which earlier were extracted from the independent experiment of Österlund [7], thus attesting to the universality of the Reynolds-number dependency that we derived for each of the three parameters.

## Conclusions

A mixing-length approach applied to the generalized logarithmic law for high Kármán numbers has been presented. The new theory exhibits the correct  $y^{+3}$  dependence of the Reynolds shear stress in the vicinity of the wall. It has been found that all parameters appearing in the velocity profile and in the expression for the mixing length are Kármán-number dependent. Extending the generalized log law to the wall provides precise mean velocity profiles to be used for many practical applications over a broad range of Reynolds numbers.

## References

- [1] Wosnik, M., Castillo, L., and George, W. K., 2000, "A Theory for Turbulent Pipe and Channel Flows," *J. Fluid Mech.*, **421**, pp. 115–145.
- [2] Buschmann, M. H., and Gad-el-Hak, M., 2003, "Debate Concerning the Mean-Velocity Profile of a Turbulent Boundary Layer," *AIAA J.*, **41**, pp. 565–272.
- [3] Buschmann, M. H., and Gad-el-Hak, M., 2004, "Reynolds-Number-Dependent Scaling Law for Turbulent Boundary Layers," in *IUTAM Symp. on Reynolds Number Scaling in Turbulent Flow*, A. J. Smits, ed., pp. 5–10, Kluwer, Dordrecht, The Netherlands.
- [4] Buschmann, M. H., and Gad-el-Hak, M., 2003, "Generalized Logarithmic Law and Its Consequences," *AIAA J.*, **41**, pp. 40–48.
- [5] Lindgren, B., Österlund, J. M., and Johansson, A. V., 2002, "Evaluation of Scaling Laws Derived From Lie Group Symmetry Methods in Turbulent AIAA, Boundary Layers," *AIAA Paper No. 2002-1103*.
- [6] Oberlack, M., 2001, "Unified Approach for Symmetries in Plane Parallel Shear Flows," *J. Fluid Mech.*, **427**, pp. 299–328.
- [7] Österlund, J. M., 1999, "Experimental Studies of Zero-Pressure Gradient Turbulent Boundary-Layer Flow," Ph.D. thesis, Stockholm, Sweden.
- [8] Buschmann, M. H., and Gad-el-Hak, M., 2004, "Comments on 'Evaluating the Law of the Wall in Two-Dimensional Fully-Developed Turbulent Channel Flows'," *Phys. Fluids*, **17**, pp. 3507–3508.
- [9] Sreenivasan, K. R., and Sahay, A., 1997, "The Persistence of Viscous Effects in the Overlap Region, and the Mean Velocity in Turbulent Pipe and Channel Flows," *Self-Sustaining Mechanisms of Wall Turbulence*, R. L. Panton, ed., pp. 253–272, Computational Mechanics, Southampton, UK.
- [10] Pope, B. S., 2000, *Turbulent Flows*, Cambridge University Press, London.
- [11] Head, M. R., and Bandyopadhyay, P. R., 1981, "New Aspects of Turbulent Boundary Layer Structure," *J. Fluid Mech.*, **107**, pp. 297–338.
- [12] Granville, P. S., 1989, "A Modified van Driest Formula for the Mixing-Length of Turbulent Boundary Layers in Pressure Gradient," *ASME J. Fluids Eng.*, **111**, pp. 94–97.
- [13] Prandtl, L., 1925, "Bericht über Untersuchungen zur ausgebildeten Turbulenz," *Z. Angew. Math. Mech.*, **5**, pp. 136–139.
- [14] van Driest, E. R., 1956, "On Turbulent Flow Near a Wall," *J. Aeronaut. Sci.*, **23**, pp. 1007–1011.
- [15] Chapman, D. R., and Kuhn, G. D., 1986, "The Limiting Behaviour of Turbulence Near a Wall," *J. Fluid Mech.*, **170**, pp. 265–292.
- [16] Sreenivasan, K. R., 1989, "The Turbulent Boundary Layer," *Frontiers in Experimental Fluid Mechanics*, M. Gad-el-Hak, ed., pp. 159–209, Springer-Verlag, Berlin.
- [17] Gill, P. E., Murray, W., and Wright, M. H., 1981, *Practical Optimization*, (Section 4.7.3, The Levenberg–Maquardt Method, pp. 136–137), Academic Press, London.
- [18] Gersten, K., and Herwig, H., 1992, *Strömungsmechanik*, Verlag Vieweg, Wiesbaden, Germany.
- [19] Nockemann, M., Abstiens, R., Schober, M., Bruns, J., and Eckert, D., 1994, "Messungen in einer turbulenten Wandgrenzschicht bei großen Reynolds-Zahlen im Deutsch-Niederländischen Windkanal," *Messbericht, RWTH Aachen, Germany*.
- [20] DeGraaff, D. B., 1994, "Reynolds Number Scaling of the Turbulent Boundary Layer on a Flat Plate and on Swept and Unswept Bumps," Ph.D. thesis, Stanford University, Palo Alto, CA.

# Effect of Initial Temperature Profile on Recovery Factor Computations

**B. W. van Oudheusden**

Department of Aerospace Engineering, Delft University of Technology, P.O.Box 5058, 2600 GB Delft, The Netherlands

e-mail: B.W.vanOudheusden@LR.TUdelft.nl

## Background

In many aeronautical applications the interaction between fluid flow and a high-speed vehicle is of crucial practical relevance, in view of vehicle performance as well as mechanical and thermal loading of the structure. Viscous flow effects, such as frictional drag and thermodynamic heating, usually play a dominant role in high-speed flight. Surface heating due to frictional effects becomes a design concern for flight Mach numbers of two and above. The elevated temperature that is reached under thermal equilibrium conditions (adiabatic wall temperature  $T_{aw}$ ) is described by the recovery factor  $r$ , as [1–3]

$$T_{aw} = T_e + r \frac{u_e^2}{2c_p} \quad (1)$$

where  $u_e$  and  $T_e$  are the velocity and temperature outside the boundary layer and with the specific heat  $c_p$  constant. In the context of the incompressible flat plate boundary layer the recovery effect was investigated already in 1921 by Pohlhausen [4], who showed that  $r \approx \sqrt{\text{Pr}}$ , where  $\text{Pr}$  is the Prandtl number. Several studies have revealed that this applies also under more general conditions, i.e., with arbitrary pressure gradient [1–3]. A recent perturbation analysis by the present author confirmed that indeed the first-order pressure-gradient effect on the Prandtl number influence on  $r$  is absent, in the case of constant fluid properties (density, viscosity, and conductivity) [5].

However, at the conditions where thermal effects become significant the approximation of constant fluid properties is no longer accurate. A common engineering approach to predict the recovery factor in compressible flow is that it can still be computed with the above approximation, provided that fluid properties are evaluated at an appropriate “reference temperature” [1–3]. Van Driest [6] showed, however, that for the flat plate flow there is also a direct effect of the viscosity variation on the recovery factor, whereas in the case of compressible flow there is a non-negligible effect of the pressure gradient as well [7].

The above arguments indicate that accurate recovery temperature data in compressible flow cannot rely on theoretical predictions derived from incompressible flow conditions. Instead, one has to resort to accurate numerical solutions to the viscous flow equations (boundary layer or Navier-Stokes), to determine the actual surface temperature for the case under study [1–3]. Rather than analyzing the complete surface it may be sufficient and more convenient to analyze only critical details of the design, say at locations where strong nonequilibrium conditions occur. This suggests starting the (boundary layer) computation at some convenient upstream location with appropriate initial profiles of the required flow variables. The common procedure for this is to generate an initial velocity profile with an appropriate value of the momentum thickness, which models the integrated drag of the upstream surface. The initial temperature profile is then typically

derived from the velocity profile by invoking the Crocco-Busemann relation [1–3], modified for incomplete recovery

$$T = T_e + r \frac{(u_e^2 - u^2)}{2c_p} \quad (2)$$

and using an estimate for the recovery factor, say  $r \approx \sqrt{\text{Pr}}$ . Any inaccuracies in the initial velocity and temperature profiles are assumed to diffuse out when advancing the computation from the initial position downstream.

However, one may not be aware that the initial temperature profile given above introduces an error that may seriously affect the computation of the adiabatic wall temperature development. This is explained by realizing that in the absence of heat transfer, the boundary layer has to satisfy the following integral energy relation [1]:

$$\frac{d}{dx} \int_0^\delta \rho u (H - H_e) = 0 \quad (3)$$

where  $H$  is the total enthalpy. For an adiabatic wall boundary layer starting from uniform initial conditions, the integral in Eq. (3) should be zero, expressing that the (mass flux weighted) average value of the total enthalpy should be constant and equal to its free-stream value. This is a simple and direct consequence of the integral conservation of energy. This implies that when  $r < 1$ , hence, the recovery temperature being lower than the free stream total temperature, this needs to be balanced by another region in the flow where the total temperature is higher than that in the free stream [2]. For the temperature profile of Eq. (2), however, the total enthalpy in the boundary layer is everywhere smaller than  $H_e$ . So, although giving possibly a reasonable estimation of the recovery temperature initially, it introduces an energy defect in the boundary layer, which affects the ensuing computation of the recovery temperature development downstream. If this energy defect is assumed to be redistributed over the boundary layer in a similar way as the total enthalpy itself, it is likely that it will result in a decrease of the recovery temperature, which will only gradually vanish as the boundary layer grows and the energy defect is redistributed over an increasing mass flow. In the following section this effect of the initial temperature profile is illustrated and assessed by means of a simple numerical test case.

## Test Case: Flat-Plate Boundary Layer

The compressible flat-plate boundary layer is chosen as a test case. A linear relation between viscosity and temperature is assumed, for the attractive feature that it makes the problem independent of the Mach number, without losing the major aspects of compressibility. This allows the analysis to be focused on the effect of the initial temperature profile. In view of the self-similarity of the exact solution, the problem is conveniently formulated by applying a standard compressibility transformation [1–3]

$$f'(x, \eta) = u/u_e, \quad \theta(x, \eta) = (h - h_e)/\frac{1}{2}u_e^2, \quad \eta = \sqrt{\frac{u_e}{2\rho_e\mu_e x}} \int_0^y \rho dy \quad (4)$$

where a prime indicates a derivative with respect to the similarity coordinate  $\eta$ . Expressing the energy in terms of the enthalpy, rather than temperature, allows the results to be applicable to the case of variable specific heat. It may be noted that the recovery factor is equal to the value of  $\theta$  at the wall ( $\eta=0$ ). The equations to solve for velocity and enthalpy in the case of constant pressure, linear viscosity law, and constant Prandtl number are then given by, compare [1–3,5]

Contributed by the Fluids Engineering Division for publication in the JOURNAL OF FLUIDS ENGINEERING. Manuscript received by the Fluids Engineering Division April 14, 2004; revised manuscript received, November 8, 2004. Review conducted by M. Andrews.

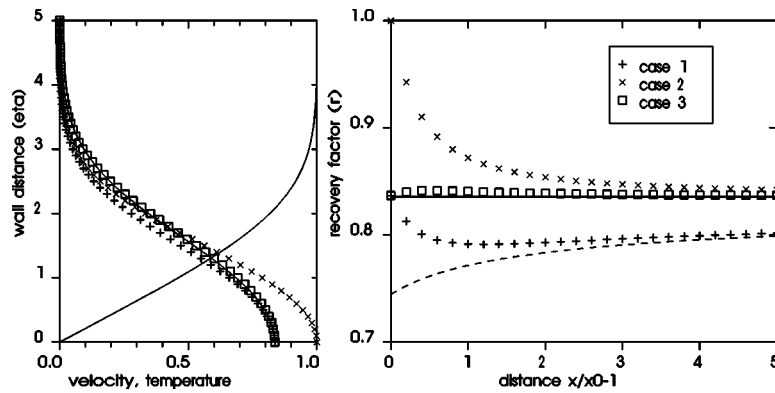


Fig. 1 Effect of initial temperature profile (left) on the computed recovery factor (right), for  $Pr=0.7$ , linear viscosity relation, and arbitrary Mach number. Solid lines: exact solution; symbols: numerical solutions; dashed line: approximate error decay, see text.

$$f''' + ff'' = 2x \left( f' \frac{\partial f'}{\partial x} - f'' \frac{\partial f}{\partial x} \right) \quad (5)$$

$$\frac{\theta'}{Pr} + f\theta' + 2f''^2 = 2x \left( f' \frac{\partial \theta}{\partial x} - \theta' \frac{\partial f}{\partial x} \right) \quad (6)$$

This reveals that all variable-property effects have been absorbed in the transformation, making the analysis and recovery results independent of Mach number. The equations were solved numerically with a finite-difference scheme, fourth- and second-order accurate in the wall-normal and streamwise direction, respectively. Numerical accuracy was assessed for the chosen settings, showing the error in the computed recovery factors to be below  $10^{-6}$  for self-similar solutions and below  $10^{-4}$  for nonsimilar cases. Computations were started at an initial station  $x=x_0$  with the exact velocity profile and using different algebraic expressions for the initial temperature profile:

- Case 1: The initial temperature profile is taken as  $\theta=r_0(1-f'^2)$ , which corresponds to the standard Crocco-Busemann relation, Eq. (2), estimating the recovery factor as  $r_0=\sqrt{Pr}$ .
- Case 2: The same as above, but now with  $r_0=1$ . Clearly the initial value of the recovery factor is incorrect, but no enthalpy defect is introduced.
- Case 3: The initial temperature profile is taken as  $\theta=r_0(1-f'^2)+2(1-r_0)ff''$ , which corresponds to a modified Crocco-Busemann relation that is the asymptotically correct first-order extension obtained from perturbation analysis [5] and that introduces no enthalpy defect. The estimate for  $r_0$  is the same as for case 1.

Results of computations are displayed in Fig. 1, which depicts the initial temperature profiles (left) and computed recovery factor development with streamwise distance (right), for  $Pr=0.7$ . The

Table 1 Relative errors in recovery computations (in percent)

$x/x_0-1$	case 1	case 2	case 3
0	0.11	19.7	0.11
1	-5.3	4.2	0.56
5	-4.1	0.7	0.14
10	-3.1	0.3	0.06
25	-2.1		
100	-1.1		

solid lines indicate the exact (self-similar) solution. Further quantitative assessment of the error with respect to the exact solution is given in Table 1.

The results show that for case 1 the enthalpy defect that is introduced indeed lowers the computed recovery value and introduces an appreciable error ( $>5\%$ ) that persists and decays only very gradually, notwithstanding that the initial temperature profile appears in reasonable agreement with the exact solution. The final decay behavior approximately follows the dashed line, which corresponds to a relative error of  $0.11(x/x_0)^{-1/2}$ , the inverse square-root behavior being in agreement with boundary layer growth according to laminar flow theory. Case 2, without enthalpy defect, although starting with much larger initial error on the recovery factor (as much as 20%), rapidly approaches the correct value. The error has dropped below 1% after five initial distances ( $x-x_0=5x_0$ ), whereas for case 1 this value is reached only after 100 initial distances. Finally, case 3 clearly gives the best results with a relative error never more than 0.7%.

## Conclusions

The effect of the initial temperature profile on the computation of compressible boundary layer development over an adiabatic wall was discussed and assessed numerically for the laminar flat-plate boundary layer. It was shown that an initial temperature profile that contains an integral total-enthalpy defect, as is the case for the classic Crocco-Busemann relation, gives rise to significant errors (up to 5% underestimation of  $r$  for the present case of  $Pr=0.7$ ) that decay only very gradually. In this sense, it is to be advised that the initial temperature profile should not contain such a defect. The use of an initial profile with constant total enthalpy may, therefore, be more acceptable because although the error is initially relatively large it decays rapidly and is therefore already after one initial length much better than the first choice. The best result was obtained with an extended Crocco-Busemann expression, which models the temperature-velocity relation more correctly. Errors are almost an order smaller than for case 2.

Although the present computation was performed for the laminar flow of a perfect gas, in view of the fundamental underlying mechanism it is to be expected that similar effects of the initial temperature profile occur under more general conditions, for example, with turbulence or real gas effects present.

## References

- [1] White, F. M., 1991, *Viscous Fluid Flow*, 2nd Edition, McGraw-Hill, New York.
- [2] Schetz, J. A., 1993, *Boundary Layer Analysis*, Prentice Hall, Englewood Cliffs, NJ.

- [3] Anderson, J. D., 1989, *Hypersonic and High Temperature Gas Dynamics*, McGraw-Hill, New York.
- [4] Pohlhausen, E., 1921, "Der Wärmeaustausch Zwischen Festen Körpern und Flüssigkeiten mit Kleiner Reibung und Kleiner Wärmeleitung." *Z. Angew. Math. Mech.*, **1**, pp. 115–121.
- [5] Van Oudheusden, B. W., 1997, "A Complete Crocco Integral for Two-Dimensional Laminar Boundary Layer Flow Over an Adiabatic Wall for Prandtl Numbers Near Unity," *J. Fluid Mech.*, **353**, pp. 313–330.
- [6] Van Driest, E. R., 1959, "Convective Heat Transfer in Gases," *High Speed Aerodynamics and Jet Propulsion, Volume V, Turbulent Flows and Heat Transfer*, C. C. Lin ed., Princeton University Press, Princeton, NJ. pp. 339–427.
- [7] Van Oudheusden, B. W., 2004, "Compressibility Effects on the Extended Crocco Relation and the Thermal Recovery Factor in Laminar Boundary Layer Flow," *ASME J. Fluids Eng.*, **126**, pp. 32–41.

# Measurements in the Transition Region of a Turbine Blade Profile Under Compressible Conditions

E. J. Walsh

M. R. D. Davies

Stokes Research Institute, Department of Mechanical & Aeronautical Engineering, University of Limerick, Plassey Technological Park, Limerick, Ireland

## Introduction

The transition region plays a critical role in the design of turbine blades, as it is accompanied by higher losses [1] and higher heat transfer rates [2]. Most of the transition onset and length correlations have been developed from incompressible measurements with only a limited number of investigators addressing the effect of Mach number. Narasimha [3] investigates the  $Re_{\theta(ST)}$  and concludes that it increases with Mach number; thereby delaying transition onset. In contrast, Schook et al. [4] found the  $Re_{\theta(ST)}$  from compressible measurements to be consistently lower than that correlated by Mayle [5] for the incompressible range. Thus the experimental evidence is contradictory.

Dey and Narasimha [6] suggest a variation in the spot formation rate with no change up to a Mach number of 2, which would suggest that the incompressible correlations could be used when predicting the transition length for the Mach numbers of turbomachinery. In contrast, Clark [7] found a significant decrease in the spot-spreading angle for Mach numbers  $< 1$ . This combined with the data of Simon [8] implies a change in the transition length. Again, the data are conflicting. Boyle and Simon [9] implemented the model of Simon [8] in a prediction code and found the resultant agreement with measurement to improve substantially from that of neglecting Mach number effects.

This work aims to provide an additional set of experimental data to help resolve the contradicting evidence through an experimental investigation on the suction surface of a linear transonic turbine cascade. By adapting the incompressible correlations in the literature to account for the effect of Mach number reasonable agreement with the current measurements is found.

## Experimental Facility

The transonic facility, shown in Fig. 1, is an open circuit, blow-down wind tunnel that operates from a reservoir of compressed air, with its operation and control system described in detail by Davies and Breathnach [10]. The working section is fitted with a linear cascade consisting of eight blades representing the midspan of the turbine blade designed by Santoriello et al. [11]. Steady-state conditions are achieved for approximately 0.6 s in an experimental run, during which time a measurement window is available. From hot-wire measurements upstream of the cascade Walsh [12] found the turbulence intensity to be 3.5%. The integral length scale was calculated from a single hot-wire measurement by applying the method of Roach [13]. This is achieved through the use of

$$\Lambda_x = U \int_0^{\infty} R(t) dt \quad (1)$$

where  $R(t)$  is the autocorrelation function. From Roach [13] the micro length scale equation is given by

$$\lambda_x = U \sqrt{\frac{-2}{(\partial^2 R(t)/dt^2)_{t=0}}} \quad (2)$$

Following the technique of Butler et al. [14] the first two temporal terms of the autocorrelation are used to approximate the second derivative. The second derivative in Eq. (2) may be determined to be equal to  $2[R(\Delta t) - 2]/\Delta t^2$  from a finite-difference method by knowing that the autocorrelation function is one when time equals zero and also knowing that the function is symmetric about time zero. The resultant values of the integral and micro length scales for this work were 15.5 and 7.2 mm, respectively. It should, however, be noted that the sampling frequency did not satisfy the criterion set forth by Roach [13] for the determination of the micro length scale and thus this value should only be used with caution. The other variable parameters of the test cases considered in the experimental investigation are summarised in Table 1, along with the inferred transition onset locations.

## Experimental Techniques and Data Acquisition

The transition region was measured by utilizing hot film anemometry, the full details of which are given by Walsh [12]. The cascade was instrumented with an array of Senflex nickel heated hot film sensors at the midspan on the suction surface of the central blade, with a spacing of 5 mm between each measuring element. This distance corresponded to increments of 10% SSL. The hot film sensors were operated in constant temperature mode at an over heat temperature of 110 °C. After sampling at 50 kHz for a period of 0.2 s, the skew function was applied to the raw hot film voltage to determine the transition region. Figure 2, taken from Walsh [12], shows a typical set of measurements obtained from the hot films on the suction surface of the linear transonic cascade. By applying the hot film interpretation technique of Hodson et al. [15] transition is seen to have commenced by 55% SSL and is completed by 75% SSL.

To determine the boundary layer edge Mach number distribution for the compressible test cases, pressure measurements were obtained in the settling chamber and at a number of locations on the suction surface. Owing to the small chord length of the transonic blade profile the number of pressure measurements on the suction surface was insufficient to determine the entire Mach

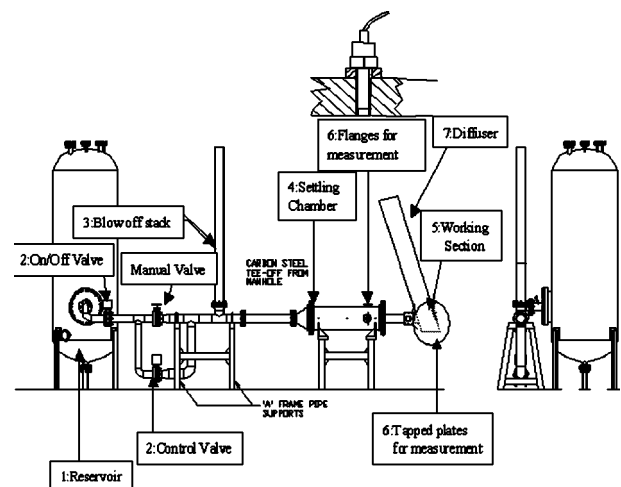


Fig. 1 The transonic blow-down wind tunnel facility utilized in this investigation

Contributed by the Fluids Engineering Division for publication in the JOURNAL OF FLUIDS ENGINEERING. Manuscript received by the Fluids Engineering Division November 22, 2004; revised manuscript received November 22, 2004. Review conducted by W. Copenhaver.

**Table 1 Summary of examined test cases**

Case number	Re <sub>c</sub> number at inlet *10 <sup>-3</sup> , measured	Mach number at outlet, measured	Transition onset %SSL, inferred
Test 1	163	0.37	47
Test 2	283	0.61	46
Test 3	369	0.74	39
Test 4	382	0.79	33
Test 5	418	0.86	31
Test 6	452	0.91	29
Test 7	489	0.97	28
Test 8	514	1	27
Test 9	551	1.06	26

number distribution. Thus inviscid calculations, using FLUENT 5, were performed for all test conditions to complete the Mach number distribution on the suction surface. The agreement between the predictions and measurements was found to be reasonably good and are used in this analysis; a comparison is shown in Fig. 3. Further details may be found in Walsh [12].

**Transition Region Parameters**

Numerous techniques have been developed over the years to reduce the probability of making an incorrect turbulent/nonturbulent decision from measurements in transitional flows. For the present work the technique employed is similar to that of Clark [7], which was based on a technique described by Hedley and Keffer [16] in a detailed review on the subject. Figure 4 illustrates the resultant indicator function as obtained from one set of hot film data. The top plot shows a portion of the raw hot film voltage. The second plot illustrates the normalized detector function, which is applied to emphasize the high-frequency components, which, as noted by Keller and Wang [17], is equivalent to conducting a digital high pass filter, and is calculated from

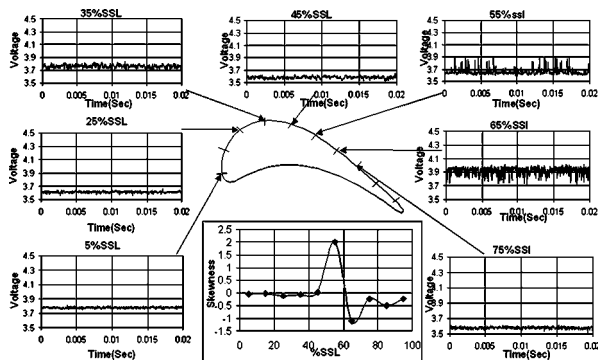
$$D_i = m \dot{V}'_i \tag{3}$$

where the relative magnitude of the signal *m* and the first derivate of the instantaneous voltage  $\dot{V}'$  are given, respectively, by

$$m = \frac{\dot{V}'_i - \dot{V}'_{\min}}{\dot{V}'_{\max} - \dot{V}'_{\min}}$$

$$\dot{V}' = \frac{\dot{V}'_{i+1} - \dot{V}'_{i-1}}{2h}$$

The probability of making an incorrect turbulent/nonturbulent decision is further reduced by smoothing or short-term integrating



**Fig. 2 Measured hot film signals and skew distribution showing the transition region along the suction surface of the linear transonic cascade with an inlet Re<sub>c</sub> and exit Mach numbers of 283 k and 0.61, respectively**

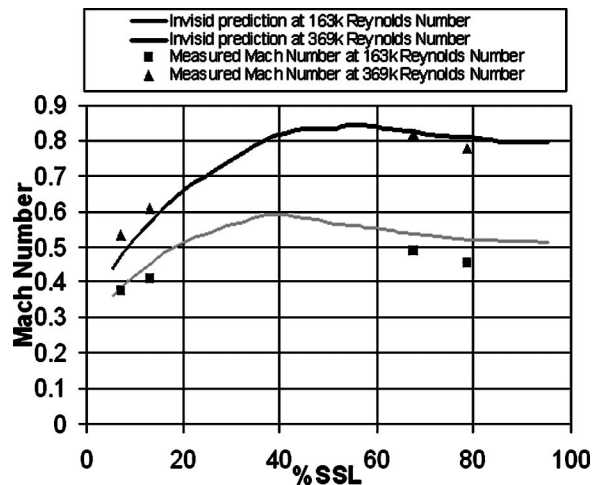
the detection function, the result of which is the criterion function as shown in the third plot of Fig. 4. This is achieved by applying the following equation to the detector function:

$$Cr_i = \frac{h^2}{1 + (\tau_s/h)} \sum_{j=i-(\tau_s/2h)}^{j=i+(\tau_s/2h)} D_j$$

Finally, a threshold level is set, with the first approximation of this value obtained from the “dual slope” method of Kuan and Wang [18] and refined using the judgment of the authors. Such judgment was particularly necessary for the high intermittency measurements. The result of this process is shown in the bottom plot of Fig. 4 as the indicator function, which was ultimately used to determine the intermittency at the hot film locations. When the indicator function is high the flow is taken to be turbulent and when it is low the flow is taken to be laminar. Thus, time averaging the indicator function over the entire sampling period results in an intermittency of 28% for the data of Fig. 4.

**Experimental Measurements**

Figure 5 shows the resultant data obtained from the hot film sensors, with the predicted acceleration parameter at transition onset also displayed. The results shown in the bottom plot of Fig. 5 are for all the choked flow measurements, Re<sub>c</sub> above 369 k (tests 3–9 from Table 1), and for the lowest Re<sub>c</sub> number of 163 k (test 1 from Table 1) as indicated on the plot. For the Re<sub>c</sub> of 163 k the inlet Mach number was ~0.2. Interestingly, above a Re<sub>c</sub> number of 369 k all the data points fall on a single linear curve fit, while below this Re<sub>c</sub> number a distinct shift in both the slope and the intersection of the data points with the x-axis is found. This is as expected since the pressure gradient parameter changes only



**Fig. 3 Comparisons between measured and predicted Mach number**

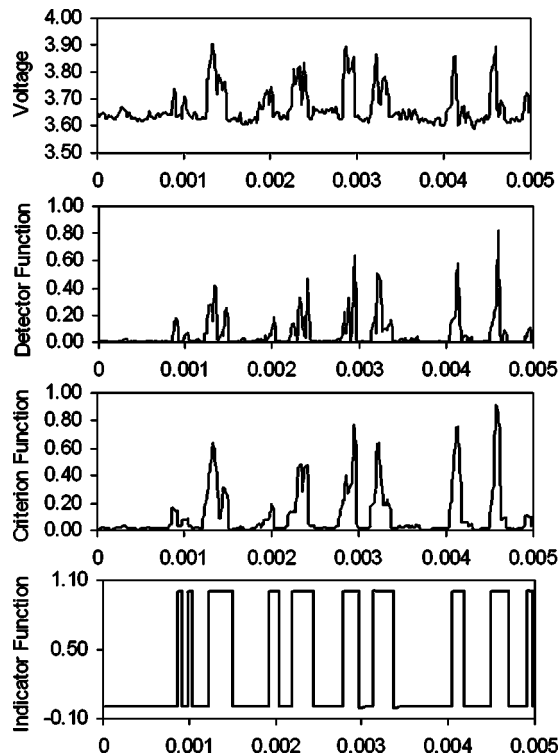


Fig. 4 Method to determine the intermittency from the hot film measurements. Raw voltage was captured from 55% suction surface length of the linear transonic cascade with an inlet  $Re_c$  and exit Mach numbers of 283 k and 0.61, respectively; fulltime trace shown in Fig. 2.

slightly after the flow has choked, as shown in the middle plot of Fig. 5. Therefore the  $Re_x$  value at transition onset would also be expected to remain constant as the turbulence intensity remains unchanged. The data indicates no evidence of a subtransition process.

The value of  $n\sigma$  is found from the square of the slope from a linear fit of  $F(\gamma)$  after Narasimha [3]. A distinct reduction in  $n\sigma$  is evident between the choked flow Mach number cases and the low Mach number case. This may not be explained singularly by a Mach number effect, as the change in pressure gradient at transition onset is most likely playing a substantial role. Data on the behavior of  $n\sigma$  in favorable pressure gradients remains scarce and thus comparisons with the literature is attempted but should be treated with caution. Mayle [5] provides a plot of spot production rate normalized on the value of flat plate flow,  $n\sigma = 1.5 \times 10^{-11} Tu^{7/4}$ , over a range of acceleration parameters where it is noted that the turbulence intensity plays a large role in adverse pressure gradients but is less critical in favorable pressure gradients. Applying an inlet turbulence intensity of 3.5% and using the correlation of Steelant and Dick [19], which is a best fit of the plot of Mayle [5], gives predicted  $n\sigma$  values of  $4.06 \times 10^{-10}$  and  $2.46 \times 10^{-11}$  for the low Mach number flow and the choked compressible flows, respectively. Adapting the correlation as suggested by Narasimha [3] to account for the effect of Mach num-

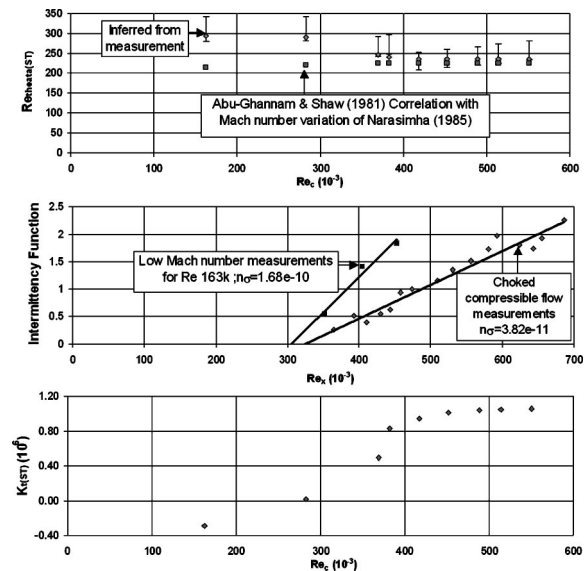


Fig. 5 Measured transition region parameters: (top)  $Re_{\theta}$  at transition onset, (middle) acceleration parameter at transition onset and (bottom) spot formation rate.

ber,  $n\sigma$  proportional to  $(1 + 0.38 M^{0.6})^{-1.5}$ , results in predicted  $n\sigma$  values of  $2.86 \times 10^{-10}$  and  $1.35 \times 10^{-11}$ , respectively. This adaptation results in an improved prediction of the low Mach number case, but an increase in the deviation between measurement and prediction for the choked flow case, where the data agrees reasonably well with the incompressible measurements found in Mayle [5]. A possible hypothesis to explain this may be that in favorable pressure gradients not only is the spot formation rate weakly dependent on the turbulence intensity as shown by Mayle [5], but it may also be weakly dependent on the Mach number. Thus making spot formation rate predictions dependent only on the acceleration parameter in favorable pressure gradient flows. Such a hypothesis requires a detailed examination before general use.

The location of transition onset was determined by the intersection of the  $F(\gamma)$  distribution with the  $x$ -axis in accordance with Narasimha [3]. This gives the location of transition onset in terms of  $Re_x$ . The first point to note is that the  $Re_{x(ST)}$  decreases for the lower inlet Mach number when compared to the choked compressible flow measurements. Thus indicating a delay in transition onset. This delay may not be solely a Mach number effect as the pressure gradient is varying. By using the transition onset location found from the intermittency measurements and the predictions of the Mach number distribution, the  $Re_{\theta(ST)}$  may be calculated by using the approximate solution for compressible laminar boundary layers due to Gruschwitz [20]. The top plot of Fig. 5 shows the resultant  $Re_{\theta(ST)}$  data with error bars applied representing the locations of the hot films before and after transition onset and completion. Also shown in this figure is the predicted  $Re_{\theta(ST)}$  using the incompressible transition onset model of Abu Ghannam and Shaw [21], with the inlet turbulence level applied, adapted to include the Mach number variation of Narasimha [3]. These models are given as

$$\left. \begin{aligned} Re_{\theta(M=0)} &= 163 + \exp \left[ F(A) - \left( \frac{F(A)}{6.91} Tu \right) \right] \\ F(A) &= 6.91 + 12.75\lambda_{\theta} + 63.64\lambda_{\theta}^2 \text{ for } \lambda_{\theta} < 0 \\ F(A) &= 6.91 + 2.48\lambda_{\theta} - 12.27\lambda_{\theta}^2 \text{ for } \lambda_{\theta} > 0 \end{aligned} \right\} \text{ AbuGhannam and Shaw [21]}$$



Good agreement is found for all the choked flow calculations. The lower  $\text{Re}_c$  numbers addressed do not show such good agreement. This implies that the correction factor for Mach number effect on  $\text{Re}_{\theta(ST)}$  may need some modification to distinguish between favorable and adverse pressure gradients just as in the transition model of Abu-Ghannam and Shaw [21] for incompressible flows. From this novel set of data it may be concluded that the effect of Mach number on the transition region needs further work before prediction methods can be used reliably. The current data set being a contribution to this work.

## Conclusions

- All the intermittency measurements in the choked flow experiments were found to fall on a linear  $F(\gamma)$  line for the current data set. This interesting result would need further validation before its widespread use was feasible.
- The introduction of correlations to include the effect of Mach number for transition onset, in general, resulted in better agreement with the measurements. Again, further experimental evidence is needed under a variation of conditions to fully resolve this issue.

## Nomenclature

$F(\gamma)$	= intermittency function (–)
$K_t$	= acceleration parameter, $(v/U_e^2)/(dU_e/dx)$
$M$	= mach number,
$\text{Re}_c$	= inlet Reynolds number, $U_i c/v$
$\text{Re}_x$	= local Reynolds number, $U_e x/v$
$\text{Re}_\theta$	= momentum thickness Reynolds number, $U_e \theta/v$
SSL	= suction surface length, m
$Tu$	= percentage turbulence intensity, %
$c$	= chord length, m
$h$	= sampling period
$n$	= dimensionless spot formation rate (–)
$T$	= time
$U$	= mean velocity, m/s
$V$	= hot film voltage, V
$X$	= curvilinear streamwise coordinate, m

## Greek

$\Lambda_x$	= integral length scale, m
$\gamma$	= intermittency, (–)
$\theta$	= momentum thickness, m
$\lambda_\theta$	= pressure gradient parameter, $(\theta^2/v)/(dU_e/dx)$
$\lambda_x$	= micro length scale m
$\sigma$	= spot propagation parameter (–)
$\tau_s$	= smoothing period
$\nu$	= kinematic viscosity, $\text{m}^2/\text{s}$

## Suffices

$( )_{ST}$	= start of transition
------------	-----------------------

$( )'$	= fluctuating measurement
$( )_c$	= chord length
$( )_e$	= boundary layer edge conditions
$( )_i$	= inlet conditions

## References

- [1] Denton, J. D., 1993, "Loss Mechanisms in Turbomachines," *ASME J. Turbomach.*, **115**, pp. 621–656.
- [2] Kim, J., Simon, T. W., and Kestoras, M., 1994, "Fluid Mechanics and Heat Transfer Measurements in Transitional Boundary Layers Conditionally Sampled on Intermittency," *ASME J. Turbomach.*, **116**, pp. 415–416.
- [3] Narasimha, R., 1985, "The Laminar Turbulent Transition Zone in the Boundary Layer," *Prog. Aerosp. Sci.*, **22**, pp. 29–80.
- [4] Schook, R., de Lange, H. C., van Steenhoven, A. A., 1998, "Effects of Compressibility and Turbulence Level on Bypass Transition," *ASME Congress and Exhibition*, ASME Paper No. 98-GT-286.
- [5] Mayle, R. E., 1991, "The Role of Laminar Turbulent Transition in Gas Turbine Engines," *ASME J. Turbomach.*, **113**, pp. 509–537.
- [6] Dey, J., and Narasimha, R., 1985, "Spot Formation Rates in High Speed Flows," Report 85 FM 11, Dept. Aero. Eng., Indian Inst. Science.
- [7] Clark, J. P., 1993, "A Study of Turbulent Spot Propagation in Turbine Representative Flows," Ph.D. thesis St. Catherine's College, University of Oxford, UK.
- [8] Simon, F. F., 1995, "The Use of Transition Region Characteristics to Improve the Numerical Simulation of Heat Transfer in Bypass Transitional Flows," *Int. J. Rotating Mach.*, **2**, pp. 93–102.
- [9] Boyle, R. J., and Simon, F. F., 1999 "Mach Number Effects on Turbine Blade Transition Length Prediction," *ASME J. Turbomach.*, **121**(4), pp. 694–702.
- [10] Davies, M. R. D., and Breathnach, E., 2002, "Operation and Preliminary Measurements From a New Transonic Wind Tunnel," *Proc. of XVth Bi-annual Symposium on Measuring Techniques in Transonic and Supersonic Flows in Cascades and Turbomachines*, September 21–22, Florence, Italy.
- [11] Santoriello, G., Colella, A., and Colantuoni, S., 1993, "Investigation of Aerodynamics and Cooling of Advanced Engine Turbine Components: Rotor Blade Aerodynamic Design," *Brite/Euram Area 3 Aeronautics Technical Report*, AER2-CT92-0044 IACA Package A.
- [12] Walsh, E., 2002, "The Measurement, Prediction and Minimization of Viscous Entropy Generation in Transitional Boundary Layers," Ph.D. thesis, Mechanical and Aeronautical Department, University of Limerick, Ireland.
- [13] Roach, P. E., 1987, "The Generation of Nearly Isotropic Turbulence by Means of Grids," *Int. J. Heat Fluid Flow*, **8**, pp. 82–91.
- [14] Butler, R. J., Byerley, A. R., VanTreuren, K., and Baughn, J. W., 2001, "The Effect of Turbulence Intensity and Length Scale on Low-Pressure Turbine Blade Aerodynamics," *Int. J. Heat Fluid Flow*, **22**, pp. 123–133.
- [15] Hodson, H. P., Huntsman, I., and Steele, A. B., 1994, "An Investigation of Boundary Layer Development in a Multistage LP Turbine," *ASME J. Turbomach.*, **116**, pp. 375–383.
- [16] Headley, T. B., and Keffer, J. F., 1974, "Turbulent/Non-Turbulent Decisions in an Intermittent Flow," *J. Fluid Mech.*, **64**(4), pp. 625–644.
- [17] Keller, F. J., and Wang, T., 1995, "Effects of Criterion Functions on Intermittency in Heated Transitional Boundary Layers With and Without Streamwise Acceleration," *ASME J. Turbomach.*, **117**, pp. 154–165.
- [18] Kuan, C. L., and Wang, T., 1990, "Investigation of the Intermittent Behavior of a Transitional Boundary Layer Using a Conditional Averaging Technique," *Exp. Therm. Fluid Sci.*, **3**, pp. 157–170.
- [19] Steelant, J., and Dick, E., 1996, "Modelling of Bypass Transition With Conditioned Navier-Stokes Equations Coupled to an Intermittency Transport Equation," *Int. J. Numer. Methods Fluids*, **23**, pp. 193–220.
- [20] Gruschwitz, E., 1950, "Calcul Approche de la Couche Limite Laminaire en Ecoulement Compressible Sur Une Paroi Non-Conductrice de la Chaleur," ONERA, Publication No. 47, Paris.
- [21] Abu-Ghannam, B. J., and Shaw, R., 1980, "Natural Transition of Boundary Layers—The Effect of Turbulence, Pressure Gradient, and Flow History," *J. Mech. Eng.*, **22**(5), 213–228.

**Erratum: “A Simplified Model for Determining Interfacial Position in  
Convergent Microchannel Flows”**

**[Journal of Fluids Engineering, 2004, 126(5), pp. 758–767]**

**T. R. Harris**

**D. L. Hitt**

**N. Macken**

---

The name of the lead author, T. R. Harris, was omitted from the paper.